PREFACE

The 2023 Geophysical Fluid Dynamics Summer Study Program started on June 20th on the topic of GFD on other worlds. The principal lectures were given by Professors Heather Knutson (Caltech) and Geoff Vallis (University of Exeter). Heather's lectures described what we can find out about GFD on other worlds from observations of extrasolar planets, and reminded everyone of the power of well-designed blackboard talks in engaging their audience. Geoff's lectures covered a number of 'hot' theoretical topics on the atmospheric dynamics of our solar system planets as well as giant and terrestrial exoplanets. We also had two tutorials: a fun "DYNamics" demonstration of properties and instabilities of rotating fluids by Jonathan Aurnou (UCLA) and the now yearly "Dedalus tutorial" by Keaton Burns (MIT).

Pascale Garaud (UC Santa Cruz) and Tiffany Shaw (University of Chicago) were co-directors. They welcomed many long- and short-term visitors, and the atmosphere at Walsh Cottage was finally back to its pre-COVID self. Almost all of the long-term visitors were able to advise fellows, either individually, or in group.

The fellows this year were:

Nathan Magnan, University of Cambridge
Yifeng Mao, University of Colorado Boulder
Hao Fu, Stanford University
Quentin Nicolas, University of California Berkeley
Arefe Ghazi Nezami, University of Texas Austin
Quentin Kriaa, Aix-Marseille University
Nimrod Gavriel, Weizmann Institute of Science
Ellie Ong, University of New South Wales
Yaoxuan Zeng, University of Chicago
Deborah Cotton, University of Oxford

As usual, laboratory experiments were facilitated by able support from Anders Jensen. Janet Fields and Julie Hildebrandt made sure that the administrative side of the summer ran smoothly.

This year's Distinguished Scholar Award was presented to Alexis Kaminski, for her academic excellence and dedication to mentoring the next generation of fellows. The 2023 Sears Public Lecture was delivered by Professor Sara Seager, of the Massachusetts Institute of Technology, on ``Planetary Atmospheres, and the search for signs of life beyond Earth''.

For the first time perhaps in the history of GFD, the staff vs. fellows softball game was replaced by a staff vs. fellows volleyball game. Only the future will tell whether this trend will catch on.

Table of Contents

Preface i
2023 GFD Participants iv
2023 GFD Principal Lecturers vi
2023 Group Photo vii
Lecture Schedule viii

Principal Lectures

Lecture 1: Exoplanet Demographics *(Heather Knutson)* 1
Lecture 2: Techniques for Characterization, Bulk and Atmospheric Compositions *(Heather Knutson)* 10
Lecture 3: Structure and Circulation of Terrestrial Planets: Atmospheric Structure and Circulation *(Geoffrey Vallis)* 21
Lecture 4: Circulation of Tidally Locked Planets *(Geoffrey Vallis)* 36
Lecture 5: Observations of Atmospheric Circulation on Short-period Gas Giants *(Heather Knutson)* 51
Lecture 6: Cold Giants: Jets, Deep Convection and Shallow Weather *(Geoffrey Vallis)* 59
Lecture 7: Atmospheric Characterization of Young, Hot, Gas Giant Planets and Brown Dwarfs *(Heather Knutson)* 71
Lecture 8: Atmospheric Characterization of Terrestrial Planets *(Heather Knutson)* 83
Lecture 9: Exo-Oceans and Icy Moons *(Geoffrey Vallis)* 93
Lecture 10: Steam Atmospheres and Runaway Greenhouse *(Geoffrey Vallis)* 101

Fellows Reports:

Convection in the Ice Shells of Icy Moons
Nathan Magnan, University of Cambridge 113
Chemical Transport by Waves in Stars
Yifeng Mao, University of Colorado, Boulder 145

Boiling Stratified Flow: A Lab Analog of Quasi-equilibrium Moist Convection
Hao Fu, Stanford University 172
Simple Models of Superrotation in Planetary Atmospheres
Quentin Nicolas, University of California, Berkeley 203
Stratified Turbulence: A Black Hole for Internal Waves?
Arefe Ghazi Nezami, University of Texas, Austin 231
Transport of Microplastics in Turbidity Currents
Quentin Kriaa, Aix-Marseille Université 249
Can AI-based Climate Models Learn Rare, Extreme Weather Events?
Nimrod Gavriel, Weizmann Institute of Science 282
Asymmetries in Formation of Gulf Stream Warm Core Rings and Filaments
Ellie Ong, University of New South Wales 299
Jets on Gas Giants—A Tale of Two Forcings
Yaoxuan Zeng, University of Chicago 320
Into the Mix: How Biological Dynamics Affect the Turbulent Transport
Deborah Cotton, University of Oxford 351

2023 Participants

FELLOWS

Deborah Cotton	University of Oxford
Hao Fu	Stanford University
Nimrod Gavriel	Weizmann Institute of Science
Arefe Ghazi Nezami	University of Texas Austin
Quentin Kriaa	Aix-Marseille Université
Nathan Magnan	University of Cambridge
Yifeng Mao	University of Colorado Boulder
Quentin Nicolas	University of California Berkeley
Ellie Ong	University of New South Wales
Yaoxuan Zeng	University of Chicago

STAFF AND VISITORS

Jonathan Aurnou	University of California Los Angeles
Anthony Bonfils	Nordic Institute of Theoretical Physics
Keaton Burns	Massachusetts Institute of Technology
Elizabeth Carlson	University of Victoria
Colm-cille Caulfield	University of Cambridge
Claudia Cenedese	Woods Hole Oceanographic Institution
Gregory Chini	University of New Hampshire
Janggeun Choi	University of New Hampshire
Raffaele Ferrari	Massachusetts Institute of Technology
Glenn Flierl	Massachusetts Institute of Technology
Basile Gallet	CEA Saclay
Pascale Garaud	University of California Santa Cruz
David Goluskin	University of Victoria
Pedram Hassanzadeh	Rice University
Karl Helfrich	Woods Hole Oceanographic Institution
Eric Hester	University of California Los Angeles
Christopher Howland	University of Twente
Malte Jansen	University of Chicago
Blair Johnson	University of Texas Austin
Edward Johnson	University College London
Keith Julien	University of Colorado
Alexis Kaminski	University of California Berkeley
Wanying Kang	Massachusetts Institute of Technology
Yohai Kaspi	Weizmann Institute of Science

Heather Knutson	California Institute of Technology
Zhiming Kuang	Harvard University
Michael Le Bars	Institut de Recherche sur les Phenomenes Hors Equilibre
Daniel Lecoanet	Northwestern University
Adrien Lefauve	University of Cambridge
Detlef Lohse	University of Twente
James McElwaine	Durham University
Brett McKim	University of Exeter
Colin Meyer	Dartmouth College
Jonathan Mitchell	University of California Los Angeles
Philip Morrison	University of Texas Austin
Jeremy Parker	ECPS, EPFL
Joseph Pedlosky	Woods Hole Oceanographic Institution
Matthew Scase	University of Nottingham
Tiffany Shaw	University of Chicago
Nicole Shibley	Princeton University
Valentin Skoutnev	Columbia University
Andre Souza	Massachusetts Institute of Technology
Bruce Sutherland	University of Alberta
Barbara Turnbull	University of Nottingham
Geoffrey Vallis	University of Exeter
Claire Valva	New York University
Kasia Warburton	Dartmouth College
Nash Ward	University of Utah
Baole Wen	New York Institute of Technology
Jack Whitehead	Woods Hole Oceanographic Insitution
Beth Wingate	University of Exeter
Da Yang	University of California Davis

2023 Principal Lecturers

Heather Knutson

Geoffrey Vallis

2023 Geophysical Fluid Dynamics Summer School Participants

First Row (L-R): Hao Fu, Quentin Kriaa, Yaoxuan Zeng, Arefe Ghazi, Ellie Ong, Nimrod Gavriel, Nathan Magnan, Quentin Nicolas, Yifeng Mao, Deborah Cotton

Second Row (L-R): Greg Chini, Eric Hester, David Goluskin, Bruce Sutherland, Elizabeth Carlson, Keaton Burns, Jeremy Parker, Pascale Garaud, Joe Lacasce

Third Row: Tiffany Shaw, Anthony Bonfils, Colin Meyer, Xi Zhang, Yohai Kaspi, Glenn Flierl, Wanying Kang, Geoff Vallis, Malte Jansen, Jack Whitehead

Not in photo: Jonathan Aurnou, Colm-cille Caulfield, Claudia Cenedese, Jang-Geun Choi, Basile Gallet, Pedram Hassanzadeh, Karl Helfrich, Chris Howland, Blair Johnson, Ted Johnson, Keith Julien, Alexis Kaminski, Heather Knutson, Zhiming Kuang, Anuj Kumar, Michael LeBars, Daniel Lecoanet, Adrien LeFauve, Cheng Li, Detlef Lohse, Jim McElwaine, Jonathan Mitchell, Phil Morrison, Joe Pedlosky, Matthew Scase, Nicole Shibley, Valentin Skoutnev, Andre Souza, Barbara Turnbull, Zhan Wang, Kasia Warburton, Beth Wingate, Da Yang, Xi Zhang, Claire Valva, Brett McKim

Lecture Schedule

PRINCIPAL LECTURES

Tuesday, June 20

Exoplanet Demographics
Heather Knutson

Wednesday, June 21

Techniques for Characterization, Bulk and Atmospheric Compositions
Heather Knutson

Thursday, June 22

Terrestrial Planets: Atmospheric Structure and Circulation
Geoffrey Vallis

Friday, June 23

Circulation of Tidally Locked Planets
Geoffrey Vallis

Observations of Atmospheric Circulation on Short-period Gas Giants
Heather Knutson

Monday, June 26

Cold, Giant Planets: Jets, Deep Convection and Shallow Weather
Geoffrey Vallis

Tuesday, June 27

Atmospheric Characterization of Young, Hot, Gas Giant Planets and Brown Dwarfs
Heather Knutson

Wednesday, June 28

Atmospheric Characterization of Terrestrial Planets
Heather Knutson

Thursday, June 29

Exo-oceans and Icy Moons
Geoffrey Vallis

Friday, June 30

Steam Atmospheres and Runaway Greenhouse
Geoffrey Vallis

SEMINARS

Friday, June 23

Dedalus tutorial Keaton Burns, Massachusetts Institute of Technology

Monday, June 26

DIYnamics
Jonathan Aurnou, University of California, Los Angeles

Wednesday, June 28

Dedalus tutorial Keaton Burns, Massachusetts Institute of Technology

Monday, July 3

Integrating Physics, Data & Scientific ML to Better Understand and Model Climate Variability and Extremes
Pedram Hassanzadeh, Rice University

Wednesday, July 5

Atmospheric Dynamics of Giant Planets: Insights from the Juno Mission
Yohai Kaspi, Weizmann Institute of Science

Thursday, July 6

The Interplay between Ocean and Ice on Icy Satellites
Wanying Kang, Massachusetts Institute of Technology

Friday, July 7

Modeling Multiphase Matter
Eric Hester, University of California, Los Angeles

Weather Impact on Cooling the Giant Planets
Xi Zhang, University of California, Santa Cruz

Monday, July 10

Energetic Constraints for Ocean Dynamics on Icy Worlds
Malte Jansen, University of Chicago

Tuesday, July 11

Verifying Global Stability of Fluid Flows Despite Transient Growth of Energy
David Goluskin, University of Victoria

Wednesday, July 12

Kelvin-Helmholtz Instability Near Boundaries
Alexis Kaminski, University of California, Berkeley

Thursday, July 13

Insights into Turbulence: Modifying Old Techniques for New Understanding
Elizabeth Carlson, University of Victoria

Ghosts in Rayleigh Bénard Convection
Jeremy Parker, École Polytechnique Fédérale de Lausanne

Friday, July 14

A Mushy Source for the Geysers of Enceladus
Colin Meyer, Dartmouth College

Monday, July 17

Three-dimensional Structure of Buoyancy Transport by Ocean Baroclinic Turbulence
Basile Gallet, CEA Saclay

Tuesday, July 18

Transmission Spectroscopy of Exoplanet Atmospheres
Sara Seager, MIT

Wednesday, July 19

Simple Models of Clouds and Convection in the Solar System
Jonathan Mitchell, UCLA

Thursday, July 20

Shaken by Physics or Stirred by Machine? Modelling Stratified Mixing (with a Twist)
Colm-cille Caulfield, University of Cambridge

Entrainment in Plumes with Turbidity Currents
Jim McElwaine, University of Durham

Friday, July 21

Critical Balance in Anisotropic Wave Systems: Strongly Stratified Turbulence at Low Prandtl Number
Valentin Skoutnev, Columbia University

Monday, July 24

What the Ultimate Regime in Rayleigh-Bénard Convection and Radiatively Heated Melt Ponds Have in Common: Bistability and Subcritical Transitions
Detlef Lohse, University of Twente

Tuesday, July 25

Fluid Dynamics of Jupiter in the Lab: Deep Jets and Vortices
Michael LeBars, University of Aix-Marseille

Wednesday, July 26

The Stratified Inclined Duct (SID) Experiment: A Rich Paradigm for Stratified Turbulence
Adrien LeFauve, University of Cambridge

Thursday, July 27

The Lightness of Water Vapor and Climate Stability
Da Yang, University of California, Davis

Internal Wave Packet Tunneling through a Thermohaline Staircase
Bruce Sutherland, University of Alberta

Friday, July 28

Enhancement of Ice Melting in Isotropic Turbulence
Blair Johnson, University of Texas

Monday, July 31

Turbulence, Waves, and Stars
Daniel Lecoanet, Northwestern University

Tuesday, August 1

Curious Convection in Vertical Channels
Chris Howland, University of Twente

Wednesday, August 2

Rotationally Driven Kelvin-Helmholtz Instability
Matthew Scase/Barbara Turnbull, University of Nottingham

Thursday, August 3

What Sets the Vertical Profile of Stratification in the Deep Ocean?
Raffaele Ferrari, MIT

Experimental Numerical Methods for Navier-Stokes
Keaton Burns, MIT

Friday, August 4

Channelization of Subglacial Water Flow: Stability and Channel Distribution
Kasia Warburton, Dartmouth College

Monday, August 7

Ice-Ocean Interactions in the Solar System
Nicole Shibley, Princeton University

Tuesday, August 8

Linear Time-invariant Models of a Large Cumulus Ensemble and Convective Memory
Zhiming Kuang, Harvard University

Wednesday, August 9

Tilt! Non-hydrostatic Geostrophy
Joe Pedlosky, WHOI

Thursday, August 10

Fast Jet Stream Winds Get Faster Under Climate Change
Tiffany Shaw, University of Chicago

Friday, August 11

Jovian Jets and Vortices
Glenn Flierl, MIT

FELLOWS' PRESENTATIONS

Monday, August 21

Convection in the Ice Shells of Icy Moons
Nathan Magnan, University of Cambridge

Chemical Transport by Waves in Stars
Yifeng Mao, University of Colorado Boulder

Boiling Stratified Flow: A Lab Analog of Quasi-equilibrium Moist Convection
Hao Fu, Stanford University

Tuesday, August 22

Simple Models of Superrotation in Planetary Atmospheres
Quentin Nicolas, University of California, Berkeley

Stratified Turbulence: A Black Hole for Internal Waves?
Arefe Ghazi Nezami, University of Texas, Austin

Wednesday, August 23

Transport of Microplastics in Turbidity Currents
Quentin Kriaa, Aix-Marseille Université

Can AI-based Climate Models Learn Rare, Extreme Weather Events?
Nimrod Gavriel, Weizmann Institute of Science

Asymmetries in Formation of Gulf Stream Warm Core Rings and Filaments
Ellie Ong, University of New South Wales

Thursday, August 24

Jets on Gas Giants – A Tale of Two Forcings
Yaoxuan Zeng, University of Chicago

Into the Mix: How Biological Dynamics Affect Turbulent Transport
Deborah Cotton, University of Oxford

GFD 2023 Lecture 1: Exoplanet Demographics

Heather Knutson; notes by Yaoxuan Zeng and Deborah Cotton

January 31, 2024

Exoplanets are planets outside our solar system. Detecting exoplanets is a challenge due to the fact that we are trying to spot a dim planet next to a high luminosity star. The challenge is analogous to trying to spot a firefly by a spotlight in Hollywood, when you are taking measurements from New York City. Nevertheless, more than 10,000 exoplanets and exoplanet candidates have been found so far[1]. Here we introduce two major methods to detect exoplanets: the radial velocity method and the transit method, and the categories and occurrence rates of exoplanets.

1 Techniques for Detecting Exoplanets

1.1 Radial velocity (RV) method

If the star has a planet, they will orbit around their common center of mass (Fig. 1a). If their velocity has a radial component relative to us, this radial velocity will result in a Doppler shifting in their spectrum. By analyzing the time series of radial velocity of the star (it is hard to observe the planet), we can learn about the orbital period and mass of the planet. This is called the *radial velocity method* to detect exoplanets.

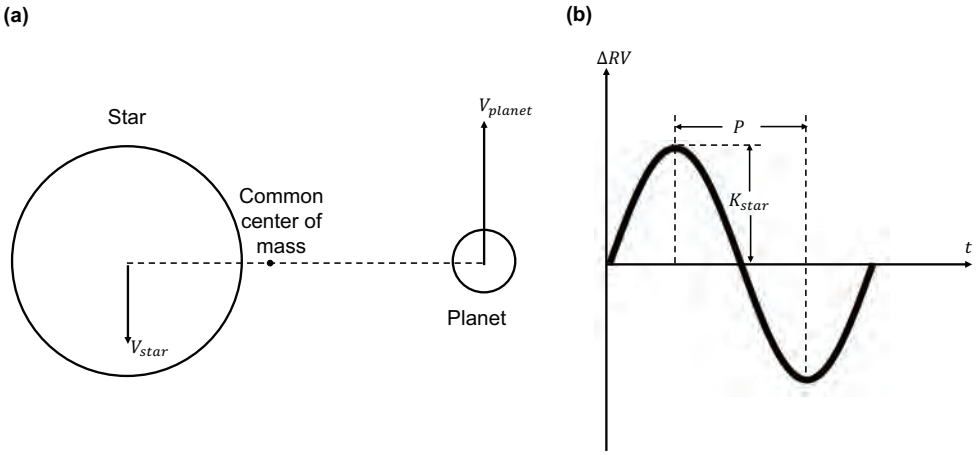

Figure 1: (a): sketch of the star-planet system. (b) sketch of the radial velocity variation (ΔRV) as a function of time. Notations can be found in the text.

[1]NASA Exoplanet Archive: https://exoplanetarchive.ipac.caltech.edu/

Here, we consider a simple case that there is only one planet in the planetary system[2], and the eccentricity of the orbit is zero (Fig. 1). Therefore, we can learn the orbital period of the planet from the period in the signal of radial velocity variation of the star. The amplitude of the variation of the star's radial velocity, K_{star}, is a function of the mass of the star, M_{star}, the mass of the planet, M_{planet}, and the orbital period, P. The distance between the star and the common center of mass, r, is

$$r = d\frac{M_{star}}{M_{star} + M_{planet}}, \tag{1}$$

where d is the distance between the star and the planet. The equations for the motion of the star can be written as,

$$M_{star}\left(\frac{2\pi}{P}\right)^2 r = \frac{GM_{star}M_{planet}}{d^2}, \tag{2}$$

$$V_{star} = \frac{2\pi r}{P}, \tag{3}$$

where V_{star} is the velocity of the star. If the orbital plane has an inclination angle i towards us ($i = 0$ means the plate directly facing us) there will be a radial velocity component of the star,

$$K_{star} = V_{star}\sin i. \tag{4}$$

By solving Eq. 1 to 4, and assuming that $M_{planet} \ll M_{star}$, we have the relationship

$$K_{star} \approx (2\pi G)^{1/3} M_{planet} M_{star}^{-2/3} P^{-1/3} \sin i \tag{5}$$

$$\approx 8.95 \text{ cm/s} \left(\frac{\mathrm{M_{planet}}}{\mathrm{M_{Earth}}}\right)\left(\frac{\mathrm{M_{star}}}{\mathrm{M_{Sun}}}\right)^{-2/3}\left(\frac{\mathrm{P}}{1\,\mathrm{yr}}\right)^{-1/3}\sin \mathrm{i}, \tag{6}$$

where M_{Earth} and M_{sun} are the mass of the Earth and the sun, respectively. Consequently, we can infer the planet's mass from the variation amplitude in the star's radial velocity. The threshold to detect the radial velocity variation is about 1 m/s. From Eq. 5 we learn that the radial velocity method is most sensitive to *massive* planets orbiting *close* to the star.

1.2 Transit method

When the planet passes in front of the star, the radiation of the star will be partially obscured, shown as a dip in the curve of solar flux as a function of time (Fig. 2). This is called *transit* and is currently the most effective way to detect exoplanets[3].

We can infer the radius of the planet based on the transit depth δ (decreasing amplitude of the radiation flux) with the relationship

$$\delta = \left(\frac{R_{planet}}{R_{star}}\right)^2, \tag{7}$$

[2]If there are more than one planet in the system, we can separate the signal for each planet as long as the planets' gravitational fields are not affecting each other's orbit.

[3]When the planet passes behind the star, the planet's radiation will be obscured by the star and form another dip, called *occultation* (Fig. 2). This signal is harder to detect.

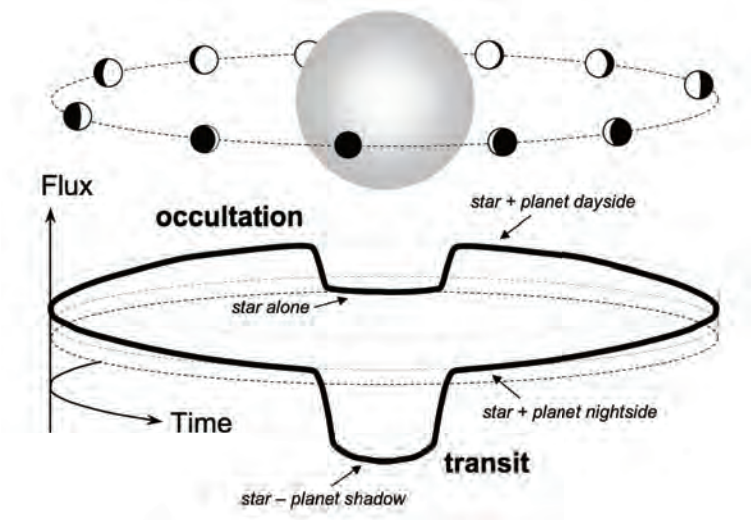

Figure 2: Sketch of transit method (taken from Fig. 1 in [5]).

where R_{planet} is the radius of the planet and R_{star} is the radius of the star[4]. The probability of transit p_{tr} is [5]

$$p_{tr} \approx \frac{R_{star}}{a} = 0.005 \left(\frac{R_{star}}{R_{sun}}\right) \left(\frac{a}{1\text{AU}}\right)^{-1}, \tag{8}$$

where a is the semi-major axis of the planet's orbit and R_{sun} is the radius of the sun. As a result, similar to the radial velocity method, the transit method is most sensitive to planets that are close to the host star.

2 Locations of Detected Exoplanets

Among the 10,000+ confirmed exoplanets and exoplanet candidates, most of them are within a few hundreds of pc around the sun (for comparison, the sun is about 8 kpc from the center of the Milky Way, Fig. 3). This is because the two main methods to find exoplanets, the radial velocity method and the transit method, both require enough photons to be detected to distinguish the planet from noise and distant planetary systems are too dim to detect. One way to detect the distant exoplanets is the *gravitational microlensing method*, which uses the effect that the gravitational field of the planets will bend the light from the star.

3 Categories of Detected Exoplanets

We can use a mass-period diagram to delineate the current extrasolar planetary catalogue (Fig. 4). Exoplanets are broadly categorised into four different types:

- Hot Jupiters are planets with a mass close to or larger than the mass of Jupiter and with small orbital period, meaning they are located close to the star they are orbiting.

[4]With both radial velocity and transit method, we can get the mass the radius and hence the bulk density of the planet, from where we can infer the composition of the planet.

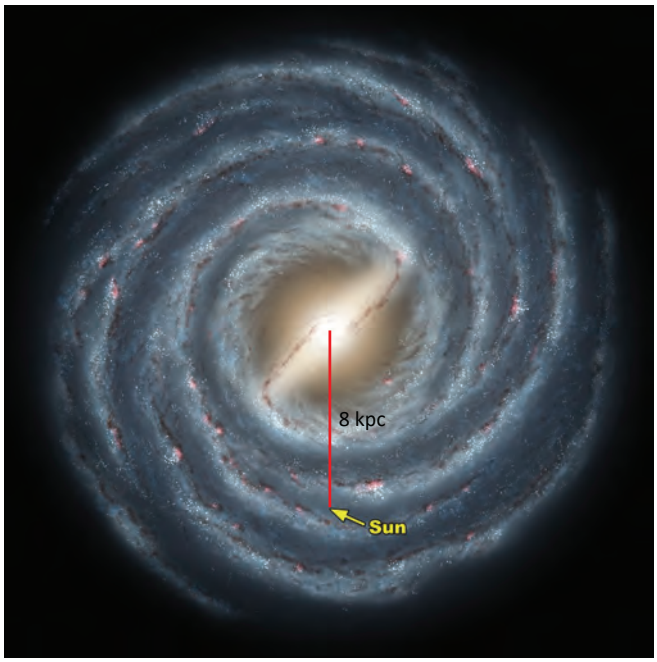

Figure 3: The Milky Way and the Sun. Figure credit: NASA/JPL-Caltech/R. Hurt (SSC)

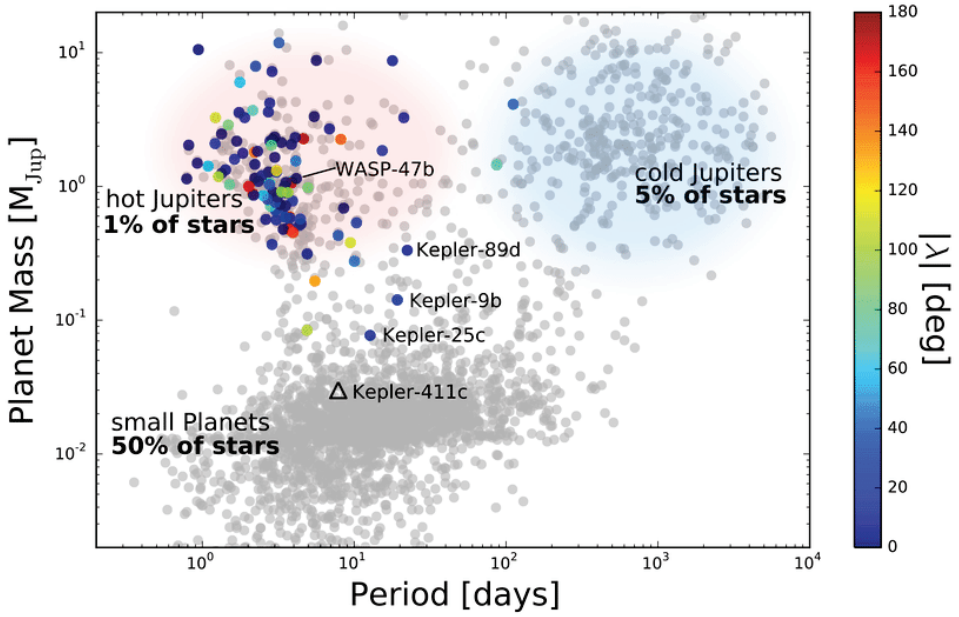

Figure 4: Categories of exoplanets. Exoplanets are split into giant planets (hot Jupiters and warm/cold Jupiters) and small planets (super-Earths and sub-Neptunes). λ refers to the spin orbit angle of the planet. The mass of each planet is plotted relative to the mass of Jupiter (M_J). The right bottom part of the diagram are small and distant planets that are unexplored. Taken from Fig. 5 in [4].

- Warm/cold Jupiters are planets with a mass close to or larger than the mass of Jupiter and with larger orbital period, meaning they are located further away from the star they are orbiting.
- The small planets are categorised either as super-Earths or as sub-Neptunes. They are planets with a significantly lower mass than that of Jupiter.
- For planets with a mass more than $\sim 13 M_J$, we categorise them as a Brown Dwarf and not a planet.

3.1 Super-Earths and Sub-Neptunes

Super-Earths and sub-Neptunes both have a rocky core. In sub-Neptunes the rocky core is surrounded by a gaseous envelope (Fig. 5). In sub-Neptunes, from measurements of outflows from young sun-like stars and from detecting atmospheric absorption, it is likely that this envelope is composed of hydrogen and helium gas. For sub-Neptunes orbiting around low mass stars there is potential for the gaseous envelope to be a water envelope. However, currently there is no confirmation that water worlds exist.

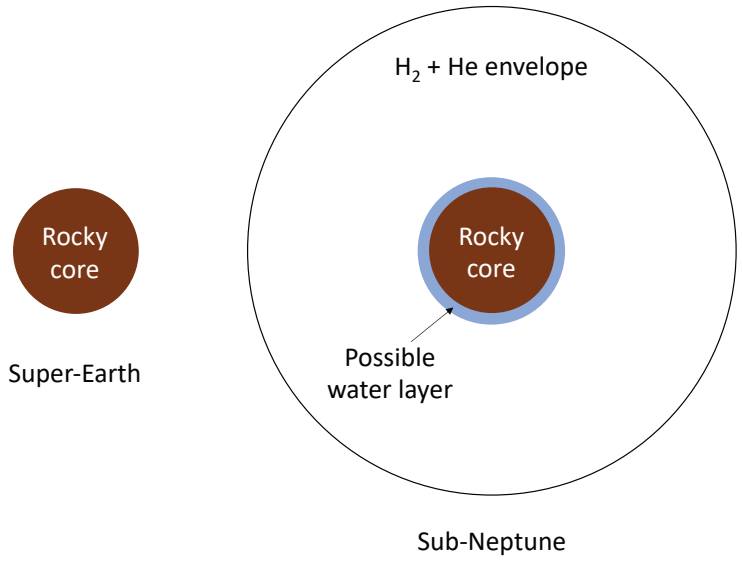

Figure 5: Sketch for the structure of the super-Earth and sub-Neptune.

3.1.1 Aside: on the formation of water worlds

For every planetary system we can define an ice line, where at closer radii, the water in the protoplanetary disk is in the gaseous state and at larger radii the water is in the solid state[5]. For sun-like stars, this line is very far from the star (1-2 AU); however, for smaller stars this line is closer in. Planets are usually formed in the inner disk, close to the host stars. For smaller stars, it is possible that the planet-forming region is outside the ice line, the planets are able to accumulate ice during its formation, and a water envelope may form above the rocky core. As the sub-Neptune migrates inward, the ice sublimates to create a gaseous, water atmosphere.

[5]The pressure of the planetary disk does not allow liquid water to exist.

3.2 Potentially "habitable planets"

For a planet to be habitable we need liquid water on the surface. Therefore, we are searching for roughly Earth-sized planets with Earth-like insolation rates. We define Earth-sized planets as planets with a radius of $0.7 - 1.5R_E$, where R_E is the radius of Earth. We choose an upper limit of $1.5R_E$ as, for planets with a radius higher than $1.5R_E$, the pressure and temperature in the atmosphere becomes too thick for liquid water to exist on the surface. The lower limit of $0.7R_E$, is partly determined by observational limitations and partly by the requirement that the planet must be of a sufficient size to hold its atmosphere.

4 Occurrence Rates

4.1 Giant planets

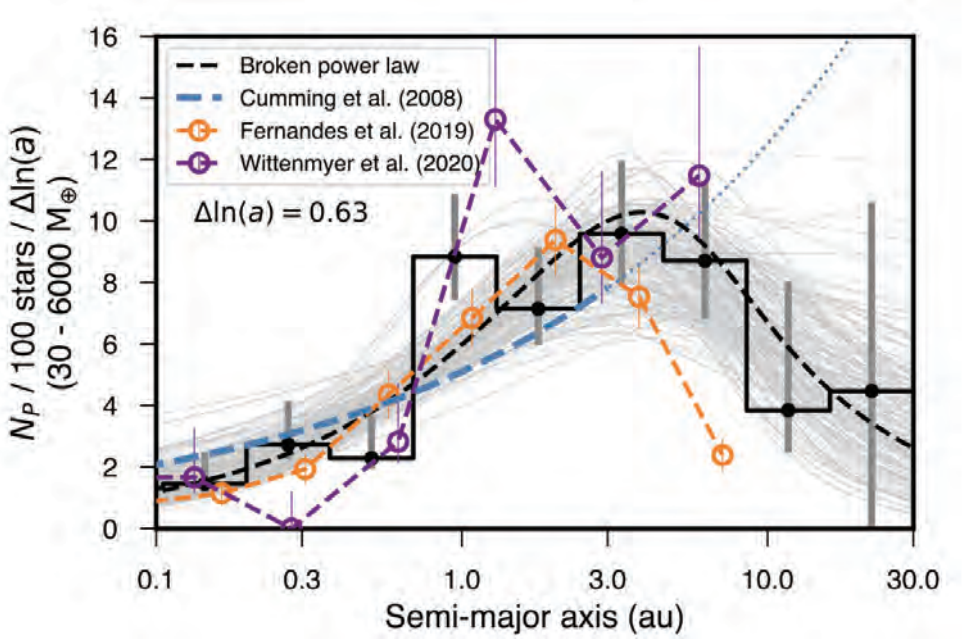

Figure 6: The occurrence rate of giant planets as a function of the semi-major axis of the orbit. Taken from Fig. 3 in [3].

The occurrence rate of hot Jupiters is about 1-2% for sun-like stars[6]. For sun-like stars, the preferred region to find giant planets is about 3-5 AU from the host star (Fig. 6). There is much discussion about what happens to the occurrence rate beyond ∼10 AU, see [3]. Cold Jupiters, which are further away from the host stars (2-8 AU), have an occurrence rate of 14% for sun-like stars. Hot Jupiters are likely to have formed further out in the solar system and migrated into their current location.

Giant planets are less common around low-mass stars. This is because we require the mass of the protoplanetary disk to be sufficiently large for giant planets to form. Further, as giant planets commonly contain a rocky core, we need the disk to contain a certain amount of solid elements. Generally, the mass of a disk is about 10% of the mass of the star and about 1% of the star disk is

[6]We define sun-like stars as stars with spectral types of F, G and K.

composed of solid elements. However, as the distribution of elements in the star generally matches the distribution of elements in the disk, giant planets can form around small, metal-rich stars. The occurrence rate of giant planets broadly decreases with stellar mass, with the occurrence rate for stars, 0.088–0.71$M_\odot$ found to be 0.194 ± 0.072% [1].

4.2 Super-Earths and sub-Neptunes

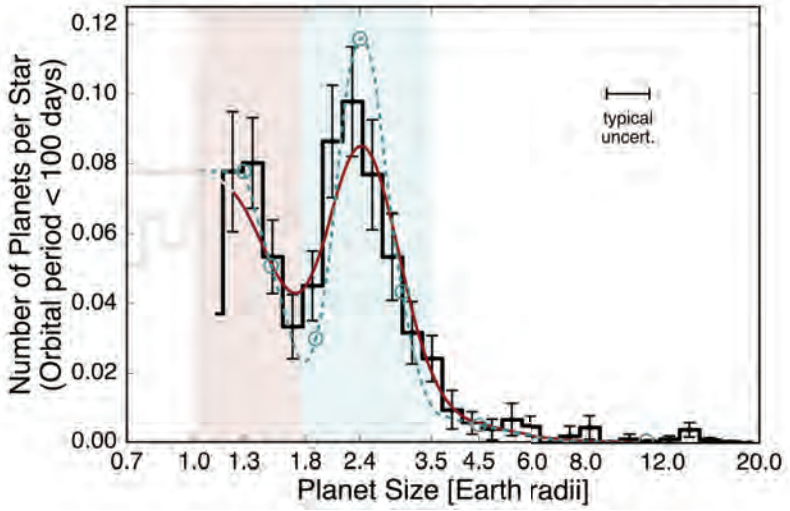

Figure 7: The occurrence rate of small planets as a function of the planetary radius. Lightly shaded regions encompass our definitions of "super-Earths" (light red) and "sub-Neptunes" (light cyan). Taken from Fig. 7 in [2].

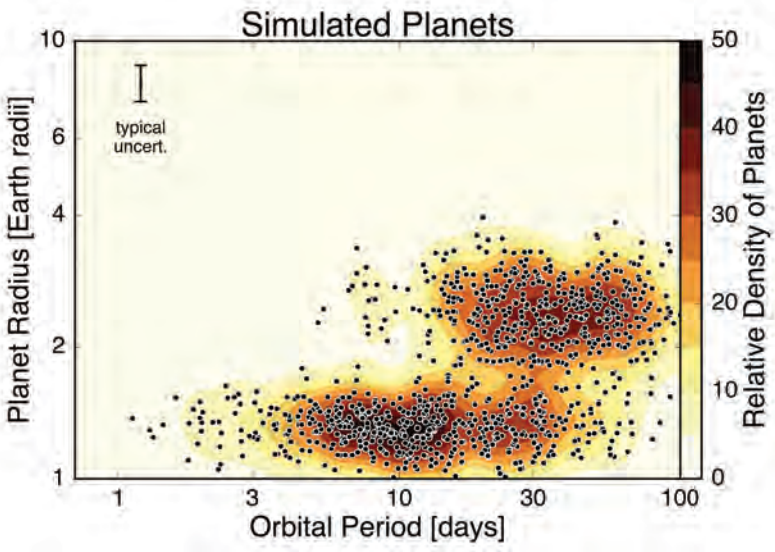

Figure 8: Radius vs. period distribution of small planets. The lower group is super-Earths and the upper group is sub-Neptunes. In between there is an "evaporation valley" where there are few planet samples. Taken from Fig. 16 in [2].

Super-Earths and sub-Neptunes have an occurrence rate of about 50% for sun-like stars, and about 100% for M-dwarfs. There is a separation in the size between super-Earths and sub-Neptunes (Fig. 7 and Fig. 8). If the planets are too close to the star (periods shorter than several days), the X-ray and UV radiation from the star will expand the hydrogen and helium envelope and these gases will escape. As a result, the sub-Neptunes, which have a hydrogen and helium envelope, are further from the star (and larger) than the super-Earths[7].

4.3 Earth-sized planets with Earth-like insolation rates

Earth-sized planets with Earth-like insolation rates have an occurrence rate of $\sim 10\%$ for sun-like stars and $\sim 30\% \pm 10\%$ for M-dwarfs. It is harder to observe these planets for larger stars because the optimal region of insolation is further away. However, in order to determine if these planets are habitable, we need to characterise their atmospheres.

5 Summary

In the RV method, the radial velocity of the star is $K_{star} \propto M_{star}^{-2/3}$. In the transit method, the transit depth is $\delta \propto R_{star}^{-2}$. Both methods are more sensitive to smaller stars. Among different exoplanets, the super-Earths and sub-Neptunes are more common than the giant planets. As a result, it is easier to find *small* planets around *small* stars. Table 1 gives a summary of the occurrence rates of the different categories of exoplanets.

	Giant planet		Small planet	
Occurrence rate (%)	Hot Jupiter	Warm/cold Jupiter	Small planet	'Potentially habitable planet'
Sun-like stars	1	14	50	10
M-dwarfs	0.2		100	30 ± 10

Table 1: Occurrence rates of different exoplanet categories.

References

[1] E. M. Bryant, D. Bayliss, and V. Van.Eylen, *The occurrence rate of giant planets orbiting low-mass stars with TESS*, Monthly Notices of the Royal Astronomical Society, 521 (2023), pp. 3663–3681.

[2] B. J. Fulton, E. A. Petigura, A. W. Howard, H. Isaacson, G. W. Marcy, P. A. Cargile, L. Hebb, L. M. Weiss, J. A. Johnson, T. D. Morton, et al., *The california-kepler survey. iii. a gap in the radius distribution of small planets*, The Astronomical Journal, 154 (2017), p. 109.

[3] B. J. Fulton, L. J. Rosenthal, L. A. Hirsch, H. Isaacson, A. W. Howard, C. M. Dedrick, I. A. Sherstyuk, S. C. Blunt, E. A. Petigura, H. A. Knutson, et al., *California legacy survey. ii. occurrence of giant planets beyond the ice line*, The Astrophysical Journal Supplement Series, 255 (2021), p. 14.

[7] There are sub-Neptunes that are close to the star, which are likely formed farther away and then migrate in

[4] S. Wang, B. Addison, D. Fischer, J. Brewer, H. Isaacson, A. Howard, and G. Laughlin, *Stellar spin–orbit alignment for kepler-9, a multi-transiting planetary system with two outer planets near 2:1 resonance*, The Astronomical Journal, 155 (2017).

[5] J. N. Winn, *Exoplanet transits and occultations*, vol. 55, University of Arizona Press Tucson, AZ, 2010.

GFD 2023 Lecture 2: Techniques for Characterization, Bulk and Atmospheric Compositions

Heather Knutson; notes by Arefe Ghazi Nezami and Quentin Kriaa

January 30, 2024

1 Introduction

This lecture focuses on the various techniques developed for characterizing the elements present in planets. In the previous lecture, we learned that the mass of a planet can be determined using radial velocity measurements, and the radius of a planet can be found using the transit technique. With this information we can find the bulk density of the planet that can be used to determine whether the planet is mostly rocky (i.e., dominated by a solid core) versus if it is mostly hydrogen and helium gas. The bulk density gives more detailed information on the bulk composition of the planet. By knowing the bulk density, we can estimate the relative proportion of hydrogen gas versus heavier elements within the planet.

For gas giant planets, two extreme scenarios can be assumed for planets with the same bulk density (which have mostly been measured for hot Jupiters); in one extreme, all the condensed material (such as metal, rock, and ice) are in the core of the planet with an envelope of H and He, another case is that the planet is a uniform mixture of these components. Both Jupiter and Saturn lie in between these two cases, as they have both a solid core and heavier elements mixed into their envelopes. It is not crucial to assume a specific extreme scenario when estimating the total heavy element content of a giant planet from its measured mass and radius. Therefore, for the sake of simplicity, in this discussion, we assume that all the heavy elements are located in the core, while the surrounding envelope is composed only of H and He (although in reality, some of the heavy elements may be dispersed in the atmosphere).

2 Planet Bulk Composition and Structure

Observationally, there is an empirical correlation between the masses of gas giant exoplanets and the relative fraction of their mass that comprises elements heavier than H and He (often referred to by astronomers as 'metals'). More massive gas giants tend to have relatively small fractions of their mass in the form of heavy elements, while less massive gas giants (analogous to Uranus and Neptune) tend to have much larger fractional heavy element masses. To highlight this relationship, $Z_{\rm planet}$ is used to indicate the number ratio of heavy elements other than H and He in the planet and is normalized relative to the Z of its parent star, $Z_{\rm star}$. $Z_{\rm planet}$, referred to as the planetary metal fraction, has been shown to have relationship with the mass of the planet. However, this relationship is stronger when $\frac{Z_{\rm planet}}{Z_{\rm star}}$ is considered, shown in figure 1. The metal fractions of the stars are smaller than their giant planets; for reference, for the sun $Z = 0.0134$. It is believed that almost all gas giant exoplanets are formed via core accretion, which is based on the fact that all of these planets have enhanced heavy element contents relative to their host stars. Additionally, giant

planets are more common around stars with higher metal abundances, indicating that metal-rich protoplanetary disks (which are assumed to share the same starting composition as their host star) are more likely to form giant planets.

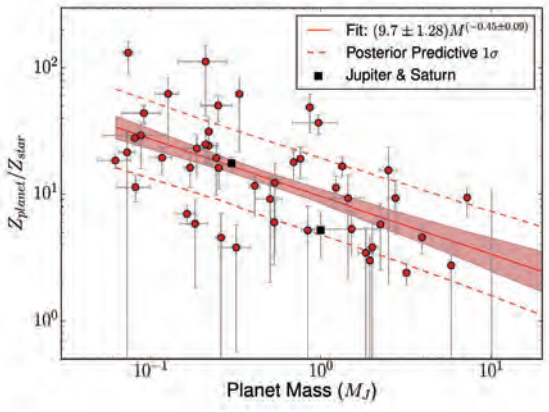

Figure 1: The relationship between the inferred planetary metal fraction relative to its parent star and planet mass in the units of mass of Jupiter. Figure adopted from reference [4]

When measuring the mass-radius relationship for smaller exoplanets ($1 - 3$ R_{Earth}), many planets are well-matched by an Earth-like mixture of rock and iron. These planets are referred to as 'super-Earths', as shown in figure 2(a). If these planets deviate from the Earth-like composition model, we can increase the content of heavier (iron) or lighter (water, hydrogen gas) materials to find the best match for the corresponding mass and radius. There is a second sub-population of small exoplanets called 'sub-Neptunes,' which have lower bulk densities than super-Earths. Two possible types of structures can be considered for these planets, which reflect a different potential formation locations. The first type, shown in figure 2(b), consists of only a rocky core with an envelope of H and He gas. The relative mass of the envelope to the planet mass is usually 1%. The second type, shown in figure 2(c), has a rocky core with water envelope (typical super-critical water with a steam envelope). Planets with envelopes of H and He are assumed to have formed close to the star and accreted their atmospheres directly from the protoplanetary disk. While, in case of the planets with water-dominated atmospheres, the planet presumably formed farther out, beyond the water-ice line, and then migrated inward. In this case, the atmosphere is formed from the melting of materials that were originally accreted as solids.

This information is obtained solely from the mass and radius data, which are obtained using the radial velocity measurements and the transit technique measurements, respectively. However, we are capable of measuring the atmospheric compositions of these planets using other methods, which can provide us with more information.

2.1 Beyond bulk composition: open questions for exoplanet atmospheres

Here we list some current open questions and problems linked to studies of exoplanet atmospheric compositions:

- Where in the disk did hot Jupiters originate based on the elemental abundances of their atmospheres? In the outer part of the disc more heavy elements and noble gasses are condensed and can be accreted as solids that are then vaporized and mixed into the atmosphere,

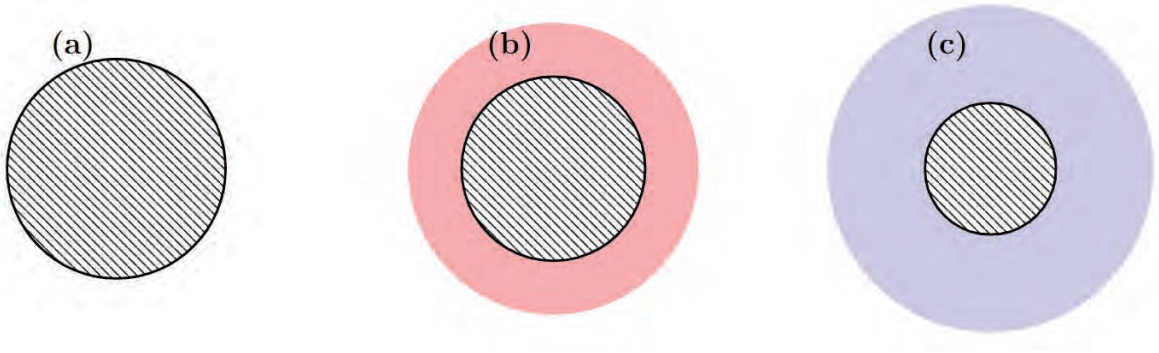

Figure 2: The possible atmospheric components for super-Earths and sub-Neptunes: (a) Rocky core only, (b) Rocky core with an envelope of H and He, and (c) Rocky core with a water-dominated envelope.

whereas in the inner disk most solids are either a mixture of rocks and metals, or (if beyond the water-ice line) water ice.

- How much H and He gas can small planets (1-10x mass of the Earth) accrete? Which small planets keep or lose their atmospheres? Additionally, how are their atmospheric compositions modified by this mass loss?
- Do water worlds exist? If so, how common are they?
- What types of outgassed atmospheres (i.e. atmospheres formed by the vaporization of materials originally accreted as solids) do terrestrial planets have?

To answer these questions, further studies of the atmospheric compositions of exoplanets are needed. The following sections present new techniques for observations to characterize exoplanetary atmospheres.

3 Techniques to Characterize the Atmospheric Compositions of Exoplanets

The previous section highlights the importance of identifying and characterizing the compositions of exoplanet atmospheres. Numerous methods have been developed for this purpose, providing insights into the dominant molecular and atomic content of these atmospheres, which, when combined with temperature data, allow for a more comprehensive understanding of their composition. Most of the methods developed for this purpose rely on observations of transiting planets, which pass in front of their host stars as seen from the Earth. Here we will focus on two of these techniques that have been successfully used in recent years. The first technique is *transmission spectroscopy*: when the planet passes in front of the star during the transit, part of the star's light is transmitted through the planet's atmosphere, imprinting a signature of atmospheric absorption. The second technique is *emission spectroscopy*: when the planet passes behind the star during the secondary eclipse, the decrease in light indicates the relative wavelength-dependent amount of light emitted (infrared) or reflected (optical) by the planet. Furthermore, a phase curve can be extracted by observing the changes in the planet's brightness as a function of orbital phase, further enhancing our understanding of the exoplanet's atmospheric dynamics.

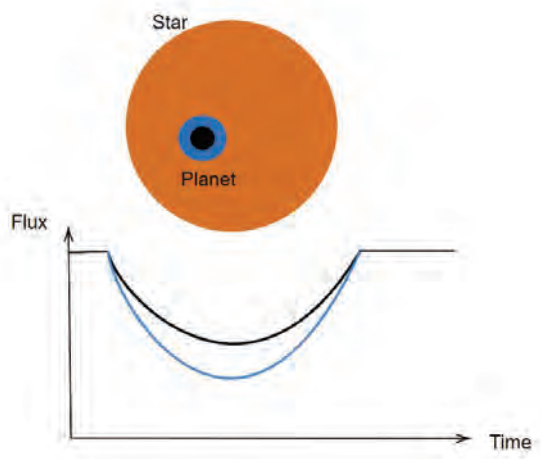

Figure 3: Two representative transit light curves showing the decrease in light when a planet atmosphere is passing in front of its host star, consider two different λ where the atmosphere is either opaque (blue colour) or transparent (black colour).

3.1 Measurements by transmission spectroscopy

Transmission spectroscopy measures the wavelength-dependent transit depth when the planet passes in front of its parent star. The amount of the star's light blocked by the planet will vary at different wavelengths if the planet possesses an atmosphere – this atmosphere will be transparent at some λ and opaque at others. Therefore, when we measure the *transit depth* $\left(\frac{R_{\rm planet}}{R_{\rm star}}\right)^2$, at a specific λ where the atmosphere is transparent (shown with black in figure 3), it will have a shallower transit depth compared to a λ where the atmosphere is opaque (shown with blue line in figure 3). Therefore, we can find the imprint of atmospheric absorption on the light of the star transmitted through the planet's atmosphere. If the planet does not have an atmosphere, the transit depth is constant across all wavelengths.

The magnitude of this absorption signal during transit can vary significantly among different exoplanets. Therefore, it is crucial to estimate the predicted depth of this absorption to find the sensitivity of these measurements to different atmospheric compositions. One way of approaching this question is to take the derivative of the transit depth with respect to the radius of the planet:

$$\Delta depth = \frac{2R_{\rm planet}}{R_{\rm star}^2} dR_{\rm planet} \tag{1}$$

This equation gives the relative change in transit depth when comparing measurements at wavelengths where the atmosphere is relatively opaque versus relatively transparent. The question is then: What is a representative value for $dR_{\rm planet}$ for an arbitrary absorber? Because the thickness of the annulus of the atmosphere of the planet determines the amount of absorption by the atmosphere (e.g., a larger annulus has a bigger area for absorption and the opposite is true for a smaller annulus), $dR_{\rm planet}$ is proportional to the atmospheric scale height. We will use the homogeneous atmospheric height, H, as the scale height. We adopt $dR_{\rm planet} \approx 1 - 5H$, where 5 is used for a highly absorbing atmosphere (no clouds, strong absorber) and 1 corresponds to a more conservative case (some high clouds and/or a weaker absorber) as a reasonable rule of thumb based on published

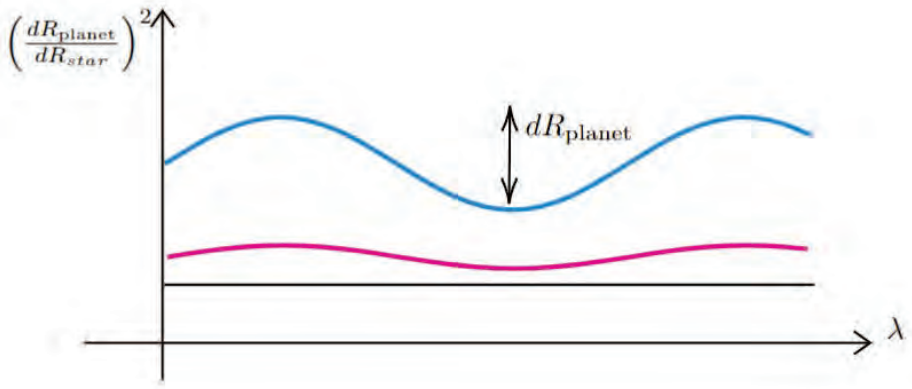

Figure 4: The transit depth of the planets as the function of λ for planets with atmosphere of smaller μ denoted by pink, larger μ denoted by blue, and for planet with no atmosphere denoted by black.

measurements of exoplanet transmission spectra. H is derived from the equation of pressure as a function of height for an isothermal hydrostatic atmosphere, when applying the ideal gas law to the hydrostatic pressure equation. H is given in equation 2, where R is the gas constant, T is the temperature, μ is the mean molecular weight, and g is the gravity. In this equation, we can estimate T based on the amount of light the planet receives from its host star, and can calculate g using the planet's measured mass and radius. Therefore, the only unknown that remains is μ. If the the planet has a H and He-dominated atmosphere, μ is around 2 M_H, and if it has a water-dominated atmosphere, μ is around 18 M_H. These two values are an order of magnitude different from each other, indicating that the strength of the absorption in the transmission spectrum is very sensitive to the mean molecular weight of the atmosphere.

$$H = \frac{RT}{\mu g} \tag{2}$$

Based on the arguments above, the best candidates for this method are hot Jupiters, which have relatively low μ (H and He rich atmospheres), large T, and large R_{planet}. Figure 4 shown the difference in the transit depth for a planet with a smaller or larger μ, and for a planet with no atmosphere. Untill now, relatively few good measurements are available using this techniques to measure the elemental abundances of C, O, etc.; this is now changing with the recent launch of JWST. This method is also less sensitive to atmospheric absorption when clouds are present in the atmosphere; since most hot Jupiters have clouds, this is another reason why there are not very many good measurements available yet.

3.1.1 Atmospheric mass loss

So far, our focus has been primarily on the bound part of the exoplanet's atmosphere. However, transmission spectroscopy can also be used to detect escaping gas from exoplanet atmospheres and calculate the corresponding mass loss rate of the atmosphere over time. This escaping gas is characterized by a very low density and corresponding low optical depth at most wavelengths. However, specific wavelengths can be selected that exhibit high absorption even at low densities. For instance, Lyman-alpha (Ly-α- absorbs in the UV) and certain meta-stable states of helium (absorbs in the near infrared, around 1083 nm) are highly absorptive under low-density conditions and can be utilized for this purpose. By measuring the absorption at these wavelengths, the planet may appear larger (in some cases, as much as a factor of a few larger), indicating the presence of unbound gas flowing away from the planet. By fitting these data with mass loss models, we can estimate the mass loss rates of these planets.

Quantifying the mass loss rates of exoplanets is crucial for understanding various aspects of their formation mechanisms. Transmission spectroscopy can be employed not only for studying atmospheric composition but also for measuring atmospheric mass loss rates. This method has enabled the observation of young sub-Neptunes transitioning into super Earths as they undergo catastrophic atmospheric loss.

3.2 Measurements by emission spectroscopy

The atmospheric composition of exoplanets can be characterized during a secondary eclipse, when the exoplanet passes behind the star it orbits around. Before the eclipse, the instrumentation measures the total flux $F_* + F_p$ (in units of $\mathrm{W.m^{-2}.Hz^{-1}}$)[1] coming from the star (F_*) and the exoplanet (F_p); during the eclipse, the planet is hidden and the flux that is measured now reduces to F_* only. As shown in figure 5, the relative amplitude of the flux decrease is given by:

$$\frac{F_p}{F_* + F_p} \simeq \frac{F_p}{F_*} \ , \tag{3}$$

where the right-hand side of equation (3) is obtained under the assumption that the planet's flux is much smaller than the star's flux. The signal-to-noise ratio of the quantity F_p/F_* is maximized for planets with relatively high values of F_p and stars with relatively small values of F_*. The ratio F_p/F_* varies with the wavelength because the fluxes of the planet and the star are not constant in wavelength. This is illustrated using black-body spectra in figure 6. Assuming the star and the planet are respectively a hot and a cold black body, figure 6 shows that the longer the wavelength, the larger the planet flux becomes relative to the stellar flux. This implies that the ratio R_p/F_* generally increases with the wavelength in the near- and mid-infrared ($1 - 10$ μm), so emission spectroscopy is best-suited to infrared observations.

Finally, note that the slopes of the spectra in figure 6 follow the same asymptote at longer wavelengths. This results in a plateau of the quantity F_p/F_* at the longest wavelengths (the Rayleigh-Jeans limit). In this limit, and under the assumption that both the star and the planet are black bodies, one can derive the following relation (see equation 3 in Reference [3])

$$\frac{F_p}{F_*} \simeq \left(\frac{R_p}{R_*}\right)^2 \frac{T_p}{T_*} \ , \tag{4}$$

[1]Note that any alternative flux unit can be adopted since we will ultimately consider a flux ratio, thus cancelling these units out.

where R_p and R_* are respectively the planet and the star radii, and T_p and T_* are respectively the planet and the star temperatures. Equation (4) reveals that, in the limit of long wavelengths, the signal-to-noise of emission spectroscopy measurements is maximized for planets orbiting relatively small cool stars, and has the advantage of being insensitive to the planet's atmospheric mean molecular weight μ. Therefore, by contrast with the transmission spectroscopy, this technique is well-suited to characterize planetary atmospheres of both small and large mean molecular weights.

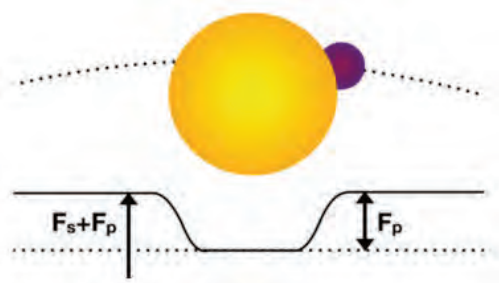

Figure 5: Sketch extracted from Reference [2]. Secondary eclipse of a planet (in pink color) passing behind a star (in yellow color). The curvilinear dotted line corresponds to the planet's orbit around the star. The solid dark line corresponds to the total flux that is measured. The flux F_p corresponds to the planet's flux. The variable F_s corresponds to the star's flux which we denote F_* in the main text.

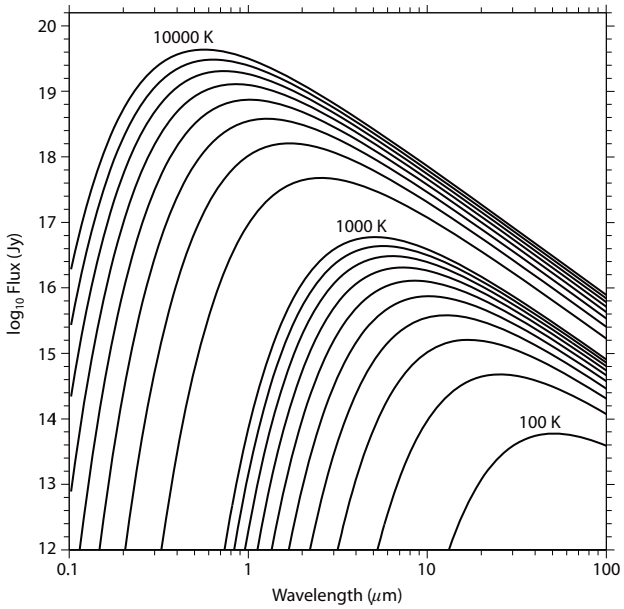

Figure 6: Figure extracted from Reference [1]. Spectra of surface fluxes (in units of $\mathrm{W.m^{-2}.Hz^{-1}}$) of black bodies of various temperatures, as a function of the wavelength (see Reference [1] for details).

3.3 Estimating the equilibrium temperature of the planet

We can predict the *equilibrium temperatures* of exoplanet atmospheres using a simple energy balance argument. This assumes that the emitting layers on these planets are isothermal, that they are in

radiative equilibrium with their parent star, and that their emission can be modelled as a blackbody. Let us define $\mathcal{F} = \int_\nu F d\nu$ as the total flux integrated over all wavelengths – or equivalently over all frequencies ν in Hz. The power $\mathcal{P}_{\rm out} = 4\pi R_p^2 \mathcal{F}_p$ going out to space from the planet's atmosphere is balanced by the fraction of incident power $(1 - A_B)\mathcal{E}_{\rm inc}$ that is absorbed from the star – which depends on the planet's Bond albedo A_B –, and by the power that the atmosphere receives from the planet's interior. The latter source of energy is negligible for most exoplanets, which orbit close to their stars [1]. The energy balance equation then reads:

$$4\pi R_p^2 \mathcal{F}_p = (1 - A_B)\pi R_p^2 \mathcal{F}_* \left(\frac{R_*}{a}\right)^2 \ , \tag{5}$$

where a is the semi-major axis of the planet's orbit around the star. Note how the amount of radiation that the planet absorbs from the star depends on the cross-sectional surface area πR_p^2 of the planet. The term $(R_*/a)^2$ is a geometric factor reflecting the solid angle that the star subtends from the planet's viewpoint [1]. Assuming that the planet and the star are black-bodies, the total fluxes are proportional to the fourth power of temperature, and equation (5) yields [1, 3]

$$T_{\rm eq} = T_* \sqrt{\frac{R_*}{a}} \left[\frac{1}{4}(1 - A_B)\right]^{1/4} \ , \tag{6}$$

where $T_{\rm eq}$ is the planet equilibrium temperature. In this last equation, the unknown planetary albedo plays a relatively minor role for hot Jupiters as their Bond albedos are usually lower than 10%. The albedo can therefore be considered negligible ($A_B \simeq 0$), and the equilibrium temperature of the exoplanet can be estimated with equation (6).

With typical values that are relevant for different categories of planets, one finds that typical hot Jupiters have an equilibrium temperature $T_{\rm eq} \sim 1000 - 2000$ K. Super-Earths can be as hot as 2000 K, which is sufficiently hot for them to be have magma oceans[2] on the day side, in which case they are called *lava-worlds*. Sub-Neptunes, in turn, are further out from the star and hence colder, with temperatures typically in the range $500 - 1000$ K.

3.4 Predictions for the atmospheric compositions of H/He-dominated planets

Once we know the approximate temperature of a hydrogen-dominated atmosphere, we can predict its expected equilibrium composition. Observationally, we are most sensitive to absorption from H_2O, CO, CO_2, and CH_4, which are predicted to be abundant in these atmospheres and have relatively high opacities across a broad range of infrared wavelengths. Elemental abundances are often estimated by scaling from the solar composition [3]. We can then translate these elemental abundances into predicted molecular abundances by assuming that the atmosphere is in thermo-chemical equilibrium. This equilibrium chemistry solution is determined by minimization of the Gibbs free energy of the chemical system. The solution to this problem of optimization gives the characteristic composition as a function of the temperature (and, to a lower extent, the pressure) in each atmospheric layer. In this framework, the dominant reservoir for atmospheric carbon is expected to transition from methane to carbon monoxide for temperatures higher than $\sim 1000K$ in gas giant atmospheres, through the following chemical equation:

$$\underbrace{\rm CO + 3H_2}_{\text{large } T} \leftrightarrow \underbrace{\rm CH_4 + H_2O}_{\text{low } T} \ . \tag{7}$$

[2]The typical value of the melting temperature of rocks is $1300 - 1400$ K for a pressure near 0 bar

A similar transition is expected in the case of nitrogen, which is primarily bound up in the form of ammonia in cooler atmospheres and then transitions to N_2 when the temperature increases above $\sim 500K$, as captured by the chemical equation:

$$\underbrace{N_2 + 3H_2}_{\text{large } T} \leftrightarrow \underbrace{2NH_3}_{\text{low } T} \ . \tag{8}$$

Surprisingly enough, the abundances of these molecules measured in exoplanet atmospheres do not always match the predictions based on these models. In the case of equation (7), methane should be more abundant than carbon monoxide for sufficiently cold planets, but many relatively cool exo-Jupiters show no clear signatures of CH_4 absorption, probably due to vertical mixing that advects some deep warm CO-laden layers upward, reducing the abundance of methane in the uppermost layers of the atmosphere [3].

There is a broad range of species that can be detected in the atmospheres of hot Jupiters. For ultra-hot Jupiters, their high temperatures ($T \gtrsim 2000K$) enables many refractory species like Li, Mg, Ca, V, Cr, Mn, Fe, Ni, Sr, Ti, Al to remain in gas phase. For most hot Jupiters, water, carbon monoxide and carbon dioxide are usually measured. Recent observations by the James Web Space Telescope also revealed the presence of SO_2 in the atmosphere of a hot Jupiter. The existence of this molecule, which is a product of photochemical reactions, is another example of disequilibrium chemistry in these atmospheres. This is an increasingly promising direction to take for future studies of the atmospheric composition of gas giant exoplanets.

3.5 Clouds and hazes

Clouds are key elements of a planet's atmosphere that notably control its climate and play a part in the atmosphere dynamics [5]. Since they control the planet's Bond albedo, they also determine the energy balance between the planet and its parent star (see section 3.3), and they alter measurements of transmission spectra by masking the planet's atmosphere during its transit, particularly when they are located at relatively low pressures (high altitudes) near the planet's day-night terminator.

Although clouds are complicated to model, they cannot be ignored since most hot Jupiters appear to have clouds. The compositions of condensate clouds can be inferred by combining models of thermochemical equilibrium, which predict the gas-phase abundances of various condensible species, along with the condensation curves for those species as a function of pressure and temperature. For a given pressure P in the planet atmosphere, when the local temperature $T_p(P)$ is lower than the condensation curve of a given element (say, $MgSiO_3$), the latter condenses. Cloud particles can be present in all regions that are cooler than the local condensation temperature – see an illustration for four planets in figure 7.

In order to determine the likely compositions of the clouds observed in hot Jupiter atmospheres, we must first search for species that can condense in the uppermost layers of these planets,and that are sufficiently abundant to produce an optically thick cloud mass, and sufficiently high in the atmosphere to substantially modify the transmission spectra through the atmosphere. Several promising candidates have been identified, as shown in figure 7. This figure reveals that the temperature has a decisive impact on the type of clouds that can form. Most hot Jupiters likely have some form of silicate clouds (enstatite $MgSiO_3$, forsterite Mg_2SiO_4) between $1500 - 2000$ K. Metal clouds (Fe, TiO_2, Al_2O_3) can form at higher temperatures near ~ 2000 K, while salt clouds (KCl) form at somewhat lower temperatures around ~ 1000 K. Discriminating between different condensates is important since they control the clouds' reflectivity, thus modifying the planet albedo, and the aerosol scattering and absorption modify the transmission spectra of the atmosphere [5]. Since some of these clouds have distinct spectral features in the mid-infrared, we expect that future

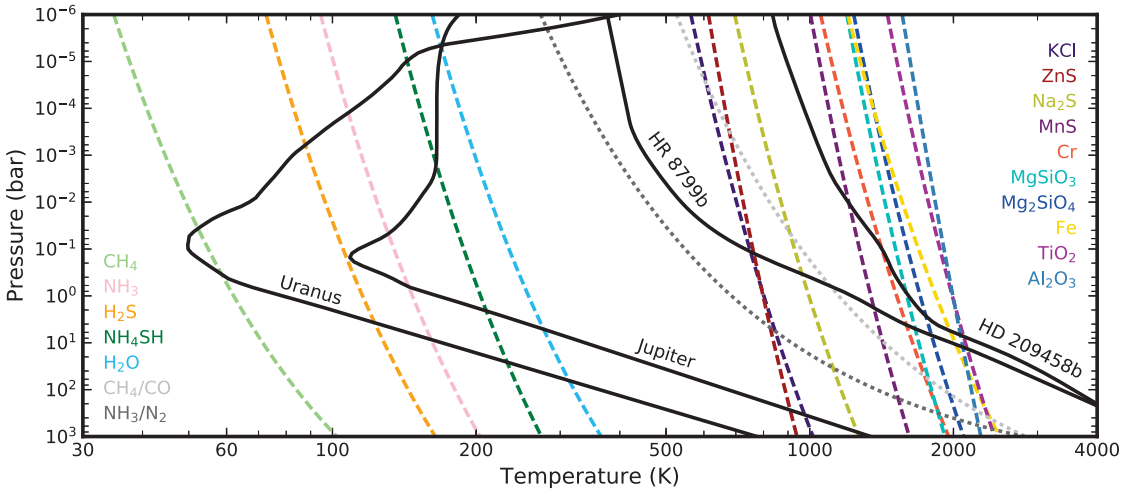

Figure 7: Figure extracted from Reference [5]. Solid dark lines show the temperature-pressure profiles of different planets. Dashed and dotted lines show the condensation curves of various species. These curves are obtained under the assumption that the composition is solar. See Reference [5] for additional details.

observations with JWST will soon be able to measure such features in emission or transmission spectra of these planets, confirming their compositions.

Finally, photochemical hazes are another important type of aerosol that may be present in these atmospheres. Such aerosols can be found on Titan, where photochemistry converts methane into long hydrocarbon chains, and when the temperature is sufficiently low for these chains to survive (typically cooler than ~ 1000 K).

As discussed above, hot Jupiters are the most favorable targets to characterize using these techniques. Due to their hydrogen-dominated atmospheres, sub-Neptunes are the next most favorable targets for transmission spectroscopy after hot Jupiters. Unfortunately, data on the atmospheric properties of these relatively small planets remains scarce. Because the range of wavelengths that was available for the Hubble Space Telescope was limited to < 1.6 μm, published observations of exoplanet atmospheres using this telescope are primarily sensitive to the presence of water vapour in a hydrogen-rich background atmosphere. There are currently no detections of atmospheric absorption from planets with non-hydrogen-dominated atmospheres. Super-Earths are doubly challenging, as they have small radii and high atmospheric mean molecular weights. To date, no one has detected atmospheric absorption from this class of planets, either in transmission or emission.

References

[1] Seager, S. (2010). Exoplanet Atmospheres: Physical Processes. *Princeton University Press.*

[2] Alonso, R. 2018. Characterization of Exoplanets: Secondary Eclipses. In: Deeg, H., Belmonte, J. (eds) Handbook of Exoplanets. *Springer, Cham.*

[3] Madhusudhan, N., Knutson, H., Fortney, J., and Barman, T. 2014. Exoplanetary atmospheres. *arXiv preprint arXiv:1402.1169.*

[4] Thorngren, D. P., Fortney, J. J., Murray-Clay, R. A., and Lopez, E. D. (2016). The mass–metallicity relation for giant planets. *The Astrophysical Journal, 831(1), 64.*

[5] Gao, P., Wakeford, H. R., Moran, S. E., and Parmentier, V. 2021. Aerosols in exoplanet atmospheres. *Journal of Geophysical Research*, 126(4)

[6] Winn, Joshua N. (2010). Transits and occultations. arXiv preprint arXiv:1001.2010.

GFD 2023 Lecture 3: Structure and Circulation of Terrestrial Planets: Atmospheric Structure and Circulation

Geoffrey K. Vallis; notes by Yifeng Mao and Hao Fu

July 6, 2024

1 Introduction

In this lecture, the first on the theory and dynamics of planetary atmospheres, we discuss terrestrial (also known as telluric) planets, which are, as the name implies, planets resembling Earth. More specifically, they are planets that have a shallow gaseous atmosphere overlying a solid or possibly liquid planetary surface. If such a planet is considerably larger than Earth it might be called a 'super Earth', and if a planet is particularly similar to Earth it may be called 'Earth-like', but such distinctions do not especially concern us in this lecture. (A more complete taxonomy of planets can be found in Chapter 13 of [6].) In this lecture our goal is to informally introduce the equations of motion for such atmospheres and describe some of the most basic features of their circulation and structure.

2 Equations of Motion

We start with the Navier-Stokes equations. The momentum equation in a rotating frame is

$$\frac{\partial \boldsymbol{v}}{\partial t} + (\boldsymbol{v}\cdot\nabla)\boldsymbol{v} + 2\boldsymbol{\Omega}\times\boldsymbol{v} = -\frac{1}{\rho}\nabla p + \nu\nabla^2\boldsymbol{v} + \boldsymbol{g}, \tag{1}$$

and the mass continuity equation is

$$\frac{\partial \rho}{\partial t} + \nabla\cdot(\rho\boldsymbol{v}) = 0. \tag{2}$$

Here, $\boldsymbol{v}$ is the three-dimensional velocity, ρ is density, p is pressure, $\boldsymbol{g}$ is gravity and we omit viscous terms. The term $2\boldsymbol{\Omega}\times\boldsymbol{v}$ in the momentum equation is the Coriolis force that results from the body rotation and is perpendicular to the velocity, and the centrifugal term is absorbed into gravity. The term $\nu\nabla^2\boldsymbol{v}$ represents the effects of molecular viscosity; its direct effects on large scales are nearly always negligible and we will nearly always omit the term in what follows.

The equation for the internal energy I per unit mass (i.e., the specific internal energy, but we shall usually omit the 'specific' qualifier) is

$$\frac{\mathrm{D}I}{\mathrm{D}t} + \frac{p}{\rho}\nabla\cdot\boldsymbol{v} = Q, \tag{3}$$

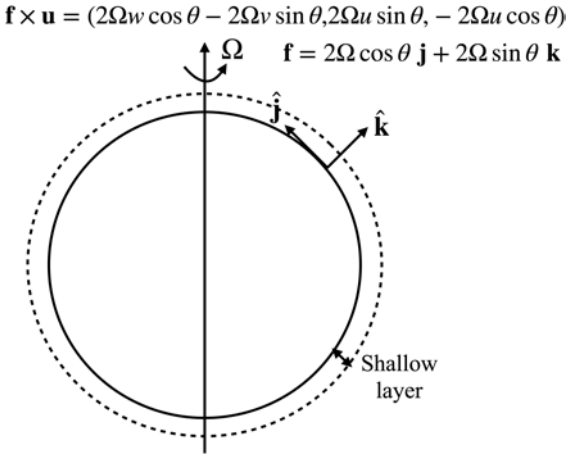

Figure 1: A schematic diagram for the illustration of Coriolis force and the shallow layer around planets. The traditional approximation of the Coriolis parameter takes $\boldsymbol{f} = 2\Omega \sin\theta \mathbf{k}$, which only retains the component aligned with gravity. The figure also shows the meridional component, $2\Omega \cos\theta \mathbf{j}$, and $\mathbf{i}$ is the unit vector direction into the paper.

where $\mathrm{D}/\mathrm{D}t = \partial/\partial t + \boldsymbol{v} \cdot \nabla$ is the total derivative operator, Q is the total rate of diabatic heating (per unit mass). In an ideal gas $I = c_v T$ where c_v is the specific heat capacity at constant volume and T is temperature.

We will simplify the equations of motion and think about how to apply them to Earth and other terrestrial planets. On an Earth-like planet we have the following equation for the horizontal velocity

$$\frac{\mathrm{D}\boldsymbol{u}}{\mathrm{D}t} + \boldsymbol{f} \times \boldsymbol{u} = -\frac{1}{\rho}\nabla p, \tag{4}$$

where $\boldsymbol{u}$ is the horizontal velocity, and $\boldsymbol{f} \approx 2\Omega \sin\theta \mathbf{k}$ is the vertical component of the Coriolis term (see fig. 1). Here $\mathbf{k}$ is the vertical unit vector (in the direction of gravity) and θ is the latitude.

Equation (4) has used a 'traditional' approximation of the Coriolis term by only retaining the component aligned with gravity. This only works for a shallow layer of fluid on a sphere, with the layer thickness much smaller than its horizontal extent. Examples of the layers are ocean and atmosphere. In Fig. 1, we illustrate the direction of the Coriolis force and the aspect ratio of the layer. Finally, we remark that it is common when dealing with terrestrial atmospheres to use a Cartesian co-ordinate system, (x, y, z) where x is the coordinate in the zonal direction, y in the meridional direction and z in the vertical direction, with corresponding unit vectors $\mathbf{i}, \mathbf{j}$ and $\mathbf{k}$ and velocities, u, v and w. On the sphere u, v and w are also used to denote the zonal, meridional and vertical velocities.

3 The Boussinesq Approximation

The Boussinesq approximation presumes that the density is nearly constant, with only a small variation $\delta\rho$ around its constant background value ρ_0:

$$\rho = \rho_0 + \delta\rho, \quad \text{where} \quad \rho_0 \gg \delta\rho(x, y, z, t). \tag{5}$$

Pressure variations are correspondingly given by:

$$p = p_0(z) + \delta p(x, y, z, t) \tag{6}$$

where the basic state pressure field is chosen to satisfy $\mathrm{d}p_0/\mathrm{d}z = -\rho_0 g$. Variations of density are then only allowed in the vertical momentum equation where they arise in conjunction with g. Thus, beginning with the vertical momentum equation

$$\rho \frac{\mathrm{D}w}{\mathrm{D}t} = -\frac{\partial p}{\partial z} - \rho g, \tag{7a}$$

giving

$$(\rho_0 + \delta\rho)\frac{\mathrm{D}w}{\mathrm{D}t} = -\frac{\partial p_0}{\partial z} - \frac{\partial \delta p}{\partial z} - \rho_0 g - \delta\rho g \tag{7b}$$

whence, neglecting the $\delta\rho$ term on the left-hand side and cancelling the basic state pressure gradient and density terms,

$$\frac{\mathrm{D}w}{\mathrm{D}t} = -\frac{\partial \phi}{\partial z} + b, \tag{7c}$$

where

$$b = -g\frac{\delta\rho}{\rho_0}, \tag{7d}$$

is the *buoyancy*. If the equation of state is a simple one, for example $\rho = \rho_0(1 - \beta_T(T - T_0))$ where β_T is a coefficient of expansion and T_0 and ρ_0 are constants, then changes in buoyancy are directly related to changes in temperature, $b = g\alpha T$. Alternatively, if we are imagining an application to an ideal-gas atmosphere then instead of $b = -g\delta\rho/\rho_0$ then b can be related to potential temperature, ϑ, rather than density, and $b = g\delta\vartheta/\vartheta_0$ (see e.g.,[5]).

The three-dimensional momentum equation can then be written in compact form as

$$\frac{\mathrm{D}\boldsymbol{v}}{\mathrm{D}t} + 2\boldsymbol{\Omega} \times \boldsymbol{v} = -\nabla\phi + b\mathbf{k}, \tag{8}$$

where $\mathbf{k}$ is the unit vector in the vertical direction (i.e., the direction aligned with gravity).

Another component of Boussinesq approximation is the simplification of the continuity equation from mass conservation to volume conservation. Neglecting the variations of density, as they are presumed small, (2) becomes

$$\nabla \cdot \boldsymbol{v} = 0. \tag{9}$$

In making this approximation we have also eliminated sound waves, which is an acceptable approximation if the flow speed is much less than the sound speed, as is the case for many geophysical applications. An upshot of this is that the pressure in the Boussinesq equation acts as a medium to guarantee the volume conservation of a parcel. One consequence of this is that the internal energy is no longer connected to the kinetic energy — note that the divergence term in (3) vanishes — and the energy cycle of the system is between kinetic energy and potential energy. Spiegel and Veronis [4] and Vallis [5] provide more discussion. Although the Boussinesq approximation is not a particularly good one for many problems in planetary atmospheres, it is a very *useful* approximation. The essence of many problems can be understood by using it, and we will employ it frequently to obtain understanding.

4 The Hydrostatic Approximation

4.1 What is it?

Hydrostatic balance, or hydrostasy, is the state in which the dominant balance in the vertical momentum equation lies between the pressure gradient force and gravity. Consider the vertical

component of the momentum equation for the vertical velocity w,

$$\frac{\mathrm{D}w}{\mathrm{D}t} + \text{Coriolis term} = -\frac{1}{\rho}\frac{\partial p}{\partial z} - g. \tag{10}$$

Often, in the case of the terestrial atmospherse and ocean, the large aspect ratio makes the vertical acceleration $\mathrm{D}w/\mathrm{D}t$ small compared to gravity, and the small relative shell depth compared to Earth's radius makes the Coriolis term negligible. (If the rotation vector is aligned with gravity and so pointed in the vertical direction then the Coriolis term is identically zero in this equation.) With these approximations, we arrive at the hydrostatic balance equation:

$$\frac{\partial p}{\partial z} \approx -\rho g. \tag{11}$$

Let us know look at this approximation a little more systematically.

4.2 Scaling and the aspect ratio

We now show that hydrostatic balance is valid when the aspect ratio α (the ratio of vertical to horizontal scales, $\alpha \equiv H/L$) is low, and it is even better if the flow is geostrophic. We will use the Boussinesq equations for simplicity and we will initially assume that the rotation vector is aligned with gravity.

The mass continuity equation in the Cartesian coordinate can be rewritten as

$$\frac{\partial u}{\partial x} + \frac{\partial v}{\partial y} + \frac{\partial w}{\partial z} = 0, \tag{12}$$

where u, v, w are the velocity components. Suppose the following scaling $w \sim W$, $u \sim v \sim U$, $x \sim y \sim L$ and $z \sim H$.[1] Matching the order of magnitude in equation (12) implies the scaling of the vertical velocity with the horizontal velocity

$$\text{nonrotating flow}: \quad W \sim \frac{H}{L}U = \alpha U, \tag{13}$$

where $\alpha = H/L$ is the aspect ratio. In most cases, we have $H \ll L$ so that $W \ll U$. As we show below, in the case of rotating flow, the magnitude of the horizontal divergence $\partial u/\partial x + \partial v/\partial y$ in (12) is actually smaller than U/L because the horizontal flow is non-divergent to a first approximation. Then, because W/H is given by the magnitude of the horizontally divergent wind, the vertical velocity is *smaller* than the estimate HU/L.

Indeed, in rapidly rotating flow the magnitude of the horizontal rotational wind can be estimated from the vertical vorticity equation which, to a decent approximation, is

$$\frac{\mathrm{D}\zeta}{\mathrm{D}t} = f\frac{\partial w}{\partial z}, \tag{14}$$

where ζ is the vertical relative vorticity, namely $\mathbf{k} \cdot \nabla \times \boldsymbol{v}$. (We have omitted various small terms. See [5] chapter 4 for detail.) Suppose $\mathrm{D}/\mathrm{D}t \sim U/L$, and $\zeta \sim U/L$, we obtain

$$\text{Rotating flow}: \quad \frac{U^2}{L^2} \sim f\frac{W}{H} \quad \Rightarrow \quad W \sim \mathrm{Ro}\frac{H}{L}U. \tag{15}$$

[1] What determines H? Hydrostatic balance relation and the ideal gas law yield $\partial p/\partial z = -\rho g = -pg/RT$ where R is the ideal gas constant. If T is constant the solution to this equation is $p = p|_{z=0}\exp(-z/H_*)$, where $H_* = RT/g$ is the atmospheric scale height. This scale is often used as a representative vertical scale in studies of planetary atmospheres and, at least on Earth, it is similar to the depth of the troposphere.

where $\mathrm{Ro} = U/(fL)$ is the Rossby number (an important parameter that we return to later). This scaling indicates that the vertical velocity is suppressed by the background rotation. (We may note that other ways to arrive at a scaling for W are possible, invoking the thermodynamic equation. See [5] for details.) Because the rotational scaling is valid only for $Ro \ll 1$, we can combine (13) and (15) to get a general scaling of W:

$$W \sim \min\{Ro, 1\}\, \alpha U. \tag{16}$$

Evidently, the background rotation tends to suppress vertical motion. Let us now consider how these scalings determine whether the flow is hydrostatic or not.

4.2.1 An inertial scaling

In the absence of rotation the vertical momentum equation is, in the Boussinesq approximation,

$$\frac{\mathrm{D}w}{\mathrm{D}t} = -\frac{\partial \phi}{\partial z} + b. \tag{17}$$

The hydrostatic approximation will hold when $|\mathrm{D}w/\mathrm{D}t| \ll |\partial\phi/\partial z|$, since then we must have $\partial\phi/\partial z = b$, which is hydrostatic balance for a Boussinesq system. To obtain a scaling for ϕ we use the horizontal momentum equation (8), which gives

$$\frac{\partial \boldsymbol{u}}{\partial t} + \boldsymbol{v}\cdot\nabla\boldsymbol{u} = -\nabla\phi \tag{18}$$

giving, assuming W is no bigger than U,

$$\frac{U^2}{L} \sim \frac{\Phi}{L} \implies \Phi \sim U^2. \tag{19}$$

Thus,

$$\frac{\partial \phi}{\partial z} \sim \frac{U^2}{H}. \tag{20}$$

If time scales advectively (so that $T = L/U$), the vertical momentum equation then scales as

$$\frac{\mathrm{D}w}{\mathrm{D}t} \sim \frac{UW}{L} \sim \frac{U^2 H}{L^2}. \tag{21}$$

Thus, the ratio of the material derivative to the vertical pressure gradient term is

$$\frac{|\mathrm{D}w/\mathrm{D}t|}{|\partial\phi/\partial z|} \sim \frac{U^2H/L^2}{U^2/H} = \frac{H^2}{L^2}, \tag{22}$$

implying that flows with a small aspect ratio, specifically with $\alpha^2 \ll 1$, will be in hydrostatic balance.

4.2.2 A geostrophic scaling

Let us now consider fluid in a rotating frame of reference, with gravity aligned with rotation (as on a terrrestial planet). Let us assume that the leading-order balance in the horizontal momentum equation is between the Coriolis force and the pressure gradient force; that is

$$\boldsymbol{f}\times\boldsymbol{u} \approx -\nabla\phi. \tag{23}$$

This is known as geostrophic balance, or geostrophy, and we look at this in more detail in the next section. From (23) we infer the scalings relating velocity, U, and pressure, Φ,

$$fU \sim \Phi/L \quad \Rightarrow \quad \Phi \sim fUL. \tag{24}$$

From (15) we have, in the rotating case, $W \sim \mathrm{Ro}\,\alpha U$ so that $\mathrm{D}w/\mathrm{D}t \sim Ro\,U^2H/L^2$. Using this with (24) gives

$$\frac{|\mathrm{D}w/\mathrm{D}t|}{|\partial\phi/\partial z|} \sim \frac{RoU^2H/L^2}{fUL/H} = Ro^2\frac{H^2}{L^2}. \tag{25}$$

That is, the criterion for hydrostatic balance is now

$$Ro^2\,\frac{H^2}{L^2} \ll 1. \tag{26}$$

This criterion is easier to satisfy than in the non-rotating case due to the suppression of vertical motion by rotation. In both cases, flows with a small aspect ratio ($\alpha^2 \ll 1$) tend to be in hydrostatic balance.

4.2.3 Misaligned gravity and rotation

Except at the poles, the direction of gravity and rotation are, in truth, misaligned. Incorporating this introduces the so-called nontraditional Coriolis terms ($2\Omega\cos\theta w$ term in the zonal momentum equation and $-2\Omega u\cos\theta$ in the vertical momentum equation). Let us use scale analysis to see if and when these terms can be neglected.

In a local Cartesian coordinate that treats the sphere as a local tangential plane, the zonal and vertical momentum equations with nontraditional Coriolis terms are:

$$\frac{Du}{Dt} - 2\Omega v\sin\theta + \underbrace{2\Omega\cos\theta w}_{\text{nontraditional}} = -\frac{\partial\phi}{\partial x}, \tag{27}$$

$$\frac{Dw}{Dt}\underbrace{-2\Omega\cos\theta u}_{\text{nontraditional}} = -\frac{\partial\phi}{\partial z} + b. \tag{28}$$

Here x denotes the coordinate along the west-east direction ($\mathbf{i}$), and y (not appearing here) denotes the coordinate along the south-north direction ($\mathbf{j}$). Unlike the traditional Coriolis terms that vanish at the equator (due to the $\sin\theta$ factor), the nontraditional terms vanish at the poles (because of the $\cos\theta$ factor).

If the flow is in geostrophic balance at the large scale then pressure scales as in (19), namely $\Phi = fUL$. The relative magnitude of the nontraditional terms to pressure gradient terms in the u and w equations are:

$$\frac{2\Omega w\cos\theta}{\partial\phi/\partial x} \sim \frac{2\Omega W}{fU} \sim \frac{2\Omega U}{fU}\frac{H}{L}Ro \sim \frac{H}{L}Ro, \tag{29}$$

and

$$\frac{-2\Omega u\cos\theta}{\partial\phi/\partial z} \sim \frac{2\Omega U}{fUL/H} \sim \frac{H}{L}, \tag{30}$$

where we have used (16): $W \sim Ro\frac{H}{L}U$ to estimate W. Because $H \ll L$ and $Ro \ll 1$, The nontraditional terms in the u and w momentum equations can be neglected.

At the tropics, or in weakly rotating systems, the flow is not strongly constrained by rotation, and we need to use (18): the $\Phi \sim U^2$ scaling. We get:

$$\frac{2\Omega w \cos\theta}{\partial\phi/\partial x} \sim \frac{2\Omega W}{U^2/L} \sim \frac{2\Omega H}{U} \sim Ro^{-1}\frac{H}{L}, \tag{31}$$

$$\frac{2\Omega u \cos\theta}{\partial\phi/\partial z} \sim \frac{2\Omega U}{U^2/H} \sim \frac{2\Omega H}{U} \sim Ro^{-1}\frac{H}{L}. \tag{32}$$

In deriving (31), we have used (13): $W \sim UH/L$, which is more appropriate for flows that are not rotationally constrained. On Earth, using $2\Omega \sim 10^{-4}$ s^{-1}, $H = 10^4$ m, and $U = 10$ m.s^{-1}, we get $2\Omega H/U \sim 10^{-1}$. Thus, the nontraditional Coriolis term is small but not wholly negligible in the Earth's tropics. In other planets where the atmosphere is much deeper, this term may become important, and not only in the tropics. We refer the readers to [7] for more details on nontraditional Coriolis terms.

In summary, the nontraditional Coriolis terms are non-negligible for a very deep fluid layer and they play a key role in deep convective layer of a gas giant, as will be discussed in Chapter 3. The traditional and nontraditional Coriolis terms work together to guarantee the Taylor-Proudman theorem, which states that the flow tends to have little variation in the rotating axis direction. In this case, a cylindrical coordinate whose axis is aligned with the rotation axis is useful for studying the general circulation of the planet.

4.3 Pressure coordinates

Knowing that pressure, in most cases, has a one-to-one correspondence with the vertical coordinate z and varies monotonically with z, it is often useful to express the equations of motion in pressure coordinates. This provides a useful simplification and a more direct connection with observations that are often taken at fixed values of pressure. Here we just provide an extremely brief introduction by writing down a few key equations without derivation. The reader interested in the derivations of these equations will find it in a number of textbooks, for example [5].

The horizontal momentum equation in pressure coordinates is

$$\frac{D\boldsymbol{u}}{Dt} + \boldsymbol{f} \times \boldsymbol{u} = -\nabla_p \varphi = \left(\frac{\partial\varphi}{\partial x}\right)_p \mathbf{i} + \left(\frac{\partial\varphi}{\partial y}\right)_p \mathbf{j}, \tag{33}$$

where the advective derivative is given by $D/Dt = \partial/\partial t + \boldsymbol{u}\cdot\nabla_p + \omega\partial/\partial p$, $\varphi \equiv gz$ is the geopotential (note the difference from ϕ), and $\omega \equiv \mathrm{D}p/\mathrm{D}t$ is the pressure velocity. The subscripts indicate that the derivatives are taken at constant p. The mass conservation in pressure coordinates is simplified as

$$\left(\frac{\partial u}{\partial x}\right)_p + \left(\frac{\partial u}{\partial y}\right)_p + \frac{\partial\omega}{\partial p} = 0. \tag{34}$$

The hydrostatic equation in height coordinates $\partial p/\partial z = -\rho g$ is written in pressure coordinates using the ideal gas law as

$$\frac{\partial\phi}{\partial p} = -\frac{RT}{p}. \tag{35}$$

4.4 Aside: surface pressure in a deep atmosphere

For a thin-layer atmosphere, hydrostatic balance indicates that the surface pressure p_s is proportional to the total mass in the air column above the ground:

$$p_s = g\int_0^H \rho\,\mathrm{d}z. \tag{36}$$

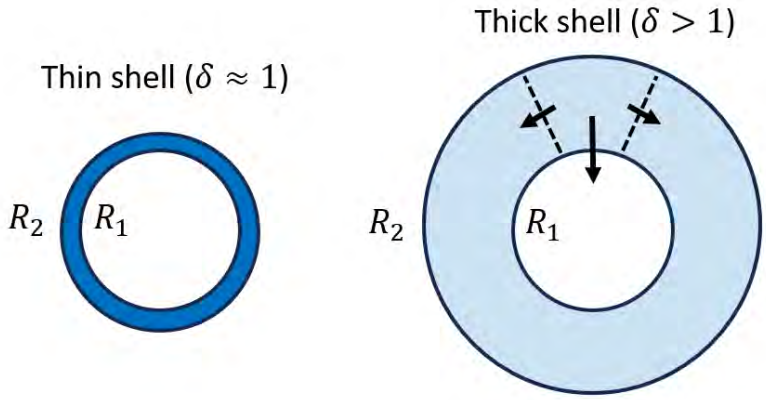

Figure 2: A schematic of, on the left, a thin atmosphere with high density, and on the right a thick atmosphere with low density. The inner radius of the shell is fixed to R_1, and the outer radius R_2 is different. A shell thickness parameter may be defined as $\delta \equiv R_2/R_1$. The blue shading denotes density, with the deeper blue denoting higher density. The arrow illustrates the normal stress at the wedge.

Integrating over the surface of the planet then suggests that the integral of surface pressure is essentially equal to the total weight of the atmosphere. For a thick atmosphere in a spherical shell, does (36) still hold (discounting the effect that gravity diminishes with height)? And does surface pressure integrated over the surface area still equal the weight of the atmosphere?

In fact, hydrostatic balance still holds (there is absolutely no reason it should not if the atmosphere is static) but the the integral of pressure over the surface does *not* equal the weight of the atmosphere, as might be envisioned by shrinking the planet to the size of a tennis ball. This is because the curvature of the atmosphere leads to partial cancellation of the stress (Fig. 2). The mechanism is similar to why an arch bridge (or a wedge) can hold more load than a flat bridge. Let us explore this a little more in a simple case with both gravity (g) and fluid density constant.

Consider the atmosphere in a spherical shell with a lower radius R_1 and an upper radius R_2, as in Fig. 2, with gravity constant. The atmospheric density ρ is assumed to be uniform within the shell, and the total atmospheric mass M_a is fixed to:

$$M_a = \rho \frac{4\pi(R_2^3 - R_1^3)}{3}. \tag{37}$$

Letting R_1 be fixed, we consider two cases: a small R_2 with a dense atmosphere and a large R_2 with a thin atmosphere but the same atmospheric mass. As noted, the hydrostatic approximation still holds even in a stationary, thick atmosphere (with $R_2 \gg R_1$) so that the surface pressure depends only on gravity and the mass of atmosphere above it. As R_1 diminishes the surface pressure will increase linearly as $R_2 - R_1$ increases. However, at the same time the integral of the surface pressure will diminish rapidly, since the surface area varies as R_1^2 What then 'holds up' the atmosphere? The answer is that the atmosphere holds itself up, in the same way as an arched bridge holds itself up, as in the right-hand panel of Fig. 2.

In the more general case gravity diminishes with height, but this does not change the above argument in any essential way. If the rock below the atmospheric lower surface contributes to most of the planetary mass (M_p) the gravitational acceleration g is given by

$$g = \frac{GM_p}{r^2}, \tag{38}$$

where r is the distance from planet's center and G is the gravitational constant. Now, hydrostatic balance is expressed as

$$\frac{\partial p}{\partial r} = -\rho g \quad \Rightarrow \quad p_s = \int_{R_1}^{R_2} \rho g dr. \tag{39}$$

Note that p_s equals the integral for mass at each vertical layer (dr) without a weight factor of the surface area that scales as r^2. This means the contribution of atmospheric mass to the surface pressure gets smaller and smaller as r increases.

Substituting (37) and (38) into (39), we get an expression of p_s:

$$p_s = \int_{R_1}^{R_2} \rho g dr = GM_p \int_{R_1}^{R_2} \frac{\rho}{r^2} dr = GM_p \rho \left(\frac{1}{R_1} - \frac{1}{R_2} \right) = \frac{GM_p M_a}{(4\pi/3)(R_2^3 - R_1^3)} \left(\frac{1}{R_1} - \frac{1}{R_2} \right). \tag{40}$$

Introducing a shell thickness parameter $\delta \equiv R_2/R_1$, we rewrite (40) as:

$$p_s = \underbrace{\frac{GM_p M_a}{R_1^2}}_{\text{gravity}} \underbrace{\frac{1}{4\pi R_1^2}}_{\text{surface area}} \underbrace{\frac{3}{\delta(\delta^2 + \delta + 1)}}_{\text{thickness factor}}. \tag{41}$$

Equation (41) shows that p_s is determined by the gravity imposed on a given surface area, weighted by a thickness factor that decreases as δ increases. When the shell gets thicker, δ increases while holding R_1 constant, the surface pressure p_s reduces. This is because the lateral normal stress partially cancels out the gravity, analogous to an arch bridge.

When $\delta \approx 1$, the problem reduces to a thin atmosphere. The gravitational acceleration reduces to $g \approx GM_p/R_1^2$. Substituting this approximate expression of g into (41), we get:

$$\delta \approx 1: \quad p_s \approx \frac{gM_a}{4\pi R_1^2}. \tag{42}$$

That the surface pressure is proportional to the total mass in the air column is recovered. Note, though, that the essential result that the integral of surface pressure does not necessarily equal the mass of the atmosphere does not depend on the gravity diminishing with distance; it is true even for a constant value of g.

5 Geostrophic and Thermal Wind Balance

We now consider the scaling of the horizontal momentum equation

$$\frac{\partial \boldsymbol{u}}{\partial t} + (\boldsymbol{v} \cdot \nabla)\boldsymbol{u} + \boldsymbol{f} \times \boldsymbol{u} = -\frac{1}{\rho} \nabla p. \tag{43}$$

The advective terms scale as $(\boldsymbol{v} \cdot \nabla)\boldsymbol{u} \sim U^2/L$ and the Coriolis term scales as $\boldsymbol{f} \times \boldsymbol{u} \sim fU$. The ratio of the magnitudes of the advective and Coriolis terms is given by the Rossby number,

$$\text{Ro} = \frac{|\text{Inertial (or advective) term}|}{|\text{Coriolis term}|} = \frac{U}{fL}, \tag{44}$$

just as encountered in the previous section. When the Coriolis term is much larger than the advective terms ($Ro \ll 1$), the dominant balance of the horizontal momentum equation is then between the Coriolis term and the horizontal pressure force. This is called geostrophic balance (and 'geostrophy' is the state of geostrophic balance). In this case, rotation effects are important.

The geostrophic velocity components in Cartesian coordinates (x, y, z) are

$$fu = -\frac{1}{\rho}\frac{\partial p}{\partial y}, \quad fv = \frac{1}{\rho}\frac{\partial p}{\partial x}. \tag{45}$$

where u is the velocity in the zonal, or x direction and v is the velocity in the meridional, or y, direction. The velocity in the vertical, or z direction is conventionally denoted w. In the Boussinesq approximation, geostrophic balance is

$$fu = -\frac{\partial \phi}{\partial y}, \quad fv = \frac{\partial \phi}{\partial x}. \tag{46}$$

In pressure coordinates, the corresponding equations are

$$fu = -\left(\frac{\partial \varphi}{\partial y}\right)_p, \quad fv = \left(\frac{\partial \varphi}{\partial x}\right)_p. \tag{47}$$

Combining geostrophy with hydrostasy $\partial\phi/\partial z = b$, a vertical derivative of (46) yields

$$f\frac{\partial u}{\partial z} = -\frac{\partial b}{\partial y}. \tag{48}$$

In pressure coordinates the corresponding equation is

$$f\frac{\partial u}{\partial p} = \frac{R}{p}\frac{\partial T}{\partial y}. \tag{49}$$

An important implication is that the vertical shear is proportional to the horizontal buoyancy gradient, which in the Boussinesq approximation is proportional to the temperature gradient.

$$\text{zonal shear} : f\frac{\partial u}{\partial z} \sim \frac{R}{p}\frac{\partial T}{\partial y} : \text{meridional temperature gradient.} \tag{50}$$

Thus, a meridional temperature gradient (as is common on many planets) is associated with a vertical shear of the zonal wind.

6 The Thermal Rossby Number

We now introduce a key parameter for studying the atmospheric general circulation - the thermal Rossby number $\mathrm{Ro_T}$, which depends on the meridional temperature difference ΔT. This is most easily done in pressure coordinates

The thermal wind balance in pressure coordinates, $f\partial u/\partial p = (R/p)\partial T/\partial y$, suggests the scaling

$$\frac{fU}{\Delta P} \sim \frac{R}{P}\frac{\Delta T}{a} \tag{51}$$

where U is the zonal velocity scale, P is the surface pressure, ΔP the vertical pressure difference, R is the gas constant, and a is the planet's radius. If we take $\Delta P = P$ (since we are considering the whole depth of the atmosphere) we obtain

$$U \sim \frac{R\Delta T}{\Omega a}, \tag{52}$$

Substituting (51) into the definition of Rossby number (U/fL), and using Ω in place of f and a (the planet's radius) in place of L, we obtain

$$\mathrm{Ro_T} \equiv \frac{R\Delta T}{\Omega^2 a^2} \tag{53}$$

This is the thermal Rossby number, one of the most important nondimensional numbers in planetary science.

For Earth we have, approximately,

$$\mathrm{Ro_T} = \frac{R\Delta T}{\Omega^2 a^2} \approx \frac{300\ \mathrm{m^2\ s^{-2}\ K^{-1}} \times 40\ \mathrm{K}}{(10^{-4}\ \mathrm{s^{-1}})^2 \times (6 \times 10^6\ \mathrm{m})^2} \approx \frac{1}{30} \approx 0.03, \tag{54}$$

which is quite small, indicating that geostrophy dominates the atmospheric general circulation. In section 1.5, we study the zonally symmetric overturning in the tropics - the Hadley Cell. We will show that the latitudinal span of the Hadley Cell is proportional to $\mathrm{Ro_T}^{1/2}$.

7 The Hadley Cell

The Hadley Cell is the meridional overturning circulation in the Earth's tropical and subtropical atmosphere. It is driven by the meridional gradient of solar heating, which generates a thermally direct circulation (i.e., it is directly driven by heating and cooling). Here we briefly introduce a model of the Hadley Cell width developed by [2] following work by [3]. It is shown to be constrained by a dynamical requirement from angular momentum conservation and a thermodynamic requirement from radiative equilibrium. One feature of this model is that it can be expected to apply fairly generally to terrestrial atmospheres with low obliquity; indeed, it may be more applicable to slowly rotating (high thermal Rossby number) planets than it is to Earth, for baroclinic instabilities in the mid-latitudes (neglected in the model) are then less important. We leave the effects of such eddies, as well a description of planets with a high obliquity, to another day.

7.1 Angular momentum conservation

We will construct an axisymmetric model of the Hadley cell in a shallow atmosphere in which parcels above the boundary layer conserve their angular momentum. The specific angular momentum, m, of a parcel around a planets axis of rotation is

$$m = (u + \Omega a \cos\theta) a \cos\theta, \tag{55}$$

where u is the zonal wind, Ω is Earth's rotating angular velocity, a is Earth's radius, and θ is the latitude. We assume that the parcel is initially at rest high in the planet's tropopshere and then moves poleward, conserving its angular momentum. This is illustrated in Fig. 3. The parcel's angular momentum takes its initial (equatorial) value:

$$m_{eq} = \Omega a^2 \tag{56}$$

assuming $u = 0$ at $\theta = 0$. Letting $m = m_{eq}$ gives, at some latitude θ

$$m(\theta) = (u + \Omega a \cos\theta) a \cos\theta = \Omega a^2 \tag{57}$$

giving

$$u = \frac{\Omega a^2 (1 - \cos^2\theta)}{a \cos\theta} = \Omega a \frac{\sin^2\theta}{\cos\theta}. \tag{58}$$

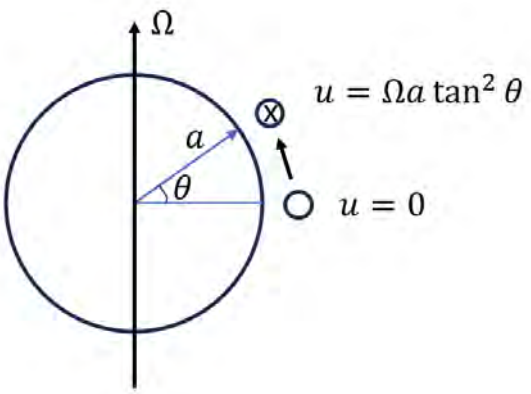

Figure 3: Schematic diagram showing the zonal velocity of a parcel that conserves its angular momentum as it moves poleward from the equator.

That is, u increases as the parcel moves poleward (i.e., as θ increases), giving rise to an eastward flow.

The expression of u can also be derived from the zonal momentum equation that is equivalent to angular momentum conservation. Under the assumption of axisymmetry and with no vertical advection the u equation may be written, in a steady state, simply as

$$(f + \zeta)v = 0, \tag{59}$$

where ζ is, as before, the vertical component of the relative vorticity, and in spherical coordinates $\zeta = -1/(a\cos\theta)\partial(u\cos\theta)/\partial\theta$. (The derivation of (59) is left to the reader.) Because the meridional velocity v is nonzero the absolute vorticity, $\zeta + f$, must be zero, which yields the simple expression: $\zeta = -f = 2\Omega\sin\theta$. We can solve u from ζ:

$$-\frac{1}{a\cos\theta}\frac{\partial u\cos\theta}{\partial\theta} = -2\Omega\sin\theta \quad \text{giving} \quad u = \Omega a\frac{\sin^2\theta}{\cos\theta}, \tag{60}$$

as before.

Because the poleward edge of the Hadley Cell is, on Earth, at about $\theta \sim 25°$N, then $\sin\theta \approx \theta$ and $\cos\theta \approx 1$, so that u can be simplified as:

$$u \approx \Omega a\theta^2. \tag{61}$$

7.2 The thermodynamic budget

Now we solve the meridional temperature of the poleward-moving parcel, invoking the thermal wind balance. As we recall, the thermal wind relation denotes the change of geostrophic wind with height due to horizontal temperature gradient, a consequence of the geostrophic balance and hydrostatic balance. Supposing the height of the polewards motion is H and that the wind increases from a state of rest at the surface, an approximate vertical finite-difference form of the thermal wind relation is

$$2\Omega\sin\theta\frac{u}{H} \sim -\frac{g}{T_0}\frac{1}{a}\frac{\partial T}{\partial\theta}. \tag{62}$$

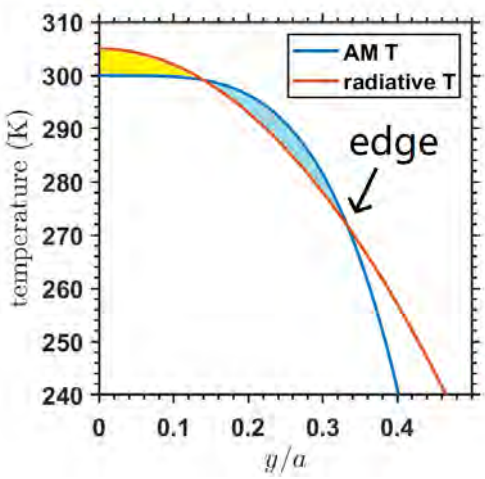

Figure 4: A schematic diagram for how the width of the Hadley Cell is calculated in the Held-Hou theory [2]. The blue line denotes the angular momentum temperature, and the red line denotes the radiative equilibrium temperature. Because there should not be net diabatic heating in a steady Hadley Cell, the area of the yellow region must equal that of the blue region.(In the text ϑ is used for temperature.)

Now, the wind, u, is given by (61), and for small values of θ $\sin\theta \approx \theta$. Using these values and integrating from the equator, (62) gives

$$T(\theta) = T(0) - \frac{\Omega^2\theta_0}{2gHa^2}y^4, \tag{63}$$

where $y = a\theta$ is the meridional distance away from the equator. (A similar expression may be obtained in pressure coordinates.) We might call this temperature the 'angular momentum temperature', because it is determined by the conservation of angular momentum in conjunction with the thermal wind relation.

At the same time the atmosphere is forced by radiation, and if the atmosphere is at rest the temperature is given by the radiative equilibrium temperature T_R, which rather approximately is given by

$$T_R(\theta) = T_{eq} - \Delta T_R\left(\frac{y}{a}\right)^2, \tag{64}$$

where T_{eq} is the radiative equilibrium temperature at the equator.

7.2.1 Solving for the Hadley Cell width

At very low latitudes the atmospheric temperature is lower than the radiative equilibrium temperature, yielding diabatic heating. Further polewards, in the subtropics, the temperature is higher than the radiative equilibrium, yielding diabatic cooling. If the Hadley Cell is a steady, closed circulation, there can be net diabatic heating within it, as illustrated in Fig. 4. Thus, to close the budget we require

$$\int_0^{y_H} \frac{T - T_R}{\tau} dy = 0, \tag{65}$$

where $y_H = a\theta_H$ defines the poleward edge of the Hadley Cell, and θ_H is as yet undetermined. Poleward of this the atmosphere is in radiative balance and $T = T_R$. We can then determine the

latitude of the edge of the Hadley Cell by solving the following constraints:

$$\int_0^{y_H} T dy = \int_0^{y_H} T_R dy = 0, \tag{66}$$

$$T(y_H) = T_R(y_H) \tag{67}$$

where T and T_R are given by (63) and (64) respectively. After some algebra we obtain

$$\theta_H = \frac{y_H}{a} = \left(\frac{2\Delta T g H}{\Omega^2 a^2 T_0} \right)^{1/2}, \tag{68}$$

which indicates that the Hadley Cell increases as Ω decreases. This may be written as

$$\theta_H = \left(\mathrm{Ro_T} \frac{2gH}{RT_0} \right)^{1/2} = \left(\mathrm{Ro_T} \frac{2H}{H_*} \right)^{1/2} \tag{69}$$

where Ro_T is the thermal Rossby number written as $R\Delta T/(\Omega^2 a^2)$and $H_* = RT_0/g$ is the atmospheric scale height.

7.2.2 A Variation

In the original formulation of the model above, the temperature is required to stay continuous at the edge of the Hadley Cell but its meridional gradient is discontinuous with the consequence that the zonal wind is discontinuous. An alternative formulation [1] posits that the zonal wind remain continuous and the temperature is allowed to have a discontinuity. Numerical simulations show that continuity of both fields is achieved by the presence of an overturning circulation poleward of the point of maximum zonal wind. Zonally symmetric simulations generally fall between the two sets of theoretical scalings. Three-dimensional simulations, which allow for the eddy motion that is missing from both theoretical models, tend to fall closer to the scalings of the variant model than the original theory, although neither theory is quantitatively satisfied even by axisymmetric simulations. At very low rotation rates the maximum zonal wind falls with falling planetary rotation rate, and is zero at zero rotation. The interested reader is referred to [1] for more detail.

7.3 Remark

Although the analysis above is informal and approximate, there is one robust conclusion, and it is that the extent of the Hadley Cell diminishes as the rotation rate of the planet diminishes. Thus, we might expect the Hadley Cell to extend further polewards in a planet like Venus, that has a slower rotation rate than Earth but is otherwise similar. In fact this is observed to be the case.

References

[1] G. Colyer and G. K. Vallis, Zonal-mean atmospheric dynamics of slowly-rotating terrestrial planets, J. Atmos. Sci., 76 (2019), pp. 1397–1418.

[2] I. M. Held and A. Y. Hou, Nonlinear axially symmetric circulations in a nearly inviscid atmosphere, J. Atmos. Sci., 37 (1980), pp. 515–533.

[3] E. K. Schneider, Axially symmetric steady-state models of the basic state for instability and climate studies. Part II: Nonlinear calculations, J. Atmos. Sci., 34 (1977), pp. 280–297.

[4] E. A. Spiegel and G. Veronis, On the Boussinesq approximation for a compressible fluid, Astrophys. J., 131 (1960), pp. 442–447. (Correction: *Astrophys. J.,* **135,** 655–656).

[5] G. K. Vallis, Atmospheric and Oceanic Fluid Dynamics, Cambridge University Press, Cambridge, U.K., 2nd ed., 2017.

[6] ——, Essentials of Atmospheric and Oceanic Dynamics, Cambridge University Press, Cambridge, U.K., 2019.

[7] A. A. White and R. Bromley, Dynamically consistent, quasi-hydrostatic equations for global models with a complete representation of the coriolis force, Quart. J. Roy. Meteor. Soc., 121 (1995), pp. 399–418.

GFD 2023 Lecture 4: Circulation of Tidally Locked Planets

Geoff Vallis; notes by Ellie Ong and Nathan Magnan

September 5, 2024

1 Introduction

This lecture focuses on the dynamics of tidally locked planets. These are planets that take just as long to rotate around their own axis as they do to orbit around their host star, and so have one side facing their host star at all times (the day side) and a side that never does (the night side). Tidal locking is almost inevitable for planets that are close to their host star. The process can be explained in the following way, as illustrated in Fig 1: (i) the gravitational pull from the star is not uniform over the planet, it is stronger on the star-facing side; (ii) this deforms the planet, which becomes an ellipsoid; (iii) if ever the major axis of this ellipsoid is not aligned with the star, the tidal forces add up to a net torque on the planet; (iv) the state that emerges is one of tidal locking, with the planet's major axis being aligned with the star.

Tidally locked planets can, in principle, be giant planets ('hot giants' in this case), or terrestrial planets, or some other form of planet. Many of them thus far are likely to be hot giants, although much of the theoretical and numerical development concerning their circulation has treated them more as terrestrial planets, partly for ease of numerical simulation. Although this may seem a little perverse, tidally locked planets are, like terrestrial planets, heated from above and it is this heating that drives the circulation that observations detect. This circulation is likely to penetrate only a small fraction of the planet's radius into the interior, although how far, and what the appropriate boundary conditions are at the base of the circulation, are not known. Since this lecture is but a first incursion into the dynamics of such systems let us not be overly ambitious. The objective of the present lecture is simply to estimate the broad circulation pattern that emerges from the permanent day-night forcing. It may later serve as a leading-order background flow upon which to study more intricate and dynamical effects.

In keeping with the Geophysical Fluid Dynamics (GFD) tradition, our strategy is to simplify the situation enough that we can study aspects of the problem analytically (where possible) and understand the relevant physics. First we work where possible in Cartesian coordinates (and in particular on the β-plane centered on the equator, a construction that will be described more fully later on) rather than on a true sphere. Then we assume the atmosphere is thin compared to the radius of the planet and use the shallow water equations (again, as explained more fully below). Finally we model the radiative heating from the star by imposing a high temperature in a circular patch positioned at the origin $(0, 0)$. This setup might remind some readers of the Matsuno–Gill problem, in which the atmospheric circulation responds to a sea surface temperature anomaly over the Earth's tropical Pacific [1]. But the other readers need not be scared, these lecture notes do not assume any prior knowledge of Matsuno & Gill's work.

First in §2 we study how the hot spot's information is transmitted eastward by Kelvin waves, then in §3 we show that information is also transmitted westward by Rossby waves. This is enough to estimate the steady state circulation induced by a small hot spot, in a simplified solution to the

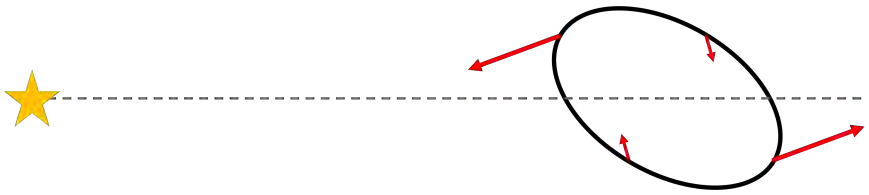

Figure 1: Schematic diagram of tidal torque. In orange is the star, in gray is the star-planet axis, and in black is the planet whose ellipsoid is misaligned with the star. The red arrows, which represent the tidal forces exerted at different points of the planet's surface, add to a non-zero torque acting in favor of alignment. A perfectly spherical planet with a uniform distribution of density would experience no tidal torque and would not become tidally locked.

Matsuno-Gill problem. In §4 we use this work to draw some basic conclusions about the circulation of tidally locked exoplanets. We also validate and extend our simple model using a global circulation model, and briefly discuss the effect of superrotation.

2 Kelvin Waves and the Kelvin Lobe

A single-layer, shallow water model is sufficient to capture the circulation induced by the hot spot. So, we remind the reader of the shallow-water equations in §2.1. Essentially, the hot spot is an unbalanced perturbation that pumps all sorts of waves, which then propagate away and transmit the hot spot's influence to the far field. In §2.2 we show that in the eastward direction the information is carried by Kelvin waves. To balance the constant input of energy from the hot spot, we need to invoke a dissipative process. In §2.3 we find that this dissipation damps the Kelvin waves, thereby limiting the hot spot's impact to a localized region called the Kelvin lobe.

2.1 The shallow water equations

Shallow water models consider the evolution of vertical fluid columns, thus reducing the dimension of the problem from 3D to 2D. Conventional shallow water models make three key hypotheses: that the fluid is of constant and uniform density ρ, that the fluid is in hydrostatic equilibrium, and that the horizontal velocity $\boldsymbol{u} = (u, v)$ only depends on the horizontal coordinates (x, y). These assumptions are not always satisfied but nevertheless provide a model that can make useful predictions.

There is a whole zoo of shallow water models: one could include topography, several fluid layers, or a lid at the top. But for the purpose of this lecture, we only need the simplest model, whose set-up is depicted in Fig. 2. Using Cartesian coordinates, x, y, where x increases in the zonal direction and y increases in the meridional direction, the equations of motion are

$$\frac{\partial h}{\partial t} + \boldsymbol{u} \cdot \nabla h + h \nabla \cdot \boldsymbol{u} = 0, \tag{1a}$$

$$\frac{\mathrm{D}u}{\mathrm{D}t} - fv = -g\frac{\partial h}{\partial x}, \tag{1b}$$

$$\frac{\mathrm{D}v}{\mathrm{D}t} + fu = -g\frac{\partial h}{\partial y}. \tag{1c}$$

On the sphere the Coriolis parameter, f, is a function of latitude and $f = 2\Omega \sin\theta$. We approximate that in Cartesian coordinates by letting $f = f_0 + \beta y$ and β is a constant; this is known as the β-plane approximation. Also, h is the height of the fluid layer, g is the acceleration due to gravity,

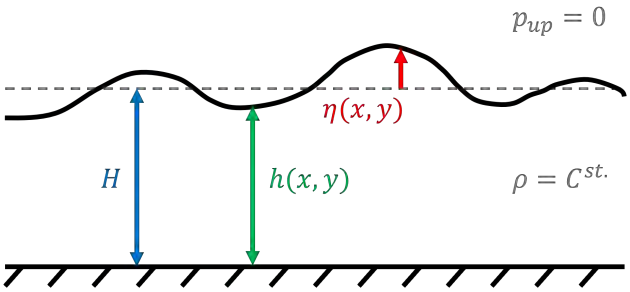

Figure 2: A shallow water model. We consider a single layer of density ρ, mean thickness H, local thickness h and elevation anomaly η. It sits on top of a solid surface of negligible topography, and below a fluid layer of negligible mass.

and the gradients ∇ are taken within the horizontal plane. If there is no bottom topography (as we assume) then $\nabla h = \nabla \eta$. These equations cannot capture sound waves, but can describe many of the large-scale phenomena that are of interest to geophysicists.

Since here we study a small-amplitude phenomenon, we can linearize these equations around the state of rest $\{h = H, \boldsymbol{u} = 0\}$ giving

$$\frac{\partial h}{\partial t} = -H \nabla \cdot \boldsymbol{u}, \tag{2a}$$

$$\frac{\partial u}{\partial t} - fv = -g \frac{\partial h}{\partial x}, \tag{2b}$$

$$\frac{\partial v}{\partial t} + fu = -g \frac{\partial h}{\partial y}. \tag{2c}$$

2.2 Equatorial Kelvin waves

Our shallow water model can potentially support both geostrophically balanced waves (and in particular Rossby waves, discussed below) and gravity waves (and in particular Kelvin waves) that may be out of geostrophic balance. In the linear approximation these waves will not interact with each other. Kelvin waves are a particular form of gravity wave that exists in the presence of rotation and a boundary, such as the equator, and let us first discuss them.

Equatorial Kelvin waves are solutions of the equations with the property that $v \simeq 0$. This characteristic allows us to simplify the equations to

$$\frac{\partial h}{\partial t} = -H \frac{\partial u}{\partial x}, \tag{3a}$$

$$\frac{\partial u}{\partial t} = -g \frac{\partial h}{\partial x}. \tag{3b}$$

The Coriolis parameter does not appear in these equations. The equations combine to give

$$\frac{\partial^2 u}{\partial t^2} = gH \frac{\partial^2 u}{\partial x^2}. \tag{4}$$

This wave equation is extremely simple (it is sometimes called *the* wave equation), and it indicates that two waves can propagate without dispersion and at velocity $c = \pm\sqrt{gH}$: one wave to the right (eastward) and one wave to the left (westward). In the most general form, we write the solution as

$$u_{\mathrm{E}}(x, y, t) = c\, F_{\mathrm{E}}(x - ct, y), \qquad \text{and} \qquad u_{\mathrm{W}}(x, y, t) = c\, F_{\mathrm{W}}(x + ct, y), \tag{5}$$

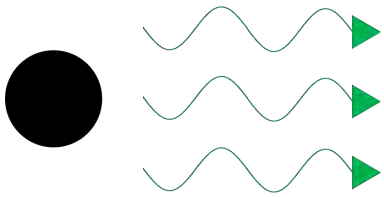

Figure 3: Schematic diagram of the situation. The black spot represent the hot spot, and Kelvin waves propagate eastward from it. With no dissipation the Rossby waves propagate all the way to infinity.

where $F_{\rm E}$ and $F_{\rm W}$ are dimensionless functions. Using either Eq. (3a) or Eq. (3b), we then get

$$h_{\rm E}(x,y,t) = H\,F_{\rm E}(x-ct,y), \qquad \text{and} \qquad h_{\rm W}(x,y,t) = -H\,F_{\rm W}(x+ct,y). \tag{6}$$

However, still need to satisfy the meridional momentum equation (2c), which gives

$$\frac{\partial F_{\rm E}}{\partial y} = \frac{-1}{L_{\rm d}} F_{\rm E}, \qquad \text{and} \qquad \frac{\partial F_{\rm W}}{\partial y} = \frac{1}{L_{\rm d}} F_{\rm E}, \tag{7}$$

where $L_{\rm d} = \sqrt{gH}/f$ is the 'Rossby deformation radius' (or just the deformation radius). However, f is not a constant: on a tangent plane we have in general $f = f_0 + \beta y$ and if we center the plane at the equator (giving the 'equatorial beta-plane') we take $f_0 = 0$. Thus, $L_{\rm d}$ is not constant and it is convenient to define the *equatorial* deformation radius,

$$L_\beta = \left(\frac{\sqrt{gH}}{\beta}\right)^{1/2} = \left(\frac{c}{\beta}\right)^{1/2}, \tag{8}$$

where $c = \sqrt{gH}$ is the gravity wave speed.

Eq. (7) are

$$\frac{\partial F_{\rm E}}{\partial y} = -\frac{\beta y}{c} F_{\rm E}, \qquad \text{and} \qquad \frac{\partial F_{\rm W}}{\partial y} = \frac{\beta y}{c} F_{\rm W}, \tag{9}$$

with solutions

$$F_{\rm E}(x-ct,y) = \tilde{F}_{\rm E}(x-ct)\,\exp\left[-y^2/(2L_\beta)^2\right], \tag{10}$$

and

$$F_{\rm W}(x+ct,y) = \tilde{F}_{\rm W}(x+ct)\,\exp\left[+y^2/(2L_\beta)^2\right]. \tag{11}$$

The westward propagating wave is evidently unphysical, for its amplitude diverges with y, and only the eastward propagating mode remains.

It is interesting to wonder why Kelvin waves can only propagate eastward. In the direction perpendicular to the direction of travel of the wave, namely the meridional direction, the flow is in geostrophic balance with

$$fu = -g\frac{\partial h}{\partial y}. \tag{12}$$

Consider the flow under a fluid crest in an equatorial Kelvin wave, as illustrated in Fig. 4. The pressure gradient force is directed away from the equator and, if the wave is travelling eastward the pressure force can balanced by the Coriolis force directed toward the equator. Under a trough the fluid is flowing in the opposite direction to the wave itself, and both the pressure gradient force and the Coriolis force are reversed and geostrophic balance still holds. If the wave were to travel westwards, no such balances could be achieved.

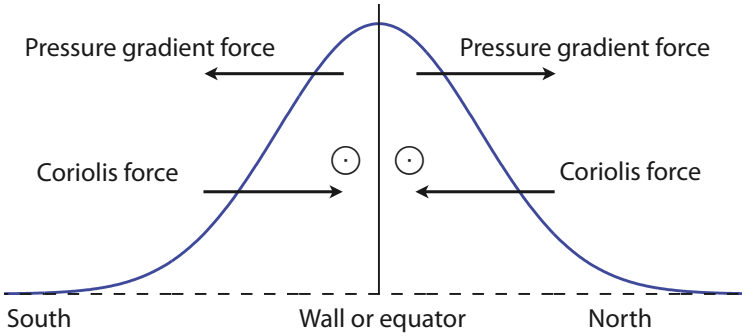

Figure 4: Balance of forces across a Kelvin wave. The solid line is the fluid surface and the phase speed is directed out of the page. Beneath a crest the fluid flow is in the direction of the phase speed and produces Coriolis forces as shown, so balancing the pressure gradient forces. If the wave were travelling in the opposite direction no such geostrophic balance could be achieved.

2.3 The eastward Kelvin lobe

Section 2.2 might seem to imply that Kelvin waves would propagate from the hot spot all the way to infinity. But it is much more reasonable to think that there is some dissipative effect of one form or another that is going to damp the Kelvin waves as they propagate. So let us adopt a crude model of the dissipation: we assume it scales with the amplitude of the wave and a single parameter the dissipation rate α. The shallow water equations become

$$\frac{\partial h}{\partial t} = -H\,\nabla\cdot\boldsymbol{u} - \alpha h, \tag{13a}$$

$$\frac{\partial u}{\partial t} - fv = -g\,\frac{\partial h}{\partial x} - \alpha u, \tag{13b}$$

$$\frac{\partial v}{\partial t} + fu = -g\,\frac{\partial h}{\partial y} - \alpha v. \tag{13c}$$

The secular dynamics of the system seem quite simple: as we 'turn on' the hot spot, the Kelvin waves start to propagate eastward and dissipate as they travel. The layer thickness, which may be taken as a proxy for temperature, increases in the region just east of the hot spot until a balance between the heating and dissipation is reached. At steady state and in the absence of meridional motion, Eqs. (13) become

$$\alpha h = -H\,\frac{\partial u}{\partial x}, \tag{14a}$$

$$\alpha u = -g\,\frac{\partial h}{\partial x}, \tag{14b}$$

$$fu = -g\,\frac{\partial h}{\partial y}. \tag{14c}$$

We can combine (14a) with (14b) to obtain

$$\frac{\partial^2 h}{\partial x^2} = \left(\frac{\alpha}{c}\right)^2 h, \tag{15}$$

whose general solution is

$$h(x,y) = \tilde{h}_+(y)\,\mathrm{e}^{-\alpha x/c} + \tilde{h}_-(y)\,\mathrm{e}^{+\alpha x/c}. \tag{16}$$

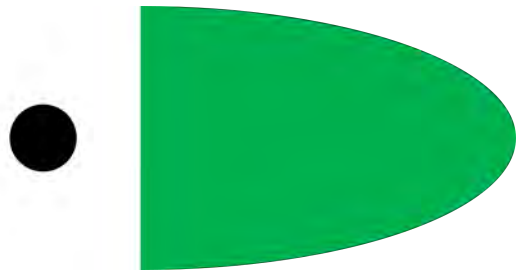

Figure 5: Schematic of a steady Kelvin lobe (in green), east of the forcing location (dark circle). In Fig. 3 we sketched a propagating wave; once we include dissipation, we obtain a steady pattern called the Kelvin 'lobe'.

In order to ensure that the wave amplitude is bounded the $\tilde{h}_-$ term must be null. (This is the same argument that we used to discard the westward wave in Eq. (10).) Therefore, the steady-state solution is

$$\forall x > 0 : \qquad h(x,y) = h_0 \, \mathrm{e}^{-1/2(y/L_\beta)^2} \, \mathrm{e}^{-\alpha x/c}. \tag{17}$$

This elevation pattern is called the **Kelvin lobe**, and is illustrated in Fig. 5. Note that we have not provided a full solution here – we have not specified the nature of the wave source for example, so the above solution applies eastward of that source source.

3 Rossby Waves and the Rossby Lobes

As announced earlier, we need to understand how the hot spot's information is transmitted westward. The key actors in that regard are Rossby waves, which are most easily extracted from the quasi-geostrophic shallow-water equations in an equatorial setting. So let us first derive these equations §3.1, then the Rossby wave solution in §3.2, and finally turn on the α damping in §3.3.

3.1 The equatorial quasi-geostrophic shallow water equations

We can start again from the linearised shallow water equations:

$$\frac{\partial u}{\partial t} - fv = -g \frac{\partial h}{\partial x}, \tag{18a}$$

$$\frac{\partial v}{\partial t} + fu = -g \frac{\partial h}{\partial y}, \tag{18b}$$

$$\frac{\partial h}{\partial t} = -H \, \nabla \cdot \boldsymbol{u}. \tag{18c}$$

These are, respectively, the zonal-momentum equations in the x- and y-directions and the height equation, which is the thermodynamic equation for this system. As before, the Coriolis parameter varies as $f = \beta y$, and $c^2 = gH$ is the gravity wave speed. Following [7] we take the curl of the (vectorial) shallow water momentum equation (18a, 18b) and arrive at

$$\frac{\partial \zeta}{\partial t} + f \left(\frac{\partial u}{\partial x} + \frac{\partial v}{\partial y} \right) + \beta v = 0, \tag{19}$$

where $\zeta = \partial_x v - \partial_x y$ and $f = \beta y$. By substituting the divergence term in (19) with the time evolution of surface elevation in (18c), we arrive at the linearized shallow water potential vorticity

equation

$$\frac{\partial}{\partial t}\left(\zeta - \frac{f}{H}\,h\right) + \beta v = 0. \tag{20}$$

We now assume the flow is divergence free. This is identially true if the flow is geostrophically balanced with a constant Coriolis parameter, but since the Coriolis parameter varies here this should be regarded as an additional assumption. We can then define a stream function ψ such that

$$u = -\frac{\partial \psi}{\partial y} \qquad \text{and} \qquad v = \frac{\partial \psi}{\partial x}. \tag{21}$$

The relative vorticity is then given by

$$\zeta = \nabla^2 \psi \tag{22}$$

and, if the flow is also in geostrophic balance, the height field is given by

$$h = \frac{f}{g}\,\psi. \tag{23}$$

Substituting these expressions into the potential vorticity equation (20) gives

$$\frac{\partial}{\partial t}\left(\nabla^2 \psi - \frac{f^2}{gH}\psi\right) + \beta \frac{\partial \psi}{\partial x} = 0, \tag{24}$$

which is a linearized, quasi-geostrophic, shallow-water, potential vorticity equation, although here we are allowing f to vary as $f = \beta y$.

3.2 Rossby waves

We can seek wavelike solutions of this in the form

$$\psi = \widetilde{\psi}(y) \mathrm{e}^{\mathrm{i}(kx - \omega t)}, \tag{25}$$

and (24) becomes

$$\frac{\mathrm{d}^2 \widetilde{\psi}}{\mathrm{d}y^2} - \left(k^2 + \frac{\beta k}{\omega} + \frac{\beta^2 y^2}{c^2}\right)\widetilde{\psi} = 0. \tag{26}$$

Some algebra is required to obtain a solution (the reader may consult [6]) but we finally obtain

$$\omega = \frac{-\beta k}{(2m+1)\beta/c + k^2}, \tag{27}$$

(where c is still $\sqrt{gH}$), which is a dispersion relation for equatorial Rossby waves. The phase speed is always negative, meaning that Rossby waves only propagate westward, as in Fig. 6.

3.3 The westward Rossby lobe

Following the same method as in §2.3, now we want to add a linear damping term in the momentum and thermodynamic equations. This is explicitly written as

$$\frac{\partial u}{\partial t} - fv = -\frac{\partial \phi}{\partial x} - \alpha_m u, \tag{28a}$$

$$\frac{\partial v}{\partial t} + fu = -\frac{\partial \phi}{\partial y} - \alpha_m v, \tag{28b}$$

$$\frac{\partial \phi}{\partial t} = -gH\,\nabla \cdot \boldsymbol{u} - \alpha_\phi\,\phi - Q, \tag{28c}$$

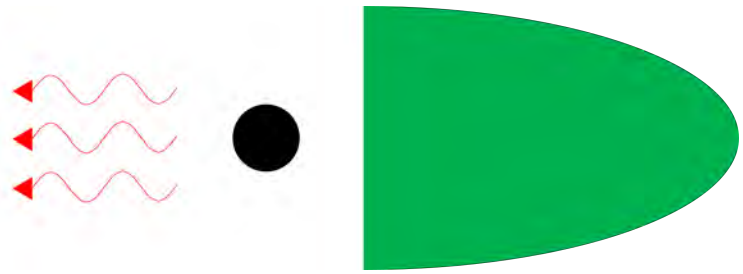

Figure 6: Schematic diagram of the situation, using the same drawing rules as Fig. 3 but adding that anything red is related to Rossby waves. At this stage of the derivation, they simply carry the hot spot's influence all the way to the western infinity.

where the αs are damping rates, $\phi = gh$ is proportional to layer thickness, and Q is a thermodynamic source. We keep the time-dependence for familiarity, but will shortly seek steady solutions. For now we assume the momentum and thermal damping rates are equal and that there is no heating, but we will relax these assumptions later on.

Applying the same method as in §3.2, we obtain the vorticity equation

$$\left(\frac{\partial}{\partial t} + \alpha\right)\left(\zeta - \frac{(\beta y)^2}{c^2}\psi\right) + \beta v = 0. \tag{29}$$

where, as before, $f = \beta y$. Let us now suppose that the divergence is small and that the velocity, vorticity and height fields can all be written in terms of a stream function,

$$u = -\frac{\partial \psi}{\partial y}, \qquad v = \frac{\partial \psi}{\partial x}, \qquad \zeta = \nabla^2 \psi, \qquad \phi = f\psi, \tag{30}$$

giving

$$\left(\frac{\partial}{\partial t} + \alpha\right)\left(\nabla^2 - \frac{(\beta y)^2}{gH}\right)\psi + \beta\,\frac{\partial \psi}{\partial x} = 0. \tag{31}$$

This equation may be put into a standard form by using the substitution $\psi = \Psi \exp(-\hat{y}^2/2)$ (and we may note the connection to the solution for the stationary Kelvin wave). With this substitution, (31) becomes

$$\frac{\mathrm{d}^2\Psi}{\mathrm{d}\hat{y}^2} - 2\hat{y}\;\Psi + \left(\hat{k}^2 + \frac{\hat{k}}{\hat{\alpha}} - 1\right)\Psi = 0. \tag{32}$$

Eq. (32) is known as Hermite's equation. If we let $\lambda = (\hat{k}^2 + \frac{\hat{k}}{\hat{\alpha}} - 1)$ then the solution is Hermite polynomials $\Psi(\hat{y}) = H_m(\hat{y})$ with $\lambda = 2m$ and

$$(H_0, H_1, H_2, H_3, H_4) = (1,\ 2\hat{y},\ 4\hat{y}^2 - 2,\ 8\hat{y}^3 - 12\hat{y},\ 16\hat{y}^4 - 48\hat{y}^2 + 12). \tag{33}$$

The values of k are quantized by this condition; that is to say

$$\left(\hat{k}^2 + \frac{\hat{k}}{\hat{\alpha}}\right) = 2m + 1, \tag{34}$$

or, in dimensional form,

$$\left(c^2k^2 + \beta c^2\frac{k}{\alpha}\right) = (2m+1)\beta c. \tag{35}$$

This is analogous to the dispersion relation for low frequency waves when time-dependence but not dissipation is included, namely

$$-c^2k^2 - \beta\frac{kc^2}{\omega} = (2m+1)\beta c. \tag{36}$$

The difference is that (36) is generally regarded as an equation for the frequency, given the spatial dependence. In (35) the decay rate, α, is a given physical parameter and the equation then yields the spatial rate of decay.

The solutions are symmetric or antisymmetric around $y = 0$ according as to whether m is even or odd, respectively. If we recall that $\psi = \phi/f$ then mirror symmetry (i.e., $\phi(y) = \phi(-y)$) implies that m has to be odd. The solution for the gravest mode, $m = 1$, then has the form,

$$\phi = \phi_0 \exp(-\beta y^2/2c) y^2 \exp(kx), \tag{37}$$

where k is given by the solution of (36), and $\phi = 0$ for $x > 0$ to satisfy boundedness at infinity. If we further simplify to the small-wavenumber case, and neglect the term in k^2 (36), then, for any m have $k = (2m+1)\alpha/c$ and for the gravest mode $k = 3\alpha/c$. The solution is then

$$\phi = \begin{cases} \phi_0 y^2 \exp(-\beta y^2/2c)\exp(3\alpha x/c), & x < 0 \\ 0. & x > 0. \end{cases} \tag{38}$$

In this case the decay rate is precisely three times as rapid as it is for the decaying Kelvin mode given by (17). Also, and importantly, the solution decays in the *westward* direction, reflecting the westward propagation of Rossby waves. East of the wave source there is no disturbance, and there is no Rossby wave propagation at the equator.

Taken together, (38) and (17) comprise the Gill solution away from the source region; that is, they are the solution to the homogeneous problem. These, and as the full solution obtained by adding the particular solution with a particular source confined about the origin, are illustrated in Fig. 8.

Combining the Rossby and Kelvin wave solutions to the localized hot spot on a hypothetical tidally locked planet, we obtain an approximate solution of the Matsuno-Gill problem. Qualitatively, the equatorial Kelvin waves induce eastward propagation originating from the hot spot and decaying at a rate of c/α, forming a Kelvin lobe extending East from the origin. The Rossby wave carries influence westward but decays more quickly than the Kelvin wave and forming two smaller Rossby lobes, one on each side of the equator: the leading order Rossby wave solution is null at the equator, but has a maximum offset from the equator by $y \approx 2c/\beta$. The upper panel of Fig. 8 shows the approximate solution to the Gill problem, treating the Rossby and Kelvin waves separately, and the lower panel shows the complete solution, including the solution in the vicinity of the source

4 Exo-Planet Considerations

The situation on tidally locked exoplanets differs in a number of ways from that considered above (and from the original problems considered by Matsuno and Gill). The main differences are likely to be:

- The thermal forcing is quite large scale. Heating can be expected to be at a maximum at the sub-stellar point, but extending considerably in both the zonal and meridional directions from there.

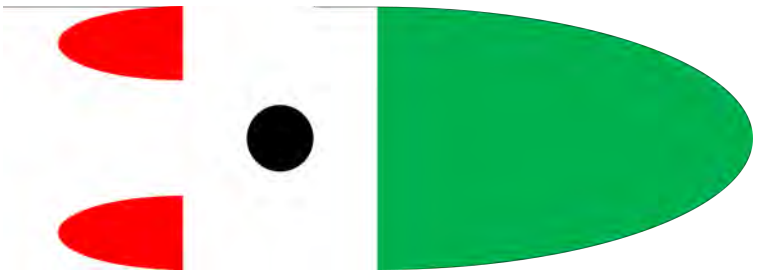

Figure 7: Schematic diagram of the solution to the Gill problem, using the same drawing rules as Fig. 3 and Fig. 6.

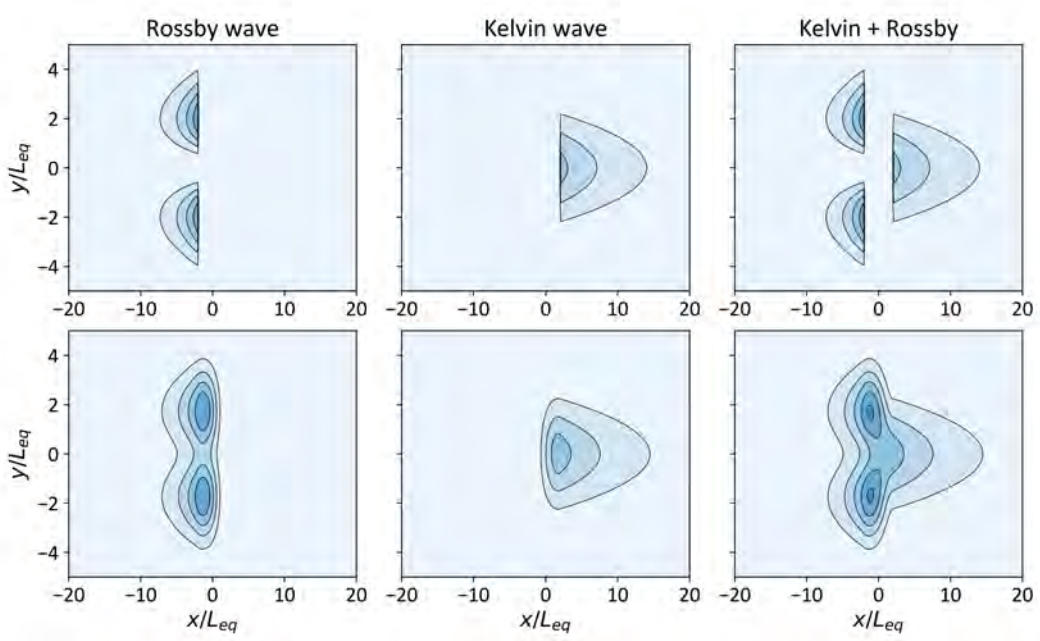

Figure 8: Top: Approximate solution to the Gill problem, treating the Kelvin and Rossby Wave solutions separately and approximately. Bottom: The complete solution. Solutions are given away from the origin in the top plot, and everywhere in the bottom plot. The approximate solution is that obtained in the text here and is a 'far-field' solution that does not depend on the details of the forcing. The full solution requires considerably more algebra and depends on the precise form of the forcing. See [1].

- Most tidally locked planets, unless they are in an extremely close orbit to their host star, will have a slower rotation rate than Earth, with a correspondingly large radius of deformation. The mid-latitude deformation radius in a stratified atmosphere is NH/f, where N is the Brunt-Väisälä frequency and H is a characteristic vertical scale. In a shallow water model the corresponding deformation scale is $\sqrt{gH}/f$ where H is the thickness of the layer. Similar considerations apply to the equatorial deformation radius. In all cases, the deformation radius increases as rotation rate diminishes.

- The momentum dissipation may be noticeably weaker than the thermal dissipation. On a gas giant the fluid in the gaseous weather layer overlays another fluid (or simply gets more

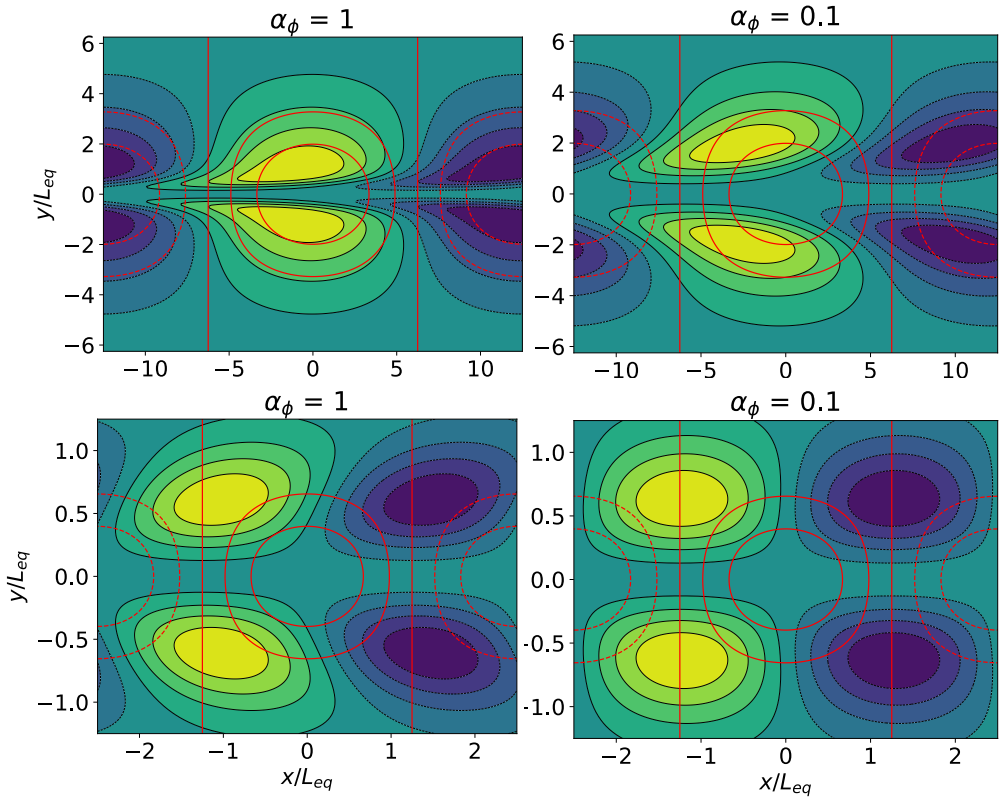

Figure 9: Analytic solutions of the linear shallow water equations showing the steady response of the height field to a stationary, tidally locked, thermal forcing with zero momentum damping and various values of thermal damping coefficient, α_ϕ and deformation radius L_{eq}, relative to the size of the planet. Length scales are nondimensionalized by L_{eq}, so that larger values in the x and y axes indicate a larger planet or smaller deformation radius. The red contours show the location of the heating, with solid contours positive, and the lighter shading (the yellows) correspond to higher temperatures.

dense with depth) rather than overlaying a solid or liquid with a rough surface. The frictional dissipation may then be relatively small, whereas the thermal dissipation may remain large. This difference can lead to noticeable differences in the phase of the Rossby wave response. In some contrast the Kelvin wave response may be only quantitatively altered: with separate damping coefficients for momentum (α_m) and height α_ϕ then the only change in the Kelvin-wave solution is that α^2 is replaced by $\alpha_\phi\alpha_m$.

- The stratification of exo-planetary atmospheres is not known and will depend on both the level at which solar heating occurs and the composition of the atmosphere. This then affects the deformation radius.

We will now discuss some of these effects.

4.1 Approximate Analytic Solution

To explore parameter space generally requires a numerical approach, but we can make some headway by obtaining an approximate analytic solution in some special cases. We will assume that the zonal

wind is in geostrophic balance with the meridional pressure gradient (this is called the longwave approximation, for reasons we do not delve into), but we allow different thermal and momentum damping rates. The governing equations are then, for a steady state and in the linear approximation,

$$\alpha_m u - fv + \frac{\partial \phi}{\partial x}, \quad fu + \frac{\partial \phi}{\partial y} = 0, \quad \alpha_\phi \phi + c^2 \left(\frac{\partial u}{\partial x} + \frac{\partial p}{\partial y} \right) = Q, \tag{39a,b,c}$$

where α_m and α_ϕ are the momentum and thermal damping rates, respectively, and we imagine $Q(x, y)$ to be a heating term provided by the planet's star, and thus centered at the substellar point which we take to be at $x = y = 0$. With a little bit of algebra we obtain a single equation for ϕ, namely

$$\frac{f^2}{c^2}\alpha_\phi \phi - \beta \frac{\partial \phi}{\partial x} - \alpha_m \frac{\partial^2 \phi}{\partial y^2} + \alpha_m \frac{2\beta}{f} \frac{\partial \phi}{\partial y} = \frac{f^2}{c^2} Q. \tag{40}$$

On the equatorial β-plane $f = \beta y$ and $k_{eq} = (\beta/c)^{1/2} = L_{eq}^{-1}$ so that the above equation may be written

$$k_{eq}^4 y^2 \alpha_\phi \phi - \beta \frac{\partial \phi}{\partial x} - \alpha_m \frac{\partial^2 \phi}{\partial y^2} + \alpha_m \frac{2\beta}{f} \frac{\partial \phi}{\partial y} = k_{eq}^4 y^2 Q. \tag{41}$$

This equation is hard to solve in full generality, but we can at least eliminate the explicit x dependence by expanding ϕ and Q as Fourier modes; that is, we let

$$\phi(x, y) = \Re \widetilde{\phi}(y) \exp(\mathrm{i}kx), \qquad Q(x, y) = \Re \widetilde{Q}(y) \exp(\mathrm{i}kx), \tag{42}$$

or a sum of such Fourier modes, whence (and henceforth omitting the $\Re$ decorator)

$$\left(\alpha_\phi k_{eq}^4 y^2 - \mathrm{i}k\beta\right)\widetilde{\phi} + \alpha_m \frac{\partial^2 \widetilde{\phi}}{\partial y^2} + \alpha_m \frac{2\beta}{f} \frac{\partial \widetilde{\phi}}{\partial y} = k_{eq}^4 y^2 \widetilde{Q}(y). \tag{43}$$

Let us now neglect the friction terms involving α_m, giving

$$\left(\alpha_\phi k_{eq}^4 y^2 - \mathrm{i}k\beta\right)\widetilde{\phi} = k_{eq}^4 y^2 \widetilde{Q}(y), \tag{44}$$

with solution

$$\widetilde{\phi} = \frac{\widetilde{Q}_\phi(y)\ k_{eq}^4 y^2}{\alpha_\phi k_{eq}^4 y^2 - \mathrm{i}k\beta}, \tag{45}$$

or with nondimensional variables

$$\widehat{\widetilde{\phi}} = \frac{\widetilde{Q}_\phi(y)\ \hat{y}^2}{\hat{\alpha}_\phi \hat{y}^2 - \mathrm{i}\hat{k}}. \tag{46}$$

Approaching the equator the variations thus become completely out of phase with the forcing, although at the same time the response weakens. For small enough thermal damping the height field will be in quadrature with the thermal forcing over most of the planet. Various solutions with different damping can be seen in Fig. 9 and Fig. 10. The length scales are nondimensionalized by the equatorial deformation radius $\sqrt{c/\beta}$, so solutions with apparently smaller scales can be considered to be either more slowly rotating or to be smaller, or to be more strongly stratified. For comparison, Earth with a rotation period of about 24 hours and a stratification corresponding to a buoyancy frequency of about 10 minutes has a gravity wave speed of about 20 m s^{-1} and an equatorial deformation radius of about 1000 km, giving an equatorial circumference of about 40 such radii.

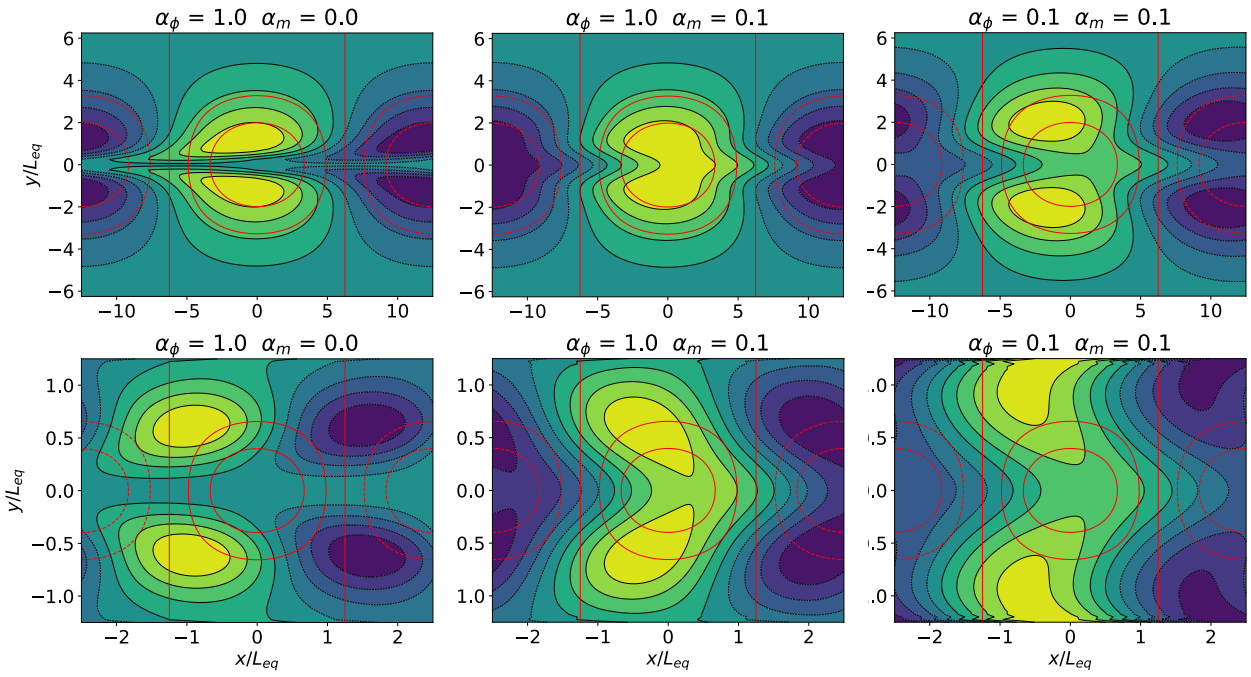

Figure 10: Similar to Fig. 9, but now showing full numerical solutions to the linear shallow water equations for various values of thermal and momentum damping coefficients α_ϕ and α_m . The panels with $\alpha_m = 0$ have the same parameters as the equivalent panels in Fig. 9.

5 Super-rotation

Super-rotation, or superrotation, is the term used to describe the situation where the relative equatorial flow is eastward, or equivalently when equatorial fluid parcels rotate faster than the planet. Such a flow might be expected to displace the hottest regions East of the sub-stellar point, as in Fig. 10. These displaced hot spots on hot Jupiters have also been predicted in various more complete simulations (e.g. [4]) and observed [3].

Prograde equatorial jets can be generated by Rossby waves propagating away from the region of their generation. However, we need to generate Rossby waves for this to be a viable mechanism. In midlatitudes on Earth-like atmospheres Rossby waves arise as a product of baroclinic instability, but there is no obvious mechanism to generate Rossby waves at the equator. In slowly rotating planets it seems that superrotation arises because of an interaction between Rossby waves and Kelvin waves that generates an instability that converges eastward momentum toward the equator. Specifically, stationary patterns illustrated in Fig. 10 suggest that off equatorial eddies may have a tilted structure and thus might converge momentum toward the equator, as in Fig. 11. Interested readers should consult the report by Q. Nicolas in this volume.

6 Conclusion

In this lecture we gave an introduction to the circulation of tidally locked planets, and among them will be hot Jupiters, super-Earths and sub-Neptunes. We spent most of our time on a horizontal circulation pattern similar to [1]. These patterns can, in some circumstances, give rise to superrotation and that superrotation is often posited to be responsible for (or is be least consistent with) the observed shift between the hottest point and the sub-stellar point [3]. A schematic of the components

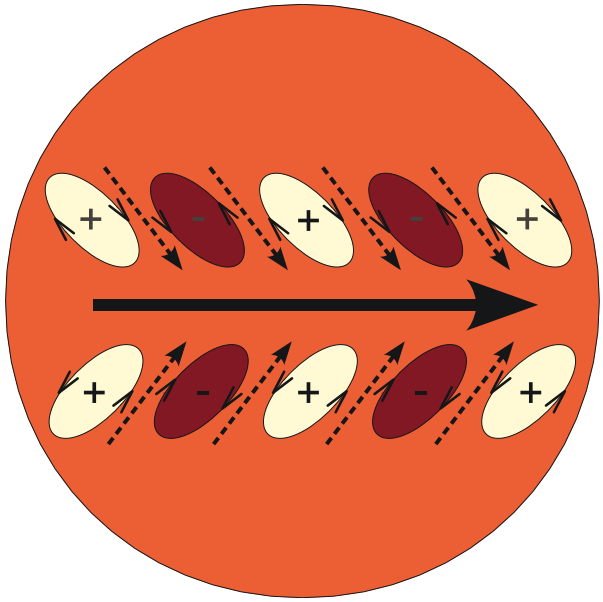

Figure 11: Schematic of the generation of superrotation in a tidally locked planet. The tilted off-equatorial eddies, perhaps similar to those in Fig. 10, converge eastward momentum toward the equator, so producing superrotation, provided that nonlinear effects are included. (From [5].)

of the general circulation on a tidally locked planet is given in Fig. 12.

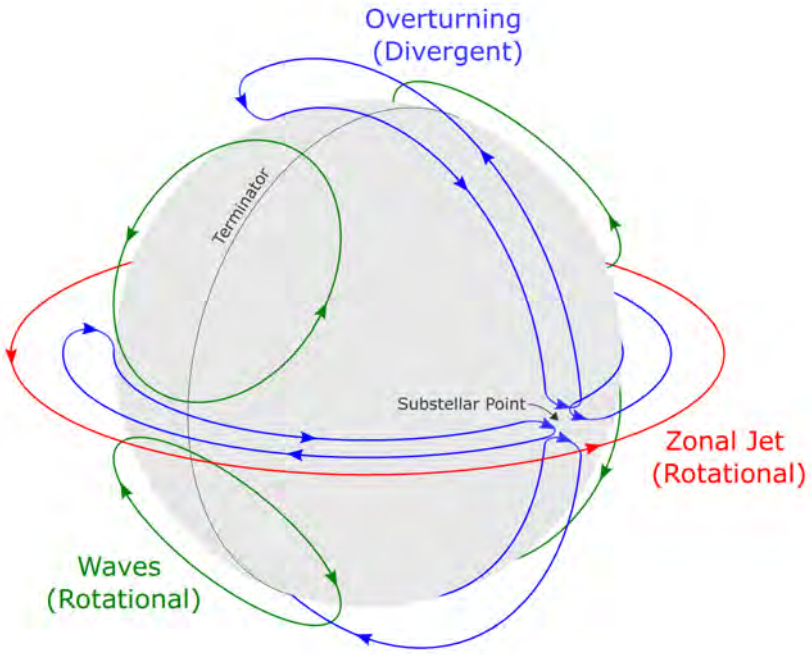

Figure 12: Schematic diagram from [2], outlining the rotational and divergent components of circulation on a tidally locked planet, driven by the horizontal temperature gradients.

References

[1] A. E. Gill, Some simple solutions for heat induced tropical circulation, Quart. J. Roy. Meteor. Soc., 106 (1980), pp. 447–462.

[2] M. Hammond and N. T. Lewis, The rotational and divergent components of atmospheric circulation on tidally locked planets, Proc. Nat. Acad. Sci., 118 (2021), p. e2022705118.

[3] H. A. Knutson, D. Charbonneau, L. E. Allen, J. J. Fortney, E. Agol, N. B. Cowan, A. P. Showman, C. S. Cooper, and S. T. Megeath, A map of the day–night contrast of the extrasolar planet HD 189733b, Nature, 447 (2007), pp. 183–186.

[4] A. P. Showman and T. Guillot, Atmospheric circulation and tides of "51 Pegasus b-like" planets, Astro. & Astrophys., 385 (2002), pp. 166–180.

[5] A. P. Showman and L. M. Polvani, Equatorial superrotation on tidally locked exoplanets, Astrophys. J, 738 (2011), pp. 1–24.

[6] G. K. Vallis, Atmospheric and Oceanic Fluid Dynamics, Cambridge University Press, Cambridge, U.K., 2nd ed., 2017.

[7] W. T. M. Verkley and I. R. V. D. Velde, Balanced dynamics in the tropics, Quart. J. Roy. Meteor. Soc., 136 (2010), pp. 41–49.

GFD 2023 Lecture 5: Observations of Atmospheric Circulation on Short-period Gas Giants

Heather Knutson; notes by Nimrod Gavriel and Quentin Nicolas

March 27, 2025

This lecture focuses on the observations of short-period gas giants, also known as hot Jupiters (HJs). More specifically, we ask what aspects of the global atmospheric circulation of these planets can be inferred from these observations.

1 Comparing the Properties of Our Jupiter and Hot Jupiters

Being faraway from its host star, Jupiter receives little external radiation, and its dynamics are thus also driven by comparable internal heating. Hot Jupiters, in contrast, are so strongly irradiated that any internal heat flux is negligible in their global energy balance. The thermal structure of gas giants can be approximated by a layer in radiative equilibrium overlying a deep convective layer. The depth at which the transition occurs is widely different between Jupiter and HJs: In Jupiter, the internal heat flux and weak irradiation keep its radiative layer above $P \simeq 1$ bar. By contrast, in HJs, it reaches as deep as 100 to 1000 bar. The infrared photosphere for Jupiter lies around 300 mbar, which means we do see through its convective layer [7]. Comparatively, we cannot "see" deeper than 0.1 bar in the atmospheres of HJs, i.e. observations are limited to the very top of their radiative layers[1].

HJs are widely believed to be tidally locked due to their close proximity with their host star. Their rotation period is thus equal to their orbital period, typically around 1 to 3 days. Combined with estimates of characteristic large-scale wind speeds from GCMs (and observations, see section 3.2) and using the radius of Jupiter as a characteristic length, this yields a Rossby number estimate of

$$Ro_{\mathrm{HJ}} \simeq \frac{1000 \text{ m/s}}{7 \times 10^7 \text{ m} \times 1.4 \times 10^{-5} \text{ s}^{-1}} \simeq 1. \tag{1}$$

In contrast, Jupiter's rotation period is around 0.4 Earth days, which puts it in a strongly rotating regime:

$$Ro_{\mathrm{J}} \simeq \frac{40 \text{ m/s}}{7 \times 10^7 \text{ m} \times 3.6 \times 10^{-4} \text{ s}^{-1}} \simeq 0.02. \tag{2}$$

Jupiter and HJs are thus in a vastly different dynamical regime.

[1] The optical depth profile of a planet's atmosphere can be inferred from assumptions on the chemical species that compose it (themselves predicted from elemental abundances in the host star) and its temperature structure. For HJs, unit optical depth is usually around 0.1 bar.

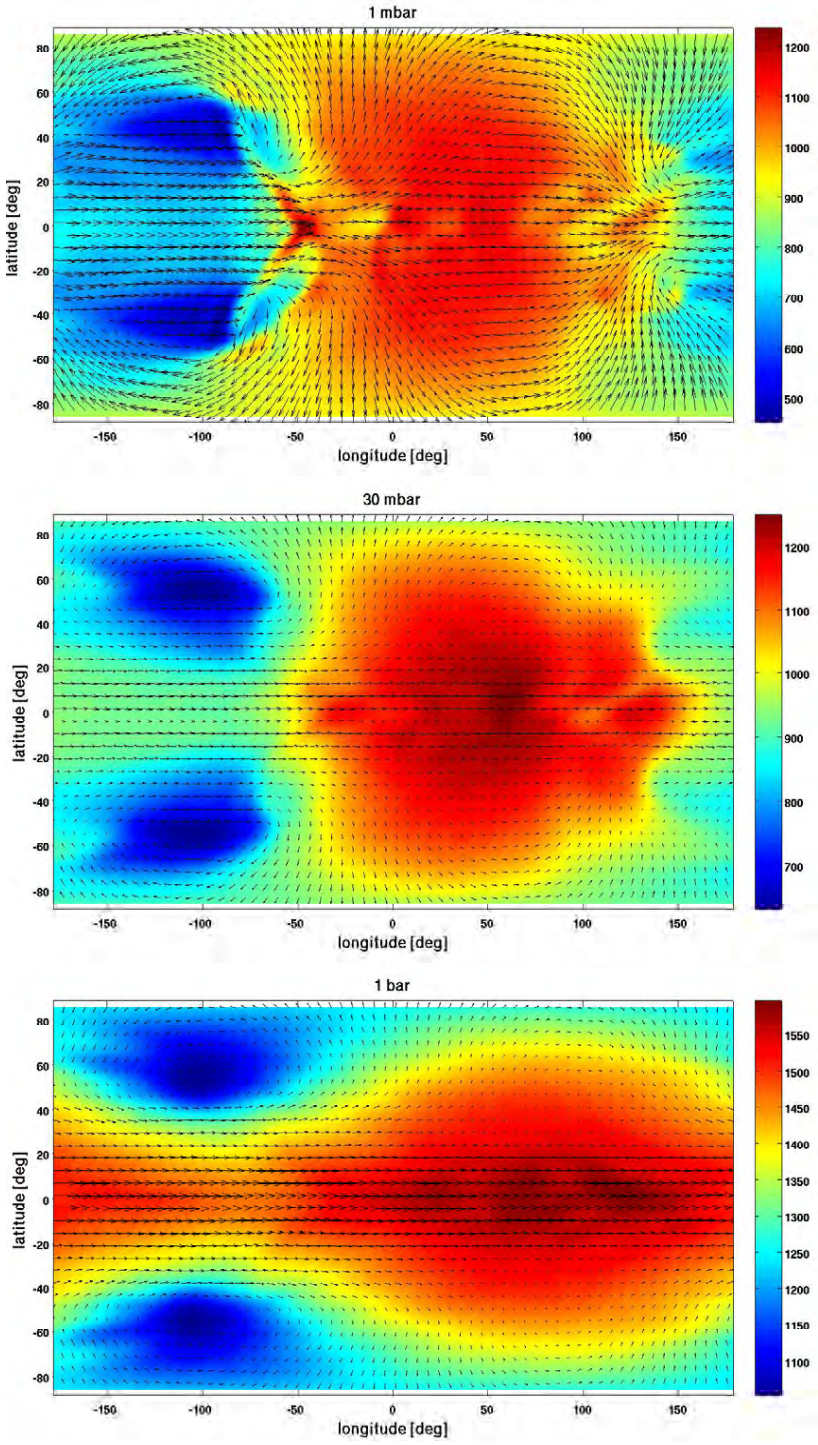

Figure 1: Taken from Showman et al., (2009)[8]. Simulation results for a hot Jupiter (from a coupled radiative-dynamical general circulation model at $\sim 2.5°$ resolution). Color is the temperature (in °K). Black arrows are velocity vectors; equatorial wind speeds are on the order of 3000 m s^{-1}. The panels represent three pressure levels. Longitude 0° is the substellar point.

2 The Thermal Structure of Hot Jupiters

2.1 Model characterization

General circulation models (GCMs) are important tools for estimating the thermal distribution and flow structure on hot Jupiters. Figure1 shows mean temperature and winds at three different depths from one such GCM run. The most prominent feature is a strong zonal temperature contrast due to tidal locking: the dayside to nightside temperature difference is on the order of several hundred K. Because this simulation (and most others) features equatorial superrotation[2], the warmest spot is located east (downstream) of the substellar point. This location is determined by a balance between heat advection and radiative cooling. While the advective timescale is similar at all depths considered here, the radiative cooling timescale increases with depth. Hence, the hotspot ventures farther from the substellar point as we look deeper, and the day-night temperature difference at the equator strongly decreases.

2.2 Observational characterization

The hemispheric temperature contrast predicted for HJs can be detected in observations. Consider a system composed of a star and its counterclockwise orbiting HJ. Suppose the ecliptic plane is oriented such that the planet passes in front of the star once per orbit for the observer. The radiative flux coming from the star+planet system undergoes variations according to the orbital phase. These variations are sketched in Figure 2. Two dips are observed per orbit: the larger one when the planet eclipses the star (the "transit"), and a smaller one, termed a "secondary eclipse", when the planet transits behind the star from the observer's perspective. As the planet orbits the star, the temperature of the hemisphere facing the observer varies. Before and after the transit, we are primarily facing its cold nightside, resulting in a lower overall flux, approaching the flux emitted only by the star (dashed line in Figure 2); around the secondary eclipse, the flux is higher as we also observe emissions from the planet's dayside. The fact that the maximum flux occurs slightly before the secondary eclipse indicates that the hotspot is shifted off the substellar point in the planet's prograde direction.

Taking into account the orbital period and phase, the brightness curve sketched in Figure 2 can be translated into a longitude-dependent brightness of the planet (Figure 3). Assuming blackbody radiation, one can infer a longitudinal temperature profile from this brightness map. The amplitude of its primary harmonic informs us of the day-night temperature contrast. Its phase gives the offset of the hotspot from the planet's substellar point.

More precise information on the longitude, and importantly the latitude of the hotspot can be inferred from detailed observations of the secondary eclipse, precisely the phases where the planet progressively disappears behind its star (the ingress) and later re-appears (egress). With a planet of uniform temperature (or a hotspot collocated with the substellar point), the ingress and egress flux curves would be mirror images of each other (Figure 4). If the hotspot is located east of the substellar point, then the flux will decrease quickly during the ingress (for a clockwise-orbiting planet) and increase quickly during the egress, creating asymmetry between the ingress and egress slopes (see Figure 4). If the planet passes above or below the star's equator, then an off-equatorial hotspot location will further distort the flux curve. Thus, assuming a given temperature structure around the hotspot, its precise location can be inverted from the ingress and egress slopes.

[2] Superrotation refers to the presence of zonal-mean prograde wind at the equator

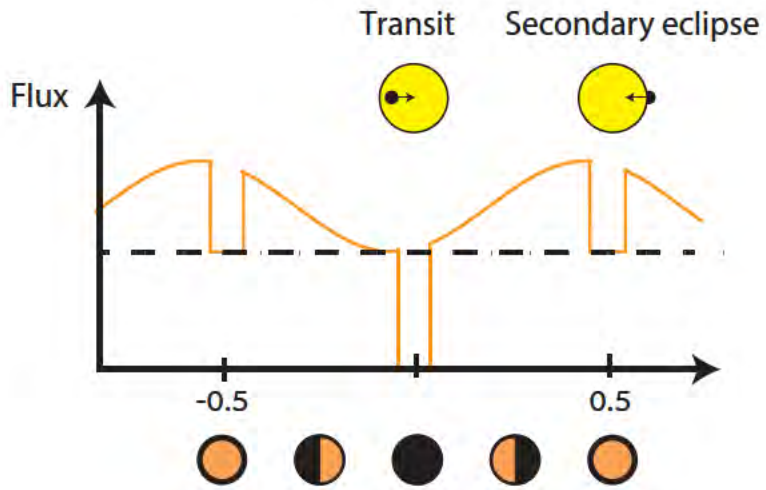

Figure 2: An illustration of a radiative flux from a star+planet system as a function of the planet's orbital phase. The dashed line represents the radiative flux emitted only by the star. The dips in the flux represent the transit and the secondary eclipse of the system, as seen by an observer (top illustrations).

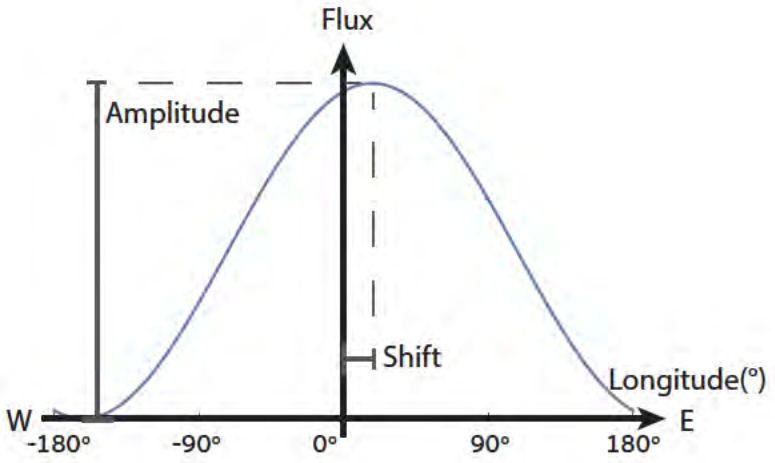

Figure 3: Sketch of the planet's radiative flux as a function of the planet's longitude. The amplitude informs on the dayside-nightside temperature difference, and the phase gives the zonal shift of the hotspot relative to the substellar point.

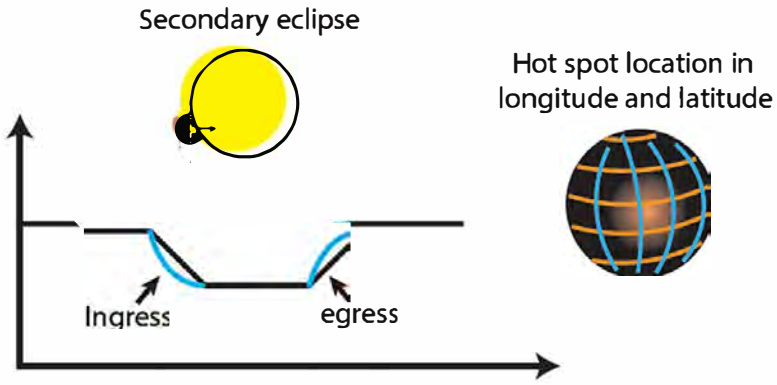

Figure 4: An illustration of a planet's radiative flux as a function of orbital phase, zoomed around the secondary eclipse. Note that the planet is orbiting clockwise on this figure. The black curve corresponds to a planet whose hotspot is located on the substellar point. A shifted hotspot results in asymmetries between the ingress and egress slopes (blue curve).

3 Existing Observations and Key Takeaways

Due to Earth's rotation, continuous observations of distant star systems are limited to a few hours. As observing phase curves (as sketched in Figure 2) requires continuous observations over several days, space telescopes such as Spitzer, Hubble, and James Webb are required. Because of this, current phase curve observations only amount to several dozen observations for Hot Jupiters. Most of these observations are in the infrared, with some in visible light (thus allowing to build longitude-dependent albedo maps). The ingress and egress phases (Figure 4) only last around 30 minutes, and several observations of these precise time frames are needed to filter out the noise. As such, secondary eclipse maps are only available for two HJs.

We now provide five key takeaways from these existing observations.

3.1 Zonal energy transport

One key element to characterize the zonal energy transport on tidally locked HJs is its efficiency, which can be defined as the fraction of the energy received by the dayside being redistributed to the nightside (varying between O and 0.5). Observations indicate that this efficiency is a decreasing function of the irradiation received by the planet, or equivalently that the hottest HJs are less efficient at redistributing the stellar energy absorbed on the dayside than their colder analogs. One theoretical argument supporting this finding was given by Perez-Becker and Showman (2013)[5]. They argue that similarly to Earth's tropics, gravity waves are a primary mechanism for tempera-ture homogenization in Hot Jupiters. The efficiency is thus set by a competition between radiative heating/ cooling and heat redistribution by waves, and as the radiative timescale decreases faster with temperature than the time scale of gravity waves, the efficiency of zonal heat transport de-creases with temperature.

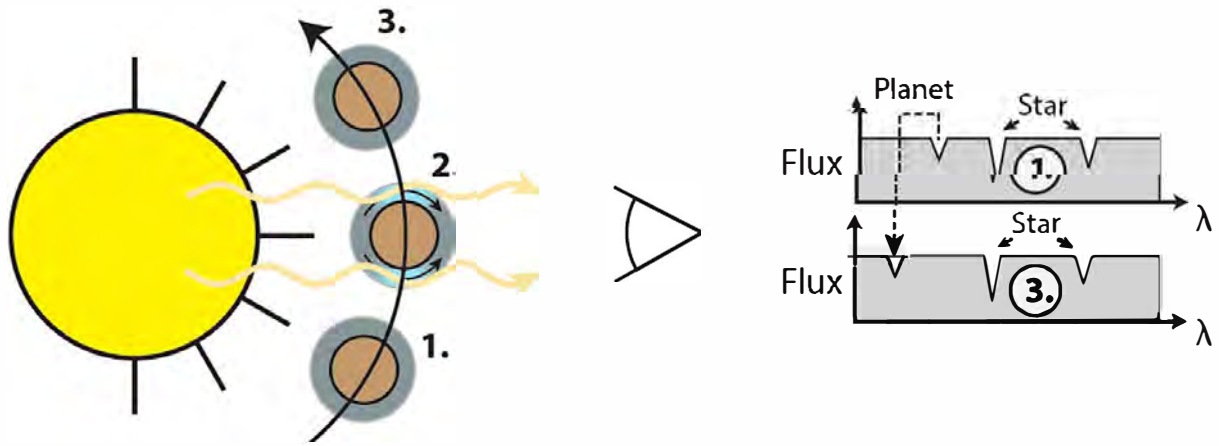

Figure 5: Sketch of the procedure used to measure large-scale winds during the transit. As the planet passes in front of the star, its atmosphere absorbs part of the incident light. Absorption lines pertaining to the star and the planet's atmosphere can be discriminated from Doppler shifting (see text), and anomalies in this Doppler shifting relative to a quiescent atmosphere are used to infer atmospheric winds.

3.2 Structure of the large-scale winds

Observations indicate that most HJs have their hotspot shifted in the prograde direction relative to the substellar point, suggesting that they likely have superrotating winds at the equator.

Measurements of transmission spectra during the transit offer a more direct way to probe at-mospheric winds. As the planet passes in front of its star, its atmosphere absorbs part of the radiation originating from the star before it reaches the observer, as illustrated in Figure 5. The measured radiation spectrum contains various absorption lines, some originating from the star and some from the planet's atmosphere. During the transit, the planet will transition from moving towards the observer (phase 1 in Figure 5) to moving away from them (phase 3). Thus, the atmospheric absorption lines will be blueshifted in phase 1, and redshifted in phase 3. This allows us to discriminate these from the star's absorption lines, which should not significantly move during the transit. Because the planet's orbital characteristics are known, the expected blueshifting and redshifting can be predicted assuming a quiescent atmosphere. Any deviation from this prediction indicates large-scale atmospheric motion. Planetary-scale energy transport tends to favor winds directed from dayside to nightside (black arrows drawn in phase 2 of Figure 5), creating an anoma-lous blueshifting of the lines for the observer. Transmitted radiation primarily comes from shallow regions of the atmosphere, and different depths can be probed from different absorption lines.

3.3 Clouds

Despite the large-scale energy redistribution, dayside and nightside temperatures differ by hundreds of K in HJs (e.g., Figure 1). These differences can lead to some chemical species existing in both vapor and condensed phases in different regions of the atmosphere. The most likely type of clouds are silicate clouds (e.g., $MgSiO_3$), which are very reflective. Given the typical thermal structure of HJs (and in accordance with model predictions), one would expect cloud structures having very large scales, with hemisphere-sized cloud patches and cloud-free regions. The best evidence we have

for the existence of patchy clouds in HJs comes from phase curve observations of the planet Kepler-7b [1]. The visible light phase curve for Kepler-7b has its maximum flux after the secondary eclipse. This indicates a westward shift in its brightest spot. This visible light signal is unlikely to come from thermal emission—in that case, the brightest spot could correspond to the hot spot, which one expects to be shifted eastward. The most likely explanation is that highly reflective clouds west of the substellar point account for the longitude of the flux maximum. This is consistent with the western part of the dayside hemisphere being generally cooler than the eastern part (see Figure 1).

For HJs, Kepler-7b is an outlier: it has a high geometric albedo of 0.3, whereas 90% of HJs have low albedos on the order of 0.05. This does not, however, mean that most HJs are cloud-free, and several lines of evidence from transmission spectroscopy indicate otherwise. For most HJs, absorption spectra do not strongly depend on wavelength in the infrared range, which is indicative of the presence of high clouds. At optical wavelengths, Rayleigh scattering by small cloud particles implies a strongly wavelength-dependent opacity [9]. Hence, HJs with low albedos are unlikely to be cloud-free but are simply devoid of widespread, highly reflective clouds.

Clouds are expected to alter the large-scale atmospheric circulation. For example, nightside clouds trap thermal emissions, lowering the hemispheric temperature gradients. A lower dayside-nightside temperature contrast would also lower the strength of equatorial winds, yielding a smaller offset of the hotspot relative to the substellar point. Observed HJs do have smaller hotspot offsets than cloud-free GCMs. Recent GCM simulations including simple cloud parameterizations confirmed that the presence of clouds can reduce the eastward shift of the hotspot [4, 6].

3.4 Large-scale chemical gradients

Different physical properties between the dayside and the nightside of HJs should also yield varying chemical compositions. In the hot dayside, carbon is expected to be present in the form of CO and CO_2. In contrast, nightside temperatures would favor CH_4 in equilibrium. However, the timescale for this chemical transition is slow enough that GCM models that allow disequilibrium chemistry due to transport predict CO-dominated atmospheres, even on the nightside [10]. Some nightside spectra have been observed and confirm that methane concentrations are low, even in conditions where methane should dominate at equilibrium.

In ultra-hot Jupiters (whose equilibrium temperatures are higher than 2000 K), chemical reaction timescales decrease. Hence, chemical reactions should be in a local equilibrium state throughout the atmosphere. If the dayside is hot enough, H_2 can be dissociated into atomic H ($H_2 \longrightarrow 2H$). Its recombination on the nightside ($2H \longrightarrow H_2$) releases heat, providing a means of cross-hemispheric energy transport.

3.5 Magnetic fields

Some HJs are hot enough that parts of the atmosphere get ionized. For example, sodium and potassium are ionized around 1500 K. Assuming a background dipolar magnetic field, ions in the equatorial jet would feel a Lorentz drag as they travel across field lines. This could reduce the overall strength of the jet, and therby the hotspot offset. There is potential observational evidence for this effect, with a couple of highly irradiated HJs having small hotspot offsets.

Some HJs (though very few) have a westward-shifted hotspot, which may be a manifestation of magnetohydrodynamic effects. Indeed, some MHD models do feature westward (more generally retrograde) equatorial flow [2], an effect attributed to the westward-tilting nature of equatorial magneto-Kelvin waves. Bounds on the strength of the background field and equilibrium temperature required to drive this effect were proposed by Hindle et al. (2019) [3], with lower thresholds of

approximately 2000 K and 1 G. Although the strength of the magnetic field remains an unknown parameter (no observations of exoplanet magnetic fields exist to date), this second bound is not unrealistic.

References

[1] B.-O. Demory, J. de Wit, N. Lewis, J. Fortney, A. Zsom, S. Seager, H. Knutson, K. Heng, N. Madhusudhan, M. Gillon, T. Barclay, J.-M. Desert, V. Parmentier, and N. B. Cowan, *Inference of inhomogeneous clouds in an exoplanet atmosphere*, The Astrophysical Journal Letters, 776 (2013), p. L25.

[2] A. W. Hindle, P. J. Bushby, and T. M. Rogers, *Shallow-water magnetohydrodynamics for westward hotspots on hot jupiters*, The Astrophysical Journal Letters, 872 (2019), p. L27.

[3] ——, *Observational consequences of shallow-water magnetohydrodynamics on hot jupiters*, The Astrophysical Journal Letters, 916 (2021), p. L8.

[4] V. Parmentier, A. P. Showman, and J. J. Fortney, *The cloudy shape of hot Jupiter thermal phase curves*, Monthly Notices of the Royal Astronomical Society, 501 (2021), pp. 78–108.

[5] D. Perez-Becker and A. P. Showman, *Atmospheric heat redistribution on hot jupiters*, The Astrophysical Journal, 776 (2013), p. 134.

[6] M. T. Roman, E. M.-R. Kempton, E. Rauscher, C. K. Harada, J. L. Bean, and K. B. Stevenson, *Clouds in three-dimensional models of hot jupiters over a wide range of temperatures. i. thermal structures and broadband phase-curve predictions*, The Astrophysical Journal, 908 (2021), p. 101.

[7] A. P. Showman, J. Y.-K. Cho, and K. Menou, *Atmospheric circulation of exoplanets*, 2009.

[8] A. P. Showman, J. J. Fortney, Y. Lian, M. S. Marley, R. S. Freedman, H. A. Knutson, and D. Charbonneau, *Atmospheric circulation of hot jupiters: Coupled radiative-dynamical general circulation model simulations of hd 189733b and hd 209458b*, The Astrophysical Journal, 699 (2009), p. 564.

[9] D. K. Sing, J. J. Fortney, N. Nikolov, H. R. Wakeford, T. Kataria, T. M. Evans, S. Aigrain, G. E. Ballester, A. S. Burrows, D. Deming, J.-M. Désert, N. P. Gibson, G. W. Henry, C. M. Huitson, H. A. Knutson, A. L. d. Etangs, F. Pont, A. P. Showman, A. Vidal-Madjar, M. H. Williamson, and P. A. Wilson, *A continuum from clear to cloudy hot-jupiter exoplanets without primordial water depletion*, Nature, 529 (2016), pp. 59–62.

[10] M. E. Steinrueck, V. Parmentier, A. P. Showman, J. D. Lothringer, and R. E. Lupu, *The effect of 3d transport-induced disequilibrium carbon chemistry on the atmospheric structure, phase curves, and emission spectra of hot jupiter hd 189733b*, The Astrophysical Journal, 880 (2019), p. 14.

GFD 2023 Lecture 6: Cold Giants; Jets, Deep Convection and Shallow Weather

Geoff Vallis; notes by Quentin Kriaa and Yaoxuan Zeng

September 5, 2024

1 Introduction

We now turn our attention to gas giants, and in particular to 'cold' gas giants. All the giants in the solar system – Jupiter, Saturn, Uranus and Neptune – are cold. Jupiter and Saturn are 'gas giants', composed mainly of hydrogen and helium (even in their interiors), with only traces of methane, ammonia, water and some other elements, whereas Uranus and Neptune are 'ice giants', with ammonia, methane and water (commonly if somewhat confusingly known as 'ices') forming much of the planets' mass. We will mainly focus on the gas giants here. The interior flux of energy of Jupiter and Saturn is comparable to the solar radiation, typically of order 5 $\mathrm{W/m^2}$. The internal flux for Uranus and Neptune is smaller, about 0.04 and 0.4 $\mathrm{W/m^2}$, respectively, although that for Neptune is comparable to the radiation received from the Sun.

The case of Jupiter (see its radial structure in Fig. 1) has received considerable attention from the scientific community due to the structures that are manifestly visible in its atmosphere, and the large amount of data that have already been collected by space missions and that will be extended by the upcoming measurements from the Juice mission. Jupiter is the largest planet in the Solar System with a radius, a, of about 71,000 km, a gravitational acceleration, g, of about $25\,\mathrm{m\,s^{-2}}$ (near the surface) and a period of rotation $2\pi/\Omega$ of about 10 hours. Consider the thermal Rossby number

$$\mathrm{Ro}_T = \frac{R\Delta T}{\Omega^2 a^2}, \tag{1}$$

where R is the specific gas constant. Compared to Earth's properties which we denote with the symbol $\oplus$, we have $\Omega \simeq 2.5\Omega_\oplus$ and $a \simeq 11 a_\oplus$ so that for the same ΔT the thermal Rossby number on Jupiter is considerably lower than that of the Earth. (In fact, ΔT is also much smaller on Jupiter than Earth, making Ro_T smaller still, but the winds on Jupiter are not directly a consequence of thermal wind balance with an equator–pole temperature gradient.) Consequently, Jupiter's dynamics are much more constrained by the influence of planetary rotation, as evidenced by its zonal winds that organize as jets – see Fig. 2. Those jets alternate as bands of prograde and retrograde winds, which balance out when averaged over all latitudes, but which still evidence a net superrotation near the equator. Several candidate models can explain this equatorial superrotation, but none has yet been definitively identified as being *the* relevant mechanism responsible for this observation. Saturn also has superrotation, over a broader range of latitudes near the equator, and with zonal velocities that are about twice larger. In contrast, Uranus and Neptune both have retrograde equatorial jets.

How do these jets form? What sets their direction near the equator? Are they deep jets that are present in the deep convective zone? Or do they belong in the surface shallow weather layer, perhaps forced by turbulence and emerging when rotation overcomes stratification? Or do they

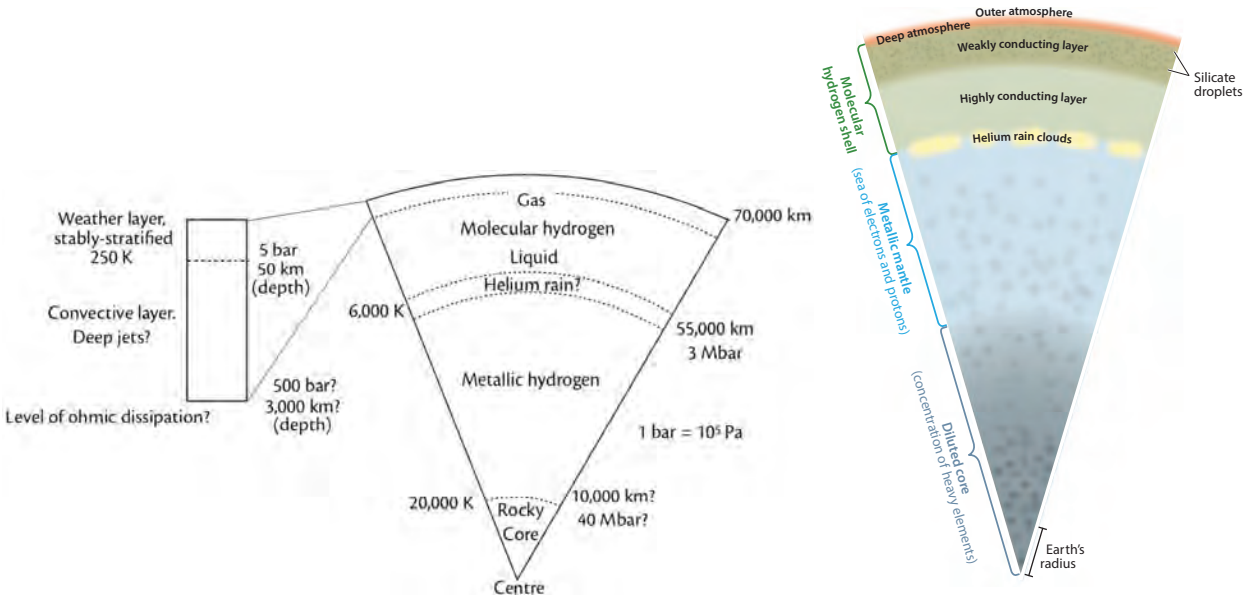

Figure 1: Possible radial structure of Jupiter. The plot on the right, from [6], incorporates data from the Juno mission that suggests that the rocky core is quite dilute.

exist in both layers and interact? The next sections discuss these guiding questions, considering first the weather layer jets and second the deep jets.

2 Weather Layer Jets

Rossby waves are likely a major agent driving the formation of zonal jets in stratified environments. Their ability to induce a zonal flow from a statistically uniform flow can be illustrated with the following simple model. Consider a flow that is barotropic, presumably hydrostatic, two-dimensional, incompressible, and with an infinite Rossby deformation radius. In that case, the inviscid vorticity equation boils down to

$$\frac{\partial \zeta}{\partial t} + \boldsymbol{u} \cdot \nabla \zeta + \beta v = 0, \tag{2}$$

where $\boldsymbol{u} = (u, v)$ is the horizontal velocity field with u the zonal velocity and v the meridional velocity, β is the gradient of the Coriolis parameter along the meridional direction (and we will assume β to be constant), and

$$\zeta = \frac{\partial v}{\partial x} - \frac{\partial u}{\partial y} \tag{3}$$

is the vertical component of vorticity. Eq. (2) may also be written as

$$\frac{\mathrm{D}q}{\mathrm{D}t} = 0 \tag{4}$$

where $q = \zeta + f$ and $f = \beta y$. The variable q is the potential vorticity in this two-dimensional system (other more general, and three-dimensional, forms are possible) and evidently (in the absence of a dissipative term on the right-hand side) it is a Lagrangian invariant.

The flow being incompressible, let us introduce the stream function ψ such that

$$u = -\frac{\partial \psi}{\partial y}; \quad v = \frac{\partial \psi}{\partial x}; \quad \zeta = \nabla^2 \psi \ . \tag{5}$$

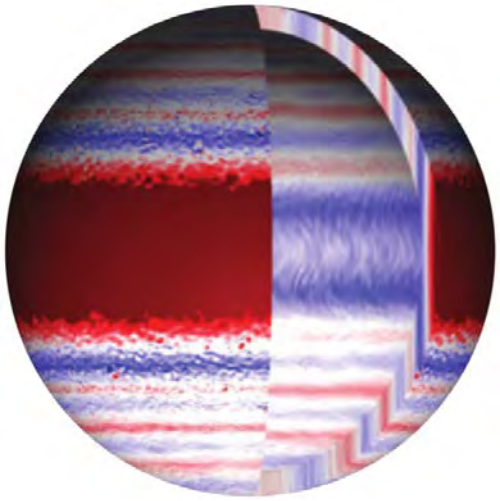

Figure 2: Zonal jets on a giant, Jupiter-like, planet according to simulations of [1] in a spherical shell of inner radius $0.9a$, where a is the planetary radius. Colors correspond to the velocity field: red jets are eastward, blue jets are westward.

Using the stream function, Eq. (2) can be linearised and reads:

$$\frac{\partial}{\partial t}\nabla^2\psi + \beta\frac{\partial\psi}{\partial x} = 0 \ . \tag{6}$$

Since the coefficients of this equation are constant, we can look for solutions in the form

$$\psi = \Re[\psi_0 e^{i(kx+ly-\omega t)}] \ , \tag{7}$$

where ψ_0 is the amplitude, k is a zonal wavenumber, l is a meridional wavenumber, and ω is an angular frequency. Injecting the solution (7) into (6) readily yields the dispersion relation of Rossby waves without mean background flow:

$$\omega = -\frac{\beta k}{k^2+l^2} \ , \tag{8}$$

whose minus signs indicates that this wave propagates westward with respect to the mean zonal flow. Suppose Rossby waves are triggered by a uniform band of perturbations along the longitude – either baroclinic instabilities if radiative heating is sufficient or, more likely for Jupiter, due to the effects convection below the weather layer. The Rossby waves then propagate energy away from the source. This transport is performed by the meridional component $c_{g,y}$ of their group velocity

$$c_{g,y} = \frac{\partial\omega}{\partial l} = \frac{2\beta kl}{(k^2+l^2)^2} \ . \tag{9}$$

Assuming $\beta > 0$, because energy is transported away from the source, we can infer from Eq. (9) that $kl > 0$ northward of the perturbation and that $kl < 0$ southward of the perturbation – see the blue text in Fig. 3.

Let us show that the velocity fluctuations (u, v) transport momentum eastward in the region of stirring, and westward on either side. From the definitions (5), the following expressions of u and v are readily obtained

$$u = -\psi_0 il e^{i(kx+ly-\omega t)}; \quad v = \psi_0 ike^{i(kx+ly-\omega t)} \ . \tag{10}$$

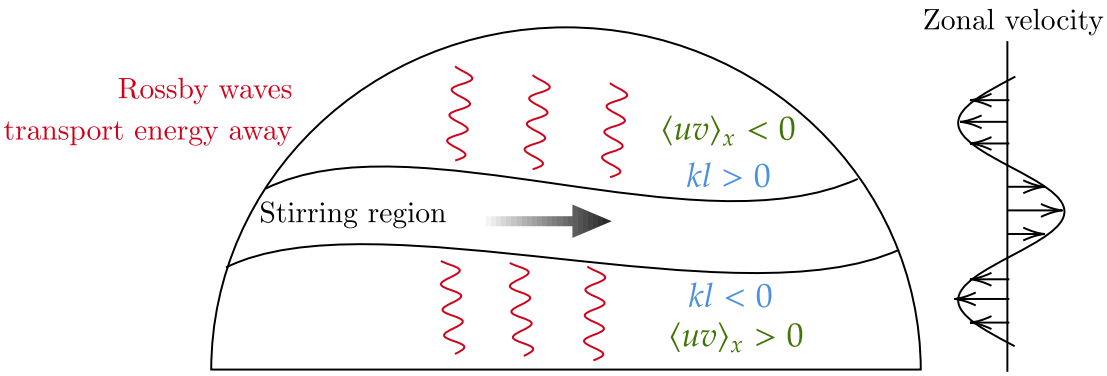

Figure 3: When a region stirs the fluid, Rossby waves are generated that transport energy outward along the meridional direction. This results in the formation of an eastward jet – see main text for details.

We finally deduce

$$uv^* = -\psi_0^2 kl \propto -kl \ , \tag{11}$$

where v^* is the complex conjugate of v. Considering the zonal average $\langle uv \rangle$ of this product (we thereafter drop the star for simplicity), the latter proves to be negative northward of the stirring region, and positive southward, meaning the momentum converges towards the source of the perturbations. Let us show that this converges and nourishes an eastward zonal flow. With the same assumptions as above, the momentum equation for the two-dimensional flow reads

$$\frac{\partial u}{\partial t} + u\frac{\partial u}{\partial x} + v\frac{\partial u}{\partial y} - fv = 0 \ , \tag{12}$$

with f the Coriolis parameter. Under the assumption that the flow is incompressible, this equation simplifies as

$$\frac{\partial u}{\partial t} + \frac{\partial u^2}{\partial x} + \frac{\partial uv}{\partial y} - fv = 0 \ . \tag{13}$$

After noticing that the v component of the solenoidal velocity field is the zonal derivative of a stream function, and then taking the zonal average $\langle \cdot \rangle_x$ of the last equation, we end up with

$$\frac{\partial \langle u \rangle_x}{\partial t} = -\frac{\partial \langle uv \rangle_x}{\partial y} > 0 \ , \tag{14}$$

which confirms the emergence of an eastward jet in the stirring region – see Fig. 3.

The key remaining question is: what is the latitudinal scale of these jets? The forcing, which nourishes the jets in the first place, and planetary rotation that constrains their dynamics, can both influence this length scale. If the forcing region is sufficiently wide, the meridional scale of the jets can be expected to result from a balance between the inertial term $\boldsymbol{u} \cdot \nabla \zeta$ and the Coriolis term βv. The simplest assumption to make is that the turbulent motion embedded within the jets (which will tend to be at a somewhat smaller scale than the jets) is approximately isotropic. A simple scaling argument then gives

$$|\boldsymbol{u} \cdot \nabla \zeta| \sim |\beta v|, \tag{15}$$

$$\frac{U^2}{L_R^2} \sim \beta U, \tag{16}$$

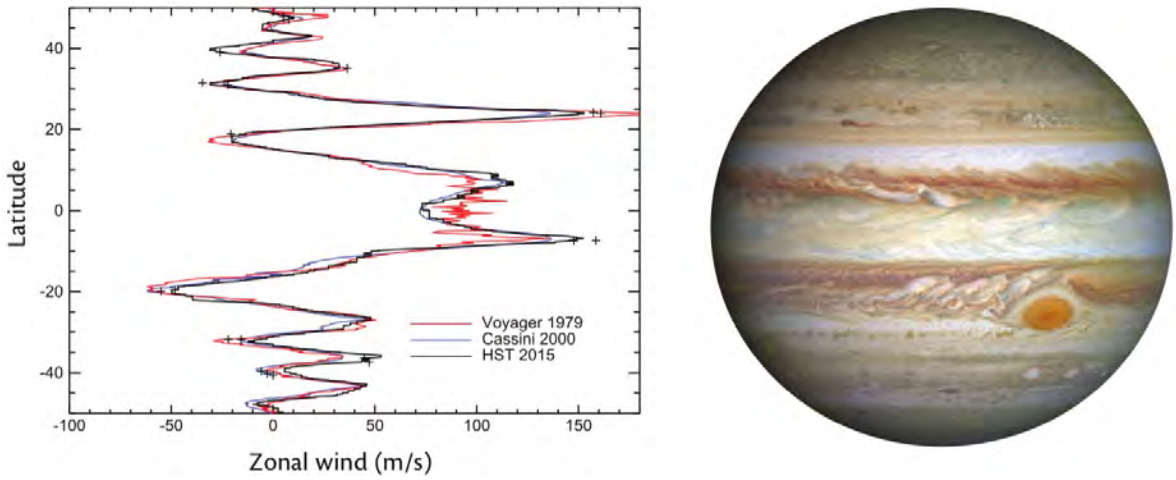

Figure 4: Left: Zonal average of the zonal winds on Jupiter at cloud top. The blue line is the Cassini profile in late 2000 [2], the red line is from Voyager in 1979 [5], the black line is from the Hubble Space Telescope in 2015 [4], from which the figure is adapted). Right: Atmosphere of Jupiter in the visible light (photo from the Cassini mission) showing ammonia clouds. The dark 'belts' are relatively warm downwelling regions, whereas the light 'zones' are relatively cool upwelling regions.

where L_R is the meridional scale of the jets, giving

$$L_R = \sqrt{\frac{U}{\beta}}. \tag{17}$$

The scale L_R is known as the Rhines scale, following [3]. Note that U is the velocity scale of the eddying flow in the jet, not the magnitude of the jet velocity itself. Other derivations of this scaling are possible, and other scalings are also possible, for example $L \sim \mathcal{Z}/\beta$ where $\mathcal{Z}$ is the mean amplitude of the vorticity, or $L \sim (\varepsilon/\beta^3)^{1/5}$ where ε is the energy cascade rate [8]. This last expression is useful if the energetic forcing rate is known independently as an external parameter (for the Rhines scale requires knowledge of the solution, i.e., the magnitude U). However, the Rhines scale is a very useful practical measure, as U may often be observed.

The flow that is of a smaller scale than L_R is dominated by turbulence (i.e., advective terms in the vorticity equation) but scales larger than this tend to be dominated by the Rossby waves (i.e., linear terms). A typical order of magnitude of the Rhines scale of Jupiter is $L_R \simeq 5000$ km, which is consistent with the typical length scale deduced from the 10°-wide jets observed in Fig. 4, up to a prefactor ~ 2.

Another perspective of jet formation arises if we think about the problem in physical space and the evolution of potential vorticity. This perspective is valuable both for deep and shallow jets, so let us turn our attention to this.

3 Potential Vorticity: Homogenization and Staircases

Although the principles we shall describe in this section are actually quite general it is easiest to describe them by way of a simple example of two-dimensional incompressible flow with an infinite deformation radius.

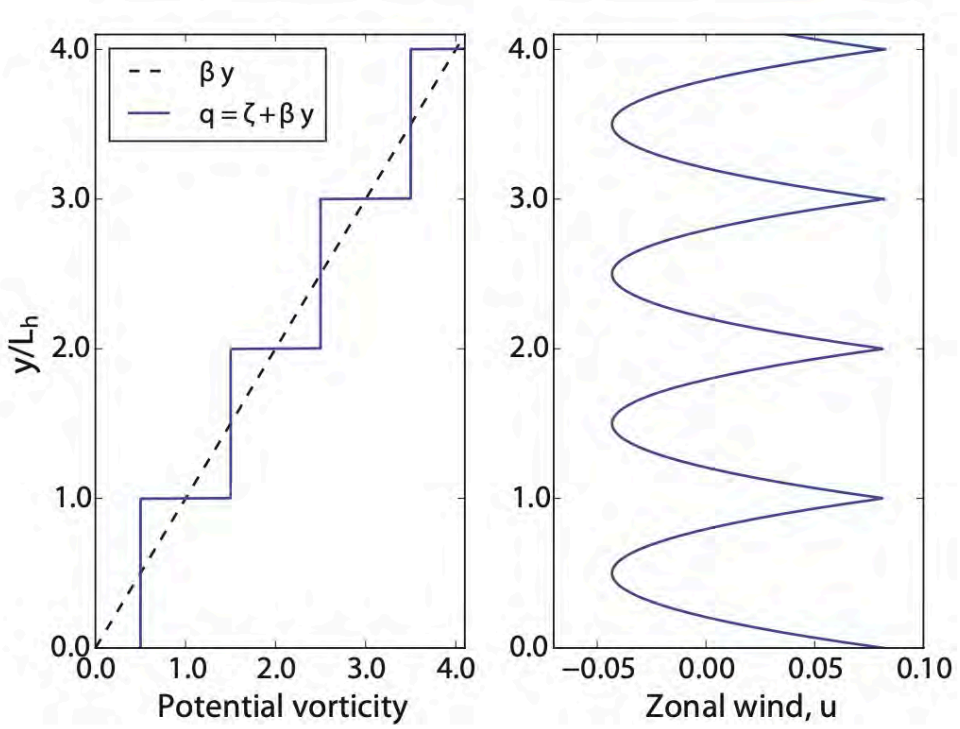

Figure 5: An idealized potential vorticity staircase on a β-plane with $\beta = 1$. The left panel shows homogeneous regions of potential vorticity of meridional extent L_h separated by potential vorticity jumps. The right panel shows the corresponding zonal flow, calculated using (25) with u_0 chosen to be such that the averaged zonal flow is zero. Taken from Fig. 12.6 in [7].

The potential vorticity, q, of such a flow on a β-plane is $q = \zeta + \beta y$, where $\zeta = \partial v/\partial x - \partial u/\partial y$ is the relative vorticity and $\beta = \partial f/\partial y$ is the meridional gradient of the Coriolis parameter, f (Eq. 2).

The premise made is that in a turbulent flow, the gradients of a scalar that is both advected and diffused will become smeared out as much as possible: diffusion will dissipate any extrema and advection cannot recreate them. Potential vorticity is a scalar, so we might expect it to become homogenized, but it is not passive and therefore the process of homogenization will affect the flow itself, preventing complete homogenization. One reason for that may be the boundary conditions, another that the process of homogenization requires more energy than the flow contains. To see this, consider a freely evolving flow on a beta-plane obeying the barotropic vorticity equation

$$\frac{\partial \zeta}{\partial t} + J(\psi, \zeta + \beta y) = \nu \nabla^2 \zeta, \tag{18}$$

where ν is sufficiently small that energy is well conserved over the timescales of interest. If potential vorticity, $q = \zeta + \beta y$, is to be homogenized over some meridional scale L then, in the homogenized region, $\zeta \approx -\beta y$. If the flow is predominantly zonal then this gives the estimate $U \sim \beta y^2$ and the energy in the region is, very approximately,

$$\frac{1}{2} \int u^2 \, dx \, dy \approx \int (\beta y^2)^2 \, dx \, dy, \tag{19}$$

giving the estimate $U^2 L \sim \beta^2 L^5$. If we suppose that the initial root-mean square velocity is also U, and that the flow becomes predominantly zonal, then solving the above estimate for L suggests

that the potential vorticity will become homogenized over the scale

$$L_h \sim \left(\frac{U}{\beta}\right)^{1/2}. \tag{20}$$

This is the same as the Rhines scale given previously, as it has to be by dimensional analysis, although now it is supposed that much of the energy lies in the zonal flow. Although the scale is the same, this way of looking at the problem adds something to the physical picture — *an asymmetry between eastward and westward flow,* as we now discuss.

In the idealized staircase of Fig. 5 potential vorticity is piecewise continuous and given by

$$q = \zeta + \beta y = q_0, \qquad 0 < y < L_h, \tag{21a}$$

$$q = \zeta + \beta y = q_0 + \beta L_h \equiv q_1, \qquad L_h < y < 2L_h, \quad \text{and so on.} \tag{21b}$$

In any one of the homogenized regions the flow is given by solving

$$\frac{\partial u}{\partial y} = \beta y - q_n \quad \text{giving} \quad u = \frac{1}{2}\beta y^2 - q_n y + \text{constant}, \tag{22}$$

where $q_n = \beta L_h/2 + n\beta L_h$. The constant may be determined by requiring continuity of u across the regions, and we then obtain

$$u = \frac{1}{2}\beta(y - L_h/2)^2 + u_0, \qquad 0 < y < L_h, \tag{23}$$

$$u = \frac{1}{2}\beta(y - 3L_h/2)^2 + u_0, \qquad L_h < y < 2L_h, \tag{24}$$

or in general,

$$u = \frac{1}{2}\beta\left(y - (n-1/2)L_h\right)^2 + u_0, \qquad (n-1)L_h < y < nL_h, \qquad n = 1, 2, 3\ldots\ , \tag{25}$$

where u_0 is a constant. Relative to u_0, the flow is weakly westward in the homogenized regions, whereas in the transition region the flow has a sharp eastward peak, as shown in Fig. 6.

Potential vorticity homogenization may also play a role in the formation of deep jets, so let us now discuss those.

4 Deep Convection and Jets

An alternative viewpoint to supposing that the jets on giant planets are shallow and confined to a weather layer at most a few hundred kilometers thick, is to suppose that they are deep, extending a few thousand kilometers into the interior, with cores that are aligned with the rotation axis. The foundation for this lies with the Taylor–Proudman result, which we now describe.

4.1 Taylor-Proudman result

Recall from Lecture 3 that the equation of motion for an inviscid fluid is[1]

$$\frac{D\boldsymbol{v}}{Dt} + 2\boldsymbol{\Omega} \times \boldsymbol{v} = -\frac{1}{\rho}\nabla p + \boldsymbol{g}. \tag{26}$$

[1] As usual we use $\boldsymbol{v}$ to indicate 3-D velocity (u, v, w) and $\boldsymbol{u}$ to indicate 2-D velocity (u, v). Also, strictly speaking, the viscous term in (26) is not exact unless ρ is constant, but we will subsequently ignore viscous effects.

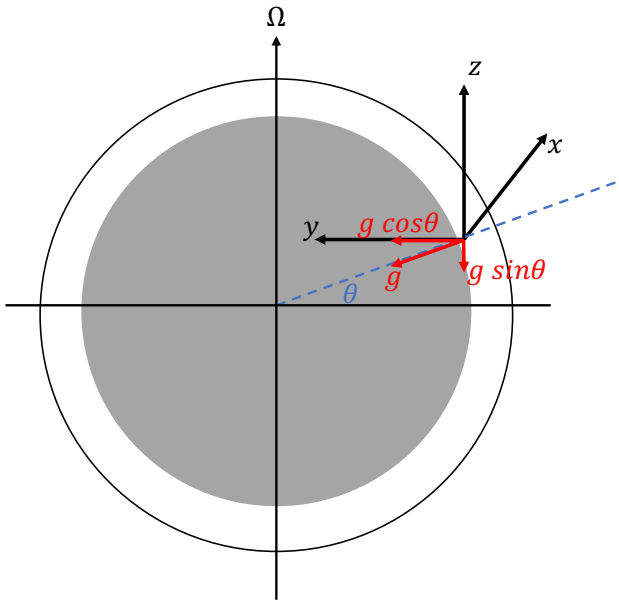

Figure 6: Sketch of the local Cartesian coordinate. The z direction is parallel to the rotation axis, the y direction is pointing inwards and perpendicular to the rotation axis, and the x direction is the prograde direction. Note that the gravity has components on both y direction ($g\cos\theta$) and z direction ($-g\sin\theta$).

If the flow is in geostrophic and hydrostatic balances, and ρ is constant (so that $\nabla\cdot\boldsymbol{v}=0$) the equation is reduced to

$$2\boldsymbol{\Omega}\times\boldsymbol{v}=-\nabla\phi+\boldsymbol{g}, \tag{27}$$

where $\phi=p/\rho$. By taking the curl of (27), and noting that $\boldsymbol{g}$ and $\boldsymbol{\Omega}$ are constant, and that the flow is non-divergent, (27) reduces to

$$2\Omega\frac{\partial\boldsymbol{v}}{\partial z}=0, \tag{28}$$

where z is taken to be the direction parallel to the rotation axis. Eq. (28) suggests that all three components of velocity, u, v, and w, are uniform along the rotation axis. In realistic settings this result will not hold exactly, but it does suggest that the flow may form columnar structures.

4.2 The topographic β-effect and jet formation

4.2.1 Column geometry

Assuming that in a rapidly rotating planet like Jupiter the flow does form into columns, let us first look at how column height, such as the one labeled H in Fig. 7, varies with latitude ϑ.

From the figure, for a column within the tangent cylinder, the following two equations connect the column height, h, its latitudes, θ and ϕ, the radius of the whole sphere, a, and the thickness of the outer region, d:

$$a\sin\theta=(a-d)\sin\phi+h, \tag{29a}$$

$$a\cos\theta=(a-d)\cos\phi. \tag{29b}$$

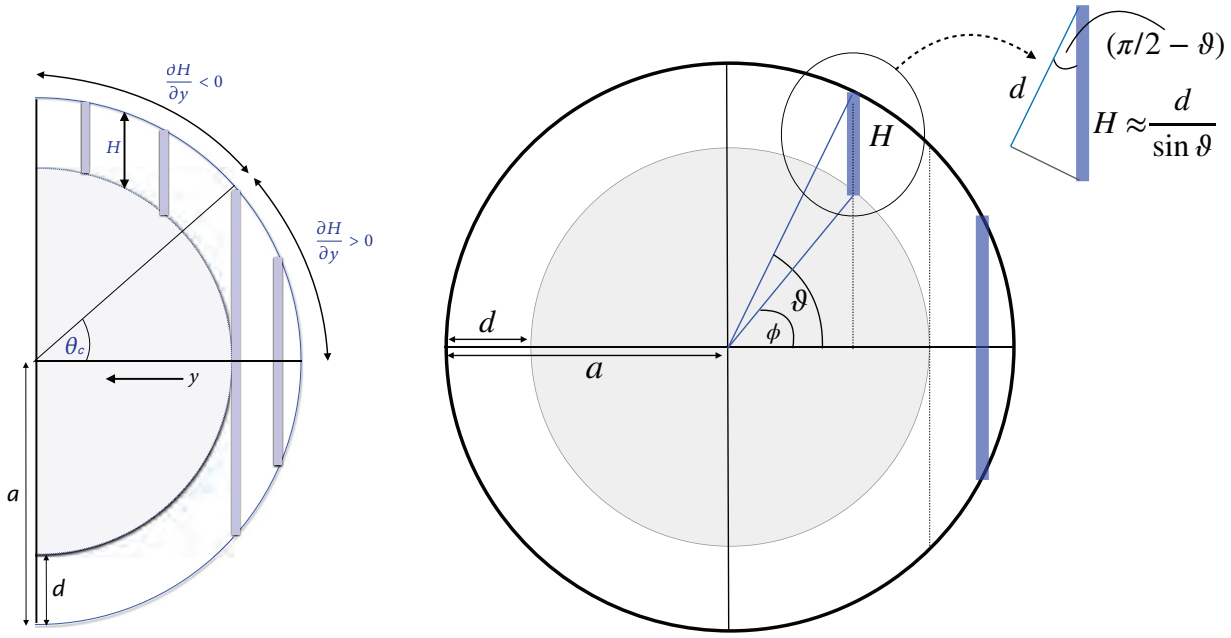

Figure 7: Geometry of columns in the convective zone in a spherical shell. For columns poleward of latitude θ the column height diminishes with latitude and $\partial H/\partial y < 0$, whereas the column height increases with latitude outside the tangent cylinder and $\partial H/\partial y > 0$. The consequence is that the beta parameter, β^*, is positive inside the tangent cylinder (i.e. at higher latitudes) and negative outside the tangent cylinder in the tropical region.

From these we easily find that

$$H = a\sin\theta - (a-d)\left[1 - \left(\frac{a}{a-d}\right)^2 \cos^2\theta\right]^{1/2}. \tag{30}$$

If the shell is sufficiently thin then this expression reduces to

$$H \approx \frac{d}{\sin\theta}, \tag{31}$$

as can be seen from Fig. 7. The rate of change of column height with latitude is, in this approximation,

$$\frac{\partial H}{\partial\theta} \approx -\frac{d\cos\theta}{\sin^2\theta}. \tag{32}$$

This expression reflects the fact that the column shrinks in height as it approaches the pole. We may also note that

$$\frac{1}{H}\frac{\partial H}{\partial\theta} \approx -\frac{1}{\tan\theta}. \tag{33}$$

For columns outside of the tangent cylinder the geometry is easier and we simply have, without approximation,

$$H = 2a\sin\theta, \tag{34}$$

and

$$\frac{\partial H}{\partial\theta} = 2a\cos\theta. \tag{35}$$

We also have

$$\frac{1}{H}\frac{\partial H}{\partial \theta} \approx \frac{1}{\tan\theta}, \tag{36}$$

which is just the negative of (33).

4.2.2 Dynamics

Let us now suppose that we can model the convective region as a layer of shallow water, obeying the shallow-water equations

$$\text{momentum:} \qquad \frac{\mathrm{D}\boldsymbol{u}}{\mathrm{D}t} + \boldsymbol{f}\times\boldsymbol{u} = -g\nabla\eta, \tag{37}$$

$$\text{mass continuity:} \qquad \frac{\mathrm{D}h}{\mathrm{D}t} + h\nabla\cdot\boldsymbol{u} = 0, \quad \text{or} \quad \frac{\partial h}{\partial t} + \nabla\cdot(h\boldsymbol{u}) = 0, \tag{38}$$

where $\boldsymbol{u}$ is the horizontal velocity, h is the total fluid thickness and η the surface height. If there is topography at the bottom then $h(x,y,t) = \eta(x,y,t) - \eta_B(x,y)$. The above equations give the potential vorticity equation

$$\frac{\mathrm{D}Q}{\mathrm{D}t} = 0, \qquad Q = \left(\frac{\zeta + 2\Omega}{h}\right). \tag{39}$$

In the planetary context, quantity h is the thickness of the convecting layer and we write this as $h = H + h'$, where H is the mean shell thickness and h' are small, time-dependent, deviations of that due to fluid motion, and $H \gg h'$. From Fig. 7 we see that H varies in the y direction, decreasing toward the pole in the region poleward of the intersection with the tangent cylinder, but decreasing toward the equator in the region equatorward of the intersection with the tangent cylinder. It is this variation with mean thickness, and hence the variation of the background potential vorticity, that gives rise to a 'topographic beta effect' and hence to zonal jets. To see this explicitly, we make two more assumptions:

1. The small Rossby number assumption, that $|2\Omega| \gg |\zeta|$.
2. The variations in mean height occur on a larger scale than the variations in vorticity.

The potential vorticity is then given by

$$Q = \left(\frac{\zeta + 2\Omega}{h}\right) \approx \left(\frac{\zeta + 2\Omega}{H}\right), \tag{40}$$

and, using the assumptions above, its evolution is given by

$$\frac{\mathrm{D}Q}{\mathrm{D}t} \approx \frac{1}{H}\frac{\mathrm{D}\zeta}{\mathrm{D}t} + 2\Omega\frac{\mathrm{D}}{\mathrm{D}t}\left(\frac{1}{H}\right) = \frac{1}{H}\frac{\mathrm{D}\zeta}{\mathrm{D}t} - \frac{2\Omega}{H^2}\boldsymbol{v}\cdot\nabla H, \tag{41}$$

and (39) becomes

$$\frac{\mathrm{D}\zeta}{\mathrm{D}t} + \beta^* v = 0 \quad \text{where} \quad \beta^* = -\frac{2\Omega}{H}\frac{\partial H}{\partial y}, \tag{42a,b}$$

where v is the velocity in the y-direction (see Fig. 7). We see that β^* is positive in the region inside the tangent cylinder (the extra-tropics) and negative outside the tangent cylinder, in the tropics. Using (33) we obtain, inside the tangent cylinder,

$$\beta^* \approx \frac{2\Omega}{a\tan\theta}, \tag{43}$$

and the negative of that outside the tangent cylinder.

The topographic β^* is thus

$$\beta^* = \begin{cases} -\dfrac{2\Omega}{a\tan\theta}, & \text{if } |\theta| < |\theta_c| \\ \dfrac{2\Omega}{a\tan\theta}, & \text{if } |\theta| > |\theta_c|. \end{cases} \tag{44}$$

taking $y \approx a\theta$. The topographic effective β^* thus changes sign from inside to outside the tangent cylinder. Depending on the layer thickness, it may be of the same order of magnitude as the traditional β in the weather layer (namely $2\Omega\cos\theta$) but will have quantitatively different values.

4.2.2.1 Tropical superrotation

In the tropical region the zonal flow on Jupiter is *prograde,* that is, in the direction of the planetary rotation, and the atmosphere superrotates. The analogous jet on Saturn is also prograde. Why should this be so? The mechanism must involve eddy motion and a plausible explanation is related to the nature of the beta effect in this region. In the tropical region outside the tangent cylinder the beta parameter, β^* given by (42b), is negative because the length of the convecting column *increases* with the y-coordinate. (In this region it is given by $H = 2a\sin\theta$, where θ is latitude and a is the planetary radius.) To simplify matters, let us suppose that β^* in (42) is a constant in which case we can write, again using Cartesian co-ordinates

$$\frac{\mathrm{D}Q^*}{\mathrm{D}t} = 0, \qquad Q^* = \zeta + \beta^* y, \tag{45}$$

where y is the direction toward the axis of rotation. If the dynamics are turbulent in the tropical region (for example, if they are stirred by convection) then they will seek to homogenize the potential vorticity and the zonally-averaged flow is given by

$$\frac{\partial \overline{u}}{\partial y} + |\beta^*| y = A, \qquad \text{or} \qquad \overline{u} = Ay - \frac{1}{2}|\beta^*| y^2 + B, \tag{46}$$

where A and B are constants. If $\partial\overline{u}/\partial y = 0$ at $y = 0$ then $A = 0$ and $\overline{u}$ takes its *maximum* value at $y = 0$; that is, we expect the flow to be prograde, or super-rotating, at the equator.

5 Remarks

The atmospheres of giant planets differ in significant ways from those of terrestrial planets, yet are similar in some others. A robust feature of the gas giants in our Solar System is the presence of superrotation. We have given one model for that in this lecture, but other mechanisms are possible. In particular, the interaction of the deep convective layer and the shallower weather layer, and whether and how the jets in the former imprint themselves on the latter, has not been properly determined. Another challenge is to better understand the causes of the differences between the gas giants and ice giants in our Solar System, for the latter do not exhibit superrotation. To see some preliminary investigations of these problems see the report by Y. Zeng in this volume.

References

[1] M. Heimpel, T. Gastine, and J. Wicht, Simulation of deep-seated zonal jets and shallow vortices in gas giant atmospheres, Nature Geos., 9 (2016), pp. 19–23.

[2] C. C. Porco, R. A. West, A. McEwen, A. D. Del Genio, A. P. Ingersoll, P. Thomas, S. Squyres, L. Dones, C. D. Murray, T. V. Johnson, et al., Cassini imaging of Jupiter's atmosphere, satellites, and rings, Science, 299 (2003), pp. 1541–1547.

[3] P. B. Rhines, Waves and turbulence on a β-plane, J. Fluid. Mech., 69 (1975), pp. 417–443.

[4] A. A. Simon, M. H. Wong, and G. S. Orton, First results from the Hubble OPAL program: Jupiter in 2015, The Astrophysical Journal, 812 (2015), p. 55.

[5] A. A. Simon-Miller and P. J. Gierasch, On the long-term variability of Jupiter's winds and brightness as observed from Hubble, Icarus, 210 (2010), pp. 258–269.

[6] D. J. Stevenson, Jupiter's interior as revealed by Juno, Ann. Rev. Earth Plan. Sci., 48 (2020), pp. 465–489.

[7] G. K. Vallis, Atmospheric and Oceanic Fluid Dynamics, Cambridge University Press, Cambridge, U.K., 2nd ed., 2017.

[8] G. K. Vallis and M. E. Maltrud, Generation of mean flows and jets on a beta plane and over topography., J. Phys. Oceanogr., 23 (1993), pp. 1346–1362.

GFD 2023 Lecture 7: Atmospheric Characterization of Young, Hot, Gas Giant Planets and Brown Dwarfs

Heather Knutson; notes by Yifeng Mao and Nathan Magnan

June 27, 2023

In the first few lectures we focussed on planets that are quite close to their stars, detected either through the radial velocity method or the transit method, or both. It is now time to focus on young gas giant planets on wide orbits, which are harder (but not impossible) to detect and characterize.

1 The Direct Detection Method

The transit technique is not suitable for studying planets that are located far away from their star. We may require alternative detection methods.

We will see a planet transit in front of its star only if its orbital plane is aligned so that the planet passes in front of its host star relative to our line of sight. The exact criterion depends on the star's radius and the planet's orbital distance. Planets in close proximity to their star have a high chance of transiting. However, those located at distances similar to Jupiter's only have a tiny probability of transiting. Additionally, Jupiter's orbital period of 12 years means that we must wait for a once-in-a-decade opportunity if we want to detect such a widely separated planet.

There are also limitations to the radial velocity method. For instance, we generally require observations over a full orbital period in order to confirm that the orbiting companion is planetary in nature and to determine its precise mass and orbital period. However, there are relatively few stars that have been observed with this technique over multi-decadal timescales, limiting our sensitivity to long-period planets using this technique.

Instead, we need to revisit a concept discussed in the first lecture, called direct detection. The idea is to obtain an image of the star and the planet, where we can resolve the planet separately from its star [1]. Although technically challenging, this is not impossible.

1.1 Principles and challenges

The key is to obtain high-resolution images so that the star and planet can be resolved. The main limits on resolution are diffraction and atmospheric turbulence. They can be mitigated by employing large telescopes equipped with adaptive optics, or by utilizing interferometers. Another constraint involves the planet-star contrast ratio and projected star-planet separation in the sky, which can be overcome by using big telescopes and selecting appropriate sources.

1.2 Preferred sources

The easiest planets to image are typically the ones that are far from their star and relatively bright. However, the equilibrium temperatures and corresponding luminosities of planets decrease with increasing orbital separation. A planet located farther away from the star is colder, and consequently less luminous. Therefore, our preferences for planets being far from their star and being luminous are two competing wishes that need to be balanced.

Fortunately, temperature is not entirely fixed by the distance of the planet to its star. Exploring very young planetary systems allows the acquisition of both orbital distance and brightness. Indeed, the accretion of material onto young planets converts gravitational potential energy to kinetic energy, heating the planet's interior and atmosphere. This energy is then gradually radiated away once accretion ends, so young planets can be quite warm. Ideally, we aim to observe planets that are still forming or just formed. Therefore, we need to consider stars that are $\sim 10^{7\text{-}8}$ years old. We also aim for big gas giant planets, because size also factors into luminosity.

We might also try to maximize the planet-star brightness ratio by looking for planets with relatively low albedos, and/or those that orbit relatively small, dim stars. However, varying the albedo between 0-0.5 has a relatively small effect on the equilibrium temperatures of these planets. Although small stars are favorable targets for this technique, it is relatively rare for them to host gas giant planets.

2 Demographics of Directly Imaged Exoplanets (DIEs)

We use sophisticated instruments to observe young nearby sun-like stars. There are approximately 500 such stars within a few hundred parsecs of the Sun. Because we are biased towards big and hot companions, some will be planets but some will be low-mass stars. We address this problem in §2.1, then move on to planetary statistics.

2.1 Caveat: How to differentiate between a big planet and a small star?

We need to draw a boundary between planets and brown dwarfs, which is the name given to the lowest mass stars. There are two competing criteria in that regard.

Stars generate energy through fusion, while planets are too small to do so. The first element to fuse is deuterium, so the boundary between stars and planets could be set by whether or not the object is massive enough to fuse deuterium in its core. This boundary is around $\sim 13\ M_J$. Companions more massive than this value would then be called brown dwarfs, while smaller/less massive companions would be classified as planets.

This criterion is straightforward to apply, because it only requires us to estimate the companion mass. But it creates unnecessary complexity down the line, because there are examples of objects less massive than $13\ M_J$ that live in isolation (without a host star), and big "brown dwarves" that are found in orbit around stars with relatively small companion-star mass ratios.

Maybe considering the formation mechanism of these companions may provide a better classification. We could decide that planets are objects that are formed in a proto-planetary disk, while brown dwarfs form like stellar binaries.

Stars form within dense molecular clouds, which contain filaments of high-density gas. Within these filaments are dense cores that may collapse under their own weight and become stars. If two cores are close to each other, they can be gravitationally bound and form a stellar binary. The initial separation between these cores is typically at least $a_0 \gtrsim 500$ au. By contrast, planets form in proto-planetary disks, which rarely extend beyond a few hundred au.

Therefore, the second common criterion sets a limit at $a \lesssim 200$ au, where a is the companion's semi-major axis. Companions located beyond that value are considered too far away to be formed within the disk, and are called stars. Usually, the mass ratio q between the companion and the primary is also included in that criterion. The value $q \lesssim 0.025$ is indicative of a planet rather than a stellar binary system [1].

2.2 Raw demographics

Using both of these criteria, there are only 20 or so objects that are both directly detected and classified as planets. There are also several dozen directly detected companions categorized as brown dwarfs, but they are either too large or too distant to be considered planets. Only $\sim 1\%$ of surveyed stars, which were selected to be young and are typically Sun-like, possess a directly imaged exoplanet (DIE). The occurrence rate of gas giant exoplanets decreases with increasing planet mass. For example, super-Jupiters are less common than Jupiters, which are less common than Saturns. The occurrence rate of gas giants is also maximized between $\sim 1-10$ au, and declines at wider separations. Most direct imaging surveys are only sensitive to planets that are $\gtrsim$ a few times more massive than Jupiter (most directly imaged planets are closer to 10 M_J) on relatively wide ($\gtrsim$ tens to hundreds of au) orbits [2]. This is an intrinsically rare type of planet.

These planets typically have host stars ranging from 10 to 100 million years old. For ages between $1 - 10$ million years, some objects are still embedded in their protoplanetary gas disks and are actively accreting hydrogen-rich gas. At ages of $10 - 100$ million years, the architectures of these systems may evolve due to dynamical three-body interactions. The majority of the 20 planets have a host star that is heavier than the sun.

These planets have masses ranging from 2 M_J to 13 M_J, and semi-major axes ranging from 10 au to 100 au.

2.3 Observables and estimates

There are a few quantities that we can measure directly once we have imaged a planet:

- First, we can measure the projected separation between the planet and the star. After accounting for uncertainties in the planet's orbital inclination and eccentricity, this can be converted into a constraint on the planet's semi-major axis a.
- Then, Kepler's third law gives a straightforward conversion between the semi-major axis and the period, $\frac{a^3}{P^2} = \frac{GM_\star}{4\pi^2}$, where a is the semi-major axis, P is the period, G is the gravitational constant and $M_\star$ is the mass of the host star.
- Independently, we can sum the number of photons received by each pixel from the planet, and obtain the planet's luminosity L. Or we can break this down into wavelengths and obtain a spectrum $F(\lambda)$.

There are a few other quantities that we can estimate but not measure precisely:

- One is the age of the planet. One could assume it is close to the age of its host star, and try to estimate the age of the star. There are a few ways to do that, reviewed in [3]. A simple one is to look at the size of all the stars in the parent cluster. Bigger stars have shorter lifetimes, so if we assume (i) that all the stars in this cluster formed at the same time, and (ii) that all clusters in the galaxy form the same proportions of heavy and light stars, then the number of "missing" big stars tells us how old the remaining stars are. This is not the best method, especially for young stars, but it gives an idea of how indirect these "measurements" are. One key takeaway from [3] is that if the cluster contains a big population of young stars, the age estimates tend to be more accurate.
- We cannot directly measure the planet's radius on the image, because the point spread function of the image is much larger than the angular size of the planet in the image. We can calculate radius if we know the luminosity and the effective temperature of the planet as $L = 4\pi\sigma R_p^2 T_{\rm eff}^4$, if we assume it radiates as a blackbody. Alternatively, the same evolution models shown in Fig. 1 also provide us with a predicted radius along with the planet mass for a given luminosity and age.
- From there, we can estimate the *effective temperature* $T_{\rm eff}$, which is the temperature a blackbody would need to have to match the observed luminosity. This is a proxy for the temperature in the emitting layer of the atmosphere, more on that in §3.1.
- Finally, we want to estimate the planet's mass, but this is challenging for DIEs. One way is to convert luminosity into mass using a model that describes how luminosity changes with age, as illustrated in Fig. 1. If we know the age of the system and the luminosity of the companion, we can determine its mass by identifying the intersecting line on the plot. However, the uncertainty in the age of the system leads to uncertainties in the estimated masses. Plus, there are uncertainties in the model, which requires assumptions about the planet's starting mass, starting temperature and starting entropy, all of which are poorly constrained because we do not know the exact formation process of these planets. All of this is in contrast to transiting planets, for which we can measure precise dynamical masses using the radial velocity technique.

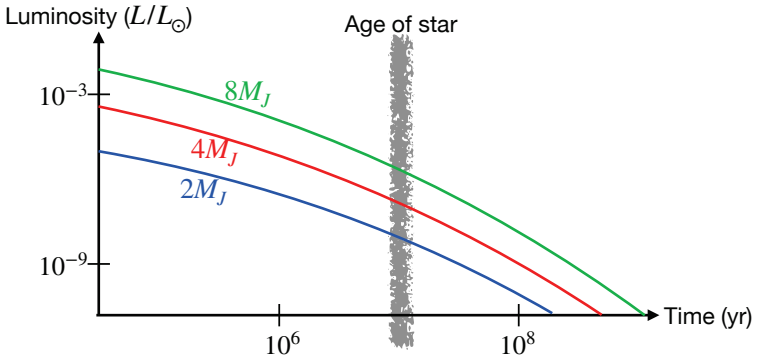

Figure 1: Luminosity of planets as a function of time. The system's age and the planet's luminosity establish a range for the planet's mass. Details can be found in [4].

2.4 Population diagram

Figure 2 presents a population diagram of most planets detected to date. It depicts their measured mass and semi-major axis, and from there makes three groups. Group I contains the giant planets that we studied in the previous lectures, including hot Jupiters, warm Jupiters and cold Jupiters. Group II is the population of small, close-in planets including super-Earths and sub-Neptunes. The majority of planets in groups I and II were discovered using the transit method, with a smaller subset being detected through the radial velocity measurement. All group III planets were identified through direct imaging, although it is important to note that some of the dots are low-mass stars.

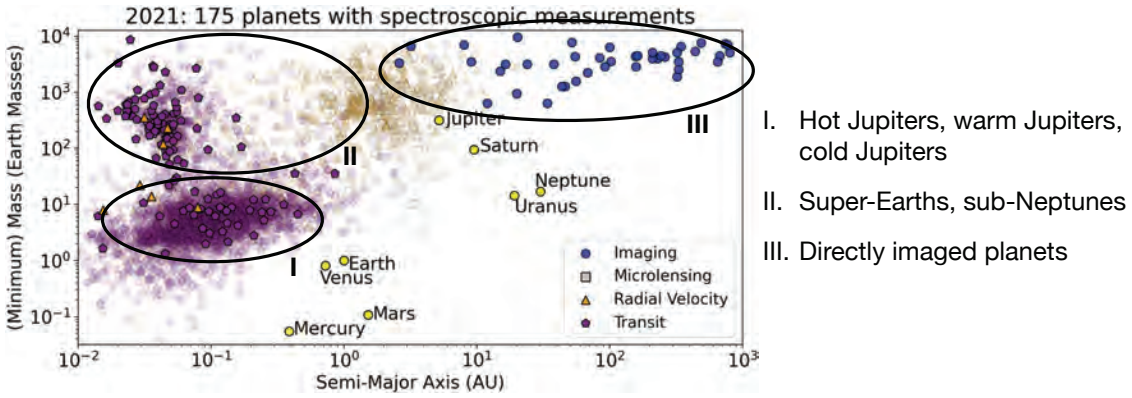

Figure 2: Demographics of planetary-mass companions detected with the transit method and radial velocity in groups I and II, and direct imaging in group III. The original plot is from [1].

2.5 Some notable DIEs

The HR 8799 system (see Fig. 3-*left*) is the most well-known DIE system, with four planets that have been directly imaged. The host star has a mass of approximately 1.5 $M_\odot$, and the planets have masses ranging from 5 M_J to 10 M_J and orbital semi-major axes from 15 au to 70 au. Notably, these planets are in a 1:2:4:8 orbital resonance chain. This indicates that the planets formed in a flat gas disk.

The 51 Eri system (see Fig. 3-*middle*) contains the DIE that is the closest to its star. It has a semi-major axis of ~ 13 au, similar to the gas giants in the solar system. The mass of the companion is not accurately known, but is around a few M_J. The mass of the primary star is ~ 1.8 $M_\odot$. The system is about 20 million years old.

PDS 70 is a famous two-planet system (Fig. 3-*right*). The star is young enough (about 5 million years old) that it is still surrounded by its proto-planetary disk. Interestingly, the outer planet is located just inside the inner edge of the disk, maybe indicating that this planet is carving the disk. At any rate, these planets are known to be actively accreting, thanks to emission lines of infalling hydrogen gas. The planets' mass are somewhere between a few M_J to 10 M_J, and their semi-major axes are 20 au and 34 au.

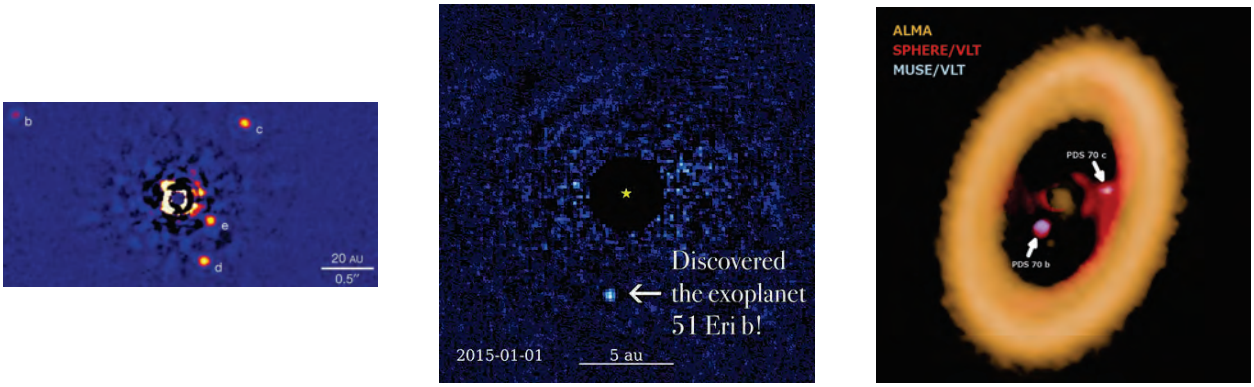

Figure 3: Three notable DIE systems. *Left*: HR 8799. Credit: Marois et al (2010). *Middle*: 51 Eri. Credit: Wang and De Rosa (2015). *Right*: PDS 70. Credit: ALMA A. Isella; ESO.

3 Atmospheric Properties of DIEs

Considering the difficulties we already face detecting these objects or measuring their bulk properties, it might come as a surprise that we are able to say anything about their atmospheres. Yet, by plowing through the data, we find that DIEs are hot, cloudy and rotating quickly.

3.1 High temperatures

Temperature is a tricky quantity to measure, because it is not uniform nor independent of time. It varies between the equator and the pole, between the interior and the upper atmosphere, and as a newly formed planet cools down. With the current instrumental resolution, we can at best discuss averaged forms of temperature.

One such averaged form of temperature, which we have already met in previous lectures, is the *equilibrium temperature* $T_{\text{eq.}}$. It is the temperature the planet (seen as a blackbody) needs to have in order to radiate away exactly as much energy as it receives from the star.

Unfortunately, this quantity is not very relevant for DIEs. Indeed, these planets (like any other) formed through a collapse or accretion process of some sort, which transformed a lot of gravitational potential energy into a lot of internal energy. DIEs are young, so they are still in the process of radiating this extra heat away. This radiation is what makes DIEs bright enough that we can detect them.

Since the internal heat flux is orders of magnitude larger than stellar irradiation, we could try to estimate the temperature from the initial amount of internal energy (which is related to mass), the energy lost since formation (which is related to age), and the average heat capacity (which is related to composition). But we just saw that none of these bulk properties are easy to measure.

What we can do is define the *effective temperature* T_{eff} as the temperature a blackbody would need to have to explain the observed luminosity. This is the temperature of the radiating layer of the atmosphere, and as such it only provides indirect information about the temperature structure in the interior. We find $T_{\text{eff}} \approx 1000 - 2000$ K for typical directly imaged exoplanets.

To measure the effective temperature we need a direct observable (the luminosity) but also an indirect observable (the radius of the planet), which is unideal. An alternative would be to look for a blackbody that has the right temperature to match the shape of the observed spectrum. But it turns out that this is also challenging, because the characteristic shape of the blackbody spectrum is polluted by broad and strong absorption bands from water, carbon monoxide, and other species. This problem is further exacerbated by scattering from small aerosols.

3.2 Patchy clouds

The first evidence we have for clouds is linked to the point of detail made above: we see features in the spectrum that hint at scattering by silicate particles in the upper atmosphere.

Specifically, we see a reddening of the spectrum due to scattering. This is a reasonably intuitive concept: (i) The planet has a certain temperature, and so must radiate away a fixed amount of energy; (ii) At the surface, we can expect blackbody radiation. (iii) But if there are clouds in the upper atmosphere, they will scatter the short wavelengths preferentially; (iv) The atmosphere compensates by radiating more long wavelengths than it receives; (v) As a consequence, the observed spectrum is biased to the red compared to a blackbody. A diagram of the resulting spectrum is provided in Fig. 4-*left*.

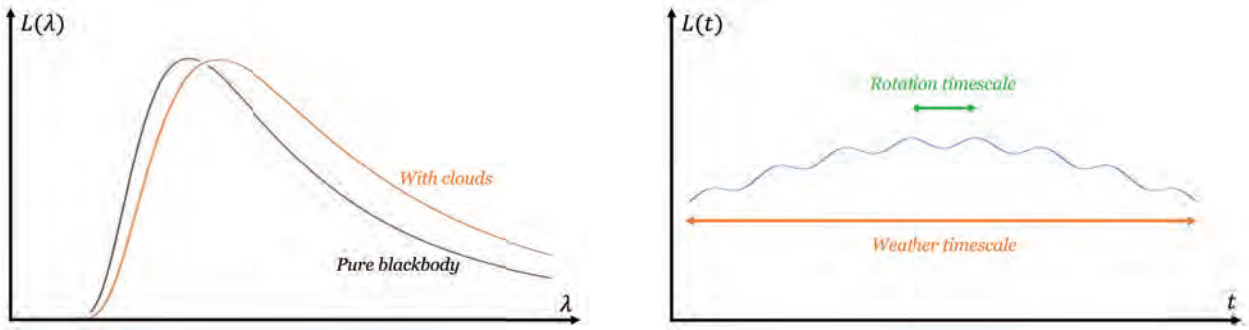

Figure 4: *Left:* Overly simplified diagram of the effect of silicate clouds on the spectrum. The black line is the surface's pure blackbody spectrum, and the orange line is the spectrum radiated from the upper atmosphere, after scattering. *Right:* Schematic diagram of a typical DIE light curve, $L(t)$. The light curve, in blue, varies over two different timescales. The short time scale corresponds to the planet's "day" and is evidence of patchy clouds. The long time scale corresponds to the planet's weather evolution. Just like on Earth, the weather takes a few days to evolve significantly.

A second piece of evidence comes from plotting the planet's total observed luminosity over time, $L(t)$. As shown in Fig. 4-*right*, we find that it varies on the timescale of the planet's day-night cycle. Since the brightness comes mainly from the planet's thermal emission, and since we believe the deep atmosphere to be relatively uniform in temperature, we do not expect any brightness variation in the deep. The observed variation must therefore be due to an upper atmospheric structure. The easiest explanation is clouds, but they must be patchy, not uniform.

It has been known for a while that brown dwarfs also exhibit rotational light curve variability [5]. The magnitude of this rotational variability can be as high as 30% [6]. These studies conclude that most of this rotational variability is likely due to inhomogenous clouds in the atmosphere, but temperature variations could play a minor role.

3.3 Fast rotation

The same light curve also gives the planet's spin period. We find that DIEs typically rotate in 4 to 20 hours, which is similar to Jupiter. This is quite a fast rotation, especially considering how big these planets are. As a consequence, we expect circulation in those planets' atmosphere to happen at a very low Rossby number, $\mathrm{Ro} \ll 1$. This is in opposition to hot Jupiters (HJs), for which we expect Rossby numbers closer to unity, since they are often tidally locked.

Another method to estimate the spin period of these planets is to use the Doppler broadening of emmission lines. Due to rotation and at any given time, one side of the planet is coming towards us, and one side is going away from us. If we find a thin molecular line that is absorbed or emitted in the upper atmosphere, we expect it to broaden from the purple shape to the green shape in the figure opposite. The level of broadening is dictated by $v \sin(i)$, where v is the speed of the planet's surface and i the inclination of the planet's spin axis with respect to the observer's line of sight. Since $v = \Omega_p \, t_p$, this can be used to estimate a lower bound on Ω_p, provided we have an estimate of the planet's radius. Reassuringly, the two methods give spin periods that are consistent with each other.

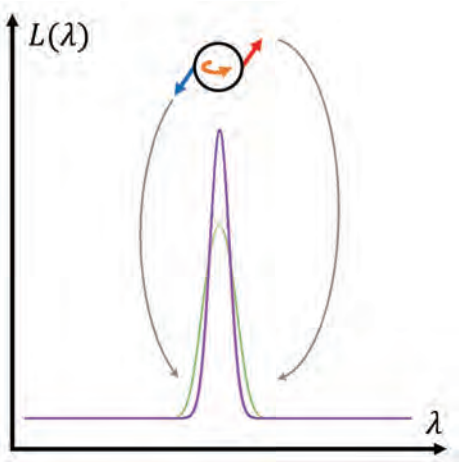

4 What Does This Imply for the Atmospheric Dynamics?

Besides this difference in Rossby number, the other difference between HJs and DIEs is that the latter are internally heated instead of irradiated, as shown in Fig. 5. Let us explore the consequences of this novelty on atmospheric dynamics.[1]

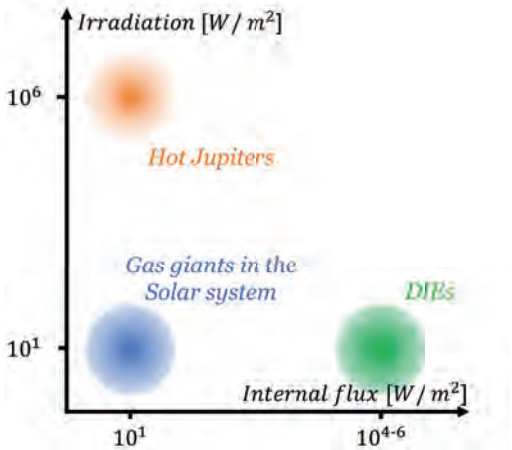

Figure 5: Approximate position of HJs, gas giants and DIEs in the (Irradiation, Internal flux) plane. This figure is inspired by [7].

[1] "Explore" being the key word here.

4.1 Convection-dominated atmospheres

First, we can expect the planet's interior to be quite hot and the upper layers of the atmosphere to be cooler. This implies that the vertical gradient of temperature is steep, which will inevitably lead to convection. Quantitatively, we expect most of the atmosphere to be convective, except the uppermost $P < 1$ bar layer.

This is very different from the atmospheres of HJs, whose vertical temperature gradient is quite small since they are heated from the top by stellar radiation. It is thought that in HJs, the radiative zone extends quite deep.

4.2 Origin of the patchy clouds

On Earth, clouds are ultimately due to horizontal temperature gradients. But the temperature of DIEs is dictated by their internal flux, which is uniform over the interior. As such, the process behind cloud formation on DIEs is worthy of some reflection.

One line of thinking invokes radiative instability. Imagine an infinitesimal "cloud seed". As shown in Fig. 6, this cloud bars some of the surface's blackbody radiation from reaching space. This heats up the column, which puffs up. In consequence, the cloud rises, and as it rises, it encounters a colder environment, so some of its molecular content condensates. The cloud seed grows, which closes the positive feedback loop. The end result of this instability is a full-fledged cloud [8].

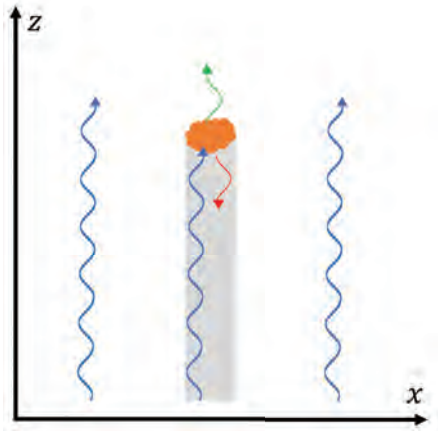

Figure 6: Schematic diagram of radiative transfer in a cloudy column. The planetary surface emits a certain amount of radiation (in blue). Usually, these rays will reach space, as happens on the left and the right. But if there is a cloud (in orange) on its way, only part of the ray is transmitted (in green), and the rest is reflected (in red). This heats up the column below the cloud (in grey).

4.3 First insights from a Global Circulation Model (GCM)

As far as the lecturer is aware, the literature only contains one global circulation model (GCM) paper on directly imaged exoplanets and brown dwarfs that includes the aforementioned radiative feedback loop [9]. The results are presented in Fig. 7.

Essentially, these simulations validate the radiative instability intuition, it does indeed lead to patchy clouds. The size of this cloud correlates with the spin period, which is perhaps not surpising

since the Rossby deformation radius is proportional to the spin period. The author also checked that these clouds lead to the variability of the right magnitude in the light curve.

The simulation also show a global circulation pattern, with an equator band whose width also correlates to the spin period. By opposition to Jupiter and Saturn, there is no other band North and South of the Equator.

5 Conclusion

DIEs live in a peculiar forcing regime, different from that of the solar system's gas giants or HJs. This will lead to different and interesting dynamics that have not yet been explored in any amount of detail. And, for once in astrophysics, this is not by lack of observational constraints. There are a few quantitative measurements that could be used to discriminate between models, for instance the light curve variability.

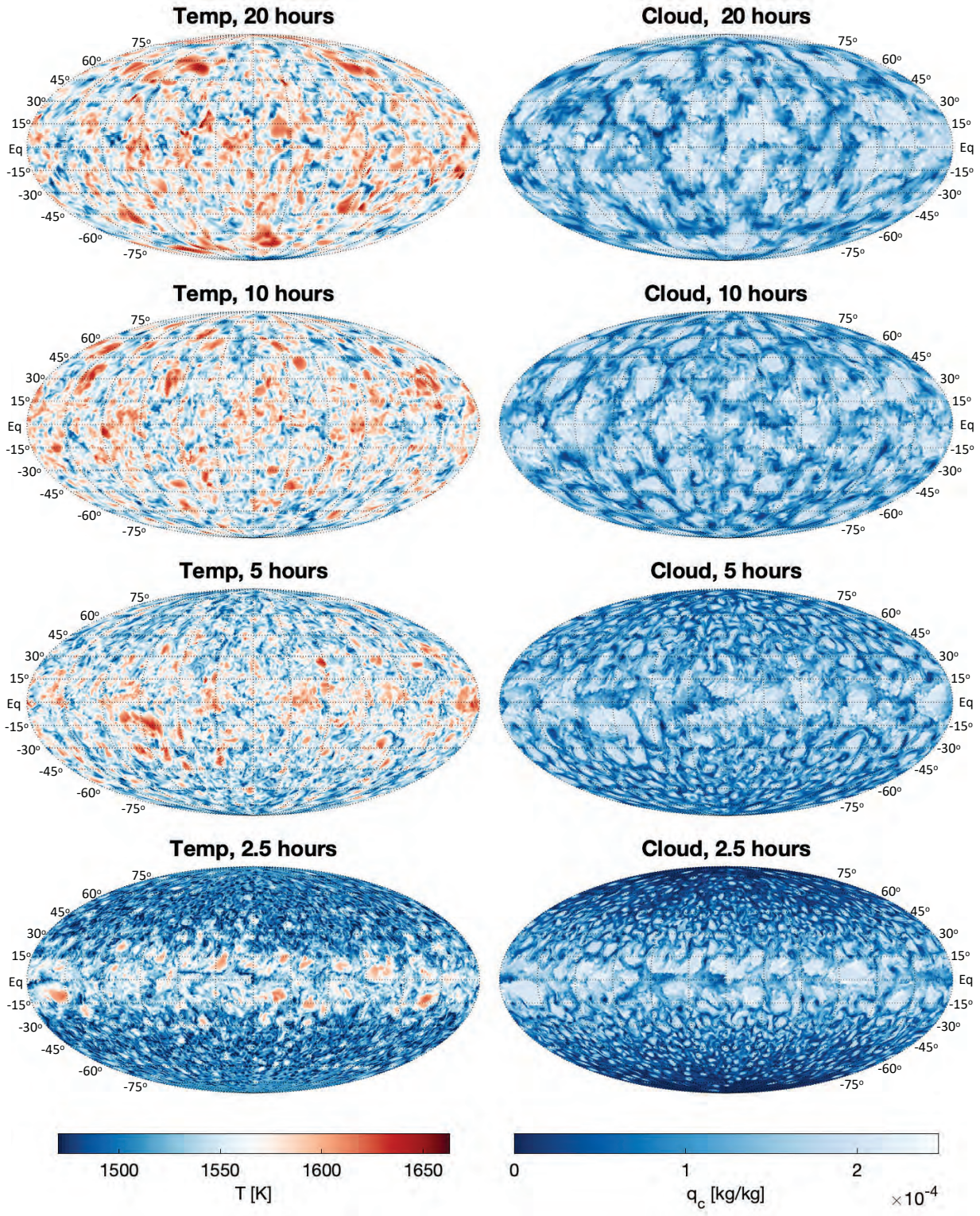

Figure 7: Temperature (on the left) and humidity (on the right) outputs from the GCM run at different spin frequencies [9]. In all simulations, we see patchy clouds, but their size correlates with the spin period. In the fastest rotators, we see an equatorial band. We never see as many meridional bands as in Jupiter or Saturn.

References

[1] Currie, T., *et al.*, 2022, Direct Imaging and Spectroscopy of Extrasolar Planets, *Arxiv preprint*, 2205.05696.

[2] Fulton, B. J., *et al.*, 2021, California Legacy Survey. II. Occurrence of giant planets beyond the ice line, *The Astrophysical Journal Supplement Series*, 255.1: 14

[3] Soderblom, D. R., *et al.*, 2014, Ages of young stars, *Protostars and planets VI*, 3.1.

[4] Marley, M. S., *et al.*, 2007, On the luminosity of young Jupiters, *The Astrophysical Journal*, 655.1: 541.

[5] Biller, B., *et al.*, 2018, Exoplanet Atmosphere Measurements from Direct Imaging, *Handbook of Exoplanets*, p. 101

[6] Zhou Y., *et al.*, 2022, Roaring Storms in the Planetary-mass Companion VHS 1256-1257 b: Hubble Space Telescope Multiepoch Monitoring Reveals Vigorous Evolution in an Ultracool Atmosphere, *Arxiv preprint*, 2210.02464.

[7] Showman A. P., *et al.*, 2020, Atmospheric Dynamics of Hot Giant Planets and Brown Dwarfs, *Space Science Reviews*, 216, 8, 139.

[8] Tan X. and Showman A. P., 2019, Atmospheric Variability Driven by Radiative Cloud Feedback in Brown Dwarfs and Directly Imaged Extrasolar Giant Planets, *The Astrophysical Journal*, 874, 2, 111.

[9] Tan X. and Showman A. P., 2021, Atmospheric circulation of brown dwarfs and directly imaged exoplanets driven by cloud radiative feedback: global and equatorial dynamics, *MNRAS*, 502, 2, 2198-2219.

GFD 2023 Lecture 8: Atmospheric Characterization of Terrestrial Planets

Heather Knutson; notes by Hao Fu and Ellie Ong

April 13, 2025

In the previous lecture we discussed the atmospheric composition of gas giants, methods of measuring their atmospheric properties, and notable exoplanetary systems. In this lecture, we move on to terrestrial/rocky planets and their atmospheric characteristics. In §1 we review the types of small rocky planets: sub-Neptunes, super-Earths, and water worlds. In §2 we look at the evidence for the existence of water worlds and their hypothesized atmospheric properties. In §3-4, we discuss predictions and detection methods of super-Earth atmospheres and in §5 we look at notable measurements of super-Earths in a few examples. Finally, in §6 we look at possible atmospheric circulations on super-Earths as a precursor to Lectures 9 and 10.

1 Types of Small Terrestrial Exoplanets

Small exoplanets are categorised as those of radius $R \sim 1-3R_\oplus$, with mass $M \sim 1-10M_\oplus$. They can be classified further into:

- sub-Neptunes, with H-He atmospheres and a rocky core;
- super-Earths, with a rocky core and an outgassed atmosphere; and
- Water worlds, characterized by an atmosphere rich in H_2O.

Due to the methods used to measure the mass and radius of exoplanets, smaller exoplanets around smaller stars are easier to characterize. The transit method, which is used to measure the radius of exoplanets relative to their host star, and the radial velocity method, which is used to measure the mass of the planets, are most effective when the host star is small, as detailed in the previous lecture.

In Luque and Palle, 2022 [1], observational data has been aggregated for exoplanets around small stars, with mass and radial measurements. Comparing the theoretical mass-radius relation for planets with an Earth-like mixture of rock, exoplanets that lie near this line are *super-Earths*, and they likely have a similarly rocky core with little atmosphere. For exoplanets of larger radii ($\sim 2-3R_\oplus$) but similar mass to Earth, we deduce that the presence of a less dense H and He atmosphere increases the radius of the exoplanets. Hence, we can classify them as *sub-Neptunes*. However, if we plot a line of the bulk density of planets with a 50% H_2O and 50% rock ratio, we find that there is a third sub-population of planets with masses between $\sim 2-5M_\oplus$ that appear to lie along this line. This line characterizes the bulk density of *candidate water worlds* but these could also be planets composed of a rocky core and thin H-He atmosphere [2].

As we have already covered exoplanets with H-He atmospheres in the previous lecture, we will skip over sub-Neptunes and discuss only water worlds and super-Earths in this lecture.

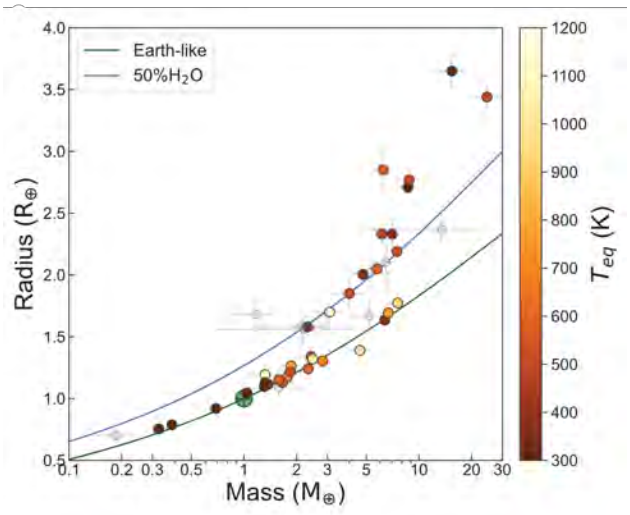

Figure 1: Plot of mass vs. radius of exoplanets, along with lines of bulk density corresponding to Earth-like planets and those with 50% H_2O composition. Replicated from Luque and Palle, 2022 [1]

2 Water Worlds

All currently known candidate water worlds are found on relatively close-in orbits, with an orbital period of < 100 days. It is thought that these planets likely formed near or outside the water-ice line and then migrated inward to their current locations. They can have up to 50% of their mass in the form of water, as this is the maximum water content that can be held by the solids located outside the water-ice line. It is thought that these water worlds may be more likely to form around cool, dim stars, as smaller host stars have a water-ice line closer to the star, making a water-rich atmospheric composition more likely. Please refer to Lecture 1 for further explanation of the water-ice line.

The second line of evidence for the existence of water worlds relies on models of atmospheric mass loss. Smaller, hotter water world candidates are predicted to have lost any primordial H + He envelopes, leaving behind a water atmosphere. This mass loss is driven by high-energy photons from the host star, in the form of the extreme UV of short wavelengths (EUV) and X-ray flux in flares, which cause the upper atmosphere of the planet to heat and expand, eventually becoming unbound [3]. In addition to their steady-state emission, small stars also flare frequently, which can further increase the mass loss rates of orbiting planets. These flares arise from the magnetic field around stars, where short energetic events can release high energy particles from the upper layer of the star. As the absorption of high-energy photons causes the atmosphere to heat and expand, and the uppermost layers become unbound, atmospheric mass loss occurs, and is considered the *photoevaporative escape* of the atmosphere (also called "hydrodynamic escape"). An illustration of this process is in Figure 3, and this outflow is also enhanced by stellar winds sculpting the flow of the atmosphere and inducing instabilities, but not a key outflow process, as further highlighted in §4. Additionally, low-mass stars are more magnetically active than sun-like stars, emitting a larger fraction of EUV and X-ray flux. This magnetic activity might make it harder for smaller planets to retain the atmosphere around these stars.

Assuming no albedo and treating the planet as a black body, the typical equilibrium temperatures of water worlds are $T_{eq} \sim 300 - 1000$ K as seen in lecture 1, where H_2-dominated atmospheres

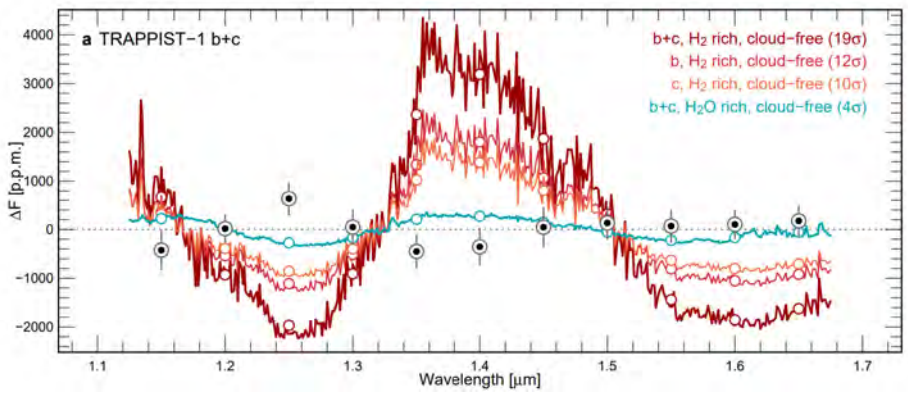

Figure 2: Transmission spectrum of Trappist-1 b and c (in black dots), compared to predicted spectra from atmospheres of different compositions. The predicted spectrum with the water world composition (in blue) has a low scale height compared to that of the H_2 composition (in red and brown). Replicated from Wordsworth and Kriedberg, 2021. [4]

are more susceptible to loss as T_{eq} is increased. Predicted photoevaporative mass loss rates for these planets depend on the assumed value of η, the fraction of the high energy flux F_{EUV} that is converted to heat, which depends on the unknown atmospheric composition. These estimates of energy flux and equilibrium temperature allow us to predict the escape rates of a hydrogen-rich atmosphere, and mass loss models suggest that the most highly irradiated water world candidates are unlikely to have retained any primordial hydrogen-rich atmospheres.

These predicted mass loss rates, however, have uncertainties of up to a factor of 10, but measurements will soon be able to directly confirm the existence of water worlds. The James Webb Space Telescope can detect water absorption from the atmospheres of water worlds. Using the transmission spectroscopy method, the magnitude of the absorption signal during transit from water world atmospheres is expected to be much smaller than those of exoplanets with H-He atmospheres, as water world atmospheres have a higher mean molecular weight than H-He atmospheres. This results in transmission spectra with a smaller scale height based on the equation for transit depth: $H = kT/\mu g$ where k is the Boltzmann constant, T is the atmospheric temperature (assumed isothermal), μ is the molecular weight of the atmospheric species, and g is the gravitational acceleration.

Clouds or hazes can, however, result in featureless transmission spectra due to the increased opacity of the atmosphere. If the transmission spectra were extended to include the visible light spectrum, we would be able to detect clouds due to their scattering in spectra of the visible light wavelengths. Detecting and correcting for the effects of clouds in these exoplanetary atmospheres, therefore, remains an active area of research.

3 Predicting Atmospheric Compositions of Super-Earths

Now moving onto the atmospheric composition of super-Earths: these exoplanets have an Earth-like bulk density, without a thick H_2O or H_2 atmosphere, but may still have atmospheres of heavier molecules, such as CO_2, N_2, etc. that would not significantly increase their measured radii. For example, Venus's atmosphere is only 1% of its planet's radius, and its atmosphere consists mostly of carbon dioxide. Therefore, we aim to understand the types of atmosphere that these super-Earths have.

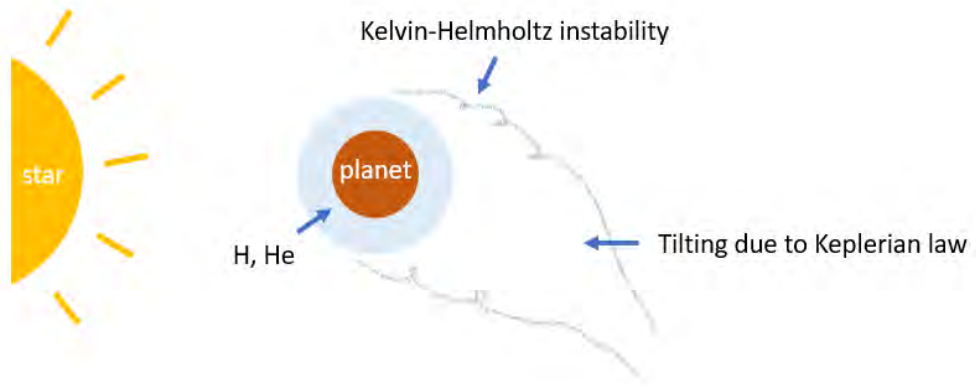

Figure 3: A schematic diagram for the hydrodynamic escape of planetary atmospheres.

The atmospheric composition of exoplanets can be greatly influenced by atmospheric escape processes, even when they are too cool for hydrodynamic escape. High energy photons provide energy to atmospheric molecules and raise their thermal velocity. Whether a given particle tends to escape depends on the relative magnitude of gravitational escape speed v_{esc} and the thermal velocity v_{th}. When a particle is at v_{esc}, the centrifugal force balances the gravity:

$$m\frac{v_{esc}^2}{R_P} = \frac{GM_\oplus m}{R_P^2} \quad \Rightarrow \quad v_{esc} = \left(\frac{GM_\oplus}{R_P}\right)^{1/2}, \tag{1}$$

where G is the gravitational constant, $M_\oplus$ is the planetary mass, and m is the molecular mass. The thermal velocity, which has to exceed the escape velocity, is expressed with temperature:

$$\frac{1}{2}v_{th}^2 = kT \quad \Rightarrow \quad v_{th} = \left(\frac{2kT}{m}\right)^{1/2}, \tag{2}$$

High energy photons from the host star heat the exoplanetary atmosphere. Lighter atoms (with a smaller m) in the exoplanets' atmosphere, such as H and He, tends to have a high v_{th} and escapes more easily.

Taking atmospheric escape into account can help us infer the atmospheric composition of exoplanets. Even more fundamentally, we want to confirm if these exoplanets even have atmospheres. Super-Earths around cool stars can experience even stronger atmospheric mass loss than those around warmer stars. The greater mass loss is due to cool stars having higher X-ray and EUV fluxes as a fraction of their total (bolometric) flux, resulting in higher predicted hydrodynamic mass loss rates. Some super-Earths have equilibrium temperatures of up to ~ 2000 K, and at such high temperatures, it is difficult for planets to hold on to their atmosphere.

To predict the existence and atmospheric composition of rocky planets without observational constraints (yet), we can go back to planet formation models and observations of solar system terrestrial planets. We assume that matter is accreted as solids and then heated, releasing gases, with H, C, N, O, and S combined to form a variety of gas phase molecules. Outgassing from meteorite samples, representative of materials from planetary building blocks, have been found to include water, CO_2, CO, and trace amounts of H_2, H_2S and N_2 [5]. Photoionization of water and other hydrogen-bearing molecules can result in the preferential loss of hydrogen atoms to space over time. However, upward mixing in the atmosphere can replace the lost H_2O until all the H_2O is lost. Together with the knowledge that lighter H-He molecules are easily lost through hydrodynamic

escape, we can therefore assume for now that CO_2, CO and N_2 are likely to be dominant in terrestrial exoplanets at later times.

This process in action can be seen in planets in our own solar system, looking at the three rocky planets:

- **Venus**: 92 bar surface pressure, 700K surface temperature, and a thick atmosphere of 92% CO_2 and 3% N_2
  - Venus likely formed with a lot of water but lost >99% of the initial water mass. Evidence of this process is found in the concentration of D in the atmosphere of Venus. D will escape more slowly than H, and the presence of a high D/H ratio in the sulphuric acid in Venus' atmosphere indicates that most of the H mass has been lost.
- **Earth**: 1 bar surface pressure, 78% N_2 and 21% O_2
  - We said earlier that H_2O and CO_2 are likely produced by outgassing, but Earth does not have a high concentration of these in the atmosphere. Atmospheric H_2O is instead condensed into oceans, while CO_2 is incorporated into the Earth's crust and ocean via the ocean-driven carbonate cycle and is also sequestered into carbonate rock. The larger proportion of O_2 in the Earth's atmosphere is produced by photosynthesis and is therefore relatively recent (began 2.4 Gyr ago) [6] [1]
- **Mars**: 7 mbar surface pressure, with 140-300K surface temperature and an atmospheric composition of 95% CO_2 and 3% N_2.
  - Again, we would have expected higher concentrations of H_2O. However, present-day Mars is so cold that atmospheric water is largely condensed onto the surface as ice. There is evidence of liquid H_2O on the surface of Mars 3.56 years ago, which required a $> 0.5 - 1$ bar CO_2 atm in order to create sufficiently warm surface conditions. This early CO_2 atmosphere was likely either lost due to non-thermal escape processes, e.g. photochemical or stellar wind processes, and/or sequestered on the surface in the form of CO_2 ices and carbonate rocks.

4 Detecting Atmospheres of Super-Earths

What about exoplanets? We focus on super-Earths orbiting small stars, which typically denote M dwarfs. These are the only exoplanets we can characterize. Because the planets are close to the star, they are tidally locked.

Recall from previous lectures, that near the secondary eclipse, the ratio of planetary emission to the star emission is:

$$\frac{F_P}{F_*} \approx \left(\frac{R_P}{R_*}\right)^2 \frac{T_P}{T_*}. \tag{3}$$

where R_P is the planetary radius, R_* is the star radius, T_P is the planetary temperature, and T_* is the star temperature. The T_P/T_* is the ratio of emission power at the longwave limit (Rayleigh-Jeans limit). This means that small planets orbiting small stars, which have smaller radii and lower temperatures than Sun-like stars, are easier to characterize than their counterparts orbiting hotter stars.

[1] For an interesting Earth related sidenote on the effect of tides and planetary rotation on oxygen levels, see Klatt et al. 2021, Possible link between Earth's rotation rate and oxygenation, Nature Geosciences.

For planets with different R_P, the change of transmission spectrum $\frac{F_P}{F_*}$ is proportional to the change of $\left(\frac{R_P}{R_*}\right)^2$, which equals $\Delta_{depth} \approx \frac{2R_p}{R_*^2} dR_p$. Here dR_p is the perturbation radius of the planet, which is between 1 to 5 scale height H. The H is expressed as $H = kT/(\mu g)$ as in §3. This indicates that a smaller R_* leads to a higher Δ_{depth} that makes the planet's atmosphere easier to detect when it orbits a small star.

We next ask: Do rocky super-Earths keep or lose their outgassed atmosphere? There are two possible scenarios:

- Scenario 1: From Sub-Neptune to Super-Earth.
- Scenario 2: Some planets, like the solar system's territorial planets, are born rocky.

In the first scenario, where sub-Neptunes transform into super-Earths, the uppermost layers of the planetary atmosphere are heated by X-ray and UV photons from the host star. This drives hydrodynamic escape, which can strip away the atmosphere of a sub-Neptune and turn it into a super-Earth. This hydrodynamic escape is expected to remove heavier molecules along with the molecular hydrogen and thus would also remove any initial inventories of outgassed water, CO_2, N_2, and other similar molecules. If these planets have atmospheres, they must comprise materials outgassed after the initial H-rich envelope was lost. For planets that formed without primordial H-rich atmospheres (i.e., analogous to the terrestrial planets in the solar system), it may be easier to form a thick atmosphere since primordial outgassed materials are retained.

5 Super-Earth Atmospheric Measurements

For tidally locked planets, we can infer the presence or absence of a thick atmosphere using phase curves of the emission flux (Fig. 4). For a planet without an atmosphere, the total emission of the star and the planet is periodic with respect to the orbital phase, except at the transition (the planet is in front of the star) and the secondary eclipse (the star is in front of the planet). During the transition, the planet blocks the star's light. At the secondary eclipse, the planet is hidden, so the emission flux equals the star's basic level flux.

For a planet with a thick atmosphere, the atmosphere can reduce the day-night side temperature difference by its circulation, so the amplitude of the phase curve is reduced. In addition, the atmosphere may have super-rotation, which makes the hot spot shift eastward (suppose the planet rotates anti-clockwise). This causes the peak in the planet's emission flux to occur early, before the secondary eclipse, as sketched in Fig. 4.

Let's see an example where these measurements can be used to infer the atmospheric composition of an exoplanet: LHS 3844b, as documented in [7]. The planet has a radius of $1.3R_\oplus$ and an orbital period of 11 hours. The star's mass is $0.15M_\odot$. The equilibrium temperature T_{eq} is diagnosed to be around 800 K, with a 3.5 μm emission flux (assuming blackbody). The day-side temperature is $T_{day} = 1000$ K, and the night-side temperature is $T_{night} = 700$ K. On the day side of LHS 3844b, the hottest temperature is at the substellar point, which indicates a lack of superrotation. Reaching $T_{day} = 1000$ K requires a low day-side albedo, possibly due to dark basaltic crust, and a large temperature difference compared to the night side indicates a lack of atmospheric circulation, with no energy distribution to the night side. Thus, the atmosphere must be absent or tenuous, likely with an atmospheric pressure of $P < 0.06$ bar with O_2 or N_2 dominating. [2] However, such an atmosphere is unstable (due to the hydrodynamic escape) and must be constantly replenished.

[2]Note that O_2 could be the remnant of a primordial H_2O-rich atmosphere.

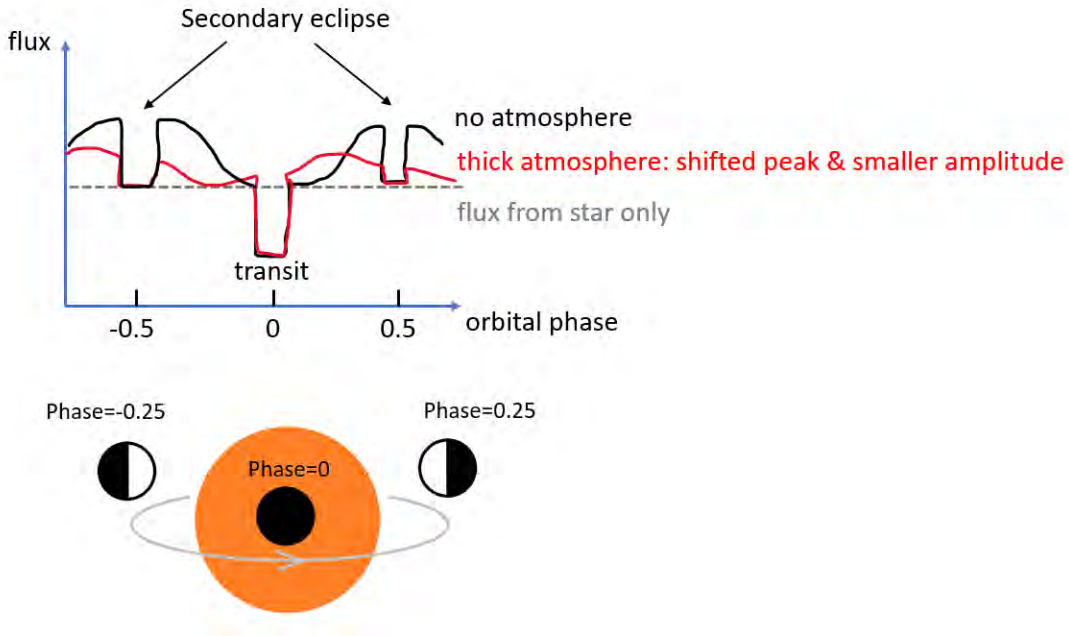

Figure 4: The upper panel is a schematic diagram for the emission flux of the star for a planet with no atmosphere (solid black line) and a planet with a thick atmosphere (solid red line). The dashed grey line denotes the flux from the star only, which does not change with the orbital phase. The lower panel illustrates why the emission flux is periodic - analogous to the moon phase.

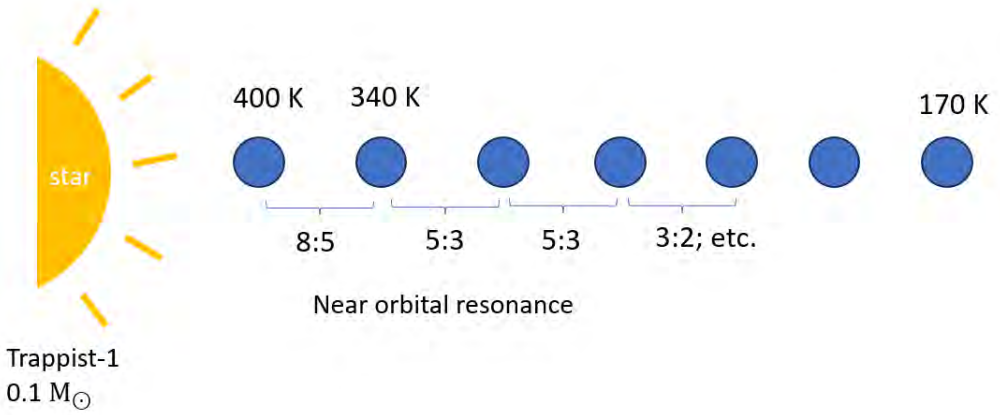

Figure 5: A schematic diagram for the Trappist-1 system. The spacing between the planets is found by Agol et al. (2021) [8] to be near orbital resonance.

LHS 3844b is relatively hot, and therefore may be more likely to have lost its atmosphere. Are there colder rocky planets with atmospheres? Let's consider an example - Trappist-1, which is a star with $0.1M_{\odot}$. The system is illustrated in Fig. 5. All planets are between $0.8 - 1.1R_{\oplus}$, and the period is between $P = 1.5 - 18$ days. The three planets closest to the star are named a, b, and c. Assuming tidally locked exoplanets, we can use the brightness temperature T_{bright} from each of these planets, relative to their expected equilibrium temperatures, to infer the existence of atmospheric circulation. [3]

Going back to the planets of Trappist-1, the day-side brightness temperatures measured by *JWST* are T_{bright} are:

- Planet b: $T_{bright} \approx 500 \pm 30$ K [9] .
- Planet c: $T_{bright} \approx 380 \pm 30$ K [10].

Therefore, the brightness temperatures for both planets are higher than their predicted equilibrium temperatures for the efficient circulation case. Why is it? We can therefore infer that both planets have low albedos and weak day-night circulation, implying that they likely have little to no atmosphere.

6 Possible Circulation on Temperate Super-Earths

We assume synchronous rotation for close-in rocky planets orbiting M-dwarf stars (a cold, low-mass star). What effect does this have on their ability to potentially retain liquid water on their surfaces? The incident heating concentrates on one side of the planet (a permanent day-side), driving a convergent circulation at the lower level and a divergent circulation at the upper level (Fig. 6). The circulation also excites Rossby waves, which converge momentum to the equator and generate a super-rotating jet. The convergent circulation can produce water clouds at the sub-stellar point if the atmosphere is cool enough. This can increase the day-side albedo, making the temperature there cooler and could maintain surface liquid water at higher solar incident fluxes than the Earth-Sun analog. Thus, the clouds could make the inner edge of habitable zone closer to the star.

Meanwhile, if the night side is sufficiently cold, the circulation can trap condensible species (e.g., CO_2 and/or H_2O) at the anti-stellar point. This could lead to a collapse of the atmosphere, as probably has occurred for Mars and Pluto.

[3] As a review, for a well-mixed atmosphere with no day-night temperature difference, the brightness temperature T_{bright} should equal the equilibrium temperature T_{eq} of the exoplanet. However, the equilibrium temperature of the planet's day side can be higher if the planet is tidally locked with weak day-night energy transport. For a planet with no day-night temperature gradient (efficient heat tranpsort by a thick atmosphere), the T_{eq} is given by:

$$\text{Efficient day-night circulation:} \quad 4\pi R_{\oplus}^2 \sigma T_{eq}^4 = \pi R_{\oplus}^2 S(1-\alpha) \quad \Rightarrow \quad T_{eq} = \left[\frac{S(1-\alpha)}{4\sigma}\right]^{1/4}. \tag{4}$$

where S is the solar heating power at the planetary orbit, α is the albedo, $R_{\oplus}$ is the planetary radius. A lower α makes T_{eq} higher because more solar heating is reflected. For a tidally locked planet with weak day-night energy transport (e.g., little to no atmosphere), the day-side temperature can be much higher than the night-side temperature. In this case, the area for radiative cooling (compared to the left-hand side of (5)) is halved, yielding:

$$\text{Weak day-night circulation:} \quad 2\pi R_{\oplus}^2 \sigma T_{eq,day}^4 = \pi R_{\oplus}^2 S(1-\alpha) \quad \Rightarrow \quad T_{eq,day} = \left[\frac{S(1-\alpha)}{2\sigma}\right]^{1/4}, \tag{5}$$

where $T_{eq,day} \approx 2^{1/4} T_{eq} \approx 1.2 T_{eq}$.

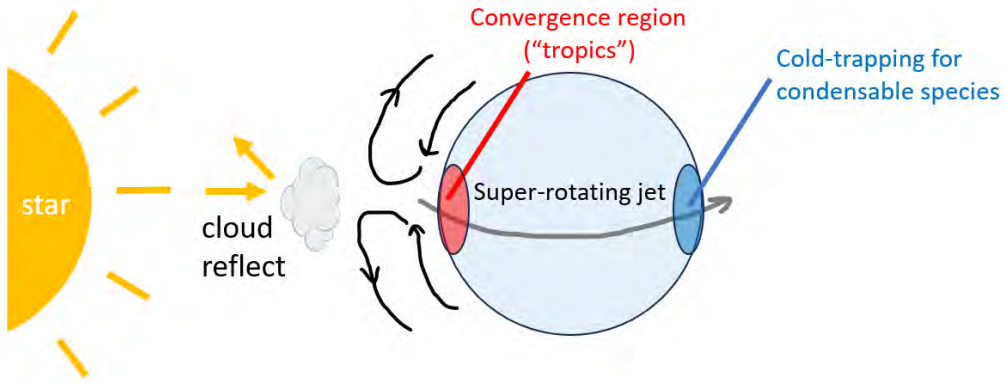

Figure 6: A schematic diagram for a tidally locked planet with clouds. The review of rocky exoplanets by Wordsworth and Kreidberg (2022) [11] provides more details.

7 Concluding Remarks

Throughout this lecture series, we have explored the current literature on exoplanet types and their atmospheric compositions. We have explored methods used to observe their atmospheres and their limitations in sampling exoplanetary systems. Especially in §6, we see how even with very limited observations, an inference can be made about the atmospheric circulation on these planets, and we look forward to the final two lectures on the circulation and atmospheric processes occurring on exoplanets.

References

[1] Luque R. and Palle' E., 2022. Density, not radius, separates rocky and water-richsmall planets orbiting M dwarf stars. *Science* 377, 1211–1214.

[2] Rogers J., Schlichting H., Owen J., 2023. Conclusive Evidence for a Population of Water Worlds around M Dwarfs Remains Elusive. *The Astrophysical Journal Letters*. 947(1).

[3] Owen J. E., 2019. Atmospheric Escape and the Evolution of Close-In Exoplanets. *Annual Review of Earth and Planetary Sciences*. 47:67–90.

[4] Wordsworth R. and Kreidberg L., 2021. Atmospheres of Rocky Exoplanets. *Annual Review of Astronomy and Astrophysics*. 60:159-201.

[5] Thompson M. et al., 2021. Composition of terrestrial exoplanet atmospheres from meteorite outgassing experiments. *Annual Review of Earth and Planetary Sciences*. 575-585, 5(6).

[6] Catling D. and Zahnle K., 2020. The Archean atmosphere. *Sci. Adv.* 6.

[7] Kreidberg, Laura, et al. 2019. "Absence of a thick atmosphere on the terrestrial exoplanet LHS 3844b." *Nature*. 573.7772, 87-90.

[8] Agol, Eric, et al. "Refining the transit-timing and photometric analysis of TRAPPIST-1: masses, radii, densities, dynamics, and ephemerides." The planetary science journal 2.1 (2021): 1.

[9] Greene, Thomas P., et al. "Thermal emission from the Earth-sized exoplanet TRAPPIST-1 b using JWST." Nature 618.7963 (2023): 39-42.

[10] Zieba, Sebastian, et al. "No thick carbon dioxide atmosphere on the rocky exoplanet TRAPPIST-1 c." Nature (2023): 1-4.

[11] Wordsworth, Robin, and Laura Kreidberg. "Atmospheres of rocky exoplanets." Annual Review of Astronomy and Astrophysics 60 (2022): 159-201.

GFD 2023 Lecture 9: Exo-Oceans and Icy Moons

Geoffrey K. Vallis; notes by Deborah Rhee (née Cotton) and Nimrod Gavriel

September 6, 2024

1 Introduction

With the recent launch of the JUICE (Jupiter Icy Moon Explorer) mission by ESA, and the upcoming Clipper mission, the various icy moons of Jupiter will be the subject of new and exciting observations. It seems almost certain that both Europa, orbiting Jupiter, and Saturn's icy moon Enceladus contain a subsurface water ocean beneath an icy shell (Fig. 1). It is also speculated that all of the Galilean moons of Jupiter (Io, Europa, Ganymede, and Callisto) have (liquid) water oceans between their icy surface and a rocky interior, as may Titan, Jupiter's largest moon. These moons can form the archetypes of a planetary class of icy moons and exo-ocean worlds, motivating the development of theoretical models that would predict their physical characteristics. In this lecture, a basic level of the current understanding of large-scale flows in such moons and planets is laid out. We focus on general issues such as how the ocean energetics depend on the location (and in particular the altitude) of the heating and cooling, rather than on considering particular icy moons. There are, perhaps surprisingly, many similarities between the circulations of icy moons and those of gas giants, for both are rotating, spherical objects driven in part by heating from below, with the dynamics determined by various non-dimensional numbers such as the Rayleigh and Rossby numbers. Let us begin with a description of a particular icy moon, Enceladus.

1.1 Enceladus

The icy moon Enceladus was observed by Voyager 2 (1981) and during the Cassini mission (2004-2017). It orbits around Saturn every 1.4 days. As it is tidally locked (to Saturn), this is also its rotation period around itself. The moon is only 500 km in diameter (small compared to our moon that has a diameter of 3200 km), and accordingly, the surface gravity is only $0.113\,\mathrm{m\,s^{-2}}$. In terms of heat balance, the surface of Enceladus is highly reflective, and thus the equilibrium surface temperature is 745 K. However, tidal and geothermal interior heating account for a total global heat flux of 20GW ($0.02\mathrm{Wm^{-2}}$), 10 GW of which is thought to escape through the warmer south pole region [1]. The structure of the moon (Fig. 1) is currently thought to be composed of three layers: an icy shell, whose thickness is modulated by heat to vary between 5-30 km (average 20 km, thinner in the south pole)[2], a global ocean and a rocky core.

While the existence of a subsurface ocean on Enceladus is still unproven, multiple arguments suggest that it indeed exists. One piece of evidence is that there are crater-free regions on the moon's surface. This indicates resurfacing by plumes, plate motions, and ice-breaking. On the south pole, plumes of water vapor and dust are ejected, suggesting pressurized subsurface chambers of liquid water, similar to Earth's 'geysers.'

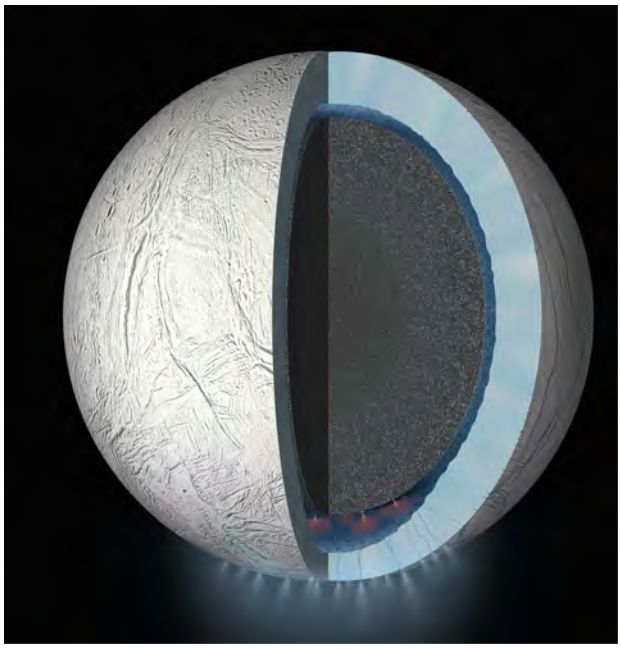

Figure 1: An artist's impression of the internal structure of Enceladus. Credit: NASA/JPL-Caltech. In the illustration, a rocky core is surrounded by a global ocean and by a thick icy shell.

1.2 Europa

Europa, the icy moon of Jupiter, was observed by Pioneer 10,11 (1973-4), the Voyager 1&2 flybys (1979), and the Galileo mission orbiting around Jupiter (1995-2003). Europa is much larger than Enceladus, with a diameter of 3100 km and gravity of 1.3 ms^{-2}. A weak magnetic field was measured for Europa, which was suggested to result from saltwater in a subsurface ocean. Another evidence for a subsurface ocean is the largely crater-free surface with cracks due to tidal forcing. Current estimates for the layering of Europa are of a 100 km deep ocean and a 10-17 km ice cover [6]. The internal heating of Europa, also due to tidal and geothermal forcing, amounts to a total of 1.6TW, or 0.05 $\mathrm{W\,m}^{-2}$, whereas the temperature varies between 60–130 K.

1.3 Snowball Earth

In Earth's past climate, it is commonly thought that there was an era (or multiple periods) of runaway glaciations of the ocean. This state, termed "snowball Earth" can happen due to the positive ice-albedo feedback, in which a climate cooling leads to increased ice coverage that in turn increases the Earth's albedo and drives more cooling, and so on. There may still be a meridional temperature gradient (Fig. 2) due to the inclination of the Sun's radiation, but that temperature gradient is likely to be much smaller than today simply because the meridional gradient of incoming solar radiation will have been small. Rather like the case on icy moons, it is thought that the oceans on Snowball Earth were not frozen all the way down; rather, there was a layer of ice on top, perhaps up to a kilometer deep, underneath which was liquid water. At low latitudes there may have been no ice cover at all, with liquid water at the surface, but observations (or really the interpretation of proxy data) are somewhat ambiguous. Nevertheless, the resemblance to icy moons is clear.

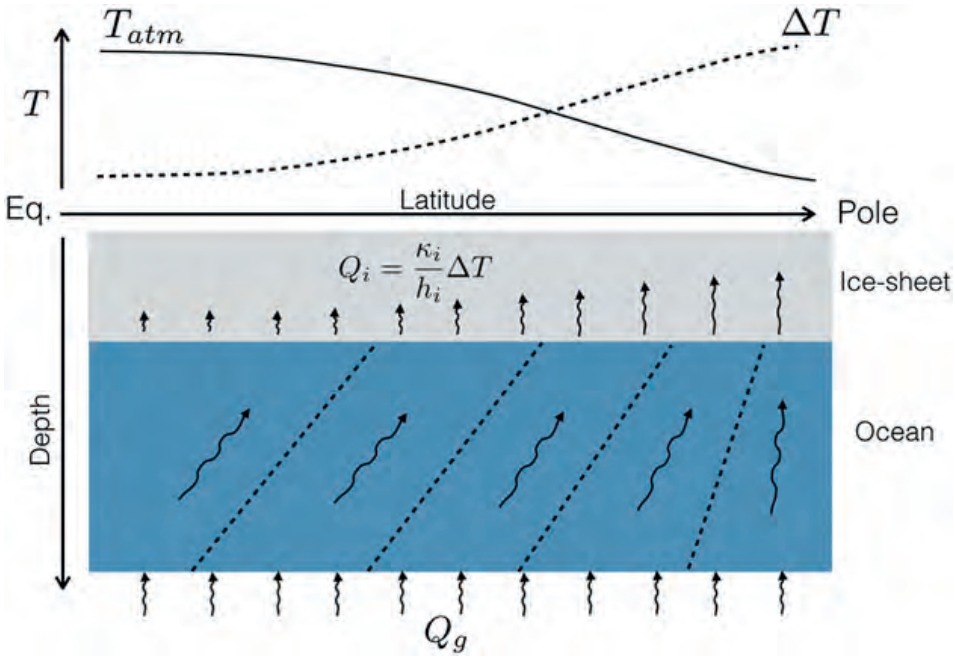

Figure 2: A sketch of possible heat transport in an ice-covered world with a horizontal heat gradient. Taken from [3]. Q_g is the heating from below, ΔT is the meridional temperature contrast, κ_i is the thermal diffusivity and h_i is the thickness of the ice cover.

2 Energetics of a Thermally Driven Ocean

To model the ocean circulation on icy moons, we consider a simple case with no atmosphere and, in the first instance, with interior heating. That is, we consider a case with thermal forcing at the surface arising from insolation from the host star, and with no wind stress. As such we model the circulation on icy moons as horizontal convection, driven by a horizontal heat gradient at the surface (Fig. 2). We assume exo-oceans on icy planets can be modeled using the Boussinesq approximation. This ignores density differences except in cases where terms are multiplied by g . This is generally a good approximation for exo-oceans because very large pressures are required to significantly alter the density of water. We ignore centrifugal terms and assume rotation is aligned with gravitational forces and obtain,

$$\frac{\mathrm{D}\boldsymbol{v}}{\mathrm{D}t} + \boldsymbol{f} \times \boldsymbol{v} = -\nabla\phi + b\hat{\boldsymbol{k}} + \nu\nabla^2\boldsymbol{v}. \tag{1}$$

The notation is conventional, with $\boldsymbol{f} = 2\boldsymbol{\Omega}$ being the Coriolis parameter which we take to be constant. (It plays no role in the energetics.) The variable b is the buoyancy, $b = -g\delta\rho/\rho_0$ and as before, $\phi = p/\rho_0$. With an equation of state of the form $\rho = \rho_0(1 - \beta_T(T - T_0))$, where β_T is a coefficient of expansion with respect to temperature, then $\delta\rho/\rho_0 = -\beta_T\delta T$ and $b = g\beta_T\delta T$.

The other equations in the Boussinesq approximation are,

$$\frac{\mathrm{D}b}{\mathrm{D}t} = Q = J + \kappa\nabla^2 b, \tag{2}$$

$$\nabla \cdot \boldsymbol{v} = 0. \tag{3}$$

Using $(\boldsymbol{v}\cdot\nabla)\boldsymbol{v} = \boldsymbol{\omega}\times\boldsymbol{v} - 1/2\nabla(\boldsymbol{v}^2)$ (where $\boldsymbol{v}^2 = \boldsymbol{v}\cdot\boldsymbol{v}$) we can write (1) as,

$$\frac{\partial \boldsymbol{v}}{\partial t} + (2\boldsymbol{\Omega} + \boldsymbol{\omega})\times\boldsymbol{v} = -\nabla B + b\hat{\mathbf{k}} + \nu\nabla^2\boldsymbol{v}, \tag{4}$$

where $B = \boldsymbol{v}^2/2 + \phi$ is the Bernoulli function for this system.

3 Energy Budget and Statistically Steady States

Taking $\boldsymbol{v}\cdot$ (4) and using $\boldsymbol{v} = (u, v, w)$ and $\nabla\cdot\boldsymbol{v} = 0$, we obtain an energy equation,

$$\frac{1}{2}\frac{\partial|\boldsymbol{v}|^2}{\partial t} = -\nabla\cdot(\boldsymbol{v}B) + wb + \nu\boldsymbol{v}\cdot\nabla^2\boldsymbol{v}, \tag{5}$$

$$= -\nabla\cdot(\boldsymbol{v}B) + wb + \nu\nabla\cdot(\boldsymbol{v}\times\boldsymbol{\omega}) - \nu\boldsymbol{\omega}^2, \tag{6}$$

where the last expression was derived using the fact that for the divergence-free velocity field, $\nabla^2\boldsymbol{v} = -\nabla\times(\nabla\times\boldsymbol{v}) = -\nabla\times\boldsymbol{\omega}$ and the fact that $\nabla\cdot(\boldsymbol{A}\times\boldsymbol{B}) = \boldsymbol{B}\cdot(\nabla\times\boldsymbol{A}) - \boldsymbol{A}\cdot(\nabla\times\boldsymbol{B})$ for any two vector fields $\boldsymbol{A}$, $\boldsymbol{B}$.

We assume periodic boundary conditions or equivalently that $\boldsymbol{v} = 0$ on the boundary and take the volume average over the whole domain to obtain,

$$\frac{1}{2}\frac{\partial\langle|\boldsymbol{v}|^2\rangle}{\partial t} = \langle wb\rangle - \varepsilon, \tag{7}$$

where $\varepsilon = \nu\langle\boldsymbol{\omega}^2\rangle$ is the average dissipation rate of kinetic energy. Here, the kinetic energy of the system is increased by hotter-fluid with a lower density rising (so $\langle wb\rangle > 0$), leading to a decrease in the overall center of gravity of the fluid. This decrease in gravitational potential energy leads to an increase in kinetic energy of the system. Kinetic energy is dissipated by friction. In the statistically steady state $\varepsilon = \langle wb\rangle$.

We can use (2) and the fact that $w = \mathrm{D}z/\mathrm{D}t$ to obtain an equation for the potential energy budget of the system,

$$\frac{\mathrm{D}(bz)}{\mathrm{D}t} = z\frac{\mathrm{D}b}{\mathrm{D}t} + b\frac{\mathrm{D}z}{\mathrm{D}t} = zQ + bw. \tag{8}$$

Again, taking a volume integral over the whole domain,

$$\frac{\mathrm{D}\langle bz\rangle}{\mathrm{D}t} = \langle zQ\rangle + \langle wb\rangle. \tag{9}$$

Here, energy increases from heating and buoyant rise. In the steady state $\langle zQ\rangle = -\langle wb\rangle$. Combining this with our steady state condition from (7) we require,

$$\langle zQ\rangle = -\varepsilon. \tag{10}$$

Since $\varepsilon \geq 0$, for a steady state to exist in which kinetic energy is dissipated, we require that z and Q are anti-correlated. Thus, *in order to maintain a circulation in which kinetic energy is dissipated, the heating (including diffusive heating) must occur, on average, at lower levels than the cooling.* This effect was pointed out, using very different reasoning, about a century ago by Sandström and is known as Sandström's effect. In Earth's ocean most of the heating occurs predominantly at the surface and (except for the small effects of hydrothermal vents) and the difference in height between where cooling and heating occurs is small. As a consequence, thermal forcing is, of itself, a very inefficient way to drive a circulation and Earth's ocean relies heaving on winds to drive it. (In part the winds directly drive the circulation, and in part the winds give rise to small-scale turbulent flows that in turn give rise to large turbulent diffusivities that enable the thermal effects to be larger.) On the icy moon there are no winds and buoyancy effects are the main driving force and as a consequence the circulation is considerably weaker than that in Earth's oceans, as we now explore.

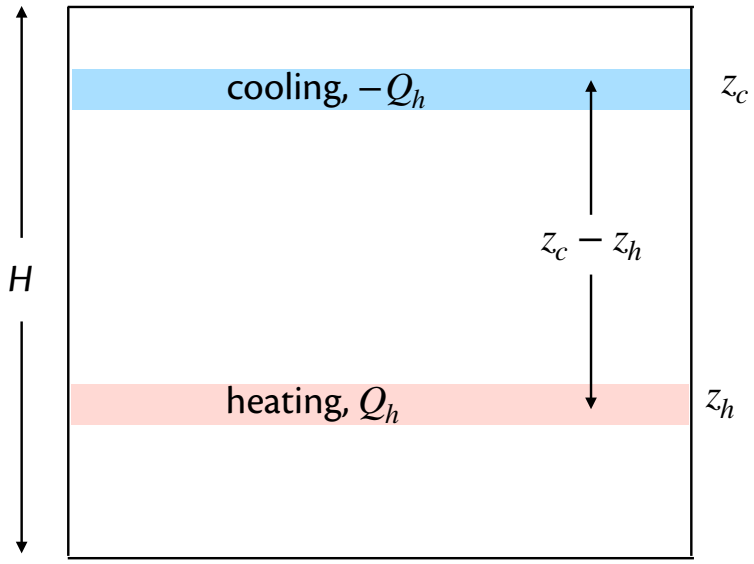

Figure 3: Heating and cooling at two levels in a box.

4 Strength of the Circulation

We start off by modelling our heating and cooling by considering two source terms approximated as delta distributions, with a cooling term, Q_c located at z_c and a heating term, Q_h located at z_h, as in Fig. 3.

From (10), and remembering that we are supposing that the Q terms include all the diabatic terms including diffusion, we have

$$\frac{1}{H}\int_z \overline{zQ}\,\mathrm{d}z = -\varepsilon, \tag{11}$$

where the overbar denotes a horizontal average and H is the total depth of the domain.

Suppose there is heating, $Q_h > 0$ over a small thickness centered around one height, z_h and cooling, $Q_c < 0$ at another height, z_c, both being within the domain, and there is no heating elsewhere (Fig. 3). Idealizing this with a δ-function we write

$$Q = HQ_c\delta(z - z_c) + HQ_h\delta(z - z_h), \tag{12}$$

so that Q_c and Q_h are the magnitudes of the heating and cooling, and the factor of H simply provides the correct dimensionality. Substituting into (11) gives

$$(Q_h z_h + Q_c z_c) = -\varepsilon. \tag{13}$$

If Q_h is the heating and is taken to be positive, and $Q_c = -Q_h$, in order that no heat (buoyancy) is added to the system overall, we have

$$\varepsilon = Q_h(z_c - z_h) = Q_h h, \tag{14}$$

where $h = z_c - z_h$. That is to say, the potential energy generation (and consequent conversion to kinetic energy) is proportional to the height difference between heating and cooling.

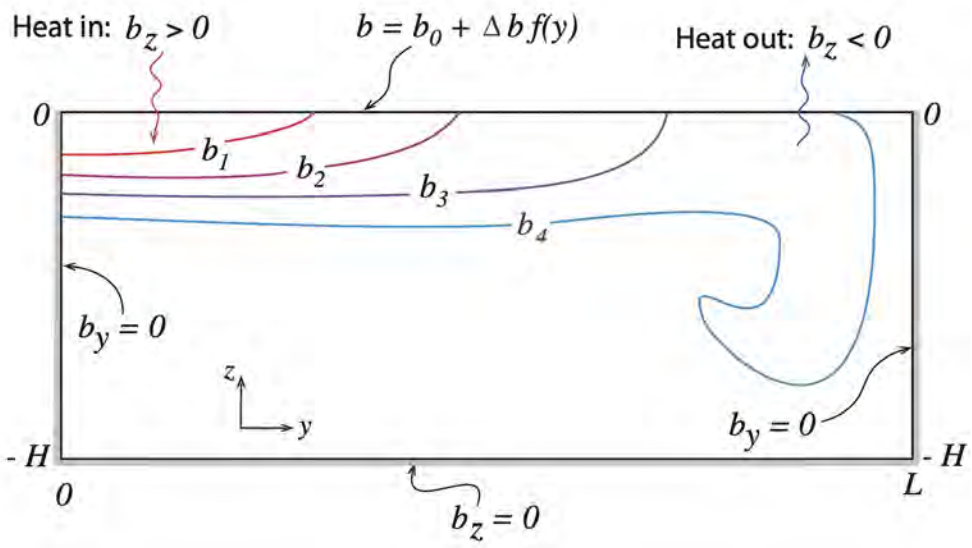

Figure 4: Sketch of sideways convection. The fluid is differentially heated and cooled along its top surface, whereas all the other walls are insulating. Taken from [5], which in turn is modeled on a figure by [4].

5 Sideways Convection

We now consider the case when $h = 0$ but there is some lateral differential heating at the top boundary. We consider a 2D model of the ocean of length L and height H (Fig. 4) where $\boldsymbol{v} = (0, v(y,z), w(y,z))$ and $b = b(y,z)$. We use the Boussinesq approximation and assume no rotation and interior heating,

$$\frac{\partial \boldsymbol{v}}{\partial t} + \boldsymbol{\omega} \times \boldsymbol{v} = -\nabla B + b\hat{\boldsymbol{k}} + \nu \nabla^2 \boldsymbol{v}, \tag{15}$$

$$\frac{\mathrm{D}b}{\mathrm{D}t} = \kappa \nabla^2 b, \tag{16}$$

$$\nabla \cdot \boldsymbol{v} = 0. \tag{17}$$

Taking the curl of (15), and using (17), we obtain the vorticity equation

$$\frac{\partial \zeta}{\partial t} + \boldsymbol{v} \cdot \nabla \zeta = \frac{\partial b}{\partial y} + \nu \nabla^2 \zeta, \tag{18}$$

where $\zeta = \partial w/\partial y - \partial v/\partial z$. We assume that the motion is dominated by vertical diffusion to obtain characteristic length and time scales,

$$\hat{y} = \frac{y}{L}, \qquad \hat{z} = \frac{z}{H}, \qquad \hat{t} = \frac{t}{H^2/\kappa}, \qquad \hat{b} = \frac{b}{\Delta b}, \tag{19}$$

where Δb is a measure of the buoyancy difference across the top surface. Defining $w = \widehat{w}/(H/\kappa)$, $v = \hat{v}/(H^2/L\kappa)$ and $\zeta = (\kappa/HL)\partial\widehat{w}/\partial\hat{y} - (L\kappa/H^3)\partial\hat{v}/\partial\hat{z} = (L\kappa/H^3)\left[(H^2/L^2)\partial\hat{w}/\partial\hat{y} - \partial\hat{v}/\partial\hat{z}\right] =$

$(L\kappa/H^3)\hat{\zeta}$. We non-dimensionalize (18) as

$$\frac{L\kappa^2}{H^5}\left\{\frac{\partial}{\partial\widehat{t}}\left[\gamma_T^2\partial\widehat{w}/\partial\hat{y}-\partial\hat{v}/\partial\hat{z}\right]+\hat{\boldsymbol{v}}\cdot\hat{\nabla}\left[(H^2/L^2)\partial\widehat{w}/\partial\hat{y}-\partial\hat{v}/\partial\hat{z}\right]\right\}$$
$$=\frac{\Delta b}{L}\frac{\partial\hat{b}}{\partial\hat{y}}+\frac{\nu L\kappa}{H^5}\left[\frac{\partial^2}{\partial\hat{z}^2}\left[(H^2/L^2)\partial\widehat{w}/\partial\hat{y}-\partial\hat{v}/\partial\hat{z}\right]+\gamma_T^2\frac{\partial^2}{\partial\hat{y}^2}\left[(H^2/L^2)\partial\hat{w}/\partial\hat{y}-\partial\hat{v}/\partial\hat{z}\right]\right], \quad (20)$$

which we can write as

$$\frac{\partial}{\partial\hat{t}}\left(\gamma_T^2\frac{\partial\hat{w}}{\partial\hat{y}}-\frac{\partial\hat{v}}{\partial\hat{z}}\right)+\hat{\boldsymbol{v}}\cdot\hat{\nabla}\left(\gamma_T^2\frac{\partial\hat{w}}{\partial\hat{y}}-\frac{\partial\hat{v}}{\partial\hat{z}}\right)$$
$$=\mathrm{Ra}\sigma\gamma_T^5\frac{\partial\hat{b}}{\partial\hat{y}}+\sigma\left[\frac{\partial^2}{\partial\hat{z}^2}\left(\gamma_T^2\frac{\partial\widehat{w}}{\partial\hat{y}}-\frac{\partial\hat{v}}{\partial\hat{z}}\right)+\gamma_T^2\frac{\partial^2}{\partial\hat{y}^2}\left(\gamma_T^2\frac{\partial\widehat{w}}{\partial\hat{y}}-\frac{\partial\hat{v}}{\partial\hat{z}}\right)\right], \quad (21)$$

where

$$\mathrm{Ra}=\frac{\Delta bL^3}{\nu\kappa},\qquad\sigma=\frac{\nu}{\kappa},\qquad\gamma_T=\frac{H}{L}. \quad (22)$$

There are two limiting cases.

Case 1: H $\lesssim$ L

In the case where $H\lesssim L$, we obtain

$$\frac{\partial\widehat{\zeta}}{\partial\widehat{t}}+\hat{\boldsymbol{v}}\cdot\widehat{\nabla}\widehat{\zeta}=\mathrm{Ra}\sigma\gamma_T^5\frac{\partial\hat{b}}{\partial\hat{y}}+\sigma\left[\frac{\partial^2\hat{\zeta}}{\partial\hat{z}^2}+\gamma_T^2\frac{\partial^2\hat{\zeta}}{\partial\hat{y}^2}\right]. \quad (23)$$

Recall that the only way the fluid is forced is by the buoyancy gradient at the surface, and in order for this to drive the flow we require

$$\mathrm{Ra}\sigma\gamma_T^5\sim\sigma. \quad (24)$$

If the buoyancy term is smaller than this, then buoyancy cannot drive the flow. If it is larger than this then there is nothing to enable the flow to reach statistically steady state. Given this, we can obtain an approximation for H, the vertical length scale for the motion of the fluid,

$$H\sim\mathrm{Ra}^{-1/5}L,\sim\left(\frac{L^2\nu\kappa}{\Delta b}\right)^{1/5}. \quad (25)$$

If $Ra\gg1$ then $H\ll L$ so that the vertical length scale is always much less than the horizontal length scale. But let us see what happens if we assume $H\gg L$.

Case 2: H $\gg$ L

In the case where $H\gg L$, where H is the scale of the fluid motion and not the depth of the container, $\gamma_T\gg1$ so letting $\hat{\zeta}\simeq\gamma_T^2\partial\hat{w}/\partial\hat{y}$ in (21) we obtain

$$\frac{\partial(\partial\widehat{w}/\partial\hat{y})}{\partial\widehat{t}}+\hat{\boldsymbol{v}}\cdot\hat{\nabla}(\partial\widehat{w}/\partial\hat{y})=Ra\sigma\gamma_T^3\frac{\partial\hat{b}}{\partial\hat{y}}+\sigma\gamma_T^2\frac{\partial^2(\partial\hat{w}/\partial\hat{y})}{\partial\hat{y}^2}. \quad (26)$$

In this case in order for buoyancy to drive the flow we require

$$\mathrm{Ra}\sigma\gamma_T^3\sim\sigma\gamma_T^2. \quad (27)$$

We can again obtain an approximation for H,

$$H\sim L/\mathrm{Ra} \quad (28)$$

We see that the condition $H\gg L$ is incompatible with the assumption $\mathrm{Ra}\gg1$, suggesting that this scaling cannot be achieved and thus the true scaling for H is, in fact, given by (25).

6 Conclusions and Challenges for Icy Moons

There are many, many complications regarding the study of ocean circulation in icy moons. Here we have mainly concentrated on the constraints imposed by the fact that there is no wind forcing from above so that the motion is purely thermally forced. The relative locations of the heating and cooling (including diffusive effects) then makes a big difference to the circulation, for its strength is proportional to the height difference between the two.

If this difference is small then the ocean will fall into the regime of sideways convection, in which the circulation is driven purely by diffusive effects, because diffusion is the only way that buoyancy can enter the ocean and there is no wind to mechanically force the ocean. In this case we obtain an approximate scaling for the vertical motion of the fluid as $H \sim L\mathrm{Ra}^{-1/5}$. In such cases, or more generally when the thermal forcing is small, saline effects will almost certainly play a role and these have not been considered in this chapter.

For Enceladus, the ice is thicker at the equator than at the poles (Fig. 1), creating a pressure difference across the ocean and providing some thermal forcing to the system, potentially driving sideways convection. However, Enceladus also has internal heating from the core $\sim 0.1\mathrm{Wm}^{-2}$, which is likely to drive Rayleigh-Bénard-like convection in the interior. This can be much more efficient than sideways convection, since the height difference between heating and cooling is essentially the depth of the ocean. If we include the effects of internal heating, we might calculate that the velocity of the fluid is ~ 1 cm/s. Putting this all together, we conclude that one possible way to model Enceladus would be to include the effects of internal heating driving some Rayleigh-Bénard-like convection in the interior, combined with some sideways convection at the top where the strength of the convection depends on the variation in thickness of the ice, the changing in depth of the ocean, the overall depth of the ocean and the strength of the internal heating, as well as saline effects. Putting all these factors together in a coherent form is a significant challenge.

References

[1] G. Choblet, G. Tobie, C. Sotin, M. Běhounková, O. Čadek, F. Postberg, and O. Souček, Powering prolonged hydrothermal activity inside Enceladus, Nature Astronomy, 1 (2017), pp. 841–847.

[2] D. Hemingway, L. Iess, R. Tajeddine, and G. Tobie, The interior of Enceladus, Enceladus and the icy moons of Saturn, (2018), pp. 57–77.

[3] M. F. Jansen, The turbulent circulation of a snowball Earth ocean, J. Phys. Oceanogr., 46 (2016), pp. 1917–1933.

[4] F. Paparella and W. R. Young, Horizontal convection is non-turbulent, J. Fluid Mech., 466 (2002), pp. 205–214.

[5] G. K. Vallis, Atmospheric and Oceanic Fluid Dynamics, Cambridge University Press, Cambridge, U.K., 2nd ed., 2017.

[6] M. E. Walker and A. R. Rhoden, Tidal heating at Europa using the multifrequency analysis of tidal heating toolkit, The Planetary Science Journal, 3 (2022), p. 149.

GFD 2023 Lecture 10: Steam Atmospheres and Runaway Greenhouse

Geoffrey Vallis; notes by Arefe Ghazi Nezami and Quentin Nicolas

September 6, 2024

Some exoplanets have densities that are compatible with a water-rich composition. These candidates orbit close to their host stars and any hydrogen in the atmosphere may well have been stripped away through hydrodynamic escape, implying that their atmospheres could be mainly composed of water vapor. This lecture aims to present a few aspects of the atmospheric circulation on these "water worlds" with "steam atmospheres". We then consider briefly one other aspect of water vapor, namely its greenhouse effect leading to possible runaway greenhouse.

1 Neutral Lapse Rates in Dry and Moist Atmospheres

We start this section by recalling some basic thermodynamics rules that will be used throughout. We will assume that all gases considered follow the ideal gas law:

$$p = \rho R T, \tag{1}$$

where p is pressure, ρ is density and T is temperature. $R = R^*/M$ denotes the specific gas constant, with R^* the molar gas constant and M the molar mass of the gas. This relationship can be rewritten $p\alpha = RT$, where $\alpha = \rho^{-1}$ is the specific volume. (Unfortunately it is standard practice to use α to mean both aspect ratio and specific volume, but the context should make the meaning clear.)

The first law of thermodynamics states that the internal energy of a body changes when work is done on it, when heat is added to it or when its chemical composition changes. For a gas at fixed chemical composition, this reads

$$\mathrm{d}I = đQ - p\,\mathrm{d}\alpha = T\,\mathrm{d}\eta - p\,\mathrm{d}\alpha, \tag{2}$$

where I is the specific internal energy of the fluid, η is the specific entropy, $đQ$ denotes the amount of heat added per unit mass of fluid, and $p\ \mathrm{d}\alpha$ is the work done on it. The second equality stems from the second law of thermodynamics, which states that in a reversible process the change in specific entropy, $\mathrm{d}\eta$ is given by $đQ/T$, where đ is a so-called imperfect differential. (Ideally, the development of thermodynamics would avoid the use of đ, and some thermodynamic texts use the notation δQ where δ denotes an infinitesimal quantity. But we will let such nuances pass us by here.)

Supposing hydrostatic balance, equation (2) can be used to infer the vertical structure of temperature in an idealized atmosphere. We proceed to determine this vertical structure for three limiting cases: a dry atmosphere, an atmosphere with a small amount of one condensible substance, and a steam atmosphere (which is composed exclusively of a condensible substance).

1.1 Dry atmosphere

In the absence of external diabatic sources, the first law reduces to

$$\mathrm{d}I = -p\,\mathrm{d}\alpha. \tag{3}$$

Let us suppose that the atmosphere is composed of a *perfect gas*, for which I is related to temperature by a constant factor c_v (called the heat capacity at constant volume). In reality, c_v is a weak function of temperature. Equation (3) becomes

$$\begin{aligned} 0 &= c_v \mathrm{d}T + p\,\mathrm{d}\alpha \\ &= c_v \mathrm{d}T + \mathrm{d}(\alpha p) - \alpha\,\mathrm{d}p \\ &= (c_v + R)\mathrm{d}T - \alpha\,\mathrm{d}p, \end{aligned} \tag{4}$$

where we have used the ideal gas law to obtain the last equality. The quantity $c_v + R$ is another constant, called the isobaric heat capacity, and denoted c_p. We deduce that in an adiabatic process

$$\frac{\mathrm{d}T}{\mathrm{d}p} = \frac{\alpha}{c_p}. \tag{5}$$

Combining this with hydrostatic balance, $\mathrm{d}p/\mathrm{d}z = -\rho g$, we obtain the vertical temperature gradient in an adiabatic dry atmosphere:

$$\frac{\mathrm{d}T}{\mathrm{d}z} = -\frac{g}{c_p}. \tag{6}$$

The negative of this quantity, which here is g/c_p, is called the dry adiabatic lapse rate and in Earth's atmosphere it is about 9.8 K/km. Any temperature profile that decreases more steeply with height is unstable, as exemplified by the red profile in Figure 1. A parcel of air lifted adiabatically from z_1 to z_2 cools by $g(z_2 - z_1)/c_p$, following the dashed blue line. It is warmer than its environment when it reaches z_2, which means it is positively buoyant and will keep rising. Conversely, any perturbation to the yellow temperature profile will be damped (a parcel lifted from z_1 to z_2 will be negatively buoyant and sink back down), meaning this profile is stable. It should be noted that the viscous effects are negligible since we are away from the boundaries.

1.2 Earth-like moist atmosphere

The presence of a condensible substance in an atmosphere has two effects: variations in its amount yield changes in the density of the fluid (e.g., in Earth's atmosphere, water vapor has a smaller molar mass than dry air, so a moist parcel will be lighter than a dry one with equal temperature and pressure), and its phase changes release or take up latent heat into/from the surrounding air. On Earth, where water vapor makes up a small fraction of the atmosphere, the second effect dominates over the first one in setting the atmosphere's temperature structure.

We will use q to denote the specific humidity of an air parcel, defined as the ratio of the mass of vapor (i.e. the condensible substance) to the total mass of the parcel, and e to denote the partial pressure of the condensible. There is an upper limit to the vapor pressure that a parcel can achieve without condensing, called the saturation vapor pressure denoted e_s, with corresponding saturation specific humidity (q_s). The quantity e_s is a function only of temperature – for a range of temperatures e_s increases almost exponentially with temperature — and the expression determining this is called the Clausius–Clapeyron relation and it is derived in the appendix.

As an unsaturated air parcel rises, it cools following equation (6), and in the absence of any mass transfer it conserves its specific humidity. Once it reaches saturation, any cooling will lower

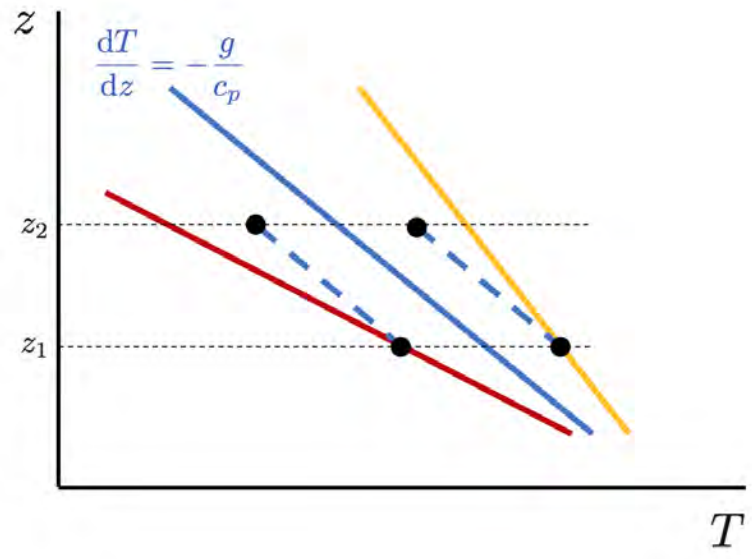

Figure 1: Stability of various temperature profiles with respect to dry convection. A temperature profile that follows the dry adiabatic lapse rate (Eq. (6)) is represented in blue. The yellow and red lines show, respectively, examples of stable and unstable temperature profiles.

q_s and lead to condensation of the excess water vapor, a process that releases latent heat. As a result, in a saturated Earth-like atmosphere, temperature decreases less steeply with height than in a dry atmosphere. The expression of its lapse rate, valid only for a dilute atmosphere (meaning the concentration of water vapor in the atmosphere is small) is (for a derivation see [3])

$$\frac{\mathrm{d}T}{\mathrm{d}z} = -\frac{g}{c_p}\frac{1 + Lq_s/(R^dT)}{1 + L^2q_s/(c_pR^vT^2)}, \tag{7}$$

where L is the latent heat of condensation, R^d is the specific gas constant of dry air and R^v is the specific gas constant of vapor. At 300 K, this lapse rate is around 4 K/km, i.e. much less steep than its dry counterpart! This means that a moist atmosphere is likely to be more unstable than a dry one, and this accounts for the prevalence of convection in Earth's tropics where the moisture content is high.

All of the above relations are independent of the presence or otherwise of another gas in the volume. If (as on Earth) a noncondensing gas is present alongside the condensible one then pressure is the just the partial pressure. In that case, when the temperature increases so that the partial pressure equals the ambient pressure any condensible liquid present will *boil*. If the condensible is the only substance present then its partial pressure is also the total pressure, and if the volume is also saturated the temperature profile with height is determined by the Clausius–Clapeyron relation. Atmospheres composed only of a single condensible are sometimes called 'steam atmospheres', a variation of the common usage in which steam refers to a mixture of water vapor, condensed water and air at temperatures near the boiling point. Atmospheres (like that of Earth) with a small proportion of condensible material are called dilute, and those with a large proportion are called nondilute. Finally, is common in the atmospheric sciences to write the vapor pressure as e, and e_s for its saturation value, to distinguish it from the total or ambient pressure p.

In the Solar System the only other body that has a hydrology cycle at all resembling that of

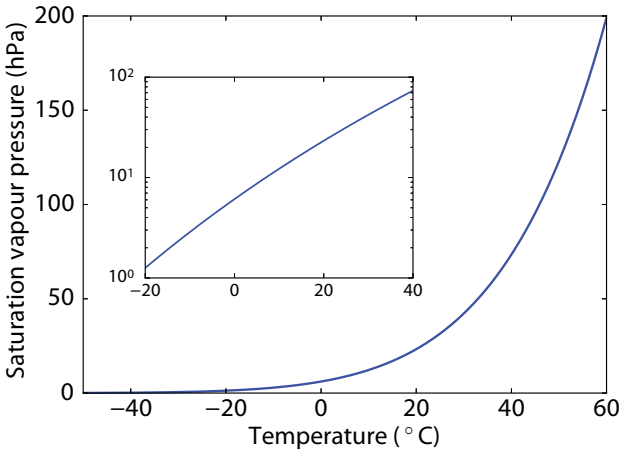

Figure 2: The equilibrium (or saturation) vapor pressure of water vapor as a function of temperature. The inset plots the same quantities on a log scale over a smaller range. The plot is made using (42) with $e_0 = 6.12\text{hPa}$, $L = 2.44 \times 10^6\,\text{J}\,\text{kg}^{-1}$ and $R = 462\,\text{Jkg}^{-1}\,\text{K}^{-1}$. Using a more accurate empirical formula that accounts for changes in L makes little difference over the range shown.

Earth is Titan, where the condensate is methane and the surface pressure about $1.5{\times}10^5$ Pa. (On Earth, surface pressure is about 10^5 Pa.) The surface temperature of Titan is around 95 K, not far from the triple point of methane, and methane rain collects in liquid lakes on Titan's surface. On Mars, about 95% of the atmosphere is carbon dioxide and in winter up to 25% of that carbon dioxide will condense over the polar caps. However, the surface pressure is so low (about 600 Pa) that the gas condenses into a solid, often forming dry ice sheets over a meter thick; the sheets sublime back into the atmosphere in the warmer summer and there is little if any liquid carbon dioxide on Mars today. The atmosphere of Mars generally behaves like a dilute one, but can be nondilute when extensive condensation occurs.

1.3 Lapse rate in a steam atmosphere

Let us now consider the limit where an atmosphere is made up entirely of one condensible substance like water vapor. Consider a mixture of liquid water and water vapor in thermodynamic equilibrium at some temperature T and pressure p. In this case equilibrium is achieved when the pressure of the gaseous substance and its temperature are related by the Clausius–Clapeyron relation, as derived in the appendix to this chapter, namely

$$\frac{\mathrm{d}p}{\mathrm{d}T} = \frac{Lp}{RT^2}\,. \tag{8}$$

A direct consequence of equation (8) is that in a saturated steam atmosphere pressure uniquely depends on temperature. Although this is only true in a saturated atmosphere, a large fraction of a steam atmosphere can be expected to be saturated. A steam atmosphere is thus constrained to be *barotropic,* meaning isolines of pressure and density are parallel. To the atmosphereic scientist or GFDer, this result has a lot of unintuitive consequences such as the absence of baroclinic instabilities, or even more fundamentally the absence of a thermal wind balance (see next section).

Combining equation (8) with hydrostasy, $dp - \rho g \mathrm{d}z$, one obtains the lapse rate in a steam atmosphere:

$$\frac{\mathrm{d}T}{\mathrm{d}z} = -\frac{gT}{L}. \tag{9}$$

The temperature scale height (i.e. the characteristic length scale over which the temperature decreases with height) is given by L/g, which for an Earth-sized planet is about 250 K/km. Evidently, the temperature would be nearly constant in a 10-km thick column.

2 Large-scale Winds in a Steam Atmosphere

One of the fundamental relationships governing the dynamics of a rotating atmosphere is the thermal wind balance. This relationship between vertical wind shear and horizontal temperature gradients arises when combining geostrophic and hydrostatic balances. In pressure coordinates, the meridional component of geostrophic balance reads

$$fu = -\left(\frac{\partial \Phi}{\partial y}\right)_p, \tag{10}$$

with the p subscript stressing the fact that the partial derivative is taken on a constant pressure surface, f is the Coriolis parameter and $\Phi = gz$ is the geopotential. Hydrostatic balance reads:

$$\frac{\partial \Phi}{\partial p} = -\frac{RT}{p}, \tag{11}$$

which can be obtained by combining the classic form $\partial p/\partial z = -\rho g$ with the ideal gas law, $p = \rho RT$. Combining equations (10) and (11) yields the thermal wind balance equation in pressure coordinates:

$$f\frac{\partial u}{\partial p} = \frac{R}{p}\left(\frac{\partial T}{\partial y}\right)_p. \tag{12}$$

Now, remember from section 1.3 that in a steam atmosphere, temperature is solely a function of pressure (they are related by the Clausius-Clapeyron equation). Hence, $\left(\partial T/\partial y\right)_p = 0$, meaning that **there is no thermal wind balance in a steam atmosphere**.

Although there is no thermal wind, large scale winds will likely still be generated, and an estimate of the large-scale zonal wind speed can be obtained from geostrophic balance alone. This scaling is best illustrated in height coordinates, where geostrophic balance reads

$$fu = -\frac{1}{\rho}\frac{\partial p}{\partial y} = -\frac{1}{\rho}\frac{\mathrm{d}p}{\mathrm{d}T}\frac{\partial T}{\partial y} = -\frac{L}{T}\frac{\partial T}{\partial y}, \tag{13}$$

where to obtain the last equality we have used the Clausius-Clapeyron equation. Denoting by ΔT the pole-to-equator temperature difference, the geostrophic wind in a steam atmosphere is thus of order

$$u_g \sim \frac{L}{fT_0}\frac{\Delta T}{a}, \tag{14}$$

where T_0 is a mean temperature scale and a is the planet's radius. In an equivalent atmosphere where thermal wind balance holds, and with the same ΔT and a, one would obtain from (12):

$$u_T \sim \frac{R}{f}\frac{\Delta T}{a}, \tag{15}$$

where we have assumed $\partial u/\partial \log p \sim u_T$. Using $L = 2.5 \times 10^6$ J kg^{-1}, $R = 460$ J kg^{-1} K^{-1} (for a steam atmosphere) and $T_0 \sim 300$ K, one obtains

$$u_g = \frac{L}{fT_0}\frac{\Delta T}{a} \sim 700\,\mathrm{m\,s^{-1}}, \tag{16}$$

and

$$\frac{u_g}{u_T} \sim \frac{L}{RT_0} \sim 20. \tag{17}$$

The geostrophic wind in a steam atmosphere is thus about an order of magnitude larger than the thermal wind of a hypothetical equivalent planet with a dry atmosphere.

3 Runaway Greenhouse Effect

Let us now switch gears, and consider another large effect of water vapor, namely that it is an efficient absorber of infra-red radiation and hence gives rise to a greenhouse effect. A *runaway greenhouse* is a state where the concentration of greenhouse gases is high enough that the surface fails to cool by longwave emission, leading to a dramatic temperature increase and a runway state. This section presents the simplest physical picture that describes the concept of runaway greenhouse effect. We will assume the atmosphere to be *gray*, meaning that it absorbs and emits similarly at all wavelengths in the infra-red. This assumption is quantitatively poor (spectroscopic effects *are* important) but the essential physics is still captured. We begin by introducing some elementary radiative transfer concepts.

3.1 Elements of Radiative Transfer

Radiative transfer is a complex subject and in order to make progress we will simplify it in two main ways:

1. Rather than treating an entire spectrum of wavelengths, we suppose that the radiation exists only in two well-separated bands, namely solar (or shortwave) radiation and infra-red (or longwave) radiation. In each band the absorption is not a function of wavelength, and this is called the gray approximation (or the semi-gray approximation, considering that there are two bands of radiation). We will suppose that the planet only emits longwave radiation, and its host star only emits shortwave radiation.

2. We suppose that the radiation travels only vertically (up or down) through the planetary atmosphere. This is the *two-stream* approximation.

Consider a beam of radiation propagating through a thin slab of gas, as in Fig. 3. Some of the incoming radiation may be absorbed, some reflected, and the slab may emit radiation of its own. In the three-dimensional problem some radiation may also be scattered into the beam from radiation travelling in other directions. Let us neglect scattering and reflection, a good approximation for longwave radiation. The difference between the outgoing and incoming radiation is then

$$\mathrm{d}I = I^{\mathrm{out}} - I^{\mathrm{in}} = -\mathrm{d}\tau\, I + \mathrm{d}E, \tag{18}$$

where I is the irradiance or radiant intensity (with units of power per unit area, or $\mathrm{W\,m^{-2}}$), the term $-\mathrm{d}\tau I$ is the absorption and $\mathrm{d}E$ is the thermal emission. The quantity $\mathrm{d}\tau$ is the nondimensional optical depth; it may be written as $\mathrm{d}\tau = e_L \mathrm{d}s$ where $\mathrm{d}s$ is the slab thickness, and e_L is the *emissivity* of the medium. The minus sign on $\mathrm{d}\tau$ in (18) is appropriate when τ increases in the direction of the beam. The emission of radiation is, in thermal equilibrium, the Planck function, B, such that $\mathrm{d}E = B\ \mathrm{d}\tau$. If the atmosphere is gray (as in assumption 1 above) then $B = \sigma T^4$ where $\sigma = 5.67 \times 10^{-8} \mathrm{W\,m^{-2}\,K^{-4}}$ is Stefan's constant. With all this, (18) becomes

$$\mathrm{d}I = -\mathrm{d}\tau(I - B) \qquad \text{or} \qquad \frac{\mathrm{d}I}{\mathrm{d}\tau} = -(I - B). \tag{19}$$

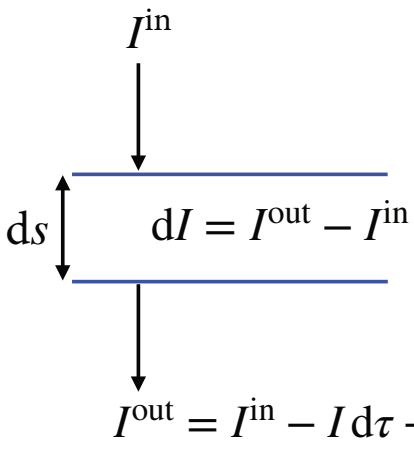

Figure 3: Radiative transfer across a thin slab, with no scattering or reflection and the radiation travelling in a single direction only, here denoted s. I is the radiative flux, τ is the optical depth and E is the emission by the slab.

In planetary atmospheres it is common to choose τ increasing downward, from 0 at the top of the atmosphere. The downward (D) and upward (U) irradiances are then

$$\frac{\mathrm{d}D}{\mathrm{d}\tau} = B - D\,, \qquad \frac{\mathrm{d}U}{\mathrm{d}\tau} = U - B\,. \tag{20a,b}$$

These equations are sometimes known as the *Schwarzchild equations.* The net flux of radiation is $N = U - D$ and the radiative heating is proportional to the net flux divergence, $-\partial N/\partial z$.

The gray assumption is not particularly accurate for many planetary atmospheres but for conceptual or approximate calculations it is often useful to suppose that the atmosphere is gray in the infra-red, in which case (20) applies to infra-red radiation. Similar but separate equations (that would normally include reflection, but not thermal emission) are then used for solar radiation. In Earth's atmosphere the absorption of solar radiation in the atmosphere is quite small, and although there is considerable reflection due to clouds most of the net incoming solar radiation is absorbed at the surface.

3.2 Radiative Equilibrium

A *radiative equilibrium* state has, by definition, no net radiative heating. If the atmosphere is transparent to solar radiation then the condition implies that the vertical divergence of the longwave radiation (denoted with a subscript L) is zero:

$$\frac{\partial(U_L - D_L)}{\partial z} = 0 \qquad \text{implying} \qquad \frac{\partial(U_L - D_L)}{\partial \tau} = 0. \tag{21a,b}$$

This condition is normally *not* satisfied in the atmosphere because the air moves. But if it were satisfied then (20) and (21b) form three equations in three unknowns, U_L, D_L and B, and a solution can be found as follows.

Consider an atmosphere with net incoming solar radiation S_{net} and suppose the planet is in radiative equilibrium with the incoming solar radiation balanced by outgoing infra-red radiation. That is, $U_{Lt} \equiv U_L(\tau = 0) = S_{\text{net}}$ where U_{Lt} is the net outgoing longwave radiation (OLR) at the top of the atmosphere. The downward infra-red radiation at the top of the atmosphere is zero, so

that the boundary conditions on the radiative transfer equations at the top of the atmosphere are

$$D_L = 0, \quad U_L = U_{Lt} \qquad \text{at} \qquad \tau = 0. \tag{22}$$

A little algebra reveals that a solution of (20) and (21b) that satisfies (22) is

$$D_L = \frac{\tau}{2} U_{Lt}, \qquad U_L = \left(1 + \frac{\tau}{2}\right) U_{Lt}, \qquad B = \left(\frac{1+\tau}{2}\right) U_{Lt}, \tag{23a,b,c}$$

as can be easily verified by substitution back into the equations.

It remains to explicitly relate τ to z, and one approximate recipe is to suppose that τ has an exponential profile,

$$\tau(z) = \tau_0 \exp(-z/H_a), \tag{24}$$

where τ_0 is the optical depth at $z = 0$ and H_a is the scale height of the absorber. In the Earth's atmosphere the optical depth is determined by the concentrations of water vapor (primarily) and carbon dioxide (secondarily), and τ_0 (the scaled optical depth) typically varies between 2 and 4, depending on the water vapor content of the atmosphere, and $H_a \approx 2\,\text{km}$, this being a typical scale height for water vapor. Using (23c) with $B = \sigma T^4$ the temperature then varies as

$$T^4(z) = U_{Lt} \left(\frac{1 + \tau_0 e^{-z/H_a}}{2\sigma} \right). \tag{25}$$

Of specific interest to us is the relation between surface temperature and outgoing IR, namely

$$T_s^4 = \frac{U_{Lt}}{2\sigma}(1 + \tau_0) = \frac{1}{2} T_e^4 (1 + \tau_0), \tag{26}$$

where T_e is the emission temperature. The expression for the ground temperature turns out to be slightly different and is given by

$$T_g^4 = \frac{U_{Lt}}{\sigma}(1 + \tau_0/2) = T_e^4 (1 + \tau_0/2). \tag{27}$$

This temperature is defined as the temperature that a black surface needs to have to provide the same upwards radiative flux as is given by the solution of the radiative transfer equations at $z = 0$, namely (23). A slightly different form was written down in a paper by Komabayasi (1967) [2], namely

$$\sigma T_g^4 = U_{Lt}(1 + 3\tau/4). \tag{28}$$

While quantitatively inaccurate because of the numerous approximations made, these equations will allow us to elucidate the mechanism behind the runaway greenhouse effect, as described below. We emphasize that the emission temperature, T_e is to be regarded as given: the outgoing longwave radiation is given by σT_e^4 and if the planet is in radiative equilibrium with its host star then the outgoing longwave radiation is equal to the net incoming solar radiation.

3.3 The runaway greenhouse effect

Let's consider an atmosphere containing some greenhouse gas (such as CO_2) and water vapor. We suppose that the surface optical depth is proportional to the concentration of greenhouse gases, and that the water concentration is proportional to $e_s(T_g)$, the saturation vapor pressure at the surface. Following Clausius-Clapeyron, e_s depends approximately exponentially on temperature, and we

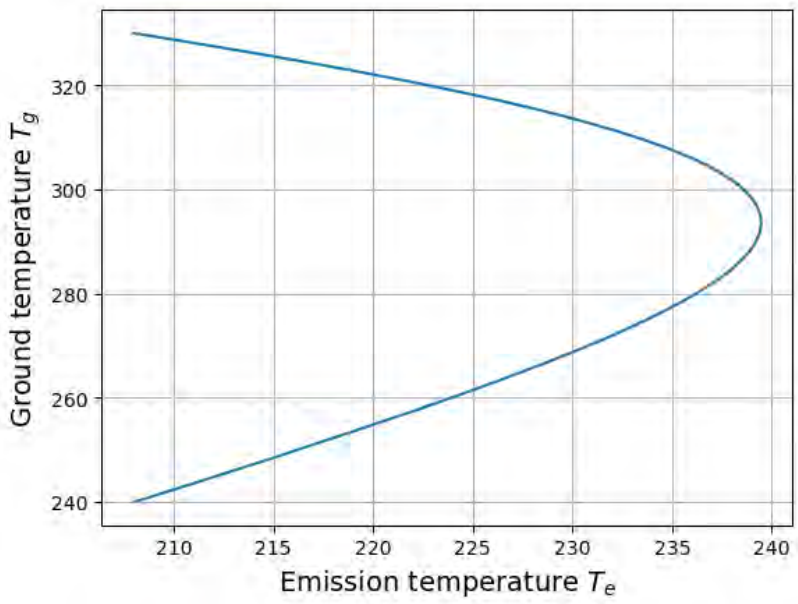

Figure 4: Ground temperature T_g as a function of emission temperature T_e (equivalent to the absorbed solar shortwave radiation at equilibrium), in radiative equilibrium. The atmosphere is supposed to contain a fixed concentration of one infra-red absorbing species, and a concentration of water vapor that scales exponentially with T_g.

will assume $e_s(T_g) \propto \exp(\gamma T_g)$, which is a rather approximate solution to the Clausius–Clapeyron equation (cf., equation (42)), valid over a limited range of temperatures, as the reader may verify. Thus, one can write

$$\tau_0 = A + B\mathrm{e}^{\gamma T_g}, \tag{29}$$

where A and B are two constants. A is the longwave optical depth of the atmosphere excluding water vapor, and $B\exp(\gamma T_g)$ scales the optical depth due to water vapor. Combining this equation with (27), one obtains a relationship between T_g and T_e:

$$\frac{T_g^4}{1 + 1(A + Be^{\gamma T_g})/2} = T_e^4, \tag{30}$$

with a very slightly different expression if (28) is used in place of (27). The left-hand side is positive and goes to 0 for small values of T_g and also as $T_g \to +\infty$; therefore, it is bounded by a threshold value of T_e from above, in which no surface temperature permits radiative equilibrium to be attained. (What might happen in reality would be that T_g strongly increases until the planet can cool by radiating outside of the absorption bands of water vapor, but let us omit that effect here.)

One can represent this situation graphically by plotting the equilibrium T_g as a function of T_e (Figure 4). For purposes of illustration, we choose $A = 1$. An approximate value of γ can be obtained by linearizing the expression for $e_s(T)$ around a basic state temperature T_0, resulting in $\gamma = L/(R^v T_0^2) \simeq 0.06\ \mathrm{K}^{-1}$. B is chosen such that $Be^{\gamma T_g} = 1$ at 300 K. It can be seen that at low values of T_e, there are two radiative equilibrium values of T_g: a case with lower value that has small amount of water vapor that is stable, and a case with high values of T_g with a large water vapor content that is unstable. To better understand the instability, consider a slight increase in

T_g around its high equilibrium value. In response, T_e decreases, hence longwave cooling decreases. This further drives an increase in T_g, and the runaway greenhouse effect occurs. As mentioned above, there are no equilibrium values of T_g for sufficiently high emission temperatures, and so for sufficiently high solar forcing. This is a runaway state. In reality, an equilibrium is reached through processes neglected in this simple model, namely emission outside of the absorption band of the greenhouse gases that are present.

4 Remarks

In this lecture we have considered two extreme consequences that the presence of water vapor, or any other condensible, might have on the climate of a planet. The first occurs when water vapor is the sole constituent of an atmosphere, giving rise to what is sometimes called a steam atmosphere. In this case, if the atmosphere is everywhere in equilibrium with liquid water (i.e., the atmosphere is 'saturated') the pressure is determined solely by temperature. This means there is no thermal wind – that is, unlike on Earth, a meridional temperature gradient is not accompanied by a vertical shear of the zonal wind. Similarly, because isosurfaces of pressure do not intersect isosurfaces of density, the atmosphere is not baroclinic and baroclinic instability thus does not occur.

A second consequence can occur if the condensible is a greenhouse gas – as water vapor. If the planet moves sufficiently close to its host star then the planet will warm. This increases the amount of water vapor, in accord with the Clausius-Clapeyron equation. The greenhouse effect increases, warming the planet still more, and the temperature 'runs away'. This is the famous runaway greenhouse effect, first described independently by Komabayasi [2] and Ingersoll [1] (who coined that most evocative phrase). Venus, in our Solar System, is believed to have passed through such a state. If the Earth were to move closer to the Sun (fortunately a very unlikely occurrence) it too could undergo a runaway greenhouse effect.

Appendix: the Clausius-Clapeyron Relation

In this section we ascertain what conditions need to be satisfied in order that equilibrium be maintained between two phases of the same substance. Suppose that, for example, water and water vapor are in contact with each other in a closed, isolated container; under what conditions is there no net transfer of material from one phase to another? And how might that change if heat is added and the temperature changes?

The energy per unit mass, Q, required to pass from one phase to another at constant temperature and pressure is given by

$$Q = T(\eta_v - \eta_l), \tag{31}$$

where T is the temperature, η_v is the specific entropy in the vapor phase and η_l the specific entropy in the liquid phase. In the phase-change context, the energy Q is denoted L and is called the 'latent heat of condensation' and, for water and water vapor, it is approximately a constant, decreasing by about 10% as temperature increases from 0° C (where $L \approx 2.5 \times 10^6 \mathrm{Jkg}^{-1}$) to 100° C.

Suppose that an amount of substance ΔM changes phase then the energy required or released is given by

$$L\Delta M = T\Delta M(\eta_v - \eta_l) = \Delta M(I_v - I_l) + \Delta M p(\alpha_v - \alpha_l), \tag{32}$$

where I is the internal energy, p is the pressure and α_v and α_l are the specific volumes of the vapor and liquid. Eq. (32) may be written as

$$L = T(\eta_v - \eta_l) = (I_v - I_l) + p\alpha_v - p\alpha_l. \tag{33}$$

The quantity $I + p\alpha$ is the enthalpy, h, so we obtain a well-known expression

$$L \equiv T(\eta_v - \eta_l) = h_v - h_l. \tag{34}$$

That is to say, the latent heat of condensation is equal to the difference in enthalpies of the two states, a useful result that we will use later on. It is not a general result that changes in entropy and enthalpy are so related, but it is true here because the temperature and pressure are constant.

Re-arranging (32) gives

$$T\eta_v - p\alpha_v - I_v = T\eta_l - p\alpha_l - I_l. \tag{35}$$

The expression $I + p\alpha - T\eta$ is known as the Gibbs function, and we have established that the Gibbs function for two phases of a substance in contact with each other and in equilibrium are equal to each other.

Let us now perturb the system slightly, for example adding some heat to it or displacing the parcel. If it then forms a new equilibrium the changes in temperature and pressure are, using (35), related by

$$T\delta\eta_v + \eta_v\ \delta T - p\ \delta\alpha_v - \alpha_v\ \delta p - \delta I_v = T\delta\eta_l + \eta_l\ \delta T - p\ \delta\alpha_l - \alpha_l\ \delta p - \delta I_l. \tag{36}$$

Using $\delta I = T\delta\eta - p\delta\alpha$ (the first law of thermodynamics) the above expression simplifies to

$$\delta T\eta_v - \alpha_v\delta p = \delta T\eta_l - \alpha_l\delta p, \tag{37}$$

or, in differential form

$$\frac{\mathrm{d}p}{\mathrm{d}T} = \frac{\eta_v - \eta_l}{\alpha_v - \alpha_l}. \tag{38}$$

Since, by definition, $L = T(\eta_v - \eta_l)$ we have

$$\frac{\mathrm{d}p}{\mathrm{d}T} = \frac{L}{T(\alpha^v - \alpha^l)}\ . \tag{39}$$

This is the *Clausius–Clapeyron* equation, which tells us how the pressure of a vapor that is in thermodynamic equilibrium with an adjacent liquid varies with temperature. In most circumstances $\alpha_v \gg \alpha_l$ (i.e., the density of the liquid is much greater than the density of the gas), and using the ideal gas relation ($\alpha_v = RT/p$) gives

$$\frac{\mathrm{d}p}{\mathrm{d}T} = \frac{Lp}{RT^2}\,. \tag{40}$$

This is the most common form of the Clausius–Clapeyron equation, and it gives the relation between temperature and vapor pressure of an ideal gas when the system is in equilibrium. If a system is in equilibrium and the temperature falls (perhaps because the system is cooled) then the system falls out of equilibrium. Some of the vapor then condenses into liquid form, reducing the vapor pressure. This is how rain forms. At the temperature at which the saturation vapor pressure of a substance equals that of the ambient pressure then any liquid present will *boil*. Note that p is the pressure due to the condensate, namely the partial pressure of the vapor, not the total pressure due to all gases present, and R is the specific gas constant of the condensate. When set in the context of an atmosphere that contains a non-condensible substance (such as Earth's atmosphere) p is commonly denoted e_s to distinguish it from the total pressure, commonly denoted p.

Eq. (40) may also be written

$$\frac{\mathrm{d}p}{\mathrm{d}T} = \frac{L\rho}{T}. \tag{41}$$

If L is constant then (40) can be solved analytically, giving

$$p_s = 0_0 \exp\left[\frac{L}{R}\left(\frac{1}{T_0} - \frac{1}{T}\right)\right], \tag{42}$$

using p_s to denote the pressure at saturation of the condensible, and where p_0 is the pressure at T_0, a value that is normally determined by experiment. These values come in pairs of values, since p_0 and T_0 are any values on the phase boundary. In many circumstances the increase in equilibrium vapor pressure with temperature is approximately exponential (inset to Fig. 2). (It is common in the atmospheric sciences, especially when dealing with dilute gases, to write the vapor pressure as e_s, with the subscript s denoting saturation.)

We can invert the above relation to give

$$T_s(p) = \frac{T_0}{1 - (RT/L)\ln(p/p_0)}, \tag{43}$$

using T_s to denote a 'saturation temperature' at pressure p. This is the temperature below which condensation will normally occur and is known as the dew point or frost point temperature. If the temperature falls below T_s, or the pressure rises above p_s, and condensation does not occur because thermodynamic equilibrium is not achieved, the gas is said to be supersaturated.

References

[1] A. P. Ingersoll, The runaway greenhouse: A history of water on Venus, J. Atmos. Sci., 26 (1969), pp. 1191–1198.

[2] M. Komabayasi, Discrete equilibrium temperatures of a hypothetical planet with the atmosphere and the hydrosphere of one component-two phase system under constant solar radiation, Journal of the Meteorological Society of Japan. Ser. II, 45 (1967), pp. 137–139.

[3] G. K. Vallis, Atmospheric and Oceanic Fluid Dynamics, Cambridge University Press, Cambridge, U.K., 2nd ed., 2017.

The Surface Temperature of Icy Moons is Nearly Insensitive to Solid-state Convection in the Ice Shell

Nathan Magnan

June 19, 2024

1 Introduction

1.1 Icy moons

The Solar system contains numerous icy moons. The ones we have the most data on are Europa and Enceladus, which, respectively, orbit Jupiter and Saturn. Other large icy moons include Ganymede and Callisto around Jupiter, Titan and Rhea around Saturn, Titania and Oberon around Uranus, or Triton around Neptune.

Icy moons get their name from their thick ice shell. Most of it is water ice, although there are always pollutants. In fact, Callisto's ice shell may only be 50% water [53, 54, 78]. For some moons this shell is in direct contact with space, but Ganymede, Callisto, Europa, Titan, and Triton all have an atmosphere [18, 24, 31, 32, 34, 37]. Triton is also covered by a thin crust of nitrogen ice [56].

There is also some variation in the deep internal structure of icy moons. Ganymede, Europa and Triton are fully differentiated, meaning that they have an iron core and a silicate mantle [2–4, 23, 56, 72]. From theory and modelling, we would expect that all icy moons have a similar structure [12]. Yet Callisto, for which we have good data, appears to only be weakly differentiated, *i.e.* its core still contains water ice [23].

Between the core and the ice shell, there may be a liquid water ocean. It is on Enceladus that we can make the strongest case for this idea. Indeed, the moons's south polar plumes, its moment of inertia and its libration pattern all hint at a hidden ocean [40, 55, 69, 70, 86]. Another moon for which we have compound evidence is Europa. Indeed, Galileo's magnetometric data, the moon's cycloidal surface features and its south polar plumes all suggest an ocean [43–45, 60, 75, 82]. Magnetometric data, which signals an ocean on Callisto [89]and maybe one on Ganymede [46], could also be used on Triton in the future [60]. Finally, there is some tentative evidence for an ocean on Titan from Huygens's detection of certain electromagnetic waves in the atmosphere, as well as from the moon's obliquity and response to tides [11, 13, 14, 39].

This possible large body of liquid water makes icy moons prime candidates in the search for extra-terrestrial life. Consequently, space agencies have devoted considerable ressources to learning more about those worlds. Voyager, Galileo, Huygens and Cassini all spent part of their mission collecting data on Jupiter and Saturn's icy moons. This trend will continue in the near future with JUICE and Europa clipper [29, 38, 67].

1.2 Why we care about convection in the ice shell

Whether those oceans host life or not depends on whether the ice shell is convecting or not.

First, because if the shell is convecting, then heat is efficiently transported upward and lost to space. Now if the shell loses more energy than it gains from tidal heating and conduction, then some water must freeze to release latent heat. Therefore, convection diminishes the ocean's life expectancy [74]. This can be compensated by the presence of antifreeze compounds such as amonia in the ocean [51].

Second, biochemistry requires oxidants, which are mostly produced at the surface by photochemistry. So, we need convective downdrafts to carry oxidants from the surface to the ocean [33]. Conversly, if there is life in the ocean, then updrafts could carry biochemicals to the surface were we could see them [1]. That being said, detecting those biotracers in the plume seems easier.

Another reason to care about convection is that it can explain some confusing surface features. For instance, we see chaos regions, lenticulae, bands and domes on Europa. Those structures could all be caused by convective updrafts in the ice shell [58, 64, 71]. Similar reasons have been advanced for why the south polar terrain (SPT) of Enceladus is deformed and has a high heat flux [59]. Additionally, the weirdly low number of craters on Europa and Enceladus indicates surface renewal, possibly by tectonics [20, 69]. More precisely, the distribution of surface ages on Enceladus hints at episodic tectonics [62]. This concurs with the observation that Europa's different types of surface features have different ages, indicating temporal variation in the updrafts' characteristics [71].

1.3 What we know (and ignore) about convection in the ice shell

At this stage, one may question how a solid like ice can exhibit fluid motions like convection.

This is because the words 'solid' and 'liquid' do not qualify a material, but its behavior. Any given material can behave both like a solid or a liquid, depending on the timescale: "everything flows if you wait long enough" [8]. For example, the typical flow speed for terrestrial ice sheets and glaciers is of order 10^{-5} m/s [57].

So, ice can flow. Now, since the interior of icy moons are hotter than their surface, and since ice is less dense when it is hot, ice may convect within the shell. This is called solid-state convection, and it also happens in the Earth's mantle. In some respects, solid-state convection is less complex than standard convection. Indeed, the extremely high viscosities make turbulence unlikely, though not impossible [88].

Unfortunately, this good news is largely compensated by how tricky it is to model ice:

First, its rheology is complicated. Indeed, the macroscopic flow is due to an accumulation of microscopic deformations, which can arise from four different creep mechanisms: dislocation creep, grain boundary sliding, basal slip and volume diffusion [9, 27]. Which mechanism prevails depends on the stress, temperature and grain size in your system [35, 68]. And of course, it is challenging to constrain the size of ice grains hidden deep in the shell of a distant world. Plus, it is risky to extrapolate viscosity laws derived from laboratory experiments to the extremely high-pressures and low-stress conditions relevant to icy moons [81].

Second, the thermodynamics of ice are hard to constrain. This is partly linked to the previous point in that the rates of tidal and shear heating in the shell depend on viscosity [87],

which comes with a large error bar. But another difficulty is that the thermal properties (heat capacity, conductivity, expansivity) of ice are temperature-dependent [19,66]. Conductivity is particularly treacherous because it depends on how the ice has crystallized [15, 47], and we do not know that for icy moons.

Third, the viscosity of ice is temperature-dependent. This non-linearity makes convection a sub-critical instability [10, 80]. Thus, the shell's convection status depends not only on the shell's current characteristics, but also its history. Moreover, viscosity gains twenty orders of magnitude between the bottom and the top of the shell [27,77].[1] This high dynamic range increases the cost of numerical simulations. Finally, the enormous viscosity of the upper shell prevents it from convecting, creating a stagnant lid [79] which eliminates the link between convection and surface features. It may be restored by allowing the stagnant layer to fracture [62], but that adds new physics and poorly constrained coefficients to the model.

For all of those reasons, we remain unsure of whether ice shells convect or not.

Indeed, surface features are not strong evidence. For example, Europa's chaos regions may be due to convection in the shell, but also to oceanic hydrothermal plumes deforming the shell [28,30]. Even though we have good observations of the chaos regions, we have not been able to disprove either option. That is because they make similar qualitative predictions, and our models of surface feature creation are crippled with so many uncertainties that we cannot make quantitative predictions.

We are also unlucky that the Rayleigh numbers of Europa and Enceladus' shells are close to the critical Rayleigh number for the onset of convection [60]. It means we would need very precise modelling to answer the convection question from the shell's global characteristics.

1.4 Objectives of the present work

Another way to detect convection is to quantify how convection would affect the shell's observables and parse the data for such patterns. Here we focus on the first step: we perform a suite of simulations of solid-state convection, incorporating various physics relevant to the shells of icy moons. We aim to determine the observable consequences of these effects.

Specifically, we consider the possibility that convective updrafts warm the surface, thereby inducing spatial variations in surface temperature. If so, one could search for periodic patterns in Galileo and Cassini's surface temperature data [73,84,85]. To test our hypothesis, we run 2D simulations of Rayleigh-Benard convection [52], but we replace the fixed-temperature boundary condition at the surface by a radiative boundary condition. It allows the surface temperature to respond to what happens below in the shell. There is already a few papers on convection under a simplified version of the radiative boundary condition called the Robin boundary condition [17, 22, 83], but none cover the solid-state regime.

We also study how the radiative boundary condition affects other observables. Those include the size of the convective cells, their flow rate, the diffuseness of the drafts, and other things that might be measured by the radars on JUICE and Europa clipper [29, 38, 41, 67].

[1] Actually, this figure was derived from an experimental law, but the experiments were all performed above $200K$. Since the surface is near $100K$, it is possible that the law fails in the upper shell, in which case the viscosity contrast may be less than 10^{20}. Yet the experiments showed a viscosity range of 10^4, so that much is undeniable.

Our observables also include the heat exchange rate between the ocean and the shell, because it determines whether the ocean freezes. Finally, we include the critical Rayleigh number, first unstable mode and growth rate of convection because those things matter to fluid dynamicists.

The plan of the report is as follows: we start in §2 by describing how we represent the ice shell; then §3 presents our numerical solver, Dedalus, and the exact equations that we feed it; The results are presented in §4, and discussed in §5; Finally, we conclude in §6.

2 Model of the Ice Shell

Let us first describe our model of the ice shell. It includes a radiative boundary condition at the surface, accounts for the high viscosity of ice, and includes the temperature dependence of viscosity. However, it does not include tidal heating.

We start in §2.1 by choosing the internal equations and the boundary conditions. Then in §2.2 we solve those equations in the case of a static shell. This provides us with orders of magnitude for all the variables, helping us adimensionalise the governing equations in §2.3.

2.1 Governing equations

We want a model that is as simple as possible. So, let us make several simplifications right off the bat: we work in a 2D rectangular box of dimensions (L, H) and axes (x, z); we assume that the gravitational field is uniform and along z; we pretend that ice is a Newtonian fluid; we neglect the temperature dependencies of heat capacity, thermal conductivity and expansivity; and we do not include internal heating.

2.1.1 Internal equations

Since the density of ice does not vary by more than 1% between the top and the bottom of the shell [66], we can safely make the Boussinesq approximation. It leads to the Oberbeck-Boussinesq equations

$$\nabla \cdot \boldsymbol{u} = 0, \tag{1a}$$

$$\partial_t \boldsymbol{u} + \boldsymbol{u} \cdot \nabla \boldsymbol{u} = -\frac{1}{\langle\rho\rangle} \nabla p + b\, \boldsymbol{e}_z + \nabla \cdot (\nu\, \nabla \boldsymbol{u}), \tag{1b}$$

$$\partial_t b + \boldsymbol{u} \cdot \nabla b = \kappa\, \nabla^2 b, \tag{1c}$$

where $\boldsymbol{u}$ is the ice's velocity, $\langle\rho\rangle$ its average density, p its pressure, b its buoyancy, ν its kinematic viscosity, and κ its thermal conductivity.

Now, because the viscosity of ice is enormous, we can simpify things further. Indeed, let us compare the sizes of the inertial, advective and viscous terms in Eq. (1b). If we choose a lengthscale $\bar{l}$ and a timescale $\bar{t}$, and if we assume the velocity scales as $\bar{l}/\bar{t}$, the ratio of the *r.h.s.* terms to the viscous term is $\bar{l}^2/\bar{t}\,\nu$. The buoyancy equation gives us $\bar{l}^2/\bar{t} = \kappa$, so the ratio simplifies to κ/ν. For ice, $\nu > 10^{11}\, m^2 s^{-1}$ and $\kappa \sim 10^{-6}\, m^2 s^{-1}$ [66, 81], so we can

neglect the inertial and advective terms in (1b). The internal equations become

$$\nabla \cdot \boldsymbol{u} = 0, \tag{2a}$$

$$\boldsymbol{0} = -\nabla h + b\,\boldsymbol{e}_z + \nabla \cdot (\nu\,\nabla \boldsymbol{u}), \tag{2b}$$

$$\partial_t b + \boldsymbol{u} \cdot \nabla b = \kappa\,\nabla^2 b \tag{2c}$$

where $h = p/\langle\rho\rangle$ is a convenient pseudo-pressure. Those are the archetypal equations of solid-state convection. Physically what happens is that velocity diffuses much faster than buoyancy. As such, we can work on the slow buoyancy timescale and assume that, at each instant, the velocity instantly relaxes to a viscous steady state that accommodates the current buoyancy distribution. This inertia-less regime is called the Stokes regime.

2.1.2 The temperature dependence of viscosity

As stated in the introduction, the macroscopic flow of ice is due to an accumulation of microscopic deformations. Those are less frequent at low temperature, so the viscosity of ice skyrockets in the upper shell. We want to include this leading-order effect in our model, so we follow [19, 27, 77] and use the Arrhenius law

$$\nu = \nu_\mathrm{m}\,\mathrm{e}^{\,N_\nu\left(\frac{T_\mathrm{m}}{T}-1\right)}, \tag{3}$$

where T is the local temperature, T_m is the melting temperature of ice (accounting for antifreeze coumpounds), ν_m is the viscosity of ice at that temperature, and $N_\nu = E_\mathrm{a}/RT_\mathrm{m} \sim 22$ is a dimensionless constant linked to the activation energy E_a of the creep mechanisms.

Note that the internal equations (2) apply to h, $\boldsymbol{u}$ and b, whereas Eq. (3) introduces T. Therefore, we need a link between T and b. Assuming that the variations in density are entirely due to thermal expansion, the Boussinesq definition of buoyancy leads to

$$\mathrm{d}b = \frac{g\alpha}{\langle\rho\rangle}\,\mathrm{d}T,$$

where g is the gravitational acceleration and α the thermal expansivity of ice. Now since b is only defined up to a constant, we can integrate the equation above to obtain

$$b = b_\mathrm{m} + \frac{g\alpha}{\langle\rho\rangle}(T - T_\mathrm{m}), \tag{4}$$

where b_m is an arbitrary constant setting the freezing-point buoyancy.

2.1.3 Boundary conditions

We try to inherit as many of our boundary conditions as possible from the standard Rayleigh-Benard setup [52]. As such, we use periodic boundary conditions for all the variables on the sides of the box (Eq. 5a), no-normal-flow boundary conditions at the top and the bottom of the box (Eq. 5b), and a fixed-temperature boundary condition at the bottom (Eq. 5d). Indeed, the base of the shell is in phase equilibrium with the ocean, so it must be at the melting temperature T_m.

One difference between our setup and Rayleigh-Benard's is that we use stress-free rather than no-slip boundary conditions (Eq. 5c). This is because the ocean acts as a lubricant, and because the shell's surface is in contact with space.

But the main novelty is in the upper boundary condition on temperature. We want to study how surface temperature responds to convection, so we need a boundary condition which reflects the physics that set the surface temperatures of ice shells. The surface layer receives energy from below by conduction, receives energy from the Sun, and loses energy via blackbody radiation. Since the layer is infinitely thin, it cannot store energy. So, the influxes and outfluxes must compensate each other, leading to the radiative boundary condition

$$-k\,\partial_z T|_{z=H} + F_* = \epsilon\sigma\,T^4(z=H),$$

where ϵ is the emmisivity of ice (accounting for pollutants), σ is the Stefan-Boltzmann constant, and F_* is the portion of the solar flux that enters the shell. Note that if the blackbody term dominates over the conductive term, we get a fixed-temperature boundary condition. Conversly, if the conductive term dominates, we get a fixed-flux condition. The radiative boundary condition covers the continuum between those two common models.

Bringing everything together into a single equation, our boundary conditions are

$$\forall f \in \{h, \boldsymbol{u}, b\},\ f(x=0) = f(x=L), \tag{5a}$$
$$u_z(z=0) = 0 \quad \text{and} \quad u_z(z=H) = 0, \tag{5b}$$
$$\partial_z u_x|_{z=0} = 0 \quad \text{and} \quad \partial_z u_x|_{z=H} = 0, \tag{5c}$$
$$T(z=0) = T_\mathrm{m}, \tag{5d}$$
$$k\,\partial_z T|_{z=H} + \epsilon\sigma\,T^4(z=H) = F_*. \tag{5e}$$

Nota bene: Clarté *et al.* [22] studies the effect of a slightly simpler boundary condition called the Robin condition. To obtain it, they introduce a nominal temperature field $T_\mathrm{n}(z)$ that satisfies Eq. (5e). Typically, one would choose for T_n the temperature profile of the conductive shell. By linearizing the radiative boundary condition around T_n, they get

$$k\,\partial_z \delta T|_{z=H} + 4\epsilon\sigma\,T_\mathrm{n}^3(z=H)\,\delta T(z=H) = 0, \tag{6}$$

where $\delta T = T - T_\mathrm{n}$ is the deviation to nominal temperature.

2.2 The conductive shell

Our research focuses on the effects of convection, so we need to compare the convective shell to something else. The relevant point of comparison is the static, conductive ice shell. Let us derive its characteristics by solving Eqs. (2-5).

The shell is static, so $\boldsymbol{u} = \boldsymbol{0}$ and the energy equation (2c) becomes $\Delta^2 b = 0$. From the symmetries of the system, it is reasonable to expect that nothing depends on x. Therefore, the energy equation becomes $\mathrm{d}^2_{zz} b = 0$, whose general solution is $b = c_1 + c_2 z$, where c_1 and c_2 are constants. The lower thermal boundary condition (5d) gives $c_1 = b_\mathrm{m}$, and if we call b_s the surface buoyancy of the conductive shell, we get $b = b_\mathrm{m} + (b_\mathrm{s} - b_\mathrm{m})\,z/H$. Injecting that

into the momentum equation (2b) gives $\mathrm{d}_z h = b_\mathrm{m} + (b_\mathrm{s} - b_\mathrm{m})\, z/H$, whose general solution is $h = h_\mathrm{m} + b_\mathrm{m} z + (b_\mathrm{s} - b_\mathrm{m})\, z^2/H$. Since pressure is only defined up to an additive constant, we are free to choose h_m. So, the only thing left to do is determine b_s.

To do so, we inject the buoyancy solution into Eq. (4). It gives $T = T_\mathrm{m} + (T_\mathrm{s} - T_\mathrm{m})\, z/H$, where T_s is the surface temperature of the conductive shell. The upper thermal boundary condition (5e) gives

$$k\,\frac{T_\mathrm{s} - T_\mathrm{m}}{H} + \epsilon\sigma\, T_\mathrm{s}^4(z = H) = F_*, \tag{7}$$

which is a fourth-degree polynomial equation. It has an analytical solution, but it looks terrible and does not give much insight. We prefer to solve the equation numerically, using the insight from Fig. 1-*left* that $T_\mathrm{s} \in [0, T_\mathrm{m}]$. These bounds allow us to use iterative root finding algorithms (dichotomy, Newton, ...) to find T_s. Finally, Eq. (4) gives $b_\mathrm{s} = b_\mathrm{m} + \frac{g\alpha}{\langle\rho\rangle}\,(T_\mathrm{s} - T_\mathrm{m})$.

We define the irradiation temperature T_* as the temperature the surface of the shell would take in the absence of conduction: $F_* = \epsilon\sigma\, T_*^4$. Figure 1-*right* shows that for icy moons, T_s is within one Kelvin of T_*. This explains why T_* is a convenient notation, and indicates that the conductive term in Eq. (7) is subdominant. This may change in the presence of internal heating or convection.

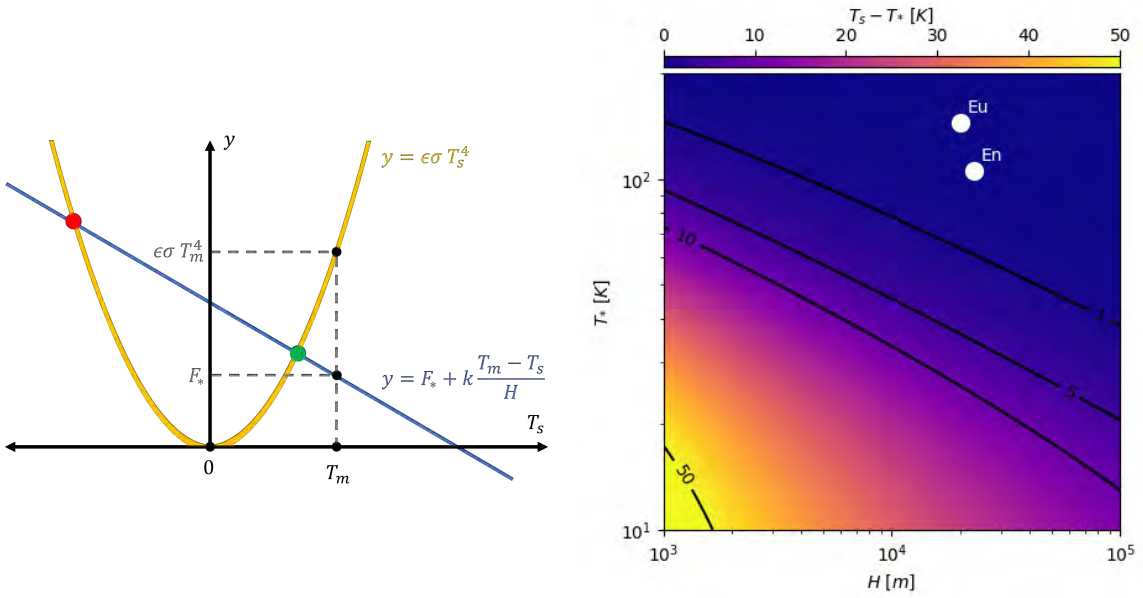

Figure 1: *Left:* Graphical solution to Eq. (7). The equation can be seen as the search for the intersections between a quartic (heat loss, in yellow) and a line (heat gain, in blue). There are two such points, one corresponds to a negative temperature (in red) and the other to a positive temperature (in green). Of course, only the latter matters. As long as the shell does not receive too much energy from the Sun, T_s is below T_m. *Right:* Surface temperature of the conductive shell T_s as a function of the shell's thickness H and of the irradiation temperature T_*. The two white dots indicate roughly the positions of the Europa and Enceladus within that plane. Notice how icy moons are in the regime where $T_\mathrm{s} \approx T_*$.

2.3 Adimensional equations

The conductive shell gives us an idea of the size of the different variables. Let us use those estimates to adimensionalise the equations. We shall use a tilde $\widetilde{\ }$ to denote adimensionalised quantities.

First, we choose T_s as our temperature scale, meaning that we define $\widetilde{T}$ as $T = T_\mathrm{s}\,\widetilde{T}$. This choice makes the radiative boundary condition (5e) look simple. Second, we set $\Delta b = \frac{g\alpha}{\langle\rho\rangle}(T_\mathrm{m} - T_\mathrm{s})$ as our buoyancy scale, meaning that we define $\widetilde{b}$ as $b = \Delta b\,\widetilde{b}$. This choice leads to the standard definition of the Rayleigh number and makes the link between buoyancy and temperature (4) look simple. Third, we saw in §2.2 that the important lengthscale is the vertical size of the box H, so we set $\mathbf{x} = H\widetilde{\mathbf{x}}$. Similarly, we saw in §2.1.1 that solid-state convection happens on the thermal diffusion timescale $\overline{t} = H^2/\kappa$, so we set $t = \overline{t}\,\widetilde{t}$. With those scales and if we adimensionalise velocity as $\boldsymbol{u} = [H/\overline{t}]\,\widetilde{\boldsymbol{u}}$, the energy equation (2c) looks simple. Fourth, we choose the basal viscosity ν_m as our viscosity scale, because it makes the viscosity law (3) look simple. Finally, we choose $\overline{h} = \nu_\mathrm{m}/\overline{t}$ as our pressure scale, because it makes the momentum equation (2b) look simple.

• With all those choices, the internal equations (2) adimensionalise to

$$\widetilde{\nabla}\cdot\widetilde{\boldsymbol{u}} = 0, \tag{8a}$$

$$\mathbf{0} = -\widetilde{\nabla}\widetilde{h} + \mathrm{Ra}\,\widetilde{b}\,\boldsymbol{e}_z + \widetilde{\nabla}\cdot(\widetilde{\nu}\,\widetilde{\nabla}\widetilde{\boldsymbol{u}}), \tag{8b}$$

$$\partial_{\widetilde{t}}\widetilde{b} + \widetilde{\boldsymbol{u}}\cdot\widetilde{\nabla}\widetilde{b} = \widetilde{\nabla}^2\widetilde{b}, \tag{8c}$$

where $\mathrm{Ra} = g\alpha(T_\mathrm{m} - T_\mathrm{s})H^3/\kappa\nu_\mathrm{m}$ is the Rayleigh number of the shell.

• Similarly, the Arrhenius law for viscosity (3) becomes

$$\widetilde{\nu} = \mathrm{e}^{\,N_\nu\left(\frac{N_T}{\widetilde{T}} - 1\right)}, \tag{9}$$

where $N_T = T_\mathrm{m}/T_\mathrm{s}$ is a dimensionless number encoding the temperature contrast between the base of the shell and the surface. This equation is nice because it gives $\widetilde{\nu} = 1$ at the bottom of the box.

• Next, remember that b_m is a free parameter. We choose $b_\mathrm{m} = \Delta b$ so that the link between buoyancy and temperature (4) becomes

$$\widetilde{b} = \frac{\widetilde{T} - 1}{N_T - 1}. \tag{10}$$

This equation is nice because it gives $\widetilde{b} = 1$ at the bottom of the box, as well as $\widetilde{b} = 0$ at the top in the conductive case.

• Finally, the adimensional forms of the boundary conditions (5) are

$$\forall f \in \{\widetilde{h}, \widetilde{\boldsymbol{u}}, \widetilde{b}\},\ f(\widetilde{x} = 0) = f(\widetilde{x} = \mathrm{Ar}), \tag{11a}$$

$$\widetilde{u}_z(\widetilde{z} = 0) = 0 \quad\text{and}\quad \widetilde{u}_z(\widetilde{z} = 1) = 0, \tag{11b}$$

$$\partial_{\widetilde{z}}\,\widetilde{u}_x|_{\widetilde{z}=0} = 0 \quad\text{and}\quad \partial_{\widetilde{z}}\,\widetilde{u}_x|_{\widetilde{z}=1} = 0, \tag{11c}$$

$$\widetilde{T}(\widetilde{z} = 0) = N_T, \tag{11d}$$

$$\partial_{\widetilde{z}}\,\widetilde{T}|_{\widetilde{z}=1} + \frac{\mathrm{Bi}}{4}\widetilde{T}^4(\widetilde{z} = 1) = \frac{\mathrm{Bi}}{4}N_*, \tag{11e}$$

where $\mathrm{Ar} = L/H$ is the aspect ratio of the box, $N_* = (T_*/T_\mathrm{s})^4$ is a dimensionless number encoding the amount of energy received from the Sun, and $\mathrm{Bi} = 4\epsilon\sigma H T_\mathrm{s}^3/k$ is called the

Biot number. The factor 4 is traditional, it makes the Robin condition look nicer. Figure 2 indicates the typical values of all those dimensionless numbers for icy moons.

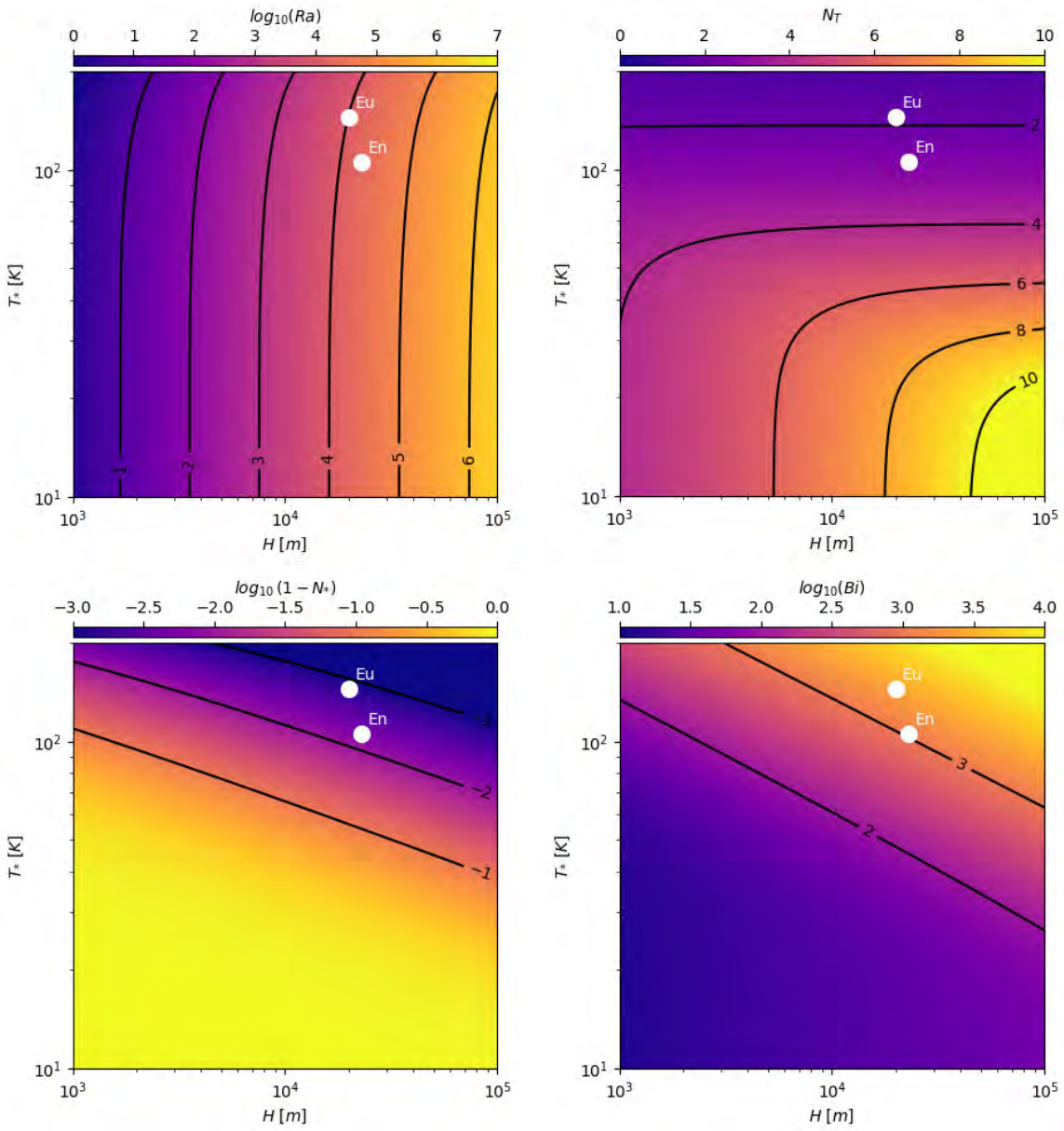

Figure 2: *Top left:* Rayleigh number Ra as function of the shell's thickness H and of the irradiation temperature T_*. The white dots indicate roughly the positions of Europa and Enceladus within that plane. *Top right:* Same, but for N_T. *Bottom left:* Same, but for N_*. *Bottom right:* Same, but for the Biot number Bi.

3 Numerical Methods

To solve the system formed by Eqs. (8-11), we use the pseudo-spectral code Dedalus [16]. The goal of the present section is to explain briefly how Dedalus works.

We start in §3.1 by explaining how Dedalus discretizes the internal equations using spectral methods. Then in §3.2 we present the tau method that handlies the boundary conditions, and in §3.3 we show how the spectral element method helps us deal with the huge dynamic range in viscosity. Finally, we describe in §3.4 our algorithms to solve initial value problems (IVPs), boundary value problems (BVPs) and eigenvalue value problems (EVPs), and we produce in §3.5 some test results that validate our code.

3.1 Spectral, Galerkin, ultra-spherical and pseudo-spectral methods

Computers can only deal with discrete quantities, whereas our equations (8-11) apply to continuous functions. This problem arises whenever one tries to solve numerically a set of differential equations of the form $\mathcal{A}(\mathbf{f}) = \mathbf{a}$, where $\mathcal{A}$ is a differential operator. But first, to keep things simple, let us assume that $\mathcal{A}$ is linear, so that $\mathcal{A}\mathbf{f} = \mathbf{a}$

Spectral methods adress the issue by expanding the solution $\mathbf{f}$ over a basis of 'trial' functions $\{\phi_j\}_{j\in\mathbb{N}}$ and truncating the expansion at some finite order N. If $\mathbf{f}$ is infinitely differentiable, this gives a very precise approximation,

$$\mathbf{f} \approx \sum_{j=0}^{N-1} \widehat{\mathbf{f}}_j \, \phi_j.$$

Indeed, the truncation error goes to zero exponentially, which is the beauty of spectral methods.

To solve the differential equation, one still needs to find the coefficients $\widehat{\mathbf{f}}_j$. Galerkin methods do so by introducing a second basis of 'test' functions $\{\psi_i\}_{i\in\mathbb{N}}$ [61]. The solution makes $\mathcal{A}\mathbf{f} - \mathbf{a}$ the null function, so $\forall i \in \mathbb{N}$, $\langle \psi_i \,|\, \mathcal{A}\mathbf{f} - \mathbf{a}\rangle = 0$. We only keep the N first equations so as to have a well-constrained $N \times N$ linear problem,

$$\forall i < N, \; \sum_{j=0}^{N-1} \langle \psi_i \,|\, \mathcal{A}\phi_j\rangle \, \widehat{\mathbf{f}}_j = \langle \psi_i \,|\, \mathbf{a}\rangle. \tag{12}$$

The art is in finding a pair of bases (ϕ, ψ) that makes the matrix $\mathcal{M}_{i,j} = \langle \psi_i \,|\, \mathcal{L}\phi_j\rangle$ sparse.

The ultra-spherical method is a particular choice of bases that leads to a banded matrix. In our case, we decompose the solution $\mathbf{f}(\widetilde{x}, \widetilde{z}, \widetilde{t})$ into a sum of separable terms of the form $\mathbf{f}_x(\widetilde{x}, \widetilde{t}) \times \mathbf{f}_z(\widetilde{z}, \widetilde{t})$. Since the boundary conditions on the sides of the box are periodic, we use Fourier modes of the form $\phi_j(\widetilde{x}) = \mathrm{e}^{2i\pi(j\widetilde{x}/\mathrm{Ar})}$ for $\mathbf{f}_x$. Naturally, the test functions that those trial functions interact best with are themselves. As for $\mathbf{f}_z$, our trial functions are the Chebyshev polynomials of the first kind $T_n(\widetilde{z})$ and our test functions are the Chebyshev polynomials of the third kind $U_n(\widetilde{z})$. Note that this is only a spectral transform in space, not time. Consequently, $\mathcal{A}$ can only contain spatial derivatives. We will see how to deal with time derivatives in §3.4.

If the operator $\mathcal{A}$ is not linear, we enter the realm of pseudo-spectral methods. To keep things brief, those methods represent each function twice: once in the spectral domain, once on a spatial grid. They try to work in the spectral domain as much as possible, but when they need to evaluate a non-linear term, they (i) use a fast spectral transform to switch to the spatial domain, (ii) evaluate the non-linear term on the grid points, and (iii) use the inverse spectral transform to return to the spectral domain.

3.2 The tau method

The ultra-spherical spectral method gives an approximate solution to the internal equations $\mathcal{A}\mathbf{f} = \mathbf{a}$, but we also have boundary conditions. The periodic ones are automatically satisfied by the Fourier modes used to expand $\mathbf{f}_x$, but the top and bottom boundary conditions are of the form $[\mathcal{B}\mathbf{f}](\mathbf{x}) = \mathbf{b}$, where $\mathcal{B}$ is a linear functional and $\mathbf{x}$ a point on the boundary of the domain. Each such boundary condition adds a row to matrix $\mathcal{M}$,

$$\forall i < K,\ \sum_{j=0}^{N-1} [\mathcal{B}_i \phi_j](\mathbf{x}_i)\, \widehat{\mathbf{f}}_j = \mathbf{b}_i. \tag{13}$$

Therefore, the matrix becomes of size $(N+K) \times N$ where K is the number of boundary conditions. $\mathcal{M}$ is not square anymore, indicating that the linear problem is over-constrained.

The τ method adresses this issue by adding degrees of freedom called 'tau terms' [50]. The internal equations become $\mathcal{A}\mathbf{f} + \boldsymbol{\tau}_1\, g_1 + \boldsymbol{\tau}_2\, g_2 + ... + \boldsymbol{\tau}_K\, g_K = \mathbf{a}$, where the $\boldsymbol{\tau}_k$ are the extra variables and the g_k are linear combinations of the test functions $\{\psi_0,\, \psi_1,\, ...,\, \psi_{N-1}\}$. $g_k = \psi_{N-k}$ is a good option, because the rows representing internal equations remain sparse:

$$\begin{cases} \displaystyle\sum_{j=0}^{N-1} \langle \psi_i \,|\, \mathcal{A}\phi_j \rangle\, \widehat{\mathbf{f}}_j = \langle \psi_i \,|\, \mathbf{a} \rangle & \text{if } i < N-K, \\ \displaystyle\sum_{j=0}^{N-1} \langle \psi_i \,|\, \mathcal{A}\phi_j \rangle\, \widehat{\mathbf{f}}_j + \boldsymbol{\tau}_k = \langle \psi_i \,|\, \mathbf{a} \rangle & \text{if } i = N-k. \end{cases}$$

In fact, we can drop the rows $N-K$ to $N-1$, because all they do is give the values of $\boldsymbol{\tau}_k$ that allows us to enforce the boundary conditions. So in essence, this version of the tau method replaces the K last 'internal equation' rows (12) by 'boundary condition' rows (13). This is what we use for the numerical experiments with temperature-dependent viscosity.

But in general, this is not the best option. In fact, there is no general theory of what is the best choice for the g_k, only rules of thumb deduced from optimising the solution to Poisson's equation in a particular domain. In most of our numerical experiments, we let Dedalus apply those rules of thumb. But to do so, we need to reframe the internal equations (8) into their first-order formulation

$$\mathrm{Tr}[\widetilde{\mathbf{G}}_u] + \tau_{\text{gauge h}} = 0, \tag{14a}$$

$$\mathbf{0} = -\widetilde{\nabla}\widetilde{h} + \mathrm{Ra}\,\widetilde{b}\,\boldsymbol{e}_z + \nabla\cdot(\widetilde{\nu}\,\widetilde{\mathbf{G}}_u) + \boldsymbol{\tau}_{\text{mom.}}\, g(\widetilde{z}) + \tau_{\text{gauge u}}\,\boldsymbol{e}_x, \tag{14b}$$

$$\partial_{\widetilde{t}}\widetilde{b} + \widetilde{\boldsymbol{u}}\cdot\widetilde{\nabla}\widetilde{b} + \tau_{\text{ener.}}\, g(\widetilde{z}) = \widetilde{\nabla}\cdot\widetilde{\mathbf{G}}_b, \tag{14c}$$

$$\widetilde{\mathbf{G}}_u = \widetilde{\nabla}\widetilde{\boldsymbol{u}} - \boldsymbol{e}_z \otimes \boldsymbol{\tau}_u\, g(\widetilde{z}), \tag{14d}$$

$$\widetilde{\mathbf{G}}_b = \widetilde{\nabla}\widetilde{b} - \tau_b\, g(\widetilde{z})\,\boldsymbol{e}_z, \tag{14e}$$

where the $\widetilde{\mathbf{G}}$ terms are new variables representing the spatial derivatives of $\widetilde{\boldsymbol{u}}$ and $\widetilde{b}$, they make the problem first-order in $\widetilde{z}$. The tau terms $\boldsymbol{\tau}_{\text{mom.}}$, $\tau_{\text{ener.}}$, $\boldsymbol{\tau}_u$ and τ_b are linked to the top and bottom boundary conditions on $\widetilde{\boldsymbol{u}}$ and $\widetilde{b}$, the tau term $\tau_{\text{gauge h}}$ enforces the gauge condition $\int \mathrm{d}\widetilde{x}\,\mathrm{d}\widetilde{z}\,\widetilde{h} = 0$, and $\tau_{\text{gauge u}}$ deals with the gauge condition $\int \mathrm{d}\widetilde{x}\,\mathrm{d}\widetilde{z}\,\widetilde{u}_x = 0$. The incompressibility condition (8a) is managed by the pseudo-pressure h, which acts as a Lagrange multiplier. The viscosity law (9), the buoyancy-temperature link (10) and the boundary conditions (11) remain unchanged.

3.3 The spectral element method

The viscosity increases by twenty orders of magnitude between the bottom and the top of the shell. Most of this variation is in the vertical direction, where we expand variables over the Chebyshev polynomials T_n. For polynomials to cover such a large dynamic range, we would need their maximal degree $N-1$ to be enormous, but that would be expensive.

The spectral element method adresses this problem by breaking the domain into several cells. The solution $\mathbf{f}$ can be seen as a piece-wise function, with one piece $\mathbf{f}^\ell$ per cell ℓ. Each piece $\mathbf{f}^\ell$ can then be expanded over the cell's own trial functions ϕ_i^ℓ [65]. Interface conditions at the border between cells ensure that the global solution $\mathbf{f}$ is continuous, differentiable, *etc.* The benefit of this method is that we keep the fast convergence of spectral methods, but now each piece of the solution $\mathbf{f}^\ell$ only deals with a small dynamic range.

In our case, since the variations in viscosity are mostly vertical, we decompose the box into L horizontal layers extending from $\widetilde{z}=\ell/L$ to $\widetilde{z}=(\ell+1)/L$. Within each layer, we use Fourier modes as test and trial functions for $\mathbf{f}_x^\ell$ and (U_n, T_n) as test and trial functions for $\mathbf{f}_z^\ell$. We only need to impose the continuities of $\widetilde{h}$, $\widetilde{\boldsymbol{u}}$, $\widetilde{b}$, $\partial_{\widetilde{z}}\widetilde{u}_x$ and $\partial_{\widetilde{z}}\widetilde{b}$ at the interfaces between layers, because the continuities of $\partial_{\widetilde{z}}\widetilde{u}_z$ and $\partial_{\widetilde{z}}\widetilde{h}$ follow from the continuity and momentum equations. To do so, we apply the row-replacement method of §3.2 *in each cell*.

Note that we only use the spectral element method if viscosity is temperature-dependent.

3.4 Solvers

3.4.1 Initial value problems

Most of our simulations are IVPs: we start from the conductive shell plus a small perturbation, and we watch the perturbation grow over time. The spectral decomposition of §3.1 is only spatial, so we still need to determine how the coefficients $\widehat{\mathbf{f}}_j^\ell$ depend on time. Since the system (14) is first-order in time, we need a way to solve systems of the form $\mathcal{C}\dot{\mathbf{F}}=\mathcal{D}(\mathbf{F})$ where $\mathbf{F}$ is a vector containing all the $\widehat{\mathbf{f}}_j^\ell$, $\mathcal{D}$ is an evolution operator that may contain spatial derivatives, and $\mathcal{C}$ is a matrix indicating which equations contain a time derivative.

IMEX methods separate the linear $\mathcal{L}$ and non-linear $\mathcal{N}$ parts of the evolution operator, so that the system becomes $\mathcal{C}\dot{\mathbf{F}}=\mathcal{L}\,\mathbf{F}+\mathcal{N}(\mathbf{F})$. The idea is then to discretize time into steps of finite duration $\Delta\widetilde{t}$, and to propagate $\mathbf{F}$ from $m\Delta\widetilde{t}$ to $(m+1)\Delta\widetilde{t}$ using an implicit scheme for $\mathcal{L}$ but an explicit scheme for $\mathcal{N}$. Thanks to the implicit treatment of the linear terms, IMEX methods tend to be numerically stable.

We use the IMEX method from section 2.6 of Ascher 1997 [6], which is second-order accurate, meaning that its truncation error scales with $\left(\Delta\widetilde{t}\right)^2$. This Runge-Kutta-like scheme decomposes each timestep into 6 successive instructions:

$$\mathbf{F}_0^* \leftarrow \mathbf{F}_m, \tag{15a}$$

$$\mathbf{N}_1 \leftarrow \mathcal{N}(\mathbf{F}_0^*), \tag{15b}$$

$$\mathbf{L}_1 \leftarrow \mathcal{L}\,\mathbf{F}_1^* \text{ where } \mathcal{C}\mathbf{F}_1^* = \mathcal{C}\mathbf{F}_m + \gamma\Delta\widetilde{t}\,\mathbf{L}_1 + \gamma\Delta\widetilde{t}\,\mathbf{N}_1, \tag{15c}$$

$$\mathbf{N}_2 \leftarrow \mathcal{N}(\mathbf{F}_1^*), \tag{15d}$$

$$\mathbf{L}_2 \leftarrow \mathcal{L}\,\mathbf{F}_2^* \text{ where } \mathcal{C}\mathbf{F}_2^* = \mathcal{C}\mathbf{F}_m + (1-\gamma)\Delta\widetilde{t}\,\mathbf{L}_1 + \delta\Delta\widetilde{t}\,\mathbf{N}_1 + \gamma\Delta\widetilde{t}\,\mathbf{L}_2 + (1-\delta)\Delta\widetilde{t}\,\mathbf{N}_2, \tag{15e}$$

$$\mathbf{F}_{m+1} \leftarrow \mathbf{F}_2^*, \tag{15f}$$

where $\gamma=(2-\sqrt{2})/2$ and $\delta=(1-\sqrt{2})/(2-\sqrt{2})$. As advertised, steps (15b) and (15d) are explicit whereas steps (15c) and (15e) are implicit.

3.4.2 Boundary value problems

The high viscosity of ice and the low Rayleigh numbers of icy moon shells ensure that convection does not lead to turbulence. Rather, the instability drives the transition from one steady state to another.[2] Some of our simulations look for this final steady state directly, by setting the time derivatives to zero.

This leaves a non-linear BVP of the form $\mathcal{D}(\mathbf{F}) = \mathbf{0}$. Ideally, we would want a set of coefficients $\widehat{\mathbf{f}}_j^\ell$ and tau terms τ_k that solves all the internal equations and all the boundary conditions. Unfortunately, the non-linear terms mean it is possible that no exact solution exists. So in practice, we search for a vector $\mathbf{F}$ that minimizes the norm of $\mathcal{D}(\mathbf{F})$.

Dedalus uses Newton's method to minimize this 'error'. One benefit of providing the symbolic form of the equations is that Dedalus can compute the Jacobian of $\mathcal{D}$ symbolically. Precisely, it computes a band-limited approximation of the Jacobian. The algorithm terminates once the Newton steps have become smaller than a value chosen by the user.

The key is to make a good initial guess $\mathbf{F}_0$ that will help the Newton solver converge quickly to the desired steady state. Our strategy is to start by solving an IVP all the way to steady state, and use that state as our initial guess. If the parameters of the IVP's ice shell are too far from the parameters of the BVP's shell, we take small steps in parameter space. The solution of BVP_n becomes the initial guess of BVP_{n+1}.

3.4.3 Eigenvalue problems

To study the onset of convection, we consider whether an infinitesimal perturbation to the conductive shell can grow exponentially over time. To do so, we linearize all the equations around the conductive shell solution f_0, and we assume that the perturbations f_1 grow exponentially in time, $f_1(t, \mathbf{x}) = f'(\mathbf{x})\, \mathrm{e}^{-i\,\widetilde{\omega}\,\widetilde{t}}$. The internal equations (14) become

$$\mathrm{Tr}[\widetilde{\mathbf{G}}'_u] + \tau'_{\text{gauge p}} = 0, \tag{16a}$$

$$\mathbf{0} = -\widetilde{\nabla}\widetilde{h}' + \mathrm{Ra}\,\widetilde{b}'\,\boldsymbol{e}_z + \nabla\cdot(\widetilde{\nu}_0\,\widetilde{\mathbf{G}}'_u) + \boldsymbol{\tau}'_{\text{mom.}}\,g(\widetilde{z}) + \tau'_{\text{gauge u}}\,\boldsymbol{e}_x, \tag{16b}$$

$$-i\,\widetilde{\omega}\,\widetilde{b}' - \widetilde{u}'_z + \tau'_{\text{ener.}}\,g(\widetilde{z}) = \widetilde{\nabla}\cdot\widetilde{\mathbf{G}}'_b, \tag{16c}$$

where $\widetilde{\nu}_0 = \mathrm{e}^{N_\nu\left(\frac{\widetilde{z}}{1-\widetilde{z}+1/(N_T-1)}\right)}$ is the conductive shell's viscosity. Similarly, we linearize the boundary conditions (11) to

$$\forall f' \in \{\widetilde{h}', \widetilde{\boldsymbol{u}}', \widetilde{b}'\},\ f'(\widetilde{x}=0) = f'(\widetilde{x}=\mathrm{Ar}), \tag{17a}$$

$$\widetilde{u}'_z(\widetilde{z}=0) = 0 \ \text{ and } \ \widetilde{u}'_z(\widetilde{z}=1) = 0, \tag{17b}$$

$$\partial_{\widetilde{z}}\,\widetilde{u}'_x|_{\widetilde{z}=0} = 0 \ \text{ and } \ \partial_{\widetilde{z}}\,\widetilde{u}'_x|_{\widetilde{z}=1} = 0, \tag{17c}$$

$$\widetilde{T}'(\widetilde{z}=0) = 0, \tag{17d}$$

$$\partial_{\widetilde{z}}\widetilde{T}'|_{\widetilde{z}=1} + \mathrm{Bi}\,\widetilde{T}'(\widetilde{z}=1) = 0 \tag{17e}$$

and the link between buoyancy and temperature (10) to

$$\widetilde{b}' = \frac{\widetilde{T}'}{N_T - 1}. \tag{18}$$

[2] Namely, from the conductive shell to the convective shell.

The structure of this set of equations is $-i\,\widetilde{\omega}\,\mathcal{C}\mathbf{F} = \mathcal{L}\mathbf{F}$ where $\mathcal{C}$ and $\mathcal{L}$ have the same abstract meaning as in §3.4.1 (but different values, $\mathcal{L} \leftarrow \mathcal{L} + \delta\mathcal{N}$). If the resolution N is low enough, Dedalus solves such EVPs using the `scipy.linalg.eig` routine, which implements a version of the QR algorithm [25, 26, 48]. Otherwise, Dedalus combines a shift-and-inverse method with the `scipy.sparse.linalg.eig` routine, which relies on Arnoldi's algorithm [5].

3.5 Tests

To verify that our equations and codes are correct, we remove the temperature dependence of viscosity by setting $N_\nu = 0$, and we replace the radiative boundary condition (11e) by a fixed-temperature boundary condition (in a sense, we take $\mathrm{Bi} = +\infty$). This simplifies the setup to one that has been studied for more than a century: 2D Rayleigh-Benard convection with fixed-temperature and stress-free boundary conditions. That gives us a wealth of results against which to validate our code.

3.5.1 Onset of convection

Let us start with the onset of convection. We show in §A that, with the present set of boundary conditions, (i) the linear instability appears when $\mathrm{Ra} > \frac{27}{4}\pi^4 \approx 658$ and (ii) the horizontal wavenumber of the fastest-growing (or most-slowly-decaying) mode is

$$\widetilde{k}_x^2 = \frac{\sqrt[3]{\sqrt{729\,\mathrm{Ra}^4\pi^4 + 27\,\mathrm{Ra}^3} + 27\,\mathrm{Ra}\,\pi^2}}{3} - \frac{\mathrm{Ra}}{\sqrt[3]{\sqrt{729\,\mathrm{Ra}^4\pi^4 + 27\,\mathrm{Ra}^3} + 27\,\mathrm{Ra}\,\pi^2}} - \pi^2.$$

We use those two predictions to validate our EVP solver in Fig. 3. Note that for each Rayleigh number Ra, we vary the aspect ratio Ar to maximise the growth rate $\mathrm{Im}(\widetilde{\omega})$. Indeed, our finite box only allows a discrete set of modes $\widetilde{k}_x = j/\mathrm{Ar}$, $j \in \mathbb{N}$, which does not contain the fastest growing mode unless Ar is optimal.

It is also possible to use an IVP simulation to estimate the growth rate. Indeed, there exists a period[3] during which plotting $\ln\left(\sqrt{\int\int \mathrm{d}\widetilde{\mathbf{x}}\,\widetilde{b}_1^2}\right)$ against $\widetilde{t}$ gives a straight line whose slope is the growth rate. At $\mathrm{Ra} = 10^3$, we find a growth rate of $\mathrm{Im}(\widetilde{\omega}) = 7.5 \pm 0.5$. This in good agreement with the analytical prediction, $\mathrm{Im}(\widetilde{\omega}) = 7.96$, so we see this as a first validation of our IVP solver. The numerical result is a bit low because we cannot optimise Ar for an IVP simulation, the best we can do is take Ar large so that one of the allowed mode is close to the fastest growing mode. We took $\mathrm{Ar} = 64$.

3.5.2 Convective steady state

The infinitesimal perturbations grow exponentially in time, until they are so big that the quadratic term in (14c) becomes significant, causing the instability to saturate. Since we consider low Rayleigh numbers, convection should saturate in a steady state. We verify this

[3] Once the fastest growing mode dominates all others, but before the non-linear effects become relevant.

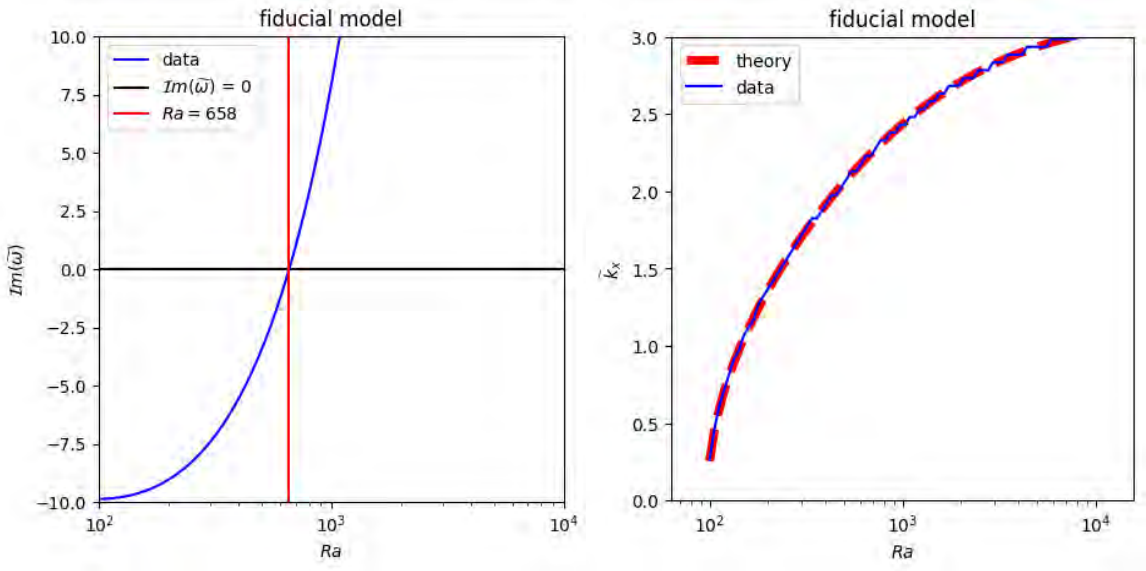

Figure 3: *Left:* Growth rate $\mathrm{Im}(\widetilde{\omega})$ of the fastest-growing (or most-slowly-decaying) infinitesimal perturbation as a function of the Rayleigh number Ra. The growth rate becomes positive when $\mathrm{Ra} = 658$, exactly as expected for Rayleigh-Benard convection (with fixed-temperature and stress-free boundary conditions). *Right:* Horizontal wavenumber $\widetilde{k}_x$ of the fastest-growing infinitesimal perturbation as a function of the Rayleigh number Ra. The agreement between our numerical results and linear theory is excellent.

by introducing the steadiness parameter

$$S(\widetilde{t}) = \frac{\sqrt{\iint \mathrm{d}\widetilde{\mathbf{x}} \ \left[\widetilde{b}_1(\widetilde{\mathbf{x}}, \widetilde{t}) - \widetilde{b}_1(\widetilde{\mathbf{x}}, \widetilde{t} - 1)\right]^2}}{\sqrt{\iint \mathrm{d}\widetilde{\mathbf{x}} \ \widetilde{b}_1^2(\widetilde{\mathbf{x}}, \widetilde{t})}} \tag{19}$$

and checking that it is below 10^{-2} throughout the last time unit of our IVP simulations.

The updrafts of hot ice and downdrafts of cold ice accelerate heat exchanges between the base and the surface. This is characterised by the Nusselt number

$$\langle \mathrm{Nu} \rangle = \int \frac{\mathrm{d}\widetilde{x}}{\mathrm{Ar}} \ \frac{\mathrm{d}_{\widetilde{z}} T_{\mathrm{conv.}}|_{\widetilde{z}=0}}{\mathrm{d}_{\widetilde{z}} T_{\mathrm{cond.}}|_{\widetilde{z}=0}}. \tag{20}$$

We average over $\widetilde{x}$ because, at steady state, layers cannot store energy, so $\int \mathrm{d}\widetilde{x} \, \mathrm{d}_{\widetilde{z}} T$ becomes independent of $\widetilde{z}$. And indeed, the conductive and convective shells are both steady. We show in Fig. 4-*left* that our numerical predictions for $\langle \mathrm{Nu} \rangle$ are in excellent agreement with the results of [36]. This is a second validation of our IVP solver.

We also quantify the horizontal size of the convective cells by locating the zeros of

$$R(\widetilde{x}) = \int \mathrm{d}\widetilde{z} \ \widetilde{b}_1 - \iint \frac{\mathrm{d}\widetilde{x}}{\mathrm{Ar}} \, \mathrm{d}\widetilde{z} \ \widetilde{b}_1.$$

They indicate the boundaries between updrafts and downdrafts, so we can use the distance $\widetilde{\lambda}$ between a zero and the second next to measure the horizontal size of a convective cell.

Different cells might have different $\widetilde{\lambda}$, so we plot the mean and standard deviation of $\widetilde{\lambda}$ in Fig. 4-*right*. We use $\mathrm{Ar} = 64$ to get many cells and thus good statistics. We find that once Ra is large enough, the cell size increases with Ra. This may be surprising, since the wavelength of the fastest growing mode always decreases with Ra. What happens is that cells merge to form convective superstructures [21,49,63]. Reproducing this well-established behavior validates our IVP solver in a third, independent way.

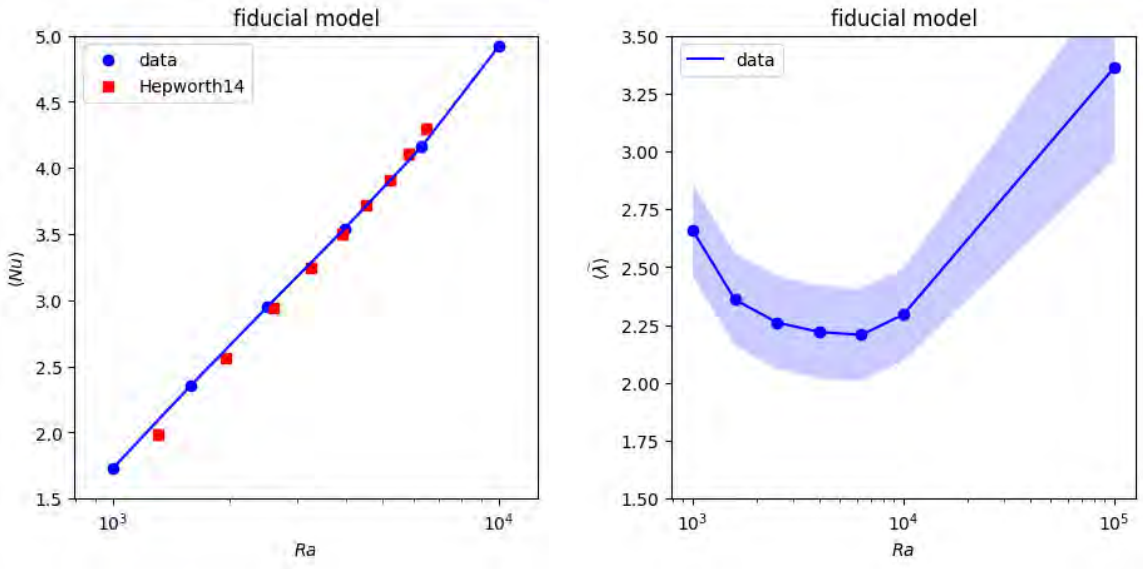

Figure 4: *Left:* Mean Nusselt number at steady state $\langle \mathrm{Nu} \rangle$ as a function of the Rayleigh number Ra. The agreement with [36] is tight, even though we used `WebPlotDigitizer` to recover the data in their figure 5.14. *Right:* Mean horizontal size of the convective cells at steady state $\widetilde{\lambda}$ as a function of the Rayleigh number Ra. Once Ra is large enough, the cell size increase with Ra, indicating the formation of convective superstructures.

In theory, we could also use a BVP solver to predict the rate of heat transport and the size of the convective cells. Unfortunately, we found that Newton's algorithm very easily diverges when faced with Eqs. (14). Consequently, we could not validate nor use the BVP solver described in §3.4.2.

4 Results

Let us now replace the fixed-temperature boundary condition used during testing by the radiative boundary condition (11e).[4] This will allow us to quantify the effect of convection on surface temperature, and also to characterise the effect of a radiative boundary condition on the onset of convection (4.1), the structure of convective rolls (4.2), and the rate of heat transport (4.3).

[4] We use a uniform viscosity ($N_\nu = 0$) in this section.

4.1 Onset of convection

First, let us study how the radiative boundary condition affects the onset of convection. This will inform future studies of shell thickness evolution(*e.g.* [76])

First, the radiative boundary condition contains a highly non-linear term (T^4) that could make the instability sub-critical. To check this idea, we plot in Fig. (5) some transition diagrams for convection. However, we find that whatever the value of the Biot number, the transition remains super-critical. We will see in §4.3 that this is because the surface temperature perturbations remain small, so the T^4 term can safely be linearized.

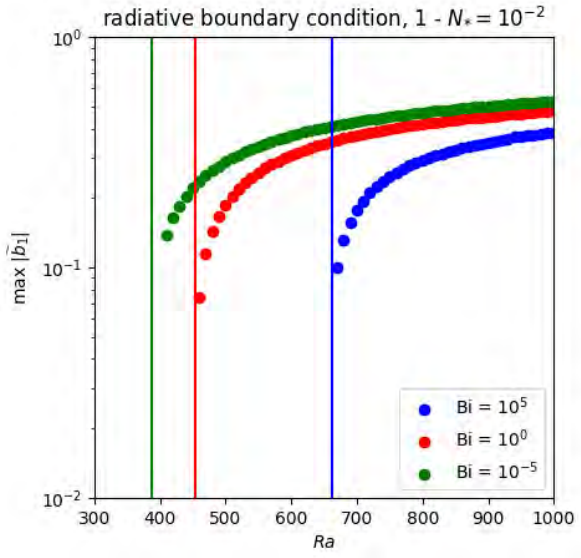

Figure 5: Transition diagram for three values of the Biot number Bi. The horizontal axis gives the Rayleigh number Ra and the vertical axis measures the strength of convection at steady state via the maximum bouyancy perturbation $\widetilde{b}_1$. The dots represent our IVP simulation data and the lines indicate the critical rayleigh numbers for the onset of convection Ra_c (as given by our EVP solver). In all three cases, the perturbations become infinitesimal as we approach Ra_c from above, meaning that the instability is super-critical.

Since the transition remains super-critical, we study how the critical Rayleigh number and fastest growing mode are impacted by the radiative boundary condition. Specifically, we consider the effect of Bi, because N_* does not appear in the linearized equations (16) and (17). We find in Fig. 6 that the fastest growing mode is almost independent of Bi.

However, the critical Rayleigh number lowers from 658 in the large-Biot (fixed temperature) limit to 390 in the small-Biot (fixed flux) limit. This does not necessarily mean that small-Biot shells are less stable. Indeed, Fig. 2 indicates that if the small Biot number is obtained by reducing the shell thickness H, then the Rayleigh number drops by so much that the shell actually gains stability. Conversely, if the small Biot number is achieved by decreasing the irradiation temperature T_*, then the Rayleigh number remains nearly constant, and a stable shell can become convective.

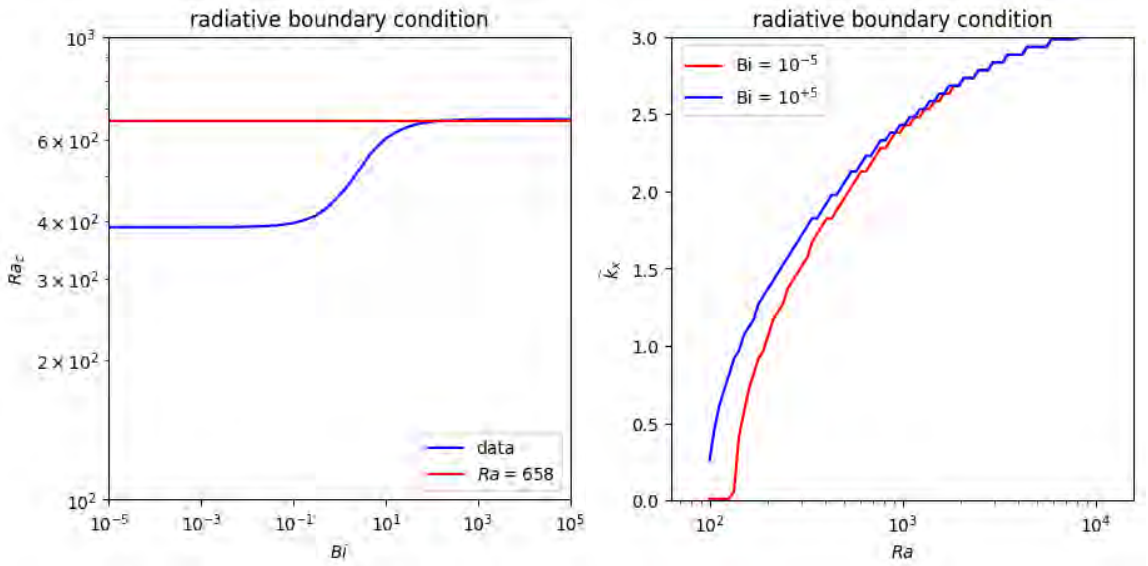

Figure 6: *Left:* Critical Rayleigh number for the onset of convection Ra_c as a function of the Biot number Bi. Ra_c is 40 % higher in the fixed-temperature limit ($\mathrm{Bi} \gg 1$) than the fixed-flux limit ($\mathrm{Bi} \ll 1$). The transition between the two regimes occurs from $\mathrm{Bi} = 10^{-1}$ to $\mathrm{Bi} = 10^2$. Icy moons typically live outside this transition zone ($\mathrm{Bi} > 10^3$, see Fig. 2). *Right:* Horizontal wavenumber $\widetilde{k_x}$of the fastest growing mode as a function of Ra, for two extreme values of Bi. The radiative boundary condition has little impact on this observable.

4.2 Bulk structure observables

The radars on JUICE and Europa clipper may detect the horizontal ice density variations that characterise convection. The goal of the present subsection is to quantify how the radiative boundary condition affects the structure of those convective rolls. It will help interpret the upcoming radar data.

We start with the amplitude of the density perturbations in Fig. 7-*left*. Since $\mathrm{d}\rho = \frac{\langle\rho\rangle}{g}\mathrm{d}b$ and $b = \frac{g\alpha}{\langle\rho\rangle}(T_\mathrm{m} - T_\mathrm{s})\,\widetilde{b}$, we have $\rho_1 = \alpha(T_\mathrm{m} - T_\mathrm{s})\,\widetilde{b}_1$. Therefore, $\widetilde{b}_1$ is a proxy for the density variations, with the added benefits of adimensionality. We find that $\widetilde{b}_1$ is unaffected by N_* but is almost 40% higher in the fixed-flux limit than the fixed-temperature limit. The true density perturbations ρ_1 can gain even more percentage points if the small Biot numbers are achieved by decreasing T_*, because then T_s decreases and $T_\mathrm{m} - T_\mathrm{s}$ increases. That being said, the icy moons of the Solar System live well into the fixed-temperature regime. Using $T_\mathrm{m} = 273K$, $T_\mathrm{s} = 100K$, $\alpha(T_\mathrm{m}) = 6 \times 10^{-5}K^{-1}$, and $\alpha(T_\mathrm{s}) = 10^{-5}K^{-1}$ [66], we predict relative density perturbations of 0.4% in the lower shell and 0.07% near the surface.

We also study the horizontal size $\widetilde{\lambda}$ of the convective cells in Fig. 7-*right*. We find that the cells grow by about 10% from the fixed-temperature regime to the fixed-flux regime. But once again, the icy moons of the Solar System live in the fixed-temperature limit, so using a radiative boundary condition does not lead to significantly better predictions than a Dirichlet boundary condition.

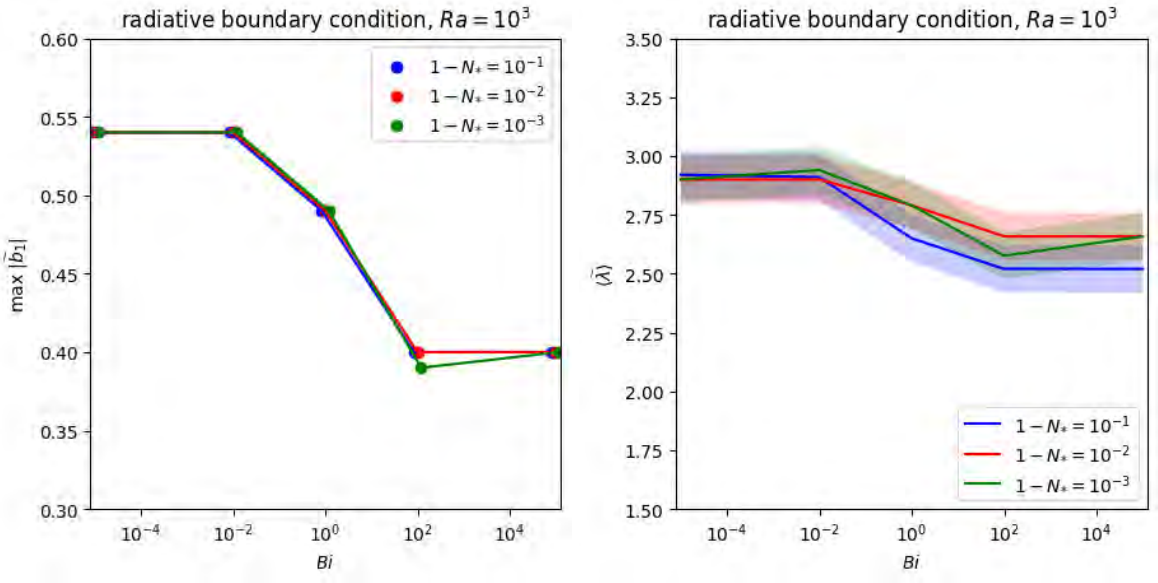

Figure 7: *Left:* Amplitude of the horizontal fluctuations in ice density due to convection, as a function of the Biot number Bi and the irradiation number N_*. We use $\widetilde{b}_1$ as a proxy for the density perturbation because $\rho_1 = \alpha(T_\mathrm{m} - T_\mathrm{s})\,\widetilde{b}_1$. If T_s is kept constant, the variations in ice density are $\sim$40% larger in the fixed-flux limit than in the fixed-temperature limit. The transition between the two regimes occur between $\mathrm{Bi} = 10^{-2}$ and $\mathrm{Bi} = 10^2$. *Right:* Mean horizontal size $\widetilde{\lambda}$ of the convective cells as a function of Bi and N_*. Cells are $\sim$10% larger in the fixed-flux limit, and the effect of N_* is not significant.

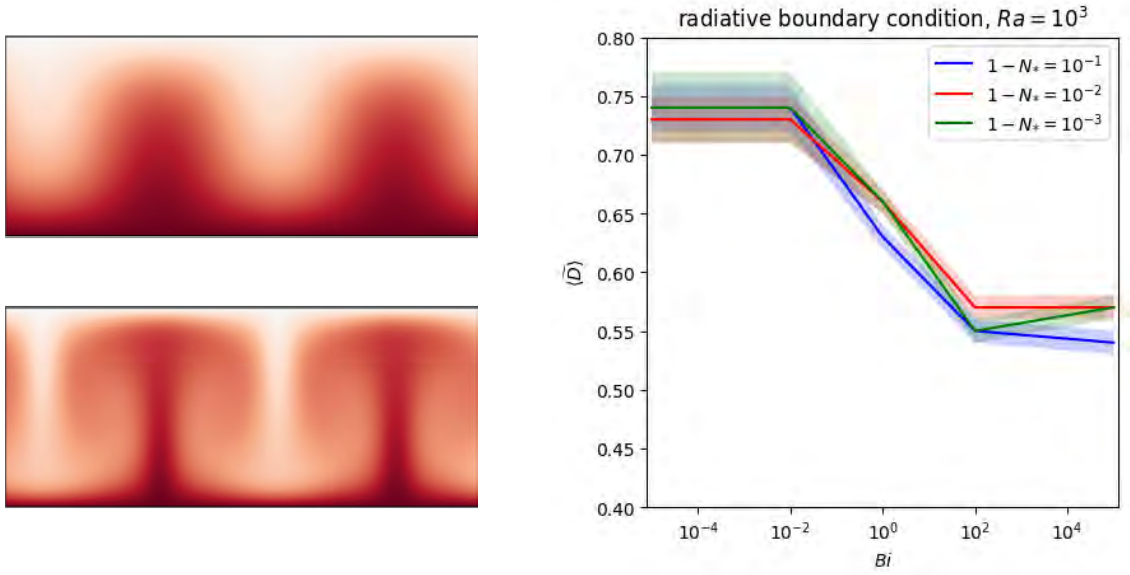

Figure 8: *Left:* Example of diffuse drafts (top) and sharp drafts (bottom). The color scale represents temperature, with red being hot and white being cold. To give a point of reference, the diffuseness parameter of the top shell is $\widetilde{D} = 0.55$, that of the bottom shell is $\widetilde{D} = 0.25$. *Right:* Mean diffusinesss of the convective drafts $\widetilde{D}$ as a function of Bi and N_*. Drafts are more diffuse in the fixed-flux limit, and the effect of N_* is not significant.

Finally, convective cells of similar size can be more or less diffuse, as shown by Fig. 8-*left*. To quantify this, we introduce a diffuseness parameter $\widetilde{D}$. Specifically, we define a convective cell as the region between a zero of $R(\widetilde{x})$ and the second next zero. Within a given cell, we consider

$$T(\widetilde{x}) = \widetilde{b}_1(\widetilde{z} = 0.25) - \int \frac{\mathrm{d}\widetilde{x}}{\mathrm{Ar}} \widetilde{b}_1(\widetilde{z} = 0.25)$$

and define $\widetilde{D}$ as the full width at 75% maximum of that quantity. This definition is by no means perfect, but it is robust enough for our purposes. We find in Fig. 8-*right* that convective drafts are already quite diffuse in the fixed-temperature limit ($\widetilde{D} = 0.55$ is a high value, as shown by Fig. 8-*left*). Yet, they become even more diffuse in the fixed-flux limit, by 25%. The increase in cell size accounts for half of those twenty-five percents, but the other half represent genuine variations of the cell structure with Bi.

4.3 Thermal observables

Convection is a heat transport mechanism, so we can expect it to strongly affect thermal observables. The heat flux from the ocean to the shell is particularly important, because it controls whether the ocean freezes and how quickly. We already know from Fig. 4-*left* that in the fixed-temperature limit, convection increases by 70% the rate of vertical heat transport. In the fixed-flux limit, the vertical heat flux is imposed by the upper boundary condition, so convection cannot affect it. Figure. 9-*left* confirms those predictions, shows that the transition between the two regimes is monotonous, and indicates that the typical Biot number of icy moons, $\mathrm{Bi} = 10^3$, is well inside the fixed-temperature regime.

Finally, remember that the main motivation for the present study is studying surface temperature. We hope that convection has a strong enough effect on this observable that we could detect it in Cassini's spectrometric data. Alas, Figure 9-*right* indicates that the mean difference in surface temperature between a convective shell and a conductive shell is less than 1K, and the order of magnitude remains identical when we consider the maximal difference. Cassini's uncertainties in surface temperature were of order 10K [84], so the signal-to-noise ratio is 0.1. The prospects of recovering the convective signal are bleak.

5 Discussion

The previous section gave a factual account of our numerical experiments. Let us now analyze the meaning of our results (§5.1), and show that they correspond to intuition (§5.2).

Of course, our numerical model overlooks several important physical effects. So, the goal of the present section is also to examine critically the robustness of our results. We shall focus on the two missing effects we believe are most relevant: the temperature-dependence of viscosity (§5.3), and internal heating (§5.4).

5.1 Meaning of our results

First, we found that convection has almost no impact on the surface temperature of icy moons. This implies that we cannot use Cassini's data to detect convection. Indeed, its

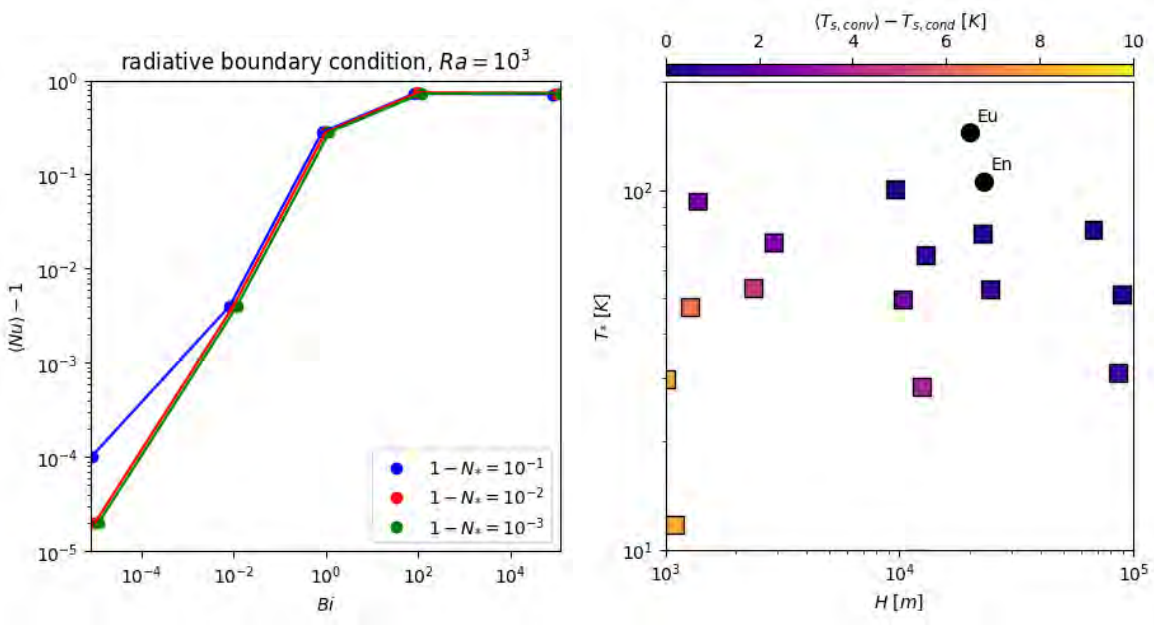

Figure 9: *Left:* Mean Nusselt number at steady state $\langle \mathrm{Nu} \rangle$ as a function of the Biot number Bi and irradiation number N_*. As expected, in the fixed-flux limit, the vertical heat flux is fixed by the boundary conditions. In the fixed-temperature limit, convection accelerates heat transport by a factor 1.7. This regime starts when $\mathrm{Bi} > 10^2$. N_* does not affect heat transport. *Right:* Difference in mean surface temperature between conductive shells and convective shells, as a function of shell thickness H and irradiation temperature T_*. Those simulations were all run with radiative boundary conditions and Rayleigh number $\mathrm{Ra} = 10^3$. The impact of convection on Europa and Enceladus' surface temperature is less than 1K.

signature is drowned by the instrument's noise, and is dwarfed by other uncertainties (over ice conductivity, shell thickness, *etc.*).

Second, we found that the radiative boundary condition has almost no impact on the onset of convection, heat transfert efficiency, or bulk structure. This means that, in order to minimize complexity, future models can safely use a fixed-temperature boundary condition.

5.2 Rationale for our results

The underlying reason for our two results is the same: the transition between the fixed-temperature and fixed-flux regimes occurs between $\mathrm{Bi} = 10^{-2}$ and $\mathrm{Bi} = 10^2$. Since icy moons typically have $\mathrm{Bi} > 10^3$, they are well inside the fixed-temperature regime.

Another, perhaps more intuitive way to phrase this is that the surface layer of icy moons receives much more energy from the Sun than from the lower shell. For instance, on Enceladus the Solar flux is of order $10^1\, W/m^2$, whereas the conductive flux is $\sim 10^{-2}\, W/m^2$. Therefore, even though convection nearly doubles the condutive term of Eq. (5e), this term remains negligible. Consequently, the blackbody term is slaved to the Solar term, and that fixes the temperature.

5.3 Temperature-dependence of viscosity

Even though our equations (8-11) cover the temperature dependence of viscosity, we only present constant-viscosity results in §4. This will need to be improved before publication.

Indeed, the extreme viscosity of ice in the cold upper shell has a leading-order effect on bulk structure (it creates a stagnant lid [79]), and the strong non-linearity of $\nu(T)$ has a leading-order effect on the onset of convection (it makes the transition sub-critical [10, 80]).

We only had time to investigate the effect of a temperature-dependent viscosity on the *linear* onset of convection. We find in Fig. 10 that the effect of the radiative boundary condition, which was already small in §4, becomes minuscule. We suspect this is due to the stagnant lid creating a diffusive buffer between the surface of the shell (where the boundary condition acts) and its lower layers (where convection occurs). If our interpretation is correct, then we expect the effect of the radiative boundary condition on *any* observable to be weaker when viscosity depends on temperature.

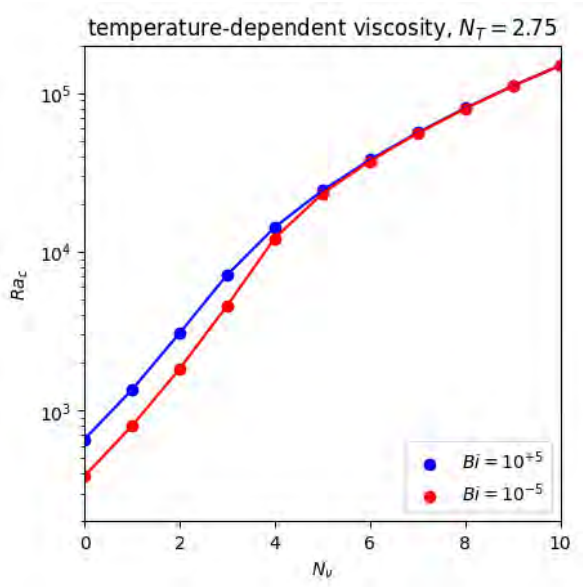

Figure 10: Critical Rayleigh number for the onset of convection Ra_c as a function of the viscosity number N_ν, for two extreme values of the Biot number Bi. When $N_\nu > 5$, the small effect of the radiative boundary condition on the linear onset of convection disappears.

5.4 Internal heating

We said in §5.2 that the radiative boundary condition (5e) has little effect because the conductive term is tiny compared to the Solar term. In our current model, the conductive term directly reflects the transfer of energy from the ocean to the shell. But in reality, the shell has access to another source of energy: internal heating.

The dominant source of internal heat is tidal friction, although shear friction and radioactive decay also play a role. If we combine figures 2 and 3 of [87], we find that tidal heating could amplify the conductive flux at the surface from $10^{-2}\,W/m^2$ to $10^{-1}\,W/m^2$.

This value remains small compared to the Solar flux ($10^1\,W/m^2$), so internal heating should not be sufficient to drive the shell out of the fixed-temperature regime. Therefore, we believe that our conclusions on surface temperature and the futility of a radiative boundary condition will remain valid in the presence of internal heating.

6 Conclusion

In this report, we present simulations of Rayleigh-Benard convection in the Stokes regime and with a radiative boundary condition. Our goal was to investigate the impact of solid-state convection on the surface temperature of icy moons.

Our logic was that convection is a heat transport process. As such, it should bring warm material close to the surface, thereby increasing the mean surface temperature and creating temperature anomalies above updrafts. If those effects are strong enough, we could use the surface temperature data from Cassini's composite infraRed spectrometer (CIRS) to detect convection (or eliminate the possibility of it).

A dataset making a convincing case for or against convection would be extremely valuable. Indeed, by regulating heat transport, convection controls the life expectancy of a possible ocean before complete freezing. Additionally, by regulating the delivery of oxidants, convection controls the maximum biomass that the ocean could support.

Alas, we find that solid-state convection in the ice shell has very little impact on the surface temperature of icy moons. The signal is at most 1K, small compared to CIRS' 10K noise level. Therefore, we conclude that surface temperature measurements will not help answer the convection question.

We were also wondering what effect the radiative boundary condition has on other observables. Specifically, we focused on the onset of convection, the rate of heat transport, and bulk structure. Once again, we find all effects to be tiny. Therefore, we conclude that the radiative boundary condition is futile: a fixed-temperature boundary condition is simpler, and precise enough for any practical purpose. This should marginally simplify the analysis of JUICE and Europa Clipper's data.

Our models ignore many physical effects. Our simulations are 2D; the geometry is Cartesian instead of spherical; the ice shell cannot deform, melt, or fracture; there is no Equator-to-pole mean flow like on Europa and Enceladus [7, 42]; *etc.* We think that the most important missing effects are the temperature dependence of viscosity and internal heating. But as discussed in §5.3 and 5.4, we expect that the former will strengthen our conclusions, and that the latter will be too weak to affect our findings.

Of course, at the moment, those claims lack credibility. Before submitting our results to a journal, we will run new simulations and verify that internal heating and the temperature dependence of viscosity do not overturn our conclusions.

7 Acknowledgements

I wish to thank my advisors C. Meyer, K. Burns and G. Chini for their invaluable help at every stage of the project. I also express my gratitude to D. Lecoanet for his help with my Dedalus scripts and for the pizzas, to this summer's directors T. Shaw and P. Garaud for the excellence of their program, to J. Fields and J. Hildebrandt and many other WHOI staff for welcoming us and making everything run smoothly, and to my fellow fellows for accomodating my incompetent swimming and generally making the summer lovely.

A The linear onset of Rayleigh-Benard convection

In §3.5.1 we made some statements about the onset of 2D Rayleigh-Benard convection with stress-free and fixed-temperature boundary conditions. Let us now justify those statements.

We decompose each variable f into a background term f_0 and a perturbation term f_1. We will take the conductive shell structure as our background. This leads to the linear perturbation equations of Rayleigh-Benard convection,

$$\widetilde{\nabla} \cdot \widetilde{\boldsymbol{u}} = 0, \tag{21a}$$

$$0 = -\widetilde{\nabla}\widetilde{h}_1 + \mathrm{Ra}\,\widetilde{b}_1\,\boldsymbol{e}_z + \widetilde{\nabla}^2\widetilde{\boldsymbol{u}}_1, \tag{21b}$$

$$\partial_{\widetilde{t}}\widetilde{b}_1 - \widetilde{u}_{1,z} = \widetilde{\nabla}^2\widetilde{b}_1. \tag{21c}$$

We still have periodic boundary conditions on the sides of the box, so we can decompose any solution in Fourier modes of the form $f_1(\widetilde{x},\widetilde{t}) = \hat{f}_1(\widetilde{z})\,\mathrm{e}^{i\,(\widetilde{k}_x\widetilde{x}-\widetilde{\omega}\widetilde{t})}$, where $\widetilde{k}_x$ is a horizontal and adimensionalised wavevector. Equations (21) become

$$\begin{aligned}
i\,\widetilde{k}_x\widehat{u}_{1,x} + \mathrm{d}_{\widetilde{z}}\widehat{u}_{1,z} &= 0,\\
0 &= -i\,\widetilde{k}_x\,\widehat{h}_1 - \widetilde{k}_x^2\,\widehat{u}_{1,x} + \mathrm{d}^2_{\widetilde{z}\widetilde{z}}\widehat{u}_{1,x},\\
0 &= -\mathrm{d}_{\widetilde{z}}\,\widehat{h}_1 + \mathrm{Ra}\,\widehat{b}_1 - \widetilde{k}_x^2\,\widehat{u}_{1,z} + \mathrm{d}^2_{\widetilde{z}\widetilde{z}}\widehat{u}_{1,z},\\
-i\,\widetilde{\omega}\,\widehat{b}_1 - \widehat{u}_{1,z} &= -\widetilde{k}_x^2\,\widehat{b}_1 + \mathrm{d}^2_{\widetilde{z}\widetilde{z}}\widehat{b}_1,
\end{aligned}$$

which, after four lines of linear algebra, combine to

$$\left[\left\{\widetilde{k}_x^2 - \mathrm{d}^2_{\widetilde{z}\widetilde{z}} - i\widetilde{\omega}\right\} \times \frac{\left\{\widetilde{k}_x^2 - \mathrm{d}^2_{\widetilde{z}\widetilde{z}}\right\}^2}{\mathrm{Ra}\,\widetilde{k}_x^2} - 1\right] \widehat{u}_{1,z} = 0. \tag{23}$$

This is a 6^{th}-order, linear ordinary differential equation (ODE) with constant coefficients. As such, if the characteristic polynomial has distinct roots, the general solution is

$$\widehat{u}_{1,z}(\widetilde{z}) = \sum_{i=1}^{6} C_i\,\mathrm{e}^{i\,\widetilde{k}_{z,i}\,\widetilde{z}},$$

where the C_i are integration constants and the $\widetilde{k}_{z,i}$ are the natural vertical wavenumbers of the system. And if we consider only the non-travelling modes, for which $\widetilde{\omega}$ is real, then the ODE has only real coefficients, so the general solution simplifies to

$$\widehat{u}_{1,z}(\widetilde{z}) = \sum_{i=1}^{3} A_i\,\cos\left(i\,\widetilde{k}_{z,i}\,\widetilde{z}\right) + B_i \sin\left(i\,\widetilde{k}_{z,i}\,\widetilde{z}\right).$$

Now we need to meet the (linearized) boundary conditions. They become, after the Fourier decomposition and a few algebraic simplifications,

$$\widehat{u}_{1,z}(\widetilde{z} = 0 \text{ or } 1) = 0, \tag{24a}$$

$$\widehat{u}^{(2)}_{1,z}(\widetilde{z} = 0 \text{ or } 1) = 0, \tag{24b}$$

$$\widehat{u}^{(4)}_{1,z}(\widetilde{z} = 0 \text{ or } 1) = 0. \tag{24c}$$

If we inject the (real) general solution into those boundary conditions, we obtain the linear problem

$$\left(\begin{array}{ccc:ccc} 1 & 1 & 1 & 0 & 0 & 0 \\ \widetilde{k}_{z,1}^2 & \widetilde{k}_{z,2}^2 & \widetilde{k}_{z,3}^2 & 0 & 0 & 0 \\ \widetilde{k}_{z,1}^4 & \widetilde{k}_{z,2}^4 & \widetilde{k}_{z,3}^4 & 0 & 0 & 0 \\ \hdashline m_{1,1} & m_{1,2} & m_{1,3} & 1 & 1 & 1 \\ m_{2,1} & m_{2,2} & m_{2,3} & \widetilde{k}_{z,1}^2 & \widetilde{k}_{z,2}^2 & \widetilde{k}_{z,3}^2 \\ m_{3,1} & m_{3,2} & m_{3,3} & \widetilde{k}_{z,1}^4 & \widetilde{k}_{z,2}^4 & \widetilde{k}_{z,3}^4 \end{array}\right) \left(\begin{array}{c} A_1 \\ A_2 \\ A_3 \\ \sin(\widetilde{k}_{z,1})B_1 \\ \sin(\widetilde{k}_{z,2})B_2 \\ \sin(\widetilde{k}_{z,3})B_3 \end{array}\right) = \mathbf{0},$$

where the $m_{i,j}$ coefficients are irrelevant. Indeed, the matrix is lower triangular, with both diagonal blocks being Vandermonde matrices. Since we assumed that the vertical wavenumbers are all different, the matrix must be invertible. As such, the only non-trivial solutions appear when one of the $\widetilde{k}_{z,i} = n\pi,\ n \in \mathbb{Z}^*$.

Consequently, we decompose any solution to Eqs. (21) into full Fourier modes of the form $f_1(\widetilde{\mathbf{x}}, \widetilde{t}) = \hat{f}_1 \sin(n\pi\widetilde{z})\, \mathrm{e}^{i(\widetilde{k}_x\widetilde{x} - \widetilde{\omega}\widetilde{t})}$. This automatically verifies the boundary conditions, and Eq. (23) becomes

$$\left[\left\{\widetilde{k}_x^2 + (n\pi)^2 - i\widetilde{\omega}\right\} \times \frac{\left\{\widetilde{k}_x^2 + (n\pi)^2\right\}^2}{\mathrm{Ra}\,\widetilde{k}_x^2} - 1\right] \widehat{u}_{1,z} = 0,$$

which leads to the dispersion relation

$$\widetilde{\omega} = -i\left[\widetilde{k}_x^2 + (n\pi)^2 - \frac{\mathrm{Ra}\,\widetilde{k}_x^2}{\left\{\widetilde{k}_x^2 + (n\pi)^2\right\}^2}\right]. \tag{25}$$

This shows an instability if $\mathrm{Im}(\widetilde{\omega}) > 0$, *i.e.* if

$$\mathrm{Ra} > \frac{\left\{\widetilde{k}_x^2 + (n\pi)^2\right\}^3}{\widetilde{k}_x^2} \geq \frac{27}{4}\pi^4$$

From Eq. (25) we also get the wave-numbers of the fastest growing mode as a function of Ra. This involves solving a cubic equation, but eventually we get

$$\widetilde{k}_x^2 = \frac{\sqrt[3]{\sqrt{729\,\mathrm{Ra}^4\pi^4 + 27\,\mathrm{Ra}^3} + 27\,\mathrm{Ra}\,\pi^2}}{3} - \frac{\mathrm{Ra}}{\sqrt[3]{\sqrt{729\,\mathrm{Ra}^4\pi^4 + 27\,\mathrm{Ra}^3} + 27\,\mathrm{Ra}\,\pi^2}} - \pi^2.$$

References

[1] D. Allu Peddinti and A. K. McNamara, *Material transport accros Europa's shell*, Geophysical Research Letters, 42 (2015), pp. 4288–4293.

[2] J. D. Anderson, R. A. Jacobson, T. P. McElrath, W. B. Moore, G. Schubert, and P. C. Thomas, *Shape, Mean Radius, Gravity Field, and Interior Structure of Callisto*, Icarus, 153 (2001), pp. 157–161.

[3] J. D. Anderson, E. L. Lau, W. L. Sjogren, G. Schubert, and W. B. Moore, *Gravitational constraints on the internal structure of Ganymede*, Nature, 384 (1996), pp. 541–543.

[4] J. D. Anderson, G. Schubert, R. A. Jacobson, E. L. Lau, W. B. Moore, and W. L. Sjogren, *Europa's Differentiated Internal Structure: Inferences from Four Galileo Encounters*, Science, 281 (1998), p. 2019.

[5] W. E. Arnoldi, *The principle of minimized iterations in the solution of the matrix eigenvalue problem*, Quarterly of Applied Mathematics, 9 (1951), pp. 17–29.

[6] U. M. Ascher, S. J. Ruuth, and R. J. Spiteri, *Implicit-explicit runge-kutta methods for time-dependent partial differential equations*, Applied Numerical Mathematics, 25 (1997), pp. 151–167. Special Issue on Time Integration.

[7] Y. Ashkenazy, R. Sayag, and E. Tziperman, *Dynamics of the global meridional ice flow of Europa's icy shell*, Nature Astronomy, 2 (2018), pp. 43–49.

[8] H. Barnes, J. Hutton, and K. Walters, *Chapter 1 - introduction*, in An Introduction to Rheology, vol. 3 of Rheology Series, Elsevier, 1989, pp. 1–10.

[9] A. C. Barr and R. T. Pappalardo, *Onset of convection in the icy Galilean satellites: Influence of rheology*, Journal of Geophysical Research (Planets), 110 (2005), p. E12005.

[10] A. C. Barr, R. T. Pappalardo, and S. Zhong, *Convective instability in ice I with non-Newtonian rheology: Application to the icy Galilean satellites*, Journal of Geophysical Research (Planets), 109 (2004), p. E12008.

[11] C. Béghin, O. Randriamboarison, M. Hamelin, E. Karkoschka, C. Sotin, R. C. Whitten, J.-J. Berthelier, R. Grard, and F. Simões, *Analytic theory of Titan's Schumann resonance: Constraints on ionospheric conductivity and buried water ocean*, Icarus, 218 (2012), pp. 1028–1042.

[12] G. K. Bhatia and S. Sahijpal, *Thermal evolution of trans-Neptunian objects, icy satellites, and minor icy planets in the early solar system*, Meteoritics and Planetary Science, 52 (2017), pp. 2470–2490.

[13] B. G. Bills and F. Nimmo, *Forced obliquity and moments of inertia of Titan*, Icarus, 196 (2008), pp. 293–297.

[14] ——, *Rotational dynamics and internal structure of Titan*, Icarus, 214 (2011), pp. 351–355.

[15] L. J. Bonales, A. C. Rodriguez, and P. D. Sanz, *Thermal conductivity of ice prepared under different conditions*, International Journal of Food Properties, 20:sup1 (2017), p. 610–619.

[16] K. J. Burns, G. M. Vasil, J. S. Oishi, D. Lecoanet, and B. P. Brown, *Dedalus: A flexible framework for numerical simulations with spectral methods*, Physical Review Research, 2 (2020), p. 023068.

[17] F. H. Busse and N. Riahi, *Nonlinear convection in a layer with nearly insulating boundaries*, Journal of Fluid Mechanics, 96 (1980), p. 243.

[18] R. W. Carlson, *A Tenuous Carbon Dioxide Atmosphere on Jupiter's Moon Callisto*, Science, 283 (1999), p. 820.

[19] E. Carnahan, N. S. Wolfenbarger, J. S. Jordan, and M. A. Hesse, *New insights into temperature-dependent ice properties and their effect on ice shell convection for icy ocean worlds*, Earth and Planetary Science Letters, 563 (2021), p. 116886.

[20] M. H. Carr, M. J. S. Belton, C. R. Chapman, M. E. Davies, P. Geissler, R. Greenberg, A. S. McEwen, B. R. Tufts, R. Greeley, R. Sullivan, J. W. Head, R. T. Pappalardo, K. P. Klaasen, T. V. Johnson, J. Kaufman, D. Senske, J. Moore, G. Neukum, G. Schubert, J. A. Burns, P. Thomas, and J. Veverka, *Evidence for a subsurface ocean on Europa*, Nature, 391 (1998), pp. 363–365.

[21] C. J. Chapman and M. R. E. Proctor, *Nonlinear Rayleigh-Benard convection between poorly conducting boundaries*, Journal of Fluid Mechanics, 101 (1980), pp. 759–782.

[22] T. T. Clarté, N. Schaeffer, S. Labrosse, and J. Vidal, *The effects of a Robin boundary condition on thermal convection in a rotating spherical shell*, Journal of Fluid Mechanics, 918 (2021), p. A36.

[23] G. Collins and T. V. Johnson, *Chapter 37 - ganymede and callisto*, in Encyclopedia of the Solar System (Third Edition), T. Spohn, D. Breuer, and T. V. Johnson, eds., Elsevier, Boston, third edition ed., 2014, pp. 813–829.

[24] J. Comas Solá, *Observations des satellites principaux de Jupiter et de Titan*, Astronomische Nachrichten, 179 (1908), p. 289.

[25] J. G. F. Francis, *The QR Transformation A Unitary Analogue to the LR Transformation—Part 1*, The Computer Journal, 4 (1961), pp. 265–271.

[26] ——, *The QR Transformation—Part 2*, The Computer Journal, 4 (1962), pp. 332–345.

[27] D. L. Goldsby and D. L. Kohlstedt, *Superplastic deformation of ice: Experimental observations*, Journal of Geophysical Research, 106 (2001), pp. 11,017–11,030.

[28] J. C. Goodman, G. C. Collins, J. Marshall, and R. T. Pierrehumbert, *Hydrothermal plume dynamics on Europa: Implications for chaos formation*, Journal of Geophysical Research (Planets), 109 (2004), p. E03008.

[29] O. Grasset, M. K. Dougherty, A. Coustenis, E. J. Bunce, C. Erd, D. Titov, M. Blanc, A. Coates, P. Drossart, L. N. Fletcher, H. Hussmann, R. Jaumann, N. Krupp, J. P. Lebreton, O. Prieto-Ballesteros, P. Tortora, F. Tosi, and T. Van Hoolst, *JUpiter ICy moons Explorer (JUICE): An ESA mission to orbit Ganymede and to characterise the Jupiter system*, Planetary and Space Science, 78 (2013), pp. 1–21.

[30] R. Greenberg, G. V. Hoppa, B. R. Tufts, P. Geissler, J. Riley, and S. Kadel, *Chaos on Europa*, Icarus, 141 (1999), pp. 263–286.

[31] D. T. Hall, P. D. Feldman, M. A. McGrath, and D. F. Strobel, *The Far-Ultraviolet Oxygen Airglow of Europa and Ganymede*, The Astrophysical Journal, 499 (1998), pp. 475–481.

[32] D. T. Hall, D. F. Strobel, P. D. Feldman, M. A. McGrath, and H. A. Weaver, *Detection of an oxygen atmosphere on Jupiter's moon Europa*, Nature, 373 (1995), pp. 677–679.

[33] K. P. Hand, R. W. Carlson, and C. F. Chyba, *Energy, Chemical Disequilibrium, and Geological Constraints on Europa*, Astrobiology, 7 (2007), pp. 1006–1022.

[34] C. J. Hansen, J. Castillo-Rogez, W. Grundy, J. D. Hofgartner, E. S. Martin, K. Mitchell, F. Nimmo, T. A. Nordheim, C. Paty, L. C. Quick, J. H. Roberts, K. Runyon, P. Schenk, A. Stern, and O. Umurhan, *Triton: Fascinating Moon, Likely Ocean World, Compelling Destination!*, The Planetary Science Journal, 2 (2021), p. 137.

[35] L. Harel, C. Dumoulin, G. Choblet, G. Tobie, and J. Besserer, *Scaling of heat transfer in stagnant lid convection for the outer shell of icy moons: Influence of rheology*, Icarus, 338 (2020), p. 113448.

[36] B. J. Hepworth, *Nonlinear two-dimensional Rayleigh-B´enard convection*, PhD thesis, University fo Leeds, 2014.

[37] S. M. Hörst, *Titan's atmosphere and climate*, Journal of Geophysical Research (Planets), 122 (2017), pp. 432–482.

[38] S. M. Howell and R. T. Pappalardo, *NASA's Europa Clipper—a mission to a potentially habitable ocean world*, Nature Communications, 11 (2020), p. 1311.

[39] L. Iess, R. A. Jacobson, M. Ducci, D. J. Stevenson, J. I. Lunine, J. W. Armstrong, S. W. Asmar, P. Racioppa, N. J. Rappaport, and P. Tortora, *The Tides of Titan*, Science, 337 (2012), p. 457.

[40] L. Iess, D. J. Stevenson, M. Parisi, D. Hemingway, R. A. Jacobson, J. I. Lunine, F. Nimmo, J. W. Armstrong, S. W. Asmar, M. Ducci, and P. Tortora, *The Gravity Field and Interior Structure of Enceladus*, Science, 344 (2014), pp. 78–80.

[41] K. Kalousová, D. M. Schroeder, and K. M. Soderlund, *Radar attenuation in Europa's ice shell: Obstacles and opportunities for constraining the shell thickness and its thermal structure*, Journal of Geophysical Research (Planets), 122 (2017), pp. 524–545.

[42] W. Kang, *Different Ice-shell Geometries on Europa and Enceladus due to Their Different Sizes: Impacts of Ocean Heat Transport*, The Astrophysical Journal, 934 (2022), p. 116.

[43] K. K. Khurana, M. G. Kivelson, D. J. Stevenson, G. Schubert, C. T. Russell, R. J. Walker, and C. Polanskey, *Induced magnetic fields as evidence for subsurface oceans in Europa and Callisto*, Nature, 395 (1998), pp. 777–780.

[44] M. G. Kivelson, K. K. Khurana, C. T. Russell, M. Volwerk, R. J. Walker, and C. Zimmer, *Galileo Magnetometer Measurements: A Stronger Case for a Subsurface Ocean at Europa*, Science, 289 (2000), pp. 1340–1343.

[45] M. G. Kivelson, K. K. Khurana, D. J. Stevenson, L. Bennett, S. Joy, C. T. Russell, R. J. Walker, C. Zimmer, and C. Polanskey, *Europa and Callisto: Induced or intrinsic fields in a periodically varying plasma environment*, Journal of Geophysical Research, 104 (1999), pp. 4609–4626.

[46] M. G. Kivelson, K. K. Khurana, and M. Volwerk, *The Permanent and Inductive Magnetic Moments of Ganymede*, Icarus, 157 (2002), pp. 507–522.

[47] J. Klinger, *Low-temperature heat conduction in pure, monocrystalline ice*, Journal of Glaciology, 14 (1975), p. 517–528.

[48] V. Kublanovskaya, *On some algorithms for the solution of the complete eigenvalue problem*, USSR Computational Mathematics and Mathematical Physics, 1 (1962), pp. 637–657.

[49] T. Käufer, P. P. Vieweg, J. Schumacher, and C. Cierpka, *Thermal boundary condition studies in large aspect ratio rayleigh–bénard convection*, European Journal of Mechanics - B/Fluids, 101 (2023), pp. 283–293.

[50] C. Lanczos, *Trigonometric interpolation of empirical and analytical functions*, Journal of Mathematics and Physics, 17 (1938), p. 123 – 199.

[51] J. S. Lewis, *Satellites of the Outer Planets: Thermal Models*, Science, 172 (1971), pp. 1127–1128.

[52] Lord Rayleigh, *On convection currents in a horizontal layer of fluid, when the higher temperature is on the under side*, The London, Edinburgh, and Dublin Philosophical Magazine and Journal of Science, 32 (1916), pp. 529–546.

[53] T. B. McCord, R. Carlson, W. Smythe, G. Hansen, R. Clark, C. Hibbitts, F. Fanale, J. Granahan, M. Segura, D. Matson, T. Johnson, and P. Martin, *Organics and other molecules in the surfaces of Callisto and Ganymede*, Science, 278 (1997), pp. 271–275.

[54] T. B. McCord, G. B. Hansen, R. N. Clark, P. D. Martin, C. A. Hibbitts, F. P. Fanale, J. C. Granahan, M. Segura, D. L. Matson, T. V. Johnson, R. W. Carlson, W. D. Smythe, and G. E. Danielson, *Non-water-ice constituents in the surface material of the icy Galilean satellites from the Galileo near-infrared mapping spectrometer investigation*, Journal of Geophysical Research, 103 (1998), pp. 8603–8626.

[55] W. B. McKinnon, *Effect of Enceladus's rapid synchronous spin on interpretation of Cassini gravity*, Geophysical Research Letters, 42 (2015), pp. 2137–2143.

[56] W. B. McKinnon and R. L. Kirk, *Chapter 40 - triton*, in Encyclopedia of the Solar System (Third Edition), T. Spohn, D. Breuer, and T. V. Johnson, eds., Elsevier, Boston, third edition ed., 2014, pp. 861–881.

[57] R. Millan, J. Mouginot, A. Rabatel, and M. Morlighem, *Ice velocity and thickness of the world's glaciers*, Nature Geoscience, 15 (2022), pp. 124–129.

[58] F. Nimmo and M. Manga, *Causes, characteristics and consequences of convective diapirism on Europa*, Geophysical Research Letters, 29 (2002), p. 2109.

[59] F. Nimmo and R. T. Pappalardo, *Diapir-induced reorientation of Saturn's moon Enceladus*, Nature, 441 (2006), pp. 614–616.

[60] F. Nimmo and R. T. Pappalardo, *Ocean worlds in the outer solar system*, Journal of Geophysical Research (Planets), 121 (2016), pp. 1378–1399.

[61] S. Olver and A. Townsend, *A fast andwell-conditioned spectral method*, SIAM Review, 55 (2013), p. 462 – 489.

[62] C. O'Neill and F. Nimmo, *The role of episodic overturn in generating the surface geology and heat flow on Enceladus*, Nature Geoscience, 3 (2010), pp. 88–91.

[63] A. Pandey, J. D. Scheel, and J. Schumacher, *Turbulent superstructures in Rayleigh-Bénard convection*, Nature Communications, 9 (2018), p. 2118.

[64] R. T. Pappalardo, J. W. Head, R. Greeley, R. J. Sullivan, C. Pilcher, G. Schubert, W. B. Moore, M. H. Carr, J. M. Moore, M. J. S. Belton, and D. L. Goldsby, *Geological evidence for solid-state convection in Europa's ice shell*, Nature, 391 (1998), pp. 365–368.

[65] A. T. Patera, *A spectral element method for fluid dynamics: Laminar flow in a channel expansion*, Journal of Computational Physics, 54 (1984), pp. 468–488.

[66] V. F. Petrenko and R. W. Whitworth, *Chapter 3 - Elastic, thermal, and lattice dynamical properties*, in Physics of Ice, Oxford University Press, 01 2002.

[67] C. B. Phillips and R. T. Pappalardo, *Europa Clipper Mission Concept: Exploring Jupiter's Ocean Moon*, EOS Transactions, 95 (2014), pp. 165–167.

[68] J.-P. Poirier, *Creep of Crystals: High-Temperature Deformation Processes in Metals, Ceramics and Minerals*, Cambridge Earth Science Series, Cambridge University Press, 1985.

[69] C. C. Porco, P. Helfenstein, P. C. Thomas, A. P. Ingersoll, J. Wisdom, R. West, G. Neukum, T. Denk, R. Wagner, T. Roatsch, S. Kieffer, E. Turtle, A. McEwen, T. V. Johnson, J. Rathbun, J. Veverka, D. Wilson, J. Perry, J. Spitale, A. Brahic, J. A. Burns, A. D. Del Genio, L. Dones, C. D. Murray, and S. Squyres, *Cassini Observes the Active South Pole of Enceladus*, Science, 311 (2006), pp. 1393–1401.

[70] F. Postberg, S. Kempf, J. Schmidt, N. Brilliantov, A. Beinsen, B. Abel, U. Buck, and R. Srama, *Sodium salts in E-ring ice grains from an ocean below the surface of Enceladus*, Nature, 459 (2009), pp. 1098–1101.

[71] L. M. Prockter, J. W. Head, R. T. Pappalardo, R. J. Sullivan, A. E. Clifton, B. Giese, R. Wagner, and G. Neukum, *Morphology of Europan bands at high resolution: A mid-ocean ridge-type rift mechanism*, Journal of Geophysical Research (Planets), 107 (2002), p. 5028.

[72] L. M. Prockter and R. T. Pappalardo, *Chapter 36 - europa*, in Encyclopedia of the Solar System (Third Edition), T. Spohn, D. Breuer, and T. V. Johnson, eds., Elsevier, Boston, third edition ed., 2014, pp. 793–811.

[73] J. A. Rathbun, N. J. Rodriguez, and J. R. Spencer, *Galileo PPR observations of Europa: Hotspot detection limits and surface thermal properties*, Icarus, 210 (2010), pp. 763–769.

[74] R. T. Reynolds and P. M. Cassen, *On the internal structure of the major satellites of the outer planets*, Geophysical Research Letters, 6 (1979), pp. 121–124.

[75] L. Roth, J. Saur, K. D. Retherford, D. F. Strobel, P. D. Feldman, M. A. McGrath, and F. Nimmo, *Transient Water Vapor at Europa's South Pole*, Science, 343 (2014), pp. 171–174.

[76] N. C. Shibley and J. Goodman, *Europa's coupled ice-ocean system: Temporal evolution of a pure ice shell*, Icarus, 410 (2024), p. 115872.

[77] A. P. Showman and L. Han, *Effects of plasticity on convection in an ice shell: Implications for europa*, Icarus, 177 (2005), pp. 425–437. Europa Icy Shell.

[78] A. P. Showman and R. Malhotra, *The Galilean satellites.*, Science, 296 (1999), pp. 77–84.

[79] V. S. Solomatov, *Scaling of temperature- and stress-dependent viscosity convection*, Physics of Fluids, 7 (1995), pp. 266–274.

[80] V. S. Solomatov and A. C. Barr, *Onset of convection in fluids with strongly temperature-dependent, power-law viscosity*, Physics of the Earth and Planetary Interiors, 155 (2006), pp. 140–145.

[81] C. Sotin and G. Tobie, *Internal structure and dynamics of the large icy satellites*, Comptes Rendus Physique, 5 (2004), pp. 769–780.

[82] W. B. Sparks, K. P. Hand, M. A. McGrath, E. Bergeron, M. Cracraft, and S. E. Deustua, *Probing for Evidence of Plumes on Europa with HST/STIS*, The Astrophysical Journal, 829 (2016), p. 121.

[83] E. M. Sparrow, R. J. Goldstein, and V. K. Jonsson, *Thermal instability in a horizontal fluid layer: effect of boundary conditions and non-linear temperature profile*, Journal of Fluid Mechanics, 18 (1964), pp. 513–528.

[84] J. R. Spencer, J. C. Pearl, M. Segura, F. M. Flasar, A. Mamoutkine, P. Romani, B. J. Buratti, A. R. Hendrix, L. J. Spilker, and R. M. C. Lopes, *Cassini Encounters Enceladus: Background and the Discovery of a South Polar Hot Spot*, Science, 311 (2006), pp. 1401–1405.

[85] J. R. Spencer, L. K. Tamppari, T. Z. Martin, and L. D. Travis, *Temperatures on Europa from Galileo Photopolarimeter-Radiometer: Nighttime Thermal Anomalies*, Science, 284 (1999), p. 1514.

[86] P. C. Thomas, R. Tajeddine, M. S. Tiscareno, J. A. Burns, J. Joseph, T. J. Loredo, P. Helfenstein, and C. Porco, *Enceladus's measured physical libration requires a global subsurface ocean*, Icarus, 264 (2016), pp. 37–47.

[87] G. Tobie, G. Choblet, and C. Sotin, *Tidally heated convection: Constraints on Europa's ice shell thickness*, Journal of Geophysical Research (Planets), 108 (2003), p. 5124.

[88] D. L. Turcotte, *Chapter13 - Is mantle convection chaotic?*, Cambridge University Press, 1997, p. 269–278.

[89] C. Zimmer, K. K. Khurana, and M. G. Kivelson, *Subsurface Oceans on Europa and Callisto: Constraints from Galileo Magnetometer Observations*, Icarus, 147 (2000), pp. 329–347.

Chemical Transport by Waves in Stars

Yifeng Mao

July 28, 2024

1 Introduction

Chemical transport in stars can be intricately related to the star evolution process. Transport plays a crucial role in the redistribution of elements within a star, affecting its overall evolution and lifecycle. One of the mechanisms driving the chemical transport in stars can be internal gravity waves (IGWs). Internal waves are ubiquitous phenomena observed in planetary atmospheres and oceans. They play a critical role because they transport angular momentum and can contribute to chemical mixing. Cores of main-sequence intermediate- and high-mass stars exhibit convective behavior, which is responsible for the excitation of IGWs [1, 2, 3, 4]. These waves are believed to be involved in physical processes including stellar rotation, chemical mixing, and magnetism.

Main-sequence intermediate and high-mass stars feature a radiative envelope that provides a supportive environment for the propagation of IGWs [5]. To better understand these environments, we must consider the properties of the radiative zones in stars. Figure 71 in the review paper by Jermyn, et al. (2022), predicts the Prandtl number (Pr) for main-sequence stellar models, revealing that the Prandtl number is very small for these stars [6]. This indicates that chemical diffusivity D is much smaller than radiative diffusivity κ with an order of $D/\kappa \sim 10^{-5}$. Low-frequency waves are strongly impacted by radiative effects as they propagate, with radiative diffusivity being of major importance since it is the primary mechanism that damps the waves. Another property of the radiative zone is its low viscosity $\nu \sim D$, which is a relatively minor effect in our problem consideration.

The internal gravity waves in stars are found to be weakly nonlinear. The prediction of amplitude spectra of internal gravity waves from simulations in [5, 7] suggests that the amplitude of internal gravity waves in the radiative zone decays quickly with radius away from the convective core. Nonlinear effects linked to large amplitude IGWs may be relevant just near the boundary of the convective core. Therefore, we do not consider strongly nonlinear waves or wavebreaking in our problem, which is different from the problems in oceans where wavebreaking happens frequently. However, the observation of IGWs excited by turbulent convection in stellar interiors is challenging.

In our project, we are particularly interested in the chemical mixing induced by IGWs in stars. Previous work has explored how fresh hydrogen fuel can be mixed into the core through convective near-boundary mixing [8, 9, 10, 4]. However, a critical question remains: does the mixing in the radiative zone occur solely due to IGWs [11, 12, 13]? Chemical transport in the radiative zone can influence whether chemical elements generated in the nuclear burning region are transported to the surface and whether fuel is brought back to

the burning region, potentially leading to a more massive core. These processes could have significant implications for the evolution and observable properties of the main-sequence intermediate and high-mass stars.

To understand the overall transport processes in stellar interiors, it is crucial to focus on the vertical transport of concentration and consider the horizontal mean of concentration. A stellar structure model is fundamentally a one-dimensional, spherically symmetric representation of a star, aiming to determine the spherically-averaged concentration of various elements. This model typically solves a reaction-diffusion equation of the form:

$$\frac{\partial c}{\partial t} = \frac{1}{r^2}\frac{\partial}{\partial r}\left(r^2 D \frac{\partial c}{\partial r}\right) + R(c),$$

where $R(c)$ represents the reaction term, D denotes the diffusivity, and $c = c(r, t)$ is the concentration as a function of radius and time. The objective is to determine the diffusivity, which generally varies with radius. Given that c is the spherically-averaged concentration, it is essential to ascertain the evolution equation for the spherical average of c.

There have been several previous studies on the amount of chemical mixing by IGWs, though their results have shown considerable variation. Rogers & McElwaine (2017) introduced tracer particles in their 2D simulation to study whether wave mixing can be treated diffusively, showing that diffusion is proportional to the square of the wave amplitude, i.e., $D \propto a^2$ [11]. A follow-up study by Varghese, et al (2022), indicated that the radial diffusion profile depends on the simulation time [12]. When comparing these two studies for the mid-main sequence stars with nominally similar parameters, for example, figure 2 in [11] and figure 7 in [12], the diffusion rates differed by an order of magnitude approximately 10^5. Additionally, Jermyn (2022) conducted a theoretical calculation that retained both thermal and chemical diffusivity D_μ, yielding the result of $D \propto D_\mu^2 a^4$ [13]. This is a different consideration from our problem, which focuses on determining how much transport is caused by radiative diffusion only.

In the following report, we will first discuss the problem setup and provide a brief review of the IGW solutions within the framework of the Boussinesq approximation. Section 2 will describe our methods, including the quasilinear decomposition of chemical transport, the Lagrangian framework, and the simulation setup. Section 3 will present the theoretical results of chemical transport by IGWs using multiscale asymptotic analysis. Transport is quantified as a diffusive equation. Section 4 will present the simulation results of transport and compare these findings with our asymptotic predictions. Finally, Section 5 will discuss the implications of our results and directions for future research.

Problem setup

We consider a 2D model with a passive tracer field in a non-rotating, stratified medium within a uniform gravitational field $-g\mathbf{e_z}$. In the linearized Boussinesq approximation when the fluid buoyancy is subject to a small variation $b = b_0 + b'$ and pressure is also perturbed

as $p = p_0 + p'$, we obtain the following normalized system

$$\frac{\partial \mathbf{u}}{\partial t} + \nabla p - b\mathbf{e}_z = -\mathbf{u} \cdot \nabla \mathbf{u}, \tag{1a}$$

$$\frac{\partial b}{\partial t} - \kappa \nabla^2 b + N^2 w = -\mathbf{u} \cdot \nabla b, \tag{1b}$$

$$\nabla \cdot \mathbf{u} = 0, \tag{1c}$$

where the prime notation is dropped for simplicity, $\mathbf{u} = (u, v)$ is the velocity field, p is the pressure perturbation, b is the buoyancy, κ is the radiative diffusivity, and $N^2 = db/dz$ is the buoyancy frequency. The transport equation for chemical concentration c is given by

$$\frac{\partial c}{\partial t} + \mathbf{u} \cdot \nabla c = 0, \quad c(\mathbf{x}, t = 0) = c_0, \tag{2}$$

which describes the evolution of the chemical concentration over time due to advection by the fluid flow, without considering chemical diffusivity.

Background of IGWs

To understand the behavior of internal gravity waves (IGWs) in such environments [14, 15, 16, 17], we start with the case of $\kappa = 0$ and neglect the nonlinear terms on the right hand side of the linearized Boussinesq approximation (1). In this case, the solutions are

$$\mathbf{u} = \mathbf{u}' \exp(i(\mathbf{k_h} \cdot \mathbf{x} + k_z z - \omega t)), \quad b = b' \exp(i(\mathbf{k_h} \cdot \mathbf{x} + k_z z - \omega t)) \tag{3}$$

where k_h represents the horizontal wavenumber, k_z is the vertical wavenumber, and ω is given by the dispersion relation

$$\omega^2 = N^2 \frac{k_h^2}{k_h^2 + k_z^2}, \quad |\omega| < N.$$

In stars, radiative diffusion transports energy but also dampens waves. Next, we consider the linear system with $\kappa > 0$, where radiative diffusion is present. In this case, the solution of the system is

$$\mathbf{u} = \mathbf{u}' \exp(i(\mathbf{k_h} \cdot \mathbf{x} + k_z z - \omega t)) e^{-z/\mu}. \tag{4}$$

With fixed wavenumber $\mathbf{k_h}$ and frequency ω, we have the dispersion relation for vertical wavenumber $k_z = k_z(\mathbf{k_h}, \omega)$ and damping rate $\mu = \mu(\mathbf{k_h}, \omega)$ (see, e.g. [17]). In the limit of weak dissipation and $\omega \ll N$, the damping rate can be approximated as

$$\mu \approx \frac{2\omega^4}{\kappa N^3 k_h^3}.$$

Several important properties emerge from this framework. The group velocity $\mathbf{v}_g$ is perpendicular to the phase velocity $\mathbf{v}_{ph}$, and the velocity $\mathbf{u}$ is perpendicular to the wave vector $\mathbf{k}$. Notably, plane waves are also exact solutions to the nonlinear Boussinesq system (1).

2 Method

2.1 Quasilinear decomposition

The quasilinear decomposition considers a theoretical framework used to simplify the analysis of fluid dynamics by separating the variables into mean fields and fluctuating components. This is realized by linearizing the small fluctuations around the mean fields. To analyze the transport processes in our study, we decompose $c(\mathbf{x}, t)$ into a horizontal mean and a fluctuating component

$$c(\mathbf{x}, t) = c_0(z, t) + c_1(\mathbf{x}, t).$$

Substituting it into the transport equation (2) and after manipulations, we obtain the equations governing the mean and fluctuations of c in the absence of mean flow

$$\frac{\partial c_0}{\partial t} + \frac{\partial}{\partial z}\langle w c_1 \rangle = 0 \quad \text{and} \quad \frac{\partial c_1}{\partial t} + w\frac{\partial}{\partial z}c_0 = 0, \tag{5}$$

where $\langle \cdot \rangle$ represents the horizontal average. Consider a single plane wave solution of the form

$$w = a\cos(k_h x + k_z z - \omega t)e^{-z/\mu}.$$

The ansatz for $c_1(\mathbf{x}, t)$ is taken as

$$c_1(\mathbf{x}, t) = \alpha_1 \sin(k_h x + k_z z - \omega t)e^{-z/\mu} + \alpha_2 \cos(k_h x + k_z z - \omega t)e^{-z/\mu}.$$

Solving Equation (5) yields $\alpha_1 = \frac{w_1}{\omega}\partial_z c_0(z, t)$ and $\alpha_2 = 0$. In this case, $\langle w c_1 \rangle = 0$, indicating that $c_0(z, t) = c_0(z, 0)$, meaning the mean concentration remains constant over time.

Leveraging the method of quasilinear decomposition, we observe that a single plane wave does not contribute to transport in either linear or nonlinear systems due to the fact that plane waves are exact solutions to the Bousinessq systems and $\mathbf{u} \cdot \mathbf{k} = 0$. This means that there is no net transport in such configurations. However, beams, or interactions of waves with different wave numbers, introduce complexities that allow for the possibility of transport.

2.2 Lagrangian framework

The theoretical study of transport by waves utilizes the Lagrangian framework to analyze the flow field [18, 19]. The Lagrangian framework involves tracking specific fluid parcels as they move through space and time. This approach contrasts with the Eulerian framework, which observes fluid motion at fixed points in space. However, to analyze mean velocities accurately, corrections known as Stokes drift must be applied [20]. Stokes drift refers to the correction needed for the mean velocity due to wave-induced motion and is defined as

$$\mathbf{u}^S = \overline{(\boldsymbol{\xi} \cdot \nabla)\mathbf{u}},$$

where $\overline{(\cdot)}$ is average over time, $\mathbf{u}$ is the fluid velocity, and $\boldsymbol{\xi} = \xi\hat{\mathbf{x}} + \zeta\hat{\mathbf{z}}$ represents the displacement of fluid parcels. This displacement evolves according to $\partial\boldsymbol{\xi}/\partial t = \mathbf{u}$ with

$\boldsymbol{\xi}_0 = 0$ as the initial condition. The Lagrangian mean velocity $\mathbf{u}^L$ is then composed of the Stokes drift velocity $\mathbf{u}^S$ and the Eulerian mean velocity $\overline{\mathbf{u}}^E$, i.e.,

$$\mathbf{u}^L = \mathbf{u}^S + \overline{\mathbf{u}}^E.$$

Here, $\mathbf{u}^S$ can be derived from the linear system which we will show in the next paragraph, while $\overline{\mathbf{u}}^E$ arises from the nonlinearity in the system and will be obtained using multiscale asymptotic analysis in Section 3.

The Stokes drift arises when we impose two plane waves propagating at an angle. Consider, for instance, waves with wavevectors $\mathbf{k} = k_h\hat{\mathbf{x}} + k_z\hat{\mathbf{z}}$ and $\mathbf{k} = -k_h\hat{\mathbf{x}} + k_z\hat{\mathbf{z}}$ [13], so that

$$w(x,z,t) = a\left[\cos(k_h x + k_z z - \omega t)e^{-z/\mu} + \cos(-k_h x + k_z z - \omega t)\right]e^{-z/\mu}, \tag{6}$$

where the wavenumber $k_z = k_z(k_h,\omega)$ and damping rate $\mu = \mu(k_h,\omega)$ satisfy the dispersion relation. This configuration results in the following expressions for the Stokes drift velocities

$$u^S = \frac{1}{2\pi/\omega}\int(\xi\partial_x u + \zeta\partial_z u)\,dt = \frac{2a^2k_z}{k_h\mu\omega}e^{-\frac{2z}{\mu}}\sin(2k_h x), \tag{7a}$$

$$w^S = \frac{1}{2\pi/\omega}\int(\xi\partial_x w + \zeta\partial_z w)\,dt = \frac{2a^2k_z}{\omega}e^{-\frac{2z}{\mu}}\cos(2k_h x). \tag{7b}$$

To understand the transport equation for linear motion in terms of the Stokes drift using the quasilinear decomposition (5), consider again the superposition of two waves propagating in opposite directions as described by (6). We assume an ansatz for solving $c_1(x,z,t)$ in (5) in the form

$$\begin{aligned} c_1(x,z,t) = [&\alpha_1\cos(k_h x + k_z z - \omega t) + \alpha_2\sin(k_h x + k_z z - \omega t)\\ &+\alpha_3\cos(-k_h x + k_z z - \omega t) + \alpha_4\sin(-k_h x + k_z z - \omega t)]\,e^{-z/\mu}. \end{aligned}$$

Solving Equation (5) yields $\alpha_1 = \alpha_3 = 0$ and $\alpha_2 = \alpha_4 = \frac{a}{\omega}\partial_z c_0(z,t)$. Consequently, we have $\overline{\mathbf{u}\cdot\nabla c_1} = \mathbf{u}^S\cdot\nabla c_0$. However, the zero horizontal average of $\langle\mathbf{u}^S\cdot\nabla c_0\rangle$ indicates there is no vertical transport at the leading order.

When considering the interaction of waves, we note that in the linear system, the Stokes drift is the mechanism that drives the transport of particles. In the nonlinear system, the interaction of wave vectors, $\mathbf{u}_1\cdot\mathbf{k}_2 + \mathbf{u}_2\cdot\mathbf{k}_1 + \cdots \neq 0$, indicates a more complex mechanism where we expect wave interactions can provide transport as also suggested in [13].

2.3 Simulation

We use the DEDALUS pseudo-spectral code simulation [21] to investigate the chemical transport induced by IGWs in stars. We solve the Boussinesq equations (1) in 2D with boundary conditions to make waves from the boundary $z = 0$ and solve the transport equation (2) simultaneously in DEDALUS.

For the linear Bousinessq system, we impose boundary conditions for waves as

$$w(x,z=0,t) = \sum_n a_n\cos(k_h^{(n)}x - \omega t)F(t), \quad w(x,z=L,t) = 0, \tag{8a}$$

$$F(t) = \frac{1}{2}\left(\tanh\frac{t-t_0}{T_0} - \tanh\frac{t-t_1}{T_0}\right), \tag{8b}$$

where $[0, L]$ is the domain for z, t_0 and t_1 represent the times at which the wave forcing is turned on and off, respectively. The function $F(t)$ ensures a smooth transition of wave forcing with constant T_0. To assess net transport, we will compare the chemical concentration before and after the wave is turned on and off, respectively. Initially, we simulate two waves, but this can be extended to multiple pairs of interactions for further analysis. The linear boundary condition at $z = 0$ for the buoyancy b in (1) satisfies

$$\frac{\partial b}{\partial t} + N^2 w = 0,$$

where diffusion is excluded at the bottom boundary. Near the top boundary $z = L$, we apply a damping layer to absorb the waves at the top and avoid wave reflection so that

$$\frac{\partial b}{\partial t} - \kappa \nabla^2 b + N^2 w = -bG(z), \quad G(z) = \frac{1}{2}[1 + \mathrm{erf}((z - z_0)/\sigma)], \tag{9}$$

where σ is constant to smooth the function and $G(z)$ is a localized damping function ensuring that b is fully damping at the top. Thereby, we apply the top boundary condition to be $b(x, z = L, t) = 0$.

To analyze the chemical transport, we initialize the concentration field as $c(z, 0) = z^2$ in the following results and examine its evolution over time. Our simulation tracks the initial concentration $c(z, t = 0)$ and compares it with the concentration profile after the wave forcing is terminated. In addition, the horizontal mean of $\langle c(z, t) \rangle$ is obtained to understand the vertical transport mechanisms, thereby mimicking the transport processes within the stellar radiative zone. To deal with the unknown boundary conditions at $z = 0$ and $z = L$ for c, we avoid the boundaries and solve c in a specific domain as a subset of $[0, L]$. Let

$$\frac{\partial c}{\partial t} = -\left(\mathbf{u} \cdot \nabla c\right) H(z), \quad H(z) = \frac{1}{2}\left[\mathrm{erf}((z - z_0)/\sigma) - \mathrm{erf}((z - z_1)/\sigma)\right]. \tag{10}$$

In the following analysis, we will avoid the boundaries for c and focus on the central domain $z \in [z_0, z_1] \subset [0, 1]$, where c is solved.

To illustrate the simulation setup, we present the propagation of a single linear wave. Figure 1 demonstrates the wave dynamics in the vertical velocity $w(x, z, t)$, concentration distribution $c(x, z, t)$, and the horizontal mean of the concentration difference compared to the initial value $c_{init}(x, z, 0) = z^2$ at an intermediate time when the wave is fully turned on. The simulation incorporates a damping layer as described in (9) and the central zone given in (10) that avoids the boundary issues, where the analysis of $c(x, z, t)$ will be performed. During wave propagation, the concentration distribution changes and oscillates with the wave. However, once the wave is fully turned off, we observe a difference in concentration $c(x, z, t_{end}) - c_{init}(x, z, 0)$ of order 10^{-10}, indicating there is no vertical transport to the precision that we achieve.

The boundary condition described by (8a) introduces certain complexities in our simulation due to the exclusion of radiative diffusivity at the boundary. This results in the generation of two distinct modes in the simulation: a gravity mode and a diffusive mode. The dual-mode wave phenomenon arises because the boundary condition allows for different solutions that can satisfy the imposed constraints. For example, when fixing the parameters

(amplitude a, horizontal wavenumber k_h, and frequency ω) at the boundary, the solutions of vertical wavenumber k_z and the damping rate μ can have multiple branches. One of these branches corresponds to the gravity mode, which can be calculated to have an amplitude of approximately $0.95a$ to $0.99a$, depending on the specific wave parameters. The other branch corresponds to the diffusive mode, characterized by a small amplitude and very rapid damping. While this effect is minimal, it can impact the quantification of chemical transport, especially when considering small transport phenomena.

To solve the nonlinear Boussinesq equations, we modify the equations used in the linear system by introducing nonlinearity above $z = 0$. The modulated equations are

$$\begin{aligned} \frac{\partial \mathbf{u}}{\partial t} + \nabla p - b\mathbf{e}_z &= -\left(\mathbf{u}\cdot\nabla\mathbf{u}\right) H(z), \\ \frac{\partial b}{\partial t} - \kappa\nabla^2 b + N^2 w &= -\left(\mathbf{u}\cdot\nabla b\right) H(z), \end{aligned}$$

where $H(z)$ is defined in (10).

3 Multiscale Asymptotic Analysis

To analyze the wave dynamics in the Boussinesq system given by (1), we consider the nondimensionalized equation and apply multiple scales analysis $t \to \tilde{t} + a\bar{t}$ [19]. Herein, we introduce two distinct time scales: the fast time scale $\tilde{t}$ and the slow time scale $\bar{t}$. The fast time scale $\tilde{t}$ captures the rapid oscillations of the internal gravity waves, while the slow time scale $\bar{t}$ describes the changes in the wave envelope. By replacing the time derivative with $\partial_t \mapsto \partial_{\tilde{t}} + a\partial_{\bar{t}}$, where $a \ll 1$ represents the small amplitude of the waves, we can separate the dynamics at different temporal scales.

We define the fast-time average of a function $f(\tilde{t})$ as

$$\overline{f(\tilde{t})} = \frac{1}{T}\int_0^T f(\tilde{t})d\tilde{t},$$

where T is the period of $f(\tilde{t})$.

3.1 Wave dynamics

We will first focus on the wave system which is decoupled from the transport equation. The background states $u_0 = 0$, $b_0 = b_0(z,\bar{t})$, $p_0 = p_0(z,\bar{t})$ are perturbed as

$$\begin{aligned} \mathbf{u}(\mathbf{x},t) &= au_1(\mathbf{x},\tilde{t}) + a^2u_2(\mathbf{x},\tilde{t},\bar{t}), \\ b(\mathbf{x},t) &= b_0(z,\bar{t}) + ab_1(\mathbf{x},\tilde{t},\bar{t}) + a^2b_2(\mathbf{x},\tilde{t},\bar{t}), \\ p(\mathbf{x},t) &= p_0(z,\bar{t}) + ap_1(\mathbf{x},\tilde{t},\bar{t}) + a^2p_2(\mathbf{x},\tilde{t},\bar{t}). \end{aligned}$$

In the following calculations, we will also separate each quantity, including concentration $c(\mathbf{x},t)$, into a fast-time component which is a function of the fast-time $\tilde{t}$, and a slow-time component which averages over $\tilde{t}$ and therefore, independent of $\tilde{t}$. The fast- and slow-time quantities will be noted using the subscripts f and s, respectively.

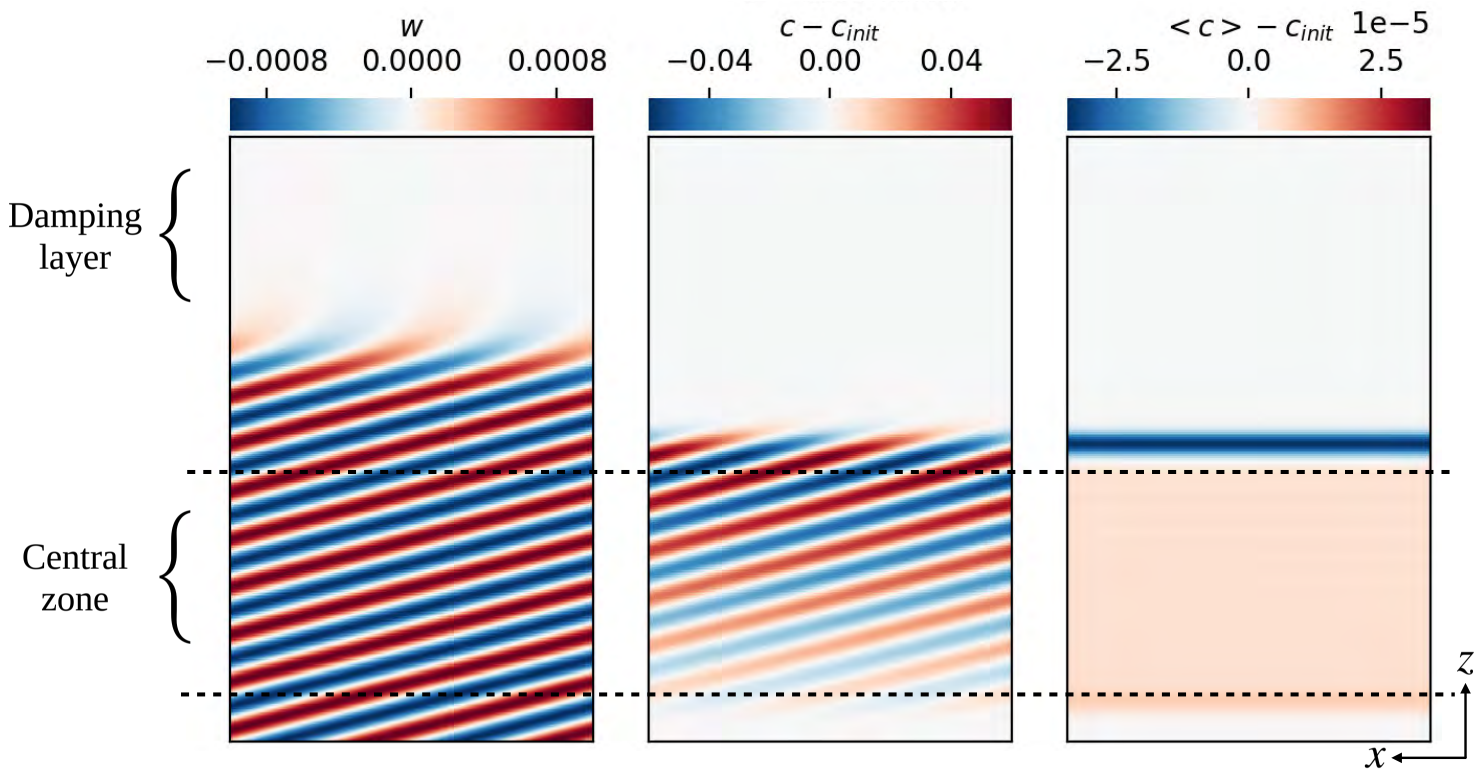

Figure 1: Illustration of the simulation result. Columns 1-3 in the figure represent the wave velocity w, the difference in the concentration distribution $c - c_{init}$, and the horizontal mean of the concentration difference $\langle c - c_{init} \rangle$, respectively, at an intermediate time when the wave is fully developed.

At the leading order $\mathcal{O}(1)$, we obtain the base states

$$\nabla p_0 - b_0 \mathbf{e}_z = 0, \quad -\kappa \nabla^2 b_0 = 0$$

so that the solutions are given by $b_0(z,\bar{t}) = z\beta_1(\bar{t}) + \beta_2(\bar{t})$ and $p_0(z,\bar{t}) = \frac{z^2}{2}\beta_1(\bar{t}) + z\beta_2(\bar{t}) + \beta_3(\bar{t})$, where $\beta_j(\bar{t})$, $j = 1, 2$, will be solved at the next order and the pressure is up to an arbitrary function $\beta_3(\bar{t})$.

At the next order $\mathcal{O}(a)$, the system incorporates the effects of wave motion and is linear. The governing equations at this order are

$$\frac{\partial \mathbf{u}_1}{\partial \tilde{t}} + \nabla p_1 - b_1 \mathbf{e}_z = 0, \tag{12a}$$

$$\frac{\partial b_0}{\partial \bar{t}} + \frac{\partial b_1}{\partial \tilde{t}} - \kappa \nabla^2 b_1 + N^2 w_1 = 0, \tag{12b}$$

$$\nabla \cdot \mathbf{u}_1 = 0. \tag{12c}$$

where $N^2(\bar{t}) = \frac{\partial b_0}{\partial z} = \beta_1(\bar{t})$ and $N_c^2(\bar{t}) = \frac{\partial c_0}{\partial z}$. As discussed in Section 2, the only possibility for transport by internal gravity waves is through the nonlinear interaction of waves with different wavenumbers. Therefore, we enforce the first-order velocity to be composed of different wave fields. We start with the simplest case of two plane waves with the same magnitude of the horizontal wavenumber $k_h > 0$ but in the opposite direction and the same frequency ω. In the $x - z$ plane, in this case, the two waves propagate towards each other in the x direction but travel upwards with the same vertical wavenumber $k_z < 0$. Consider the first-order velocity

$$w_1(x, z, \tilde{t}) = e^{-z/\mu} \left[\cos(k_h x + k_z z - \omega \tilde{t}) + \cos(-k_h x + k_z z - \omega \tilde{t}) \right], \tag{13}$$

where $\mu(k_h, \omega)$ is the damping rate. Taking the $z-$component of the curl of the curl of the first-order momentum equation (12a)

$$\frac{\partial}{\partial \tilde{t}}(-\nabla^2 w_2) + \nabla_h^2 b_2 = -\nabla \times (\nabla \times (\mathbf{u}_1 \cdot \nabla \mathbf{u}_1))_z, \tag{14}$$

we obtain the slow-time requirement of $b_1(\mathbf{x}, \bar{t})$ so that $\nabla_h^2 b_{1s}(x, z, \bar{t}) = 0$ and the fast-time component

$$\begin{aligned} b_{1f}(x, z, \tilde{t}) = \frac{2\omega}{k_h^2 \mu^2} e^{-\frac{z}{\mu}} \cos(k_h x) \big[\left(k_h^2 \mu^2 + k_z^2 \mu^2 - 1\right) \sin(k_z z - \omega \tilde{t}) \\ + 2 k_z \mu \cos(k_z z - \omega \tilde{t}) \big]. \end{aligned} \tag{15}$$

For periodic BCs, $\nabla_h^2 b_{1s}(x, z, \bar{t}) = 0$ means that $b_{1s} = b1s(z, \bar{t})$. In the first-order buoyancy equation (12b), we let $\partial b_0 / \partial \bar{t}$ compensate the slow-time variations in (12b) so that

$$\frac{\partial b_0}{\partial \bar{t}} = z\beta_1'(\bar{t}) + \beta_2'(\bar{t}) = \kappa \overline{\nabla^2 b_1}, \tag{16}$$

where $b_{1s}(z, \bar{t}) := \overline{b_1}$ remains to be solved at the next order. In addition, equating the fast-time component of (12b) with the solution (15) yields the dispersion relation.

We proceed to the next order $\mathcal{O}(a^2)$. At this order, the system now includes nonlinearity from the first-order interactions. The governing equations are

$$\frac{\partial \mathbf{u}_2}{\partial \tilde{t}} + \nabla p_2 - b_2 \mathbf{e}_z = -\mathbf{u}_1 \cdot \nabla \mathbf{u}_1, \tag{17a}$$

$$\frac{\partial b_1}{\partial \bar{t}} + \frac{\partial b_2}{\partial \tilde{t}} - \kappa \nabla^2 b_2 + N^2 w_2 = -\mathbf{u}_1 \cdot \nabla b_1, \tag{17b}$$

$$\nabla \cdot \mathbf{u}_2 = 0. \tag{17c}$$

We work from the second-order momentum equation first. Taking the $z-$component of the curl of the curl of (17a) and averaging over fast time yields $\nabla_h^2 \overline{b_2} = -\overline{\nabla \times (\nabla \times (\mathbf{u}_1 \cdot \nabla \mathbf{u}_1))_z}$ so that the slow-time component $b_{2s}(x, z, \bar{t})$ is given by

$$b_{2s}(x, z, \bar{t}) := \overline{b_2} = \frac{2k_z^2 e^{-\frac{2z}{\mu}} \cos(2k_h x)}{\mu k_h^2} + f(z, \bar{t}),$$

where $f(z, \bar{t})$ will be determined later from the buoyancy equation. Next, we take the fast-time average of (17b) and obtain

$$\frac{\partial \bar{b}_1}{\partial \bar{t}} - \kappa \overline{\nabla^2 b_2} + N^2 \overline{w_2} = -\overline{\mathbf{u}_1 \cdot \nabla b_1}. \tag{18}$$

Notice that

$$-\overline{\mathbf{u}_1 \cdot \nabla b_1} = -\frac{2\mu N^2 e^{-\frac{2z}{\mu}} \left(\kappa \left(\mu^2 \left(k_h^2 + k_z^2\right) - 1\right) + k_z \mu^2 \cos(2k_h x)(\mu\omega - 2\kappa k_z)\right)}{\kappa^2 \left(\mu^4 \left(k_h^2 + k_z^2\right)^2 - 2\mu^2 (k_h - k_z)(k_h + k_z) + 1\right) - 4\kappa k_z \mu^3 \omega + \mu^4 \omega^2}, \tag{19}$$

consisted of a horizontal mean part and an oscillation part, we require $\kappa \partial_{zz} f(z, \bar{t})$ to compensate the horizontal mean term in (19) for continuity, i.e., $\kappa \partial_{zz} f(z, \bar{t}) = \langle \overline{\mathbf{u}_1 \cdot \nabla b_1} \rangle$. This solves the only remaining unknown part of b_{2s} so that

$$f(z, \bar{t}) = \frac{\mu^3 N^2 e^{-\frac{2z}{\mu}} \left(\mu^2 \left(k_h^2 + k_z^2\right) - 1\right)}{2\left(\kappa^2 \left(\mu^4 \left(k_h^2 + k_z^2\right)^2 - 2\mu^2 (k_h - k_z)(k_h + k_z) + 1\right) - 4\kappa k_z \mu^3 \omega + \mu^4 \omega^2\right)}.$$

Meanwhile, we require $\partial b_1 / \partial \bar{t} = 0$, i.e., $b_1 = b_{1f}(\mathbf{x}, \tilde{t})$. Otherwise, b_{1s} in (18) should behave like $b_{1s} \sim e^{-2z/\mu}$ which does not satisfy (16). Consequently, we have $\partial b_0 / \partial \bar{t} = 0$ implying $\beta_1'(\bar{t}) = 0$ and $\beta_2'(\bar{t}) = 0$. In stars, the buoyancy profile $b_0(z)$ originates from the stellar structure model which can be complex as shown in figure 1 of [22]. Despite such a profile, thermal equilibrium $\kappa \nabla^2 b_0 = 0$ can still be maintained because, in stars, the diffusivity κ varies with radius r causing significant changes in the buoyancy gradient.

Now we obtain the Eulerian mean velocity $w^E := \overline{w_2}$ from (18). While the full expression for w^E is quite extensive, we can simplify it under the assumption that $\kappa \ll 1$ and $\mu\kappa = \mathcal{O}(1)$. The dominant terms are then

$$\begin{aligned} w^E = &- \frac{2k_z e^{-\frac{2z}{\mu}} \cos(2k_h x)}{\omega} \\ &+ \frac{2\kappa k_z e^{-\frac{2z}{\mu}} \cos(2k_h x) \left(\kappa \mu N^2 \left(k_h^2 + k_z^2\right)^2 - 2k_z N^2 \omega - 4k_z \omega^3\right)}{\mu N^2 \omega^3} + \dots \end{aligned} \tag{20}$$

In the absence of radiative diffusion $\kappa = 0$, we find the Eulerian mean exactly cancels out with the Stokes drift, i.e., $w^E = -w^S$ in (7b). Hence, in addition to the nonlinear interactions between waves of different wavenumbers, radiative diffusion is another key mechanism for chemical transport.

Remark. *We notice that w^E in* (20) *exponentially decays and does not oscillate in z. This is because we have a fixed frequency and the same magnitude of k_h for the wave pair. Given in* (18)*, we have $N^2 w^E = -\overline{\mathbf{u}_1 \cdot \nabla b_1} + \kappa \nabla^2 b_{2s}(x, z, \bar{t})$ and $\mathbf{u}_1 \cdot \nabla b_1 \sim e^{-2z/\mu}[\cos(2k_h x) + \cos(2k_z z - \omega t) + \sin(2k_z z - \omega t)]$. Therefore, averaging over fast time eliminates the phase in z. However, in the case that we have wavenumbers of different magnitudes, w^E is expected to oscillate in both x and z.*

One last piece that we need at this stage is the fast-time component of the wave field $w_{2f}(x, z, \tilde{t})$. The fast-time component of the momentum equation (17a) and the buoyancy equation (17b) give, respectively,

$$\frac{\partial}{\partial \tilde{t}}(-\nabla^2 w_{2f}) + \nabla_h^2 b_{2f} = 0, \tag{21a}$$

$$\frac{\partial b_{2f}}{\partial \tilde{t}} - \kappa \nabla^2 b_{2f} + N^2 w_{2f} = e^{-2z/\mu}\left[\lambda_1 \cos(2k_z z - 2\omega\tilde{t}) + \lambda_2 \sin(2k_z z - 2\omega\tilde{t})\right], \tag{21b}$$

where

$$\lambda_1 = \frac{2\mu N^2\left(\kappa\left(\mu^2(k_h - k_z)(k_h + k_z) - 1\right) + k_z\mu^3\omega\right)}{\kappa^2\left(\mu^4\left(k_h^2 + k_z^2\right)^2 - 2\mu^2(k_h - k_z)(k_h + k_z) + 1\right) - 4\kappa k_z\mu^3\omega + \mu^4\omega^2},$$

$$\lambda_2 = \frac{2\mu^2 N^2\left(\kappa k_z\left(\mu^2\left(k_h^2 + k_z^2\right) + 1\right) - \mu\omega\right)}{\kappa^2\left(\mu^4\left(k_h^2 + k_z^2\right)^2 - 2\mu^2(k_h - k_z)(k_h + k_z) + 1\right) - 4\kappa k_z\mu^3\omega + \mu^4\omega^2}.$$

Because the right-hand-side of (21b) is $x-$independent, by continuity we require

$$w_{2f}(x, z, \tilde{t}) = 0. \tag{22a}$$

Using (21a), we obtain

$$b_{2f}(x, z, \tilde{t}, \bar{t}) = e^{-2z/\mu}\big[a_1 \cos(2k_z z - 2\omega\tilde{t}) + a_2 \sin(2k_z z - 2\omega\tilde{t})\big], \tag{22b}$$

where a_1, a_2 are constant that can be solved by (21b). Again, to avoid the tedious expressions of a_1 and a_2, they are not shown here. Instead, by assuming $\kappa \ll 1$ and $\mu \sim 1/\kappa$, we reduce the constants to

$$a_1 \approx \frac{N^2\left(\kappa k_z \mu\left(k_h^2 + 3k_z^2\right) - \omega\right)}{\mu\omega^3}, \quad a_2 \approx -\frac{k_z N^2}{\omega^2}.$$

3.2 The transport equation

The concentration field $c_0 = c_0(z, \bar{t})$ is perturbed as

$$c(\mathbf{x}, t) = c_0(z, \bar{t}) + a c_1(\mathbf{x}, \tilde{t}, \bar{t}) + a^2 c_2(\mathbf{x}, \tilde{t}, \bar{t}) + a^3 c_3(\mathbf{x}, \tilde{t}, \bar{t}).$$

At each order, we collect the governing equations as

$$\mathcal{O}(a): \quad \frac{\partial c_0}{\partial \bar{t}} + \frac{\partial c_1}{\partial \tilde{t}} + N_c^2 w_1 = 0, \tag{23a}$$

$$\mathcal{O}(a^2): \quad \frac{\partial c_1}{\partial \bar{t}} + \frac{\partial c_2}{\partial \tilde{t}} + N_c^2 w_2 = -\mathbf{u}_1 \cdot \nabla c_1, \tag{23b}$$

$$\mathcal{O}(a^3): \quad \frac{\partial c_2}{\partial \bar{t}} + \frac{\partial c_3}{\partial \tilde{t}} + N_c^2 w_3 = -\mathbf{u}_1 \cdot \nabla c_2 - \mathbf{u}_2 \cdot \nabla c_1, \tag{23c}$$

where $N_c^2(z,\bar{t}) = \partial c_0(z,\bar{t})/\partial z$. Taking the fast-time average of (23a) yields $\frac{\partial c_0}{\partial \bar{t}} = 0$ so that $c_0(z,\bar{t}) = z^2$ and $N_c^2 = 2z$. The fast-time component of c_1 can be solved at $\mathcal{O}(a)$ whereas the slow component of c_1 remains to the next order, i.e.,

$$c_1(x,z,\tilde{t},\bar{t}) = \frac{2}{\omega} N_c^2 e^{-\frac{z}{\mu}} \cos(k_h x) \sin(k_z z - \omega \tilde{t}) + c_{1s}(x,z,\bar{t}). \tag{24}$$

Then taking the fast-time average over (23b) gives the net transport in c_1 as

$$\frac{\partial c_{1s}}{\partial \bar{t}} := \frac{\partial c_1}{\partial \bar{t}} = -\overline{\mathbf{u}_1 \cdot \nabla c_1} - N_c^2 \overline{w_2} = -\mathbf{u}^S \cdot \nabla c_0 - N_c^2 \overline{w_2} = -N_c^2 (w^S + w^E),$$

where $\overline{\mathbf{u}_1 \cdot \nabla c_1} = \overline{d(\xi_1)/dt \cdot \nabla c_1} = \mathbf{u}^S \cdot \nabla c_0$ is derived using integration by parts. With no radiative diffusion, we know $w^E = -w^S$ so that there is no net transport in c_1 as expected. With diffusion, we obtain

$$c_{1s} = -\frac{2\kappa k_z N_c^2 e^{-\frac{2z}{\mu}} \cos(2k_h x) \left(\kappa \mu N^2 \left(k_h^2 + k_z^2\right)^2 - 2k_z N^2 \omega - 4k_z \omega^3\right)}{\mu N^2 \omega^3} \bar{t} + h.o.t.,$$

and $\overline{c - c_0} = \mathcal{O}(a^2 t)$. In this case, the first-order transport is purely driven by the Eulerian mean of the wave field. On the other hand, notice that taking the horizontal mean of c_1,

$$\frac{\partial \langle c_1 \rangle}{\partial \bar{t}} = 0.$$

Although c_1 changes vertically, the horizontal mean of c_1 does not transport. We also comment that the asymptotic expansion is valid so long as $a^2 t \ll 1$, which is sufficient considering the small amplitude waves in stars and the stochastic generation of waves due to convection.

Since the goal is to obtain vertical transport with a nonzero horizontal mean, we will continue to the higher-order transport equations to solve for $\langle \partial c_2/\partial t \rangle$. Given the variables c_1, $\mathbf{u}_1$ and w_2 already solved in (23b), $c_{2f}(x,z,\tilde{t})$ can be derived at $\mathcal{O}(a^2)$ easily, and the full expression is omitted here for brevity. Now proceed to the next order $\mathcal{O}(a^3)$ in the transport equation to solve for $\langle \partial c_2/\partial \bar{t} \rangle$. Taking the fast-time average and horizontal mean of (23c) and using $\mathbf{u}_{1s}(x,z,\bar{t}) = 0$, $\mathbf{u}_{2f}(x,z,\tilde{t}) = 0$, we obtain

$$\langle \frac{\partial c_{2s}}{\partial \bar{t}} \rangle := \langle \frac{\partial c_2}{\partial \bar{t}} \rangle = -\langle \overline{\mathbf{u}_{1f} \cdot \nabla c_{2f}} \rangle - \langle \mathbf{u}^E \cdot \nabla c_{1s} \rangle \tag{25a}$$

$$\implies \langle c_{2s} \rangle \sim \gamma_1 e^{-4z/\mu} (z - \gamma_2) \bar{t}^2, \tag{25b}$$

where γ_1, γ_2 are solved constants. Therefore, at a fixed position z, concentration changes as $\overline{\langle c - c_0 \rangle} = \mathcal{O}(a^4 t^2)$.

3.3 Multiple wavenumbers

To gain a more general understanding of vertical chemical transport, we extend our analysis to waves with different horizontal wavenumbers (k_h, nk_h), $n \in \mathbb{R}$, instead of the previously simplified case $(k_h, -k_h)$. Specifically, we examine the forcing of waves from the boundary with these two different wavenumbers but at the same frequency. The approach and the governing equations are the same as given in the previous sections, and the procedure at each order follows the same methodology. In this section, we will highlight the differences in the solutions that arise from this setup. Consider

$$w_1(\mathbf{x}, t) = \cos(k_h x + k_{z1} z - \omega t) e^{-z/\mu_1} + \cos(n k_h x + k_{z2} z - \omega t) e^{-z/\mu_2}, \tag{26}$$

where $(k_{z1}, \mu_1) = (k_{z1}(k_h, \omega), \mu_1(k_h, \omega))$ and $(k_{z2}, \mu_2) = (k_{z2}(nk_h, \omega), \mu_2(nk_h, \omega))$ satisfy the dispersion relation for each individual wave. The Eulerian mean velocity is derived as

$$w^E := \overline{w_2} \sim e^{-z/(\frac{1}{\mu_1} + \frac{1}{\mu_2})} \big[\cos(\phi) + \sin(\phi) \big], \tag{27}$$

where $\phi(x, z) = (1 - n)k_h x + (k_{z1} - k_{z2})z$. In this case, the Eulerian mean velocity still cancels with the Stokes drift in the absence of dissipation. However, in contrast with the case when $n = -1$, now the Eulerian mean oscillates in both x and z. At this stage, we find the first order transport as

$$c_{1f}(x, z, \tilde{t}) \sim e^{-z/\mu_1} \sin(k_h x + k_{z1} z - \omega t) + e^{-z/\mu_2} \sin(n k_h x + k_{z2} z - \omega t). \tag{28a}$$

and

$$c_{1s} \sim w^E N_c^2 \bar{t}. \tag{28b}$$

Similarly, $\langle c_{1s} \rangle = 0$ indicates that there is no vertical transport of the horizontal average.

To obtain the vertical transport, we proceed to the next order. We first focus on the fast-time component of (17a) and (17b)

$$\begin{aligned}
\frac{\partial}{\partial \tilde{t}}(-\nabla^2 w_{2f}) + \nabla_h^2 b_{2f} &= -\nabla \times (\nabla(\mathbf{u}_1 \cdot \nabla \mathbf{u}_1))_z + \overline{\nabla \times (\nabla(\mathbf{u}_1 \cdot \nabla \mathbf{u}_1))_z} && \text{(29a)} \\
&\sim e^{-z/(\frac{1}{\mu_1} + \frac{1}{\mu_2})} \left[\cos(\psi - 2\omega t) + \sin(\psi - 2\omega t) \right] \\
\frac{\partial b_{2f}}{\partial \tilde{t}} - \kappa \nabla^2 b_{2f} + N^2 w_{2f} &= -\mathbf{u}_1 \cdot \nabla b_1 + \overline{\mathbf{u}_1 \cdot \nabla b_1} && \text{(29b)} \\
&\sim e^{-z/(\frac{1}{\mu_1} + \frac{1}{\mu_2})} \left[\cos(\psi - 2\omega t) + \sin(\psi - 2\omega t) \right], && \text{(29c)}
\end{aligned}$$

where

$$\psi(x, z) = (1 + n)k_h x + (k_{z1} + k_{z2})z.$$

Therefore, instead of a zero w_{2f} and an $x-$independent b_{2f} as the previous $n = -1$ case, we take the ansatz

$$w_{2f}, b_{2f} \sim e^{-z/(\frac{1}{\mu_1} + \frac{1}{\mu_2})} \left[\cos(\psi - 2\omega t) + \sin(\psi - 2\omega t) \right]. \tag{30}$$

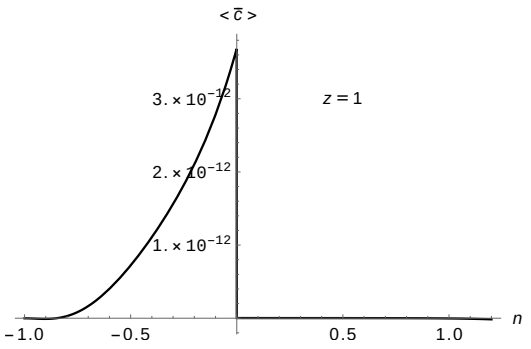

(a) $z = 1$

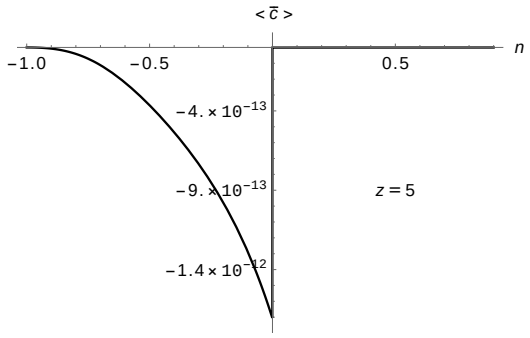

(b) $z = 5$

Figure 2: Change of $\langle \bar{c} \rangle$ in different wavenumbers nk_h in the weak dissipation and small frequency limit.

Note the difference in the phase $\phi(x, z)$ and $\psi(x, z)$. Now we are ready to solve the higher-order transport equations (23b, 23c) and obtain

$$\langle c_{2s} \rangle = D_c e^{-z/(\frac{1}{\mu_1}+\frac{1}{\mu_2})} \left(2(\mu_1 + \mu_2) N_c^2(z) - \mu_1 \mu_2 \frac{d}{dz} N_c^2(z) \right) \bar{t}^2. \tag{31}$$

Most importantly, let us rewrite (31) in the diffusive form

$$\langle \overline{c - c_0} \rangle = a^4 D_c \nabla \left(e^{-z/(\frac{1}{\mu_1}+\frac{1}{\mu_2})} \nabla c_0(z) \right) t^2, \tag{32}$$

where $N_c^2(z) = \partial c_0(z)/\partial z$ and $D_c = D_c(k_h, nk_h, k_{z1}, k_{z2}, \mu_1, \mu_2, \kappa, N^2)$ is constant. Equation (32) provides a general form for quantifying the chemical transport by the nonlinear interaction of internal gravity waves with different wavenumbers. We find that transport is proportional to $a^4 t^2$ and also depends on the initial concentration distribution.

To determine the conditions under which chemical transport is maximized, we analyze the system using equation (32). The wavenumber is given by k_z as $k_z = -\sqrt{\frac{k_h^2(N^2-\omega^2)}{\omega^2}}$. In the limit of weak dissipation and considering waves with $\omega \ll N$, we approximate μ as $\mu = \frac{2\omega^4}{\kappa N^3 k_h^2 \sqrt{k_h^2}}$. By fixing the parameters, e.g., $a = 0.001$, $k_h = 0.4\pi$, $\omega = 0.2$, $\kappa = 5 \cdot 10^{-4}$, $N^2 = 1$, and $\bar{t} = 1$, we plot $\langle \bar{c} \rangle (nk_h; z)$ in figure 2. Our results indicate that long waves propagating in opposite directions may result in a higher magnitude of chemical transport.

Remark. *Consider waves with the same horizontal wavenumber but different frequencies, for instance,*

$$w_1(\mathbf{x}, t) = \cos(k_h x + k_{z1} z - \omega t) e^{-z/\mu_1} + \cos(k_h x + k_{z2} z - n\omega t) e^{-z/\mu_2}.$$

Using trigonometric identities, we expect the terms from the interaction modes all average out over time, indicating that such wave interactions do not contribute to net transport. Therefore, we consider equation (32) *to be sufficiently general to encompass all scenarios of transport driven by nonlinear wave interactions.*

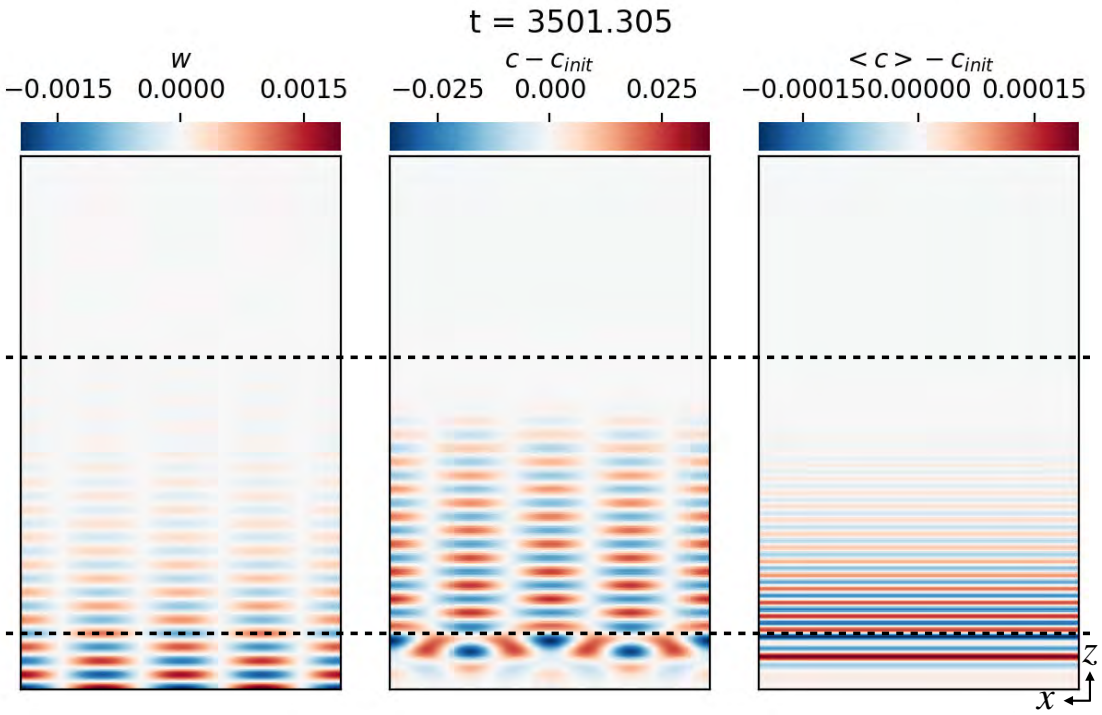

Figure 3: Simulation results at an intermediate time for solving the nonlinear Boussinesq equation and the transport equation with the boundary forcing (33). Column 1 shows the vertical velocity w, Column 2 is the change in concentration driven by the IGWs, and Column 3 is the horizontal mean of the concentration change. Inside the black dashed lines indicates the regions where analysis is performed.

4 Simulation Results

In this section, we present the results of our simulations on transport by nonlinear wave interactions using the method described in section 2.3. We first consider the case where two plane waves are forced at the boundary with wavenumbers $\mathbf{k} = k_h\hat{\mathbf{x}} + k_z\hat{\mathbf{z}}$ and $\mathbf{k} = -k_h\hat{\mathbf{x}} + k_z\hat{\mathbf{z}}$. Additionally, we examine the scenario with two different wavenumbers $\mathbf{k}_j = k_{hj}\hat{\mathbf{x}}+k_{zj}\hat{\mathbf{z}}$, $j = 1, 2$, generated from the boundary. The results from the 2D simulations will be shown and analyzed, and we will compare these findings with the asymptotic predictions provided in section 3.3.

4.1 Transport by waves with opposite wavevectors

According to the predictions in section 3.2, the net transport by nonlinear wave interactions is described by $\overline{c - c_0} \propto a^2 t$ and $\langle\overline{c - c_0}\rangle \propto a^4 t^2$. Considering how small the transport is, we opted to use larger amplitude and radiative diffusivity in our simulations. However, it is crucial to balance these parameters to avoid numerical issues and to maintain values that are physically realistic.

Figure 3 shows the simulation of the nonlinear Boussinesq equation (1) with the trans-

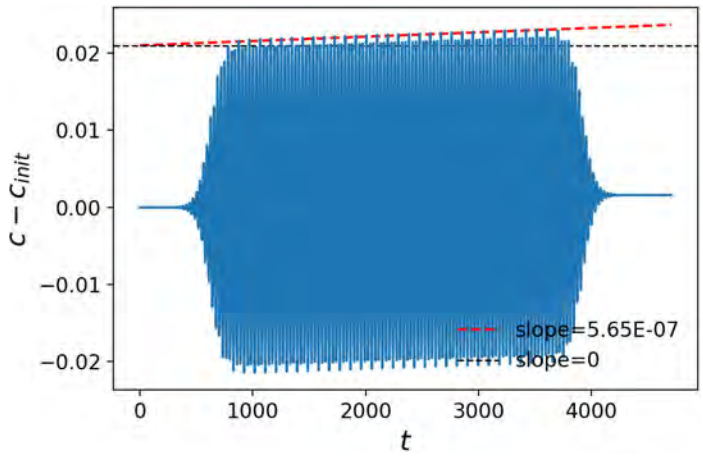

Figure 4: Temporal evolution of the concentration change in c at fixed $x = 5$ and $z = 5$. The red dashed line indicates the predicted c_{1s} from the multiscale asymptotic analysis (24), and the black dashed line is a line with slope 0 for comparison.

port equation (2) forced by the boundary data

$$w(x, z = 0, t) = a\big[\cos(k_h x - \omega t) + \cos(-k_h x - \omega t)\big]F(t), \tag{33}$$

with parameters $a = 0.001$, $k_h = 0.4\pi$, $\omega = 0.2$, radiative diffusivity $\kappa = 5 \times 10^{-4}$, and buoyancy frequency $N^2 = 1$. The function $F(t)$ is given in (8b) to turn on and turn off the wave field. The first column in Figure 3 shows the vertical velocity field at an intermediate time. The wave is damped due to the radiative diffusivity, consisting of multiple waves and therefore appearing as oscillating blocks while propagating upwards with a positive group velocity. The second column in Figure 3 shows the change in concentration that is purely driven by the traveling waves. It is noticeable that there are some boundary issues near $z = 0$ that we need to ignore due to the turning on of the nonlinearity and solving c only slightly above $z = 0$. Nevertheless, the central region is not affected by these boundary issues. The third column in Figure 3 shows the change in the horizontal mean of c, defined as

$$\langle c \rangle = \frac{1}{L_x} \int_0^{L_x} c(x, z, t)\, dx,$$

where L_x is the domain size in x.

The primary objective is to identify the net transport in c, which represents the overall transport over time despite the intermediate oscillations. To investigate this, we analyze how c evolves with time while keeping x and z fixed. Figure 4 illustrates the concentration change at $x = 5$ and $z = 5$. The oscillations observed in the figure correspond to the fast-time component of c_1 as described in (24), while the envelope of these oscillations represents the slow-time component c_{1s} in (24). The red dashed line in Figure 4 represents the predicted c_{1s} from the multiscale asymptotic analysis, which is expected to be linear in t and has the order $\mathcal{O}(a^2 t)$. The simulation results show good agreement with the asymptotic predictions, thereby validating the quantification of the first-order transport by IGWs.

Next, we examine the vertical transport in the simulation presented in figure 3 by analyzing the horizontal mean of c. Figure 5(a) shows a 2D plot depicting how $\langle c \rangle$ changes

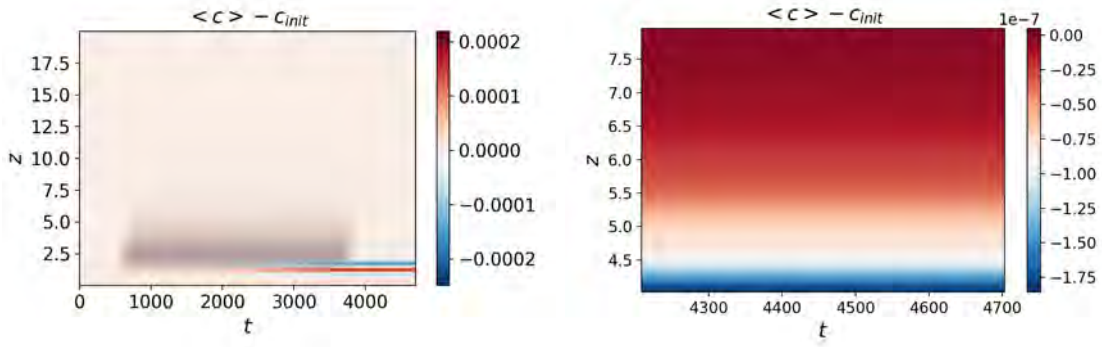

(a) (b)

Figure 5: (a) Two-dimensional plot showing the evolution of the horizontal mean of the concentration, $\langle c \rangle - c_{\text{init}}$, as a function of height z and time t. (b) Zoomed-in view of the region $z \in [4, 8]$ after the wave is turned off.

with z and t. It is clear that the wave turns on and starts to propagate around $t = 900$, initiating transport, and is turned off around $t = 4000$, allowing the chemical to return to its original position. More transport occurs at smaller z due to wave damping. We then focus on the concentration distribution after the wave has fully turned off to determine how it differs from the initial value, which indicates net transport. Figure 5(b) zooms into the region $z \in [4, 8]$ after the wave has turned off. We observe a difference of 10^{-7}, indicating that there is indeed net transport of the horizontal mean by the nonlinear wave interactions.

We proceed to compare the vertical transport observed in the simulation with the second-order asymptotic results. In figures 6(a-c), we analyze the temporal evolution of the horizontally averaged concentration, $\langle c \rangle$, at fixed vertical locations $z = 5, 6, 7$. The focus is on the envelopes of $\langle c \rangle$, which signify the net transport over time. These envelopes are then compared with the slow-time component of the horizontal mean, $\overline{\langle c \rangle} = \langle c_{2s} \rangle$, as described by the asymptotic prediction in (25b). The results demonstrate good agreement across the examined vertical locations, validating that the change in $\overline{\langle c \rangle}$ is indeed of the order $\mathcal{O}(a^4 t^2)$. Additionally, a comparison is performed in figure 6(d) between the simulation results at the final time $t = 4700$ and the transport solution given in (25b). This comparison focuses on the spatial variation of the time-average and horizontally-averaged concentration $\overline{\langle c \rangle}$ in the vertical direction z. Despite minor deviations, probably attributed to numerical issues, the second-order asymptotic solution (25b) accurately captures the transport dynamics within the examined range.

4.2 Transport by waves with different wavevectors

In this section, we examine the scenario of transport induced by two plane waves with distinct wavenumbers $\mathbf{k}_j = k_{hj}\hat{\mathbf{x}} + k_{zj}\hat{\mathbf{z}}$, $j = 1, 2$, but with the same frequency ω at the boundary. Each wave is associated with a different vertical wavenumber $k_{zj} = k_{zj}(k_{hj}, \mu)$ and a corresponding damping rate $\mu_{zj} = \mu_{zj}(k_{hj}, \mu)$, both of which satisfy the dispersion relation independently. To enhance the transport for better visualization and easier analysis,

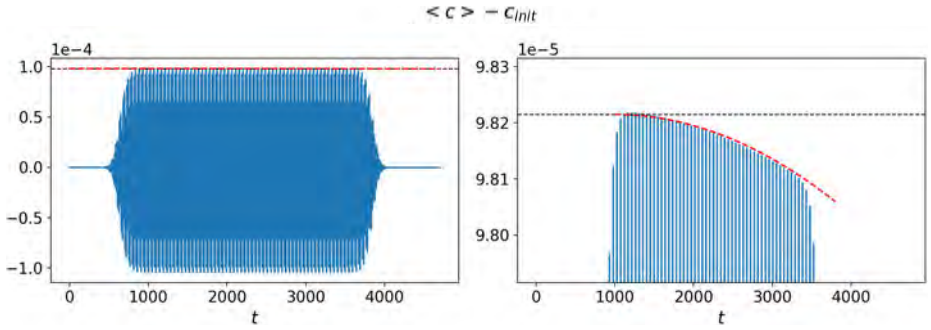

(a) $z = 4$

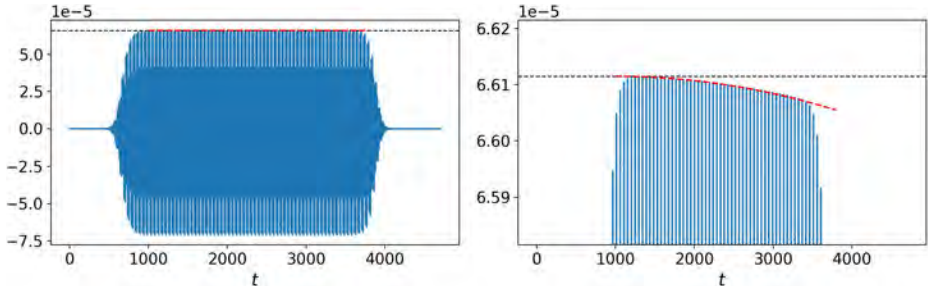

(b) $z = 5$

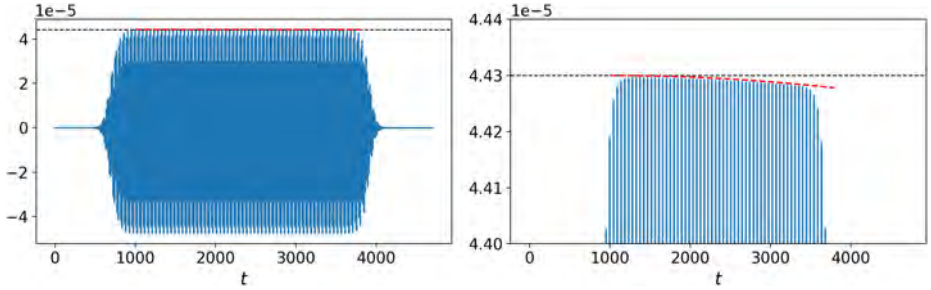

(c) $z = 6$

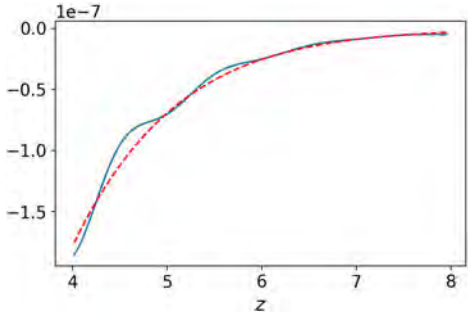

(d) $t = 4700$

Figure 6: (a-c) Evolution of the horizontal mean concentration $\langle c \rangle$ at different fixed vertical positions z over time t. The right column provides a detailed view of the envelopes from the left column. The blue lines represent the simulation results, while the red dashed lines indicate the theoretical predictions based on the slow-time component of the horizontal mean, $\langle c_{2s} \rangle$, from the asymptotic analysis. (d) Change in $\langle c \rangle$ as a function of z at the final time after wave terminates.

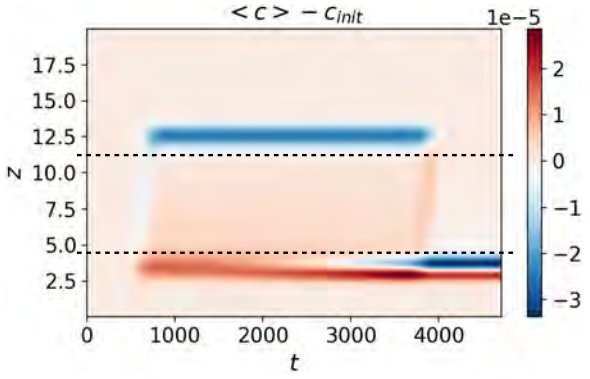

(a)

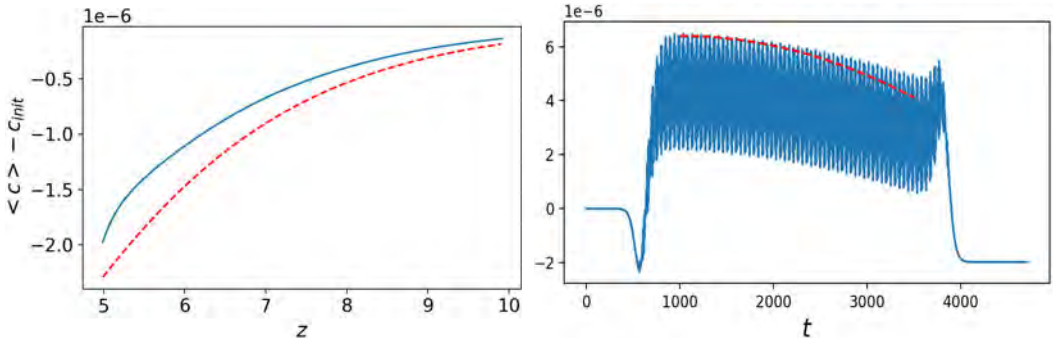

(b) $t = 4700$

(c) $z = 5$

Figure 7: (a) Vertical transport $\langle c - c_{init} \rangle$ plotted against z and t. Boundary issues are observed due to the wave addition and damping as well as the solution domain for c. (b) The net transport $\langle c - c_{init} \rangle$ at $t = 4700$. (c) Temporal evolution of $\langle c - c_{init} \rangle$ at $z = 5$.

we conduct simulations with the following parameters: $a = 0.001$, $k_{h1} = 0.4\pi$, $k_{h2} = -0.2\pi$, $\omega = 0.2$, radiative diffusivity $\kappa = 5 \times 10^{-4}$, and buoyancy frequency $N^2 = 1$.

Figure 7(a) depicts the vertical transport $\langle c \rangle$ as a function of z and t. Some boundary issues are present where nonlinearity is introduced, the waves are damped, and the transport c is solved. Despite these issues, the region between the black lines in figure 7(a) provides a suitable area for analyzing the net transport over time. In figure 7(b), the horizontal mean of the concentration field's change from its initial value is illustrated after the wave is fully turned off at $t = 4700$. This plot indicates the overall transport driven by wave propagation as a function of z. The results show more transport at smaller z values, decreasing as z increases. The simulation result is then compared with the multiscale asymptotic prediction $\langle \overline{c - c_0} \rangle$ in (32). Despite the deviations, which will be explained later, the observed values follow the predicted order of $\mathcal{O}(a^4 t^2)$ as given in (32).

In figure 7(c), we fix the location at $z = 5$ and observe how the horizontal mean of the concentration field changes with time. The oscillations in $\langle c \rangle$ are driven by the periodic wave oscillations and correspond to the fast-time changes, reflecting the circulatory behavior of the waves. The envelope in figure 7(c) represents the net transport associated with the slow-time change, which is of primary interest. We observe a shift in $\langle c \rangle$, which we verified

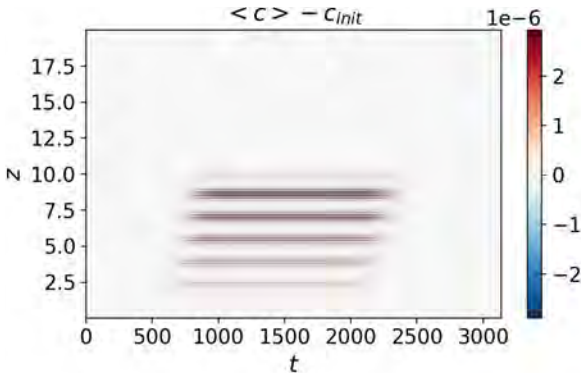

Figure 8: Illustration of vertical transport induced by the interaction of two nonlinear wave beams.

is related to the process of turning the wave on and off in the simulation. This shift is not present in the previous case shown in figure 6, likely due to the opposing wavenumbers k_h and $-k_h$, causing the shifts to cancel out. Comparing our simulation with the second-order prediction (32) at $z = 5$, we note an accumulating deviation over time. we are still investigating why there appears to be a discrepancy in these cases. Nevertheless, the order of the net vertical transport $\mathcal{O}(a^4t^2)$ appears to be correct.

5 Discussion

In this study, we investigated the coherent transport induced by internal gravity waves (IGWs) using both Dedalus simulations and multiscale asymptotic analysis. The Dedalus simulations were employed to solve the nonlinear Boussinesq equations along with the transport equation, allowing us to observe the wave dynamics and concentration changes directly. The multiscale asymptotic analysis provided a theoretical framework to compare with the simulation results. By induction, we derived the main equation describing the net vertical transport, as given by (32). This equation primarily addresses the transport due to two interacting nonlinear waves but can be extended to scenarios involving multiple waves.

Our analysis shows that the leading-order transport is negligible, and the primary contribution to transport arises from the Eulerian mean velocity in the presence of diffusivity. When there is no diffusivity, the transport by the Eulerian mean velocity cancels out with the Stokes drift, a phenomenon potentially related to the pseudo-momentum [23]. With diffusivity, the concentration change Δc scales as $\Delta c \propto a^2 t$, and the horizontal mean of the concentration change scales as $\langle \Delta c \rangle \propto a^4 t^2$, in the asymptotic limit $t \ll 1/a^2$. The net vertical concentration change is in one direction, meaning the effects from multiple waves should be added constructively, consequently yielding an effective diffusion coefficient that scales like a^4. We then expect our effective diffusivity to be proportional to the radiative diffusivity. These findings are consistent with simulation observations and are expected to align well with results from three-dimensional calculations.

When comparing our results with previous studies, we find that Rogers & McElwaine (2017) reported a diffusion scaling of a^2 [11], whereas Jermyn (2022) identified a diffusion

scaling of $D_\mu^2 a^4$ [13]. Our study examines these findings by providing a more detailed understanding of the transport mechanisms and the scaling of diffusion coefficients under different wave interaction scenarios.

In the context of stellar interiors, particularly within the radiative zones, our study provides insights into the transport purely driven by weakly nonlinear wave interactions. The primary focus is on quantifying the amount of vertical transport driven by these interactions. This study on nonlinear plane wave interactions can be further extended to beam interactions, where each beam consists of waves with multiple different wavenumber. Figure 8 illustrates the interaction of wave beams and the resulting transport processes. Beam interactions are more related to the physical scenarios of stellar interiors. Finally, we aim to compare the transport equation that we obtained in (32) with the observation data of internal gravity waves excited by the stellar convection core in [3].

Acknowledgements

I would like to thank my advisor Daniel Lecoanet for his mentorship. I appreciate and am encouraged by his patient guidance, physical insights, and inspiring spirit. The overall experience has been helpful and enjoyable. I would also like to extend my gratitude to our GFD program directors Pascale Garaud and Tiffany Shaw for their organization and care. I am grateful to Geoff Vallis and Heather Knutson for their lectures from which I have learned a lot. Special thanks to Glenn Flierl and Wanying Kang for the insightful discussions throughout the summer. I am also thankful to Greg Chini, Colin Meyer, and Keaton Burns for their softball instructions. Most importantly, I am appreciative of the friendship shared with the other nine fellows. Lastly, I would like to thank Keith Julien for his invaluable mentorship both within and outside GFD.

A Transport by the Stokes drift

The Stokes drift arises from interactions of linear internal gravity waves. As derived in section 3, the Stokes drift cancels out with the Eulerian mean velocity in the absence of diffusivity, which aligns with the concept of wave propagation being probably a reversible process. In this section, we will consider the interaction of two linear waves with an opposite wavenumber $k_h = \pm 0.4\pi$ and the same frequency $\omega = 0.3$. We solve for the Stokes drift from the linearized Boussinesq system using multiscale asymptotic analysis by introducing $t = \tilde{t} + a\bar{t}$ and compare the theoretical results with simulation.

Considering the first-order velocity (13), in the linear system, the equations at $\mathcal{O}(a)$ remain the same as (12). Thus, the leading-order solutions for $\mathbf{u}_1$, b_1, $c_0(z, \bar{t}) = z^2$, and $c_1(x, z, \tilde{t}, \bar{t}) = \frac{2N_c^2}{\omega} e^{-\frac{z}{\mu}} \cos(k_h x) \sin(k_z z - \omega \tilde{t}) + c_{1s}(x, z, \bar{t})$ are consistent with the previous derivations in section 3. Here, $c_{1s}(x, z, \bar{t})$ remains an unknown function that will be solved

at $\mathcal{O}(a^2)$. However, the equations at $\mathcal{O}(a^2)$ are collected as the following system

$$\begin{aligned} \frac{\partial \mathbf{u}_2}{\partial \tilde{t}} + \nabla p_2 - b_2 \mathbf{e}_z &= 0, \\ \frac{\partial b_1}{\partial \bar{t}} + \frac{\partial b_2}{\partial \tilde{t}} - \kappa \nabla^2 b_2 + N^2 w_2 &= 0, \\ \nabla \cdot \mathbf{u}_2 &= 0, \\ \frac{\partial c_1}{\partial \bar{t}} + \frac{\partial c_2}{\partial \tilde{t}} + N_c^2 w_2 &= -\mathbf{u}_1 \cdot \nabla c_1. \end{aligned} \tag{34}$$

Note that (34) is the same as (23b) in the nonlinear system. Given the linear boundary forcing, we take $\mathbf{u} = a\mathbf{u}_1$, implying $\mathbf{u}_j = 0$, $b_j = 0$, and $p_j = 0$ for $j = 2, 3, \ldots$. Consequently, taking the fast-time average of (34) yields

$$c_1(x, z, \tilde{t}, \bar{t}) = \frac{2N_c^2 e^{-\frac{z}{\mu}} \cos(k_h x) \sin(k_z z - \omega \tilde{t})}{\omega} - \frac{2k_z N_c^2 e^{-\frac{2z}{\mu}} \cos(2k_h x)}{\omega} \bar{t} \tag{35}$$

and $\langle c_1(x, z, \tilde{t}, \bar{t}) \rangle = 0$. The theoretical predictions are compared with observations from our simulation. Figure 9(a) depicts the concentration field $c - c_{init}(x, z)$ at an intermediate time t when the wave is actively propagating. In figure 9(b), the position is fixed at $z = 5$ and a 2D contour plot of $c(x, t)$ is presented. The waves are initiated at approximately $t \approx 500$ and deactivated at around $t \approx 2200$, leading to c oscillating in conjunction with the wave field during this interval. Finally, to validate our theoretical prediction (35), the position is fixed at $x = 5$ and $z = 5$ in figure 9(c). The red line represents the slope $\partial c_1 / \partial \bar{t}$ as derived in (35), which aligns well with the envelope of the simulation result for $c(t)$.

We proceed to higher orders to solve for a nonzero vertical transport. Subtracting the fast-time average from (34), we derive

$$\frac{\partial c_2}{\partial \tilde{t}} = -(\mathbf{u}_1 \cdot \nabla c_1 - \overline{\mathbf{u}_1 \cdot \nabla c_1}),$$

so that the fast-time component of c_2 (noted as c_{2f}) can be solved. For solving $c_{2s}(x, z, \bar{t})$, we appeal to the third-order transport equation (see also (23c))

$$\frac{\partial c_2}{\partial \bar{t}} + \frac{\partial c_3}{\partial \tilde{t}} + N_c^2 w_3 = -\mathbf{u}_1 \cdot \nabla c_2 - \mathbf{u}_2 \cdot \nabla c_1,$$

where $w_3 = 0$ and $\mathbf{u}_2 = 0$. Taking the fast-time average yields $\frac{\partial c_2}{\partial \bar{t}} = -\overline{\mathbf{u}_1 \cdot \nabla c_2} = -\overline{\mathbf{u}_1 \cdot \nabla c_{2f}}$ and consequently,

$$c_{2s}(x, z, \bar{t}) = \bar{t}^2 \frac{2k_z^2 e^{-\frac{4z}{\mu}} \left(\mu \cos^2(2k_h x) \frac{dN_c^2}{dz} - 2N_c^2 \right)}{\mu \omega^2}. \tag{36}$$

Apply the initial condition $N_c^2 = 2z$, the horizontal average of $c_2(x, z, \tilde{t}, \bar{t})$ is

$$\begin{aligned} < c_2 > = & \frac{1}{\mu \omega^2} e^{-\frac{2z}{\mu}} (2k_z \mu z \sin(2k_z z - 2\omega \tilde{t}) + (2z - \mu) \cos(2k_z z - 2\omega \tilde{t})) \\ & + \bar{t}^2 \frac{2k_z^2 e^{-\frac{4z}{\mu}} (\mu - 4z)}{\mu \omega^2}. \end{aligned} \tag{37}$$

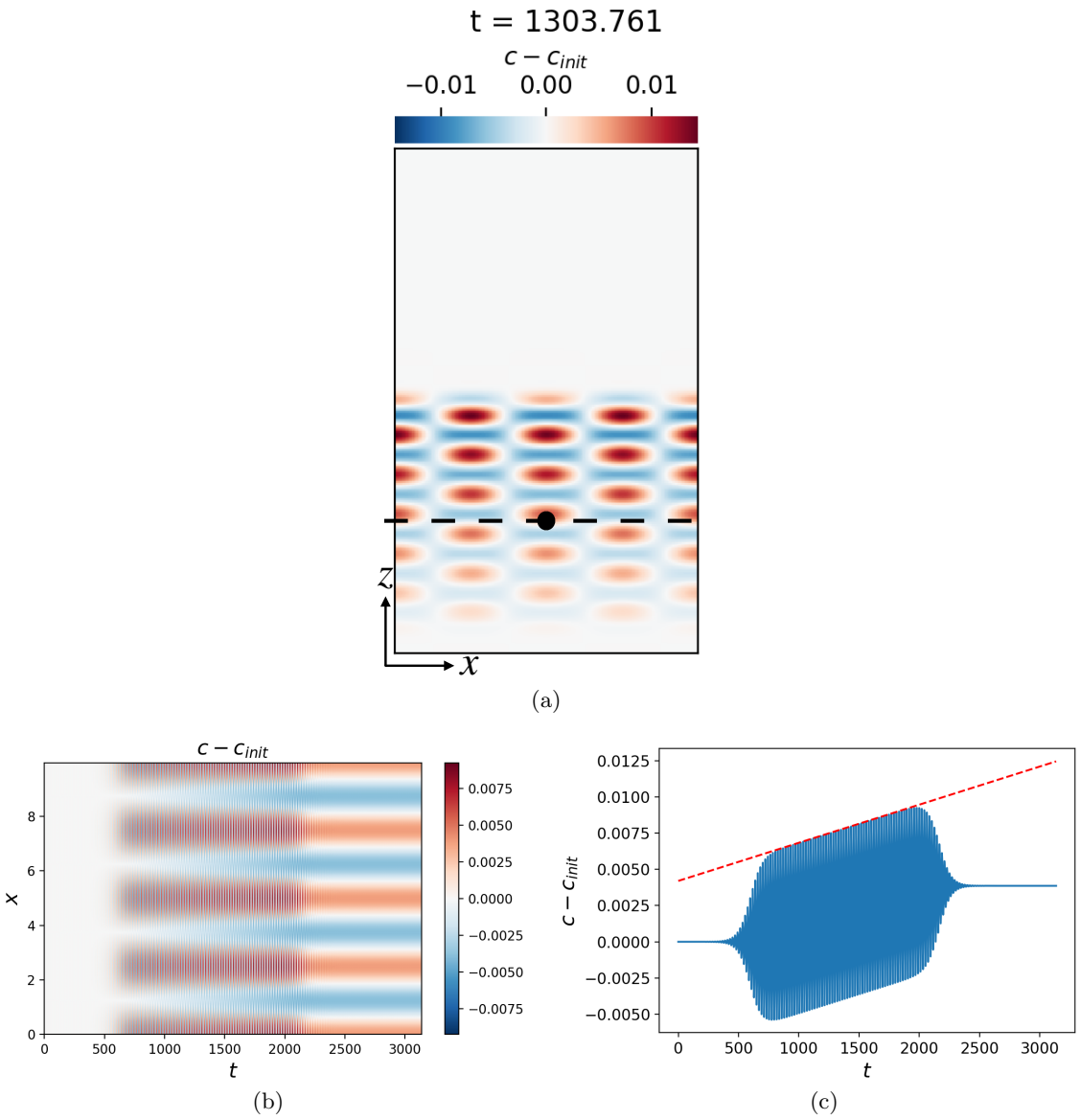

Figure 9: (a) Simulation of the concentration field $c - c_{init}$ at an intermediate time t induced by the linear wave interaction generated using $a = 10^{-4}$, $k_h = \pm 0.4\pi$, $\omega = 0.3$, and diffusivity $\kappa = 10^{-5}$. The black dot indicates the position $x = 5$, $z = 5$ used for further analysis. (b) 2D concentration field at $z = 5$. (c) Comparison of the theoretical prediction for the slow-time component $\partial c_1/\partial \bar{t}$ in (35) (red dashed) with the simulation result at $x = 5$ and $z = 5$ (blue solid).

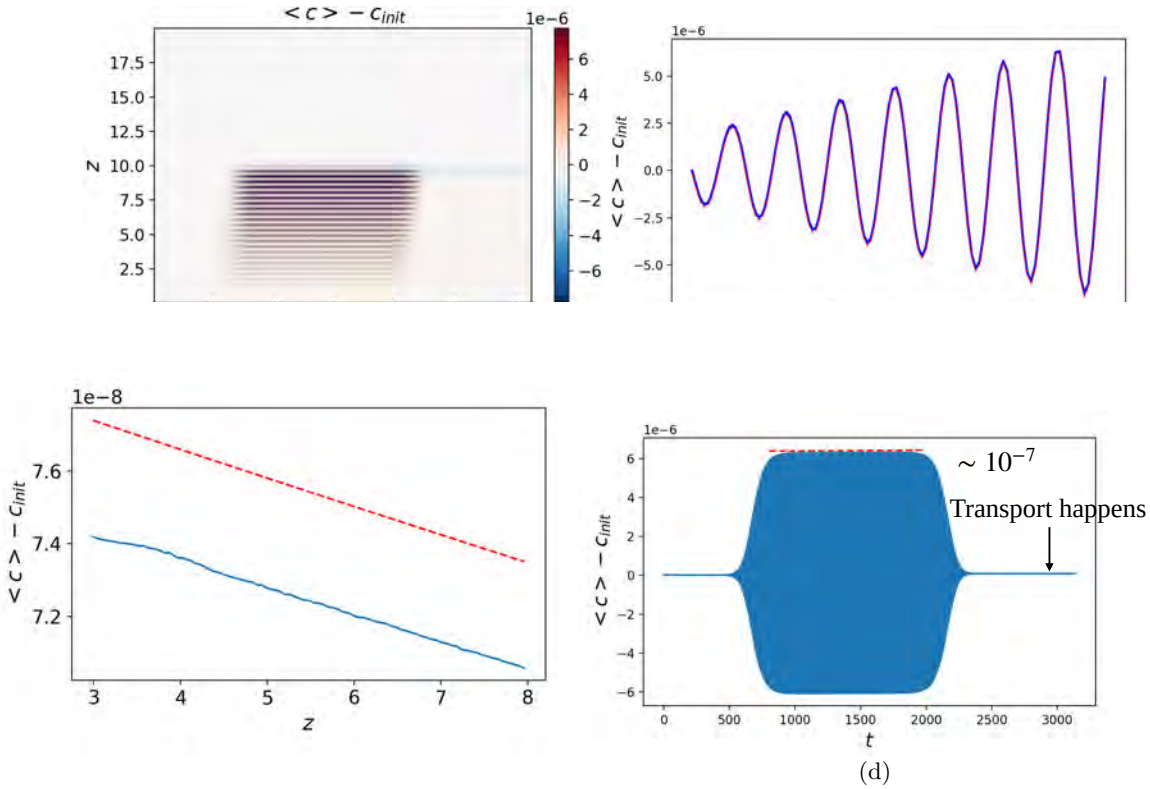

(d)

Figure 10: (a) Evolution of the horizontal mean change $\langle c - c_{init} \rangle$ extracted from the simulation of the linear wave interaction. (b) Comparison of $\langle c - c_{init} \rangle$ at an intermediate time $t = 1500$ (blue solid) with the fast-time component of the theoretical prediction (37) (red dashed), showing the oscillatory behavior. (c) The slow-time component of (37) and net transport of $\langle c - c_{init} \rangle$ at the final time $t = 3000$. (d) Evolution of $\langle c - c_{init} \rangle$ at fixed $z = 5$, with the envelope agreeing with (37).

Figure 10(a) illustrates the change in $\langle c \rangle$ over z and t extracted from the simulation shown in figure 9. To validate our simulation results, we conduct three comparisons with the second-order asymptotic prediction (37). Firstly, by fixing an intermediate time $t = 1500$, we can compare $\langle c \rangle$ with the fast-time component of (37) as shown in figure 10(b). Secondly, in figure 10(c), we fix the final time $t = 3000$ to compare with the slow-time component of (37) and analyze how the net transport changes with z. Finally, by fixing $z = 5$, we compare the slow-time $\langle c_{2s} \rangle$ with the envelope of the change in $\langle c \rangle$ in the simulation, as depicted in figure 10(d).

In summary, the transport in c by the Stokes drift generated from the interaction of two linear plane waves is of order $\mathcal{O}(a^2 t)$ and the vertical transport in $\langle c \rangle$ is of $\mathcal{O}(a^4 t^2)$.

B Chemical diffusivity

Although chemical diffusivity is very small compared to radiative diffusivity in stars and has minor effects on chemical transport, it is still valuable to include it for code validation.

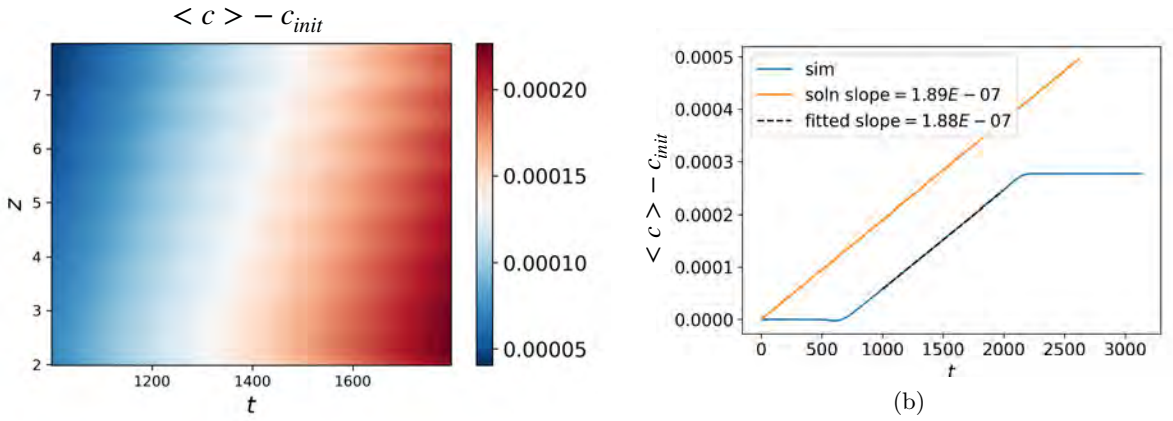

(b)

Figure 11: (a) Evolution of the horizontal mean concentration field $\langle c \rangle - c_{init}$. The transport is driven by a single plane wave with parameters $a = 10^{-4}$, $k_h = 0.4\pi$, $\omega = 0.3$, in the environment of radiative diffusivity $\kappa = 10^{-}5$ and chemical diffusivity $D = 10^{-3}$. (b) Comparison of the simulation result (blue curve) with the solution of the quasilinear decomposition (orange line).

In this section, we use the quasilinear decomposition to incorporate chemical diffusivity and analyze its impact on the transport equations.

We decompose the transport equation into the horizontal mean $c_0(z,t)$ and the fluctuating component $c_1(x,z,t)$

$$\frac{\partial c_0}{\partial t} + \frac{\partial}{\partial z}\langle w c_1 \rangle = 0, \tag{38a}$$

$$\frac{\partial c_1}{\partial t} + w\frac{\partial c_0}{\partial z} = D\nabla^2 c_1, \tag{38b}$$

where D is the chemical diffusivity. We consider only a single plane wave with the vertical velocity given by

$$w = a\cos(k_h x + k_z z - \omega t)e^{-z/\mu}.$$

Using the quasilinear decomposition in section 2.1, we know there is no transport at the leading order c_0 when there is no diffusivity. However, after including chemical diffusivity, we will observe that c_0 changes with time. Assuming an ansatz for $c_1(x,z,t)$:

$$c_1(x,z,t) = \left[\alpha_1 \sin(k_h x + k_z z - \omega t) + \alpha_2 \cos(k_h x + k_z z - \omega t)\right] e^{-z/\mu},$$

where α_1 and α_2 are coefficients to be solved using (38b). Once these coefficients are determined, we can numerically solve for $c_0(z,t)$ from (38a).

We performed the simulation for solving the linearized Boussinesq system with a single plane wave forcing at the boundary $z = 0$ with wave parameters $a = 10^{-4}$, $k_h = 0.4\pi$, and $\omega = 0.3$, and radiative diffusivity $\kappa = 10^{-5}$. The transport equation was incorporated with chemical diffusivity $D = 10^{-3}$. Figure 11(a) shows the simulation result for the horizontal mean of the transport $\langle c(z,t) - c_{init} \rangle$. Transport occurs as $\langle c(z,t) \rangle \sim a$ and accumulates over time. We then extract $\langle c - c_{init} \rangle$ at a fixed location $z = 5$ to compare with the solution obtained from the quasilinear decomposition (38). In figure 11(b), the blue curve

represents the transport observed in the simulation, with the flat platforms indicating the regions before the wave initiation and after the wave termination. We observe that the transport increases linearly over time, with a fitted slope of 1.88×10^{-7}. The solution derived from the quasilinear decomposition (38), shown in orange, exhibits a consistent slope of 1.89×10^{-7}. This agreement between the simulation result and the quasilinear decomposition confirms the validity of the simulation in capturing the transport dynamics.

References

[1] Robert F Stein. Generation of acoustic and gravity waves by turbulence in an isothermal stratified atmosphere. *Solar Physics*, 2:385–432, 1967.

[2] Louis-Alexandre Couston, Daniel Lecoanet, Benjamin Favier, and Michael Le Bars. The energy flux spectrum of internal waves generated by turbulent convection. *Journal of fluid mechanics*, 854:R3, 2018.

[3] Daniel Lecoanet, Matteo Cantiello, Evan H Anders, Eliot Quataert, Louis-Alexandre Couston, Mathieu Bouffard, Benjamin Favier, and Michael Le Bars. Surface manifestation of stochastically excited internal gravity waves. *Monthly Notices of the Royal Astronomical Society*, 508(1):132–143, 2021.

[4] Daniel Lecoanet and Philipp VF Edelmann. Multidimensional simulations of core convection. *Galaxies*, 11(4):89, 2023.

[5] Arthur Le Saux, I Baraffe, Thomas Guillet, Dimitar Georgiev Vlaykov, A Morison, J Pratt, T Constantino, and Tom Goffrey. Two-dimensional simulations of internal gravity waves in a 5 $M_\odot$ zero-age-main-sequence model. *Monthly Notices of the Royal Astronomical Society*, 522(2):2835–2849, 2023.

[6] Adam S Jermyn, Evan H Anders, Daniel Lecoanet, and Matteo Cantiello. An atlas of convection in main-sequence stars. *The Astrophysical Journal Supplement Series*, 262(1):19, 2022.

[7] Evan H Anders, Daniel Lecoanet, Matteo Cantiello, Keaton J Burns, Benjamin A Hyatt, Emma Kaufman, Richard HD Townsend, Benjamin P Brown, Geoffrey M Vasil, Jeffrey S Oishi, et al. The photometric variability of massive stars due to gravity waves excited by core convection. *Nature Astronomy*, 7(10):1228–1234, 2023.

[8] Etienne A Kaiser, Raphael Hirschi, W David Arnett, Cyril Georgy, Laura JA Scott, and Andrea Cristini. Relative importance of convective uncertainties in massive stars. *Monthly Notices of the Royal Astronomical Society*, 496(2):1967–1989, 2020.

[9] Johann Higl, Ewald Mueller, and Achim Weiss. Calibrating core overshooting parameters with two-dimensional hydrodynamical simulations. *Astronomy & Astrophysics*, 646:A133, 2021.

[10] Falk Herwig, Paul R Woodward, Huaqing Mao, William R Thompson, Pavel Denissenkov, Josh Lau, Simon Blouin, Robert Andrassy, and Adam Paul. 3d hydrodynamic simulations of massive main-sequence stars–i. dynamics and mixing of convection and internal gravity waves. *Monthly Notices of the Royal Astronomical Society*, 525(2):1601–1629, 2023.

[11] TM Rogers and JN McElwaine. On the chemical mixing induced by internal gravity waves. *The Astrophysical Journal Letters*, 848(1):L1, 2017.

[12] Ashlin Varghese, Rathish Previn Ratnasingam, Riccardo Vanon, Philipp Valentin Ferdinand Edelmann, and Tamara M Rogers. Chemical mixing induced by internal gravity waves in intermediate-mass stars. *The Astrophysical Journal*, 942(1):53, 2023.

[13] Adam S Jermyn. Nonlinear mixing driven by internal gravity waves. *arXiv preprint arXiv:2209.08344*, 2022.

[14] Michael J Lighthill and James Lighthill. *Waves in fluids*. Cambridge university press, 2001.

[15] Bruce R Sutherland. *Internal gravity waves*. Cambridge university press, 2010.

[16] Geoffrey K Vallis. *Atmospheric and oceanic fluid dynamics*. Cambridge University Press, 2017.

[17] Michael Le Bars and Daniel Lecoanet. *Fluid Mechanics of Planets and Stars*. Springer, 2020.

[18] ME McIntyre. An introduction to the generalized lagrangian-mean description of wave, mean-flow interaction. *pure and applied geophysics*, 118:152–176, 1980.

[19] GL Wagner and WR Young. Available potential vorticity and wave-averaged quasi-geostrophic flow. *Journal of Fluid Mechanics*, 785:401–424, 2015.

[20] George Gabriel Stokes. On the theory of oscillatory waves. *Trans. Cam. Philos. Soc.*, 8:441–455, 1847.

[21] Keaton J Burns, Geoffrey M Vasil, Jeffrey S Oishi, Daniel Lecoanet, and Benjamin P Brown. Dedalus: A flexible framework for numerical simulations with spectral methods. *Physical Review Research*, 2(2):023068, 2020.

[22] Daniel Lecoanet, Dominic M Bowman, and Timothy Van Reeth. Asteroseismic inference of the near-core magnetic field strength in the main-sequence b star hd 43317. *Monthly Notices of the Royal Astronomical Society: Letters*, 512(1):L16–L20, 2022.

[23] Tiffany A Shaw and Theodore G Shepherd. Wave-activity conservation laws for the three-dimensional anelastic and boussinesq equations with a horizontally homogeneous background flow. *Journal of Fluid Mechanics*, 594:493–506, 2008.

Boiling Stratified Flow: A Laboratory Analogy of Atmospheric Convection

Hao Fu

December 29, 2023

1 Introduction

Simulating weather in a beaker is the dream of many generations of scientists. When the first author was a fresh graduate student at Stanford University, Prof. Leif Thomas performed a demonstrative experiment of atmospheric convection using a two-layer configuration with freshwater on salty water and imposed heating from below. The two layers represent the stratosphere and troposphere, respectively. This elegant demonstration, originally designed by Turner [70], still has space to improve - it lacks an important factor in atmospheric convection - moisture. When ascending parcels are cooled by adiabatic expansion, water condensates from vapor to liquid and releases latent heat. This provides extra buoyancy that makes parcels penetrate the stably stratified free troposphere. As a result, in-cloud saturated parcels are unstable, but clear-sky unsaturated parcels are stable, rendering the conditional instability [8]. When a cumulus cloud is deep enough, the re-evaporation of liquid water in the dry atmosphere produces a downdraft. The downdraft brings down dry air and shuts the convection. The updraft and downdraft couplet renders a convective lifecycle [13, 50, 25, 40, 17].

Even though observation and numerical simulation has been the main tool for studying clouds, efforts to simulate clouds in the lab has never stopped. At the cloud microphysics scale, people have been studying particle-laden flow in a cloud chamber, where real droplets and ice interact with turbulence [66]. The dynamics of the whole cloud as an entity, named cloud dynamics, is much harder to reproduce. This is because the lifting condensation requires an apparatus as tall as the scale height of the saturated vapor mixing ratio, which is around 3 km [61]. To study cloud dynamics in the lab, a rule of thumb is finding analogies and being aware that no analogy is complete. There are three perspectives on the nature of moist convection, which guide people to create corresponding experiments.

In the first view, an individual cloud is considered a buoyant plume or bubble driven by a prescribed internal buoyancy source. Candidate sources include chemical reaction heat [69], gas bubbles [72], heating coil [47], and radiation [79]. This setup suits problems where feedback to the heat source can be neglected, e.g., the entrainment process or the circulation response to diabatic heating.

In the second view, moist convection is treated as a hydrodynamic instability, essentially an extension of the Rayleigh-Bénard convection problem to include moisture [7, 58, 14]. Researchers built models of conditional instability, which qualitatively reproduced the length

scale of a cloud system: with narrow ascent and a wide descent [36, 10, 11, 56, 73]. Krishnamurti [35] came up with an experiment of conditional instability using selective radiation absorption of chemicals.

In the third view, people realized that moist convection as a heat transfer mechanism tends to be in a quasi-equilibrium state (QE), especially in the tropics where radiative cooling balances condensation heating [4, 23, 77]. The QE is essentially a highly nonlinear state where conditional instability is self-regulated. It still lacks an experimental analogy. Let's briefly review the boundary layer quasi-equilibrium thinking (BLQE), which is convective quasi-equilibrium in a narrow sense [21, 59]. Whether convection can occur is sensitive to moisture in the boundary layer. Convection induces mixing that brings up moist air and brings down dry air. As a result, the boundary layer moisture is equilibrated by convection, and convection is a "valve" that releases the extra moisture. One open question attracting us is: what controls the vertical mixing near the boundary layer top, and how does it influence the adjustment to equilibrium? Mixing can be undertaken by the entrainment of boundary layer convective cells [38, 18, 4] and the transport by cumulus updraft and downdraft. One intriguing question posed by Thayer-Calder and Randall [68] is how the cumulus updraft and downdraft produce turbulence at the boundary layer top that may *indirectly* influence mixing.

An ideal experiment of cloud dynamics should reproduce both conditional instability and QE. The boiling phenomenon is a candidate that has not been considered seriously. First, the explosive buoyancy production during vaporization is analogous to the threshold-dependent latent heat release in conditional instability. Second, the boiling point is analogous to the humidity or sea surface temperature threshold for deep convection to outbreak [30, 12, 33]. Boiling limits the water temperature around the boiling point by absorbing vaporization heat and mixing the superheated water with the cold water above [15, 54], analogous to QE. However, simply boiling water is still far from an analogy to moist convection because the atmosphere is stratified. Stratification traps the moisture in the boundary layer, making convection intermittent. What about combining boiling with the two-layer convection experiment of Turner [70], making a *boiling stratified flow*? We have only seen studies on the boiling of two layers of immiscible fluids, with potential applications to heating and cooling device [44, 45, 31, 67, 26, 53, 34]. We have not seen research on the boiling of two separate layers of *miscible* fluids, likely because they are too easy to homogenize.

In this report, we use water to mimic the free troposphere and a thin layer of diluted syrup to mimic the atmospheric boundary layer (Fig. 1a). The question to study is:

- How does moist convection favor the entrainment of dry air into the boundary layer?
- How does the dry air influence moist convection?

We let the water temperature represent the atmospheric humidity and let the syrup concentration represent the atmospheric potential temperature. Translating the questions into the context of lab experiments, we ask:

- How do boiling plumes favor the entrainment of cold water into the syrup layer?
- How does the cold water influence boiling?

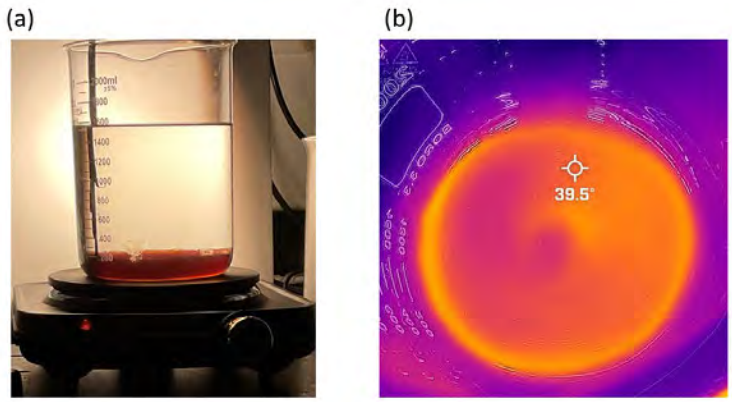

Figure 1: (a) The experimental setup. (b) The temperature map taken by an infrared camera (model: FLIR 435-0004-03-NA), with a few centimeters of water in the breaker. A lighter color denotes a higher temperature.

The report is organized in the following way. Section 2 introduces the experimental setup. Section 3 analyzes the flow evolution of the reference experiment, which inspires a theoretical framework in section 4. Section 5 applies the theory to understand experiments that sample the parameter space. Section 6 extends the theory to study the transition between two types of boiling. Section 7 concludes the report.

2 The Experiment

2.1 Experimental setup

The experimental setup is shown in Fig. 1a. The experimental beaker has a volume of 2000 ml (model: Karter Scientific 213D20), made of 3.3 borosilicate glass. The diameter is 17.48 cm. The beaker is heated on an electric hot plate (model: SUNAV-HP102-D2, 1500 W power for 110 V voltage). The heating power is controlled by a voltage regulator (brand: VEVOR), which has a ± 2 V fluctuation. For the working fluid, we use dark corn syrup (brand: Golden Barrel) with a dextrose equivalent of 42 and a density of $\rho_{s,max} = 1.4 \times 10^3$ kg m^{-3}. We use tap water, which has a density of $\rho_w = 10^3$ kg m^{-3}, as the upper-layer fresh water and for diluting the syrup to the desired concentration.

The system is required to be statically stable at the onset of boiling. The vertical gradient of syrup concentration stabilizes the two-layer configuration against the destabilizing effect of the temperature gradient. The buoyancy b (unit: m s^{-2}) is defined as:

$$b = g\left(\frac{\rho_s - \rho_w}{\rho_w} + \gamma_T T\right) = g\left(-\gamma_s S + \gamma_T T\right), \tag{1}$$

where $S \equiv (\rho_s - \rho_w)/(\rho_{s,max} - \rho_w)$ is the concentration of syrup that ranges from 0 to 1, T (unit: K) is temperature, $\gamma_s \equiv (\rho_{s,max} - \rho_w)/\rho_w = 0.4$ is the syrup concentration coefficient, $\gamma_T \approx 6 \times 10^{-4}$ K^{-1} (taken as the value of 75°C pure water) is the volumetric thermal expansion coefficient of the solution, and $g = 9.8$ m s^{-2} is the gravitational acceleration

constant. At the onset of boiling, the water layer temperature is around 30°C (slightly above the 20°C room temperature), and the syrup layer is around the boiling point (100°C). We let the temperature difference be $\Delta T = 100°\mathrm{C} - 30°\mathrm{C} = 70°\mathrm{C}$. To make the system stable, S must be above a minimum value S_{min}:

$$S_{min} \equiv \frac{\gamma_T \Delta T}{\gamma_s} \approx 0.11. \tag{2}$$

The temperature in the experiment represents the vapor mixing ratio in the atmosphere. Vapor is not only a triggering factor of moist convection but also a component of buoyancy that makes a parcel lighter [76], analogous to the temperature in the experiment that controls boiling and influences buoyancy via thermal expansion. The $(1 - S)$ in the experiment represents the potential temperature in the atmosphere, which increases with height. As the initial S of all our experiments is much larger than S_{min}, the buoyancy from syrup plays the dominant role.

Why use syrup? This is because syrup has a higher density than water and relatively high viscosity. Both effects suppress interfacial heat and mass transfer [71], enabling the syrup layer to reach the boiling point before the two-layer stratification is eroded by turbulence. The kinematic viscosity of syrup increases approximately exponentially with its concentration (Table A1.8 of [43]). We have tried a sodium chloride (NaCl) solution, whose saturated density is around 1.15×10^3 kg m^{-3}. Even for a nearly saturated NaCl solution, the two-layer stratification is eroded before boiling due to its much smaller viscosity than syrup. The high viscosity does not have a direct analogy to the atmosphere. It might be thought of as an amplifier of the stratification effect.

The other point to note is that the phenomenon is sensitive to the geometry of the beaker. Ideally, we need a beaker whose bottom is not uniformly heated and permits local superheating. For our beaker, heating is strongest on a ring near the lateral boundary (Fig. 1b). This steady heating ring produces large bubbles that mix efficiently, leading to intermittent boiling. We have tried a 3000 ml beaker from another brand (model: ULAB, UBG1029) with a more uniform surface and an electric kettle with a perfectly uniform metal surface (model: COSORI, GK172-CO). They steadily produce tiny bubbles, a regime to be classified as steady boiling in section 6. Because we are particularly interested in the intermittent boiling regime, which is relevant to cumulus convection, we decided to use the beaker with a more nonuniform surface. Despite the sensitivity to the container, once we stick to the beaker, the experimental result is quite robust.

Video and temperature are recorded, with the video information for quantitative comparison and temperature information for qualitative reference. The illumination is provided by a desk lamp diffused by a 3 mm white acrylic sheet. The light transmitted through the beaker is recorded by a cell phone camera (model: iPhone 11). The temperature is recorded with four K-type thermocouples (model: NUZAMAS) plugged into a temperature recorder (model: Gain Express). According to the manufacturer of the temperature recorder, the temperature resolution is 0.1 °C, and the accuracy is $\pm(1°\mathrm{C} + 0.3\%\mathrm{rdg})$ between 18 °C and 28 °C. The four sensors are bound by heat-shrink tubes and fixed to a portable retort stand. The sensors are located at $z = 1$ cm, 3 cm, 5 cm, and 7 cm above the bottom of the beaker. Only the $z = 1$ cm and 5 cm temperature data are used in this report.

2.2 Experimental procedure

First, we add 1400 ml of tap water to the beaker. Then, we use an injector to manually add syrup to the bottom of the beaker. The injecting process unavoidably causes mixing and dilutes the syrup. As a rule, the injection stops when the syrup layer reaches the desired height, even if the injected syrup is less than expected. The syrup "saved" due to mixing is typically $< 25\%$ of the expected injection volume. To reduce mixing, it is critical to work slowly (usually longer than 1 minute), avoid wiggling, and push the injector's piston continuously rather than intermittently. Once the two-layer stratification is set, we use a portable resonant density meter (model: Anton Paar, DMA 35) to measure the syrup density near the bottom of the beaker.

Second, we move the beaker onto the heating pad and put the temperature sensor array into it. Then, we turn on the heating pad, which is at its maximum level. The level controls the temperature of the heating pad. The power is automatically shut off when the temperature reaches an unknown desired temperature. The power rarely shuts off in the experiments, so the heating power is approximately fixed and controlled by the voltage regulator. In a specially designed experiment with 86 V heating, 1000 ml of water, and the beaker's top capped by a plastic membrane to insulate heat, the surface heat flux at the bottom of the beaker is measured to be around 19 kW m^{-2}.

Third, after an experiment is finished, we cool down the heating pad to be close to the room temperature before starting another experiment. An experimental cycle takes around two hours.

2.3 Experimental list

Several parameters govern the system:

1. The surface heating flux F_s. It is analogous to the solar heating power in the atmosphere.

2. The syrup layer thickness h_0. It is analogous to the atmospheric convective boundary layer thickness.

3. The syrup concentration S_0. It is analogous to the atmospheric stratification strength near the boundary layer top.

4. The water layer thickness. It is analogous to the tropospheric depth.

We decided to leave the investigation on the water layer thickness for future work by keeping it around 14 cm, which is much thicker than the convective penetration height. We performed four groups of experiments that changed F_s (F1-F5), h_0 (T1-T7), S_0 (S1-S7), and S and h_0 together (ST1-ST4), as shown in Table 1. Note that the labels (F3, S5) and (T7, ST2) share the same experiments. Experiment S3 is the reference experiment that will be analyzed in detail.

Note that S_0 or h_0 cannot be precisely aligned in an experimental group due to the fluctuation introduced in preparing the two-layer fluid. We strive to align them and report the measured values in Table 1. The S_0 and h_0 are measured with the density meter and the video (using a pixel-to-length scale).

Table 1: A table of experimental parameters, which include heating voltage, surface heat flux F_s, initial syrup density ρ_s, initial syrup concentration S_0, initial syrup thickness h_0. The post-boiling syrup thickness h_1 is shown in the rightmost column, with the diagnostic procedure introduced in section 5.1. For experiments in the steady boiling regime (section 5.4), their h_1 is denoted as "-". The experiments shared by different groups are marked with brackets.

Name	Voltage (V)	F_s (kW m^{-2})	ρ_s ($\times 10^3$ kg m^{-3})	S_0	h_0 (cm)	h_1 (cm)
F1	50	6.4	1.188	0.47	2.00	5.84
F2	60	9.3	1.190	0.48	2.10	5.45
F3 (S5)	86	19.0	1.184	0.46	2.05	4.35
F4	100	25.7	1.205	0.51	1.93	4.35
F5	120	37.0	1.197	0.49	1.80	3.52
S1	86	19.0	1.070	0.18	1.76	1.98
S2	86	19.0	1.112	0.28	1.83	4.74
S3	86	19.0	1.124	0.31	1.91	5.48
S4	86	19.0	1.138	0.35	1.96	5.32
S5 (F3)	86	19.0	1.184	0.46	2.05	4.35
S6	86	19.0	1.218	0.54	1.94	4.13
S7	86	19.0	1.272	0.68	1.89	4.04
T1	86	19.0	1.205	0.51	0.80	4.19
T2	86	19.0	1.203	0.51	1.20	3.90
T3	86	19.0	1.199	0.50	1.50	4.14
T4	86	19.0	1.218	0.54	1.94	4.13
T5	86	19.0	1.211	0.53	2.64	4.74
T6	86	19.0	1.204	0.51	3.40	5.24
T7 (ST2)	86	19.0	1.204	0.51	4.13	-
ST1	86	19.0	1.204	0.51	3.40	5.24
ST2 (T7)	86	19.0	1.204	0.51	4.13	-
ST3	86	19.0	1.136	0.34	4.08	6.61
ST4	86	19.0	1.133	0.33	4.74	-

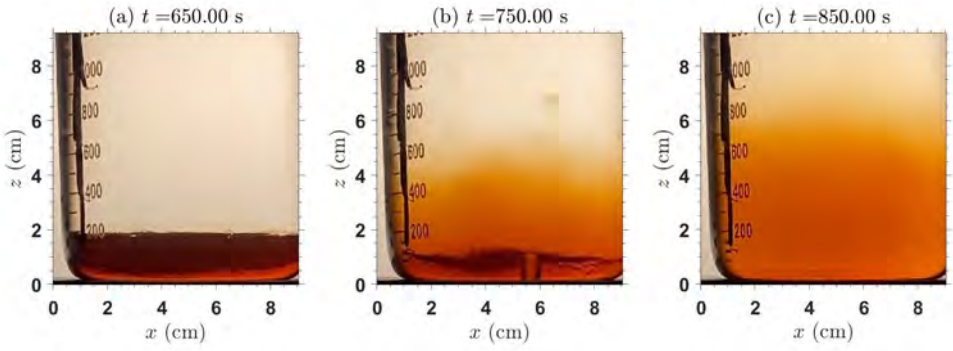

Figure 2: The flow snapshots at $t = 650$ s, 750 s, and 850 s of the reference experiment (S3), showing the initial two-layer stage, the boiling stage, and the post-boiling two-layer stage.

3 Basic Physics

We let S3 be the reference experiment for demonstrating the basic physics of boiling stratified flow. Figure 2 shows that the flow has three stages: the initial two-layer stage, the boiling stage, and the post-boiling two-layer stage.

Before boiling starts, the syrup layer temperature gradually rises, and the water layer temperature remains close to the initial temperature (Fig. 3a). This is because density stratification suppresses heat transfer by suppressing eddy mixing [70]. Boiling begins at around $t = 700$ s by which the syrup temperature reaches 100 °C (Fig. 3b). Bubbles erupt from the bottom and mostly quench before leaving the syrup layer (Fig. 2b). This is because the upper part of the syrup is still below the boiling point. It can be viewed as a sub-cooled nucleate boiling phenomenon (section 4.4.4 of [15]), with the sub-cooling substantially amplified by the two-layer stratification. Though the bubble quenches, its momentum can drive a vortex ring that rises into the freshwater layer and mixes with freshwater and sediments on the interface, producing a middle mixed layer. The middle mixed layer can also be produced by a bubble plume penetrating a two-layer stratification interface [49].

Boiling only lasts about 1 minute, during which the $z = 1$ cm temperature drops to 60°C and the $z = 5$ cm temperature slightly rises (Fig. 3b). The bubble-induced mixing brings cold freshwater to the syrup layer and quenches boiling. Such a self-regulating behavior is analogous to moist convection on Earth and gas giants [25, 78, 37, 28]. At $t = 850$ s, the system still has kind of a two-layer stratification, but the interface rises from the initial 2 cm to 6 cm, and the syrup layer is significantly diluted (Fig. 3c).

Next, we use the horizontally averaged video pixel value to track the interface height, denoted as h. The printed scale of the beaker is excluded from the averaging slot. The video records the pixel values of red, green, and blue light. Because the syrup appears red, the red light is more transmissible than the green and blue light. As the interface is essentially an outline of the syrup layer, we use the less transmissible green light. Figure 3c shows boiling significantly lifts the interface from the initial value h_0 to a post-boiling value h_1.

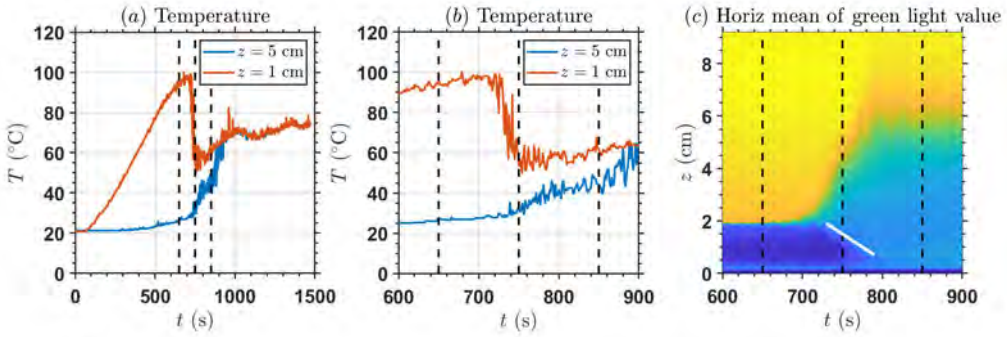

Figure 3: Quantitative measurements of the reference experiment (S3). (a) The temperature time series at $z = 5$ cm (blue line) and $z = 1$ cm (red line). The dashed black lines denote $t = 650$ s, 750 s, and 850 s, where the snapshots in Fig. 2 are taken. The origin of the time coordinate is the heating start time. (b) The same as (a), but zooming into the boiling slot. (c) The zoom-in time evolution of the video's horizontally averaged green light pixel value. The solid white line annotates the internal interface between the bottom and middle mixed layer.

Thus, boiling can be viewed as a mixing event. We ask:

- What controls the boiling duration time Δt?
- What controls the interface's rising rate dh/dt?

With Δt and dh/dt, we will be able to predict the net effect of mixing: $h_1 - h_0$,

$$h_1 - h_0 \approx \Delta t \frac{dh}{dt}. \tag{3}$$

A closer look at the green light pixel value (Fig. 3c) shows an internal interface between the bottom and middle mixed layers. The internal interface splits from the outer interface at the onset of boiling and touches the bottom at the end of boiling. The vortex rings carry syrup from the bottom mixed layer and deposit it in the middle mixed layer. Thus, the bottom mixed layer gets thinner and finally disappears, letting the relatively cold middle mixed layer touch the bottom and quench the boiling. This indicates Δt is essentially the time needed for vortex rings to eliminate the bottom mixed layer:

$$\Delta t \approx \frac{h_0}{\overline{w_+}}, \tag{4}$$

where $\overline{w_+}$ (unit: m s^{-1}) is the horizontally averaged syrup volume flux across the internal interface, analogous to the mass flux of atmospheric convection [4]. The $\overline{w_+}$ ultimately depends on the surface heating rate.

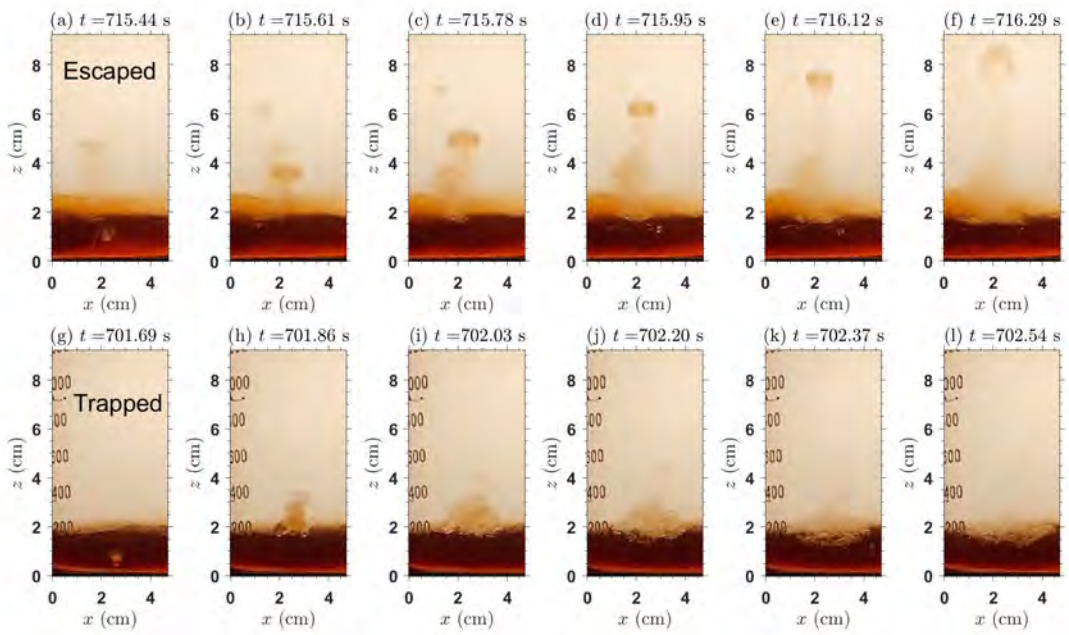

Figure 4: Examples of the vortex ring's two life paths, using the reference experiment S3. The first row shows an escaping vortex ring, and the second row shows a trapped vortex ring, with a time interval of 0.17 s.

4 A Theoretical Framework

This section builds a theoretical framework of how $h_1 - h_0$ depends on the system's control parameters, e.g., F_s, h_0, and S_0. Modeling dh/dt is equivalent to modeling the ensemble effect of vortex rings, which comes down to modeling the mixing of individual vortex rings and their nonlinear interaction. The mixing by individual vortex rings has been investigated by Olsthoorn and Dalziel [51], but the nonlinear interaction has not been addressed. The boiling stratified flow provides a unique setup to study this fundamental problem.

4.1 The two life paths of vortex ring

By inspecting the video, we identified two typical life paths of vortex rings: escaping and trapping. The first row of Fig. 4 shows an example of escaping. The bubble quenches in the syrup layer, leaving a vortex ring that rises into the water layer and sinks. The second row of Fig. 4 shows an example of trapping. The initial bubble has a similar size to the escaping case, but the vortex ring crashes near the interface, producing a wide turbulent patch. The two paths are summarized in Fig. 5. The escaping path has a relatively long mixing length, characterized by the vortex ring's penetration depth l. The trapping path, however, has a shorter mixing length, and its ability to bring down cold water is limited. Thus, we speculate that the escaped vortex rings are mainly responsible for the thickening of the middle mixed layer.

We define the escape ratio E to quantify the fraction of the vortex rings that could

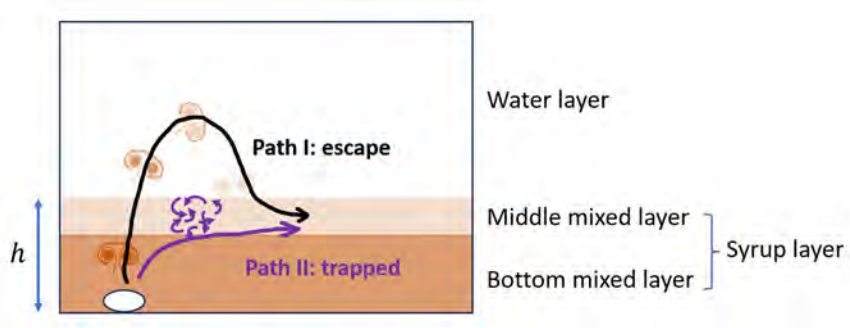

Figure 5: A schematic diagram of two life paths of a vortex ring: escaping and trapping.

escape the middle mixed layer and rise into the water layer. What determines E? We hypothesize that the stratified turbulence on the path of a vortex ring causes trapping. The turbulence can be induced by the wake of ascending vortex rings [32] or the baroclinic vorticity generated at the interface [52]. The turbulence could tilt the orientation of the vortex ring, causing an oblique incidence onto the interface. The experiments of Pinaud [57] showed that an oblique incidence could significantly tilt the vortex ring and turn it horizontal due to the interaction between the vortex ring and the baroclinically generated vorticity at the interface. Because a smaller vortex ring is more easily tilted by an eddy, and a thicker syrup layer (h_0) increases the chance of tilting, we heuristically parameterize E as:

$$E = e^{-\frac{C_E h_0}{R}}, \tag{5}$$

where C_E is a nondimensional escaping parameter depending on the turbulent kinetic energy in the syrup layer. In section 4.3, C_E will be shown to be equivalent to a drag coefficient.

We further hypothesize that C_E is smaller for a higher F_s because stronger surface heating reduces the time interval between vortex rings. The turbulent wake of the current vortex ring could trap the next one, causing stronger turbulence and, therefore, a pileup of vortex rings. This hypothesis will be tested in section 5 where experiments with different F_s are introduced.

4.2 The vortex ring penetration depth l

A hotter surface temperature generally increases the initial bubble radius R in boiling [5]. A bubble is highly buoyant but quenches (condensates) quickly once it leaves the hot bottom. A hotter fluid interior makes the bubble condensate more slowly and yields a longer acceleration path h_* for buoyancy. Combining these arguments, we see that h_* should increase with the bubble radius. For simplicity, we assume:

$$h_* \approx \beta R, \tag{6}$$

where β is a nondimensional bubble acceleration coefficient. The bubble exerts pressure on the environment and accelerates the surrounding liquid. The added mass theory [24] indicates that for a spherical bubble, the surrounding liquid moving with the bubble has

half of its volume (Fig. 6). Ignoring the mass of vapor, the mean density of the bubble and the surrounding liquid is approximately $\frac{2}{3}\rho_w$. The initial velocity of the vortex ring, w_0, is estimated with a free-fall scaling:

$$w_0 \approx \left(2\frac{2}{3}gh_*\right)^{1/2}. \tag{7}$$

After the bubble quenches, the moving liquid turns into a vortex ring of radius R.

Let's make a force analysis of an escaped vortex ring and let its vertical velocity be w. In the syrup layer, the vortex ring has neutral buoyancy, only influenced by drag:

$$\frac{dw}{dt} = -\frac{C_D}{R}w^2, \quad w|_{t=0} = w_0, \tag{8}$$

where C_D is the nondimensional drag coefficient. This drag parameterization is taken from Maxworthy [41], which is also used in modeling the drag of thermals in clouds [62, 63]. It works for a turbulent vortex ring. Let us estimate the Reynolds number Re of our problem. Most of our experiments use $S_0 \lesssim 0.6$ with a kinematic viscosity of $\nu \lesssim 10^{-5}$ m^2 s^{-1} (Table A1.8 of Mohos [43]). Combining the ν with $w \sim 0.05$ m s^{-1} and $R \sim 0.01$ m (Fig. 4), we find $\mathrm{Re} = wR/\nu \gtrsim 50$. Because $\mathrm{Re} \gg 1$, this estimation confirms that the vortex ring is turbulent. When the vortex ring rises to the water layer, the vortex ring is influenced by both drag and negative buoyancy:

$$\frac{dw}{dt} = -\frac{C_D}{R}w^2 - g\gamma_s S \approx -g\gamma_s S. \tag{9}$$

For simplicity, we only consider the buoyancy effect after the vortex ring has escaped because the vortex does not have a maximum height without considering buoyancy. The buoyancy is assumed to be controlled by S, as discussed in section 2.1.

We can solve for the kinetic energy of the vortex ring when it crosses the interface and the negative buoyancy work done in the water layer. They are linked with the interface crossing velocity w_+:

$$\frac{2}{3}gh_* e^{-\frac{2C_D h_0}{R}} = \frac{w_+^2}{2} = g\gamma_s S l. \tag{10}$$

Equation (10) yields an expression for the vortex ring penetration depth l:

$$l = \frac{2}{3}\frac{h_*}{\gamma_s S_0}e^{-\frac{2C_D h_0}{R}}. \tag{11}$$

The theory predicts that a more diluted syrup (smaller S_0) makes the vortex ring lighter and penetrates a longer distance. A thicker syrup layer (higher h_0) induces more accumulated drag and reduces l.

4.3 The post-boiling syrup layer thickness h_1

The dh/dt depends on detrainment and entrainment across the syrup-water interface. Detrainment denotes the mass leaving the syrup layer, and entrainment denotes the mass

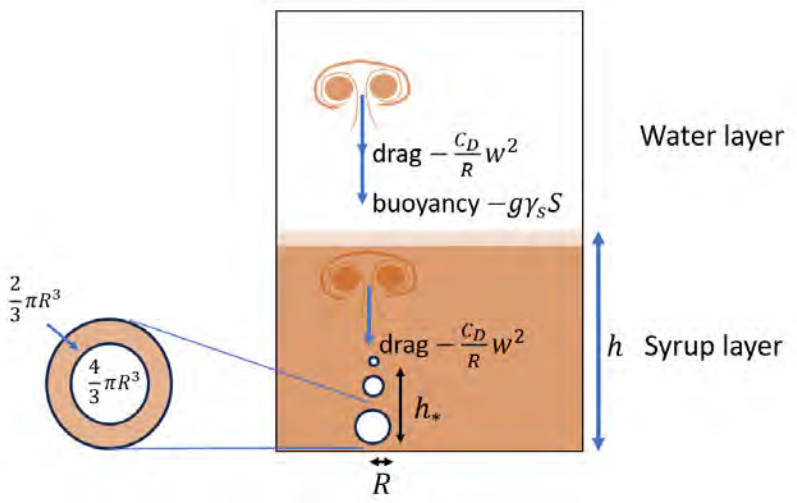

Figure 6: A schematic diagram of the vortex ring initiation and development processes. The syrup layer includes both the bottom and middle mixed layers.

entering the syrup layer. Vortex rings detrain first and then entrain. There is some net mass gain, which is related to the vortex ring's fractional entrainment rate ε (unit: m^{-1}), escape ratio E, mean volume flux $\overline{w_+}$, and the penetration depth l:

$$\frac{dh}{dt} = \underbrace{-E\overline{w_+}}_{\text{detrain}} + \underbrace{E\overline{w_+}e^{2\varepsilon l}}_{\text{entrain}} \approx 2\varepsilon E\overline{w_+}l, \tag{12}$$

where $e^{2\varepsilon l}$ is the volume expansion factor of a vortex ring, and we have used $e^{2\varepsilon l} \approx 1 + 2\varepsilon l$. Following Morton et al. [46], the ε is expressed as:

$$\varepsilon = \frac{2\alpha}{R}, \tag{13}$$

where α is the nondimensional entrainment coefficient.

Our model is consistent with the experimental result of Olsthoorn and Dalziel [51], who studied successive vortex rings impinging onto a stratification interface. Their experiments showed the ratio of net entrainment to detrainment, essentially the $e^{2\varepsilon l} - 1$ factor in our formulation, is proportional to Ri^{-1}. Here, Ri is the bulk Richardson number that obeys:

$$\mathrm{Ri} \equiv g\frac{\rho_s - \rho_w}{\rho_w}\frac{R}{w_+^2} = g\gamma_s S_0 \frac{R}{w_+^2}, \tag{14}$$

which shows $\mathrm{Ri} \propto S_0$. Substituting the expression of l (11) into $e^{2\varepsilon l} - 1$, we get:

$$e^{2\varepsilon l} - 1 \approx 2\varepsilon l \propto S_0^{-1} \propto \mathrm{Ri}^{-1}, \tag{15}$$

which explains the Ri^{-1} scaling of their measured entrainment rate.

Next, we apply the knowledge of an individual vortex ring to understand the collective effect of many vortex rings, i.e., the interface rising. Combining (3), (4), (5), (11), (12), and

(13), we obtain the expression of h_1:

$$h_1 = h_0 \left(1 + \frac{8}{3}\frac{\alpha\beta}{\gamma_s S_0} e^{-\frac{2C_D + C_E}{R} h_0}\right). \tag{16}$$

Note that the mean vertical volume flux of vortex rings, $\overline{w_+}$, is eliminated. The expression of h_1 has two uncertain nondimensional parameters:

1. $\alpha\beta$, the product of the entrainment parameter α and the bubble acceleration parameter β.

2. The effective drag coefficients $2C_D + C_E$, representing the bulk effect of the physical drag and the trapping by turbulence.

We still need to parameterize the vortex ring radius R to close the theory of h_1.

4.4 The bubble radius R

The R is the "cloud radius" in this experiment, which depends on how superheated the syrup layer is. We let the syrup layer temperature be T, and the boiling point be $T_* = 100°\mathrm{C}$. When $T \ll T_*$, there is no boiling, so $R = 0$. When $T \gtrsim T_*$, the water is superheated, and Narayan et al. [48] showed that R has an upper bound with respect to $T - T_*$, which we take as R_m. Thus, we parameterize R as an error function of $T - T_*$:

$$R = R_m \frac{1}{2}\left[1 + \mathrm{erf}\left(\frac{T - T_*}{\delta T_*}\right)\right], \tag{17}$$

where δT_* is the temperature range of the transition zone.

The T depends on the heat balance of the syrup layer, which involves the surface heat flux F_s, the ventilation by the interfacial heat transfer, and the vaporization and mixing caused by boiling. For simplicity, we use the equilibrium temperature without considering boiling to approximate T:

$$\frac{dT}{dt} \approx \underbrace{\frac{F_s}{\rho_w c_w h_0}}_{\text{surface heating}} - \underbrace{\frac{T - T_w}{h_0} w_i}_{\text{ventilation}} \approx 0, \tag{18}$$

where ρ_w is the density of pure water, c_w is the specific heat of pure water ($\rho_w c_w$ could approximately represent the volumetric heat capacity of syrup solution, see Table A1.8 of [43]), w_i is the characteristic eddy vertical velocity at the syrup-water interface, and T_w is the water temperature that is around the room temperature. One might be concerned that T could be unrealistically large without considering the cooling by mixing. We argue its consequence is limited because T only controls the bubble radius R, an error function of T with an upper bound. The R is only sensitive to T where the superheating is weak and boiling is not vigorous. Thus, an overestimation of T in the vigorously boiling regime yields little error in R.

Equation (18) shows that T depends on w_i, with more efficient ventilation reducing T. What determines w_i? The syrup-layer eddy is driven by convection. It is analogous to

Rayleigh-Bénard convection (RBC), with the beaker's bottom as the warm plate and the syrup-water interface as the cold plate. In our setup, the Rayleigh number (Ra) and Nusselt number (Nu) are defined as:

$$\mathrm{Ra} \equiv \frac{g\gamma_T(T - T_w)h_0^3}{\nu\kappa}, \quad \mathrm{Nu} \equiv \frac{w_i}{\kappa/h_0}, \tag{19}$$

where ν is the kinematic viscosity and κ is the thermal diffusivity. The Ra represents the relative strength of convective instability and the diffusive damping. The Nu represents the ratio of convective to conductive heat transfer. For the regime where the heat transfer is diffusive in the boundary layer of RBC (a thin layer attached to the beaker's bottom) and turbulent in the syrup interior, Nu obeys:

$$\mathrm{Nu} \approx c\mathrm{Ra}^{1/3}, \tag{20}$$

where $c = 0.085$ is an empirical factor reported in [70]. Substituting (19) into (20), we obtain an expression of w_i:

$$\begin{aligned} w_i \quad &= c\mathrm{Ra}^{1/3}\frac{\kappa}{h_0} \\ &\approx c\left[\frac{g\gamma_T(T_* - T_w)}{\nu\kappa}\right]^{1/3}\kappa. \end{aligned} \tag{21}$$

The w_i depends on $T - T_w$, ν, and κ. Physically, T should be around T_* for most situations of interest, so we let $\Delta T \equiv T_* - T_w \approx T - T_w$ and consider it a fixed quantity. For syrup, κ is insensitive to S_0 (Table A1.9 of [43]). However, ν is very sensitive to S_0 and approximately obeys an exponential function (Table A1.8 of [43]):

$$\nu \approx \nu_w e^{\frac{S}{S_\nu}}, \tag{22}$$

where ν_w (unit: $\mathrm{m}^2\ \mathrm{s}^{-1}$) is the reference kinematic viscosity of water and S_ν is the critical syrup concentration to feel the change of viscosity. Substituting (22) into (21), we get:

$$w_i = w_{i,ref}e^{-\frac{S}{3S_\nu}}, \quad w_{i,ref} = c\left[\frac{g\gamma_T(T_* - T_w)}{\nu_w}\right]^{1/3}\kappa^{2/3}, \tag{23}$$

where $w_{i,ref}$ is a reference convective velocity scale for $S_0 = 0$ (water). Equation (23) indicates that a denser syrup suppresses heat transfer.

Equation (23) shows the heat transfer ability of RBC, and (18) shows the requirement on w_i to make the syrup-layer temperature steady without boiling. Combining them yields a critical w_i and, therefore, a critical S_0 for boiling, S_*:

$$S_* = 3S_\nu \ln\left[\frac{\rho_w c_w(T_* - T_w)w_{i,ref}}{F_s}\right]. \tag{24}$$

For $S > S_*$, convective heat transfer is too weak to keep the syrup temperature steady, and boiling must occur. Substituting (24) into (18), we obtain the relationship between

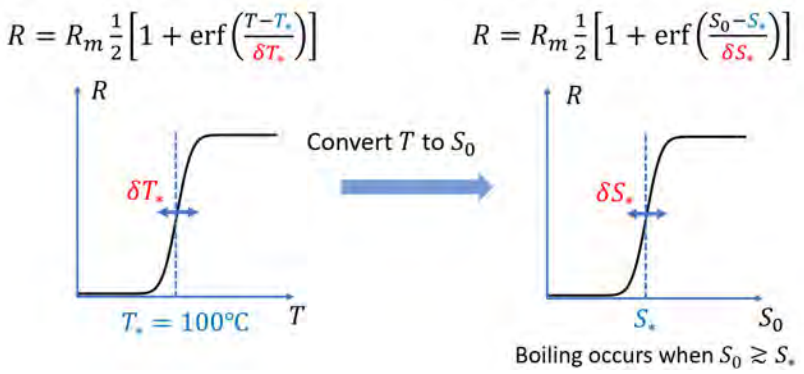

Figure 7: A schematic diagram for the parameterization of the bubble radius R as a function of T, which is ultimately linked to S_0.

supercritical syrup concentration $(S_0 - S_*)$ and the superheated temperature $(T - T_*)$:

$$\begin{aligned} T - T_* &= \frac{F_s}{\rho_w c_w w_{i,ref}} e^{-\frac{S_0}{3S_\nu}} - \Delta T \\ &= \left(e^{\frac{S_0 - S_*}{3S_\nu}} - 1\right) \Delta T \\ &\approx \frac{S_0 - S_*}{3S_\nu} \Delta T, \end{aligned} \tag{25}$$

which indicates a denser syrup increases the superheating by increasing viscosity and suppressing heat transfer.

Substituting (25) into (17), we express R as a function of S_0:

$$R \approx R_m \frac{1}{2}\left[1 + \mathrm{erf}\left(\frac{S_0 - S_*}{\delta S_*}\right)\right], \quad \delta S_* \equiv 3S_\nu \frac{\delta T_*}{\Delta T}, \tag{26}$$

where δS_* is the width of the transition zone for the initial syrup concentration. Equation (26) indicates that a denser syrup makes bubbles larger. The conversion from R vs. T relation to R vs. S_0 relation is illustrated in Fig. 7.

Equations (16) and (26) render a closed theory of how h_1 depends on h_0 and S_0:

$$h_1 = h_0 \left[1 + \frac{8}{3}\frac{\alpha\beta}{\gamma_s S_0} \exp\left(-\frac{h_0}{h_{DE}} \frac{2}{1 + \mathrm{erf}\left(\frac{S_0 - S_*}{\delta S_*}\right)}\right)\right]. \tag{27}$$

Here, h_{DE} is the vortex ring dissipation length scale:

$$h_{DE} \equiv \frac{R_m}{2C_D + C_E}, \tag{28}$$

which represents the bulk effect of drag and trapping. The system has four uncertain parameters: $\alpha\beta$, h_{DE}, δS_*, and S_*. In section 5, we validate the theory using experiments with varying F_s, S_0, and h_0.

5 Validation of the Theory

This section analyzes the h_1 diagnosed from horizontally averaged green light pixel value and applies it to validate the theory. We first introduce the diagnostic method and then discuss experiments with varying F_s, S_0, and h_0.

5.1 Diagnosing the post-boiling interface height

The diagnosis has two steps. First, we identify the syrup-water interface, essentially the top of the middle mixed layer. At each time snapshot, we vertically smooth the image pixel value with a Gaussian filter whose stencil spans 20 pixels. The width of a pixel depends on the distance of the camera to the beaker, which is around 0.03 cm. The height where the vertical gradient of the smoothed pixel value is the largest is identified as the interface. This operation renders a time series of the interface height, $h(t)$, shown as the solid black line in Fig. 8.

Second, we identify the boiling start time. We make a temporal Gaussian filter on $h(t)$ with a stencil of 20 snapshots (a time span of 101.8 s) and denote it as $\widetilde{h}(t)$. The initial value of $\widetilde{h}(t)$ is taken as h_0. The boiling start time is taken as the time by which $\widetilde{h}(t)$ first rises above $1.1h_0$.

Third, we identify the boiling end time using $\widetilde{h}(t)$. We build a moving window spanning 20 snapshots (101.8 s) and move it from the boiling start time. The range (maximum minus minimum) of $\widetilde{h}(t)$ in the window gradually decreases as the window approaches the post-boiling stage. We let the time by which the range first drops below 0.3 cm as the boiling end time and denoted it as h_1. The h_1 is shown as the dashed red line in Figs. 8 and summarized in Fig. 9. There are two exceptions. One is experiment S1 (Fig. 8f), where no significant boiling occurs, and the system directly transitions to a well-mixed state after a long time (about 1400 s). The h_1 is taken as h_0. The other is experiment T7 (Fig. 8s), where boiling is steady, and no boiling end time is found.

5.2 Experiments with varying F_s

The different surface heat fluxes (F_s) simulate the effect of different solar radiative heating rates on the atmospheric boundary layer. The theory (27) shows that F_s influences h_1 in two competing ways:

1. A higher F_s reduces the critical syrup concentration necessary to initiate boiling, S_*. It should make bubbles larger and increase h_1.

2. A higher F_s reduces the time interval between vortex rings and increases the turbulence intensity in the syrup layer. It should reduce C_E, trap more vortex rings, and reduce h_1.

For the experimental results, h_1 is generally smaller for a larger F_s (Fig. 8). It indicates that the enhanced trapping should be an important factor. For future work, we plan to perform quantitative modeling of how C_E depends on F_s, which involves a careful analysis of vortex ring interaction.

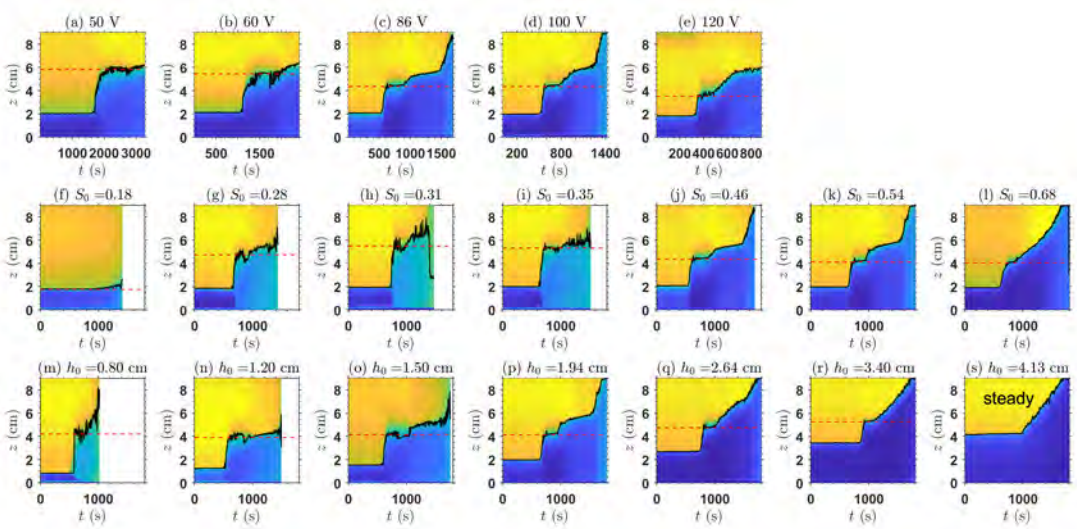

Figure 8: Evolution of the syrup layer thickness shown with the horizontally averaged green light pixel value of the video. The first row shows experiments F1-F5, where F_s is changed by varying the heating voltage. The solid black lines show the diagnosed height of the syrup-water interface. The dashed red lines show the diagnosed h_1. The second row is for experiments S1-S7 that change the initial syrup concentration S_0. The third row is for experiments T1-T7 that change the initial syrup thickness h_0. The T7 experiment is in the steady boiling regime without a well-defined h_1.

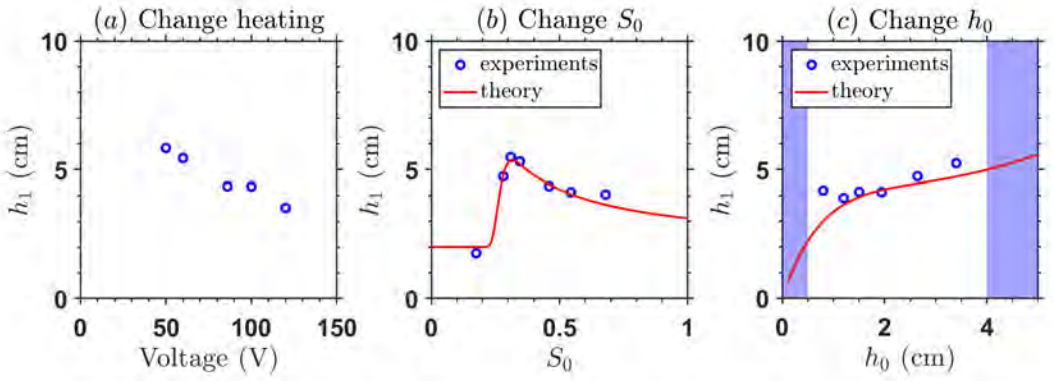

Figure 9: The post-boiling interface height h_1 of (a) experiments F1-F5 that change the surface heat flux by changing the heating voltage, (b) experiments S1-S7 that change the initial syrup concentration S_0, and (c) experiments T1-T7 that change the initial syrup thickness h_0. The blue circles denote the experimental data, and the solid red lines denote the theoretical prediction. The blue shadings show the $h_0 < 0.5$ cm regime where the post-boiling state lacks a clear interface, and the $h_0 > 4$ cm regime where the boiling is steady.

5.3 Experiments with varying S_0

The initial syrup concentration (S_0) is analogous to the atmospheric stratification near the boundary layer top. The theory predicts that S_0 influences h_1 with two competing factors:

1. A higher S_0 reduces the convective ventilation of the syrup layer, enhances the superheating, and increases the vortex ring radius R. A higher R makes the vortex ring feel less drag and trapping, penetrate deeper, and increase h_1.

2. A higher S_0 makes the vortex rings more negatively buoyant, penetrate shallower, and reduce h_1.

For the experimental results, h_1 first increases with S_0 and then decreases, yielding an optimal S_0 around 0.3 (Fig. 9b). Thus, for the relatively dilute regime ($S_0 \lesssim 0.3$), the radius effect dominates. For the relatively dense regime ($S_0 \gtrsim 0.3$), the buoyancy effect dominates.

The red lines of Fig. 9b show the quantitative prediction of h_1. We use $h_0 = 2$ cm. The value of the four uncertain parameters is prescribed as $\alpha\beta = 0.375$, $h_{DE} = 1.33$ cm, $\delta S = 0.05$, $S_* = 0.25$. This is a set of best-fit parameters, which makes the theory agree well with the experiments. The sensitivity to the four parameters is tested in the first row of Fig. 10, showing the trend is robust. The optimal S_0 mainly depends on S_* and δS_*, with a higher S_* and higher δS_* shifting the optimal S_0 higher.

5.4 Experiments with varying h_0

The initial syrup thickness (h_0) represents the thickness of the atmospheric boundary layer. The theory predicts that h_0 influences h_1 with two competing factors:

1. A higher h_0 increases the boiling duration time Δt because it takes longer to eliminate a thicker bottom mixed layer by detrainment. This effect increases h_1.

2. A higher h_0 increases the path for a vortex ring to be influenced by the drag and turbulence in the syrup layer, reducing its penetration depth l and escape ratio E. Thus, vortex rings entrain less and should yield a lower h_1.

For the experimental results, h_1 slightly increases with h_0 (Fig. 9c), indicating that the two factors roughly balance each other, and a smaller h_0 yields a more efficient dilution of the syrup layer by boiling. Experiments with $h_0 \lesssim 0.5$ cm yield a too-dilute post-boiling state that directly transitions to a well-mixed state. The post-boiling interface in our T1 experiment is marginally distinguishable. Experiments with $h_0 \gtrsim 4$ cm, including our T7 experiment (Fig. 8s), are in a *steady boiling regime* where boiling is continuous and the interfacial rising rate is steady. We name the regime with a clear end-of-boiling state the *intermittent boiling regime*.

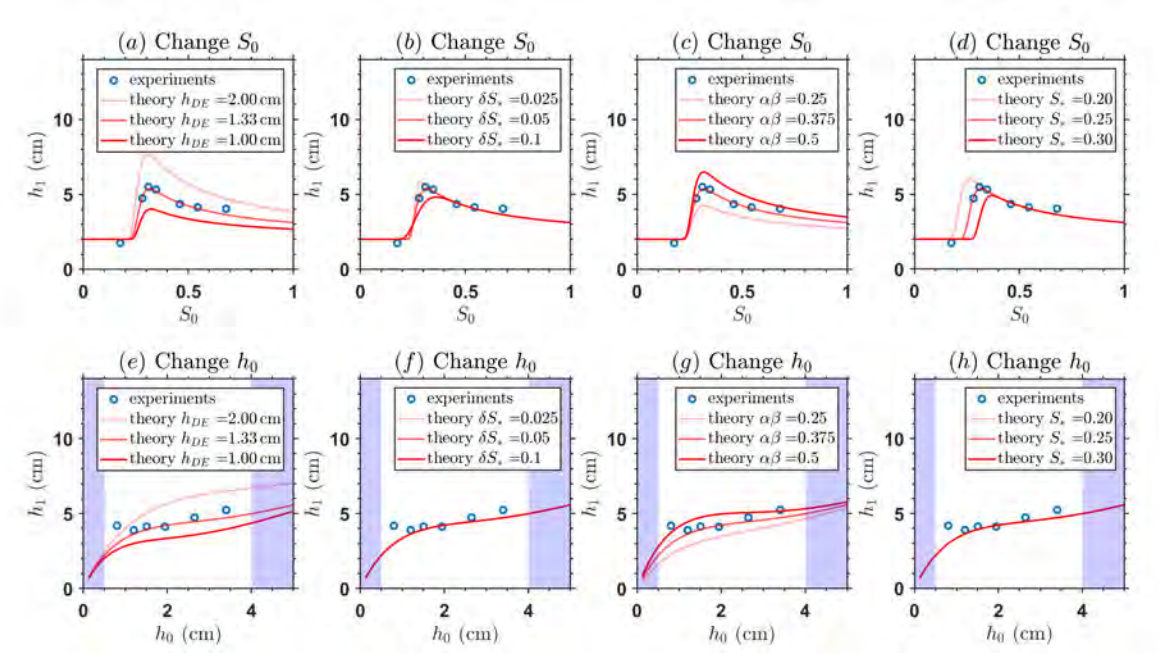

Figure 10: The first row shows the theoretical prediction of the h_1 vs. S_0 relation with perturbed parameters. The experimental results are blue circles, and the theoretical curves are solid red lines. (a) Changing h_{DE}. (b) Changing δS_*. (c) Changing $\alpha\beta$. (d) Changing S_*. The second row is the same as the first but for the h_1 vs. h_0 relation. The blue shadings show the $h_0 < 0.5$ cm and $h_0 > 4$ cm regimes.

6 Transition Between the Intermittent and Steady Boiling Regimes

6.1 Solving the transitional h_0

Section 5.4 reveals a steady boiling regime for a relatively high h_0, a regime beyond the theoretical framework of section 4. This section extends the theoretical framework to include the steady boiling regime and studies the mechanism of the transition.

In the steady boiling regime, the thick syrup layer sufficiently dissipates the vortex rings, reduces its penetrating depth, and limits the entrainment of cold water. As a result, entrainment is maintained at the minimum rate that keeps the syrup temperature around 100°C:

$$\frac{dh}{dt} = \frac{F_s}{\rho_w c_w \Delta T}. \tag{29}$$

Latent heating does not appear in (29) because all bubbles condense in the syrup layer, balancing the latent heat absorption and release. Using $F_s \approx 20$ kW m^{-2}, $\rho_w c_w \approx 4 \times 10^6$ J m^{-3} K^{-1}, and $\Delta T = 70$°C, we predict a 5.7 cm rise of the interface in 800 s, which is close to the approximately 5 cm rise in 800 s shown in Fig. 8s.

What controls the transitional h_0? If the entrainment rate by vortex rings (shown in (12)) is higher than that required to keep the syrup temperature around 100°C, boiling should be intermittent:

$$\text{Intermittent when :} \quad 2\varepsilon E \overline{w_+} l > \frac{F_s}{\rho_w c_w \Delta T}, \tag{30}$$

where we have used (12) and (29). Here, we must solve for the mean detrainment flux from the bottom mixed layer, $\overline{w_+}$, a quantity canceled out in solving h_1. The $\overline{w_+}$ depends on the vaporization rate at the bottom, which ultimately depends on the surface heat flux (F_s) and the heat transfer between the bottom and middle mixed layers. We parameterize the ratio of vaporization cooling rate to F_s as a vaporization efficiency χ, an uncertain parameter. The vertical flux of bubble number density, N (unit: m^{-2} s^{-1}), should obey:

$$N = \frac{F_s \chi}{\frac{4}{3}\pi R^3 L_v \rho_v}, \tag{31}$$

where $L_v = 2.5 \times 10^6$ J kg^{-1} is the vaporization heat and $\rho_v = 0.6$ kg m^{-3} is the density of vapor. The added mass argument introduced in section 4.2 indicates that the volume of moving syrup around a bubble is half its volume ($\frac{2}{3}\pi R^3$), so $\overline{w_+}$ obeys:

$$\overline{w_+} = \frac{2}{3}\pi R^3 N = \frac{F_s \chi}{2 L_v \rho_v}. \tag{32}$$

We need to constrain χ from experiments. Figure 2c shows that the interface between the bottom and middle mixed layers drops from 2 cm to 0 cm in around 60 s, indicating $\overline{w_+} \approx 3.3 \times 10^{-4}$ m s^{-1}. To let it meet (32), there should be $\chi \approx 0.05$. Thus, vaporization should play a minor role compared to eddy mixing in cooling the syrup layer's bottom.

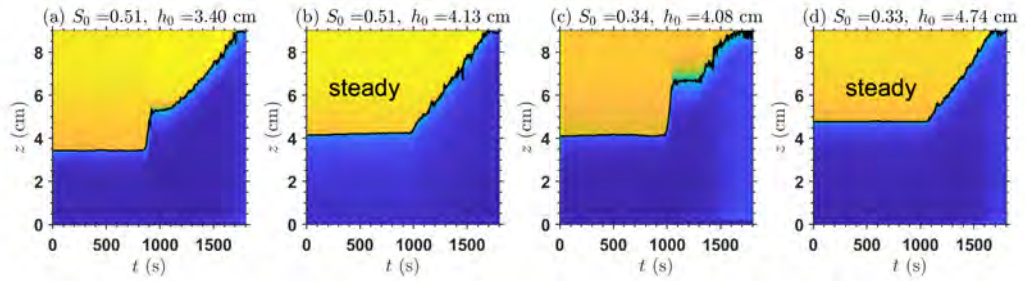

Figure 11: The same as Fig. 8, but for experiments ST1-ST4 that vary both S_0 and h_0 to study the critical h_0. ST2 and ST4 enter the steady boiling regime at the first boiling surge. ST1 and ST3 enter it at the second surge.

In other words, the mechanical removal of superheating is more important than the phase change effect. Substituting the expression of $\overline{w_+}$ (32), R (26), l (11), and E (5) into (30), we obtain the critical h_0 for transitioning to steady boiling:

$$\text{Steady when}: h_0 > h_\perp(S_0), \quad h_\perp(S_0) = h_{DE} \ln\left(\frac{4\alpha\beta\chi}{3\gamma_s S_0}\frac{\rho_w c_w \Delta T}{L_v \rho_v}\right), \tag{33}$$

where $h_\perp(S_0)$ is the transitional h_0 that is a function of S_0. In deriving (33), we have assumed the non-boiling regime ($S < S_*$) is sufficiently separated from the steady boiling regime by letting $R = R_m$. Substituting in estimated values ($\alpha\beta = 0.375$, $\chi = 0.05$, $\gamma_s = 0.4$, $\rho_w c_w \approx 4 \times 10^6$ J m^{-3} K^{-1}, $\Delta T = 70$°C, $L_v = 2.5 \times 10^6$ J kg^{-1}, and $\rho_v = 0.6$ kg m^{-3}), we get $h_\perp(S_0 = 0.5) = 4.2$ cm. It is close to the experimental results where the critical h_0 lies between $h_0 = 3.40$ cm (T6) and $h_0 = 4.13$ cm (T7).

Equation (33) predicts that the critical h_0 for steady boiling is proportional to the dissipation length scale h_{DE}, a quantity inversely proportional to the maximum bubble radius R_m. The proportional factor is higher for a smaller S_0 because a lighter syrup penetrates deeper and entrains more. To verify the dependence of the critical h_0 on S_0, we performed experiments ST1-ST4, as shown in Fig. 11. For $S_0 \approx 0.5$, the critical h_0 lies between $h_0 = 3.40$ cm (ST1) and 4.13 cm (ST2). For $S_0 \approx 0.35$, the critical h_0 lies between $h_0 = 4.08$ cm (ST3) and 4.74 cm (ST4). This confirms that a more dilute syrup yields a higher critical h_0 for steady boiling. In summary, a smaller h_0 and S_0 increase the entrainment in boiling and make it more intermittent.

The next step is to test the sensitivity to the bubble radius. We have performed preliminary experiments with an electric kettle where the bottom is a uniform metal plate (not shown). Strong superheating is prevented. The bubbles are much smaller, and boiling is always steady.

6.2 System evolution in the phase space

The above discussions are for the first surge of boiling. We can analyze the second surge using the same theoretical framework by taking h_1 as the new initial condition h_0. Some experiments enter steady boiling after the syrup-layer temperature recovers to the boiling

point. They include T5, T6, ST1, and ST3, where either S_0 or h_0 is relatively large (Fig. 8). For other experiments, the post-boiling syrup layer is too dilute to restore enough heat and boil again (i.e., $S < S_*$).

We summarize the system evolution in the phase space of the instantaneous syrup concentration S and syrup-layer thickness h, as shown in Fig. 12. Assuming the syrup layer is diluted by entraining freshwater and no syrup is released into the water layer, there should be:

$$Sh = S_0 h_0, \tag{34}$$

which sets the system's trajectory in the phase space as an inverse proportional function. The parameter space is divided into four regimes:

1. The single-layer regime ($S < S_{min}$), where a two-layer configuration is convectively unstable.

2. The non-boiling two-layer regime ($S_{min} < S < S_*$), where the ventilation by convective heat transfer prevents the syrup layer from boiling.

3. The intermittent boiling regime ($S > S_*$ and $h < h_\perp$).

4. The steady boiling regime ($S > S_*$ and $h > h_\perp$).

7 Conclusion

This report presents a novel experiment, boiling stratified flow, to investigate the vertical mixing induced by atmospheric moist convection. A thin layer of syrup is heated below a thick layer of freshwater in a beaker. The syrup layer represents the atmospheric boundary layer, and the water layer represents the free troposphere. The temperature in the experiment is analogous to the atmospheric humidity, and the boiling point is analogous to the saturated vapor mixing ratio.

When the initial syrup concentration S_0 and the syrup layer thickness h_0 are relatively small (but S_0 is not too small, see Fig. 12), the system is in the intermittent boiling regime. The bubbles generated at the bottom quench on their way up and drive vortex rings that penetrate the syrup-water interface, mix with water, and sink to the interface, producing a middle mixed layer that lies above the bottom mixed layer. The bottom mixed layer gradually diminishes due to the mass detrainment by vortex rings. The relatively cold middle mixed layer then touches the bottom and ends boiling. Boiling is intermittent because more cold water is entrained into the syrup layer than needed to remove superheating.

We built a theoretical framework to model the entrainment amount in a boiling surge, which is quantified with the interface rising distance $h_1 - h_0$. Key quantities include the escape ratio E, which measures the fraction of vortex rings that escape the syrup layer against the disturbance by turbulence, and the vortex ring penetration depth l, which determines the amount of freshwater a vortex ring can entrain. The theory can explain the trend of experiments with varying F_s (surface heat flux), S_0, and h_0. The post-boiling interface height h_1 drops with increasing F_s because the higher surface heating raises the

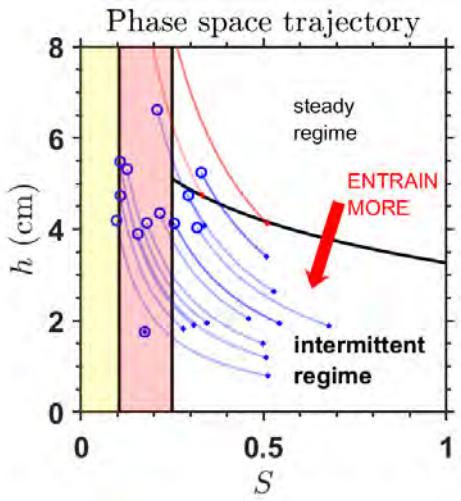

Figure 12: The system evolution in the S-h phase space. The yellow zone denotes the single-layer regime ($S < S_{min}$), and the red zone denotes the non-boiling two-layer regime ($S_{min} < S < S_*$). The white zone denotes the two boiling regimes, with the upper zone denoting the steady boiling regime ($h > h_\perp$) and the lower zone denoting the intermittent boiling regime ($h < h_\perp$). Phase trajectories of experiments S1-S7, T1-T7, and ST1-ST4 are plotted. Blue trajectories denote the experiments with intermittent boiling at the first surge. Red trajectories denote the experiments with steady boiling at the first surge, and no ending of the trajectory is set. The trajectories are assumed to obey $h = h_0 S/S_0$, with the dots denoting $h = h_0$ and the circles denoting $h = h_1$. Generally, a smaller h or S enhances the boiling entrainment.

bubble number density and the turbulent strength in the syrup layer and traps more vortex rings. The h_1 is non-monotonic with S_0. For $S_0 \lesssim 0.3$, the h_1 increases with S_0 due to the higher superheating and the larger bubble radius. For $S_0 \gtrsim 0.3$, the h_1 decreases with S_0 due to the more negative buoyancy of the vortex ring. The h_1 is relatively insensitive to h_0 because a thicker syrup layer raises the dissipation path of a vortex ring, reducing E and l. We quantitatively modeled the dependence of h_1 on S_0 and h_0. When the four uncertain parameters take the best-fit values, the agreement with experiments is very good.

When S_0 and h_0 are relatively large, E and l get smaller, and the entrainment rate drops to the minimum value for removing superheating in the syrup layer. We call it a steady regime, where boiling is continuous. The overshooting vortex rings continuously entrain cold water into the syrup layer. We match the intermittent and steady regimes theory and predict a transition curve. The theory predicts that a smaller S_0 raises the transitional h_0 to steady boiling, qualitatively agreeing with experiments.

The key aspects of comparing boiling stratified flow and atmospheric convection are their lifecycle and influence on environmental stratification. Moist convection in the atmosphere generally exhibits a self-regulating behavior, i.e., a lifecycle, primarily with three mechanisms. First, the re-evaporation of liquid droplets drives downdrafts, which brings the middle-level dry air into the boundary layer [59]. Second, the net latent heat release in condensation and evaporation, measured by surface rainfall rate, stratifies the atmosphere and reduces the convective instability [75, 10]. Third, the mechanical stirring effect of updrafts weakens the stratification at its overshooting top [39], and the mechanical stirring of evaporation-driven downdrafts could potentially weaken the stratification at the boundary layer top [68]. The mechanical stirring converts kinetic energy to potential energy, making the updrafts and downdrafts penetrative [74, 60, 3]. The ratio of stratifying to de-stratifying effects generally increases from zero as the cloud transitions from shallow cumulus to deep convection. For a shallow cumulus (Fig. 13), whose cloud top is $\lesssim 3$ km high and has little precipitation, the condensation of vapor produces liquid droplets that will re-evaporate and cause little net heating [21, 2]. Its primary role is to mix moisture vertically.

In the intermittent boiling regime of the experiments, the stirring of the syrup-water interface by vortex rings de-stratifies the system and brings down cold water, ending boiling. This is analogous to the third mechanism of the self-regulating behavior of moist convection. The dehydration effect of vaporization slightly increases the S in the syrup layer, and the S in the freshwater layer is slightly increased by gaining water from condensed bubbles. However, the bubble's vapor mass is much smaller than the syrup moving with it. The de-stratifying effect of boiling is much stronger than its stratifying effect. Thus, shallow cumulus is closest to the intermittent boiling regime among all types of moist convection.

Further analogies exist in the flow structure, parameter sensitivity, and regime transitions. As for the flow structure, the subcooled feature of the boiling, i.e., the quench of bubbles when in contact with the liquid below the boiling point, is analogous to the entrainment cooling of a shallow cumulus, where the liquid droplets mix with dry air, evaporate, and reduce the parcel's buoyancy [19]. The middle mixed layer resembles the trade cumulus layer in the subtropics, a humid layer produced by the mixture of the boundary layer and free-tropospheric air [22, 29].

The trend in experiments also yields interesting analogies with shallow cumulus. The reduction of h_1 with increasing F_s in the experiments implies that the stratified turbulence

Figure 13: Shallow cumulus in Puerto Rico, USA, December 2022, photographed by Hao Fu. This report shows the analogy between shallow cumulus and the laboratory boiling stratified flow.

produced by updrafts and downdrafts at the atmospheric boundary layer top may not always favor mixing. It might suppress a more efficient mixing mechanism - the organized updrafts and downdrafts. One possible future work is using large-eddy simulations to study whether a similar mechanism exists in the real atmosphere. The optimal S_0 in entrainment has an analogy to the atmosphere. Parker [55] studied the response of moist convection to the stratification strength. He found that a stabler stratification not only suppresses convection but also dry air entrainment. This leads to the build-up of convective available potential energy (CAPE) and deeper convection, with implications for continental convection in the midlatitude [20].

Is the transition of boiling type analogous to the transition of convective type in the atmosphere? The steady boiling regime is analogous to a strict boundary layer quasi-equilibrium (BLQE) state in the atmosphere, where the entrainment of dry air instantaneously balances the surface heat flux [59]. The nearly boiling temperature in the syrup layer requires the atmospheric analogy to be a nearly saturated atmospheric boundary layer, i.e., a stratocumulus or fog layer [42, 27]. The negligible dehydration in boiling syrup further requires the atmospheric analogy to be nonprecipitating, i.e., no net latent heat release. This analogy might be weird - does it mean "shallow cumulus" transitions to "stratocumulus" as the surface heating proceeds? The opposite is true in the atmosphere. In a diurnal cycle or for a growing sea surface temperature, stratocumulus breaks up into shallow cumulus and then transitions to precipitating deep convection [22, 16, 6]. The re-evaporation of raindrops drives gravity currents in the boundary layer, which aggregates vapor and triggers deeper convection [9, 65]. The paradox lies in the prohibition of precipitation required by the analogy. For a nonprecipitating atmosphere, we speculate the next stage of shallow cumulus should be the gradual saturation of the lower troposphere, essentially a deep stratocumulus close to our steady boiling regime. This suggests future research for the convective transition in a severely polluted atmosphere with a high concentration of aerosol, where the conversion from suspending cloud droplets to falling raindrops is suppressed [64, 1].

8 Acknowledgements

I am grateful to my advisors, Claudia Cenedese, Adrien Lefauve, and Geoff Vallis, for their insightful guidance that led to this report. They taught me how to design and do experiments professionally, helped me solidify the theoretical framework, and inspired me to dig the link to the real atmosphere. I am grateful to Yunjiao Pu for providing experimental support at the kitchen stage of this project. I thank Jim McElwaine, Anders Jensen, and Bruce Sutherland for critical experimental support. I thank Keaton Burns for teaching us softball and helping me run the Dedalus model at the early stage of this project. The great summer wouldn't be possible without the administration of the program by Tiffany Shaw, Pascale Garaud, and Julie Hildebrandt. I received guidance from numerous GFD faculties and visitors. I thank Wanying and my roommates, Yaoxuan and Quentin, for their care in life. Finally, I would like to thank the 2023 Class fellows for their kind help throughout the summer.

References

[1] T. H. Abbott and T. W. Cronin, *Aerosol invigoration of atmospheric convection through increases in humidity*, Science, 371 (2021), pp. 83–85.

[2] AMS-Glossary, *Glossary of meteorology, American Meteorological Society*, URl: http://glossary.ametsoc.org, (2012).

[3] J. K. Ansong and B. R. Sutherland, *Internal gravity waves generated by convective plumes*, J. Fluid Mech., 648 (2010), pp. 405–434.

[4] A. Arakawa and W. H. Schubert, *Interaction of a cumulus cloud ensemble with the large-scale environment, part I*, J. Atmos. Sci., 31 (1974), pp. 674–701.

[5] S. Barathula and K. Srinivasan, *Review on research progress in boiling acoustics*, Int. Commun. Heat Mass Transf., 139 (2022), p. 106465.

[6] G. Bellon and O. Geoffroy, *Stratocumulus radiative effect, multiple equilibria of the well-mixed boundary layer and transition to shallow convection*, Q. J. R. Meteorol. Soc., 142 (2016), pp. 1685–1696.

[7] H. Bénard, *Les tourbillons cellulaires dans une nappe liquide propageant de la chaleur par convection: en régime permanent*, Gauthier-Villars, 1901.

[8] J. Bjerknes, *Saturated-adiabatic ascent of air through dry-adiabatically descending environment*, Quart. J. Roy. Meteor. Soc., 64 (1938), pp. 325–330.

[9] S. J. Böing, H. J. Jonker, A. P. Siebesma, and W. W. Grabowski, *Influence of the subcloud layer on the development of a deep convective ensemble*, J. Atmos. Sci., 69 (2012), pp. 2682–2698.

[10] C. S. Bretherton, *A theory for nonprecipitating moist convection between two parallel plates. Part I: Thermodynamics and "linear" solutions*, J. Atmos. Sci., 44 (1987), pp. 1809–1827.

[11] ——, *A theory for nonprecipitating convection between two parallel plates. Part II: Nonlinear theory and cloud field organization*, J. Atmos. Sci., 45 (1988), pp. 2391–2415.

[12] C. S. Bretherton, M. E. Peters, and L. E. Back, *Relationships between water vapor path and precipitation over the tropical oceans*, J. Clim., 17 (2004), pp. 1517–1528.

[13] H. R. Byers and R. R. Braham, *The thunderstorm: report of the Thunderstorm Project*, US Government Printing Office, 1949.

[14] S. Chandrasekhar, *Hydrodynamic and hydromagnetic stability*, Courier Corporation, 1961.

[15] J. G. Collier and J. R. Thome, *Convective boiling and condensation*, Clarendon Press, 1994.

[16] W. R. Cotton, G. Bryan, and S. C. Van den Heever, *Storm and cloud dynamics*, Academic press, 2010.

[17] G. Dagan, I. Koren, A. Kostinski, and O. Altaratz, *Organization and oscillations in simulated shallow convective clouds*, J. Adv. Model. Earth Syst., 10 (2018), pp. 2287–2299.

[18] J. W. Deardorff et al., *Convective velocity and temperature scales for the unstable planetary boundary layer and for Rayleigh convection*, J. Atmos. Sci., 27 (1970), pp. 1211–1213.

[19] S. Derbyshire, I. Beau, P. Bechtold, J.-Y. Grandpeix, J.-M. Piriou, J.-L. Redelsperger, and P. Soares, *Sensitivity of moist convection to environmental humidity*, Q. J. R. Meteorol. Soc., 130 (2004), pp. 3055–3079.

[20] K. Emanuel, *On the physics of high cape*, J. Atmos. Sci., 80 (2023), pp. 2669–2683.

[21] K. A. Emanuel, *The finite-amplitude nature of tropical cyclogenesis*, J. Atmos. Sci., 46 (1989), pp. 3431–3456.

[22] ——, *Atmospheric convection*, Oxford University Press on Demand, 1994.

[23] K. A. Emanuel, J. David Neelin, and C. S. Bretherton, *On large-scale circulations in convecting atmospheres*, Quart. J. Roy. Meteor. Soc., 120 (1994), pp. 1111–1143.

[24] G. Falkovich, *Fluid mechanics: A short course for physicists*, Cambridge University Press, 2011.

[25] G. Feingold, I. Koren, H. Wang, H. Xue, and W. A. Brewer, *Precipitation-generated oscillations in open cellular cloud fields*, Nature, 466 (2010), pp. 849–852.

[26] G. Filipczak, L. Troniewski, and S. Witczak, *Pool boiling of liquid-liquid multiphase systems*, in Evaporation, Condensation and Heat transfer, IntechOpen, 2011.

[27] H. Fu, *A linear stability analysis of two-layer moist convection with a saturation interface*, J. Fluid Mech., 928 (2021), p. A13.

[28] H. Ge, C. Li, X. Zhang, and C. Moeckel, *Heat-flux limited cloud activity and vertical mixing in giant planet atmospheres with an application to uranus and neptune*, arXiv preprint arXiv:2310.15267, (2023).

[29] G. George, B. Stevens, S. Bony, R. Vogel, and A. K. Naumann, *Widespread shallow mesoscale circulations observed in the trades*, Nat. Geosci., 16 (2023), pp. 584–589.

[30] N. Graham and T. Barnett, *Sea surface temperature, surface wind divergence, and convection over tropical oceans*, Science, 238 (1987), pp. 657–659.

[31] G. A. Greene, J. C. Chen, and M. T. Conlin, *Onset of entrainment between immiscible liquid layers due to rising gas bubbles*, Int. J. Heat Mass Transf., 31 (1988), pp. 1309–1317.

[32] A. Innocenti, A. Jaccod, S. Popinet, and S. Chibbaro, *Direct numerical simulation of bubble-induced turbulence*, J. Fluid Mech., 918 (2021), p. A23.

[33] N. C. Johnson and S.-P. Xie, *Changes in the sea surface temperature threshold for tropical convection*, Nat. Geosci., 3 (2010), pp. 842–845.

[34] O. Kawanami, K. Matsuhiro, Y. Hara, I. Honda, and N. Takagaki, *Liquid-liquid interfacial instability model for boiling refrigerant transition by pool boiling of immiscible mixtures*, Int. J. Heat Mass Transf., 146 (2020), p. 118826.

[35] R. Krishnamurti, *Convection induced by selective absorption of radiation: a laboratory model of conditional instability*, Dyn. Atmos. Oceans., 27 (1998), pp. 367–382.

[36] H. Kuo, *Convection in conditionally unstable atmosphere*, Tellus, 13 (1961), pp. 441–459.

[37] C. Li and A. P. Ingersoll, *Moist convection in hydrogen atmospheres and the frequency of saturn's giant storms*, Nat. Geosci., 8 (2015), pp. 398–403.

[38] D. K. Lilly, *Models of cloud-topped mixed layers under a strong inversion*, Q. J. R. Meteorol. Soc., 94 (1968), pp. 292–309.

[39] ——, *Stratified turbulence and the mesoscale variability of the atmosphere*, J. Atmos. Sci., 40 (1983), pp. 749–761.

[40] P. Markowski and Y. Richardson, *Mesoscale meteorology in midlatitudes*, John Wiley & Sons, 2011.

[41] T. Maxworthy, *Turbulent vortex rings*, J. Fluid Mech., 64 (1974), pp. 227–240.

[42] J. P. Mellado, *Cloud-top entrainment in stratocumulus clouds*, Annu. Rev. Fluid Mech., 49 (2017), pp. 145–169.

[43] F. Á. Mohos, *Confectionery and chocolate engineering: principles and applications*, John Wiley & Sons, 2017.

[44] Y. H. Mori, *Configurations of gas-liquid two-phase bubbles in immiscible liquid media*, Int. J. Multiph. Flow, 4 (1978), pp. 383–396.

[45] ——, *Classification of configurations of two-phase vapor/liquid bubbles in an immiscible liquid in relation to direct-contact evaporation and condensation processes*, Int. J. Multiph. Flow, 11 (1985), pp. 571–576.

[46] B. R. Morton, G. I. Taylor, and J. S. Turner, *Turbulent gravitational convection from maintained and instantaneous sources*, Proc. R. Soc. Lond., Ser. A, Math. Phys. Eng. Sci., 234 (1956), pp. 1–23.

[47] R. Narasimha, S. S. Diwan, S. Duvvuri, K. Sreenivas, and G. Bhat, *Laboratory simulations show diabatic heating drives cumulus-cloud evolution and entrainment*, Proc. Natl. Acad. Sci. U.S.A., 108 (2011), pp. 16164–16169.

[48] S. Narayan, T. Singh, and A. Srivastava, *Experiments on pool boiling regimes and bubble departure characteristics of single vapor bubble under subcooled bulk conditions*, Exp. Therm. Fluid Sci., 111 (2020), p. 109943.

[49] I. E. L. Neto, S. S. Cardoso, and A. W. Woods, *On mixing a density interface by a bubble plume*, J. Fluid Mech., 802 (2016), p. R3.

[50] Y. Ogura and T. Takahashi, *Numerical simulation of the life cycle of a thunderstorm cell*, Mon. Wea. Rev., 99 (1971), pp. 895–911.

[51] J. Olsthoorn and S. B. Dalziel, *Vortex-ring-induced stratified mixing*, J. Fluid Mech., 781 (2015), pp. 113–126.

[52] ——, *Vortex-ring-induced stratified mixing: mixing model*, J. Fluid Mech., 837 (2018), pp. 129–146.

[53] S. Onishi, H. Ohta, N. Ohtani, Y. Fukuyama, and H. Kobayashi, *Boiling heat transfer by nucleate boiling of immiscible liquids*, INTERFACIAL PHENOM H, 1 (2013).

[54] P. Oresta, R. Verzicco, D. Lohse, and A. Prosperetti, *Heat transfer mechanisms in bubbly Rayleigh-bénard convection*, Phys. Rev. E., 80 (2009), p. 026304.

[55] D. Parker, *The response of cape and cin to tropospheric thermal variations*, Q. J. R. Meteorol. Soc., 128 (2002), pp. 119–130.

[56] O. Pauluis and J. Schumacher, *Idealized moist Rayleigh-bénard convection with piecewise linear equation of state*, Commun Math Sci, 8 (2010), pp. 295–319.

[57] J. Pinaud, J. Albagnac, S. Cazin, Z. Rida, D. Anne-Archard, and P. Brancher, *Three-dimensional measurements of an inclined vortex ring interacting with a density stratification*, Physical Review Fluids, 6 (2021), p. 104701.

[58] L. Rayleigh, *Lix. on convection currents in a horizontal layer of fluid, when the higher temperature is on the under side*, The London, Edinburgh, and Dublin Philosophical Magazine and Journal of Science, 32 (1916), pp. 529–546.

[59] D. J. Raymond, *Regulation of moist convection over the west pacific warm pool*, J. Atmos. Sci., 52 (1995), pp. 3945–3959.

[60] J. J. Riley and M.-P. Lelong, *Fluid motions in the presence of strong stable stratification*, Annu. Rev. Fluid Mech., 32 (2000), pp. 613–657.

[61] D. M. Romps, *An analytical model for tropical relative humidity*, J. Clim., 27 (2014), pp. 7432–7449.

[62] D. M. Romps and A. B. Charn, *Sticky thermals: Evidence for a dominant balance between buoyancy and drag in cloud updrafts*, J. Atmos. Sci., 72 (2015), pp. 2890–2901.

[63] D. M. Romps and R. Öktem, *Stereo photogrammetry reveals substantial drag on cloud thermals*, Geophys. Res. Lett., 42 (2015), pp. 5051–5057.

[64] D. Rosenfeld, U. Lohmann, G. B. Raga, C. D. O'Dowd, M. Kulmala, S. Fuzzi, A. Reissell, and M. O. Andreae, *Flood or drought: how do aerosols affect precipitation?*, Science, 321 (2008), pp. 1309–1313.

[65] L. Schlemmer and C. Hohenegger, *The formation of wider and deeper clouds as a result of cold-pool dynamics*, J. Atmos. Sci., 71 (2014), pp. 2842–2858.

[66] A. S. M. Shawon, P. Prabhakaran, G. Kinney, R. A. Shaw, and W. Cantrell, *Dependence of aerosol-droplet partitioning on turbulence in a laboratory cloud*, J. Geophys. Res. Atmos., 126 (2021), p. e2020JD033799.

[67] J. Takahashi, Y. Tasaka, Y. Murai, Y. Takeda, and T. Yanagisawa, *Experimental study of cell pattern formation induced by internal heat sources in a horizontal fluid layer*, Int. J. Heat Mass Transf., 53 (2010), pp. 1483–1490.

[68] K. Thayer-Calder and D. Randall, *A numerical investigation of boundary layer quasi-equilibrium*, Geophys. Res. Lett., 42 (2015), pp. 550–556.

[69] J. Turner, *Model experiments relating to thermals with increasing buoyancy*, Q. J. R. Meteorol. Soc., 89 (1963), pp. 62–74.

[70] ——, *The coupled turbulent transports of salt and heat across a sharp density interface*, Int. J. Heat Mass Transf., 8 (1965), pp. 759–767.

[71] ——, *Turbulent entrainment: the development of the entrainment assumption, and its application to geophysical flows*, J. Fluid Mech., 173 (1986), pp. 431–471.

[72] J. Turner and D. Lilly, *The carbonated-water tornado vortex*, J. Atmos. Sci., 20 (1963), pp. 468–471.

[73] G. K. Vallis, D. J. Parker, and S. M. Tobias, *A simple system for moist convection: the rainy–bénard model*, J. Fluid Mech., 862 (2019), pp. 162–199.

[74] G. Veronis, *Penetrative convection.*, Astrophys. J., 137 (1963), p. 641.

[75] M. Yanai, S. Esbensen, and J.-H. Chu, *Determination of bulk properties of tropical cloud clusters from large-scale heat and moisture budgets*, J. Atmos. Sci., 30 (1973), pp. 611–627.

[76] D. Yang, *Boundary layer height and buoyancy determine the horizontal scale of convective self-aggregation*, J. Atmos. Sci., 75 (2018), pp. 469–478.

[77] J.-I. Yano and R. Plant, *Convective quasi-equilibrium*, Rev. Geophys., 50 (2012).

[78] J.-I. Yano and R. Plant, *Finite departure from convective quasi-equilibrium: Periodic cycle and discharge–recharge mechanism*, Quart. J. Roy. Meteor. Soc., 138 (2012), pp. 626–637.

[79] S. Zhao, X. Xiong, F. Hu, and J. Zhu, *Rotating annulus experiment: Large-scale helical soliton in the atmosphere?*, Phys. Rev. E., 64 (2001), p. 056621.

Simple Models of Superrotation in Planetary Atmospheres

Quentin Nicolas

January 16, 2024

Abstract

Planetary atmospheres with excess angular momentum relative to the planet's equatorial surface are said to be superrotating. Superrotation is a common feature of both fast rotating gas giants (e.g., Jupiter), slowly rotating planets (e.g., Venus) planets, and tidally locked planets. While the mechanisms of superrotation in slow rotators and tidally locked planets share some commonalities, they have to date not been studied jointly. Here, we explore the physics of superrotation for a wide range of planetary sizes, rotation rates, and insolations, in a hierarchy of model complexities. We focus on atmospheres that can be modeled as thin shells, and all of our models have a finite number of fixed pressure levels extending from a solid surface (or quiescent layer) to the top of the atmosphere. Our simplest model is composed of two vertical levels, and is able to produce realistic superrotation on both tidally locked planets and slow rotators, without the need for specific tricks required by shallow-water models. We also show that some classes of tidally locked planets, specifically at low thermal Rossby numbers and large radiative relaxation times, may have subrotating atmospheres. Linearizations of this model elucidate the wave-mean-flow interactions responsible for the establishment of superrotation. They further allow an understanding of the regime transition from subrotating to superrotating atmospheres. Finally, we explore the transition in the mechanisms of superrotation from non-tidally locked to tidally locked planets by applying a progressively stronger standing asymmetric equatorial forcing. We show that a standing Gill-like pattern quickly dominates over travelling planetary Kelvin-Rossby waves in forcing superrotation. These results allow for a unified understanding of superrotation mechanisms across a wide range of planetary bodies.

1 Introduction

Axisymmetric motion in planetary atmospheres cannot produce an angular momentum maximum away from a surface or an interior quiescent layer, a consequence of Hide's theorem (Hide, 1969; Vallis, 2017). As a consequence, equatorial winds must be retrograde when the flow is purely axisymmetric. Despite this constraint, Venus, Jupiter, Saturn, Titan, and many planetary atmospheres beyond the solar system have prograde equatorial winds; they are said to *superrotate*. On these planets, non-axisymmetric wave processes presumably flux momentum from extratropical and subtropical regions towards the equator.

Three broad classes of planets exhibit superrotation (e.g. Imamura et al., 2020): fast-rotating gas giants (Jupiter and Saturn), slowly rotating terrestrial planets (e.g., Venus and Titan), and tidally locked planets. Most observed exoplanets belong to the latter group. Indeed, current detection techniques favor planets orbiting close to their host star, which tidal stresses are expected to rapidly bring to a state of tidal locking (Barnes, 2017). This group can be subdivided into terrestrial planets and gas giants, the latter often referred to as hot Jupiters.

Many attempts at explaining superrotation on fast-rotating gas giants used shallow atmospheric models (both shallow-water and primitive equation) (e.g., Lian and Showman, 2010; Liu and Schneider, 2011), developed and extensively used for the study of Earth's atmosphere. These models assume that the depth of the layer in which atmospheric flows take place is small compared to the planet's radius, which happens if the flows are confined to an upper stratified layer ($\mathcal{O}$(100 km) deep for Jupiter and Saturn). One important consequence of this assumption is that the flows primarily aligns with the local gravity. Another approach assumes that the flow extends to a much deeper convective layer (e.g., Busse, 1976). In such a scenario, the flow primarily aligns with the rotation axis, and the dynamics cannot be adequately described by shallow atmospheric models. Recent measurements from the Juno mission confirmed that the latter hypothesis was true on Jupiter and Saturn (Kaspi et al., 2020). On hot Jupiters, however, the internal heat flow is expected to be very weak compared to the stellar irradiation. The upper atmosphere is thus likely to be stably stratified and the depth of the flow is likely shallower there (following Showman et al. (2008), one might estimate this depth using the density scale height, which is a factor at least 20 smaller than the planetary radius). On terrestrial planets, it is customary to assume that the shallow atmosphere approximation holds, as higher molecular masses yield small scale heights. Thus, all classes of superrotating atmospheres except "cold" gas giants can be modeled in a single framework, that of thin or shallow atmospheres, or at least that is the approach we shall take here.

Different classes of waves have been proposed to drive superrotation on slow rotators and tidally locked planets. For the former, when the heating is axisymmetric in the time mean, an instability of the zonally symmetric basic state is likely required to create eddies. One such instability (termed Rossby-Kelvin – or RK – instability) arises in the presence of strong enough midlatitude jets. These allow midlatitude Rossby waves to phase lock with fast-travelling equatorial Kelvin waves and produce momentum-converging wind patterns (Iga and Matsuda, 2005; Wang and Mitchell, 2014). For tidally locked planets, Showman and Polvani (2010, 2011) proposed that the steady linear response to non-axisymmetric heating, a Matsuno–Gill-like solution, could itself spin-up superrotation if vertical momentum transport from a low-level quiescent layer was also taken into account.

While the mechanisms of superrotation are often examined using linearized versions of shallow water models, producing realistic superrotation with these models has proved challenging. The vertical momentum transport parameterization employed by Showman and Polvani (2011) requires some amount of retrograde flow at the equator for superrotation to exist. This prevents the emergence of pan-equatorial superrotating flows, as predicted by global circulation models (GCMs) of tidally locked planets (e.g., Showman et al., 2009; Pierrehumbert and Hammond, 2019). For slow rotators, Zurita-Gotor and Held (2018) have shown that a 1.5-layer shallow water model, even with vertical momentum transport, struggles to produce superrotation despite representing the RK instability. One goal of the present work is to present a modeling framework that contains the simplest physical processes (and allows for some analytical treatment of linear waves to be carried), but has rich enough behavior to produce realistic superrotation, and then to

explore the mechanisms involved.

We use a hierarchy of models to understand the mechanisms of superrotation on tidally locked planets and slow rotators in a unified framework. We seek to answer several questions: Do all tidally locked planets superrotate? If not, for what sets of parameters (size, rotation rate, insolation, surface drag ...) do they? What mechanisms govern the appearance of superrotation across the parameter space? Are the mechanisms of superrotation on tidally locked planets and slow rotators related? Can both coexist?

In order to answer these questions, we first explore the response to steady thermal forcing in tidally locked planets, which consists in the sum of a thermally direct axisymmetric flow and a Matsuno-Gill type response, using a linear two-level model. This allows us to make qualitative predictions about the strength of the superrotating jet as a function of input parameters. Fully nonlinear integrations of the two-level model with varying thermal Rossby number and thermal relaxation scales are conducted to verify the predictions made using linear dynamics. They confirm a weakening equatorial jet with increasing thermal relaxation scale, and feature subrotation at high values of this parameter. The robustness of the two-level results is investigated using a 10-level version of the same model, which constitutes a simplified GCM. We also present two-level simulations with axisymmetric thermal forcing, both subrotating and superrotating, and investigate the eddies causing superrotation at high thermal Rossby numbers. Finally, we explore the interplay between the superrotation mechanisms characteristic of slow rotators and tidally locked planets with a set of simulations that bridge the two cases, applying a progressively stronger zonal asymmetry in the thermal forcing.

2 Methods

The numerical models used in this study are all part of the same class of pressure-level models on the sphere. They are extensions of the models of Held and Suarez (1978), Suarez and Duffy (1992), and Saravanan (1993), who used two-level versions. We start with the dry primitive equations in pressure coordinates, and make approximations suitable for a thin atmosphere: the acceleration of gravity g is constant, the atmosphere is hydrostatic, and we only retain the component of planetary rotation that projects on the local vertical direction in calculating the Coriolis acceleration (the traditional approximation). The horizontal momentum, hydrostatic, thermodynamic, and continuity equations read

$$\frac{\partial \boldsymbol{u}}{\partial t} + \boldsymbol{u}\cdot\nabla\boldsymbol{u} + \omega\frac{\partial \boldsymbol{u}}{\partial p} + f\boldsymbol{k}\times\boldsymbol{u} = -\nabla\Phi + \boldsymbol{F_u}, \tag{1}$$

$$\frac{\partial \Phi}{\partial \Pi} = -c_p\theta, \tag{2}$$

$$\frac{\partial \theta}{\partial t} + \boldsymbol{u}\cdot\nabla\theta + \omega\frac{\partial \theta}{\partial p} = F_\theta, \tag{3}$$

$$\nabla\cdot\boldsymbol{u} + \frac{\partial \omega}{\partial p} = 0, \tag{4}$$

where $\boldsymbol{u} = (u, v)$ is the horizontal velocity vector, ω the pressure velocity, θ the potential temperature, Φ the geopotential height, $f = 2\Omega\sin\phi$ is the Coriolis parameter (Ω is the planet's rotation rate), and $\Pi = (p/p_0)^{R/c_p}$ the Exner function, where R is the specific gas constant and c_p the isobaric heat capacity. In the remainder of this work, $R/c_p = 2/7$, as for a diatomic gas. We include forcing terms in the momentum and thermodynamic equations; those represent the effects of surface friction and thermal relaxation.

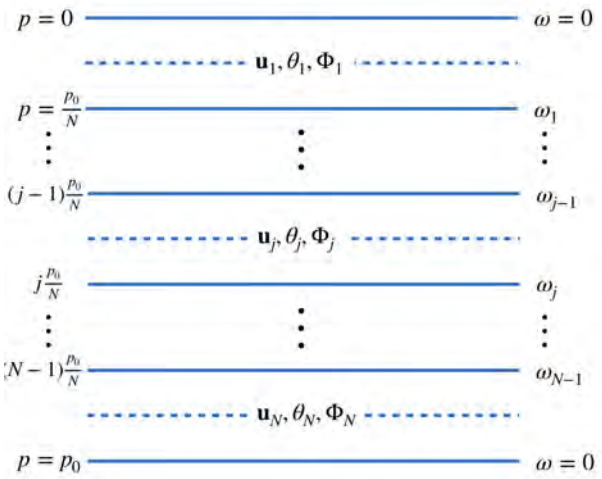

Figure 1: Sketch of the vertical discretization of the N-level atmospheric model

The atmosphere is divided into $N \geq 2$ pressure levels, evenly spaced between the $p = 0$ and $p = p_0$ levels. p_0 is taken as the mean surface pressure on a terrestrial planet. On a gas giant, it is the pressure level at which horizontal flows become negligible (compared to weather-layer flows) due to magnetic drag or Ohmic dissipation in the planet's interior. The variables are represented on a staggered vertical grid. Pressure velocities ω_i are defined on the full levels $i\Delta p$ $(0 \leq i \leq N)$, where $\Delta p = p_0/N$ is the vertical grid spacing. $\boldsymbol{u}_i$, θ_i, Φ_i are defined on the half levels $(i - 1/2)\Delta p$, for $1 \leq i \leq N$. We will henceforth refer to these levels by their value of $\sigma := p/p_0$. A schematic of this vertical discretization is provided in Fig. 1. A Rayleigh mechanical damping, with a timescale τ_{drag}, is applied in the lowermost layer. The thermodynamic forcing term consists in a relaxation towards a prescribed potential temperature profile $\theta_E(\phi, \lambda, p)$, where ϕ and λ denote latitude and longitude, on a time scale τ_{rad}. We use

$$\theta_E(\phi, \lambda, p) = \begin{cases} (\Delta\Theta_h - \Delta\Theta_v \ln \Pi)\ \cos\phi\ \max(0, \cos\lambda) & \text{for tidally locked planets,} \\ (\Delta\Theta_h - \Delta\Theta_v \ln \Pi)\ \cos\phi\ \dfrac{1}{\pi} & \text{for non tidally locked planets.} \end{cases} \tag{5}$$

The vertical structure specifies an approximately constant static stability $\partial\theta_E/\partial z$ in height. The meridional structure is taken proportional to that of the stellar irradiation in the absence of axial tilt (i.e., $\propto \cos\phi$). The same goes for the zonal structure on tidally locked planets: it varies as $\cos\lambda$ on the day side and vanishes on the nightside. The structure of this reference potential temperature profile is illustrated in Fig. 2. The first panel shows the vertical and meridional structures, common to tidally locked and axisymmetrically forced planets (we choose nondimensional values of $\Delta\Theta_h$ and $\Delta\Theta_v$ that correspond to those used henceforth.). The second panel illustrates the latitude-longitude structure on tidally locked planets. The factor $1/\pi$ in the second expression of (5) ensures that the mean θ_E, a proxy for the stellar irradiation, is the same for tidally locked and non-tidally locked planets for given $\Delta\Theta_h$ and $\Delta\Theta_v$. We pause here to note that the assumption of a zonally symmetric forcing for non-tidally locked planets is adequate when the thermal relaxation scale τ_{rad} is much longer than the planet's rotation period $2\pi/\Omega$. This is not the case, for example, on Venus: there, the effect of thermal tides is of primary importance (, e.g)[]Takagi2007.

Two versions of this model are used in this work. The first one emphasizes simplicity

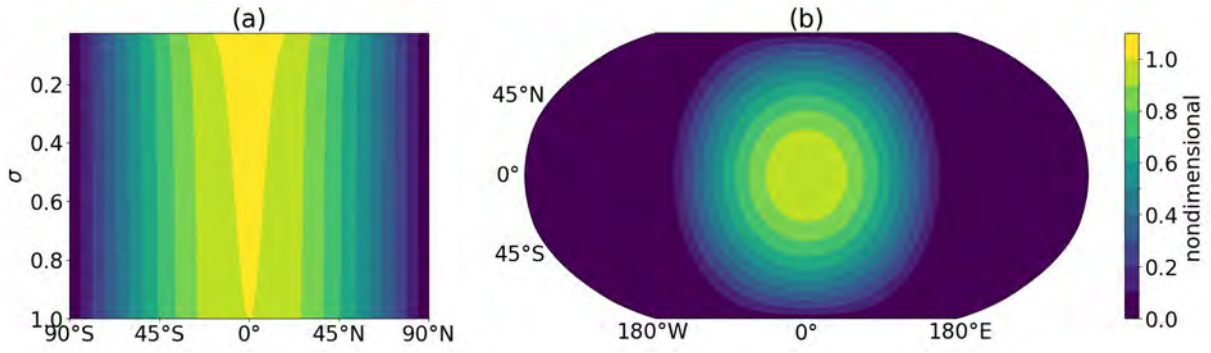

Figure 2: (a) Latitude-height structure of the reference potential temperature θ_E — i.e., $(\Delta\Theta_h - \Delta\Theta_v \ln\Pi)\ \cos\phi$ — with $\Delta\Theta_h = 1$ and $\Delta\Theta_v = 0.05$. (b) Reference potential temperature structure at the surface — i.e., $\Delta\Theta_h \cos\phi\ \max(0, \cos\lambda)$ — again with $\Delta\Theta_h = 1$.

and has two levels (i.e., $N = 2$); it is the simplest model that allows to obtain physical insights on the mechanisms of superrotation while retaining enough complexity (including vertical momentum transport) to have a rich behavior. Some analytical treatment of a linearized version of this model is presented in section 3. The other model has $N = 10$ levels. We use it to validate the results found with the two-level model. Proper evaluation of the 10-level model, namely the Held and Suarez (1994) benchmark, is carried out in Appendix A. Numerical integrations are performed using Dedalus (Burns et al., 2020), an open framework for solving partial differential equations. We use a fourth-order horizontal hyperdiffusion (but no vertical diffusion) in the momentum and thermodynamic equations to ensure numerical stability.

In order to reduce the number of input parameters to this model, we nondimensionalize equations (1)–(2) following Potter et al. (2014). Using a length scale a (the planetary radius), a time scale $(2\Omega)^{-1}$, a geopotential scale $c_p\Delta\Theta_h$, a horizontal velocity scale $c_p\Delta\Theta_h/(2\Omega a)$ (from geostrophic balance), and a vertical velocity scale consistent with continuity, the governing equations become

$$\frac{\partial \boldsymbol{u}}{\partial t} + Ro_T \left(\boldsymbol{u} \cdot \nabla \boldsymbol{u} + \omega \frac{\partial \boldsymbol{u}}{\partial p} \right) + \hat{f} \boldsymbol{k} \times \boldsymbol{u} = -\nabla\Phi - E\boldsymbol{u}, \tag{6}$$

$$\frac{\partial \Phi}{\partial \Pi} = -\theta, \tag{7}$$

$$\frac{\partial \theta}{\partial t} + Ro_T \left(\boldsymbol{u} \cdot \nabla \theta + \omega \frac{\partial \theta}{\partial p} \right) = \frac{\theta_E - \theta}{T_{\mathrm{rad}}}, \tag{8}$$

$$\nabla \cdot \boldsymbol{u} + \frac{\partial \omega}{\partial p} = 0, \tag{9}$$

where $\hat{f} = \sin\phi$ and three nondimensional control parameters appear: a thermal Rossby number, an Ekman number, and a nondimensional thermal relaxation time scale, given respectively by

$$Ro_T = \frac{c_p \Delta\Theta}{(2\Omega a)^2}, \quad E = \frac{1}{2\Omega\tau_{\mathrm{drag}}}, \quad T_{rad} = 2\Omega\tau_{\mathrm{rad}}. \tag{10}$$

A fourth nondimensional control parameter controls the vertical structure of θ_E: $\mathcal{S} = \Delta\Theta_v/\Delta\Theta_h$. In (6)–(9), all variables are nondimensional. The friction term in (6) is only effective in the lower layer in the discretized models.

For completeness, we now give the nondimensional governing equations of the two-level model, obtained by discretizing (6)–(9) in the vertical:

$$\frac{\partial \boldsymbol{u}_i}{\partial t} + Ro_T\left(\boldsymbol{u}_i \cdot \nabla \boldsymbol{u}_i + \omega(\boldsymbol{u}_2 - \boldsymbol{u}_1)\right) + \hat{f}\boldsymbol{k} \times \boldsymbol{u}_i = -\nabla\Phi_i - \delta_{i2} E \boldsymbol{u}_i, \qquad i = 1, 2, \tag{11}$$

$$\frac{\Phi_2 - \Phi_1}{\pi_2 - \pi_1} = -\frac{\theta_1 + \theta_2}{2}, \tag{12}$$

$$\frac{\partial \theta_i}{\partial t} + Ro_T\left(\boldsymbol{u}_i \cdot \nabla \theta_i + \omega(\theta_2 - \theta_1)\right) = \frac{\theta_{iE} - \theta_i}{T_{\text{rad}}}, \qquad i = 1, 2, \tag{13}$$

$$\nabla \cdot \boldsymbol{u}_1 + 2\omega = 0, \tag{14}$$

$$\nabla \cdot \boldsymbol{u}_2 - 2\omega = 0, \tag{15}$$

We note that the pressure scale used in the nondimensionalization is the lowermost pressure level of the model, p_0.

3 Processes Driving Superrotation in a Two-level Model

In this section, we explore linear wave processes that can drive superrotation on tidally locked planets and slow rotators. We do so using a two-level model, which is the simplest model containing all the necessary processes for superrotation. Indeed, superrotation cannot be sustained in the absence of vertical momentum transport (e.g., in one-level models) if the circulation is symmetric about the equator at all times (Showman and Polvani, 2011). This is best understood in the framework of the Eulerian-mean momentum equation: denoting zonal averages with an overbar, the zonal-mean zonal momentum equation can be arranged into

$$\frac{\partial \overline{u}}{\partial t} = \overline{(\hat{f} + Ro_T\zeta)v} - Ro_T\,\overline{\omega\frac{\partial u}{\partial p}} - E\overline{u}, \tag{16}$$

where ζ is the relative vorticity. For an equatorially symmetric circulation, $v = 0$ at the equator, hence the only term that can positively accelerate the equatorial jet is the vertical transport term. In the two-level system, (16) reads in the frictionless upper layer:

$$\frac{\partial \overline{u_1}}{\partial t} = \overline{(\hat{f} + Ro_T\zeta_1)v_1} - Ro_T\,\overline{\omega(u_2 - u_1)}. \tag{17}$$

Hence, superrotation requires $\overline{\omega(u_2 - u_1)} < 0$ at the equator, meaning that vertical motion generates a flux of eastward momentum from the lower to the upper layer. We now explore which planetary waves in tidally locked planets and slow rotators meet this condition.

3.1 Tidally Locked Planets

Tidally locked planets are driven by a zonally varying thermal forcing. Because the cooling is uniform on the nightside, while the heating is stronger near the equator on the dayside, there is also a zonal-mean heating gradient between the equator and the poles. Formally, one can expand the equilibrium potential temperature profile (5) in Fourier series in longitude:

$$\theta_E(\phi, \lambda, p) = \left(\frac{1}{\pi} + \frac{1}{2}\cos\lambda + \ldots\right)(1 - \mathcal{S}\ln\Pi)\,\cos\phi, \tag{18}$$

(in nondimensional terms) and understand the total circulation as a sum of the response the first term (an axisymmetric thermal forcing) and the second term (a wavenumber-1 forcing), neglecting higher-order terms in the expansion.

The axisymmetric part of the forcing leads to a thermally direct circulation, which exports momentum away from the equator and accelerates midlatitude jets. Using a simple angular-momentum conserving model of this circulation (e.g., Held and Hou, 1980), one can show that the speed of the jets scales as

$$U^* \simeq \Omega a \frac{gH}{\Omega^2 a^2} \tag{19}$$

where gH is a representative squared gravity wave speed, which corresponds to $c_p \Delta\Theta_v$ in our model. Hence, a nondimensional jet speed is

$$U \simeq \frac{\Omega a \; c_p \Delta\Theta_v / \Omega^2 a^2}{c_p \Delta\Theta_h / (2\Omega a)} \simeq 2\mathcal{S} \tag{20}$$

The linear response to the wavenumber-1 forcing part is the well-known Matsuno–Gill circulation pattern (Gill, 1980, discussed in the context of tidally locked planets by Showman and Polvani (2010)). The Matsuno–Gill problem is obtained in the two-level system by linearizing (11)–(15) about a state of rest with uniform potential temperatures Θ_1 and Θ_2, with $\Theta_1 - \Theta_2 = \mathcal{S}$:

$$\hat{f}\boldsymbol{k} \times \boldsymbol{u}_1 + \nabla\Phi_1 = 0, \tag{21a}$$

$$\hat{f}\boldsymbol{k} \times \boldsymbol{u}_2 + \nabla\Phi_2 + E\boldsymbol{u}_2 = 0, \tag{21b}$$

$$-\mathcal{S} Ro_T \omega = \frac{\theta_{1E} - \theta_1}{T_{\rm rad}}, \tag{21c}$$

$$-\mathcal{S} Ro_T \omega = \frac{\theta_{2E} - \theta_2}{T_{\rm rad}}, \tag{21d}$$

along with continuity and hydrostasy. Here, $\theta_{iE} = \cos\phi \cos\lambda \, (1 - \mathcal{S} \ln \Pi_i)/2$ for $i = 1, 2$. A sample solution of the Matsuno-Gill problem (21a)–(21d), solved on the sphere with $E = 0.02$, $\mathcal{S} = 0.05$, and $Ro_T T_{\rm rad} = 10$, is shown in Fig. 3. The lower layer geopotential field illustrates the classical structure of the response to equatorial heating, composed of an equatorial Kelvin wave and two off-equatorial Rossby waves, which together form an eastward-pointing chevron pattern. The arrows show the horizontal eddy momentum fluxes $u_2\boldsymbol{u}_2$, the meridional convergence of which forms part of the total eddy acceleration (17). They are directed equatorward, indicating that the horizontal eddy flow accelerates the mean equatorial flow eastward. In the upper layer, the eddy geopotential field is uniform at the equator, as mandated by the absence of drag. Horizontal eddy momentum fluxes are still, however, mostly equatorward. The total upper-layer eddy momentum flux convergence (which is mostly contributed to by the horizontal eddy flow, not shown) is shown in Fig. 4 (cyan line) as a function of latitude.

Our goal is to understand how this eddy acceleration depends on the various control parameters, especially Ro_T and $T_{\rm rad}$. One first observation is that the solution to this system only depends on three parameters: E, $\mathcal{S} Ro_T T_{\rm rad}$, and $\mathcal{S}$ (because the form of θ_{1E} and θ_{2E} depends on $\mathcal{S}$). Second, from continuity and the thermodynamic balance, one finds $u1, u2 \sim \omega \sim (\mathcal{S} Ro_T T_{\rm rad})^{-1}$. Hence, the magnitude of the eddy momentum flux convergence terms is expected to scale as $(\mathcal{S} T_{\rm rad})^{-2} Ro_T^{-1}$ (see (17)).

The Matsuno–Gill problem is solved for a second value of $Ro_T T_{\rm rad}$, both with and without drag. We compute the eddy momentum flux convergence (17) from these solutions, shown as a function of latitude in Fig. 4 (and scaled by $(\mathcal{S} T_{\rm rad})^2 Ro_T$). Every

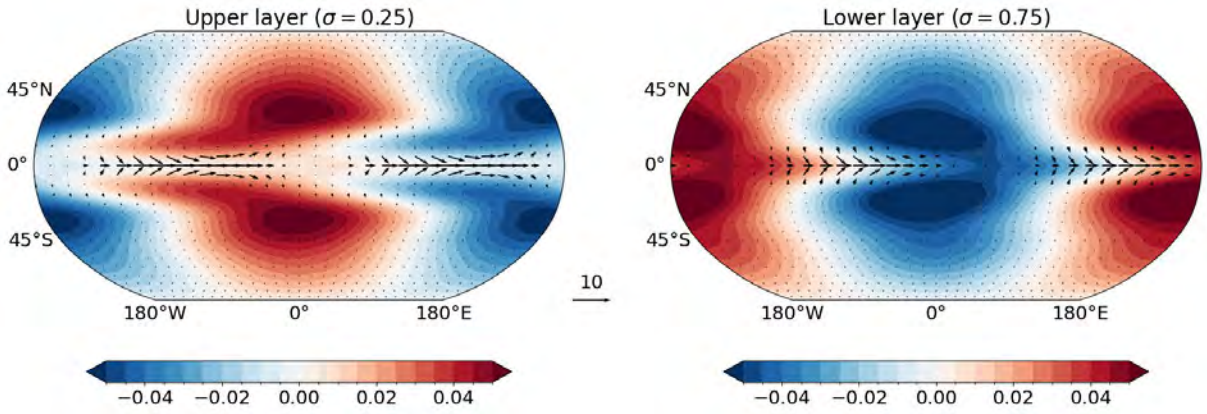

Figure 3: Solution of the Matsuno-Gill problem (21a)–(21d) with $E = 0.02$, $\mathcal{S} = 0.05$, and $Ro_T T_{\mathrm{rad}} = 10$. The left panel shows the upper-layer geopotential Φ_1 (shading) and eddy fluxes of zonal momentum $u_1 \boldsymbol{u}_1$ (arrows). The meridional component of these eddy fluxes is increased by a factor 10 relative to its zonal component for clarity. The right panel shows Φ_2 (shading) and $u_2 \boldsymbol{u}_2$ (arrows).

case contains one equatorial maximum and two off-equatorial maxima, and the latter two maxima shift poleward as $Ro_T T_{\mathrm{rad}}$ is increased. This poleward shift can be understood as follows: thermal relaxation is most effective at high latitudes, where potential temperature gradients can be balanced by the Coriolis force. A very effective thermal relaxation (small T_{rad}) yields small vertical motion at high latitudes (through (21c)–(21d)), hence weak meridional wind (through the vorticity balance, $2\hat{f}\omega = \hat{\beta} v_1$ where $\hat{\beta} = \partial_y \hat{f}$). Both of these effects lead to a small eddy momentum flux convergence at small T_{rad}.

A second observation is that the equatorial eddy momentum flux convergence strengthens relative to the off-equatorial peaks as $Ro_T T_{\mathrm{rad}}$ is decreased, but vanishes in the absence of lower-layer drag ($E = 0$ case). The latter fact can be understood by combining the vorticity equation $\nabla\times$(21a) with continuity, which gives $2\omega = -\partial_\phi u_1 / a$ at the equator. Hence,

$$\overline{\omega u_1} = 0 \tag{22}$$

In the absence of drag, we similarly obtain $\overline{\omega u_2} = 0$, and equatorially symmetric linear motions cannot drive superrotation as $\overline{\omega(u_2 - u_1)} = 0$.

In the presence of drag, the low-level wind pattern can shift eastward relative to the vertical motion pattern, which allows for positive vertical momentum transport. Specifically, one can show (see Appendix B) that the equatorial eddy momentum flux convergence is

$$-Ro_T \overline{\omega u_2} = \frac{1}{\mathcal{S} T_{\mathrm{rad}}} \overline{(\theta_{1E} + \theta_{2E}) u_2} \tag{23}$$

In Fig. 5, we show patterns of $u_2(\phi)$ at the equator (obtained by solving the linear Matsuno-Gill problem on the sphere) for two values of the control parameter $Ro_T T_{\mathrm{rad}}$, for fixed $E = 0.02$ and $\mathcal{S} = 0.05$. We also show a solution with $E = 0$ for reference. In the latter case, $\theta_{1E} + \theta_{2E}$ and u_2 are exactly in quadrature and $\overline{\omega u_2} = 0$. When friction is included, the low-level wind pattern shifts eastward (solid blue lines in Fig. 5), and more so as $Ro_T T_{\mathrm{rad}}$ is decreased. This shift can be understood in the beta-plane shallow water model of the Gill problem (Vallis, 2017). As damping is increased, the Kelvin wave cannot propagate as far to the east and shifts westward. The converse happens to the Rossby component. Because the Rossby feels a stronger damping than the Kelvin component, a

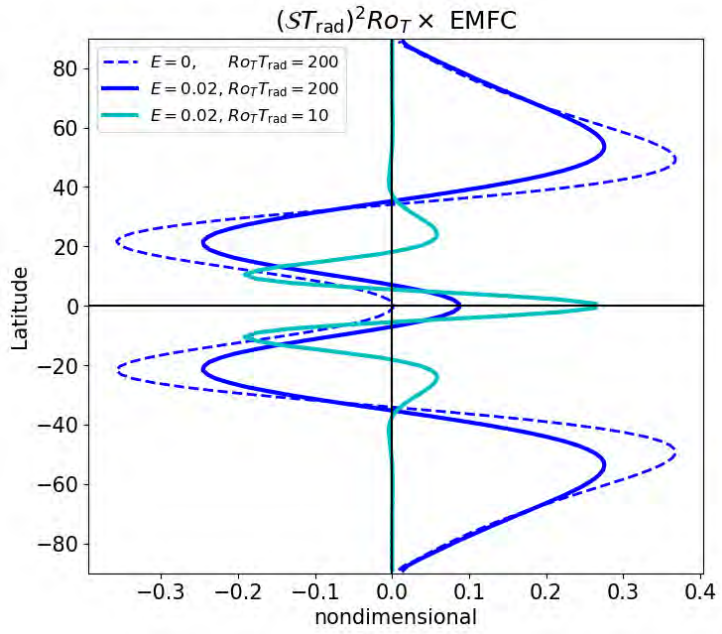

Figure 4: Scaled eddy momentum flux convergence in the two-level Gill problem on the sphere.

given increase in damping shifts it further than the Kelvin wave. This leads to an overall eastward shift in the zonal wind pattern. This explains the increase in the magnitude of the equatorial acceleration with decreasing $Ro_T T_{\mathrm{rad}}$, relative to the off-equatorial peaks.

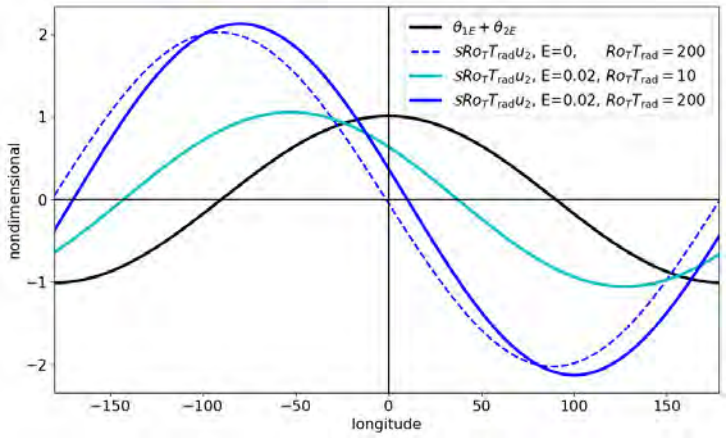

Figure 5: Equilibrium potential temperature and lower-level zonal wind at the equator in the two-level Gill problem on the sphere.

In summary, the response to the zonally asymmetric heating that characterizes tidally locked planets can be broken down in two main parts. The first one is an axisymmetric, thermally direct circulation. A simple theoretical picture of this circulation predicts two midlatitude jets whose speed is independent of Ro_T and T_{rad}. The second part is the response to the zonal wavenumber-1 component of the heating. When treated linearly, this response gives rise to a positive eddy momentum flux convergence at the equator, provided friction is present at low levels. This eddy acceleration also features two off-

equatorial peaks that shift poleward and strengthen relative to the equatorial maximum as $Ro_T T_{\rm rad}$ increases. The overall strength of this acceleration pattern is proportional to $Ro_T^{-1} T_{\rm rad}^{-2}$. Hence, high $T_{\rm rad}$ leads to weak eddy momentum flux convergence, and one may expect a circulation dominated by the midlatitude jets spun up by the thermally direct circulation. Indeed, these jets would likely become baroclinically unstable and radiate Rossby waves that deposit westward momentum when breaking at low latitudes (see, e.g, Vallis, 2017), leading to a weak, or even subrotating, equatorial jet. Low $T_{\rm rad}$ and low Ro_T, on the contrary, lead to a strong and equatorially-focused eddy acceleration, and likely to superrotation. This linear picture is unlikely to inform us about the high-Ro_T, low $T_{\rm rad}$ case due to stronger nonlinearity. Section 4 explores the equilibrated state of fully nonlinear simulations across a wide range of Ro_T and $T_{\rm rad}$ to test these ideas.

3.2 Slow rotators

In our idealized picture, non-tidally locked planets have an entirely zonally symmetric forcing. Thus, one needs an some other mechanism, for example an instability, to produce non-axisymmetric eddies that can accelerate the equatorial atmosphere. Iga and Matsuda (2005) showed that in a spherical shallow water model, various profiles of background zonal wind yield an unstable mode that results from the interaction of a midlatitude Rossby wave and an equatorial Kelvin wave (hereafter called "RK mode"). While this is reminiscent of the Matsuno-Gill pattern, this mode does not arise as a response to a standing forcing and has a fast eastward propagation speed. Wang and Mitchell (2014) extended this linear analysis using a primitive equation model with a wide range of zonal wind profiles. They found that an unstable RK mode exists whenever the midlatitude jets Doppler-shift the Rossby wave phase speed to match that of the equatorial Kelvin wave.

Being symmetric about the equator, the RK mode cannot converge momentum there in the absence of vertical momentum transport. Consequently, single-layer shallow water models cannot produce superrotation if that process is not parameterized (Zurita-Gotor and Held, 2018). Here, we show that RK modes can be captured in the 2-level model and produce equatorial acceleration. We linearize (11)–(15) about a state of horizontally uniform potential temperatures Θ_1 and Θ_2 (with $\Theta_1 - \Theta_2 = \mathcal{S}$), with a barotropic background zonal wind $\boldsymbol{U} = (U(\phi), 0)$, and without friction (the modes still appear in the presence of friction — we are merely trying to show that it isn't a necessary component). The equations read:

$$\partial_t \boldsymbol{u}_i + Ro_T \left(\boldsymbol{U} \cdot \nabla \boldsymbol{u}_i + \boldsymbol{u}_i \cdot \nabla \boldsymbol{U}\right) + \hat{f}\boldsymbol{k} \times \boldsymbol{u}_i + \nabla \Phi_i = 0, \quad i = 1, 2, \tag{24}$$

$$\partial_t \theta_i + Ro_T \left(\boldsymbol{U} \cdot \nabla \theta_i - \mathcal{S}\omega\right) + \frac{\theta_i}{T_{\rm rad}} = 0, \quad i = 1, 2, \tag{25}$$

along with continuity and hydrostasy. $\boldsymbol{u}_i$, θ_i and Φ_i are perturbation quantities. Following Zurita-Gotor and Held (2018), $U(\phi)$ is taken as angular momentum-conserving wind between the equator and a given latitude ϕ_0, and tapers off to 0 at the poles, thus having two broad midlatitude jets.

We solve for zonal-wavenumber-1 eigenmodes of the system (24)–(25) with two different background wind profiles, using $Ro_T = 10, T_{\rm rad} = 200$, and $\mathcal{S} = 0.05$. We show the upper-level winds and geopotential perturbation in the left panels of Fig. 6. In the first case, the zonal jets are close enough to the equator that the midlatitude Rossby wave can phase-lock with the equatorial Kelvin wave. This produces an eastward pointing chevron pattern. We compute the two components of eddy momentum flux convergence (see (17)),

shown on the right-hand panels. As expected, $v_1\zeta_1$ vanishes at the equator, but the vertical momentum transport term produces equatorial acceleration. Both Rossby and Kelvin waves are also observed in the second case (bottom panels), but they do not interact as strongly, as the jets are farther poleward. This results in a weaker growth rate, and weaker equatorial momentum flux convergence, relative to the midlatitudes.

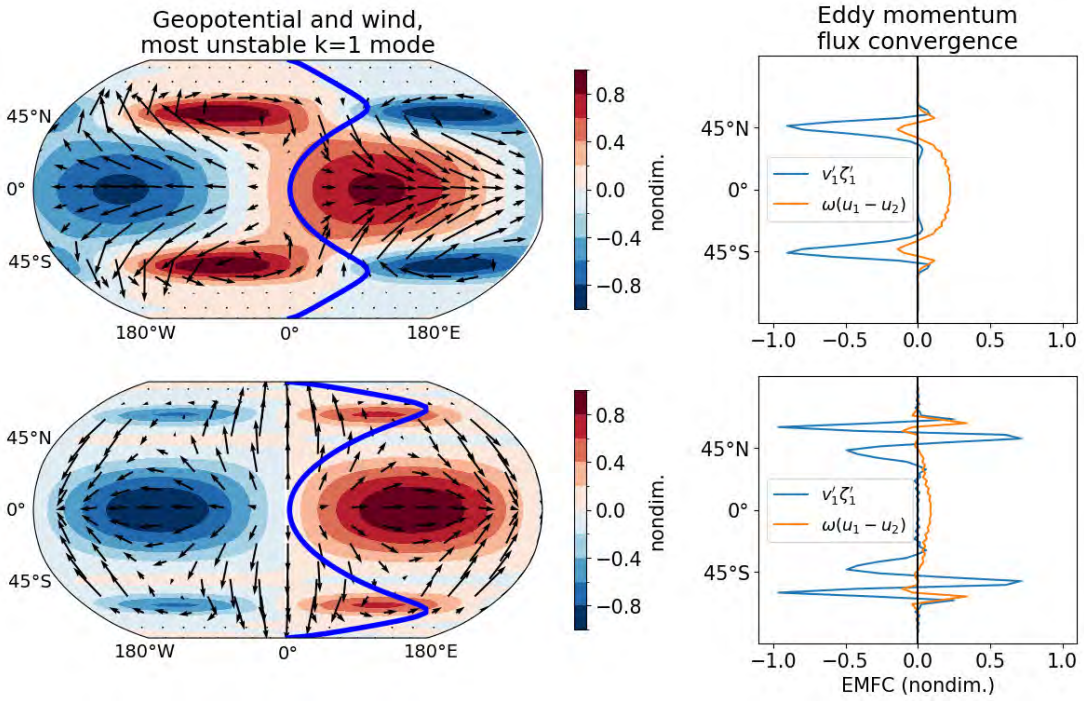

Figure 6: (Top) Most unstable eigenmode with the imposed basic-state wind shown in blue on the left panel and horizontally uniform potential temperature. The maximum speed of the basic-state zonal wind is 0.04, attained at 50°. The left panel shows upper-level geopotential (shading) and wind (arrows), and the right panel shows the two components of the eddy momentum flux convergence. These are normalized by the maximum absolute value of $v_1\zeta_1$, attained in midlatitudes. (Bottom) Same as the top row, with a different basic-state zonal wind that attains a maximum of 0.08 at 65°. The mode shown is the most unstable RK-like eigenmode. The growth rates for these modes are respectively 0.10 and 0.0072, and their frequencies are respectively 0.11 and 0.19 (the positive sign indicates eastward propagation).

This result indicates that the two-level model could be one of the simplest frameworks to be able to produce superrotation in the presence of axisymmetric forcing. We verify this claim in the next section.

4 Nonlinear Models of Superrotation

In this section, we perform fully nonlinear integrations of the 2-level model, with both tidally locked and axisymmetric thermal forcings, for a wide range of input parameters. Our goal is to test the qualitative, quasi-linear mechanisms presented in section 3, including the behavior of superrotation as a function of Ro_T and $T_{\rm rad}$ and the importance of surface friction for superrotation on tidally locked planets. Another goal is to assess

whether this simple framework can produce superrotation on slow rotators. The nonlinear 2-level model is envisioned as a step of intermediate complexity between simple linear models and GCMs, as it contains many of the processes of the latter (such as wave-mean-flow interactions and transient eddies) with the simplest possible vertical structure. The robustness of some of the results presented is verified using the 10 level model, which is a simple GCM.

4.1 Tidally locked planets in a 2-level model

All of the runs presented (except for the runs without friction at the end of this part) use $E = 0.02$ and $\mathcal{S} = 0.05$. These are both relatively low values. E is more representative of gaseous planets than rocky planets, and the low value of $\mathcal{S}$ represents relaxation towards a profile that is nearly neutral to convection. The presence of condensible species would likely increase this value. We perform a total of nine runs, spanning three values of Ro_T (0.2, 1, and 5) and three values of $T_{\rm rad}$ (10, 50 and 250). Each run is integrated for 500 rotation periods (i.e., until $t = 2000\pi$). A statistically steady state is reached after about 200, and steady-state values are obtained by averaging over the last 250 rotation periods. Finally, the hyperdiffusion coefficient is taken as 1.5×10^{-7} for all runs except the $Ro_T = 5, T_{\rm rad} = 10$ run which uses 3×10^{-7}.

Figure 7 shows the equilibrated potential temperature and winds in the upper layer. The zonal-mean wind fields possess numerous interesting features, some of which are consistent with the predictions from section 3. The most notable is that while all the simulations superrotate for $T_{\rm rad} \leq 50$, all of the high-$T_{\rm rad}$ runs subrotate[1]. This is consistent with the behavior of the linear Gill pattern, which features weaker eddy momentum flux convergence at all latitudes, and more so at the equator, at high $T_{\rm rad}$. The strength of the overall circulation, and in particular of the superrotating jet, is confirmed to be a decreasing function of both Ro_T and $T_{\rm rad}$. Midlatitude jets are present at high $T_{\rm rad}$, and we verified (not shown) that the westward acceleration of the equatorial region in the high-$T_{\rm rad}$ runs is produced by transient eddies, whereas stationary eddies accelerate the equatorial flow eastward in all cases. It remains to be shown, however, whether the eddies responsible for this westward acceleration are indeed Rossby waves radiated from the midlatitudes.

Unsurprisingly, some of the features of these simulations are not consistent with the linear picture. In the nonlinear runs, increasing Ro_T while keeping $T_{\rm rad}$ fixed tends to make midlatitude jets disappear. This seems at odds with the fact that the Gill solution produces stronger midlatitude acceleration at high Ro_T (relative to the equator), and that the Held and Hou (1980) model of the axisymmetric component of the circulation predicts a jet speed that does not depend on Ro_T. One thing we can note is that at high Ro_T, the temperature field is more strongly homogenized by gravity waves across the entire planet, as the tropical band, as defined by the region where the local Rossby number is larger than 1, significantly expands (e.g., Sobel et al., 2001; Potter et al., 2014). It is thus expected that midlatitude jets, which must respect thermal wind balance and thus require strong meridional temperature gradients, should be weaker.

The temperature field also shows some interesting features, starting with the above-mentioned fact that it becomes more homogeneous as Ro_T increases (see the range of the color scales). Evidently, temperature homogeneity also increases with $T_{\rm rad}$, as the ratio of the advective timescale to the temperature relaxation timescale decreases. Each runs

[1]We observed in another test that the $Ro_T = 5$, $T_{\rm rad} = 250$ run has a second stable configuration, which superrotates.

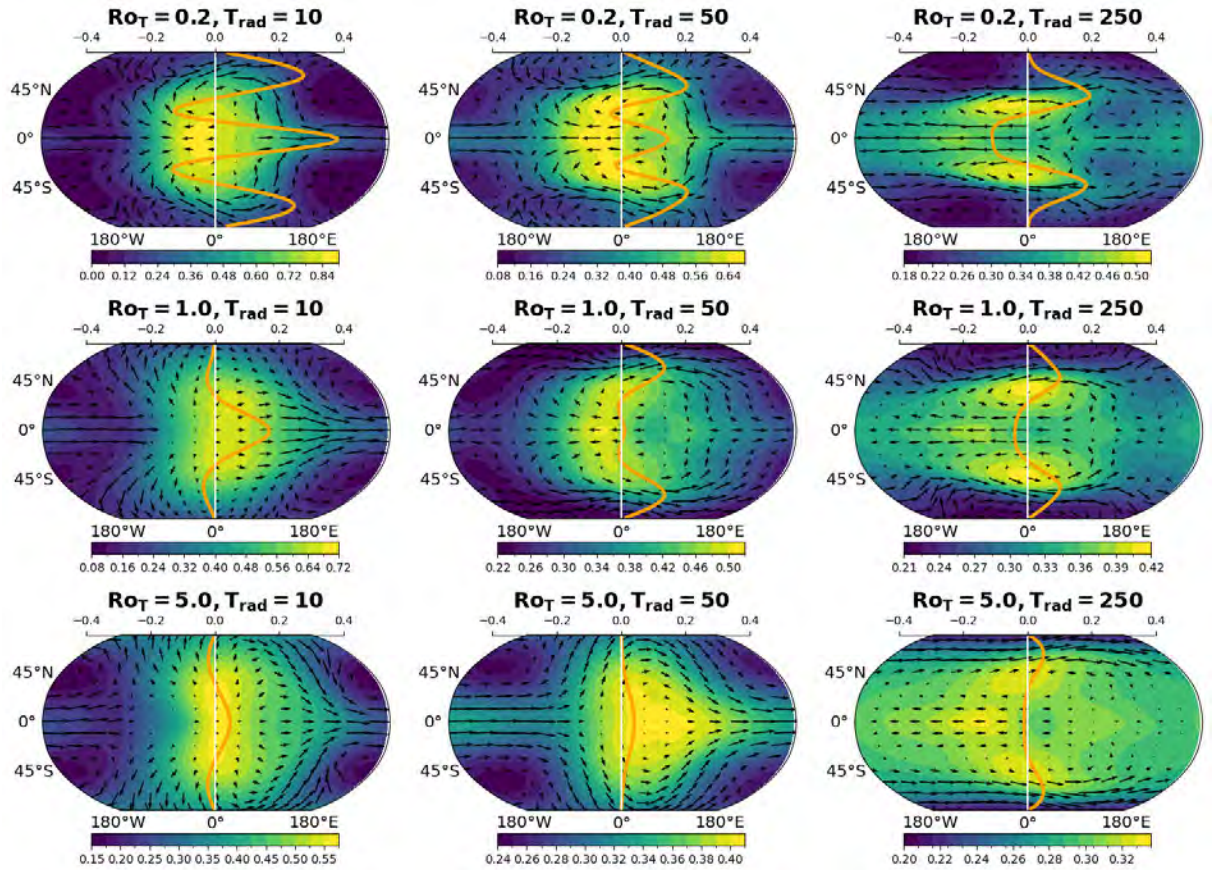

Figure 7: Mean upper level potential temperature and winds over the last 250 rotation periods of a set of fully nonlinear two-level simulations. For each simulation, $E = 0.02$ and $\mathcal{S} = 0.05$, while Ro_T and $T_{\rm rad}$ are given above each panel. Note that each panel uses a different color scale for temperature. Thick orange lines show the zonal-mean zonal wind, with a scale shown on the top axis (the same scale is used for each panel).

still features a hot region on the day side, but the hottest point (hotspot) is not always shifted eastward in the presence of superrotation. A full understanding of the position of this hotspot requires careful analysis of the response of the stationary Gill pattern to the presence of the mean flow (Hammond and Pierrehumbert, 2018), and is out of the scope of the present manuscript.

One important prediction from the linear solutions is that the Gill pattern does not accelerate superrotation in the absence of low-level drag. We re-run the $T_{\rm rad} = 50$ simulations with $E = 0$ to test this idea in fully nonlinear runs. We show the equilibrated zonal-mean u_1 in simulations with and without drag in Fig. 8. The superrotating jet indeed disappears in the low-Ro_T simulations, but remains present (albeit weaker) at $Ro_T = 5$. This may indicate that the Gill model is less relevant to describing the acceleration of superrotation at high Ro_T, where nonlinearities play a much more important role. At low Ro_T, however, the linear prediction is largely confirmed.

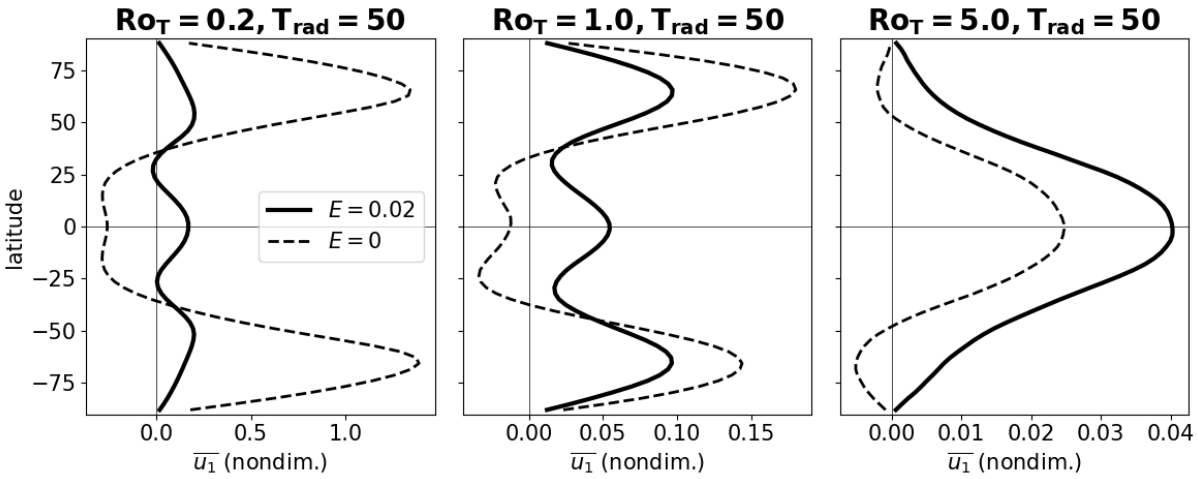

Figure 8: Upper level zonal-mean zonal wind in two-level runs with (solid lines) and without (dashed lines) surface drag.

4.2 Sensitivity of tidally locked integrations to the vertical resolution

Despite their rich behavior, the truncated vertical structure of the 2-level runs may affect the spin-up and maintenance of a superrotating jet. Here, we perform 10-level runs with the exact same parameters as in 4.1 to test the robustness of the 2-level results. One important difference between the two setups is in the surface friction: In both the 2-level and 10-level runs, it is applied in the lowermost layer only. Friction is thus felt through a much deeper layer in the 2-level runs. We have not explored the dependence of these results to the addition of a deeper friction layer in the 10-level runs. All of the 10-level simulations presented here use a fourth-order hyperdiffusion with a coefficient of 5×10^{-7}.

Fig. 9 displays zonal-mean u averaged in the upper half of the atmosphere in the 2-level and 10-level runs. Enhancing the vertical resolution results in stronger superrotating jets for all the parameters shown, and a switch from subrotation to superrotation for all of the $T_{\rm rad} = 250$ runs. The explanation for this discrepancy can be twofold: it could suggest a prominent role for vertical eddy momentum flux convergence in accelerating the jet, or point to the effect of the depth of the layer that feels the surface drag. We were not able to obtain subrotating steady-states in sensitivity tests up to $T_{\rm rad} = 1000$ (not shown).

The thermal structure and horizontal winds of the 10-level runs is shown in Fig. 10. One main difference with the 2-level integrations is that the superrotating jets are more zonally uniform: while all of the 2-level runs have regions of weak or reversed flow, none but two of the 10-level runs do. This likely explains the fact that the hotspots are all shifted eastward in the 10-level runs, as thermal advection is much stronger on the dayside.

Overall, this section suggests that further tests are needed to validate the conclusions proposed on the basis of the 2-level runs and understand the mechanisms behind the differences between these two models.

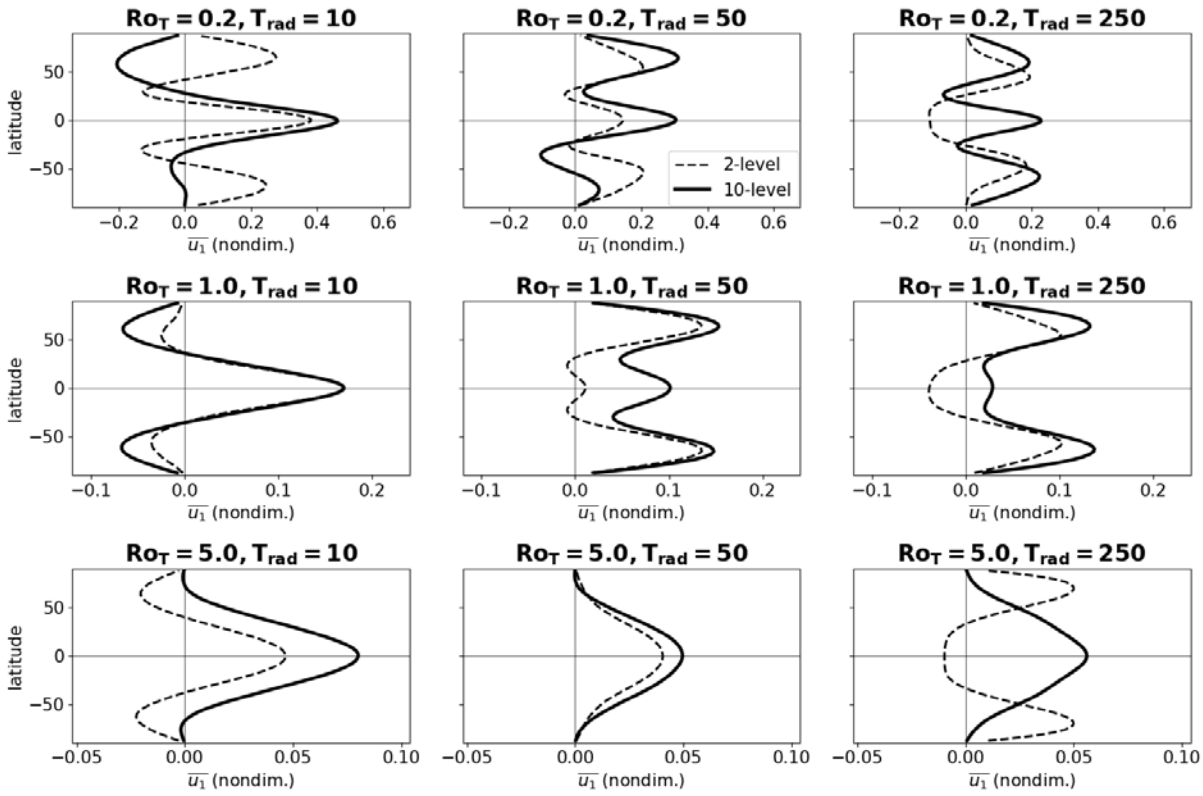

Figure 9: Upper-tropospheric zonal-mean zonal wind in 2-level and 10-level runs. For 2-level runs, we select the upper level. For 10-level runs, we show an average of the upper 5 levels.

4.3 Axisymmetric forcing in the 2-level model

We now move away from the tidally locked configuration, towards axisymmetric thermal forcing. We use the exact same setup and set of parameters as in 4.1, except for the equilibrium potential temperature profiles, which are zonally symmetric — see (5). To the best of our knowledge, superrotation in axisymmetric configurations has only been produced in GCMs (see, e.g., Williams, 2003; Mitchell and Vallis, 2010; Potter et al., 2014; Zurita-Gotor and Held, 2018). We seek to verify whether the simpler two-level model can do so and whether the mechanism can be tied to RK instability.

For the sake of brevity, we only analyze simulations with $T_{\rm rad} = 50$. The equilibrated $\overline{u}(\phi)$ is shown in Fig. 11. Aside from a poleward shift of the midlatitude jets with increasing Ro_T, the main observation is the progressive strengthening of the equatorial flow until superrotation is reached for $Ro_T = 5$. While we have not evaluated the sensitivity of these results to the vertical resolution, GCM simulations performed by Mitchell and Vallis (2010) (albeit with higher $T_{\rm rad}$) were superrotating for $Ro_T \geq 1$. This may suggest that the 2-level model, as in the tidally locked case, does not superrotate as easily as vertically resolved runs. Nevertheless, the general trend is captured and we proceed with studying the modes responsible for eastward acceleration at the equator.

While the equilibrated profiles shown in Fig. 11 are averaged over the last 250 rotation periods (out of 500), most of the acceleration takes place over the first 50. Starting with (17), we decompose the acceleration into mean flow and eddy components:

$$\frac{\partial \overline{u_1}}{\partial t} = \left(\hat{f}\overline{v_1} + Ro_T \overline{\zeta_1}\,\overline{v_1} - Ro_T \overline{\omega}(\overline{u_2 - u_1}) \right) + \left(Ro_T \overline{\zeta_1' v_1'} - Ro_T\, \overline{\omega'(u_2' - u_1')} \right), \qquad (26)$$

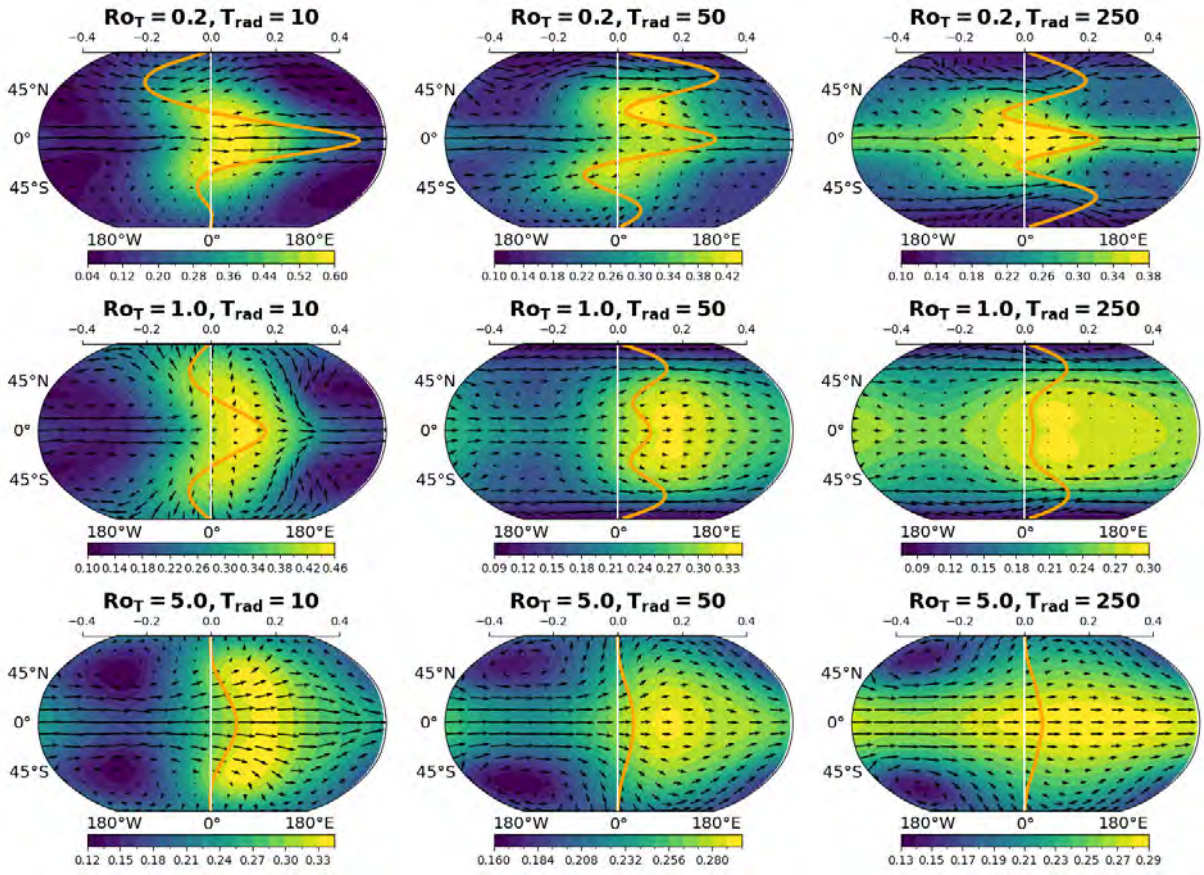

Figure 10: As in Fig. 7, but for 10-level runs with θ and $\boldsymbol{u}$ averaged in the upper 5 levels.

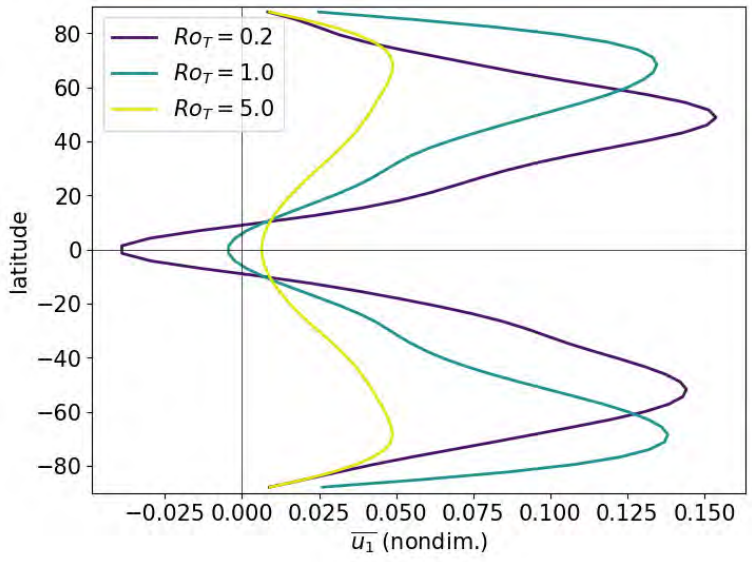

Figure 11: Upper layer zonal-mean zonal wind in two-level runs with axisymmetric thermal forcing, with $T_{\rm rad} = 50$

where primes denote deviations from a zonal average. The first and second terms on the right-hand side, respectively termed the mean meridional circulation (MMC) and eddy momentum flux convergence (EMFC) components, are calculated every quarter of

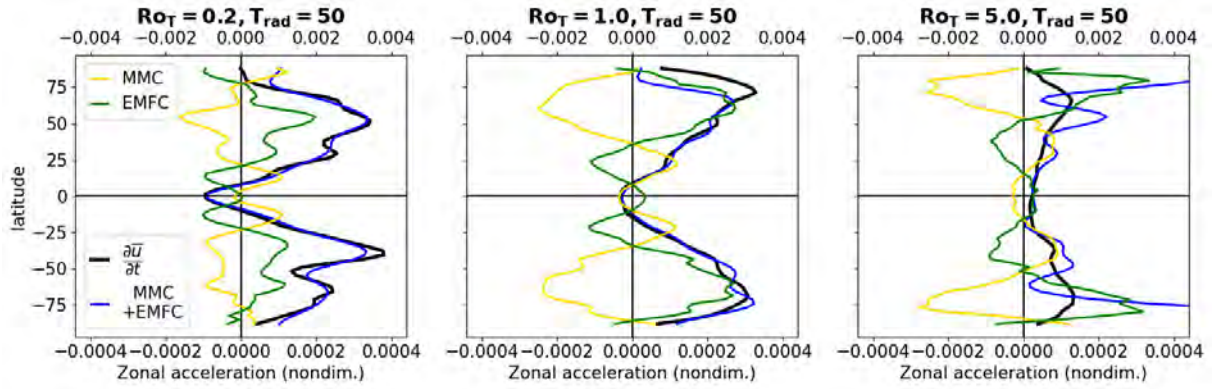

Figure 12: Upper layer zonal acceleration in two-level runs with axisymmetric thermal forcing (averaged over the first 50 rotation periods). The yellow line shows the contribution of the mean flow, $(\hat{f} + Ro_T\overline{\zeta_1})\overline{v_1} - Ro_T\,\overline{\omega}(\overline{u_2 - u_1})$. The yellow line shows the eddy contribution, $Ro_T\left[\overline{\zeta_1' v_1'} - \overline{\omega'(u_2' - u_1')}\right]$. The scale for these two quantities is shown on the top axis. The black line shows the total acceleration $\partial\overline{u_1}/\partial t$, and the blue line the total acceleration diagnosed as the sum of the yellow and green lines. The scale for these two quantities is shown on the bottom axis.

a rotation period and averaged over the first 50 rotation periods, and shown in Fig. 12. We note that the contribution from zonal-mean transients (not shown) is negligible; in other words,

$$\left\langle \hat{f}\overline{v_1} + Ro_T\overline{\zeta_1}\,\overline{v_1} - Ro_T\overline{\omega}(\overline{u_2 - u_1})\right\rangle \simeq \hat{f}\langle\overline{v_1}\rangle + Ro_T\langle\overline{\zeta_1}\rangle\langle\overline{v_1}\rangle - Ro_T\langle\overline{\omega}\rangle\langle\overline{u_2 - u_1}\rangle, \qquad (27)$$

where angle brackets denote a time average. The MMC and EMFC components mostly cancel out, and their sum (smoothed with a Gaussian filter of standard deviation 3°) is shown as a blue line in Fig. 12 (note the different scale). The total acceleration, $\langle\partial\overline{u}/\partial t\rangle$, is shown in black for comparison. At high Ro_T, the contribution from short-time transients increases and the true and diagnosed zonal accelerations differ in midlatitudes, but show decent agreement at the equator. As expected from Hide's theorem, the zonal-mean flow causes westward acceleration at the equator in all cases. The eddy contribution is weak for $Ro_T = 0.2$, suggesting the absence of any instability producing eastward equatorial acceleration. It is positive for both $Ro_T = 1$ and $Ro_T = 5$, but only stronger than the mean flow contribution in the latter case.

In order to identify the waves responsible for this eastward equatorial acceleration, we compute cospectra of the eddy momentum flux convergence. Specifically, each field ψ is Fourier-transformed in longitude and time:

$$\psi(t,\lambda,\phi) = \Re\sum_{k=0}^{N} e^{ik\lambda}\int_{-\infty}^{+\infty}\tilde{\psi}(\omega,k,\phi)e^{-i\omega t}\mathrm{d}\omega, \qquad (28)$$

and the correlation between two fields ψ and χ is decomposed as

$$\langle\overline{\psi'\chi'}\rangle = \frac{1}{2}\sum_{k=0}^{N}\int_{-\infty}^{+\infty}\Re(\tilde{\psi}\tilde{\chi}^*)(\omega,k,\phi)\mathrm{d}\omega, \qquad (29)$$

This way, we decompose the eddy momentum flux convergence at each latitude as

$$\begin{aligned} \mathrm{EMFC}(\phi) &= Ro_T \left(\langle \overline{\zeta_1' v_1'} \rangle + \langle \overline{\omega'(u_1' - u_2')} \rangle \right) \\ &= \sum_{k=0}^{N} \int_{-\infty}^{+\infty} \widetilde{\mathrm{EMFC}}(\omega, k, \phi) \mathrm{d}\omega, \end{aligned} \tag{30}$$

where

$$\widetilde{\mathrm{EMFC}}(\omega, k, \phi) = \frac{Ro_T}{2} \Re \left(\tilde{\zeta}_1 \tilde{v}_1^* + \tilde{\omega}(\tilde{u}_1^* - \tilde{u}_2^*) \right) \tag{31}$$

denotes the contribution of waves of frequency ω and zonal wavenumber k to the eddy momentum flux convergence at latitude ϕ. The cospectra $\widetilde{\mathrm{EMFC}}$ are calculated for the first 50 rotation periods, smoothed in frequency with a Gaussian filter of standard deviation 0.01, and averaged over the 5°S - 5°N band. These are shown for the two simulations that display positive equatorial acceleration, namely $Ro_T = 1$ and $Ro_T = 5$, in Fig. 13. Both cases show several peaks at $k = 2$, with both positive and negative frequencies. Weaker additional peaks are present at higher wavenumbers and, to a lesser extent, at $k = 1$. While the positive frequencies (eastward propagating waves) are compatible with RK waves, the presence of positive peaks at negative frequencies suggests that other types of waves may contribute to the spin-up of superrotation.

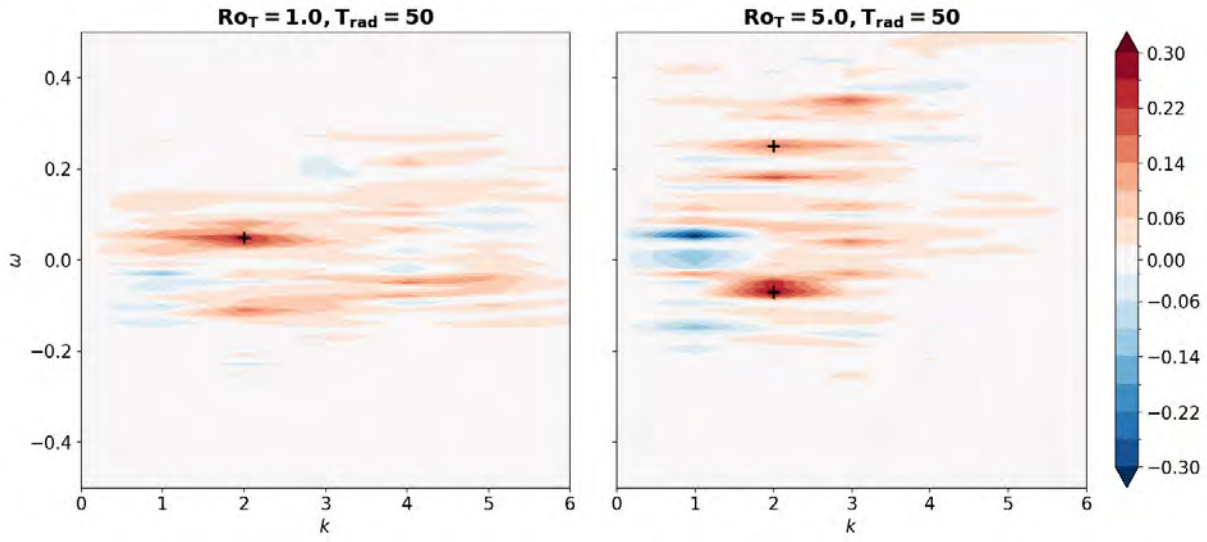

Figure 13: Spectral decomposition of the upper-layer eddy momentum flux convergence (see text for details), computed over the first 50 rotation periods, averaged over the equatorial band (5°S - 5°N). The x-axis is zonal wavenumber k and the y-axis is frequency ω. The black plus signs indicate the waves that are shown in Fig. 14.

In order to visualize the structure of the wave that yield the strongest positive EMFC peak in the $Ro_T = 1$ simulation, we select the $k = 2$, $\omega = 0.05$ component of the upper-layer wind and geopotential fields, shown on the top-left panel of Fig. 14 (again, the Fourier spectra are smoothed in frequency with a Gaussian filter of standard deviation 0.01). While the pattern is quite different from the canonical RK wave shown in Fig. 6, one can clearly distinguish a Kelvin wave structure at the equator, along with midlatitude Rossby waves. Unlike the pattern in Fig. 6, the Rossby waves are ahead of phase compared with the Kelvin wave, but the two connect in a way to produce an eastward-pointing

chevron pattern in the wind field. The resulting EMFC is positive across the 10°S-10°N region.

The $Ro_T = 5$ simulation has two EMFC peaks at positive frequencies for $k = 2$ (corresponding to $\omega = 0.18$ and $\omega = 0.25$). Both have similar structures, hence we only show the second mode in the second row of Fig. 14. Once again, the pattern connects an equatorial Kelvin wave with midlatitude Rossby waves. It thus seems likely that a form of RK instability is responsible for the appearance of these modes, both in the $Ro_T = 1$ and $Ro_T = 5$ simulation. This corroborates earlier studies by Wang and Mitchell (2014) and Zurita-Gotor and Held (2018), in a simpler framework that does not involve a GCM.

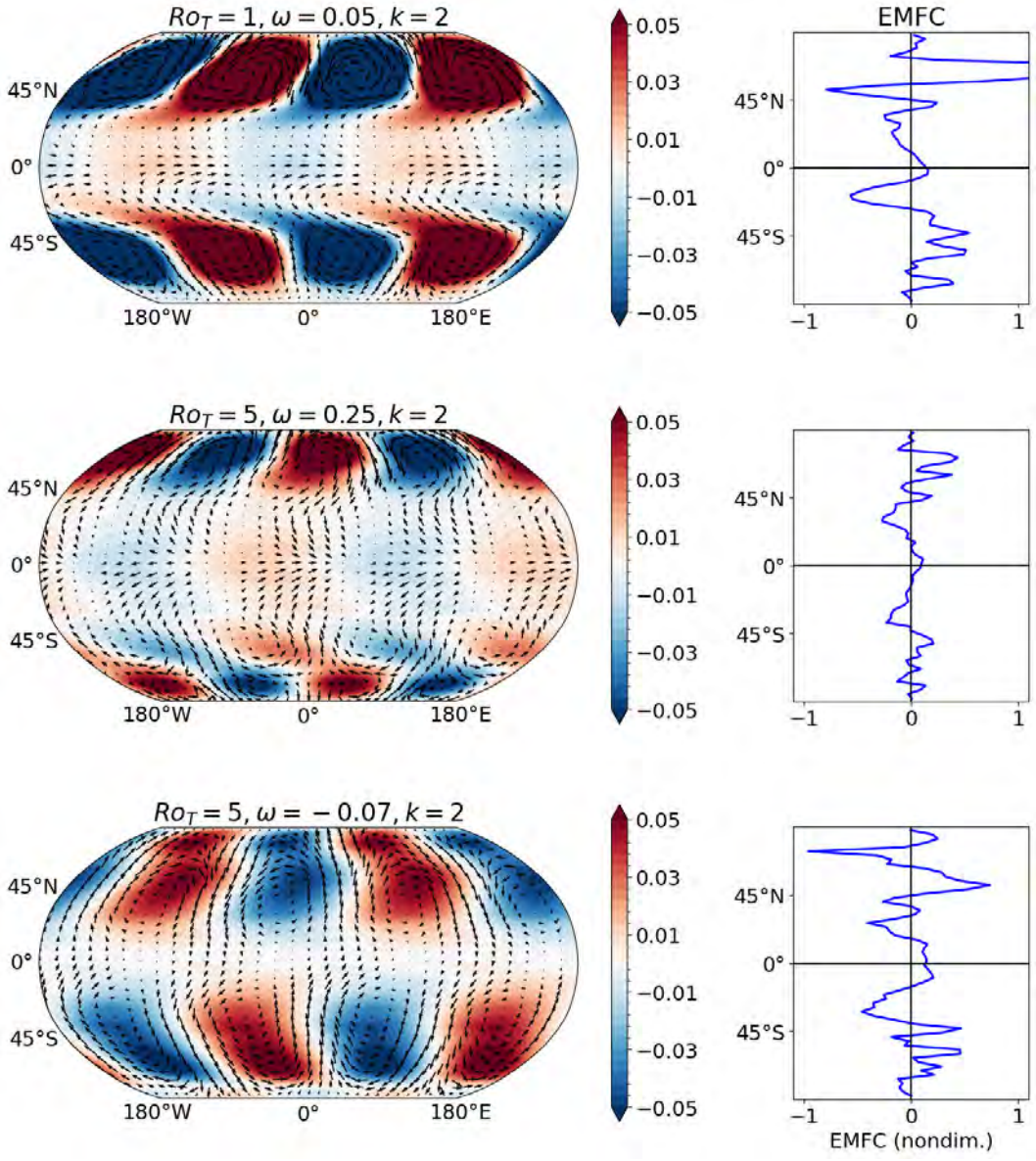

Figure 14: Sample modes from the first 50 rotation periods of the $Ro_T = 1$ and $Ro_T = 5$ axisymmetric runs. The left panels show upper layer wind and geopotential, and the right panel shows the EMFC of each mode as a function of latitude, namely $\widetilde{\mathrm{EMFC}}(\omega, k, \phi)$. The first row shows the $k = 2$, $\omega = 0.05$ component of the $Ro_T = 1$ simulation. The second and third row show, respectively, the $k = 2$, $\omega = 0.25$ and $k = 2$, $\omega = -0.07$ components of the $Ro_T = 5$ simulation.

The EMFC cospectrum of the $Ro_T = 5$ simulation (right panel of Fig. 13) shows a prominent peak at negative frequencies. This peak cannot involve equatorial Kelvin waves, as the latter propagate eastward and thus must involve positive frequencies. We plot the component of the dynamics that corresponds to this peak ($k = 2$, $\omega = -0.07$) on the third row of Fig. 14. The structure of this mode resembles a mixed Rossby-gravity (MRG) wave, with two trains of Rossby waves (one in each hemisphere) that are out of phase. A mode with similar structure, frequency and wavenumber (not shown) can be obtained as an eigenmode of the (24)-(25) system, with a basic-state wind profile taken from the $Ro_T = 5$ run. This mode has a weak negative growth rate; it conceivably become unstable with slight modifications to the basic-state profile. Overall, this suggests that RK modes may not be the only type of wave contributing to the spin-up of superrotation on slow rotators.

This section has shown that superrotation can be achieved in a simple two-level model of slow rotators. Some of the eddies that cause eastward equatorial acceleration resemble RK modes, corroborating earlier studies. However, our model suggests that other types of waves, resembling westward-traveling MRG waves, may contribute to the establishment of superrotation on slow rotators.

5 Transition from a Slow Rotator to a Tidally Locked Planet

We have now seen that the waves accelerating superrotation on tidally locked and axisymmetrically forced planets are similar but distinct. Both involve a coupling between midlatitude Rossby waves and equatorial Kelvin waves (although other types of waves may contribute to the superrotation on slow rotators, see section 4.3); however, the waves in the tidally locked case are predominantly forced standing waves wheres those on axisymmetrically forced planets arise from an instability and have a fast eastward propagation. In this section, we explore the transition between these two cases. Specifically, we fix all parameters and run a suite of simulations where we only vary the longitudinal structure of the thermal forcing, forming a continuum between axisymmetric and tidally locked thermal forcing. It is unlikely that any planet could, in reality, undergo such a transition: the switch to tidal locking would likely be accompanied with a change in the rotation rate, hence in Ro_T. Rather, our goal with this exercise is to understand the interplay between RK waves and standing waves forced by zonal asymmetries. Using a spectral decomposition of the equatorial EMFC, we identify the properties of the waves that accelerate superrotation in the various cases and illustrate their structures.

In this section, we will be analyzing six simulations, all using $\mathcal{S} = 0.05, E = 0.02, Ro_T = 5$ and $T_{\rm rad} = 50$. This set of parameters corresponds to the axisymmetrically forced simulation that superrotates in section 4.3. As in Section 4, all of the simulations are run for 500 rotation periods, although we will mostly be studying the first 50 (when most of the equatorial acceleration takes place). The runs only differ in the zonal structure of their thermal forcing. The two end-members were already described in section 4: one is axisymmetric (i.e., $\theta_{iE} = (1 - \mathcal{S} \ln \Pi_i) \cos\phi \, (1/\pi)$) and the other one is tidally locked (i.e., $\theta_{iE} = (1 - \mathcal{S} \ln \Pi_i) \cos\phi \, \max(0, \cos\lambda)$). Four runs with increasingly stronger zonal asymmetries bridge these two. Recalling that $\max(0, \cos\lambda)$ expands in Fourier series as $1/\pi + (\cos\lambda)/2 + \ldots$, we define a parameter ϵ such that θ_{iE} is given, in these runs, by

$$\theta_{iE} = (1 - \mathcal{S} \ln \Pi_i) \, \cos\phi \, \left(\frac{1}{\pi} + \epsilon \cos\lambda \right), \tag{32}$$

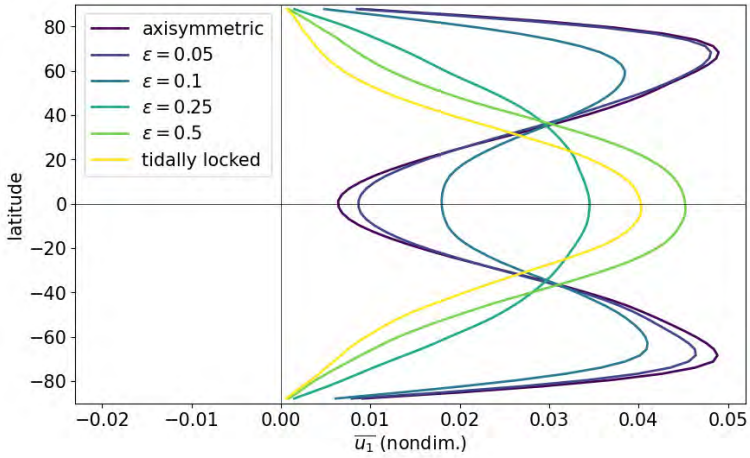

Figure 15: Upper layer zonal-mean zonal wind in a suite of two-level runs with increasing $k = 1$ heterogeneities in thermal forcing, with $Ro_T = 5$ and $T_{\text{rad}} = 50$

and we use four values of ϵ: $0.05, 0.1, 0.25$ and 0.5.

Figure 15 shows the equilibrated $\overline{u_1}$ in the six simulations of the suite. One can observe a transition from a regime with two strong high-latitude jets and weaker equatorial flow (axisymmetric or weakly zonally asymmetric cases) to a regime where the zonal wind increases monotonously from the poles to the equator ($\epsilon \geq 0.25$ and tidally locked cases). The jet strength increases with ϵ, which suggests that stronger forcing of a Gill-like pattern leads to stronger superrotation. Finally, the $\epsilon = 0.5$ and tidally locked simulations have a very similar profile, indicating that the higher-order harmonics in the zonal structure of the thermal forcing in this tidally locked case only play a weak role. This also justifies our approach of studying the transition, by only varying the strength of the $k = 1$ component of the forcing.

We now turn to the spectral decomposition of the EMFC, detailed in section 4.3. Spectra are calculated over the first 50 rotation periods in each simulation and shown in Fig. 13. One element that stands out is that while the spectrum of the axisymmetric run is broadly distributed in frequency and zonal wavenumber, all of the other runs are dominated by the standing $k = 1$ component. This is especially surprising for the $\epsilon = 0.05$ and $\epsilon = 0.1$ cases: while their $\overline{u_1}$ profiles are qualitatively similar to the axisymmetrically forced ($\epsilon = 0$) case and the zonal asymmetry in their forcing is weak, superrotation results from a wholly different process that involves standing waves rather than travelling RK waves or MRG waves. This suggests that weak zonal asymmetries are more efficient at causing superrotation than instabilities of the axisymmetric dynamics.

Fig. 17 shows the structure of the standing $k = 1$ mode in all of the non-axisymmetric runs. All of these patterns show a coupling between off-equatorial Rossby gyres (around 30° for $\epsilon \leq 0.25$ and 40° for the $\epsilon = 0.5$ and the tidally locked case) and an equatorial Kelvin wave, reminiscent of the Matsuno-Gill pattern. The $\epsilon \leq 0.25$ runs show an additional train of high-latitude Rossby wave that is likely due to the presence of high-latitude jets (the $\epsilon = 0.25$ case possesses high-latitude jets early in the simulation, before the zonal wind profile shown in Fig. 15 arises). Indeed, these waves have a westward phase propagation and need a Doppler shift to be able to phase-lock with the standing pattern.

Despite the dominance of the standing $k = 1$ component in setting the total EMFC,

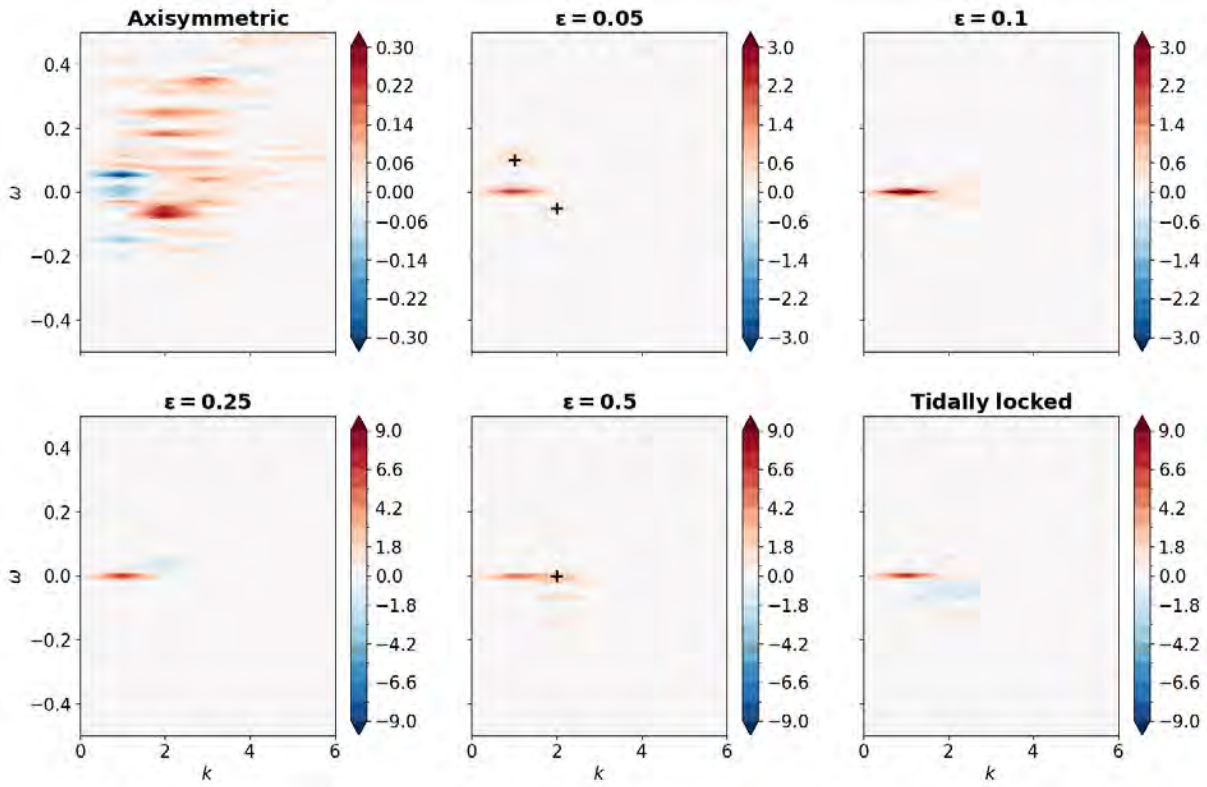

Figure 16: Spectral decomposition of the upper layer EMFC (as in Fig. 13) in the suite of two-level runs with increasing $k = 1$ heterogeneities in thermal forcing. The black "plus" signs indicate the waves shown in Fig. 18.

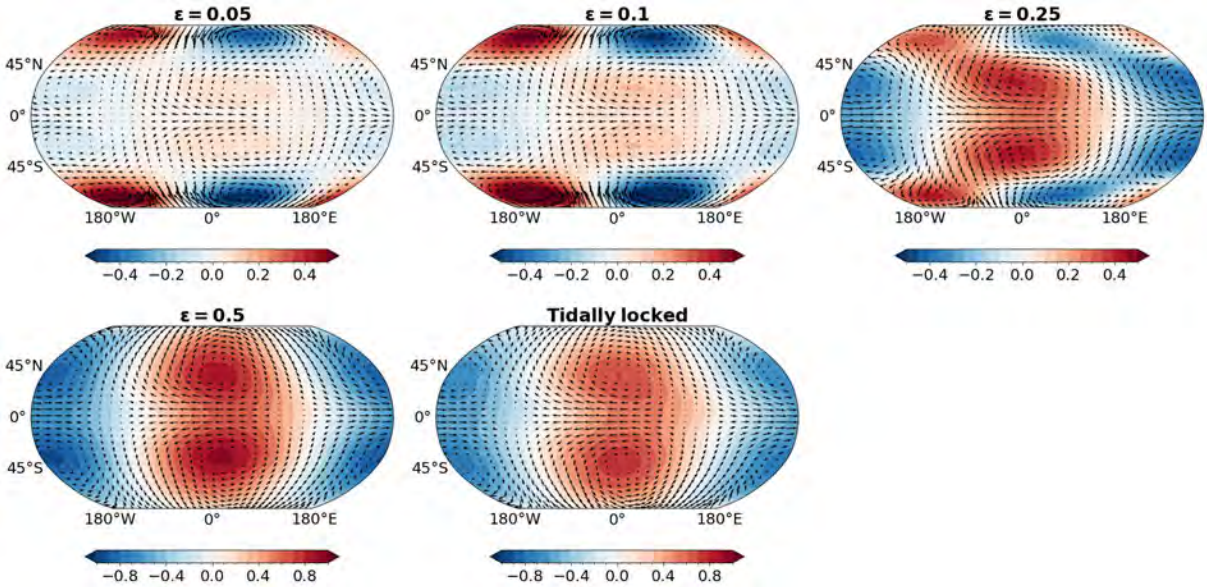

Figure 17: Standing, $k = 1$ eddy component of the upper-layer geopotential and wind in the non-axisymmetric runs of the suite.

a few secondary peaks are observed, especially in the $\epsilon = 0.05$ and $\epsilon = 0.5$ cases. We investigate three of these (identified by the black signs in Fig. 16) in Fig. 18. The first

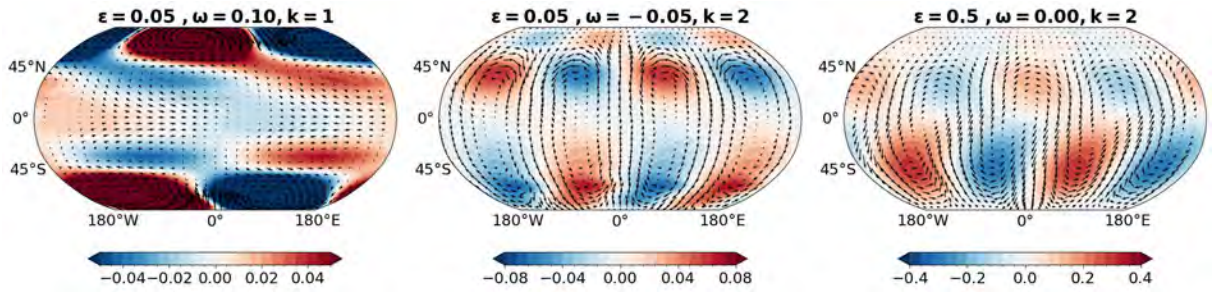

Figure 18: Upper-layer geopotential and wind in sample modes from two runs of the suite. The first two panels show propagating modes from the $\epsilon = 0.05$ run, while the third panel shows a standing $k = 2$ mode from the $\epsilon = 0.5$ run.

panel shows an eastward-propagating $k = 1$ mode from the $\epsilon = 0.05$ run. The structure of this mode is very similar to the RK wave from Fig. 6, except for the coupling with high-latitude wave trains. A similar mode exists in the $\epsilon = 0$ case (not shown). The second panel shows a westward-propagating $k = 2$ mode that is highly similar to the one illustrated in the third row of Fig. 14, i.e., a coupling between $k = 2$ Rossby waves in both hemispheres, with a westward phase propagation. Thus, some of the propagating modes from the $\epsilon = 0$ still exist in the presence of a weak zonal asymmetry — they simply aren't as efficient as the standing mode in accelerating superrotation.

Finally, the spectral patterns of EMFC in the $\epsilon = 0.5$ and tidally locked case both present a secondary peak in the $k = 2, \omega = 0$ band. We illustrate the structure of this mode in the $\epsilon = 0.5$ run, noting that it is very similar in the tidally locked run. It has a similar structure to the MRG-like waves already observed in the $\epsilon = 0$ and $\epsilon = 0.05$ cases, although the two wave trains are in quadrature (not out of phase) in this case. These relative positions of the gyres allow for the eddy wind to tilt in the Northeast-Southwest direction, and because the northern wave train is closer to the equator than the southern one, leads to eastward momentum flux convergence. The fact that this is a standing mode may be a coincidence of the fact that its intrinsic westward propagation is cancelled by the strong superrotating jet of the $\epsilon = 0.5$ simulation: indeed, there is no standing $k = 2$ forcing in this run.

We have found that despite a seemingly continuous transition in wind patterns when transitioning from an axisymmetrically forced ($\epsilon = 0$) to a tidally locked planet, the processes responsible for superrotation almost immediately switch when weak zonal asymmetries are applied. Specifically, a standing Gill-like pattern soon dwarfs the contribution from propagating waves seen in the $\epsilon = 0$ case in setting the total EMFC. However, the two processes can and do coexist (as seen for $\epsilon = 0.05$), and some of the unstable modes from the $\epsilon = 0$ case may still be present when strong zonal asymmetries are applied (as the MRG-like wave seen in the $\epsilon = 0.5$ case suggests).

6 Discussion and Conclusions

This work seeks a unified understanding of superrotation on slowly rotating and tidally locked planets. Our main tool for studying these planetary atmospheres is a two-level model, in which the dynamics are driven by a relaxation towards a specified potential temperature profile. This profile can model axisymmetrically forced slow rotators, tidally locked planets, or cases in between, which involve weak zonal asymmetries. This model

bridges the gap between single-layer shallow water models (which struggle to produce superrotation in some cases, especially on slow rotators or without parameterizations of vertical momentum transport) and GCMs. In addition to the thermal forcing profile, three parameters govern the dynamics: a thermal Rossby number (Ro_T), a radiative relaxation time scale (T_{rad}), and an Ekman number (which quantifies surface drag).

On tidally locked planets, the presence or absence of superrotation is the result of a competition between a thermally direct Hadley circulation and a wavenumber-1 standing eddy arising from the zonally asymmetric thermal forcing (Matsuno-Gill pattern). At high T_{rad}, the eddy momentum flux convergence is weak and focused in midlatitudes. This leads to the appearance of subrotating states in fully nonlinear simulations. At low T_{rad}, the Gill pattern produces stronger equatorial EMFC provided surface friction is present. This leads consistently to superrotating states in fully-nonlinear simulations. The more strongly-nonlinear high-Ro_T cases seem to evade this simple picture, as high-Ro_T nonlinear simulations without surface friction still superrotate. Preliminary tests with a multi-level GCM indicate that some of these results may not be robust, as all high-T_{rad} cases superrotate.

On slow rotators, some known results are reproduced in the simple framework of the two-level model. An unstable eigenmode of the zonally symmetric dynamics, which couples an eastward-propagating equatorial Kelvin wave with two midlatitude Rossby wave trains, is found when the model is linearized. A similar mode, albeit with higher zonal wavenumber, is shown to cause eastward equatorial acceleration in the early stages of a set of fully nonlinear simulations. However, a second, previously unidentified mode (which couples two out-of-phase Rossby wave trains, one in each hemisphere) is also shown to play a major role in the acceleration of superrotation in some runs.

Finally, we examine the interplay between the eddies causing superrotation on slow rotators and tidally locked planets in a suite of simulations that connects these two cases. It is shown that the traveling RK waves (and MRG-like waves) that cause superrotation when axisymmetric thermal forcing is applied are still present in the presence of weak zonal asymmetries. However, these play a relatively minor role compared to the standing eddies forced by the zonally asymmetric thermal forcing, in setting the total eddy-momentum flux convergence (even in cases with a weak asymmetry).

This work is a first step towards the sought-after unified understanding of superrotation, and several results remain partial. A proper understanding of the differences between two-level and 10-level results has not yet been reached. Proper evaluation of the results on axisymmetric and weakly asymmetric cases, including the existence and importance of the MRG-like mode, needs to be addressed using the multi-level model. Finally, a more refined view of the parameter dependence of superrotation (both in terms of existence and strength) needs to be established.

Acknowledgements

I want to extend my deepest thanks to my advisor Geoffrey Vallis and to Keaton Burns and Daniel Lecoanet for their invaluable help with Dedalus, and to Jonathan Mitchell for a number of useful conversations about superrotation.

Appendix A - Validation of the multi-level model

A 10-level model built in Dedalus is tested in the configuration proposed by Held and Suarez (1994), which serves as a test bed for GCMs. As in our setup, the model is forced with a Newtonian relaxation to a prescribed zonally symmetric potential temperature profile. The relaxation coefficient varies in latitude and in the vertical. The momentum equations contain a Rayleigh drag, which decreases linearly in strength until the $\sigma = 0.7$ level, above which it is absent. The hyperdiffusion coefficient is chosen, here, as 4×10^{15} m^4 s^{-1}, which corresponds to a nondimensional value of 3×10^{-8}, i.e., an order of magnitude lower than used in Section 4.2. Using the same coefficient as in Section 4.2 does not drastically change the results, but leads to a very weakly superrotating state in the mid-troposphere and slightly weakens the temperature variance.

Fig. 19 shows the various diagnostics of the original Held and Suarez (1994) article. The 10-level model is able to develop the expected circulation, with two midlatitude jets peaking around $\sigma = 0.2$ at 45° latitude, easterlies in the tropics and polar regions, and a relatively uniform temperature distribution in the tropics. The temperature variance shows the two expected midlatitude maxima, and the eddy zonal wind shows the wavenumber 5-6 peaks just equatorward and poleward of the midlatitude jets. This analysis validates our use of the 10-level model as a simple GCM in section 4.2.

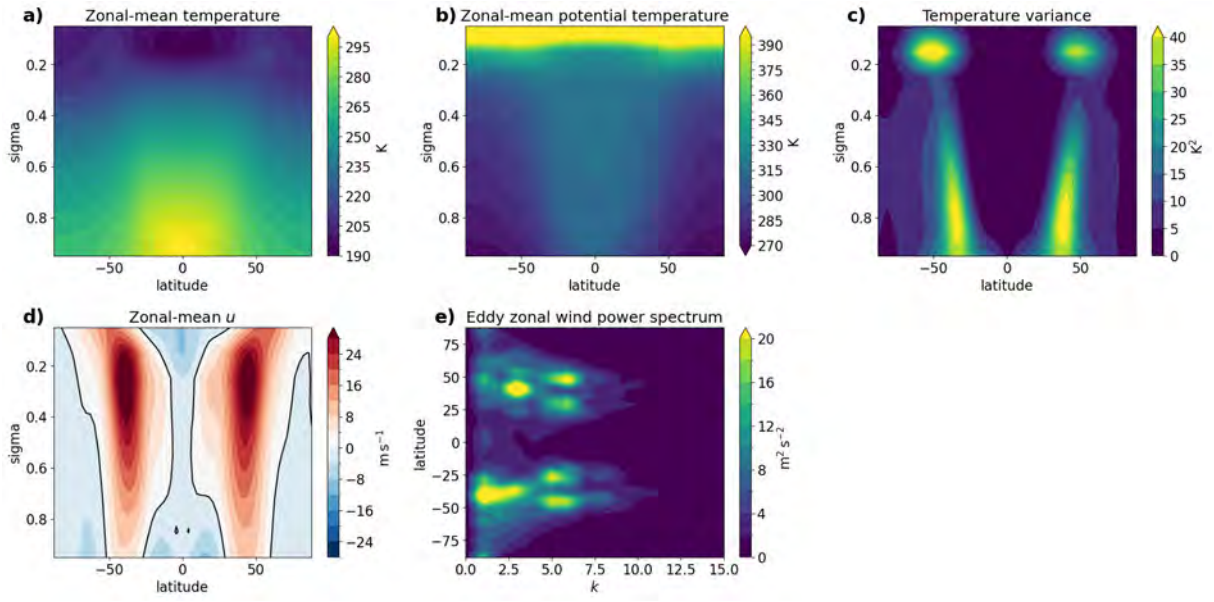

Figure 19: Set of diagnostics for the Held and Suarez (1994) test of the 10-level model. All fields are collected over the last 25 days of a 100-day simulation. (a) Zonal mean temperature $\overline{T}$. (b) Zonal mean potential temperature $\overline{\theta}$. (c) Temperature variance, $[(T - [T])^2]$ where $[\cdot]$ represents a zonal and time average. (d) Zonal mean zonal wind $\overline{u}$. (e) Zonal power spectrum of the eddy zonal wind as a function of latitude. The eddy zonal wind $u - \overline{u}$ is Fourier transformed in longitude, and the square of the Fourier coefficients is averaged in time and in the vertical.

Appendix B - Derivation of the eddy-momentum flux convergence expression in the linear two-level model

We seek to obtain a simplified expression for the eddy momentum flux convergence at the equator in the 2-level Gill model. As explained in section 3, this quantity simplifies to $-Ro_T\overline{\omega u_2}$. Summing (21c) and (21d), one obtains

$$-Ro_T\omega = \frac{\theta_{1E} + \theta_{2E}}{\mathcal{S}T_{\text{rad}}} - \frac{\theta_1 + \theta_2}{\mathcal{S}T_{\text{rad}}} \tag{33}$$

Hence,

$$-Ro_T\overline{\omega u_2} = \frac{1}{\mathcal{S}T_{\text{rad}}}\overline{(\theta_{1E} + \theta_{2E})u_2} - \frac{1}{\mathcal{S}T_{\text{rad}}}\overline{(\theta_1 + \theta_2)u_2}. \tag{34}$$

We now proceed to show that $\overline{(\theta_1 + \theta_2)u_2} = 0$. Subtracting the upper-layer momentum balance from the lower-layer one at the equator (where $v_1 = v_2 = 0$), one obtains

$$\frac{1}{\cos\phi}\partial_\lambda(\Phi_2 - \Phi_1) + Eu_2 = 0. \tag{35}$$

Combining with hydrostasy,

$$\frac{\pi_1 - \pi_2}{2\cos\phi}\partial_\lambda(\theta_1 + \theta_2) + Eu_2 = 0. \tag{36}$$

Hence,

$$\overline{(\theta_1 + \theta_2)u_2} \propto \overline{(\theta_1 + \theta_2)\partial_\lambda(\theta_1 + \theta_2)} = 0 \tag{37}$$

References

Barnes, R. (2017). Tidal locking of habitable exoplanets. Celestial Mechanics and Dynamical Astronomy, 129(4):509–536.

Burns, K. J., Vasil, G. M., Oishi, J. S., Lecoanet, D., and Brown, B. P. (2020). Dedalus: A flexible framework for numerical simulations with spectral methods. Physical Review Research, 2(2):023068.

Busse, F. (1976). A simple model of convection in the jovian atmosphere. Icarus, 29(2):255–260.

Gill, A. E. (1980). Some simple solutions for heat-induced tropical circulation. Quarterly Journal of the Royal Meteorological Society, 106(449):447–462.

Hammond, M. and Pierrehumbert, R. T. (2018). Wave-mean flow interactions in the atmospheric circulation of tidally locked planets. The Astrophysical Journal, 869(1):65.

Held, I. M. and Hou, A. Y. (1980). Nonlinear axially symmetric circulations in a nearly inviscid atmosphere. Journal of Atmospheric Sciences, 37(3):515 – 533.

Held, I. M. and Suarez, M. J. (1978). A two-level primitive equation atmospheric model designed for climatic sensitivity experiments. Journal of Atmospheric Sciences, 35(2):206 – 229.

Held, I. M. and Suarez, M. J. (1994). A proposal for the intercomparison of the dynamical cores of atmospheric general circulation models. Bulletin of the American Meteorological Society, 75(10):1825 – 1830.

Hide, R. (1969). Dynamics of the atmospheres of the major planets with an appendix on the viscous boundary layer at the rigid bounding surface of an electrically-conducting rotating fluid in the presence of a magnetic field. Journal of Atmospheric Sciences, 26(5):841 – 853.

Iga, S. and Matsuda, Y. (2005). Shear instability in a shallow water model with implications for the venus atmosphere. Journal of the Atmospheric Sciences, 62(7):2514 – 2527.

Imamura, T., Mitchell, J., Lebonnois, S., Kaspi, Y., Showman, A. P., and Korablev, O. (2020). Superrotation in planetary atmospheres. Space Science Reviews, 216(5):87.

Kaspi, Y., Galanti, E., Showman, A. P., Stevenson, D. J., Guillot, T., Iess, L., and Bolton, S. J. (2020). Comparison of the deep atmospheric dynamics of jupiter and saturn in light of the juno and cassini gravity measurements. Space Science Reviews, 216(5):84.

Lian, Y. and Showman, A. P. (2010). Generation of equatorial jets by large-scale latent heating on the giant planets. Icarus, 207(1):373–393.

Liu, J. and Schneider, T. (2011). Convective generation of equatorial superrotation in planetary atmospheres. Journal of the Atmospheric Sciences, 68(11):2742 – 2756.

Mitchell, J. L. and Vallis, G. K. (2010). The transition to superrotation in terrestrial atmospheres. Journal of Geophysical Research, 115(E12).

Pierrehumbert, R. T. and Hammond, M. (2019). Atmospheric circulation of tide-locked exoplanets. Annual Review of Fluid Mechanics, 51(1):275–303.

Potter, S. F., Vallis, G. K., and Mitchell, J. L. (2014). Spontaneous superrotation and the role of kelvin waves in an idealized dry gcm. Journal of the Atmospheric Sciences, 71(2):596 – 614.

Saravanan, R. (1993). Equatorial superrotation and maintenance of the general circulation in two-level models. Journal of Atmospheric Sciences, 50(9):1211 – 1227.

Showman, A. P., Cooper, C. S., Fortney, J. J., and Marley, M. S. (2008). Atmospheric circulation of hot jupiters: Three-dimensional circulation models of hd 209458b and hd 189733b with simplified forcing. The Astrophysical Journal, 682(1):559.

Showman, A. P., Fortney, J. J., Lian, Y., Marley, M. S., Freedman, R. S., Knutson, H. A., and Charbonneau, D. (2009). Atmospheric circulation of hot jupiters: Coupled radiative-dynamical general circulation model simulations of hd 189733b and hd 209458b. The Astrophysical Journal, 699(1):564.

Showman, A. P. and Polvani, L. M. (2010). The matsuno-gill model and equatorial superrotation. Geophysical Research Letters, 37(18).

Showman, A. P. and Polvani, L. M. (2011). Equatorial superrotation on tidally locked exoplanets. The Astrophysical Journal, 738(1):71.

Sobel, A. H., Nilsson, J., and Polvani, L. M. (2001). The weak temperature gradient approximation and balanced tropical moisture waves. Journal of the Atmospheric Sciences, 58(23):3650 – 3665.

Suarez, M. J. and Duffy, D. G. (1992). Terrestrial superrotation: A bifurcation of the general circulation. Journal of Atmospheric Sciences, 49(16):1541 – 1554.

Vallis, G. K. (2017). Atmospheric and Oceanic Fluid Dynamics: Fundamentals and Large-Scale Circulation. Cambridge University Press, 2 edition.

Wang, P. and Mitchell, J. L. (2014). Planetary ageostrophic instability leads to superrotation. Geophysical Research Letters, 41(12):4118–4126.

Williams, G. P. (2003). Barotropic instability and equatorial superrotation. Journal of the Atmospheric Sciences, 60(17):2136 – 2152.

Zurita-Gotor, P. and Held, I. M. (2018). The finite-amplitude evolution of mixed kelvin–rossby wave instability and equatorial superrotation in a shallow-water model and an idealized gcm. Journal of the Atmospheric Sciences, 75(7):2299 – 2316.

Stratified Turbulence, A Black Hole for Internal Waves?

Arefe Ghazi Nezami

April 2024

1 Abstract

Numerical simulations of internal wave beams generated as a result of the barotropic tide passing over steep topography show reflected wave beams upon interacting with the surface. However, observations do not capture such wave reflection. Instead, they indicate that the incident wave beam exhibits high levels of turbulent dissipation and wave energy in the upper ocean. We hypothesize that incident waves are absorbed by stratified turbulence near the surface, inhibiting their reflection. In this study, we perform three-dimensional direct numerical simulations, where stratified turbulence is generated in the top half and forcing is applied near the bottom, creating waves that travel toward the turbulent layer. We apply the Hilbert transform, distinguishing the upward and downward traveling waves to diagnose wave reflection, should it occur. We also examine the energy of turbulent flow, in the forms of the total kinetic energy as it evolves in time and the spectrum of horizontal kinetic energy with respect to horizontal wave numbers. We compare results for cases in which only turbulence is present with cases in which upward waves are launched in the same domain. Based on our results, we observed minimal reflection of the waves off of the interface between the turbulent and non-turbulent regions. No significant changes to the energy of the turbulent region are observed with and without waves.

2 Introduction

The ocean mixed layer is the upper part of the ocean that is relatively uniform in temperature, salinity, and density due to the mixing effects of winds, waves, and shear associated with large-scale circulations (Kara et al., 2000; D'Asaro, 2014). This layer varies in depth but is generally around 100 meters or less. The ocean mixed layer is critical to the dynamics and circulations of both the atmosphere and ocean, mediating energy and mass exchange that drives climate systems at a global and local scale (Roemmich et al., 2015; Moum et al., 2009; Ferrari and Wunsch, 2009; Kunze, 2017). The scale variability within the ocean mixed layer is notable, ranging from large-scale phenomena approximately 100 kilometers in horizontal extent to more localized, finer-scale processes which remain under-investigated (Munk and Wunsch, 1998; Sasaki et al., 2014; Riley and de Bruyn Kops, 2003; Thomson et al., 2016). Turbulence, generated from different sources in the upper ocean layer (Hibiya and Nagasawa, 2004), significantly impacts the transport of various tracers and particles, such as carbon and nutrients, therefore impacting the biological activity of this layer (Lévy et al., 2012; Denman and Gargett, 1995; Balwada et al., 2018; Mahadevan, 2014). Understanding the dynamics within this layer is crucial for unraveling its role in shaping atmospheric and oceanic dynamics.

Internal waves are oscillatory motions in a stratified fluid medium, and play an important role in ocean dynamics. Internal tides are internal waves that are generated through the interaction of barotropic tides with bottom topography. They propagate through the water column, contributing to mixing processes in the ocean, so influencing oceanic circulations and transport phenomena (Polzin et al., 1997; Roemmich et al., 2015). Various regions have been identified worldwide—such as oceanic islands, trenches, and mid-ocean ridges—where internal tides are prominently produced (Egbert and Ray, 2000; Ray and Mitchum, 1996). Some regions, including the Hawaiian Ridge, are specifically interesting as they serve as hot spots for the generation of internal tides (Martin et al., 2006).

Observations from satellite altimetry and in situ measurements reveal the extensive reach of internal tides, radiating thousands of kilometers from their generation sites at prominent mid-ocean topographic features (Ray and Mitchum,

1996, 1997; Kantha and Tierney, 1997; Dushaw et al., 1995; Lee et al., 2006). For example, in regions with steep topography, ocean observations reveal significant variability in internal wave characteristics and turbulence along with heightened turbulent dissipation and wave energy (Polzin and Lvov, 2011; St. Laurent et al., 2001; Pinkel et al., 2000; Egbert and Ray, 2000; Rudnick et al., 2003; Martin et al., 2006). This is especially true for low-mode internal waves (e.g. mode-1 internal tides (Rainville and Pinkel, 2006)). The waves exhibit spatial coherence and directional propagation, making them essential components of the oceanic energy budget; and significantly impacting mixing processes far beyond their point of origin (Ray and Mitchum, 1996; St. Laurent and Garrett, 2002).

Numerical and experimental simulations, where waves are generated by oscillatory flow over a ridge, have been performed to increase the understanding of internal wave evolution, stability, and mixing in the ocean mixed layer (Echeverri et al., 2009, 2011). While these studies offer valuable insight into the dynamics of internal waves and the flow dynamics, they do not closely follow field observations. Numerical studies such as Tabaei et al. (2005); Diamessis et al. (2014); Gayen and Sarkar (2014) and experiments such as those by Wunsch and Brandt (2012) demonstrate that an upward propagating wave beam reflects when reaching a pycnocline or the surface. In contrast, in regions around the Hawaiian Ridge, observations have shown increased turbulent dissipation rates and wave energy associated with the upward propagating beam near the surface, but no signal of wave reflection (Cole et al., 2009).

This discrepancy points to a gap in our understanding of how internal waves interact with the turbulent ocean mixed layer. In this study, we aim to address this gap by using direct numerical simulations to investigate the interaction of internal waves with stratified turbulent layer, mimicking the stratified transition region of the mixed layer (Kaminski et al., 2021). This report is organized as follows: in section 3, we discuss the governing equations and the numerical setup. In section 4, we discuss simulations of waves launched in a stratified domain. In section 5, we explain how we model the turbulence. We put all the pieces together, and in section 6, we present results of having both waves and turbulence in the same domain. Finally, conclusions are presented in section 7.

3 Governing equations

We use direct numerical simulations (DNS) to model a linearly stratified domain using the set of Navier-Stokes equations that characterize the motion of a Boussinesq fluid. The equations for momentum, internal energy, and incompresibility, respectively, are:

$$\frac{D\mathbf{u}}{Dt} = -\nabla p + \nu\nabla^2\mathbf{u} + \mathcal{F}_{\mathrm{w_u}} + \mathcal{F}_T + b\mathbf{e_z} + \mathcal{D}\mathbf{u}, \tag{1}$$

$$\frac{Db}{Dt} = \kappa\nabla^2 b - N_0^2 w + \mathcal{F}_{\mathrm{w}_b} + \mathcal{D}b, \tag{2}$$

$$\nabla \cdot \mathbf{u} = 0. \tag{3}$$

In equation 1, $\mathbf{u}(\mathbf{x}, t)$ is the vector of the fluctuating velocities with u, v, and w being components of $\mathbf{u}$ in x, y, and z directions, respectively, with z being the vertical. $\frac{D}{Dt}$ represents the material derivative. Since there is no mean flow (i.e., $\bar{\mathbf{u}} = \mathbf{0}$, the overbar represents the time average), we only include the fluctuating velocities. The buoyancy field is $b = -g\rho/\rho_0$, and the buoyancy frequency is $N_0^2 = -\frac{g}{\rho_0}\frac{d\bar{\rho}}{dz}$ with $\bar{\rho}$ being the background density profile and ρ_0 being the characteristic fluid density. ρ and p are the fluctuations to the density and pressure fields, and g represents the gravitational acceleration. We have non-dimensionalized the equations using characteristics time and velocity scales. The time has been non-dimensionalized such that N_0^2 was taken to be constant equal to 1 and therefore the inherent time scale of the system being $N_0^{-1} = 1$. The constants ν and κ are the non-dimensionalized kinematic viscosity and the diffusivity of the fluid, respectively. For all simulations, viscosity and diffusivity is selected to be $\nu = \kappa = 5 \times 10^{-4}$ with Prandtl number of $Pr = 1$, to ensure the highest turbulent Reynolds number with low computation cost.

In this set of equations, $\mathcal{F}$ represents the forcing, whith subscript w indicating the wave forcing and T indicating the turbulence forcing. The details related to the forcing will be discussed further in the report: $\mathcal{F}_w$ in section 4 and $\mathcal{F}_T$ in section 5. A damping layer is applied at the bottom boundary to remove any reflection of the downward propagating wave from the bottom boundary. $\mathcal{D}$ is applied to both buoyancy and velocity fields. The damping itself is adopted from Slinn and Riley (1998) as $\mathcal{D} = \exp(\frac{-(3.5(z-z_d)/L_d)^2}{2})$. In this formula, z_d is the location where the damping layer is located, and L_d is the depth of the damping layer. In all of our simulations, $z_d = 0.75$ and $L_d = z_d$.

The turbulent kinetic energy and the turbulent dissipation rate respectively are $KE = \langle \overline{\mathbf{u} \cdot \mathbf{u}} \rangle$ and $\epsilon = -\nu \langle \overline{\frac{1}{2} \frac{\partial u_i}{\partial x_j} \frac{\partial u_j}{\partial x_i}} \rangle$, in which the bracket indicates spatial averaging in the top half of the domain where turbulence is mainly present. Two dimensionless numbers representing the strength of the turbulence can be defined. The Taylor Reynolds number calculated as $Re_\lambda = \frac{\lambda u}{\nu}$, where the Taylor microscale is $\lambda = \sqrt{15 \frac{\nu}{\epsilon}} u_T$, with $u_T = \sqrt{KE}$ being the turbulence velocity scale calculated as the square root of turbulent kinetic energy, provides insight into the strength of the turbulence. The buoyancy Reynolds number, calculated as $Re_b = \frac{\epsilon}{\nu N_0^2}$, characterizes the relative importance of buoyancy forces to inertial forces in stratified flows.

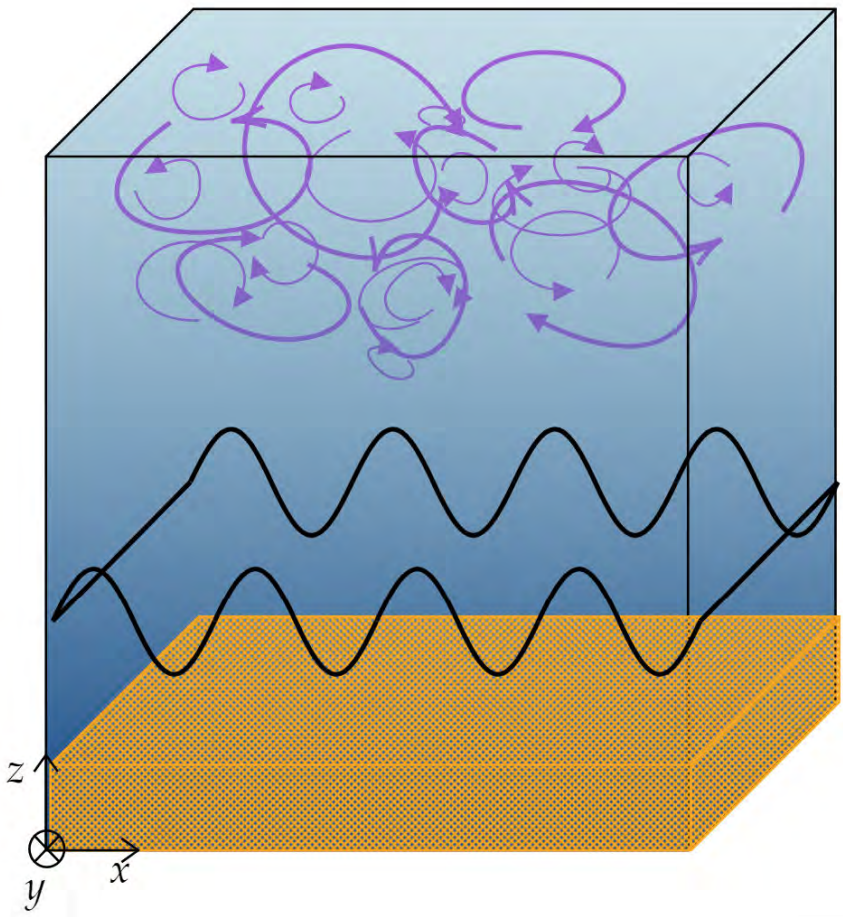

Figure 1: Schematic of the setup of the simulation domain: The pink vortices indicate the turbulent layer located at the top of the domain, the black lines represent the wave forcing, and the yellow part at the bottom of the domain represents the damping layer.

3.1 Numerical setup

The simulations are carried out with Dedalus, a flexible framework for solving partial differential equations using spectral methods (Burns et al., 2020). Our final goal is to simulate a density-stratified domain that is turbulent in the top half of the domain with waves launched toward it from the bottom half, as shown in figure 1. We simulate each component of this setup separately before integrating them into the complete system. Simulations with turbulence, with and without waves, are constructed as a three-dimensional (3D) domain with size $L_x \times L_y \times L_z$ where space scales are non nondimensionlized so $L_x = L_y = L_z = 2\pi$. Boundary conditions were free-slip and impermeable conditions at the bottom and top boundaries, with periodic boundaries on the lateral sides to simulate a horizontally unbounded oceanic environment.

For the numerical discretization a combination of spectral methods tailored to the geometry and nature of the problem, were used. For the vertical (z) direction, Chebyshev polynomials were used due to their excellent properties in resolving functions with steep gradients, which are common in stratified fluid dynamics due to density and velocity fluctuations. Chebyshev discretization is particularly advantageous in dealing with boundary layer effects and capturing the sharp interfaces between layers of different densities and velocities (e.g. turbulent and non-turbulent regions). Fourier series were employed in horizontal directions to take advantage of their periodic nature. The number of Chebyshev and Fourier modes in all direction, are set to be $N_x = N_y = N_z = 256$, and the number of grids are 1.5 times the number of modes. The resolution of simulations was set to ensure that the smallest scales of turbulence were adequately resolved. This has been tested as to ensure the size of grids are close to the size of the Kolmogorov length scale η, which means that the small scales of dissiption can be captured via our resolution. In our simulations η, calculated as $\left(\eta = \frac{\nu^3}{\epsilon}\right)^{1/4}$, was around 0.02.

The time-stepping technique utilized is the Second-order Backward Differentiation Formula (SBDF2), which is an implicit-explicit time-stepping scheme. This method is often chosen for its stability and accuracy . This method is used to advance solutions in time while handling the nonlinear terms of the equations in a stable manner, especially when the equations involve complex fluid dynamics. The Courant-Friedrichs-Lewy (CFL) condition is used to determine the maximum time step that ensures the numerical stability of the simulations. In our setup, according to the stratification and the domain size, the maximum time stepping is set to $\Delta t_{max} = \frac{2\pi}{0.05 N_0}$ with a safety factor of 0.2.

4 Internal wave forcing without turbulence

The first step in our investigation is to study upward propagating waves in a density-stratified fluid. This is simulated in a two-dimensional domain (i.e. $x - z$ plane) to simplify and reduce the numerical cost. Equations 1 and 2 in the 2-dimensional form are used here with the forcing included in them.

$$\begin{cases} \frac{Dw}{Dt} = -\frac{\partial P}{\partial z} + b + \nu\nabla^2 w + \mathcal{F}_w + \mathcal{D}w, \\ \frac{Du}{Dt} = -\frac{\partial P}{\partial x} + \nu\nabla^2 u + \mathcal{F}_u + \mathcal{D}u, \\ \frac{Db}{Dt} = -wN_0^2 + \kappa\nabla^2 b + \mathcal{F}_b + \mathcal{D}b. \end{cases} \tag{4}$$

$\mathcal{F}_b$ is directly applied to the buoyancy equation as $\mathcal{F}_b = \mathcal{A}_b e^{i(k_x x - \omega t)}$, in which k_x is the wave number in the horizontal direction and ω is the wave frequency. The forcing amplitude is $\mathcal{A}_b = A_b e^{\frac{-(z-z_w)^2}{2\sigma_w^2}}$, where A_b is the magnitude and the exponential function is used to smooth out the introduction of forcing at location z_w over a length of σ_w. We have taken $z_w = 1.5$ and $\sigma_w = 0.25$. A_b is adjusted to ensure minimal growth of nonlinear terms in simulations. The forcing is set so that $|\xi_z| \times k_z < 0.2$, where $|\xi_z|$ is the vertical displacement (equal to $\frac{A_b}{\omega}$) and $k_z = \frac{k_x N}{\omega}$ (Sutherland, 2010). Therefore, $A_b \frac{k_x N}{\omega^2}$ should be less than 0.2. Here, we explored two cases: one with $\omega = 0.2$, $A_b = 0.01$, and $k_x = 1$ leading to $|\xi_z| \times k_z = 0.25$ and the other with $\omega = 0.5$, $A_b = 0.0025$, and $k_x = 4$ leading to $|\xi_z| \times k_z = 0.04$.

Using the polarization relations for internal waves to relate buoyancy to the velocity fields, $\mathcal{F}_u$ and $\mathcal{F}_w$ are given by

$$\begin{cases} \mathcal{F}_w = -\frac{\omega}{N_0^2}\mathcal{A}_b e^{i(k_x x - \omega t)}, \\ \mathcal{F}_u = -\left(1 - \frac{\omega^2}{N_0^2}\right)^{\frac{1}{2}} \frac{1}{N_0}\mathcal{A}_b e^{i(k_x x - \omega t)}. \end{cases} \tag{5}$$

The forcing of waves increases in time as a hyperbolic tangent function given by $0.5(1 + \tanh(2(t - T_w)/T_w)$ in time, which starts near zero increasing to $\mathcal{F}_b$, $\mathcal{F}_u$, and $\mathcal{F}_w$ in time after a delay T_w over time $T_w = \frac{2\pi}{\omega}$. Figure 2 shows a 2D simulation of the wave traveling in a square domain of size $2\pi\pi$ with periodic boundaries in the x direction and free slip boundary condition at the top of the domain.

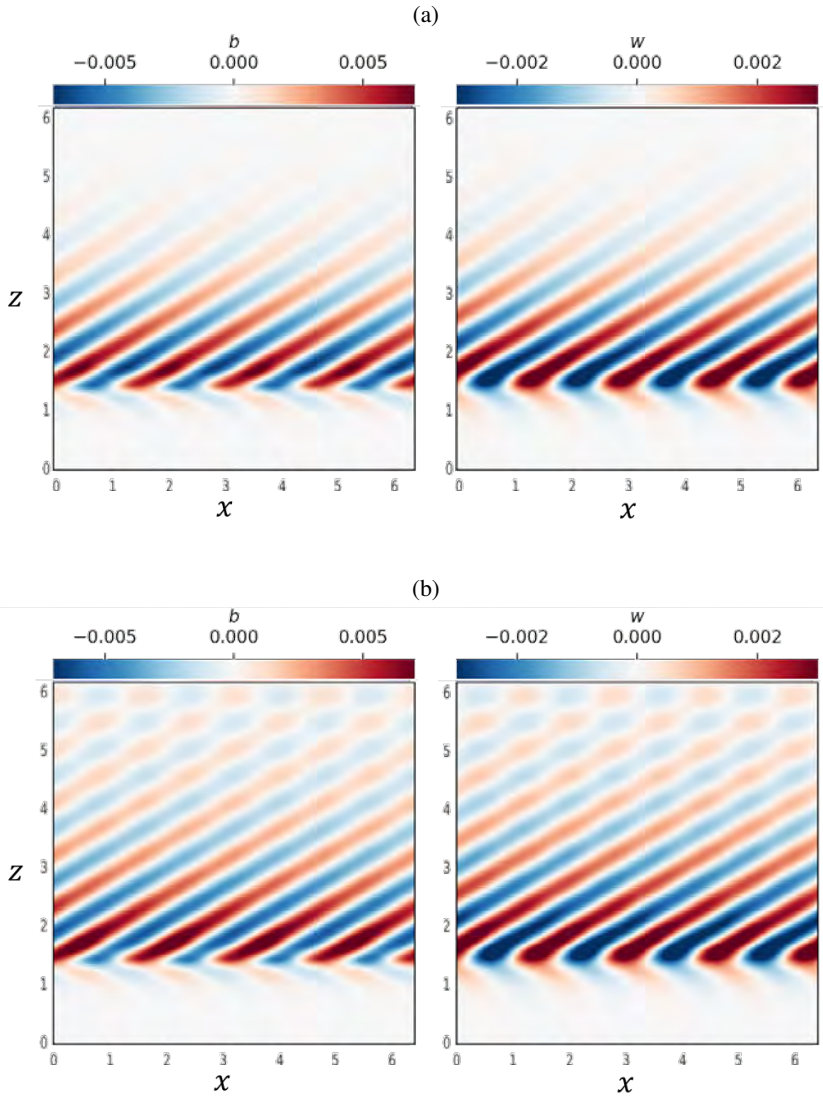

Figure 2: 2D simulations of wave in a stratified domain with $k_x = 4$, $\omega = 0.5$ at dimensionless $N_0 t$ time of a) 74 when the waves have not reached the top boundary and b) 502 where waves upon reaching the top boundary have been are reflected to the domain.

4.1 Damping length of the traveling wave

As the waves travel into the domain, they get damped by viscosity and diffusivity. In our simulations, we need to ensure that the waves can reach the turbulent layer with negligible damping. Damping happens over a length in the vertical direction as the waves travel, $\mathcal{A}e^{(-z/l_d)(i(\mathbf{k}.\mathbf{x}-\omega t))}$, where l_d is damping length. Following the calculation in Appendix 1, the damping rate can be found as:

$$l_d^{-1} = \frac{(\nu + \kappa) N_0^3 k_h^3}{2\omega^4} \tag{6}$$

From equation 6, we can understand how far a wave travels before damping becomes non-negligible. An example is shown in figure 3, where with $\omega = 0.2$, $k_x = 4$, $\kappa = \nu = 10^{-5}$, and $N_0^2 = 1$, l_d is 0.125. Thus, the waves get damped close to where they were launched originally. Figure 3 illustrates how the choice of wave-forcing variables should be scrutinized to have the waves travel further in the domain.

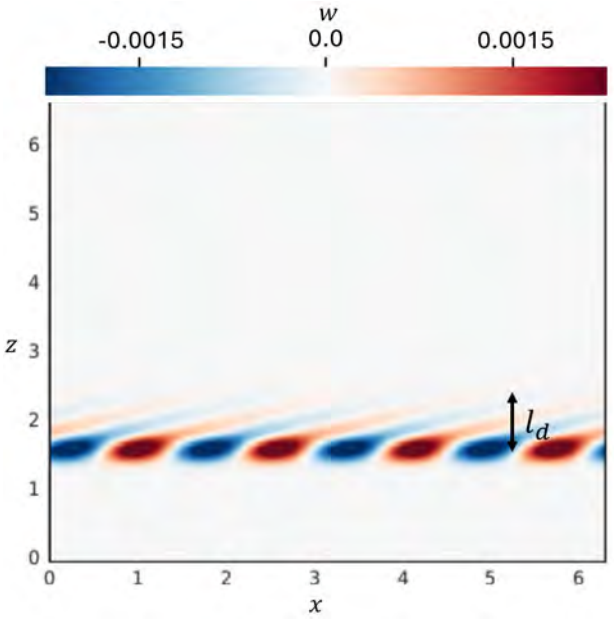

Figure 3: Vertical velocity (w) of 2D waves at N_0t=800 with damping rate of l_d^{-1} in a stratified domain with $\omega = 0.2$, $k_x = 4$, and $l_d = 0.125$.

The value of ω also affects the angle at which waves travel in a stratified fluid, depending on their frequency relative to the buoyancy frequency: $\omega = N \sin\theta$ where θ is the angle of traveling waves with the horizontal direction. The wave packet travels with the speed of group velocity $\mathbf{c_g} = \frac{\partial\omega}{\partial\mathbf{k}}$. High-mode waves typically travel at shallower angles, almost horizontally, since they have shorter vertical wavelengths and are more influenced by the ocean's stratification (St. Laurent and Garrett, 2002). As this angle decreases, the time required for the wave to travel in the horizontal direction toward the turbulent layer increases, resulting in high computational costs.

We first chose $\omega = 0.2$. However, based on equation 6, and as can be seen in figure 3, for high wave numbers (e.g. k =4), this does not work . As shown in figure 3, the waves are damped at a very short distance. Therefore, we increase ω to 0.5, which results in $l_d = 5$, eliminating this problem. This can also be achieved by reducing ν. However, reducing ν increases the cost of computations as higher resolutions are required to resolve the turbulence completely.

4.2 Hilbert transform: A method for decomposing wave signal

In various communication systems, information is often transmitted by modulated signal, and demodulation processing is extracting information from the modulated signal. The Hilbert Transform (HT), referred to as a complex demodulation process by Mercier et al. (2008), is a mathematical operation that provides a way to extract the envelope and instantaneous frequency of a signal. It is a powerful tool for analyzing and extracting information from signals in both the time and frequency domains. We use HT as a means to decompose the waves propagating in the positive z direction from the negative ones. Below is a brief description of the method introduced by Mercier et al. (2008).

Considering decomposing the signal, U in the z direction into a superposition of two wave beams propagating with the same wave number as the original signal, but in opposite directions,

$$U(z,t) = A\cos(\omega t - k_z z) + B\cos(\omega t + k_z z). \tag{7}$$

Assuming A and B are constant amplitudes in both space and time, equation 7 can be re-written as the sum of exponentials with complex arguments (i.e. calculating a Fourier transform of the signal in time), $U(z,t) = \hat{U}e^{(i\omega t)} + \hat{U}^* e^{(-i\omega t)}$. In this equation, $\hat{U} = \left(Ae^{-ik_z z} + Be^{ik_z z}\right)$ and * represents the complex conjugate form. Now we can write the real-values signal U to a complex values signal $\bar{U}$, which the real part is equal to the original signal U.

$$\bar{U}(z,t) = Ae^{(i\omega t - k_z z)} + Be^{(i\omega t + k_z z)}. \tag{8}$$

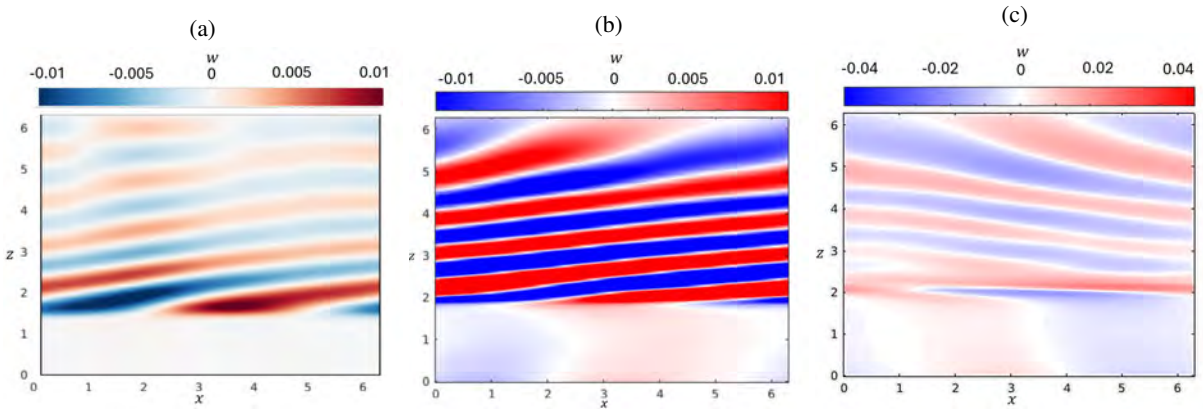

Figure 4: Vertical velocity field in simulations of wave forcing with $k_x = 1$, $\omega = 0.2$ at $N_0 t = 800$; a) the original vertical velocity field w, b) decomposed upward traveling, and c) downward traveling components.

By finding the Fourier transform of equation 8 in space, we can decompose the signal into upward propagating and downward propagating components by isolating the negative values and positive values of $Ae^{(i\omega t)}e^{(-ik_z z)} + Be^{(i\omega t)}e^{(ik_z z)}$.

To summarize the whole process, we first need to find the Fourier transform of the original signal in time, followed by a Fourier transform in space. Then, we can decompose the signal into positive and negative wave numbers and apply the inverse Fourier transform in space followed by an inverse Fourier transform in time. This procedure will provide us with a decomposition of upward propagating and downward propagating waves. The result of applying HT to this section's 2-dimensional wave field simulations is shown in figure 4. Applying HT, we can observe the upward traveling wave shown in figure 4b and the downward traveling waves that are shown in figure 4c.

5 Stratified turbulence

In our simulations, stratified turbulence in the upper part of the domain is generated by applying an artificial body force, $\mathcal{F}_\mathcal{T}$, to the momentum equation 1 using a method adopted from Maffioli (2017). The Craya-Herring reference frame is utilized to input this force in the Fourier space (Godeferd and Staquet, 2003). Maffioli (2017) selected this method over only forcing vortical modes $k_z = 0$ to avoid exciting an arbitrary spectrum of internal gravity waves directly and inducing a specific length scale in the vertical direction. Additionally, this forcing was found to reduce the growth of energy in the shear modes compared to other methods, otherwise these shear modes would grow during the simulation and dominate the total kinetic energy of the system (Maffioli, 2017).

To generate a divergence-free velocity field, the forcing must satisfy $\nabla \cdot \mathcal{F}_\mathcal{T} = 0$, which in Fourier space implies $\mathbf{k} \cdot \hat{\mathcal{F}}_\mathcal{T} = 0$, where the top hat represents the Fourier transform. Maffioli (2017) chose the power spectrum in the horizontal direction to be constant as $P_w(k_h) = \frac{1}{2}\Sigma(\hat{\mathcal{F}}\hat{\mathcal{F}}^*) = c$, with $k_h = 3$. θ is the random phase changing at each time step to remove time dependency of the forcing. Based on these conditions, the forcing adopted by Maffioli (2017) is

$$\hat{\mathcal{F}}_\mathcal{T} = \begin{cases} \frac{c}{\sqrt{\pi k_h}e^{i\theta}} & \text{for } k_h = 3, \\ 0 & \text{for } k_h \neq 3. \end{cases} \tag{9}$$

The total power P_w is kept constant to ensure smooth time evolution of velocity components and dissipation rates. Change in the input power corresponds to a change in the strength of the turbulence. P_w can be calculated as

$$P_w = \sum_{k_x,k_y,k_z} \hat{\mathbf{u}}^* \cdot \hat{\mathcal{F}}_\mathcal{T} + \frac{1}{2}\hat{\mathcal{F}}_\mathcal{T} \cdot \hat{\mathcal{F}}_\mathcal{T}^* \Delta t = cP_{\mathbf{uf}} + c^2 P_{\mathbf{ff}}. \tag{10}$$

Since P_w is a constant value, c should be calculated for each time step, as a quadratic function:

$$c = \frac{-P_{\mathbf{uf}} \pm \sqrt{P_{\mathbf{uf}}^2 + 4P_{\mathbf{ff}}P_w}}{2P_{\mathbf{ff}}}. \tag{11}$$

A value of $P_w = 1.5$ is selected as input forcing of the turbulence in all of our simulations.

As mentioned previously, the aim is to generate turbulence in the top half of the domain. To achieve this, we set the force of turbulence to be zero at the bottom half of the domain. This is done by multiplying the turbulent forcing by a hyperbolic tangent function of $P_w \times \left(\frac{1}{2}\left(1 + \tanh\frac{z-z_{\mathcal{F}_t}}{\sigma_{\mathcal{F}_t}}\right)\right)$, which introduces $\sigma_{\mathcal{F}_T}$, which is the transition width from turbulent to non-turbulent region, as another variable related to turbulence forcing. $z_{\mathcal{F}_t}$ is the transition location between the non-turbulent and turbulent region, which is equal to π in our setup. If $\sigma_{\mathcal{F}_t}$ is small, this transition happens over a short length, mimicking a step-like function, which might introduce instabilities and numerical errors. After trial and error, we found $\sigma_{\mathcal{F}_t} = 0.25$ works well with our setup.

The stratified turbulence is simulated in a three-dimensional domain. Figure 5 shows the snapshots of the dissipation field and the buoyancy field of the $x - z$ plane at $y = \pi$ at $N_0 t = 1$ (figure 5a), and when it is 131 time units advanced in the simulations (figure 5b). As can be seen from figure 5a, the forcing transition region is pronounced in the buoyancy field at the beginning of the simulations. This bold transition fades away later. In figure 5b, the buoyancy field is active in the bottom half of the domain, where the turbulent forcing was not applied. The turbulence at the top generates internal waves that can be observed at the bottom half.

Table 1 presents the statistics regarding turbulence and the dimensionless number corresponding to the developed flow in this layer, presented in details in section 3. The values of KE and ϵ are averaged from the time that turbulence has fully developed, which is equal to $N_0 t = 113$, for 450 time units. Many of the important characteristics of the stratified turbulence can be achieved when the Re_b is $O(10)$ (Bartello and Tobias, 2013); while our simulations can only get up to 1.5. This value of Re_b might not suggest high values of turbulence but the flow shows non-linearity.

P_w	KE	ϵ	Re_λ	Re_b
1.5	3	10^{-4}	50	1.5

Table 1: Statistics and dimensionless numbers of the turbulent region

(a)

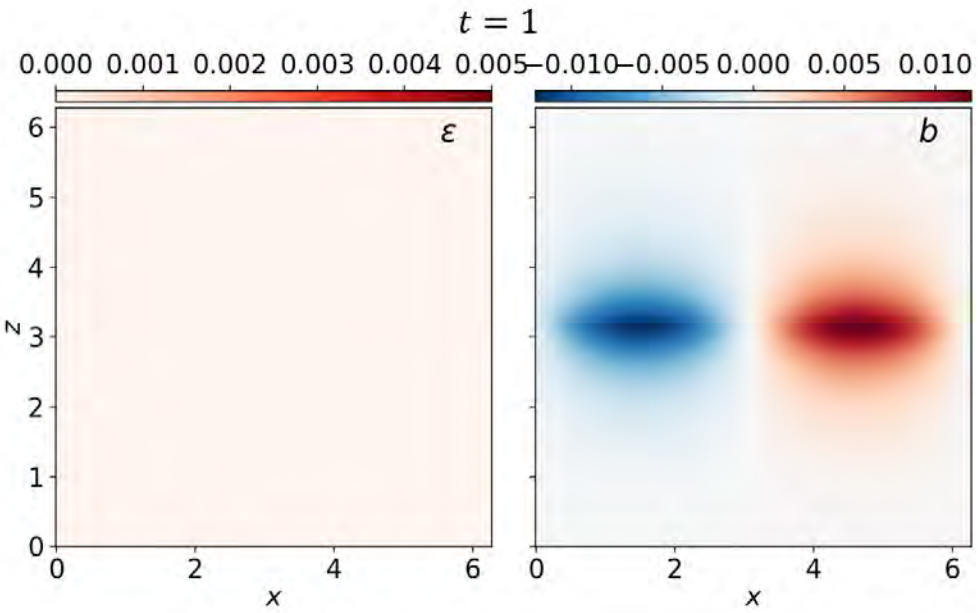

(b)

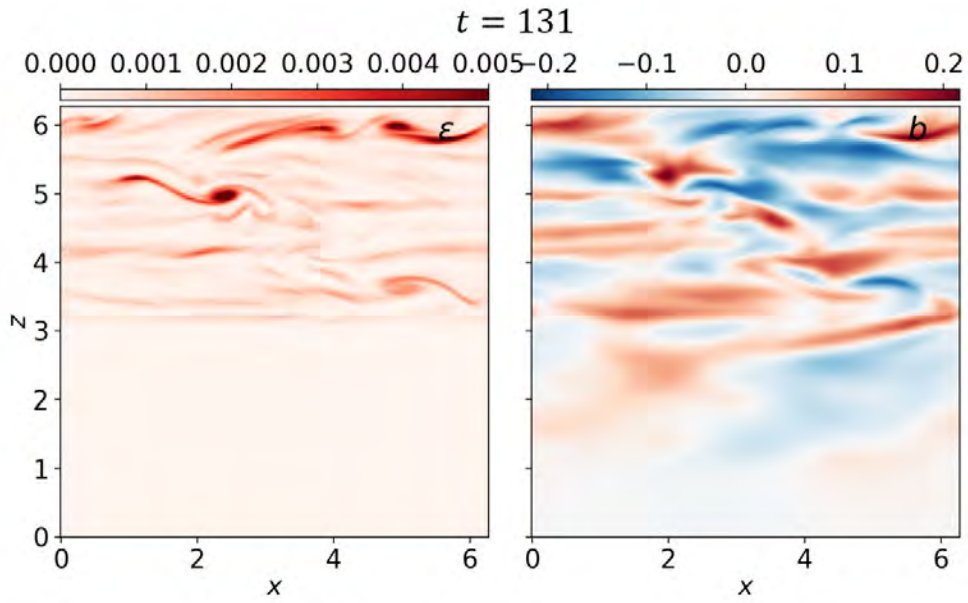

Figure 5: Buoyancy and dissipation rate fields at $y = \pi$ in the simulations of applying turbulence forcing in the top half of the domain at two different times of a) $N_0 t = 1$, which is the beginning of the simulations, and b) $N_0 t = 131$, where turbulence is fully developed.

The development of turbulent kinetic energy and the dissipation rate of turbulent kinetic energy averaged in the top half of the domain is shown in figure 6. From this figure, we can understand that after around 130 time units, the development of turbulence is complete. This trend is very similar to the result presented by Maffioli (2017). Therefore, if waves are launched, we need to ensure that they reach the turbulent layer after this point in the simulations so that they reach a completely developed turbulent layer.

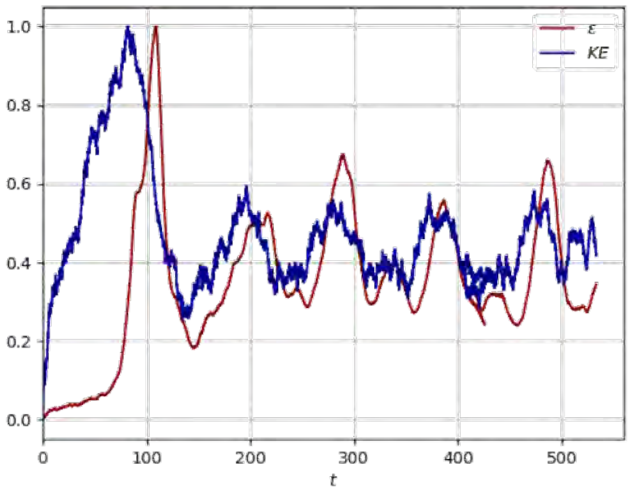

Figure 6: Development of the averaged values of turbulent kinetic energy and turbulent dissipation rate normalized by their maximum value during the simulations.

We also studied the spectrum of horizontal energy of the developed turbulence at the location $z = 3/4L_z$ (i.e. middle of the turbulent layer). The spectrum of horizontal energy can be calculated based on the Fourier transform of velocities $E_h = 1/2(\hat{u}.\hat{u}^* + \hat{v}.\hat{v}^*)$. The horizontal wave number is calculated as $k_h = \sqrt{k_x^2 + k_y^2}$. Figure 7 shows the relationship between E_h and k_h along with the $-5/3$ slope, a representative slope of the inertial subrange in a turbulent field. As expected, there is a peak in the plot of E_h shown in figure 7 around $k_h = 3$, which is the forcing wave number.

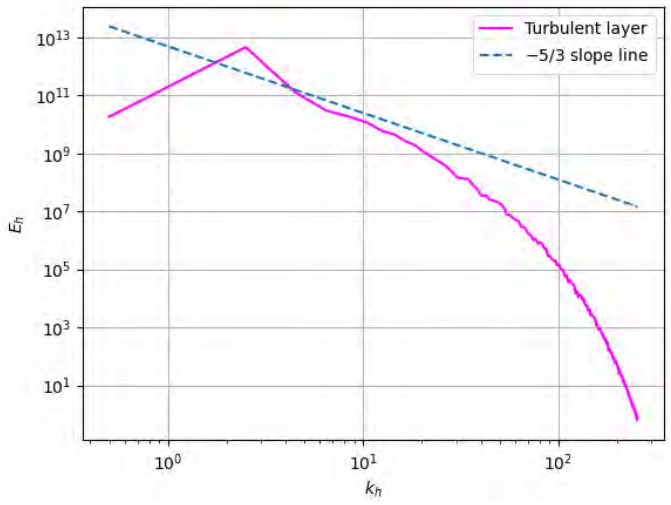

Figure 7: E_h in different horizontal wave number k_h, with the -5/3 slope.

6 Interaction of wave with a turbulent layer

Now that we have successfully simulated the turbulent layer and the wave traveling in a stratified domain, we can simulate our final model. We integrate these components and model stratified turbulence and launch waves in the same

domain to answer the question raised at the beginning of this document.

We first model the turbulent domain with the specifications presented in section 5 up to $N_0 t = 600$ units, then we perform two simulations of the same turbulence characteristics where in one waves are launched waves have wave numbers $k_x = 1$ with an amplitude of A_b of 0.01, and the other with $k_x = 4$ and $A_b = 0.0025$, based on the discussions in section 4. Figure 8 demonstrates how the buoyancy and dissipation fields evolve after launching waves in a fully developed turbulence. In the region between the wave forcing and the turbulent layer, the buoyancy field is dominated by wave-like motions (see figure 8b). However, this effect diminishes as we move up into the turbulent domain, even at later times in the simulations.

Figure 9 shows how the turbulent kinetic energy evolves when waves reach the turbulent layer. As can be seen in figure 9, after waves are launched, it takes around 70 to 80 time units for those waves to reach the turbulent layer and affect its dynamics. This can be understood as KE has the same trend for both cases up until this time, while their plots departure from each other afterwards. However, the changes in the magnitude of KE are not noticeable after the waves interact with the turbulent layer as they add negligible energy to the system. However, the two simulations might deviate at later times as they develop.

Upon finding the horizontal energy spectrum at different heights of the domain, we can understand the difference in the energy distribution at different modes and wave numbers. Frequency-wave number spectra at two different locations in the middle of the turbulent layer (i.e., $z = 3/4L_z$) and between the bottom of the turbulent layer and wave forcing (i.e., $z = 1/4L_z$) are shown in figure 10. The spectra calculated at the non-turbulent region of the domain (see figures 10a and 10c) have clear regions of high energy, indicating more pronounced activity of the waves with dependencies on specific ω and k. This is not the case for turbulent region (see figures 10b and 10d), where elevated energy levels are observed across a broader range of ω and k.

One of the main questions we wish to answer is whether the waves launched will be reflected or absorbed when interacting with the turbulent layer. In our setup, turbulence in the top layer excited internal gravity waves in the underlying stratified domain. We apply HT to distinguish between incident waves that we launch toward the turbulent layer, the reflected waves, and the waves generated by the turbulent activity in the stratified domain. This is shown in figure 11, where the upward and downward traveling waves are shown separately, which can be identified with the structured wave domain between wave forcing and the turbulent layer of figure 11b. Based on figure 11c, the upward traveling waves (shown in figure 11b) are strongly noticeable as up- and rightward oriented phase lines. This is not true for the downward traveling waves (shown in figure 4c).

We also plot the horizontal energy of this layer versus the horizontal wave number and frequency for both cases shown in figure 12. The comparison between the cases of only turbulence and turbulence with waves is shown in all figures. Similar to simulations of stratified turbulence in section 5, in the plot of E_h versus k_h, a slight peak around $k_h = 3$ is observed due to forcing. Similarly, when wave force is applied, a peak in the E_h-ω plots is observed aligned with the input force.

7 Conclusion

Here, we have performed direct numerical simulations to study the interaction of waves with a turbulent layer to investigate whether waves get reflected from or absorbed by the turbulent layer. This study is motivated by the observations in regions with steep topography and high tidal wave energy being different from the numerical studies of similar setups. To do this, we have performed DNS to simulate a linearly stratified domain in which the top half is turbulent, and the waves are launched from the bottom propagating toward the turbulent layer.

To better ensure that the turbulence and wave are simulated correctly before simulating their complicated interaction, we first modeled the waves and turbulence separately. The parameters related to wave simulation are selected so that the non-linear terms are small and the waves can fully reach the turbulent layer without being damped along the way. The parameters involved in the turbulence simulations were also adjusted so that the turbulence was fully resolved and the transition between the turbulent and non-turbulent regions did not induce any additional complexity and non-linearity to the system.

We then modeled waves and turbulence in the same domain with one input power for the turbulent layer and two different waves with two horizontal wave numbers of $k_x = 1$ and 4 and corresponding wave frequencies of $\omega = 0.2$ and 0.5, and $A_b = 0.01$ and 0.0025 respectively. To distinguish between the upward and downward traveling waves methods such as Hilbert Transform were performed on the result of the simulations. We also found the kinetic energy of the turbulent before and after launching the waves. Based on the analysis provided, no strong reflection was observed

(a)

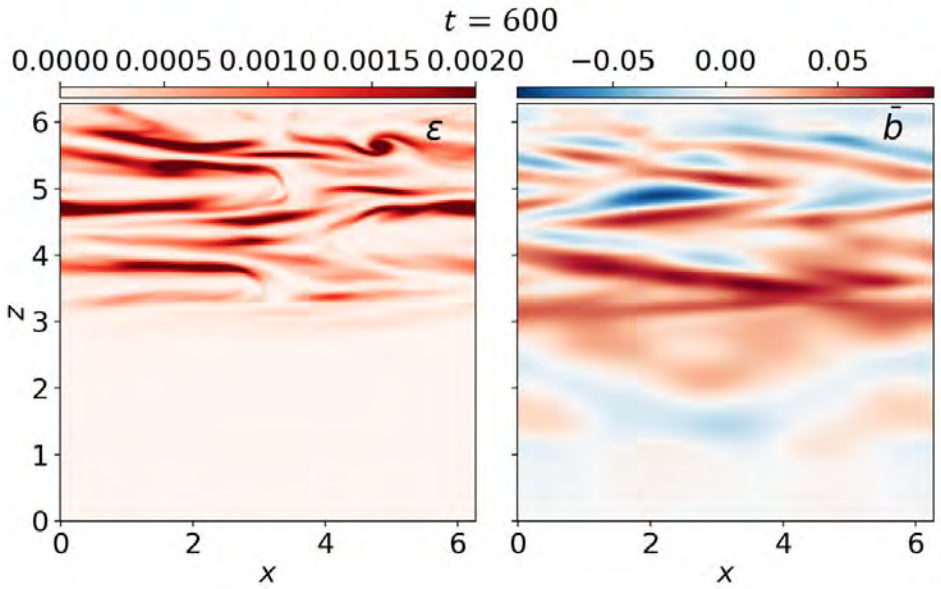

(b)

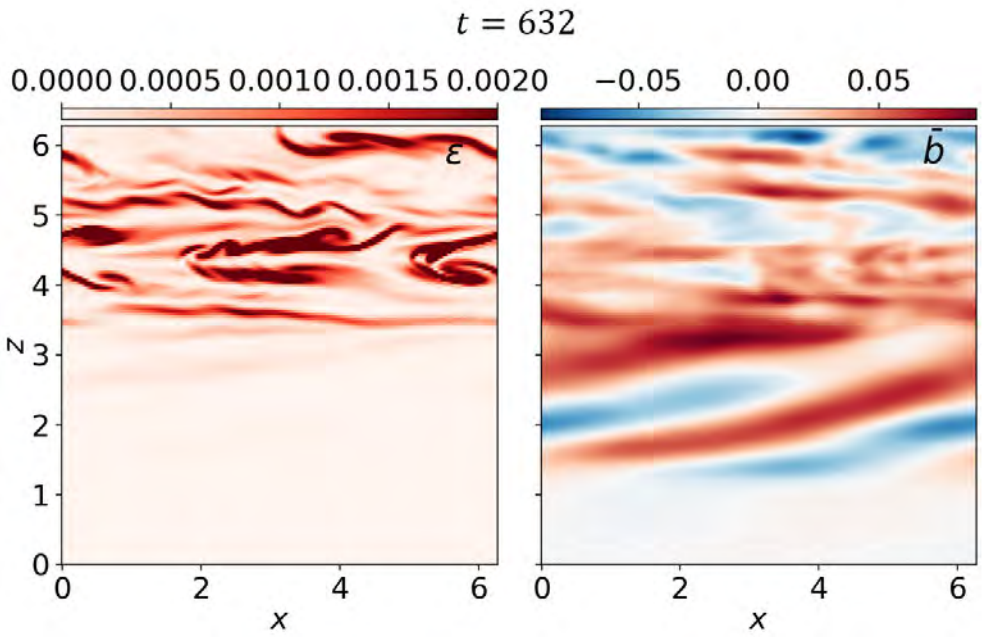

Figure 8: Buoyancy and dissipation rate at $y = \pi$ of simulations of applying wave forcing with k_x=1, A_b=0.01 and ω=0.2 in a domain that with developed turbulence at two different times of a) 600, before introducing wave forcing, and b) 632, after wave forcing is introduced.

of launched waves upon reaching the turbulent layer. Our observations suggest that the waves were absorbed into the turbulent layer. This finding aligns with the observational studies on sites such as near the Hawaiian Ridge, originally discussed in the introduction.

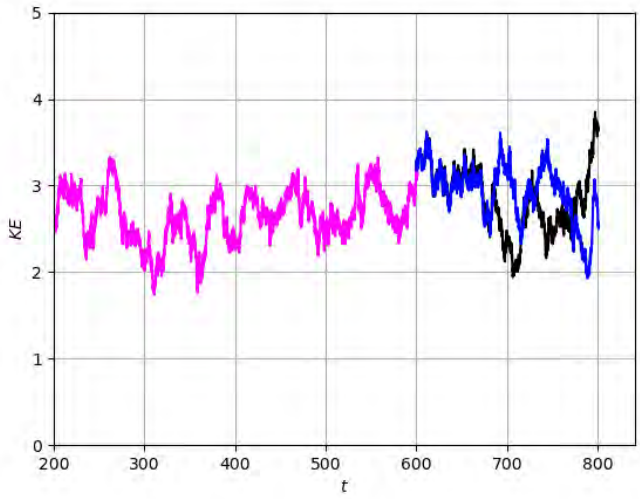

Figure 9: KE of spatially averaged over the top half of the domain at simulations with a) only waves (shown in pink), b) turbulence and wave with $k_x = 1$ and $A_b = 0.01$ and $\omega = 0.2$ (shown in blue) turbulence and waves with $k_x = 4$ and $A_b = 0.0025$. $\omega = 0.5$ (shown in black).

This problem can be investigated further by performing higher resolution simulations to achieve higher levels of turbulence. This will allow to better mimic the oceanic environment. Additionally, as we only modeled waves with a single wave number, this can be modified to model an incident wave beam. More analysis should be performed to further increase our understanding of the dynamics of the interaction of waves with stratified turbulence. By changing the amplitude and wave number, we can investigate a bigger parameter space. Finally, the energetics of the simulated flow can be compared with the field observations.

8 Acknowledgements

To me, summer at GFD was a fantastic experience. The lectures and talks in the morning, the late-night presentations and dinner with the fellows, and the occasional swim or bike around Woods Hole all contributed to my experience. The fellows made the experience 200 times more enjoyable. The coordinators, Tiffany and Pascale, made everything seem smooth, calm, and flawless. Thanks to the principal lecturers, Geoff and Heather, for the information and educational lecture.

My special thanks are to my great advisors. They all were amazing and patient with me, even at hard times. To mention just a glimpse, Bruce Sutherland being super patient when running simulations on supercomputers or writing wave equations on board; Daniel Lecoanet being super helpful when I repeatedly asked Dedalus and simulation questions; and Alexis Kaminski being extra supportive at times when I was having anxiety and panic. But more importantly, thank you all for what I have learned and experienced during the summer. I researched things I loved and tipped my toes in areas I longed for. All in all, that was one great summer.

A Appendix: Damping length

To find the damping length, based on the Dr. Lecoanet's personal notes, we take the curl of the curl of the linearized momentum equation and take the z component of it. Using the continuity equation, the resultant equation is

$$\partial_t \nabla^2 w - \nu \nabla^4 w - \nabla_h b = 0. \tag{12}$$

Where ∇_h, is the derivative in the horizontal direction. Taking the horizontal derivative of the buoyancy equation 2, and combine that with the time derivative of equation 12 and assuming $\kappa\nu$ is small, we will get

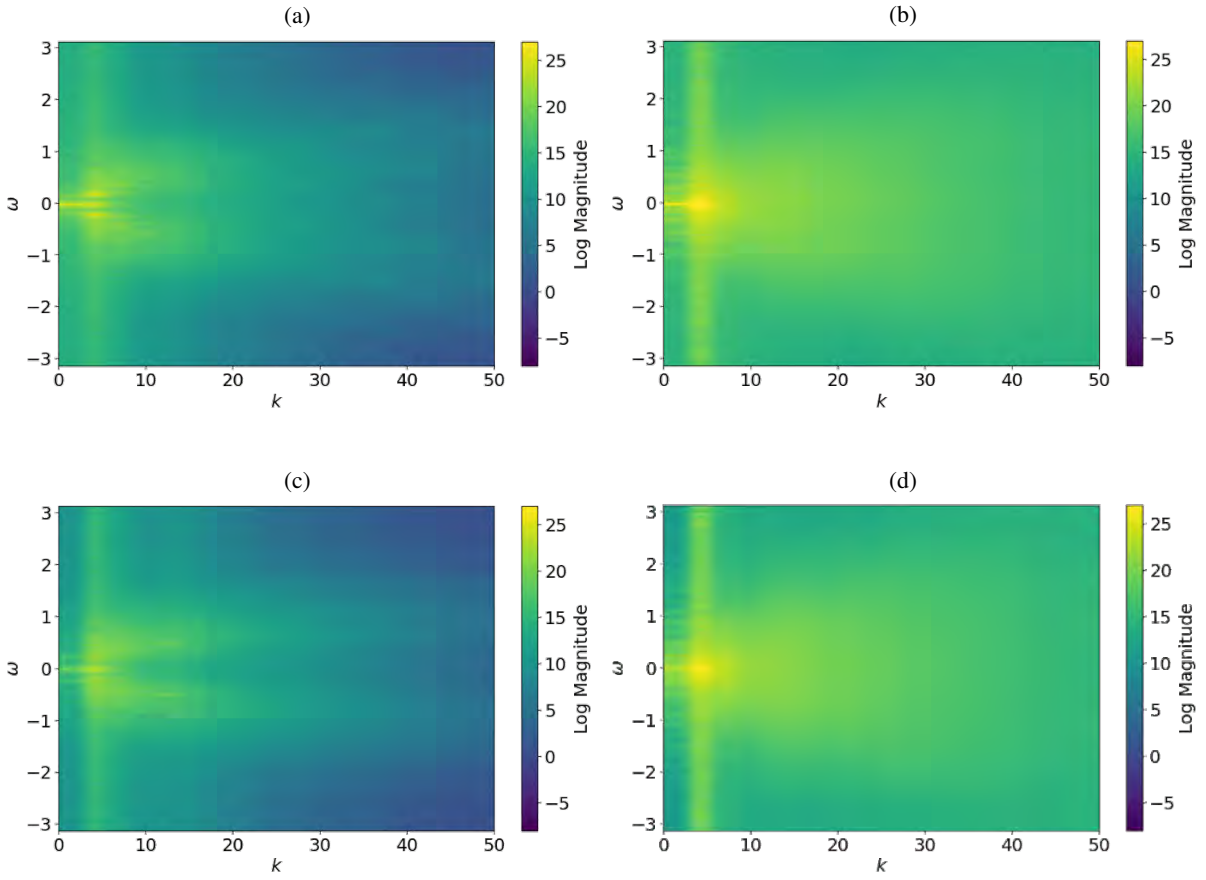

Figure 10: $\omega - k$ spectrum of horizontal energy in the non-turbulent region (left) and turbulent regions (right) calculated for simulations with waves of a) & b) $k_x = 1$, $\omega = 0.2$, and $A_b = 0.01$ and c) & d) $k_x = 4$, $\omega = 0.5$, and $A_b = 0.0025$.

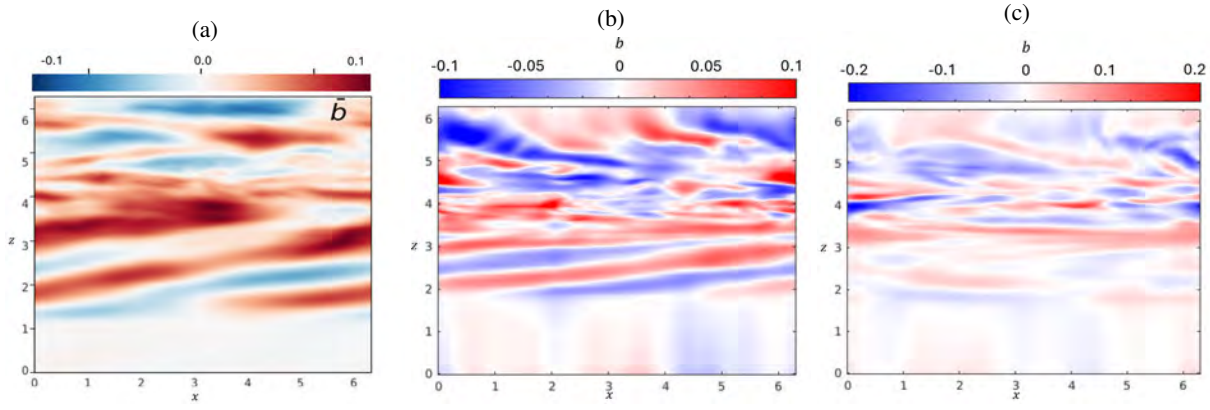

Figure 11: Buoyancy field in simulations of wave with $k_x = 1$, $\omega = 0.2$, and $A_b = 0.01$ launched in a turbulent domain at $N_0 t = 682$; a) the original buoyancy field b, b) decomposed upward traveling, and c) downward traveling components.

$$\partial_t(\partial_t - (\nu + \kappa)\nabla^2)\nabla^2 w + N_0^2 \nabla_h w = 0. \tag{13}$$

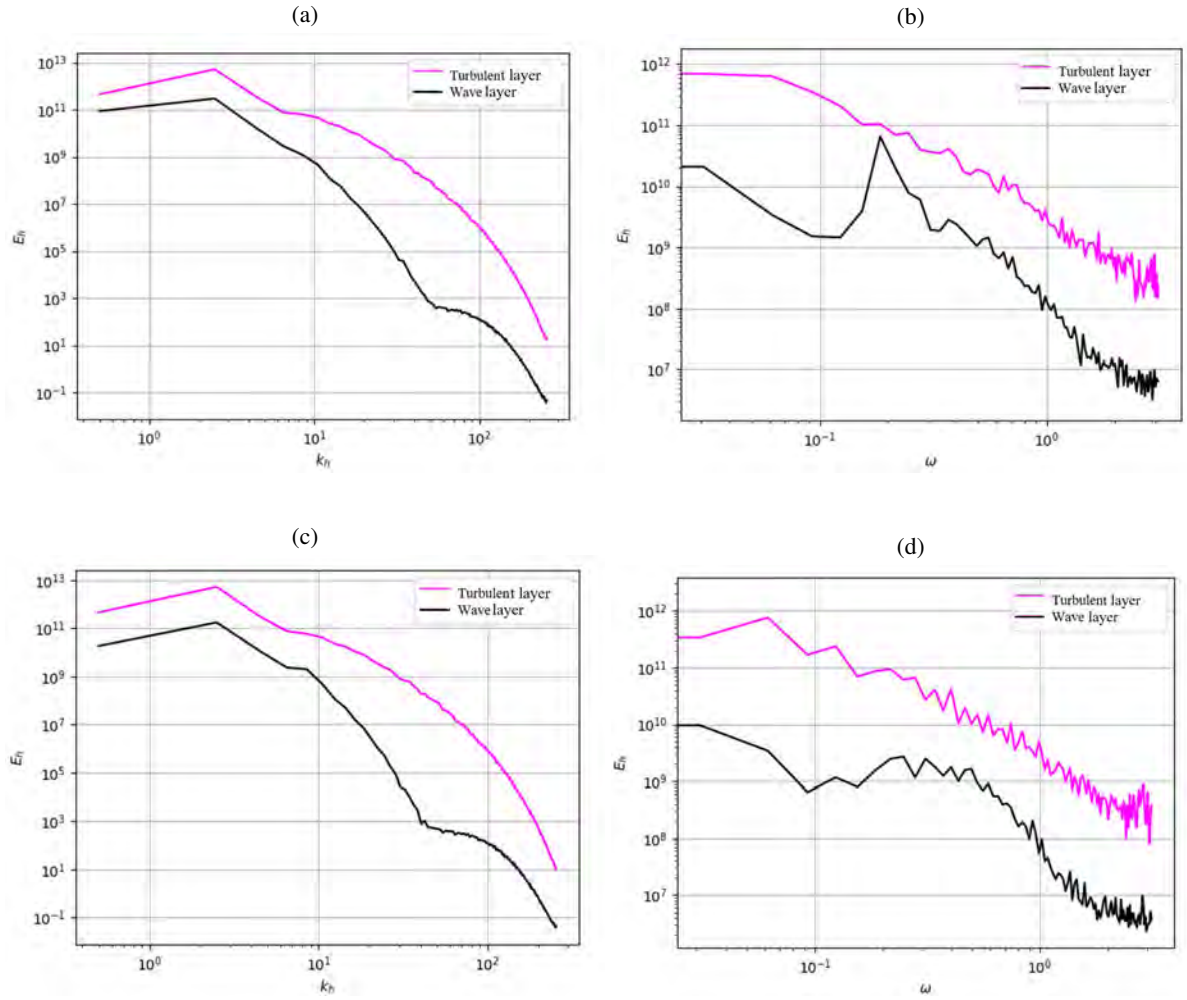

Figure 12: Variations of E_h with regards to k_h (left figures) and ω (right figures) in at $z = 3/4\pi$ in the middle of turbulent layer is available (shown in black) and at $z = 2.5$ between the wave forcing and the turbulent layer (shown in pink) with waves of a) & b) $k_x = 1$, $\omega = 0.2$, and $A_b = 0.01$ and c) & d) $k_x = 4$, $\omega = 0.5$, and $A_b = 0.0025$.

As stated in 4.1, w follows $\mathcal{A}e^{(-z/l_d)(i(\mathbf{k}.\mathbf{x}-\omega t))}$. With this relationship, the derivatives can be found as, $\partial_t = -i\omega$, $\nabla = i\mathbf{k}_h + (ik_z - l_d^{-1})\mathbf{e}_z$, and $\nabla^2 = -k^2 - 2ik_z l_d^{-1} + l_d^{-}2$. Substituting the derivatives in equation 13, we get

$$(-\omega^2 - i\omega(\nu + \kappa)(k^2 + 2ik_z l_d^{-1} - l_d^{-2}))(-k^2 - 2ik_z l_d^{-1} + l_d^{-2}) - N_0^2 k_h^2 = 0. \tag{14}$$

This can be re-written as

$$i(\omega\nu(k^4 + l_d^{-4} - 4l_d^{-4}(k^2 + k_z^2)) - 2\omega^2 k_z l_d^{-1}) - \omega^2 \tag{15}$$

$$-4\omega(\nu + \kappa)k_z L_d^{-1}(-k^2 + l_d^{-2}) - N_0^2 k_h^2 = 0. \tag{16}$$

This rearrangement, separates the imaginary and the real part of the equation 16, which then both should be equal to zero. Using the real part we can find k_z

$$k_z = \left(\omega^2 - N_0^2 \frac{k_h^2}{k^2 - l_d^{-2}}\right) \frac{l_d}{4\omega\nu}. \tag{17}$$

Substituting this into the imaginary part of the equation 16, and assuming weak viscosity and diffusivity (i.e., $\nu+\kappa \ll 1$) we can find an equation that $l_d^{-1} = \frac{\nu N_0^4 k_h^4}{2\omega^5 k_z}$. Which with the assumption of $N_0 k_h = \omega k_z$, we can find the damping rate.

$$l_d^{-1} = \frac{(\nu+\kappa) N_0^3 k_h^3}{2\omega^4}. \tag{18}$$

References

Balwada, D., Smith, K. S., and Abernathey, R. (2018). Submesoscale vertical velocities enhance tracer subduction in an idealized antarctic circumpolar current. *Geophysical Research Letters*, 45(18):9790–9802.

Bartello, P. and Tobias, S. (2013). Sensitivity of stratified turbulence to the buoyancy reynolds number. *Journal of Fluid Mechanics*, 725:1–22.

Burns, K. J., Vasil, G. M., Oishi, J. S., Lecoanet, D., and Brown, B. P. (2020). Dedalus: A flexible framework for numerical simulations with spectral methods. *Physical Review Research*, 2(2):023068.

Cole, S., Rudnick, D., Hodges, B., and Martin, J. (2009). Observations of tidal internal wave beams at kauai channel, Hawaii. *Journal of Physical Oceanography*, 39(2):421–436.

D'Asaro, E. A. (2014). Turbulence in the upper-ocean mixed layer. *Annual review of marine science*, 6:101–115.

Denman, K. and Gargett, A. (1995). Biological-physical interactions in the upper ocean: the role of vertical and small scale transport processes. *Annual Review of Fluid Mechanics*, 27(1):225–256.

Diamessis, P., Wunsch, S., Delwiche, I., and Richter, M. (2014). Nonlinear generation of harmonics through the interaction of an internal wave beam with a model oceanic pycnocline. *Dynamics of Atmospheres and Oceans*, 66:110–137.

Dushaw, B. D., Howe, B. M., Cornuelle, B. D., Worcester, P. F., and Luther, D. S. (1995). Barotropic and baroclinic tides in the central north pacific ocean determined from long-range reciprocal acoustic transmissions. *Journal of Physical Oceanography*, 25(4):631–647.

Echeverri, P., Flynn, M., Winters, K. B., and Peacock, T. (2009). Low-mode internal tide generation by topography: an experimental and numerical investigation. *Journal of Fluid Mechanics*, 636:91–108.

Echeverri, P., Yokossi, T., Balmforth, N., and Peacock, T. (2011). Tidally generated internal-wave attractors between double ridges. *Journal of Fluid Mechanics*, 669:354–374.

Egbert, G. D. and Ray, R. D. (2000). Significant dissipation of tidal energy in the deep ocean inferred from satellite altimeter data. *Nature*, 405(6788):775–778.

Ferrari, R. and Wunsch, C. (2009). Ocean circulation kinetic energy: Reservoirs, sources, and sinks. *Annual Review of Fluid Mechanics*, 41:253–282.

Gayen, B. and Sarkar, S. (2014). Psi to turbulence during internal wave beam refraction through the upper ocean pycnocline. *Geophysical Research Letters*, 41(24):8953–8960.

Godeferd, F. S. and Staquet, C. (2003). Statistical modelling and direct numerical simulations of decaying stably stratified turbulence. part 2. large-scale and small-scale anisotropy. *Journal of Fluid Mechanics*, 486:115–159.

Hibiya, T. and Nagasawa, M. (2004). Latitudinal dependence of diapycnal diffusivity in the thermocline estimated using a finescale parameterization. *Geophysical Research Letters*, 31(1).

Kaminski, A. K., D'Asaro, E. A., Shcherbina, A. Y., and Harcourt, R. R. (2021). High-resolution observations of the north pacific transition layer from a lagrangian float. *Journal of Physical Oceanography*, 51(10):3163–3181.

Kantha, L. H. and Tierney, C. C. (1997). Global baroclinic tides. *Progress in Oceanography*, 40(1-4):163–178.

Kara, A. B., Rochford, P. A., and Hurlburt, H. E. (2000). An optimal definition for ocean mixed layer depth. *Journal of Geophysical Research: Oceans*, 105(C7):16803–16821.

Kunze, E. (2017). Internal-wave-driven mixing: Global geography and budgets. *Journal of Physical Oceanography*, 47(6):1325–1345.

Lee, C. M., Sanford, T. B., Kunze, E., Nash, J. D., Merrifield, M. A., and Holloway, P. E. (2006). Internal tides and turbulence along the 3000-m isobath of the Hawaiian ridge. *Journal of Physical Oceanography*, 36(6):1165–1183.

Lévy, M., Ferrari, R., Franks, P. J., Martin, A. P., and Rivière, P. (2012). Bringing physics to life at the submesoscale. *Geophysical Research Letters*, 39(14).

Maffioli, A. (2017). Vertical spectra of stratified turbulence at large horizontal scales. *Physical Review Fluids*, 2(10):104802.

Mahadevan, A. (2014). Eddy effects on biogeochemistry. *Nature*, 506(7487):168–169.

Martin, J. P., Rudnick, D. L., and Pinkel, R. (2006). Spatially broad observations of internal waves in the upper ocean at the Hawaiian ridge. *Journal of physical oceanography*, 36(6):1085–1103.

Mercier, M. J., Garnier, N. B., and Dauxois, T. (2008). Reflection and diffraction of internal waves analyzed with the Hilbert transform. *Physics of Fluids*, 20(8).

Moum, J., Lien, R.-C., Perlin, A., Nash, J., Gregg, M., and Wiles, P. (2009). Sea surface cooling at the equator by subsurface mixing in tropical instability waves. *Nature Geoscience*, 2(11):761–765.

Munk, W. and Wunsch, C. (1998). Abyssal recipes ii: Energetics of tidal and wind mixing. *Deep Sea Research Part I: Oceanographic Research Papers*, 45(12):1977–2010.

Pinkel, R., Munk, W., Worcester, P., Comuelle, B. D., Rudnick, D., Sherman, J., Filloux, J. H., Dushaw, B. D., Howe, B. M., Sanford, T. B., et al. (2000). Ocean mixing studied near Hawaiian ridge. *Eos, Transactions American Geophysical Union*, 81(46):545–553.

Polzin, K., Toole, J., Ledwell, J., and Schmitt, R. (1997). Spatial variability of turbulent mixing in the abyssal ocean. *Science*, 276(5309):93–96.

Polzin, K. L. and Lvov, Y. V. (2011). Toward regional characterizations of the oceanic internal wavefield. *Reviews of geophysics*, 49(4).

Rainville, L. and Pinkel, R. (2006). Propagation of low-mode internal waves through the ocean. *Journal of Physical Oceanography*, 36(6):1220–1236.

Ray, R. D. and Mitchum, G. T. (1996). Surface manifestation of internal tides generated near Hawaii. *Geophysical Research Letters*, 23(16):2101–2104.

Ray, R. D. and Mitchum, G. T. (1997). Surface manifestation of internal tides in the deep ocean: Observations from altimetry and island gauges. *Progress in Oceanography*, 40(1-4):135–162.

Riley, J. J. and de Bruyn Kops, S. M. (2003). Dynamics of turbulence strongly influenced by buoyancy. *Physics of Fluids*, 15(7):2047–2059.

Roemmich, D., Church, J., Gilson, J., Monselesan, D., Sutton, P., and Wijffels, S. (2015). Unabated planetary warming and its ocean structure since 2006. *Nature climate change*, 5(3):240–245.

Rudnick, D. L., Boyd, T. J., Brainard, R. E., Carter, G. S., Egbert, G. D., Gregg, M. C., Holloway, P. E., Klymak, J. M., Kunze, E., Lee, C. M., et al. (2003). From tides to mixing along the Hawaiian ridge. *science*, 301(5631):355–357.

Sasaki, H., Klein, P., Qiu, B., and Sasai, Y. (2014). Impact of oceanic-scale interactions on the seasonal modulation of ocean dynamics by the atmosphere. *Nature communications*, 5(1):5636.

Slinn, D. N. and Riley, J. (1998). A model for the simulation of turbulent boundary layers in an incompressible stratified flow. *Journal of Computational Physics*, 144(2):550–602.

St. Laurent, L. and Garrett, C. (2002). The role of internal tides in mixing the deep ocean. *Journal of physical oceanography*, 32(10):2882–2899.

St. Laurent, L. C., Toole, J. M., and Schmitt, R. W. (2001). Buoyancy forcing by turbulence above rough topography in the abyssal Brazil Basin. *Journal of Physical Oceanography*, 31(12):3476–3495.

Sutherland, B. R. (2010). *Internal gravity waves*. Cambridge university press.

Tabaei, A., Akylas, T., and Lamb, K. G. (2005). Nonlinear effects in reflecting and colliding internal wave beams. *Journal of Fluid Mechanics*, 526:217–243.

Thomson, J., Schwendeman, M. S., Zippel, S. F., Moghimi, S., Gemmrich, J., and Rogers, W. E. (2016). Wave-breaking turbulence in the ocean surface layer. *Journal of Physical Oceanography*, 46(6):1857–1870.

Wunsch, S. and Brandt, A. (2012). Laboratory experiments on internal wave interactions with a pycnocline. *Experiments in fluids*, 53:1663–1679.

Transport and Aggregation of Microplastics in Experimental Turbidity Currents

Quentin Kriaa

July 3, 2024

Experiments are performed to gain an understanding of the transport of microplastics by turbidity currents. The first series of experiments analysed the detrainment of positively buoyant microplastics from saline gravity currents of varying Reynolds number. The non-uniform flows within the gravity current affected the detrainment of microplastics, whose rise was delayed with respect to the motion of the current's nose. A second series of experiments focused on the interaction between the same positively buoyant microplastics and glass spheres. Idealised controlled experiments revealed that these two types of particles adhered when mixed together, leading to the formation of aggregates whose modified buoyancy can turn the microplastics into negatively buoyant aggregates. Finally, we analysed the settling and transport of microplastics from microplastics-bearing turbidity currents driven by the negative buoyancy of glass spheres. We verified that this flow also produces aggregates of microplastics and glass, resulting in the deposition of up to 17% of the plastic mass at the bottom of the tank.

1 Introduction

Every year an approximate mass of plastic of 10^8 tons is produced [21], with about 20% being released into rivers and the ocean [5]. Most of the plastic produced is expected to be positively buoyant [10], and yet floating plastic waste and plastics washed onto shore are estimated to have a combined mass of about 300 kilotons [25]. This represents less than $\sim$2% of the expected mass which is produced in just one year. Since plastics can adsorb toxic substances (e.g., hydrophobic marine pollutants, pesticides, heavy metals, etc. [22, 8]), it represents a threat to living organisms that might ingest them.

Due to turbulent and abrasive processes, large pieces of plastic waste are broken up into smaller microplastics (MP) having sizes in the range $1\ \mu\text{m} - 5$ mm [12, 21], the upper bound corresponding to the minimum size that can be captured by trawling nets. These micro particles are now present in hundreds of ecosystems, down to small aquatic organisms like zooplanktons [6], and they can be transmitted through the food chain at many scales. On top of that, present-day studies reveal how smaller plastic fragments called *nanoplastics* are transported through the air [1] and can therefore be inhaled, reinforcing the need to further study the dispersal of MP in the environment.

Measurements on the sea floor have revealed the presence of MP deep in the ocean [23, 27]. Knowing that most produced plastics are expected to float, this raises the question of what mechanism turns positively buoyant MP into negatively buoyant particles. A number of mechanisms are linked to biology [24, 19]: MP can be transported deep in the ocean when ingested by or after sticking to aquatic organisms; alternatively, biofilms can grow over plastic fragments and turn the resulting 'biolfouled' assemblage into a negatively buoyant structure.

The present work focuses on a novel inorganic process that turns positively buoyant MP into negatively buoyant agglomerates. We show that glass spheres are attracted to polyethylene plastic particles, making some of the plastics settle in stationary and turbulent flows. The manuscript is organised as follows. Section 2 investigates the transport and detrainment of MP when passively advected by (saline) gravity currents. Section 3 reveals how MP and sediments attach to one another when brought in contact in idealised controlled experiments in beakers. Section 4 combines both aspects of transport and attachment: we analyse the evolution of turbidity currents that are laden with glass spheres (they drive the current through buoyancy) and MP (they are transported by the current), and show how glass-plastic interactions alter the transport of the MP. Concluding remarks are presented in section 5, and appendices are added to detail technical aspects of the experiments.

2 Transport of MP by Gravity Currents

2.1 Experimental setup

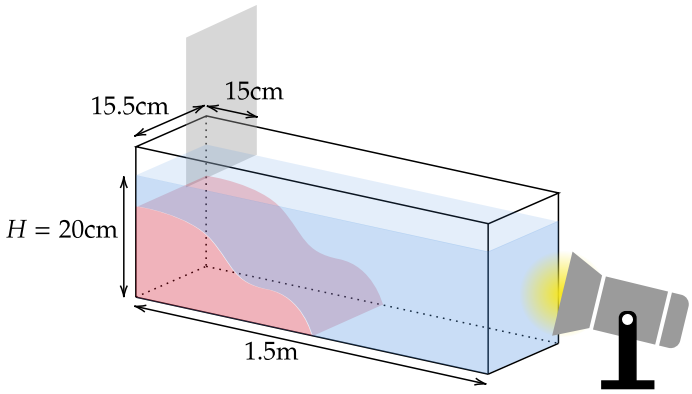

Figure 1: Setup used to generate gravity currents. The fresh tap water is shown in blue, the dyed salty water is shown in red, the grey rectangle corresponds to the gate after lifting it upward to release the dense gravity current, and light is shone from the right end of the tank.

As shown in figure 1, experiments are performed in a 150.0 cm-long and 15.5 cm-wide tank, filled with fresh tap water of density $\rho_a = 998.5$ kg m^{-3} up to a depth $H = 20.0$ cm. At a distance of 15.0 cm from the left wall, a vertical gate seals the lock region of volume $V_{\text{lock}} = 4.65$ L in which a small amount of food colouring and some salt water are added until the density in the lock reaches a value $\rho = \rho_a + \Delta\rho$. Most gravity currents are laden

with MP. In that case, a measured mass m_p of MP, usually of 1.0 g, is injected in the lock and stirred vigorously to homogenise the microplastics in the lock. When an experiment starts, stirring is stopped at $t \simeq -5$ s and at $t = 0$ the gate is quickly lifted. The gate is left partly underwater, with its lowest end 2 cm below the free surface to damp the formation of surface waves that would otherwise affect the propagation of a gravity current. Once the gate is lifted, the dense fluid from the lock is put in contact with the ambient fluid. The density difference $\rho - \rho_a = \Delta\rho$ generates a horizontal pressure gradient that drives the formation of a gravity current, whose nose rolls up, accelerates and quickly reaches a regime of constant velocity, as shown in Figure 2. The flow is visualised with a colour camera that faces the side wall of the tank over its entire length. Light is shone from the right end of the tank, illuminating its length. The colouring is visualised by light absorption, while MP are visualised as bright dots due to light scattering from the particles.

Microplastics are obtained by grinding light polyethylene beads with a cryogrinder until particles become sub-millimetric. The particles obtained are rinsed and sifted through stacks of sieves on a NORJIN lab vibrator. The particles used in this study have a maximum dimension smaller than 425 μm and larger than 250 μm.

2.2 Governing numbers

The motion of the gravity current is essentially characterised by two dimensionless numbers. The Froude number [4, 15],

$$Fr = \frac{\dot{x}_f}{\sqrt{g'H}/2}, \tag{1}$$

compares the front velocity $\dot{x}_f$ of the current (i.e., the time derivative of the front position x_f), with the characteristic speed $\sqrt{g'H}/2$ given in terms of the reduced gravity $g' = g\Delta\rho/\rho_a$ with $g = 9.81$ m.s^{-2}. As visible in the second snapshot of both figure 2a and figure 2b, despite initial perturbations introduced by the shear that develops when the gate is lifted, gravity currents have sufficient inertia to quickly reach a regime of constant front velocity. This so-called *inertial regime* is characterised by a Froude number of order unity i.e., $Fr = O(1)$. Therefore, the characteristic velocity

$$u_c = \sqrt{g'H}/2 \tag{2}$$

is a good estimate of the front velocity during experiments. Based on this estimate, the input Reynolds number

$$Re = \frac{u_c H/2}{\nu} \tag{3}$$

ranges in the interval $[378, 2858]$, with $\nu = 10^{-6}$ m^2.s^{-1}, the kinematic viscosity of water.

To describe the motion of an individual buoyant particle in a flow, we assume that the particle is only subject to buoyancy and drag, and that the particle response time is negligible compared to all other timescales that characterise the fluid motion. A straightforward consequence is that the particle velocity, $\boldsymbol{v}_p$, satisfies

$$\boldsymbol{v}_p(\boldsymbol{x}_p, t) = \boldsymbol{v}(\boldsymbol{x}_p, t) + w_s \boldsymbol{e}_z, \tag{4}$$

(a) $Re = 1459$ (b) $Re = 2843$

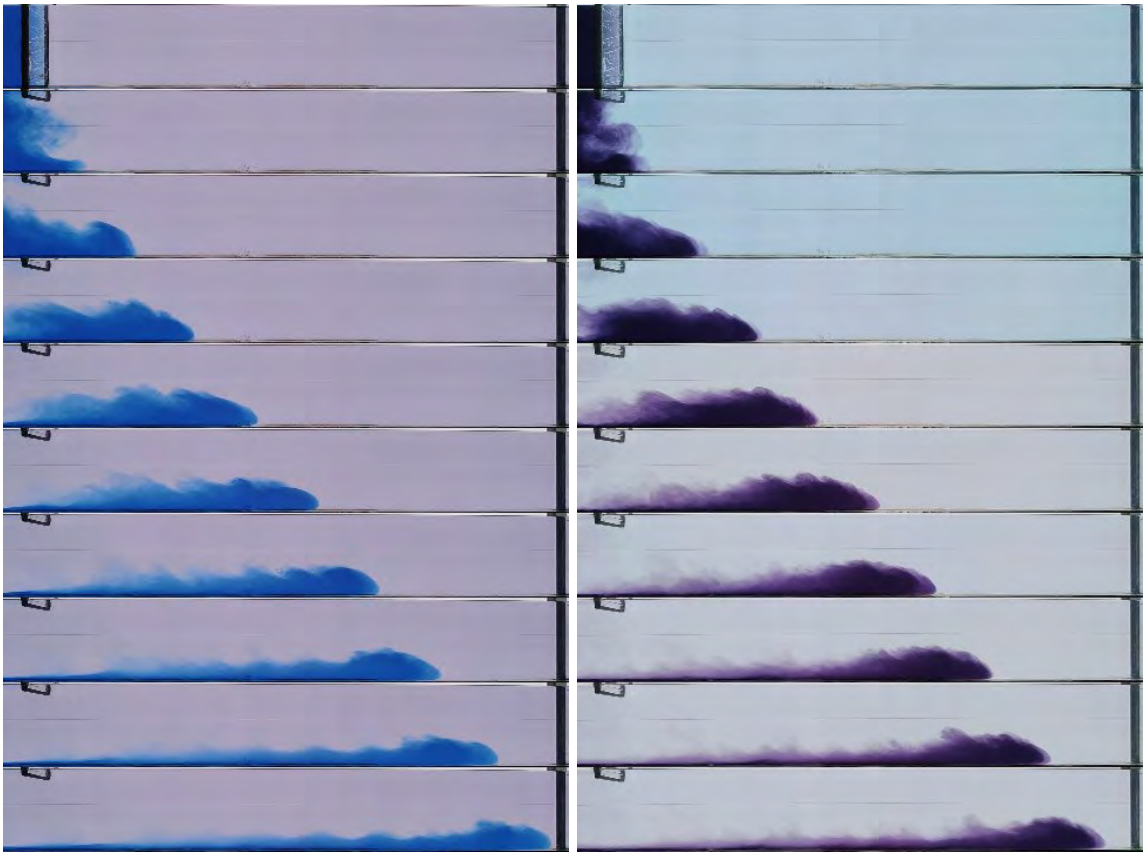

Figure 2: Snapshots of gravity currents of Reynolds numbers (a) $Re = 1459$ and (b) $Re = 2843$, respectively. The time lapse between two snapshots is, respectively, (a) $\Delta t = 14.4$ s and (b) $\Delta t = 7.2$ s. The height of every snapshot is $H = 20$ cm.

with bold symbols corresponding to vectors, $\boldsymbol{v}(\boldsymbol{x}_p, t)$ is the fluid velocity at the particle position $\boldsymbol{x}_p(t)$, the upward vertical unit vector is denoted $\boldsymbol{e}_z \equiv -\boldsymbol{g}/g$, and w_s is the rise velocity[1] of a spherical particle of radius r_p and density ρ_p, which we parameterise with the Schiller-Naumann correction to the Stokes velocity [7]

$$w_s = \frac{w_s^{\text{Stokes}}}{1 + 0.15 Re_p^{0.687}}, \tag{5}$$

where the particle Reynolds number is defined as

$$Re_p = \frac{2 r_p w_s}{\nu}, \tag{6}$$

and the Stokes velocity is

[1]The subscript s is adopted from a general notation that defines w_s as the *settling* velocity of the particle, here in the upward direction.

$$w_s^{\text{Stokes}} = \frac{2gr_p^2(\rho_a - \rho_p)}{9\nu\rho_a} \ . \tag{7}$$

In equation (5), the settling velocity is defined implicitly since the particle Reynolds number depends itself on w_s in equation (6). That is why the values of w_s are obtained by numerical integration of equation (5) for a given particle radius r_p.

The particle velocity in equation (4) reveals that small microplastics move as tracers along the horizontal direction, but they gravitationally drift upward in time, therefore crossing trajectories of fluid parcels. For light-polyethylene particles, $\rho_p = 930$ kg.m^{-3}. With the mean radius $r_p = 169$ μm, this leads to an estimated rise velocity, $w_s \simeq 3.6 \times 10^{-3}$ m.s^{-1}. The order-of-magnitude velocity of gravity currents is $u_c \sim 10^{-2}$ m.s^{-1} which is much larger than w_s. The relative rise speed of the particles can be characterised by a non-dimensional number, the Rouse number, which we denote by

$$\mathcal{R} = \frac{w_s}{u_c}. \tag{8}$$

This number can be derived by rewriting equation (4) under the form $|\boldsymbol{v}_p - \boldsymbol{v}|/|\boldsymbol{v}| = w_s/|\boldsymbol{v}| = O(\mathcal{R})$. In typical experiments, $\mathcal{R} \sim 10^{-1}$.

Exp. #	Mass of MP (g)	Mass surfactant (g)	$\Delta\rho$ (kg.m^{-3})	Re	Buoyancy ratio
1	1.0059	0	0.107	725	0.1586
2	1.0014	0	0.238	1081	0.071
3	1.0035	0	1.662	2858	0.0102
4	0.9949	0	0.942	2151	0.0178
5	1.0004	0	0.029	378	0.5821
6	1.0046	0	0.425	1445	0.0399
7	0.9999	0	0.66	1800	0.0256
8	1.0014	0	0.338	1288	0.05
9	1.0015	0	0.199	989	0.0849
10	1.0043	0	0.151	861	0.1122
11	1.0006	0	1.566	2773	0.0108
12	7.998	2.1584	1.525	2737	0.0885
13	8.0513	2.3278	0.416	1429	0.3266
14	0	0	1.646	2843	0
15	0	0	0.434	1459	0
16	1.0039	0	0.8	1983	0.0212
17	1.0016	0	0.535	1621	0.0316
18	1.0002	0	0.683	1831	0.0247

Table 1: Experimental data on gravity currents with and without the addition of microplastics and surfactants to the lock. The last column is the ratio of the buoyancy of microplastics over the buoyancy of the saline current given by $m_p(1 - \rho_a/\rho_p)/[(\rho - \rho_a)V_{\text{lock}}]$.

The contribution of suspended particles to the total buoyancy of the MP-bearing gravity current is small (see Table 1). In addition, the microplastic particles are dilute. Due to both reasons, we assume that the gravity current is uninfluenced by the presence of the MP

and that the MP follow the horizontal motion of the current. However, along the vertical direction, they additionally drift upward in time and ultimately rise above the current.

2.3 How do microplastics detrain from gravity currents?

In the reference frame of the nose of the gravity current which moves with constant speed, one might assume that particles within the current rise vertically with no additional lateral motion. We shall see that this is not the case.

We begin by assessing the influence of the current velocity on the detrainment of MP. Since their buoyancy contributes little to the total buoyancy of gravity currents, changing their total mass did not affect the process of detrainment. To modify the density contrast $\Delta\rho$ between the current and the ambient fluid, and therefore the velocity u_c, we varied the amount of salt water that was added in the lock. Figure 3 shows snapshots of MP-bearing gravity currents that gradually detrain MP above and behind them over the course of their propagation. Successive snapshots from high Reynolds number experiments show that MP are initially detrained as a particle plume near the nose of the gravity current, but gradually the source of the plume shifts upstream until the plume emanates from the tail of the gravity current, as visible when comparing the third and the last snapshots in figure 3b. For the low Reynolds number gravity current (figure 3a), the plastics detrain from the current shortly after its release from the lock. This is expected: the time for microplastics to rise over the current's height $\sim H/2$ is typically $\sim H/(2w_s)$; during that time, the current propagates over a distance $\sim u_c H/(2w_s) = Re\nu/w_s$. So for currents of low Reynolds numbers with fixed w_s, the microplastics rise before the current propagates far from the lock.

The current nose velocity is measured first by constructing time series plots of image intensity over a horizontal slice through movie frames taken at a height $z = H/12$ above the bottom of the tank, as shown for example in figure 4. The yellow crosses indicate the position where the nose of the gravity current is detected. Figure 5a plots the front position $x_f(t)$ as a function of time t for all the gravity current experiments. The slope of the best-fit line through each trajectory provides a measurement of the front velocity $\dot{x}_f$, which is compared to the estimate $\sqrt{g'H}/2$ in figure 5b. We verify in this figure that the Froude number $Fr = \dot{x}_f/u_c$ is approximately constant with an average value 0.69 ± 0.09 i.e. of order unity, which is consistent with section 2.3.

We measure the horizontal propagation velocity of the plume of MP, $\dot{x}_{\text{plume}}$. This velocity corresponds to the Lagrangian velocity of the front of the plume as detected in space-time diagrams of the light intensity recorded at mid-depth ($z = H/2$), as illustrated in figure 6: yellow crosses show the position of the front of the plume of MP in time. Figure 7a plots these measurements for all gravity current experiments. Curves show no clear trend of convexity nor concavity, meaning there appears no trend of acceleration or deceleration of the plume in time. Some curves show oscillations for intermediate values of the Reynolds number (near $Re \sim 1000$) on a time-scale of order 50 s, which is due to the presence of shear-induced billows that carry MP up-and-down the mid-water depth. Save for these few experiments, the MP plume front position x_{plume} increases relatively linearly in time. The slope of the best-fit line through each trajectory gives the plume velocity $\dot{x}_{\text{plume}}$, which is compared to the front velocity $\dot{x}_f$ for all experiments in figure 7b.

Although the Reynolds number, Re, affects the value of the ratio $\dot{x}_{\text{plume}}/\dot{x}_f$ for reasons

(a) $Re = 725$ (b) $Re = 2773$

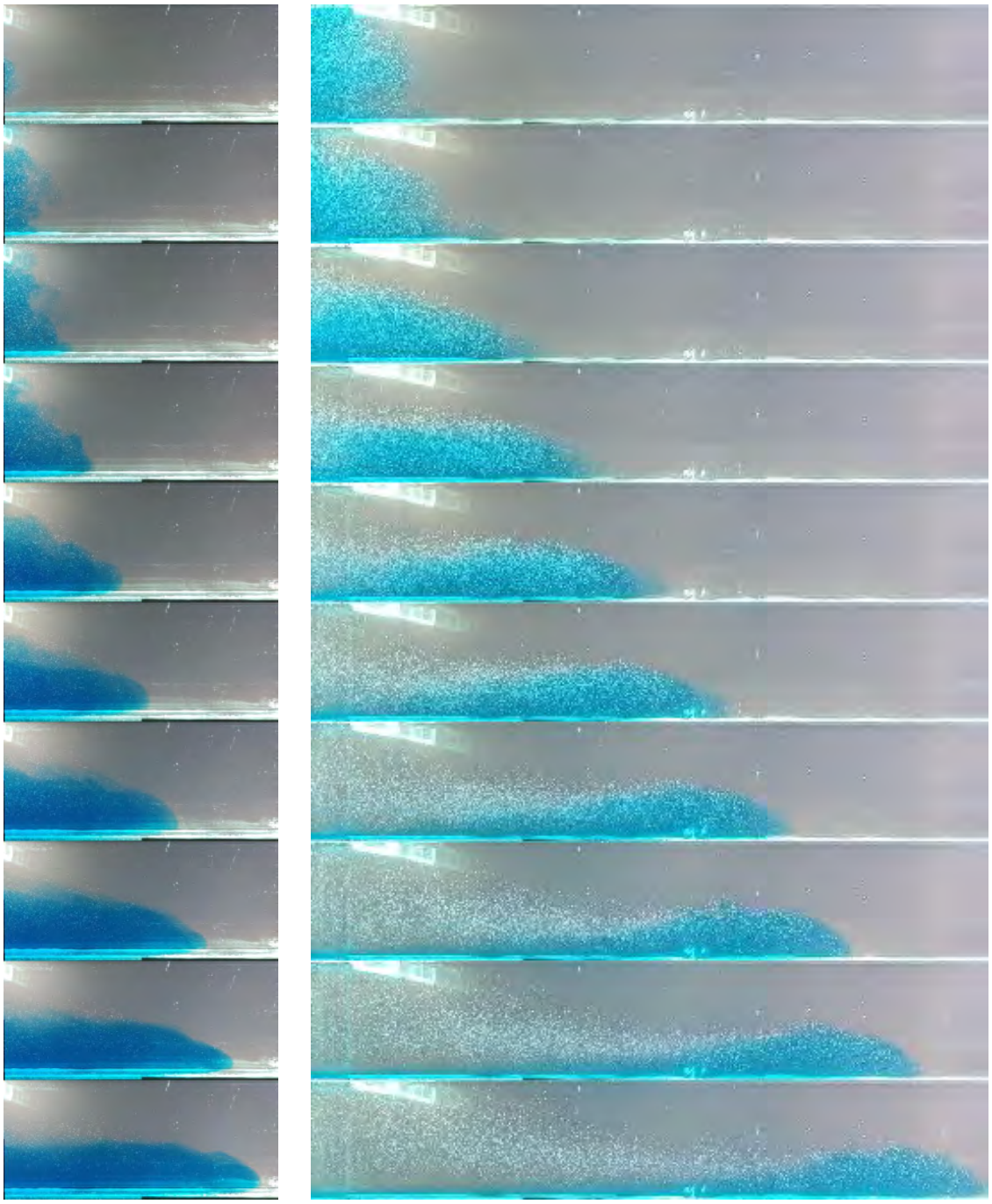

Figure 3: Snapshots of MP-bearing gravity currents of Reynolds numbers (a) $Re = 725$ and (b) $Re = 2773$, respectively. The time lapse between two snapshots is, respectively, (a) $\Delta t = 11.52$ s, and (b) $\Delta t = 5.6$ s. The height of every snapshot is $H = 20$ cm.

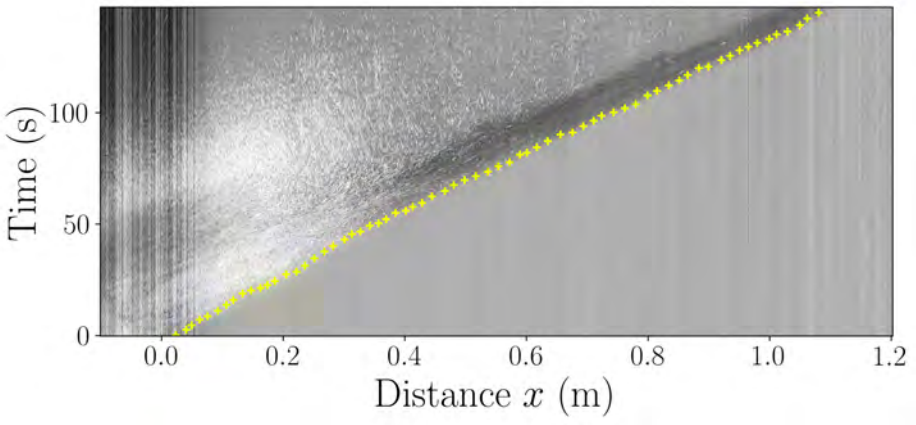

Figure 4: Space-time diagram showing the propagation of the MP-bearing gravity current of Reynolds number $Re = 1429$ as measured at a depth $z = H/12$. Yellow crosses indicate the front position of the current at different timesteps.

that remain yet to be clarified, figure 7b manifests the comparatively slower propagation of the plume of MP compared to the current's front.

The reason for the slower relative advance of the particle plume is made evident by figure 8a, which shows successive snapshots that correspond to moving standard deviations of light intensity over periods of 1.33 s. In much the same way as long-exposure photographs, these snapshots reveal the trajectories of MP during the experiments. These images show that the motion within the gravity current is not uniform, but has significant shear that carries MP downstream to the nose when they are close to the bottom, and conversely carries them upstream away from the nose when they are located higher up in the current. Such near-bottom noseward advected fluid has recently been observed by Sher and Woods in saline gravity currents with no particles [20]. A schematic illustrating this motion is shown in figure 8b. Due to the shear flow, as MP rise in a gravity current, they initially sample large horizontal velocities near the bottom that carry them to the nose of the current from which they detrain at early times. At later times, when MP have risen sufficiently high within the current above the forward advancing flow, they rise upward and backward in the reference frame of the nose. Consequently, the particles detrain farther and farther away from the nose at late times. This sequence of events explains why the plume origin drifts upstream in time. These observations and interpretations are consistent with past measurements of the mean shear profile in a gravity current (see, e.g., [14, 26]) and the observations of Sher and Woods [20].

Another influence on the slower plume advance speed is that the head of the current changes morphology in time. Once the gravity current forms, a perturbation at the interface between the saline fluid and the ambient fluid in the lock propagates from the position of the gate to the left end wall where it is reflected. After reflection, this perturbation propagates downstream as a *bore* (also called a *rarefaction wave*), that propagates faster than the current nose, and therefore leads to a shrinking of the portion of the current located between the bore and the nose [18]. This gradual reduction of the size of the current is shown in figure 9. At the back of the head, where the bore is located, the fluid motions are

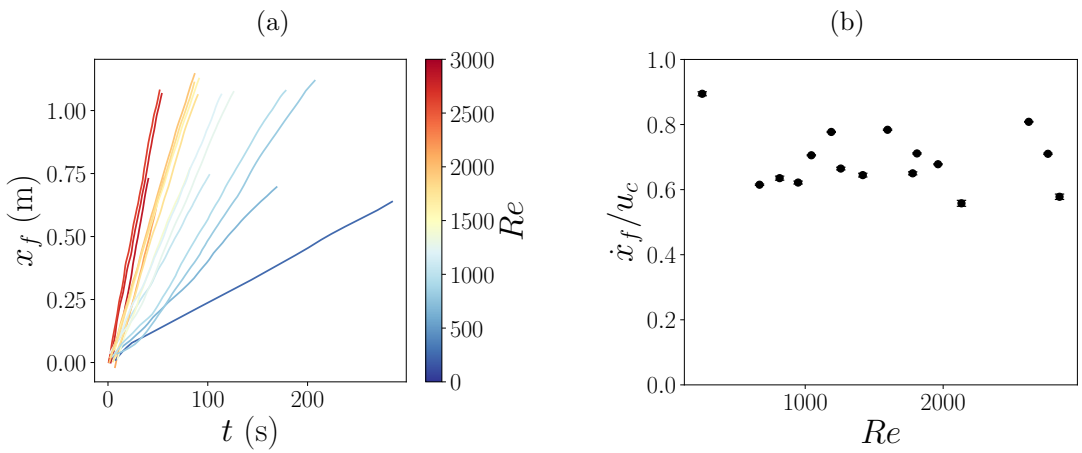

Figure 5: (a) Time evolution of the front position of all MP-bearing gravity currents. After fitting a linear law on every curve in (a), the average current velocity is extracted, normalised by $u_c = \sqrt{\overline{g'H}/2}$ and shown for each experiment of a given Reynolds number in (b). The barely visible error bars in (b) correspond to the standard error of the regression in Python.

deflected downward (see the red arrow on the last snapshot of figure 9); therefore, as the head shrinks and as the plume of MP drifts upstream, the MP ultimately feel this downward deflection that delays their ascent. This enhances the discrepancy between $\dot{x}_f$ and $\dot{x}_{\text{plume}}$.

3 MP-Sediment Interaction in Idealised Experiments

3.1 Experimental setup

When entering rivers from storm drains or municipal waste outflows, MP interact with suspended sediments in a turbulent flow. The possible adhesion of relatively dense sediments to plastics is thought to lead to the ultimate deposition of plastics on the sea floor despite the possible positive buoyancy of the plastic. Because particle-particle interactions can be highly sensitive to the details of the particles' size, shape and surface properties, idealised and controlled laboratory experiments are conducted to gain understanding into such interactions. Specifically, we examine the interaction between polyethylene plastic particles and glass spheres.

Experiments are performed in beakers containing 900 mL of fresh tap water. A controlled amount $\mathcal{C}_{\text{surf}}$ of the surfactant, TritonX 100, is added and systematically varied between experiments. A fixed mass $m_p = 0.68$ g of low density polyethylene MP of density $\rho_p = 930$ kg.m^{-3} and mean radius $r_p = 169$ μm is introduced in the beaker. Then, as a laboratory analog for sand, $m_g = 2$ g of glass spheres of radius $r_g = 37.5$ μm and density $\rho_g = 2500$ kg.m^{-3} are introduced. An electrical helical stirrer is then activated for a duration of 1 min before removing it from the beaker and rinsing it with a syringe containing the same mixture of water and surfactant as that in the beaker. The beaker is then covered with plastic wrap and left undisturbed for a minimum of 30 minutes as particles come to rest.

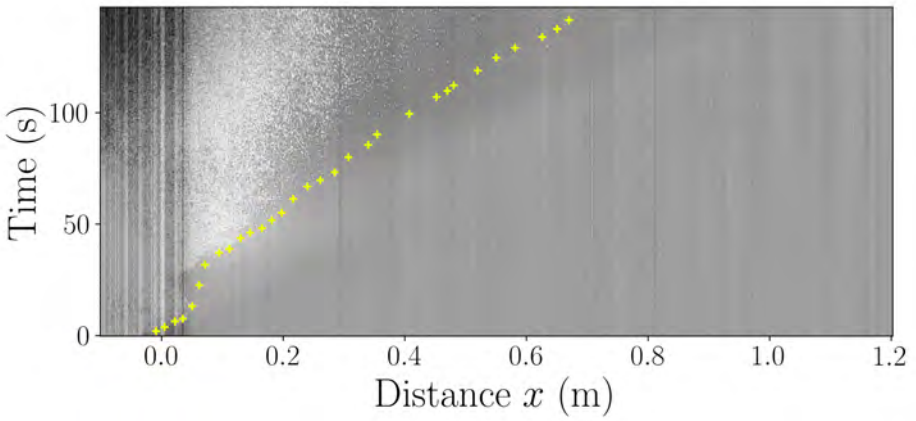

Figure 6: Space-time diagram showing the propagation of the plume of MP at mid-depth, for a Reynolds number $Re = 1429$. Yellow crosses indicate the front position of the plume of MP at several timesteps.

Table 2 summarises the main parameter values used in these experiments.

3.2 Quantifying the deposition of MP

Once fluid motions in the beaker have come to rest, most MP are found at the water's free surface. However, some MP are also detected at the bottom of the beaker amongst the glass spheres, where they stand out due to their larger size and difference in colour (glass spheres are translucent and they brightly reflect the light, whereas MP are partly opaque and white). This observation is illustrated with photographs, as shown in figure 10.

To quantify the deposition of MP at the bottom of the beaker, the mass of deposited MP is measured. A syringe is used to remove all the MP that float at the free surface. The absence of any MP particle in the meniscus is carefully inspected and confirmed by shining light from different angles and visualising the meniscus with a camera. Then, the rest of the beaker is flushed out onto moistened Whatman 8 micron filter paper sitting on a strainer above a bucket. The beaker is thoroughly rinsed by clear fresh water and so are the collected particles. The filter paper and its content are then placed in an oven for a few hours to dry. Subsequently, all the particles are poured into a stack of several sieves with mesh sizes (from top to bottom, in microns) 425-250-150-40. The first sieve essentially removes dust from the pile of particles, while the smallest mesh only collects small glass spheres. The mass of MP collected in intermediate ranges is measured on a scale with a precision of 10^{-4} g.

Figure 11 shows the results as a function of the concentration of surfactant in the beaker. These results show that the concentration of surfactant affects the total mass that deposits at the bottom of the beaker. Circles correspond to experiments performed with a fast clockwise stirring in circles with the electric stirrer; on the opposite, diamonds correspond to past experiments that were stirred slower with a wooden stick by hand, producing random turbulent motions with no clear direction of the flow. Similar observations are obtained in both cases: a lot of scatter at low concentrations of surfactant $\mathcal{C}_{\text{surf}} < 2$ g/L, a small plateau

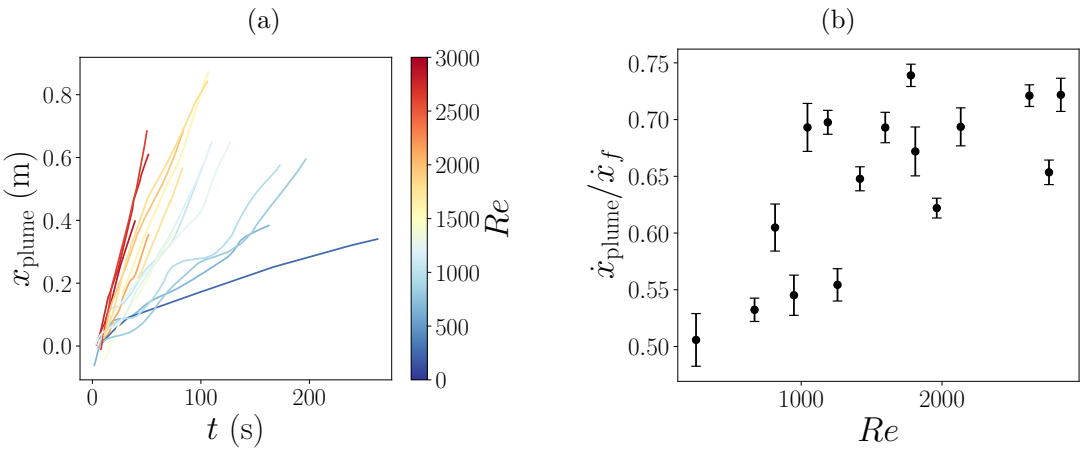

Figure 7: (a) Time evolution of the MP plume front position as detected at mid water depth. After fitting a linear law on every curve in (a), the average propagation velocity of the plume $\dot{x}_{\text{plume}}$ is extracted for all experiments and compared to the front velocity $\dot{x}_f$ in (b).

at large concentrations $\mathcal{C}_{\text{surf}} > 2$ g/L, with a possible local maximum near $\mathcal{C}_{\text{surf}} = 1-2$ g/L. Stirring faster in circles usually leads to a lower mass of deposited MP (circles tend to have lower ordinates than diamonds); this observation will be discussed below. Finally, additional experiments have been performed with various amounts of glass to vary the glass-to-plastic mass ratio. As a general trend, the larger this ratio, the more mass deposited at the bottom of the beaker.

To understand why MP become negatively buoyant when stirred with glass spheres in water, even in the absence of surfactant, the guiding hypothesis is that glass spheres and MP stick to one another, forming aggregates that are negatively buoyant and therefore sink to the bottom at the end of the experiment. To confirm this assumption, a WiFi digital microscope of 1920 × 1080 pixels magnifying up to 1000× (focus distance 3 mm) was used to closely observe the negatively buoyant MP collected at the bottom of the beaker at the end of an experiment. Figure 12 shows snapshots taken with the microscope that clearly reveal the presence of large opaque microplastic particles coated with a number of glass spheres that are easily identified due to their sphericity (the eight white stripes of light on each glass sphere correspond to reflections of the eight LEDs of the microscope).

The number of glass spheres attached to a plastic particle varies greatly. By comparing the density of fresh tap water with the average density of an aggregate of one plastic particle and one or more glass sphere(s), we can estimate the number of glass spheres that must be attached to a plastic particle for it to reach neutral buoyancy. Figure 13 shows how this number varies with the microplastic radius. For the range of sizes explored in this study, we find that if there are more than 2-9 glass spheres attached, the aggregate is negatively buoyant and should deposit at the bottom of the beaker. Otherwise, microplastics can be close to neutrally buoyant, or remain positively buoyant. Consistently, observations of floating microplastics revealed the presence of a few glass spheres attached to them – not

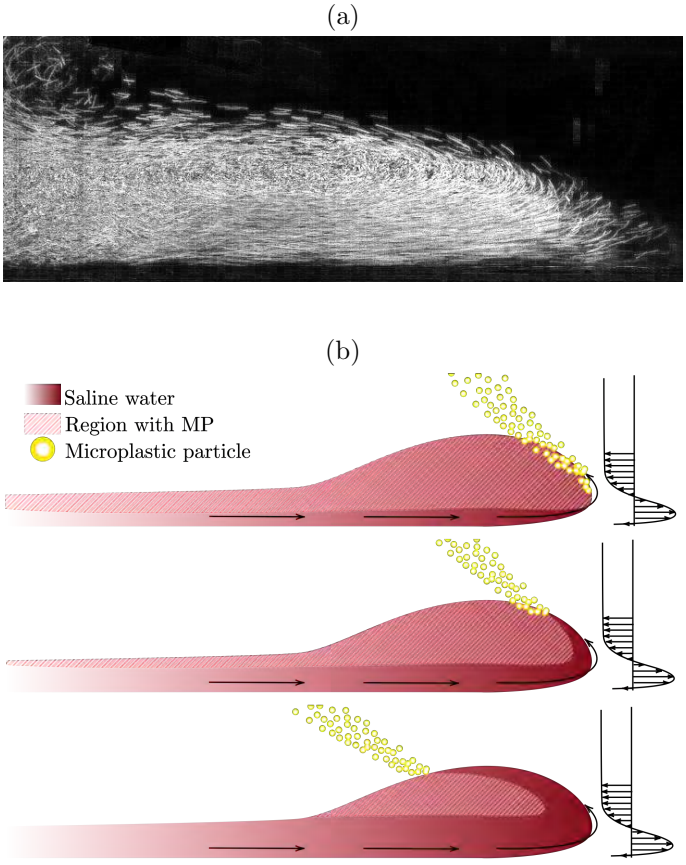

Figure 8: (a) Standard deviation of the light intensity over a duration of 1.33 s, showing in white the trajectories of MP in a gravity current of Reynolds number $Re = 2773$: MP move downstream near the bottom of the tank, change direction near the nose and move upstream near the upper edge of the current. (b) Sketch of the gradual drift of the plume of MP (yellow circles) detrained from the gravity current (shown in red). Arrows in the gravity current show the motion of MP; an illustrative sketch of the velocity profile in the current's reference frame is shown on the right of each row. First row: at early times, the region laden with MP (shown with red-white hatchings) is still close to the bottom of the tank where the velocity advects MP to the current's nose. Second row: later on, MP have risen and are advected to the front much slower, so that most of them detrain from the top of the head rather than from the very front. Third row: MP have now risen in a region of negative velocity and MP are detrained from the back of the current's head.

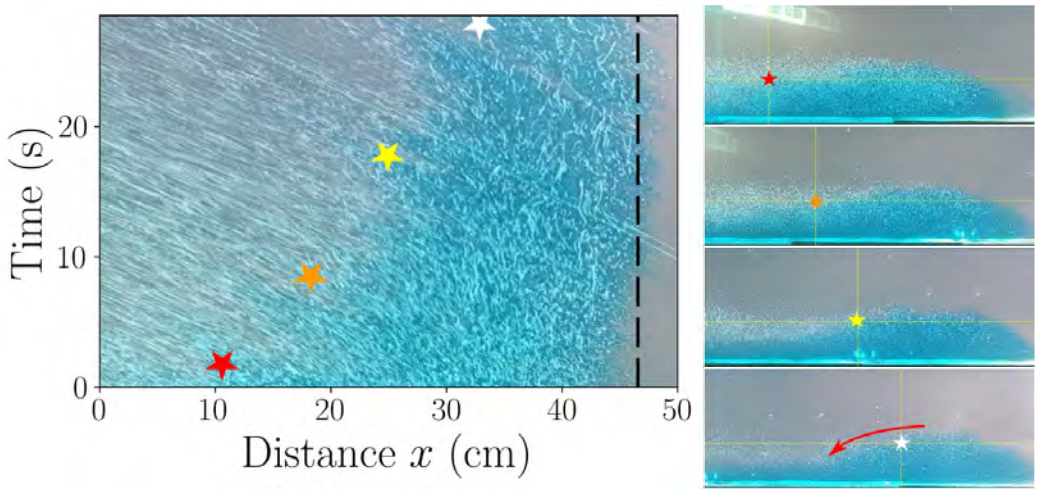

Figure 9: The space-time diagram on the left-hand side shows, in the reference frame of a gravity current's nose, the presence of white MP and blue dye at a distance $z = 6.5$ cm above the bottom of the tank. The blue dye is indicative of the presence of the gravity current's head: its horizontal extension at the height $z = 6.5$ cm proves to shrink in time. Each star corresponds to one of the four snapshots shown on the right-hand side. The Reynolds number is $Re = 2773$.

enough for them to reverse buoyancy.

The exact interactions leading to the aggregation between MP and glass spheres remain to be investigated. Possible candidates include capillary bridges, hydrophobic interactions, depletion forces, friction, electrostatic interactions, or steric hindrance. As recently pointed out by Al Harraq and Bharti [2], the interaction between microplastics and their environment can notably be determined by electrical double-layer effects, which stand as a plausible candidate to explain our observations. Microplastics are usually close to neutrally charged [29, 28] and hydrophobic [2]; when surfactant molecules are introduced in water, their long hydrophobic chain tends to adsorb on the surface of microplastics [9, 16, 12], leaving their hydrophilic part oriented towards the bulk [12]. The interaction between the glass spheres, which are negatively charged in water [3, 12, 13], and the surfactant molecules that coat the MP, determines the ability of glass spheres and MP to aggregate. Aggregation crucially depends on the microplastic-glass distance and on their potential of interaction which, under the Derjaguin Landau Verwey Overbeek (DLVO) theory, is the sum of the attractive Van der Waals forces and the double-layer repulsion [11, 2, 8]. The ambient ionic strength [11, 2], the distance between particles [29], their size and their surface roughness [12], the ionisation of functional groups at their surface [13], the concentration of surfactant [12], the vigour of the flow around particles and their collision rate can all affect the microplastic-glass interaction, whether their potential of interaction has one minimum or two minima, whether stable or fragile aggregates can exist in the flow. Measuring potentials of interaction is beyond the scope of the present study, and we call for further analyses in dedicated setups.

Let us finally discuss the substantial scatter of data points in the range $\mathcal{C}_{\text{surf}} < 1.5$ g/L in

Exp. #	m_p (g)	m_g (g)	$\mathcal{C}_{\text{surf}}$ (g/L)	Mass of MP deposited (% of m_p)
1	0.6819	1.9920	1.8233	0.2640
2	0.6749	1.9980	0.6142	0.4593
3	0.6780	2.0034	1.2283	0.5605
4	0.6790	2.0027	3.0911	0.1325
5	0.6785	2.0081	5.1291	0.1474
6	0.6808	2.0148	0.6191	0.1322
7	0.6778	2.0017	0.8337	0.1918
8	0.6804	2.0026	0.4098	0.0588
9	0.6814	1.9922	0.1318	0.4109
10	0.6810	1.9997	0.8659	0.6304
11	0.6776	1.9913	0	0.3542
12	0.6808	2.0041	0	0.2350
13	1.0003	11.9916	0	1.5895
14	0.6928	6.0155	0	0.6062
15	0.6806	5.9959	1.0598	0.5730
16	0.6806	12.0020	1.0667	1.1020
18	1.5054	2.0041	1.0802	0.1196
18	2.2927	2.0038	1.0542	0.0480

Table 2: Experimental data for the experiments perfomed in beakers with glass spheres, microplastics and surfactant (TritonX 100).

figure 11. The experiments in beakers revealed that low concentrations of surfactant result in *fragile* aggregates that are broken by extremely small degrees of turbulence. Indeed, after an experiment with a low surfactant concentration, if a beaker is slowly and gently transported from one table to another, some aggregates break and MP rise from the bottom of the beaker up to the free surface. The fragility of the aggregates is clearly correlated to the surfactant concentration: the lower the concentration, the more aggregates broken when moving the beaker[2]. This observation is consistent with the previous statement that stirring faster in circles usually leads to a lower mass of deposited MP than stirring slower a wooden stick (compare circles and diamonds in figure 11).

Therefore, based on the results of figure 11 and our experimental observations, we conjecture that the lower $\mathcal{C}_{\text{surf}}$, the more aggregates that form and the more fragile they are. Under this conjecture, the substantial scatter that we observe at low $\mathcal{C}_{\text{surf}}$ is a consequence of the intense turbulence that the stirrer produces in beakers, that breaks the aggregates shortly after we stop stirring. The next section corroborates that a lower turbulence intensity leads to more aggregates depositing during experiments in turbidity currents.

[2]After we observed this phenomenon, we decided never to transport the beakers nor even rotate them to avoid the formation of any shear in the liquid; under these conditions, we verified that the aggregates remained at the bottom of the beaker until we extracted them.

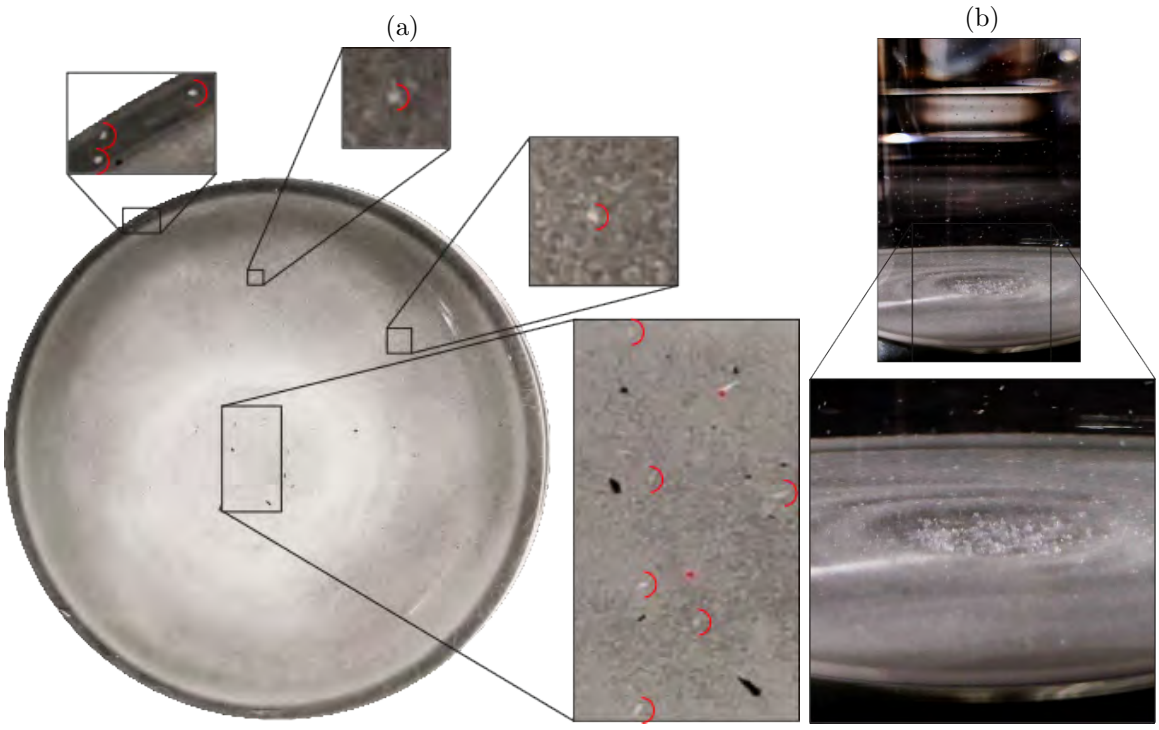

Figure 10: (a) Top photograph of the microplastics deposited at the bottom of a beaker at the end of an experiment. Most of the bottom is white due to the presence of glass spheres; some of the larger microplastic particles are highlighted by red semi-circles in four close-ups. (b) Microplastics gathered near the centre of a beaker after stirring, at the end of an experiment that contained only traces of surfactant.

4 Transport and Aggregation of MP in Turbidity Currents

Section 2 analysed how MP are transported by and detrained from a simple canonical flow, while section 3 revealed in idealised beaker experiments how MP-sediment interactions modify the coupling between fluid motions and MP by modifying their rise velocity. The present section focuses on MP-laden turbidity currents to investigate the combined roles of MP-sediment interactions and transport in a buoyancy-driven turbulent flow.

4.1 Experimental setup

The setup used to generate turbidity currents is the same as that described in section 2.1, except that before lifting the gate, the lock contains ambient fresh tap water of density ρ_a with no salt, a given mass m_p of MP of density $\rho_p = 930$ kg.m^{-3} and radius $r_p = 169$ μm, and a given mass m_g of glass spheres of radius $r_g = 37.5$ μm and density $\rho_g = 2500$ kg.m^{-3}. An additional amount of surfactant and possibly of food colouring can be added in the lock or in the entire tank. The main information about experiments is summed up in table 3.

Initially, microplastics are vigorously stirred in the lock. Then, the mass m_g of glass

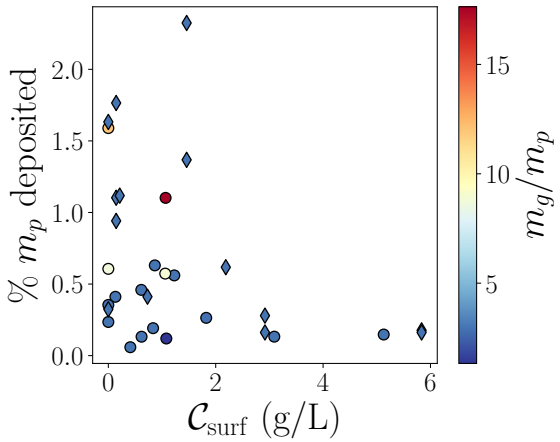

Figure 11: Evolution of the percentage of mass of microplastics deposited at the bottom of beakers, as a function of the concentration of surfactant, for different masses of glass introduced. Circles correspond to experiments with a fast clockwise stirring in circles by the electric stirrer, while diamonds correspond to a slower random turbulent stirring with a wooden stick.

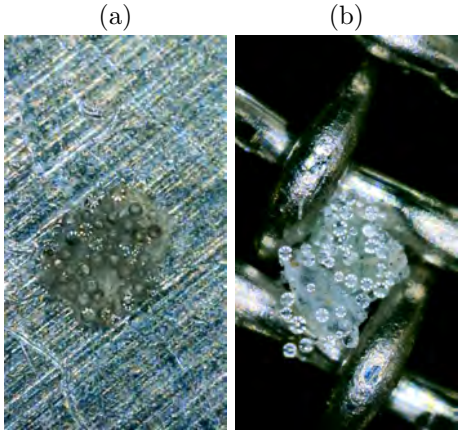

Figure 12: Photographs of microplastics – the large opaque grey or yellow particles – coated with glass spheres – the small circles each containing 8 white lines due to the reflection of the 8 microscope LEDs – when they are collected in a cup after sieving (a) or trapped in the mesh of a sieve (b). The diameter of the spheres is in the range $63 - 90$ μm, giving a scale for the images.

Exp. #	m_p (g)	m_g (g)	$\mathcal{C}_{\text{surf}}$ (g/L)	Mass of MP deposited (% of m_p)
1	0	12.0033	0	-
2	0	11.9991	0	-
3	0	12	0	-
4	0	12.0008	0	-
5	0	11.9995	0	-
6	0	12.0065	0	-
7	0	12.004	0	-
8	0	12.0163	0	-
9	0	12.0069	0	-
10	0	12.0012	0.0582	-
11	0	12.0016	0.0577	-
12	0	12.0083	0.0519	-
13	0	12.0018	0.0519	-
14	0	12.0084	0.1142	-
15	0	12.0088	0.1147	-
16	0	12.0132	0.2287	-
17	0	12.0317	0.2290	-
18	0	10.0223	0.4545	-
19	0	12.0116	0.4544	-
20	0	11.9952	0.6900	-
21	0	12.0179	0.6899	-
22	0	12.0045	0.6899	-
23	0	12	0	-
24	4.8409	12.0071	0.5	-
25	2.4289	12.018	0.5	-
26	4.7458	12.0019	0.5	0.42563951
27	2.4327	12.0006	0.5	0.67003741
28	1.0077	11.9985	0.5	-
29	1	12.0002	0	15.15
30	1.0088	12.0066	0	-
31	1.0017	12.009	0	17.0210642
32	1.0001	11.9985	0	7.18928107
33	1.0001	12.0031	0	14.8085191
34	1.0045	12.0012	0	16.8342459
35	0.9982	11.9972	0.125	5.3095572
36	1.0025	12.0035	2	1.017456359
37	8.0279	12.0059	0.5	-
38	1.0014	11.9982	0	14.6095466
39	1	8.4023	0.5	-
40	1.0019	3.0035	0.5	-
41	1.0066	27.0157	0.5	-
42	1.0036	3.004	0.5	-
43	1.0069	27.037	0.5	-
44	1.001	27.0067	0	11.2987013
45	1.0019	2.9966	0	2.07605549

Table 3: Experimental data about turbidity currents.

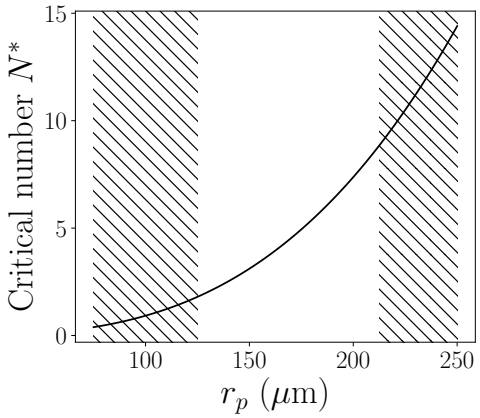

Figure 13: Evolution of the number $N^* = (r_p/r_g)^3(\rho_p - \rho_a)/(\rho_a - \rho_g)$ of glass spheres that should attach to a MP particle of radius r_p for it to become neutrally buoyant. The MP particles used for our experiments are in the range without hatchings: between 2 and 9 glass spheres must attach to a plastic particle, depending on r_p.

spheres is poured into the lock and stirred with the microplastics for about 10 s. At $t = -5$ s, stirring is stopped, and at $t = 0$ the gate is lifted and left partly underwater over its lowest 2 cm to damp surface waves.

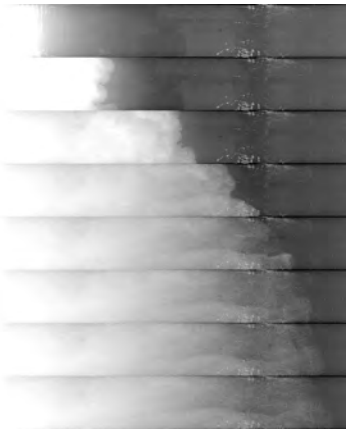

Figure 14: Time series showing, from top to bottom, the propagation of a turbidity current as seen from above ($m_g = 12.1$ g, in the lock $\mathcal{C}_{\text{surf}} = 0.229$ g/L while the rest of the tank was devoid of surfactant). The time lapse between two snapshots is $\Delta t = 2.67$ s and the horizontal length of each image is 97 cm.

Another lighting procedure consists in shining light tapes below the tank and taking photographs from above the tank. This enables us to measure the light attenuation due to its absorption by food colouring or glass spheres. It also enables us to finely measure the deposition of the glass spheres at the bottom of the tank after an experiment. To do so, a reference picture of the light intensity is taken before the experiment. Figure 14 shows the propagation of a turbidity current with no plactic particles that is filmed from above.

Finally, at the end of the experiment, a second picture captures the deposition of glass spheres at the bottom of the tank. This system enabled to verify that the stirring of lock fluid and lifting of the gate are repeatable by quantifying the deposition of glass spheres at the end of experiments of pure turbidity currents without MP (see Appendix A for details). Our turbidity currents are not energetic enough for glass spheres that settle on the bottom of the tank to be resuspended. Therefore, the total buoyancy of our turbidity currents constantly decreases in time. A consequence is that after a brief acceleration, the currents continuously decelerate in time until all glass spheres are deposited, as already visible from the snapshots in figure 14.

4.2 Aggregates form and settle down in turbidity currents

Figure 15 shows the propagation of a turbidity current containing red food colouring, a mass $m_g = 12.0$ g of glass spheres and a mass $m_p = 1.0$ g of MP. The current initially rolls up and builds up velocity in a short transient. Then, the current continuously decelerates. The red food colouring enables to track the fluid originating from the lock as well as all the fluid that is entrained at the edge of the turbidity current. The diffuse white milky region at the very front of the current near the tank floor corresponds to a concentrated region of glass spheres that drive the propagation of the current near the nose. They can easily be distinguished from the MP that are so large that they can be identified individually as large bright white dots rising towards the free surface. A close inspection of the front of the turbidity current at large times shows that several microplastics deposit onto the bottom of the tank as eddies bring them close to it, confirming the formation and deposition of aggregates.

To undoubtedly confirm that these large bright particles correspond to aggregates of MP and glass spheres, after such an experiment, the tank is left untouched for $30 - 60$ min. Then, a peristaltic pump is used to extract the MP from the free surface. Afterward, a pipe is gently introduced in the tank near the right end wall, and water is slowly extracted until only ~ 5 mm of water are left in the tank. Then, a microscope is introduced in the tank to record *in situ* photographs and videos that confirm the existence of aggregates: MP and glass spheres are not juxtaposed, they do stick to one another, and aggregates move as one solid body without deformation, as confirmed by videos that recorded the vibration of aggregates when gently shaking the microscope to disturb the fluid around the sediments (see figure 16).

As shown in table 3, the mass of aggregates found on the bottom of the tank was measured after the end of several experiments on turbidity currents. Measuring this mass required the following steps: (i) After mixing the lock fluid, lift the gate to initiate an experiment; (ii) wait for all motions to dissipate after the propagation of a current; (iii) extract all the particles found at the free surface, on the gate, and on the stick used to stir the lock at times $t < -5$ s; (iv) take pictures of the deposit to locate aggregates; (v) slowly extract most of the water out of the tank; (vi) image the aggregates with the microscope; (vii) collect all the deposited particles (glass spheres and aggregates) on filter paper in several iterations to rinse the tank and pipes; (viii) rinse the collected particles; (ix) dry the particles in an oven. Due to the large size of the tank, the small size and large number of microplastic particles, and the fragility of aggregates, these steps took 7-

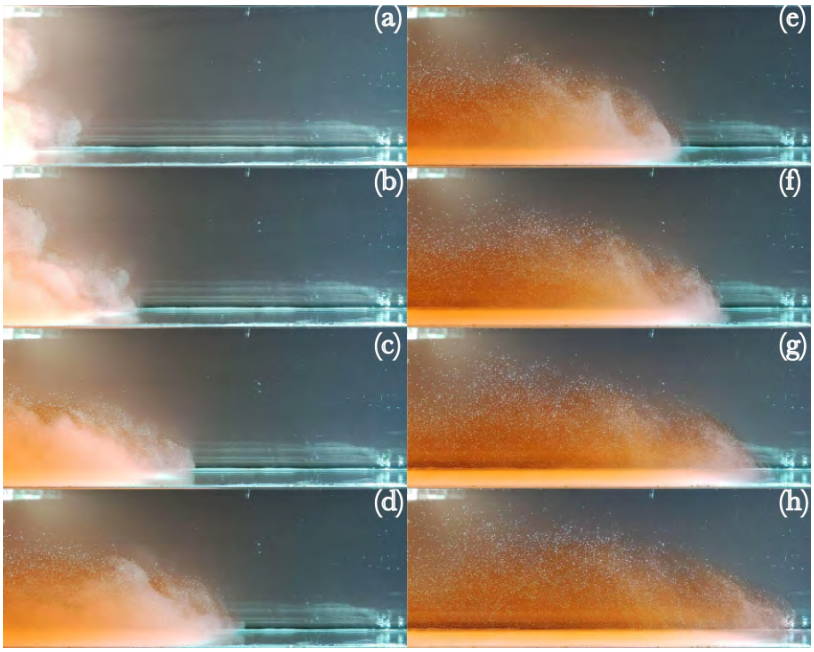

Figure 15: Time series of a turbidity current with microplastics. The glass spheres appear as a white milky region, in particular near the front of the current. The water initially in the lock is dyed red, and microplastics appear as large distinguishable white dots. The mass of glass spheres is $m_g = 12.0$ g, the mass of plastic is $m_p = 1.0$ g, and the time lapse between two snapshots is $\Delta t = 4$ s.

8h. Particles could be sorted and their mass could be measured on the following day. Due to the complexity of this protocol and its duration, these measurements were performed for dedicated experiments, mostly at low surfactant concentration since it leads to more aggregation (see figure 17), confirming the conjecture of section 3.2.

Changing the mass of plastic m_p barely affected the percentage of MP deposited. This was verified for $\mathcal{C}_{\text{surf}} = 0.5$ g/L, where the mass of MP has been varied between $\{1, 2, 4\}$ g (the size of circles is proportional to the mass of MP). On the opposite, for a fixed mass $m_p = 1$ g, the larger the mass of glass spheres in the turbidity current, the larger the percentage of m_p that deposits (see the blue and red points). This is consistent with the trends obtained in the beaker experiments, although data are lacking in both types of experiments to confirm this trend. We note that additional beaker experiments performed with a ratio $m_g/m_p \in [8 - 18]$ and stirred by the electrical helical stirrer stirrer never led to more deposition than 1.5% of m_p. Conversely, for the ratio $m_g/m_p = 12$ in the turbidity currents experiments, we obtain up to 17% of deposition. This order-of-magnitude difference is consistent with our conjecture that a lower turbulence intensity leads to more deposition, and that the vigorous stirring in beakers probably led to the breaking of aggregates.

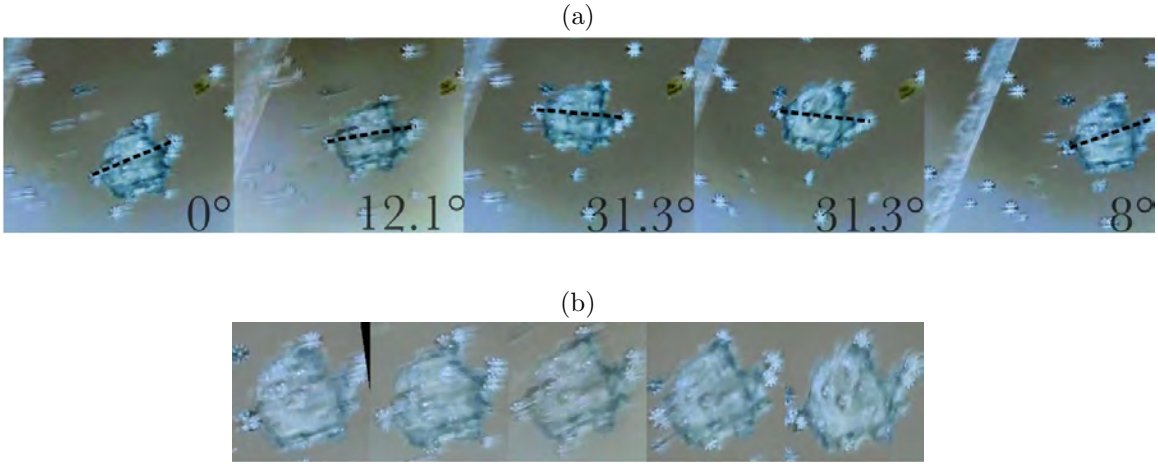

Figure 16: (a) Successive snapshots of an aggregate filmed in situ while shaking the microscope. The aggregate orientation is determined by the dashed dark line that connects the position of two attached spheres on the microplastic particle, and the corresponding angle is written in the bottom right-hand corner of each snapshot. Each snapshot is then rotated by an equal amount in the anti-clockwise direction, leading to (b). The latter figure evidences that the glass spheres are actually *attached* to the plastic particle onto which they keep the same position.

4.3 Aggregation affects the rise of MP

Within the range of masses, m_p, of MP that we used, MP only marginally contribute to the total buoyancy of the turbidity current, hence varying m_p has no clear impact on the dynamics of the turbidity current before full deposition of the glass spheres. The same conclusion holds when varying the surfactant concentration $\mathcal{C}_{\text{surf}}$. This is verified in figure 18a which shows the trajectory $x_f(t)$ of the front of the turbidity currents in time: within a margin of uncertainty due to the sensitivity of the turbulent flow to initial conditions, all currents follow the same trajectory.

This observation is consistent with section 2.2: MP essentially follow horizontal fluid motions like tracers, and their buoyancy is negligible in turbidity currents, hence the horizontal position $x_f(t)$ evolves in time essentially due to the buoyancy of glass spheres. However, along the vertical direction, MP eventually decouple from fluid motions due to their rise velocity. As shown in section 3, the concentration of surfactant affects the amount of aggregates that form, and therefore the distribution of rise velocities between rising plastic particles and sedimenting aggregates that are denser than the ambient. Hence, we now focus the analysis on the vertical motion of MP to identify a signature of the process of aggregation.

Figure 19 qualitatively shows with snapshots that the surfactant concentration considerably affects the rise time of microplastics: these two experiments reveal that, in the absence of surfactant (see the red current), MP rise much slower than when the surfactant concentration is large (see the blue current, and compare it with the red one on the three

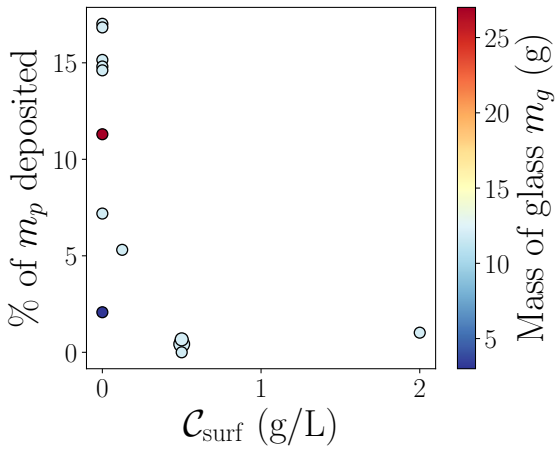

Figure 17: Evolution of the percentage of mass of MP deposited after experiments of turbidity currents, as a function of the concentration of surfactant in the tank, for different masses of glass introduced.

final snapshots of figure 19b). Figure 20 quantifies this phenomenon by showing the measured time of rise t_{rise} of MP along the water depth H (see Appendix B for details about measurements), normalised by the estimate H/w_s for pure MP, as a function of the total mass of surfactant introduced in the tank. This figure confirms the conjecture of section 3.2: the more surfactant, the less aggregation, and the closer the ratio $t_{\text{rise}}w_s/H$ is to unity. Conversely, the less surfactant, the more aggregates form; those that are negatively buoyant deposit on the ground and barely affect the measured time t_{rise}; those that are pure (i.e. with no glass sphere attached) rise as fast as w_s and contribute to reducing the measured value of t_{rise}; those that are close to neutral buoyancy take a considerable amount of time to rise, and they statistically contribute to an increase of t_{rise}. The increasing scatter in figure 20 when the surfactant concentration diminishes is consistent with the sensitivity of aggregation to details of the interaction between MP and glass spheres, which is itself sensitive on the initial conditions of the flow.

The previous two figures clearly show that after full deposition of glass spheres, the fate of MP is controlled by the amount of aggregation that happened during MP-glass interactions. The MP that remain in water for a long time are close to neutral buoyancy, hence their residual motion is due to the residual inertia in the flow. This explains the drastic deceleration of the trajectories $x_f(t)$ beyond a distance of about 0.7 m which corresponds to the maximum distance reached by the glass spheres. Similarly, the residual inertia of the fluid depends crucially on the initial conditions of the flow; this explains the large scatter in the curves $x_f(t)$ beyond ~ 0.7 m.

4.4 Deposition of aggregates up until the head's stopping point

In a moving ambient like the ocean, those aggregates that are close to neutral buoyancy will be advected away by the flow. Conversely, aggregates with a sufficiently large negative buoyancy settle on the bottom of the tank and presumably stay there. The goal in this

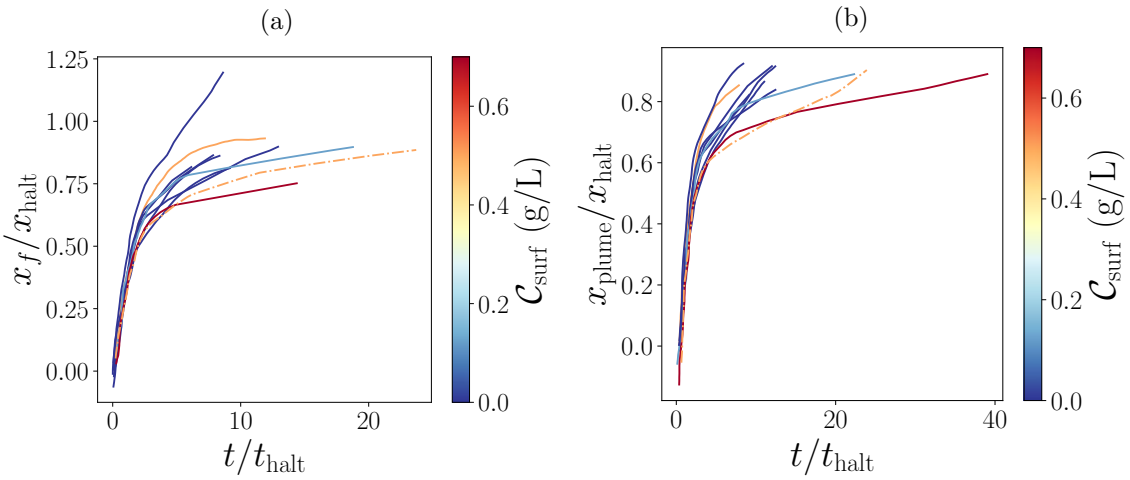

Figure 18: Time evolution of the position of (a) the front of turbidity currents, and (b) the plume of detrained microplastics detected at mid water height. Colours indicate the concentration of surfactant. Measurements are non-dimensionalised with the estimated time necessary for glass to settle over the current's height, $t_{\mathrm{halt}} = H/2w_{\mathrm{s,glass}}$, and the distance travelled by the current during that time $x_{\mathrm{halt}} = u_c t_{\mathrm{halt}}$ where u_c is based on the reduced gravity in the lock at $t = 0$.

section is therefore to determine the spatial distribution of these aggregates in the deposit after the dissipation of all fluid motions in the tank. To do so, we vary the total mass of glass spheres that is introduced in the lock to vary the maximum distance reached by the turbidity current. Figure 21 shows snapshots to compare the transport of microplastics by turbidity currents containing, respectively, $m_g \simeq 3$ g, $m_g \simeq 12$ g and $m_g \simeq 27$ g of particles. The results are in agreement with theoretical estimates (see Appendix A). The larger the total mass of glass spheres, the larger the initial (negative) buoyancy in the current, and the farther away the current comes to a halt.

Once the fluid motions come to rest, all the MP at the free surface are removed with a peristaltic pump, and a photograph is taken from above to analyse the deposit. Figure 22a shows that a deposit contains a continuous large white region containing glass spheres, as well as some isolated bright dots that correspond to deposited aggregates. After processing photographs of the deposit (see Appendix C for details), the light scattered by the glass spheres can be subtracted, and figure 22b shows the resulting image. Every bright spot is assumed to represent one aggregate. Then, the image is split in 30 bins along the horizontal direction. Figure 23 shows a histogram of the number of bright spots in each bin along the direction x for the experiment whose deposit is visible in figure 22a. By comparing figure 22a and figure 23, it appears that the maximum number of aggregates is found near the run out location of the turbidity current. As for the absence of aggregates at low values of x, it is an artefact due to the dilution of the signal of aggregates in glass spheres, which has been subtracted by image processing. Similarly in the context of MP burial by a turbidity current in the environment, plastic pollution might go unnoticed at such locations where too much

(a) $\Delta t = 8.0$ s

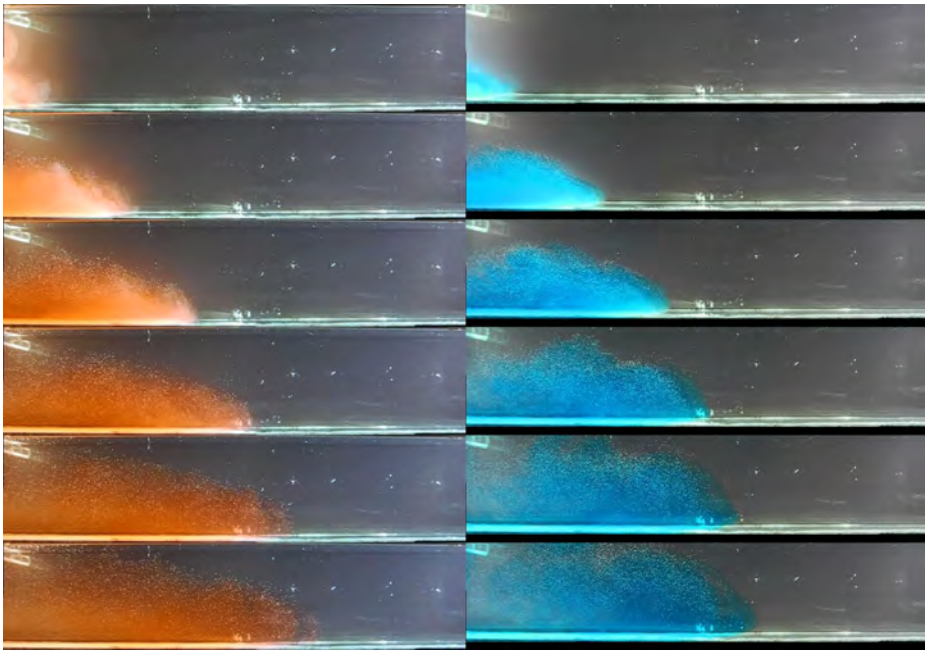

(b) $\Delta t = 24.0$ s

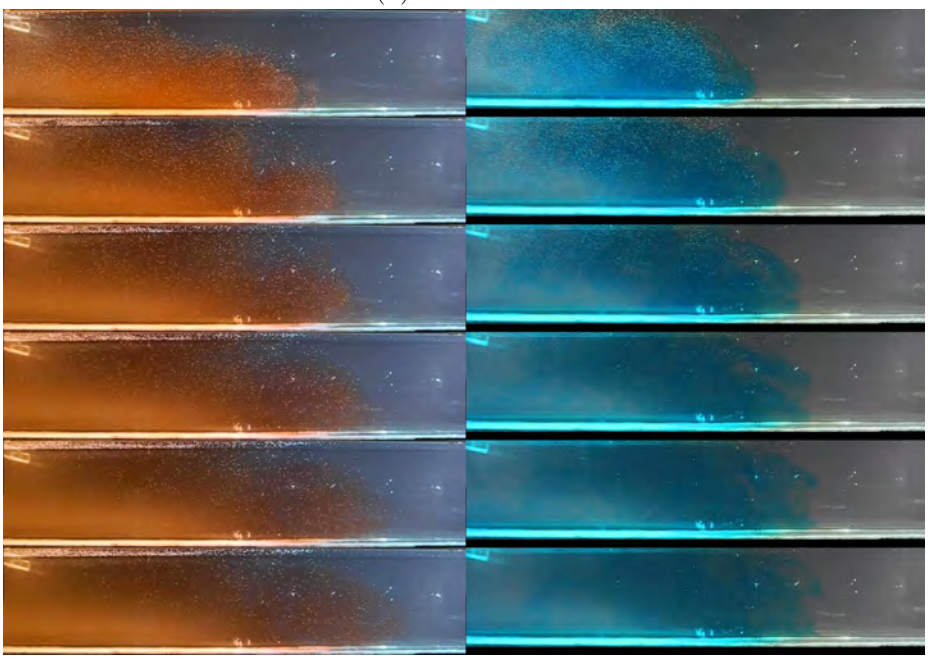

Figure 19: Propagation of two turbidity currents without surfactant (red current; see characteristics in the caption of figure 15) and with a high concentration of $\mathcal{C}_{\text{surf}} = 2$ g/L in the tank (blue current, $m_g = 12.0$ g and $m_p = 1.0$ g). The time lapse between consecutive snapshots is shown above each figure. The last snapshot of figure (a) is the same as the initial snapshot of figure (b).

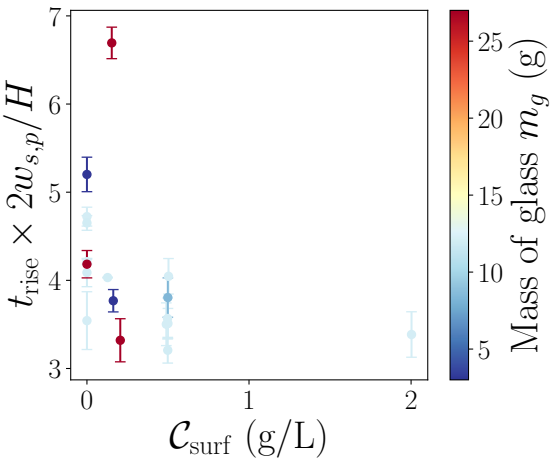

Figure 20: Time for microplastics to rise over the water height H due to their rise velocity, for various masses of glass spheres initially in the lock, and several concentrations of surfactant.

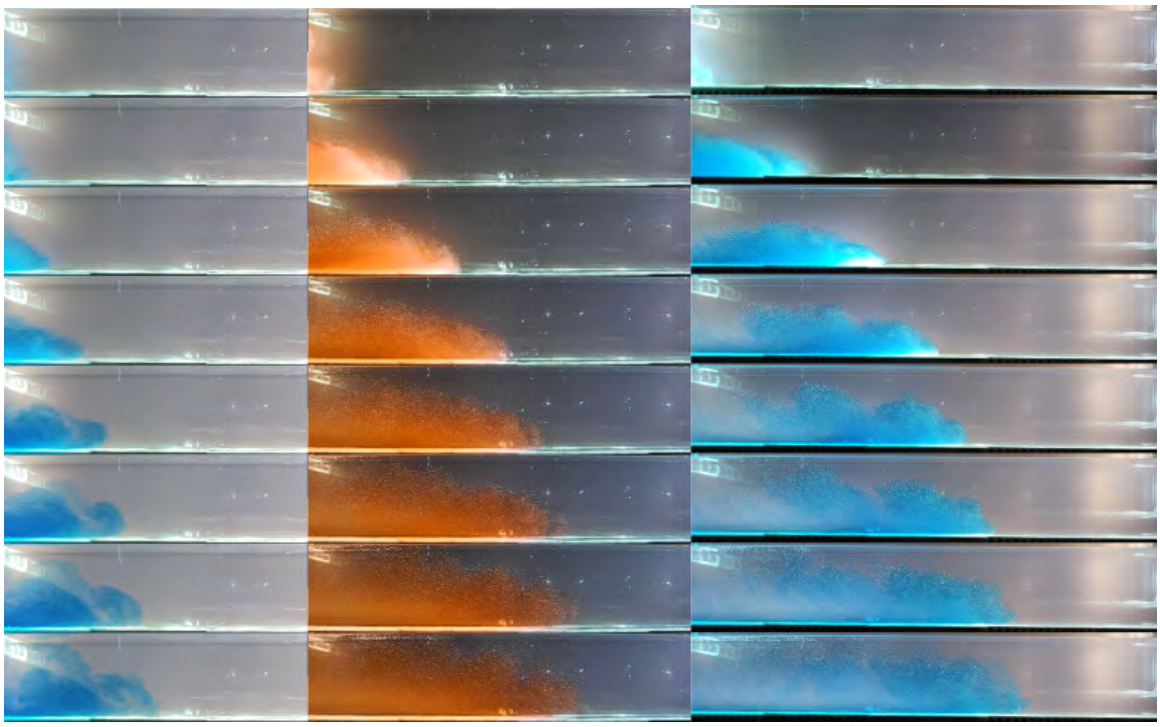

Figure 21: Time series of three turbidity currents containing 1.00 g of microplastics and no surfactant, and driven by a mass of glass spheres equal to (left) 3.00 g, (middle) 12.0 g, (right) 27.0 g, respectively. The time lapse between snapshots is $\Delta t = 8$ s for all experiments.

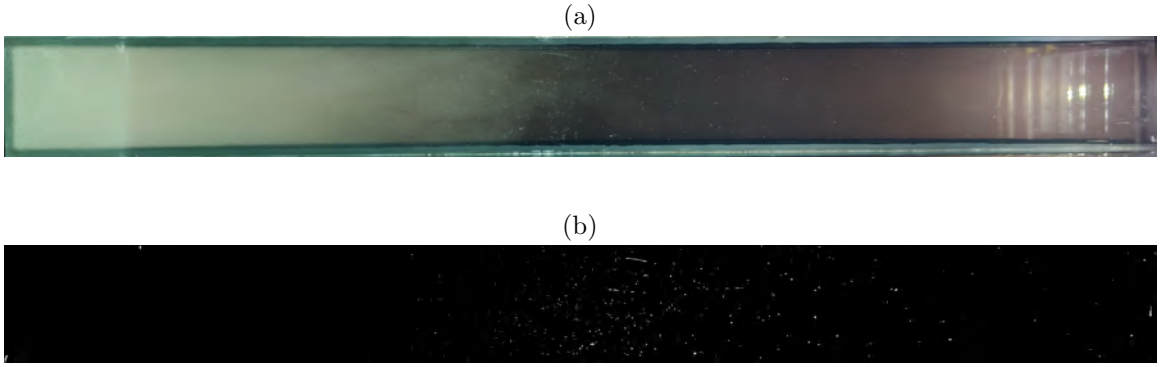

Figure 22: Deposit of glass spheres and microplastics after the propagation of a turbidity current containing $m_g = 12.0$ g of glass and $m_p = 1.0$ g of microplastics. Figure (a) shows a raw image while figure (b) shows the result after subtracting the large continuous white region at the left of the deposit (the glass spheres) to evidence the presence of microplastics (remaining white dots).

sand deposits with and above the plastic fragments, hampering their simple detection.

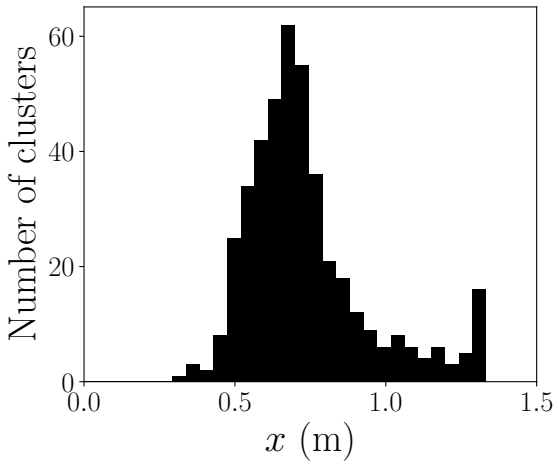

Figure 23: Distribution of aggregates along the tank, as detected using figure 22b.

To circumvent this issue of detection using the photograph, after each experiment a series of close photographs with a better resolution was recorded by moving a camera just above the tank and sliding it from $x = 0$ to $x = 1.5$ m above a transparent window. Figure 24 shows the reconstruction of the deposit by putting together the various photographs of a series. These photographs reveal the presence of aggregates at the bottom of the tank at all locations before the stopping point of the turbidity current. After a similar processing as described above, the new distribution of aggregates is shown in figure 25. The conclusion remains that most aggregates are found near the run out location of the turbidity current, but aggregates are also found in the tail. Further processing of all experiments will confirm

whether this observation holds in general.

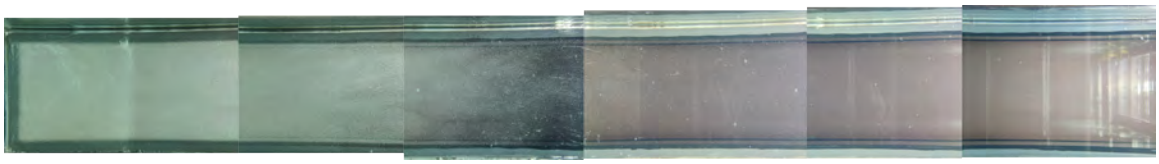

Figure 24: Stack of images taken at a short distance from the surface of the tank, showing the deposit of the same turbidity current as in figure 22.

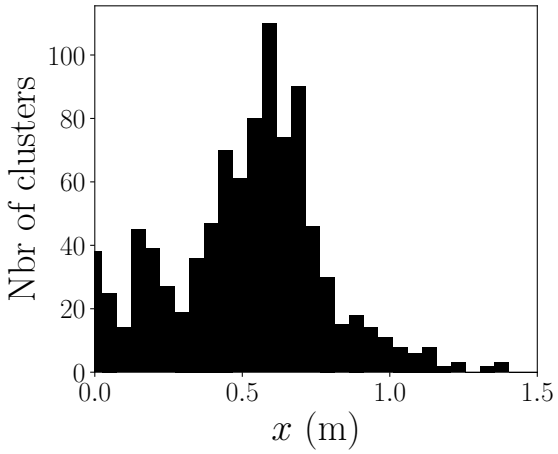

Figure 25: Distribution of aggregates along the tank, as detected using figure 24.

5 Concluding Remarks

Section 2 showed that analysing the rise of MP offers an original way of sampling the complex structure of a gravity current. Despite the fact that a gravity current is traditionally modelled as a fluid mass propagating with a constant velocity, the coupling between MP and the inner structure of a gravity current already makes it non-trivial to predict the detrainment of MP, and the gradual evolution of the current's morphology adds yet another layer of complexity. It remains to be determined how much confinement affects this observation, which could be assessed by performing similar experiments in a tank of different dimensions. Another intriguing question is: how would the dynamics of the current be altered if the buoyancy of the microplastics were non-negligible, for example by having a larger total mass of microplastics, or if their size were different and hence if they decoupled faster or slower from the gravity currents?

Section 3 revealed that when stirred together in fresh water, glass spheres can attach to microplastics and produce aggregates whose density is larger than the ambient, thus leading to their deposition. Although the literature provides some possible explanations that could be consistent with our observations, we were not able to investigate the physics at small scale that governs the attachment of glass spheres onto microplastics, thus calling for additional

experiments with a dedicated setup that could quantify the microplastics-glass interactions. One may wonder how these interactions would be modified when considering microplastics interacting with sediments in rivers or seas. As an example, the interaction of microplastics with biological media could certainly alter the picture: nature organic matters smooth the surface of microplastics and growth media cover deposition sites, thus inhibiting aggregation, yet biofilms can also trap particles during collisions [8]. As microplastics are released from rivers into the sea, the ambient concentration in salt increases whereas the concentration in surfactant likely decreases, which might both affect their ability to aggregate with sand. Aside from biological factors, the size and the anionic/cationic/non-ionic nature of the surfactant used, the size of the microplastics, their density, the turbulence intensity are some of many factors whose impact on aggregation remains to be carefully quantified.

Finally, section 4 revealed that microplastics also aggregate with glass spheres when transported in turbidity currents. As we present experiments where microplastics barely affect the carrier flow, the dynamics of the turbidity currents is unaffected by aggregation. However, the reverse does not hold: as the rise velocity of aggregates is altered, the rise of microplastics is quantitatively delayed by the process of aggregation, and the population of microplastics then spans from buoyant microplastics to sinking aggregates, including neutrally buoyant aggregates that passively drift in the remaining fluid inertia after the glass spheres have deposited. The fragility of aggregates, and the amount of glass spheres that must attach onto a microplastic to neutralise its buoyancy, are two key aspects determining the fate of the MP. Can these aggregates form in rivers, seas or oceans? How resistant are they to the surrounding turbulence and to collisions? Would the neutrally buoyant aggregates drift with the currents, while those on the ground would be buried under sediments? In connection with section 2, where would the rising microplastics be detrained? All these questions are paramount and call for additional experiments with dif-ferent sizes and densities of both microplastics and sediments, and the presence or absence of an ambient shear or some pre-existing turbulence to assess how they can create or break aggregates.

6 Acknowledgements

I warmly thank my supervisors, Claudia Cenedese, Jim McElwaine and Bruce Sutherland for their patience, advice and support all along this study – I feel extremely lucky to have had this enriching experience with them on such an exciting project! I also want to thank the directors of the 2023 GFD program, Pascale Garaud and Tiffany Shaw, for all they have organised to make this very special summer a smooth and joyful experience. More generally, I am grateful to the whole GFD community for welcoming me, and I'd like to express my affection to the other fellows, to Michael Dotzel, Nash Ward and Christian Mier who have been a fantastic support.

A Repeatability of initial conditions and runout distance

To verify the repeatability of experiments with pure turbidity currents, i.e., without microplastics, the same mass of glass spheres $m_g \simeq 12$ g is introduced in the lock, stirred, and

the gate is lifted as described in section 4.1. At the end of the experiments, glass spheres have deposited at the bottom of the tank. Then, by shining an LED panel underneath the water tank, the profile of light intensity going through the deposit is captured by a camera located above the tank. Since the distribution is close to uniform along the y direction (width of the tank), the intensity is averaged along this direction and the resulting average intensity $\mathcal{I}(x)$ only varies along the length of the tank. A similar reference photograph is recorded in the absence of glass spheres, and we denote $\mathcal{I}_{\text{bkg}}(x)$ this background intensity. In figure 26, the ratio $\mathcal{I}/\mathcal{I}_{\text{bkg}}$ proves to be lower than unity near the lock due to the absorption of light by the deposit. Beyond approximately half the length of the tank, the intensity ratio reaches unity, meaning a negligible amount of glass spheres reaches this region. The collapse of curves indicates that the release of these 14 turbidity currents is repeatable and unaffected by the concentration of surfactant (see the colours in figure 26). To determine the run-out distance, we calculate the average intensity $\langle \mathcal{I}/\mathcal{I}_{\text{bkg}} \rangle$ of the plateau near unity, as well as its standard deviation $\sigma_{\mathcal{I}}$. The run-out distance is then quantified as the position where the intensity ratio reaches the value $\langle \mathcal{I}/\mathcal{I}_{\text{bkg}} \rangle - 2\sigma_{\mathcal{I}}$. From figure 26 we find that the currents stop at $x = 0.70 \pm 0.06$ m.

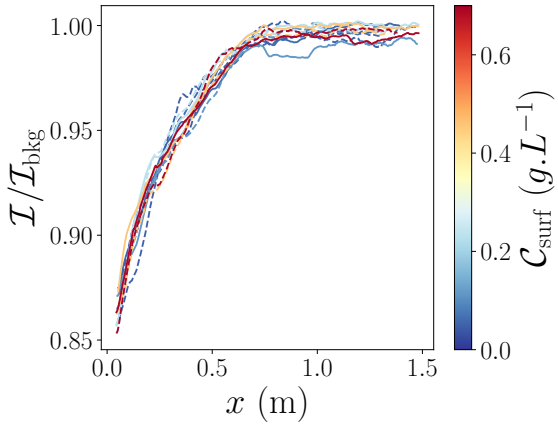

Figure 26: Profile of normalised light intensity going through the deposit of 14 experiments having turbidity current containing only glass spheres. The profile is unaffected by the surfactant concentration.

B Time of rise of microplastics

To measure the time of rise of microplastics, movies of moving standard deviations are produced: over a time window of 1 s, the pixel-by-pixel standard deviation is computed to remove any information from the background and to highlight the slow motion of microplastics. Then, space-time diagrams are extracted at mid-water depth, as shown in figure 27a. These diagrams show a quick ascent of many microplastics at early times when most of them are detrained from the turbidity current; subsequently, we observe the much slower rise of the remaining microplastics. The space-time diagram is smoothed by applying a Gaussian kernel of standard deviation equal to 10 pixels, and we average the information in

the space-time diagram and obtain intensity profiles in time – see the dark curve in figure 27b. The light intensity of all profiles initially increases when microplastics first reach the mid water height, and then decreases in time after a maximum at time $t_{\max}$. We use two methods to compute the time of rise: (i) we find the time when the light intensity decreases from its maximum to a third of the maximum value; (ii) we fit an exponential decay (see the dashed red line in figure 27b) and calculate the time of rise as the sum of $t_{\max}$ and the e-folding time of the exponential. Both methods giving close results (see figure 27b), we average these two results to compute the final times of rise shown in figure 20.

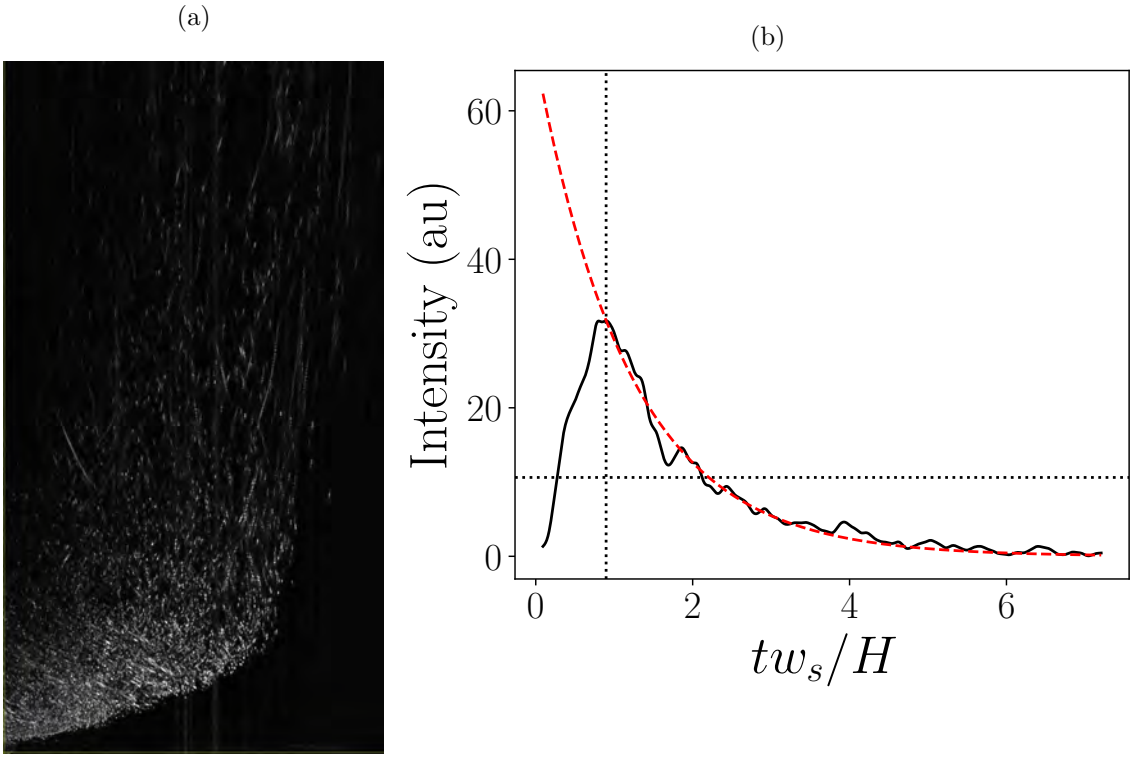

Figure 27: (a) Space-time diagram of the light intensity recorded at mid water depth. Time increases from the bottom up over a duration of 33.3 min, and the abscissa corresponds to the x position over 0.85 m starting from the gate on the left. This turbidity current contained $m_g = 12.0$ g and $m_p = 1.0$ g. (b) The solid dark line is the average intensity as a function of time corresponding to (a), while the red dashed line is the exponential fit performed to find the time of rise. The vertical dotted line shows the time when the maximum is reached, and the horizontal dotted line is located at a third of the maximum value.

C Detection of aggregates

To detect aggregates on a picture $\mathcal{I}_0$ of a deposit, a blurred version of the deposit is calculated with a Gaussian filter of standard deviation 150 pixels, and then subtracted from

the raw image to remove large-scale structures. Let us denote $\mathcal{I}_1$ the resulting image after subtraction. Then, the image $\mathcal{I}_1$ is blurred with a Gaussian kernel of standard deviation 30 pixels to remove medium-scale structures, and another subtraction is performed. Let us denote $\mathcal{I}_2$ the result. Finally, a blurred version of $\mathcal{I}_2$ based on a Gaussian kernel of size 15 pixels is subtracted to remove small-scale structures. The remaining information is binarised with Otsu's method [17], and figure 22b illustrates a typical result. Isolated clusters are then identified with the Python submodule Ndimage from the library Scipy, and counted by bins to get figure 23.

References

[1] M. Aeschlimann, G. Li, Z. A. Kanji, and D. M. Mitrano, *Potential impacts of atmospheric microplastics and nanoplastics on cloud formation processes*, Nature Geoscience, 15 (2022), pp. 967–975.

[2] A. Al Harraq and B. Bharti, *Microplastics through the Lens of Colloid Science*, ACS Environmental Au, 2 (2022), pp. 3–10.

[3] S. H. Behrens and D. G. Grier, *The charge of glass and silica surfaces*, The Journal of Chemical Physics, 115 (2001), pp. 6716–6721.

[4] T. B. Benjamin, *Gravity currents and related phenomena*, Journal of Fluid Mechanics, 31 (1968), pp. 209–248.

[5] S. B. Borrelle, J. Ringma, K. L. Law, C. C. Monnahan, L. Lebreton, A. McGivern, E. Murphy, J. Jambeck, G. H. Leonard, M. A. Hilleary, M. Eriksen, H. P. Possingham, H. De Frond, L. R. Gerber, B. Polidoro, A. Tahir, M. Bernard, N. Mallos, M. Barnes, and C. M. Rochman, *Predicted growth in plastic waste exceeds efforts to mitigate plastic pollution*, Science, 369 (2020), pp. 1515–1518.

[6] M. Cole, P. Lindeque, E. Fileman, C. Halsband, R. Goodhead, J. Moger, and T. S. Galloway, *Microplastic Ingestion by Zooplankton*, Environmental Science & Technology, 47 (2013), pp. 6646–6655.

[7] C. T. Crowe, J. D. Schwarzkopf, M. Sommerfeld, and Y. Tsuji, *Multiphase Flows with Droplets and Particles*, CRC Press, Boca Raton, 2 ed., 2011.

[8] S. Dong, Z. Yu, J. Huang, and B. Gao, *Chapter 9 - Fate and transport of microplastics in soils and groundwater*, in Emerging Contaminants in Soil and Groundwater Systems, B. Gao, ed., Elsevier, 2022, pp. 301–329.

[9] T. M. Ferreira, D. Bernin, and D. Topgaard, *Chapter Three - NMR Studies of Nonionic Surfactants*, in Annual Reports on NMR Spectroscopy, G. A. Webb, ed., vol. 79, Academic Press, 2013, pp. 73–127.

[10] R. Geyer, J. R. Jambeck, and K. L. Law, *Production, use, and fate of all plastics ever made*, Science Advances, 3 (2017), p. e1700782.

[11] M. Instruments, *Tech Note: Zeta potential - An introduction in 30 minutes*, (2005), p. 1.

[12] Y. Jiang, X. Yin, X. Xi, D. Guan, H. Sun, and N. Wang, *Effect of surfactants on the transport of polyethylene and polypropylene microplastics in porous media*, Water Research, 196 (2021), p. 117016.

[13] Y. Jiang, S. Zhou, J. Fei, Z. Qin, X. Yin, H. Sun, and Y. Sun, *Transport of different microplastics in porous media: Effect of the adhesion of surfactants on microplastics*, Water Research, 215 (2022), p. 118262.

[14] B. C. Kneller, S. J. Bennett, and W. D. McCaffrey, *Velocity structure, turbulence and fluid stresses in experimental gravity currents*, Journal of Geophysical Research: Oceans, 104 (1999), pp. 5381–5391.

[15] P. Linden, *Gravity currents – theory and laboratory experiments*, in Buoyancy-Driven Flows, C. Cenedese, E. P. Chassignet, and J. Verron, eds., Cambridge University Press, Cambridge, 2012, pp. 13–51.

[16] Y. Nakama, *Chapter 15 - Surfactants*, in Cosmetic Science and Technology, K. Sakamoto, R. Y. Lochhead, H. I. Maibach, and Y. Yamashita, eds., Elsevier, Amsterdam, 2017, pp. 231–244.

[17] N. Otsu, *A threshold selection method from gray-level histograms*, IEEE Transactions on Systems, Man, and Cybernetics, 9 (1979), pp. 62–66.

[18] J. W. Rottman and J. E. Simpson, *Gravity currents produced by instantaneous releases of a heavy fluid in a rectangular channel*, Journal of Fluid Mechanics, 135 (1983), pp. 95–110.

[19] A. Shamskhany, Z. Li, P. Patel, and S. Karimpour, *Evidence of Microplastic Size Impact on Mobility and Transport in the Marine Environment: A Review and Synthesis of Recent Research*, Frontiers in Marine Science, 8 (2021).

[20] D. Sher and A. W. Woods, *Mixing in continuous gravity currents*, Journal of Fluid Mechanics, 818 (2017), p. R4.

[21] B. R. Sutherland, M. DiBenedetto, A. Kaminski, and T. van den Bremer, *Fluid dynamics challenges in predicting plastic pollution transport in the ocean: A perspective*, Physical Review Fluids, 8 (2023), p. 070701.

[22] W. J. Sutherland, A. S. Pullin, P. M. Dolman, and T. M. Knight, *The need for evidence-based conservation*, Trends in Ecology & Evolution, 19 (2004), pp. 305–308.

[23] L. Van Cauwenberghe, A. Vanreusel, J. Mees, and C. R. Janssen, *Microplastic pollution in deep-sea sediments*, Environmental Pollution, 182 (2013), pp. 495–499.

[24] E. van Sebille, S. Aliani, K. L. Law, N. Maximenko, J. M. Alsina, A. Bagaev, M. Bergmann, B. Chapron, I. Chubarenko, A. Cózar, P. Delandmeter, M. Egger, B. Fox-Kemper, S. P. Garaba, L. Goddijn-Murphy, B. D. Hardesty, M. J. Hoffman, A. Isobe, C. E. Jongedijk, M. L. A. Kaandorp, L. Khatmullina, A. A. Koelmans, T. Kukulka, C. Laufkötter, L. Lebreton, D. Lobelle, C. Maes, V. Martinez-Vicente, M. A. M. Maqueda, M. Poulain-Zarcos, E. Rodríguez, P. G. Ryan, A. L. Shanks, W. J. Shim, G. Suaria, M. Thiel, T. S. van den Bremer, and D. Wichmann, *The physical oceanography of the transport of floating marine debris*, Environmental Research Letters, 15 (2020), p. 023003.

[25] E. van Sebille, C. Wilcox, L. Lebreton, N. Maximenko, B. D. Hardesty, J. A. van Franeker, M. Eriksen, D. Siegel, F. Galgani, and K. L. Law, *A global inventory of small floating plastic debris*, Environmental Research Letters, 10 (2015), p. 124006.

[26] M. G. Wells and R. M. Dorrell, *Turbulence Processes Within Turbidity Currents*, Annual Review of Fluid Mechanics, 53 (2021), pp. 59–83.

[27] L. C. Woodall, A. Sanchez-Vidal, M. Canals, G. L. Paterson, R. Coppock, V. Sleight, A. Calafat, A. D. Rogers, B. E. Narayanaswamy, and R. C. Thompson, *The deep sea is a major sink for microplastic debris*, Royal Society Open Science, 1 (2014), p. 140317.

[28] Y. Xia, S. Niu, and J. Yu, *Microplastics as vectors of organic pollutants in aquatic environment: A review on mechanisms, numerical models, and influencing factors*, Science of The Total Environment, 887 (2023), p. 164008.

[29] Y. Xia, J.-J. Zhou, Y.-Y. Gong, Z.-J. Li, and E. Y. Zeng, *Strong influence of surfactants on virgin hydrophobic microplastics adsorbing ionic organic pollutants*, Environmental Pollution, 265 (2020), p. 115061.

Can AI-based Climate Models Learn Rare, Extreme Weather Events?

Nimrod Gavriel

April 24, 2025

1 Introduction

1.1 Motivation

Machine learning (ML) models are becoming prominent tools for weather prediction, recently outperforming state-of-the-art physical weather models on several measures [6, 1]. However, these models are generally subject to a significant setback in ML generative models. After predicting a finite period, they become unstable and blow up. With current improvements in neural network (NN) architectures and more extensive training sets, the prediction is incrementally longer. However, the generation of long-period data sets for climate research is still far away. A recent study took the first step in this direction by pinpointing the sources of instability and addressing them directly, where a 2-layer QG model was used to train an ML model, which was able to run a long-duration emulation stably and reproduce the long-term statistics of the QG model [2]. Here, we build on this initial step to try and prove that such a stable ML weather emulator can, in principle, be used to generate valid long-term statistics of extreme weather events. Currently, such statistics, required to study the effects of climate change on weather, can only be acquired with computationally expensive hydro-dynamical models like the CMIP models (e.g., [3]). Here, we include moisture in the 2-layer QG model (see [7]) to generate the training data set. The moist QG model represents the dominant variables of the mid-latitude atmospheric dynamics well, and thus represents a good test case for the question of this project.

1.2 Extreme events under a changing climate

Climate change and its consequences on the human population and the weather system are a significant focus of the scientific community [4]. One of the most used indicators of climate change is the global mean temperature. However, fundamental aspects of climate change are the frequency and magnitude of extreme events [9]. Current studies already show significant anthropogenic changes in extreme events (Figure 1), stressing the importance of understanding how extreme events would change in a warmer climate and what are their actual re-occurrence periods in the current climate. In this project, we look at extreme events in terms of temperature and moisture in an idealized model, where "extreme" refers to anomalies with magnitudes very far from the climatology (or temporal mean).

Figure 1: Overview of already measured anthropogenic-related changes in extreme temperatures and precipitation, taken from [9]. For each region of the map, shown with squares, is how statistically significant the observed change in extreme heat, cold, or precipitation is. The circles in each region represent an assessment of how much of the change can be attributed to human influence.

1.3 Layout

In the Methods section, the hydrodynamic model is presented, as well as the details of how the prediction performance of NN models is measured for this study. Using this hydrodynamic model, I generated large data sets to train and test an NN model. I used a hierarchy of increasing complexity of NN models trained on this data, presented in the results section. Finally, I tried to use the strategy of [2] to maintain stability, in addition to novel strategies, to eliminate the evolution of instabilities in NN emulation.

2 Methods

2.1 A quasi-geostrophic 2-layer numerical model

In this project, A QG 2-layer moist model is used to generate three data sets. One set is generated to train our NN model. A second set is generated for testing our NN model. A third set is generated to produce long-term statistics that would be compared with the NN-generated statistics. The reason for choosing a QG 2-layer moist model for this project has two parts. For one, the model is simple enough and numerically light that generating very long data sets for the purposes of the project is feasible, and the dynamics are relatively simple to analyze. Second, the model is rich enough to represent long-term behavior in Earth's mid-latitudes and includes baroclinic instabilities, annular modes of the

eddy-driven jet, and moist convection, coupled to the dynamics through a linear Clausius-Clapeyron relation [7].

The model equations

Conservation of PV The model we used was created by Lutsko and Hell (2021) [7] (Herein LH21). The PV (q_k) for each layer k ($k = 1(2)$ for the upper (lower) layer) is defined by

$$q_k = \nabla^2 \psi_k + (-1)^k (\psi_1 - \psi_2) + \beta y, \tag{1}$$

where ψ is the stream function, and β is the β-plane approximation for the gradient of the Coriolis coefficient with y (latitude). The equations solved by the model are the potential vorticity (PV) conservation equation for the two layers as

$$\frac{\partial q_k}{\partial t} + J(\psi_k, q_k) = -\frac{1}{\tau_d}(-1)^k (\psi_1 - \psi_2 - \psi_R) - \frac{1}{\tau_f}\delta_{k2}\nabla^2\psi_k - \nu\nabla^4 q_k + (-1)^k LP, \tag{2}$$

where $J(a,b) \equiv a_x b_y - a_y b_x$ is the Jacobian operator, here representing the advection of PV. The first term on the right-hand side (RHS) represents solar radiation by relaxing the temperature ($T \equiv \psi_1 - \psi_2$) towards a predefined profile

$$\psi_R \equiv -\sigma A \tanh(y/\sigma), \tag{3}$$

which is asymmetric around $y = 0$, τ_d is the relaxation time, and A and σ are constants. The second term on the RHS represents surface friction at the bottom layer, where τ_f is a friction time coefficient. The third term on the RHS is a hyperviscosity term. The last term represents latent heating from precipitation, where L is a constant, and P is precipitation, controlled by the moisture equation.

Moisture conservation of mass The moisture (m) in the model is assumed to advect in the lower layer, such that the conservation equation for moisture is

$$\frac{\partial m}{\partial t} + J(\psi_2, m) = E - P - \nabla \cdot \mathbf{u}_2, \tag{4}$$

Where E and P are evaporation and precipitation, respectively, controlled by

$$E = \begin{cases} \hat{E}\,|\mathbf{u}_2|\,(m_s - m) & m < m_s \\ 0 & m \geq m_s \end{cases}, \quad P = \begin{cases} 0 & m \leq m_s \\ (m_s - m)/\tau_p & m > m_s \end{cases}, \tag{5}$$

where $\hat{E}$ is a constant, τ_p is the precipitation time constant, and m_s is the saturation moisture, determined by the linearized Clausius-Clapeyron relation

$$m_s \equiv CT = C(\psi_1 - \psi_2), \tag{6}$$

where C is a constant. Thus, everywhere the moisture is larger than m_s, precipitation occurs by moving mass between the layers, while evaporation occurs in the rest of the domain. The last term in Equation 4 is a divergence of the ageostrophic wind, which is required for consistency of the QG formulation. For more information on the model, see LH21.

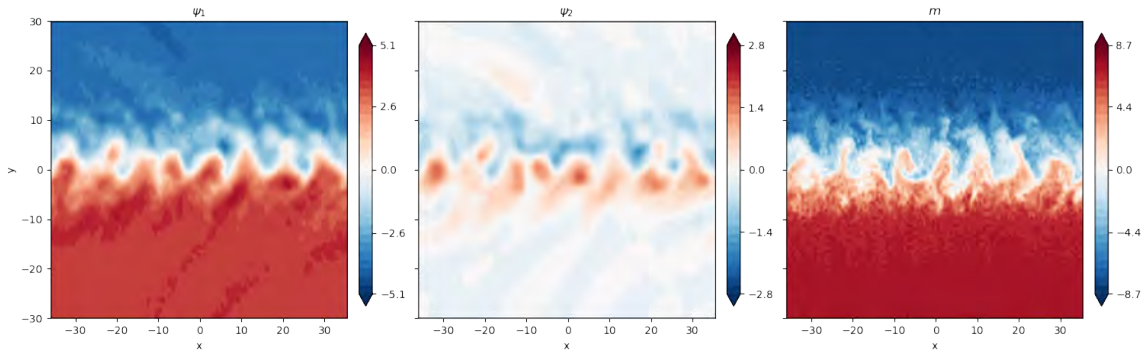

Figure 2: A snapshot from the moist two-layer QG model. The contours in the left panel represent the stream function of the upper layer. The contours in the middle panel represent the stream function of the lower layer. The contours of the right panel represent moisture. All the values in this figure are non-dimensional.

Model runs

As the purpose of the project is to be able to emulate atmospheric dynamics stably for an extended period using an ML emulator, rather than investigate the model itself, we ran the model with one set of parameter choices, similar to the choices made in LH21. These are (in order of appearance)

$$\beta = 0.2, \quad \tau_d = 100, \quad \tau_f = 15, \quad \nu = 10^{-6}, \quad L = 0.2, \quad \sigma = 3.5, \quad A = 1, \quad \hat{E} = 0.1, \tau_p = 1, \quad C = 2. \tag{7}$$

The model equations (Equations 1-6) are solved spectrally with domain size $(72, 96)$ in the zonal and meridional directions, respectively, and with 128 wavenumbers in both dimensions. In Figure 2, a snapshot from the model output is presented. It can be seen that the model produces an eddy-driven jet around $y = 0$, where the gradient of the imposed solar flux (included as a relaxation term, according to the profile in Equation 3) is largest. Looking at the moisture (Figure 2, right panel), the north-to-south zonal mean gradient is also due to the relaxation term, where the hotter south can hold more moisture according to the Clausius-Clapeyron relation (Equation 6). At this stage, it is important to note that the moisture variable has considerable amplitudes on all scales (Fig. 2, right panel). This fact would make the moist dynamics much more challenging to predict with an NN emulator than the dry ones, which have dominant scales.

2.2 Result statistics

2.2.1 NN model performance

To evaluate the performance of our NN emulations, standard tests of "root mean square error" (RMSE) and "anomaly correlation coefficient" (ACC) are used. In these tests, we take a snapshot of the state vector from the test time series and use it as an initial condition for the ML emulator. ACC and RMSE are thus two ways to compare the prediction produced from the ML emulator and the parallel "truth" time series that the QG model produced.

Here, the details of the calculation of these tests are explicitly described.

ACC We use ACC to evaluate how similar NN-predicted transient patterns are to the "truth" patterns (from the QG model). We define a "climatology" of any variable p as

$$p_{\mathrm{c}(j,k)} = \frac{1}{N_t} \sum_{i=1}^{N_t} p_{(i,j,k)}, \tag{8}$$

where N_t is the number of time steps in the time series, and (j, k) are the (y, x) indices. Thus, for each time variable p and time step i (where $i = 0$ is the identical snapshot from which the prediction starts), the ACC is calculated as the correlation,

$$\mathrm{ACC}_{p,i} = \frac{\sum_{j=1}^{N_y} \sum_{k=1}^{N_x} \left(a_{p,(i,j,k)} \cdot b_{p,(i,j,k)} \right)}{\sqrt{\sum_{j=1}^{N_y} \sum_{k=1}^{N_x} \left(a_{p,(i,j,k)} \cdot a_{p,(i,j,k)} \right) \sum_{j=1}^{N_y} \sum_{k=1}^{N_x} \left(b_{p,(i,j,k)} \cdot b_{p,(i,j,k)} \right)}}, \tag{9}$$

between the predicted anomalies

$$a_{p,i} = p_{\mathrm{pred},i} - p_{\mathrm{c}} - \frac{1}{N_y N_x} \sum_{j=1}^{N_y} \sum_{k=1}^{N_x} \left(p_{\mathrm{pred},(i,j,k)} - p_{\mathrm{c,(j,k)}} \right), \tag{10}$$

and the "truth" anomalies,

$$b_{p,i} = p_i - p_{\mathrm{c}} - \frac{1}{N_y N_x} \sum_{j=1}^{N_y} \sum_{k=1}^{N_x} \left(p_{(i,j,k)} - p_{\mathrm{c,(j,k)}} \right), \tag{11}$$

where N_x and N_y are the number of grid points in the x and y directions, respectively. This type of test neglects the amplitude difference between truth and prediction and only accounts for the accuracy of predicted patterns. To account for the fact that some snapshots may be harder to predict than others, we calculate the ACC over multiple initial conditions and present the mean between them.

RMSE The RMSE is much less sensitive to pattern matching, but provides a sense of the total error accumulated through the prediction. The RMSE is calculated simply as the root mean square difference between the truth and the prediction of each variable at each time step as

$$\mathrm{RMSE}_{p,i} = \sqrt{\sum_{j=1}^{N_y} \sum_{k=1}^{N_x} \left(p_{\mathrm{pred},(i,j,k)} - p_{\mathrm{(i,j,k)}} \right)^2}. \tag{12}$$

3 Results

The results section starts with presenting the benchmark long-term statistics from the QG model, which we aim to reproduce with NN-emulated data. Then, NN models of increasing complexity are presented and evaluated.

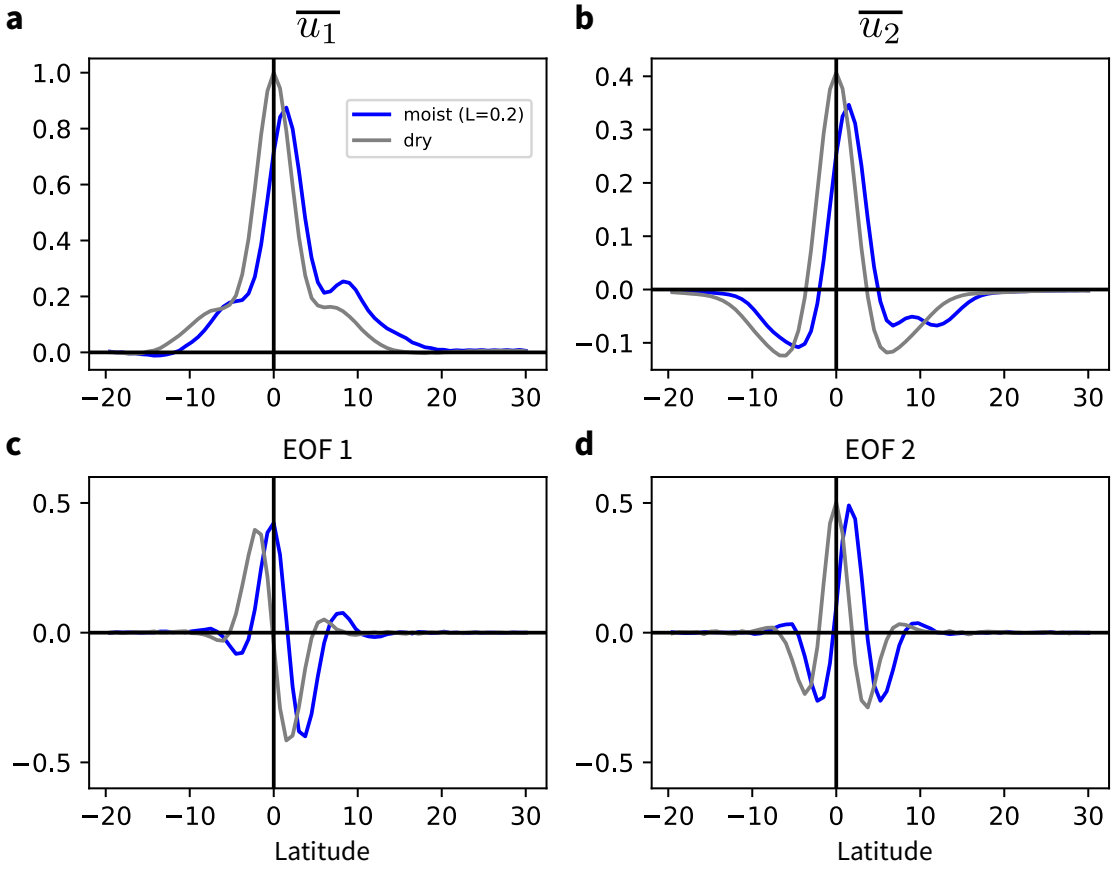

Figure 3: Long-term statistics of the zonal mean winds for moist (blue) and dry (grey) cases. **a**, The zonal mean, time-averaged, zonal wind at layer 1 as a function of latitude. **b**, The same as **a**, but for layer 2. **c-d**, The leading (**c**) and second (**d**) EOFs of the upper mean zonal wind ($\overline{u_1}$), as a function of latitude.

3.1 Benchmark QG model statistics

3.1.1 Mean state and EOFs

For this subsection, a dataset equivalent to ~ 1000 years is generated with the QG model. It does not include the data used to train the NN models presented in the following sections. To begin, validating that the model is set up correctly, I also generated an equivalent "dry" dataset with the moisture coefficients set to zero. Then, I calculated the zonal and temporal mean of the zonal wind (u_1 and u_2 for the upper and lower layers) per latitude for layer 1 (Figure 3a) and layer 2 (Figure 3b) for the dry and moist cases. Also, I calculated the orthogonal empirical functions (EOFs) of the zonal mean winds over time, representing the modes of transient change in the winds, responsible for most of the temporal variance, with lower orders responsible for a greater percentage of the change (Figure 3c-d). Comparing with the results of the original model paper [7], we see that our results are indeed identical for the two tested cases (moist with $L = 0.2$ and dry). These results (Figure 3) would also

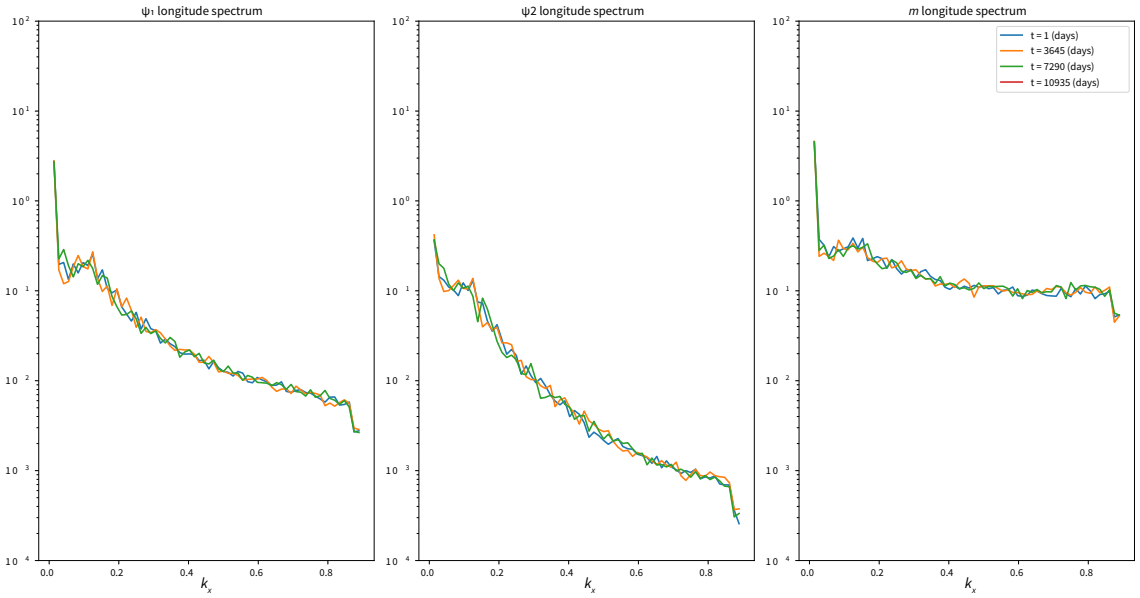

Figure 4: Meridional mean zonal spectra for ψ_1, ψ_2 and m. The abscissa is a scaled wavenumber in the zonal (x) direction.

represent a benchmark for the long-term statistics generated by the trained NN emulator.

3.1.2 Zonal Spectra

One benchmark of the QG model is also important for the training stage. Training an ML model to reduce RMSE gives disproportionate weight to the large scales (in Fourier space) since the large-scale motion has exponentially larger amplitudes, as would be described in more detail in the model-training section. Thus, to train a more physically correct model, it assists to include the spectra of the state vectors in the model-training loss function. In Figure 4, the spectra of ψ_1, ψ_2, and m are presented for 4 snapshots at different times. The spectrum for each time and each variable is calculated by performing a fast Fourier Transform (FFT) in the zonal direction at each y value and averaging it meridionally. It can be seen that the spectrum of m is more "flat" than the spectra of the stream functions in that it has similar amplitudes at all scales.

3.1.3 PDFs and extreme events

In addition to the mean winds, we aim in this project to be able to generate valid long-term statistics of extreme events. In Figure 5, these statistics are presented in the form of a probability density function (PDF) for moisture (m, ordinate) versus temperature (T, abscissa). Here, the whole dataset of $m(x, y, t)$ and $T(x, y, t)$ is inserted into the PDF calculation as a string. Darker colors represent more frequent occurrences in the data, and lighter shades are rarer. The linear blue line represents the CC relation (equation 6) where values above it are over saturated. However, to better understand the distribution of extreme events, it

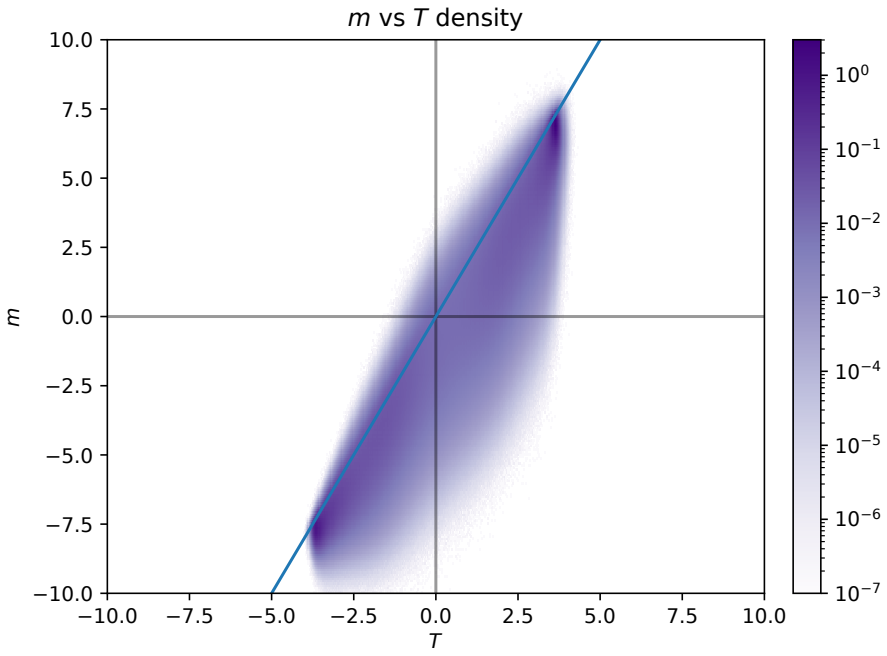

Figure 5: Probability density distribution of moisture (ordinate) and temperature (abscissa). A darker shade represents more occurrences in the data. The blue line represents the linear Clausius-Clapeyron relation.

is helpful to normalize the data set per grid point by removing the climatology and dividing the anomalies by the temporal standard deviation (STD) at that grid point. This normalized distribution is presented in figure 6, and would be our benchmark for evaluating our ML prediction of extreme events.

3.2 Training the ML model

In this section, the hierarchy of ML models that were trained in this study is described.

3.2.1 U-net

The first stage of our ML model, which is also the primary building block of all the following stages, is the U-net architecture [8]. U-net is an AI architecture used for image segmentation, like identifying different parts of an image, such as organs in medical scans, by leveraging a network that learns to outline and distinguish these parts accurately. In our context, the network is expected to take the state vector at time t ($\mathbf{X}(t)$) and predict the state vector at the next time step ($\mathbf{X}(t+\Delta t)$), according to

$$\mathbf{X}(t+\Delta t) = \mathbf{X}(t) + \int_t^{t+\Delta t} \mathbf{F}(\mathbf{X}(t))dt \approx \mathcal{M}(\mathbf{X}(t), \phi), \tag{13}$$

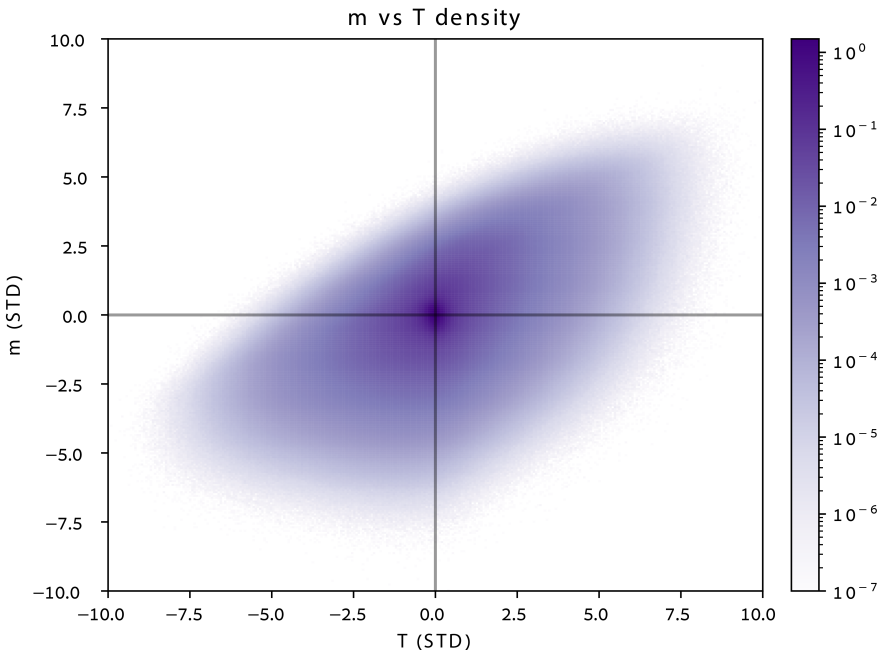

Figure 6: This figure is similar to figure 5, but here, temperature and moisture are climatology removed; also, the values are scaled by the STD per grid point.

where $\mathbf{F}$ represents the time derivatives (equations 1-6), $\mathcal{M}$ is the network operator, and ϕ are the trainable parameters. In this stage, we train the network by trying to predict from one snapshot to the next in the training dataset, having snapshots with a 0.2-day time step. Training is carried out by optimizing the parameters (ϕ) to minimize the cost function

$$L(\phi) = \| \mathcal{M}(\mathbf{X}(t), \phi) - \mathbf{X}(t + \Delta t) \|_2, \tag{14}$$

which is essentially a norm of the error between the truth and the prediction. This optimization process is repeated 15 times (termed epochs) over the training dataset. Once the network is trained, a snapshot from the testing dataset ($\mathbf{X}(t)$) is given as an initial condition to the network, and the predicted results can be used again as input. This process can be repeated to predict any number of following snapshots. The quality of this prediction over time can be seen in Figure 7. It can be seen that by 0.8 days of prediction, the moisture prediction losses correlation below 60%. One main reason for the short prediction span, highlighted in [2], is the spectral bias, where the network is trained to mainly handle the low wavenumbers, which has much bigger amplitudes, leading to larger weight in the loss function than the high wavenumbers.

3.2.2 The FouRK model

To account for the spectral bias, [2] proposed the FouRK model (Fourier Runge Kutta). In this model, the loss function is modified to amplify the weight of errors in high wavenumbers.

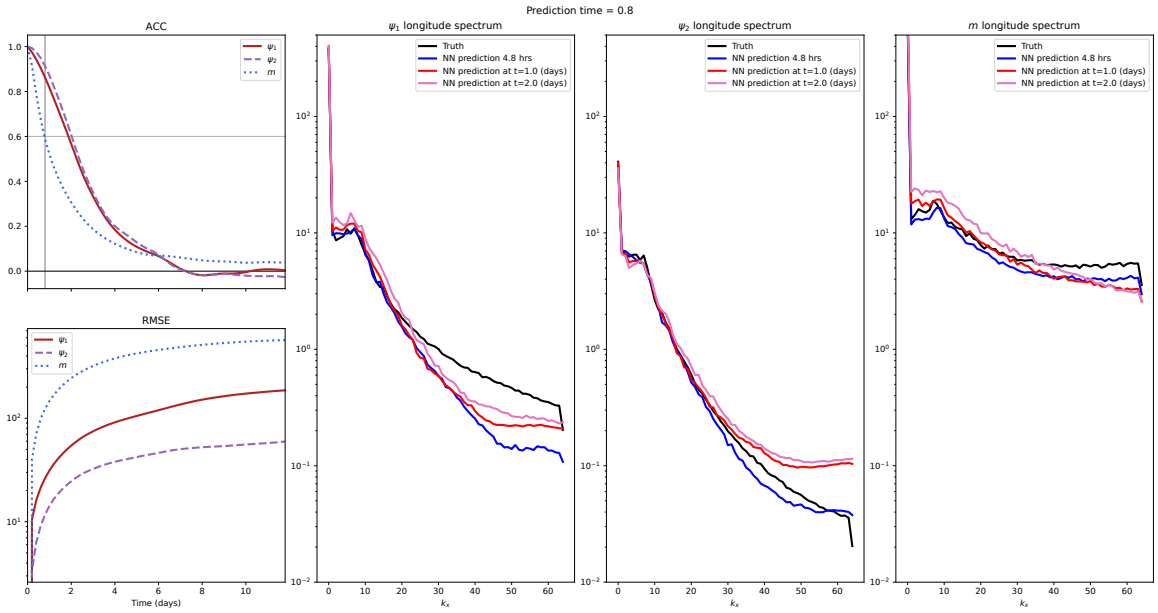

Figure 7: The prediction performance of the U-net network. The prediction time is defined here as when the ACC falls below 60% (for any predicted variables). The ACC and RMSE calculation procedures are given in section 2.2.1. The plots of the spectra are the same as in Figure 4, but here the black is a mean spectrum for the QG model, and the colors are the spectrum of the U-net prediction at different times from the initial condition snapshot.

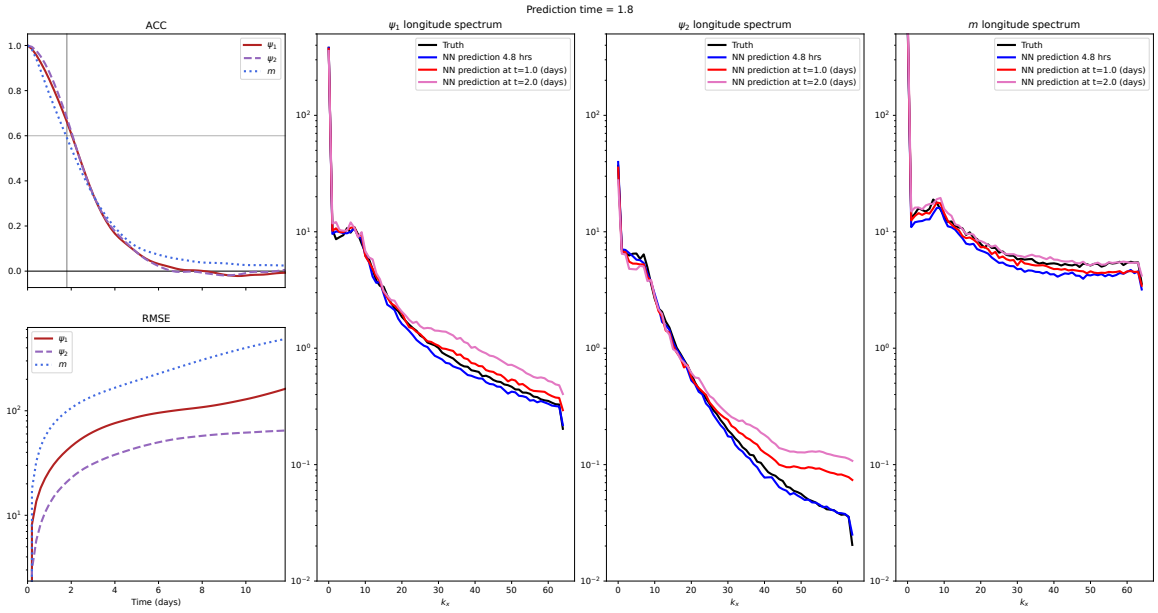

Figure 8: Similar to Figure 7, but for the FouRK model.

Formally, the modified loss function [2] is

$$L_{\text{FouRK}} = \| \mathbf{H}[\mathcal{N}(\mathbf{X}(t),\theta)] - \mathbf{X}(t+\Delta t) \|_2 + \lambda\mu(\theta), \tag{15}$$

where $\mathcal{N}$ is a U-net network, θ is its trainable parameters, and λ is a weighting coefficient for another term $\mu(\theta)$ that is in charge of giving the high wavenumbers extra weight. This term is defined by

$$\mu(\theta) = \left\| \hat{\mathbf{H}}[\mathcal{N}(\mathbf{X}(t),\theta)]\Big|_{k_x \geq k_T} - \widehat{\mathbf{X}}(t+\Delta t)\Big|_{k_x \geq k_T} \right\|_2, \tag{16}$$

where the hat sign signifies a high pass filter with cutoff frequency k_T. In addition to the spectral penalty imposed by $\lambda\mu(\theta)$, the FouRK model increases the prediction performance by stepping forward in time with a Runge-Kutta scheme, as was explored at length in previous studies [5]. Explicitly, this time integration is executed as

$$\begin{aligned}
i_1 &= \mathcal{N}[\mathbf{X}(t),\theta], \\
i_2 &= \mathcal{N}\left[\mathbf{X}(t) + \frac{1}{2} i_1, \theta\right], \\
i_3 &= \mathcal{N}\left[\mathbf{X}(t) + \frac{1}{2} i_2, \theta\right], \\
i_4 &= \mathcal{N}\left[\mathbf{X}(t) + i_3, \theta\right], \\
\mathbf{H}[\mathcal{N}(\mathbf{X}(t),\theta)] &= \mathbf{X}(t) + \frac{1}{6}\left(i_1 + 2i_2 + 2i_3 + i_4\right),
\end{aligned} \tag{17}$$

giving the model prediction a better accuracy than the standard Euler scheme for a given time step. Implementing these improvements and training the FouRK model on our moist QG model datasets (Figure 8) improves the prediction time by 225% while drastically reducing the spectral bias in the predicted variables.

3.2.3 3-net

One of the new challenges in this study, involving the moist QG model (Section 2.1), in contrast to the dry QG model of [2], is that moisture involves comparable dynamics on all scales (see Figure 4). This imposes an additional challenge for the AI network, which has a better prediction ability the narrower the spectral range of the objective variable is. An approach I tried here to improve in this aspect is by training 3 different networks in parallel, where each network predicts only one variable (from ψ_1, ψ_2, and m) and has a separate loss function. The loss function here was built like the FouRK loss function (Equation 15), but here, I did not use the Runge-Kutta scheme, and $X(t)$ represents only one variable for each network. Using this model further increased the prediction time by 133% relative to the FouRK model and improved the spectral bias on the three variables (Figure 9).

3.2.4 Adding self-supervision to the ML model to stabilize prediction over time

While the hierarchy of models presented here managed to considerably increase the prediction window of a 2-layer moist QG model relative to the baseline U-net model, errors

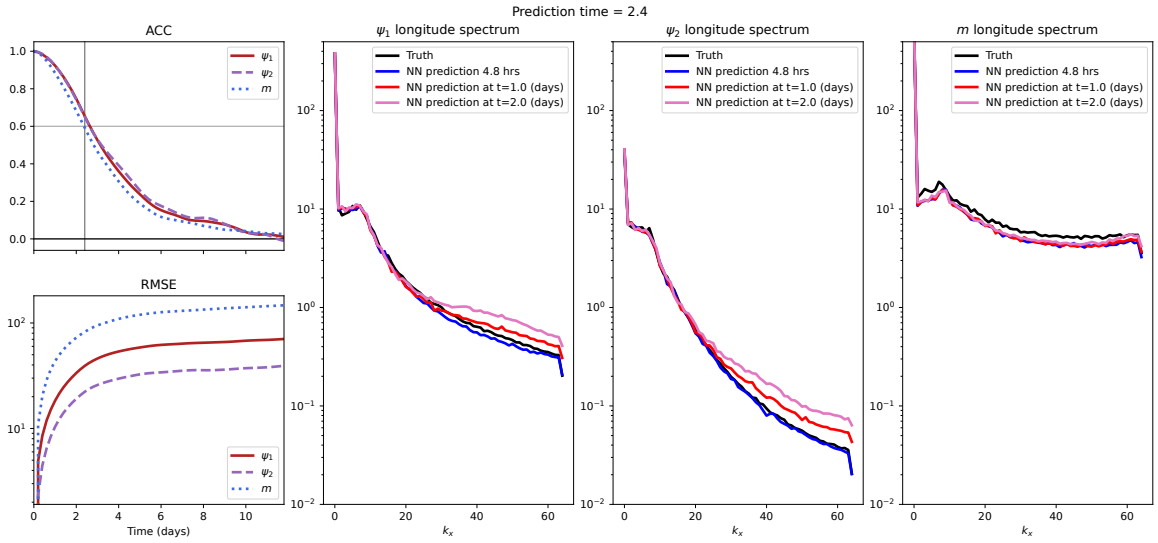

Figure 9: Similar to Figure 7, but for the 3-net model.

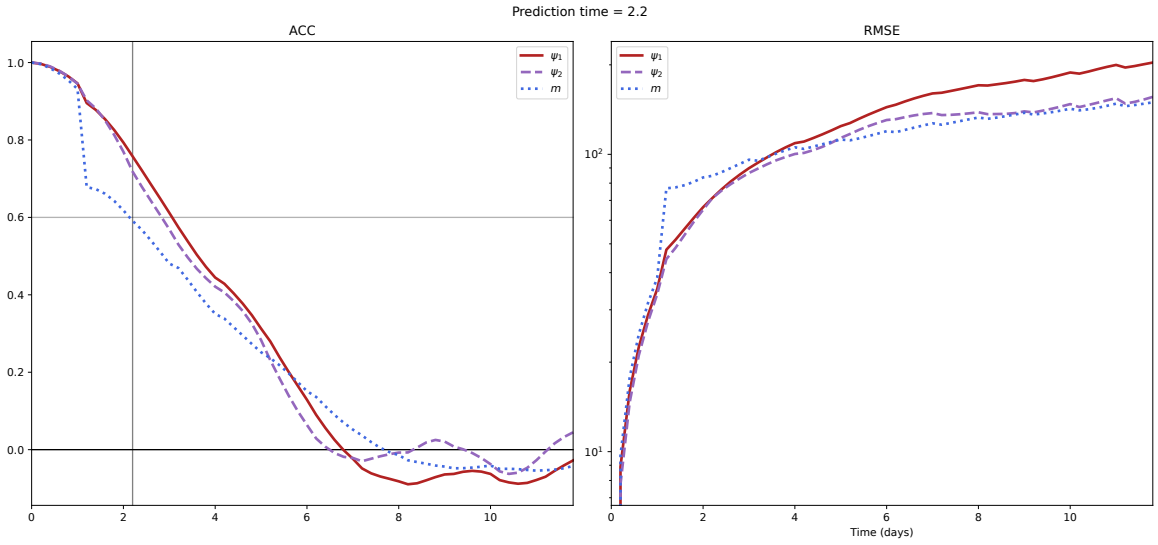

Figure 10: The ACC and RMSE over time for the 3-net model with self-supervision.

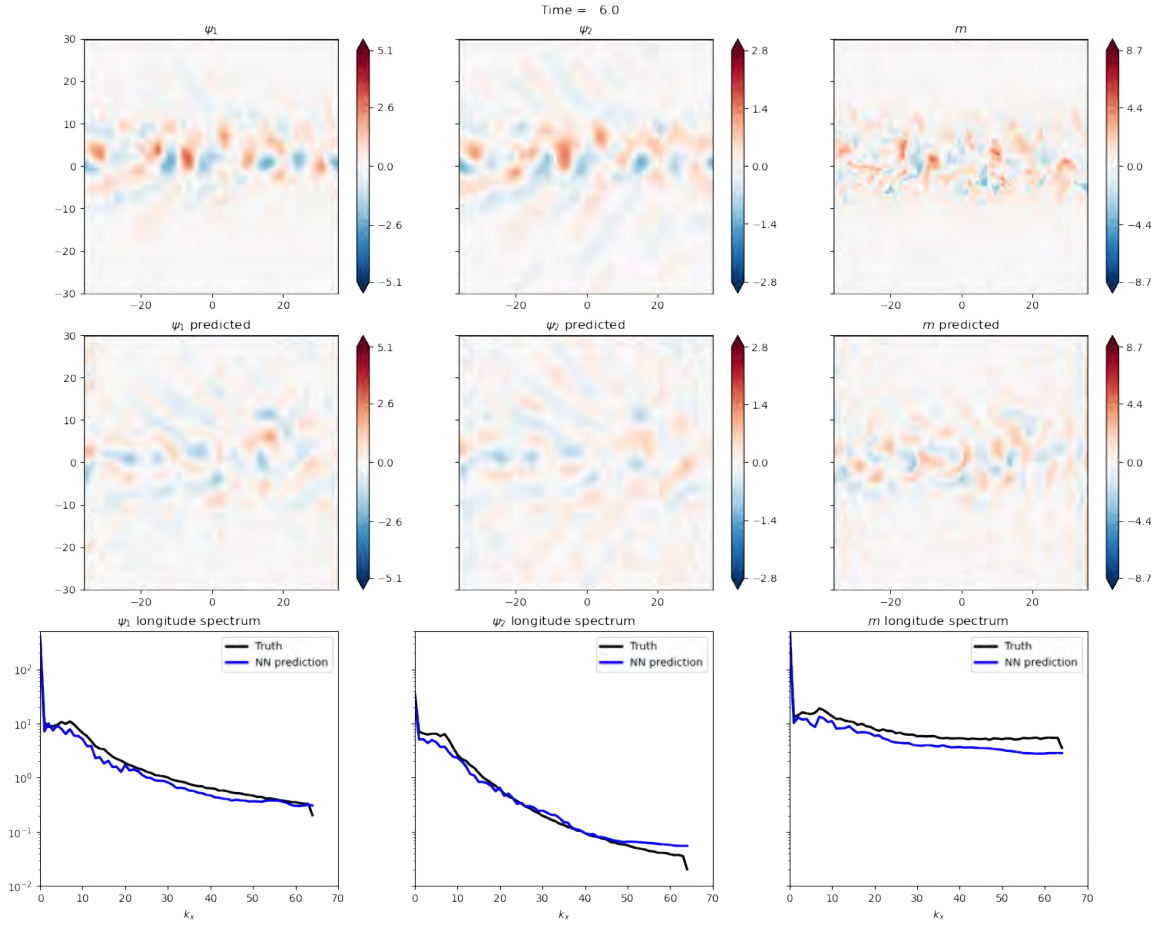

Figure 11: The upper row shows the anomalies of ψ_1, ψ_2, and m from the moist QG 6 days after an initial snapshot from which a prediction was initiated. In the middle row is the model-predicted variables at the same time. The lower row is the spectra of the variables, where black is the QG model's spectra and blue is the spectra from the prediction.

still accumulate exponentially over time (RMSE in Figures 7-9). Thus, collecting long-term statistics is impossible as the model is intrinsically unstable, and errors eventually arise that would blow the emulation, making the prediction non-physical. To achieve long-term stability, [2] suggested the FouRKS model, which adds to the FouRK model a self-supervision scheme that acts as viscosity and dissipates errors in the high wavenumbers. The way this was done is as follows. The AI model is let to progress forward with the FouRK architecture for a set number of steps, over which an error is accumulated on the small scales. Then, the current state variable is divided into two models that are retrained during this step to predict the small and large scales for the following snapshot in a manner that corrects the spectra of the variables to the mean spectra produced from the QG model in advance. Thus, the following snapshot is predicted with the errors removed so that the spectra are now correct relative to the QG model. This procedure repeats itself every few time steps (where the FouRK model progresses in between), and the AI model can remain stable indefinitely. However, the challenge is to get the AI model to maintain its "physical integrity" while it goes through this correction stage. This method was successfully applied in [2] on a dry QG model, where the FouRKS model produced long-term statistics, correctly reproducing the mean and EOFs of the dry model (Figure 3 and Figure 3 in [2]).

I applied the self-supervision algorithm to the 3-net model (Figures 10-11). Although the spectra remain correct, as imposed by the self-supervision, the variables become homogenized and non-physical (Figure 11). The self-supervision here is enacted every 1 day of prediction; the first application of it can be seen in the jump in the ACC at 1 day (Figure 11).

4 Conclusion

In this project, building on the recent achievement in NN stable and physical long-term integrator [2], I tried to expand the capability of the NN model to a more complex physical model, which now includes the moisture variable, and mainly, to assess the possibility of using such a NN integrator to generate long-term statistics of extreme events. In the project's time frame, I have come a long way in these directions. Still, eventually, the most successful version of my NN model does not maintain physicality (Figure 11). This, however, does not mean that this is not possible. When designing and training the model, many choices and hyper parameters can affect the end result. Given more time and effort, a model can plausibly be devised to perform this time integration successfully and physically. As an indication that the aim of the project is within reach, we can see from the data of [2] a comparison between the PDFs of ψ_1 from 3 different data sets (Figure 12). Here, the truth represents 1000 years of dry QG model simulation (black). The blue curve represents the data that was used for training the FouRKS model, consisting of a 10-year time series produced with the QG model. Finally, the red curve is the product of the FouRKS NN emulation of $1,000$ years. Incredibly, the $1,000$-year NN emulation captures the long-term statics much better than the shorter "truth" data on which it was trained, and that was too short to give an adequate account of the long-term behavior. This result provides the motivation to try more adjustments with the NN and its training to achieve physical emulation, like in the dry case, seeing that there, indeed, the NN emulating can predict behavior with periods much larger than the period on which it was trained.

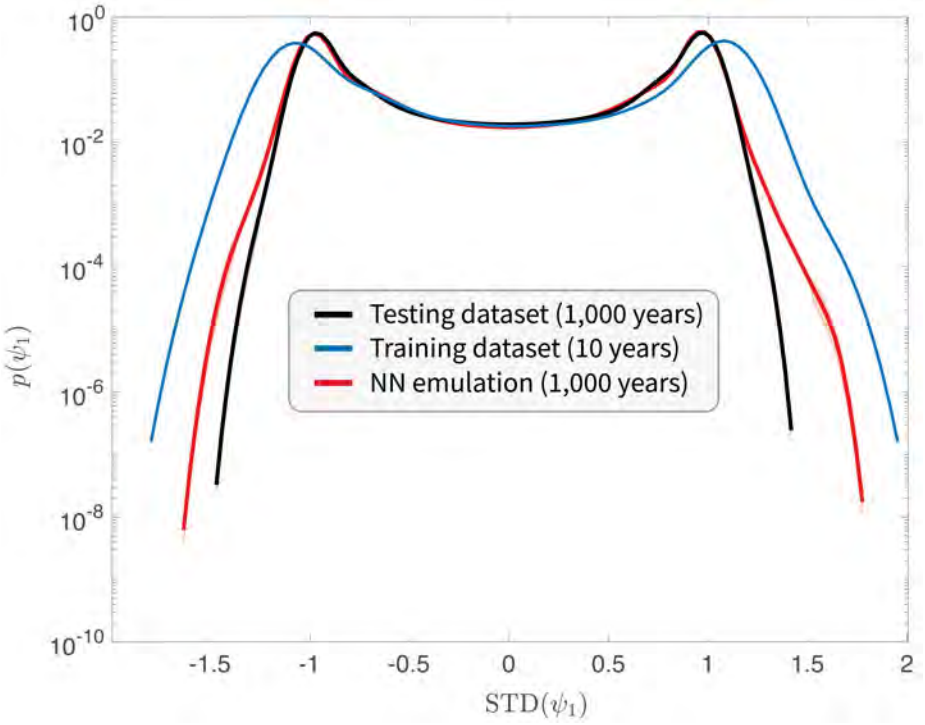

Figure 12: PDF of ψ_1 in a dry QG model [2]. The black curve represents the test data set, consisting of a $1,000$-year time series generated by the dry QG model. The blue curve is a 10-year time series generated by the QG model to train the NN model. The red curve is a $1,000$-year time series emulated by the trained NN model.

One aspect of this study that made successful long-term integration more difficult is the multi scale nature of the moisture variable. There is still a lack of understanding of how to correctly simulate such multi-scaled processes with an NN integrator. This is left for future studies. Nevertheless, generalizing the self-regularization scheme on models of increasing complexity can eventually lead to long-term emulation of data with a model trained on the high-quality, highly dense ERA5 reanalysis data (representing, to a high degree of accuracy, Earth's climate over the recent 80 years). Such statistics can assist in climate research, constraining the recurrence time of extreme events in the current climate. Lastly, I developed a novel approach through this study, namely, using multiple NN models trained in tandem to predict separate variables. This approach successfully increased the quality of integration from step to step, increasing the overall accuracy of the NN integration.

5 Acknowledgments

I would like to thank Pedram Hassanzadeh and Tiffany Shaw, who advised and guided me on this project. I came without a background in any of the methods required for this project, and they patiently guided and encouraged me through it. Thanks to them, I extensively learned and expanded my tool set this summer. Thanks also to Ashesh Chattopadhyay, whose work I followed and who agreed to spare hours guiding me through his codes and setting up my first neural networks. Big thanks to Tiffany Shaw and Pascale Garaud for directing this incredible program. I would also like to thank the principal lecturers, Heather Knutson and Geoffrey Vallis, for their compelling lecture series and the faculty, visitors and staff for making this summer so rich. Last but not least, I want to thank the nine fellows with whom I shared this program, who made this such a wonderful experience. I really enjoyed spending this summer with you and hope we'll stay in touch and run into each other in the future. Special thanks to my roommates, Quentin Nicolas (and Emma) and Nathan Magnan, for many dinners, chats and friendship.

References

[1] K. Bi, L. Xie, H. Zhang, X. Chen, X. Gu, and Q. Tian, *Accurate medium-range global weather forecasting with 3D neural networks*, Nature, (2023), pp. 1–6.

[2] A. Chattopadhyay and P. Hassanzadeh, *Long-term instabilities of deep learning-based digital twins of the climate system: The cause and a solution*, arXiv preprint arXiv:2304.07029, (2023).

[3] N. Christidis, G. S. Jones, and P. A. Stott, *Dramatically increasing chance of extremely hot summers since the 2003 european heatwave*, Nature Climate Change, 5 (2015), pp. 46–50.

[4] IPCC, *Climate Change 2021: The Physical Science Basis. Contribution of Working Group I to the Sixth Assessment Report of the Intergovernmental Panel on Climate Change*, Cambridge University Press, Cambridge, UK and New York, NY, USA, 2021.

[5] A. S. Krishnapriyan, A. F. Queiruga, N. B. Erichson, and M. W. Mahoney, *Learning continuous models for continuous physics*, Communications Physics, 6 (2023), p. 319.

[6] R. Lam, A. Sanchez-Gonzalez, M. Willson, P. Wirnsberger, M. Fortunato, A. Pritzel, S. Ravuri, T. Ewalds, F. Alet, Z. Eaton-Rosen, et al., *Graphcast: Learning skillful medium-range global weather forecasting*, arXiv preprint arXiv:2212.12794, (2022).

[7] N. J. Lutsko and M. C. Hell, *Moisture and the persistence of annular modes*, Journal of the Atmospheric Sciences, 78 (2021), pp. 3951–3964.

[8] O. Ronneberger, P. Fischer, and T. Brox, *U-net: Convolutional networks for biomedical image segmentation*, in Medical Image Computing and Computer-Assisted Intervention–MICCAI 2015: 18th International Conference, Munich, Germany, October 5-9, 2015, Proceedings, Part III 18, Springer, 2015, pp. 234–241.

[9] S. I. Seneviratne, X. Zhang, M. Adnan, W. Badi, C. Dereczynski, A. Di Luca, S. M. Vicente-Serrano, M. Wehner, and B. Zhou, *IPCC chapter 11: weather and climate extreme events in a changing climate*, (2021).

Asymmetries in Formation of Gulf Stream Warm Core Rings and Filaments

Ellie Q. Y. Ong

December 17, 2023

1 Introduction

The Gulf Stream is the surface-intensified, western boundary current of the subtropical North Atlantic gyre. It also forms the upper limb of the Atlantic Meridional Overturning Circulation. The Gulf Stream brings warm waters from the lower latitudes in the Caribbean along the coast to the high latitudes offshore from the Northeast of the U.S. At 100km in width, the Gulf Stream is a key conduit of heat transport northward, and its extension across the North Atlantic towards western Europe has large effects on the region's climate.

As the Gulf Stream travels north from the tropics and reaches Cape Hatteras at $\sim 35°N$, it is steered eastward and separates from the North American continent, where it separates the cool Slope Sea on the Northeast continental shelf in the north from the warmer Saragasso Sea in the south (see Figure 1 [14]). In this section of the Gulf Stream, the current also flows over the New England Seamount Chain, topographic features that stretch across the Gulf Stream. The Gulf Stream is also an incredibly turbulent current, with vortex rings of scale of ∼100km enclosing parcels of different water masses breaking off on its north and south side. Cold core rings form in the south, with cyclonic rings of cooler water in the Saragasso Sea, while anticyclonic Warm Core Rings (abbreviated to WCRs) form in the North. Shingles/streamers also feature in this region—where warm tongues of anticyclonically flowing near surface water extended onshore from the Gulf Stream and are folded backwards [10, 8].

Warm Core Rings have been formed in increasing frequency in recent years, and they have been shown to contribute to maxima in salinity intrusions on the Northeastern continental shelf [5]. This can have ramifications on the biology in the region, affecting fish and zooplankton populations, as well as squid catches [13]. Hence, understanding why these WCRs are formed at increasing frequency, and the mechanisms behind their formation is a key area of open research.

There has been research on the eddying Gulf Stream for decades, but recent research has shown that the new England Seamount Chain plays an important role in how warm core rings form. In a recent paper by Silver et al. 2022 [14], vortex rings formed west of the seamount chain comprising Gulf Stream and slope water but not Saragasso Sea Water,

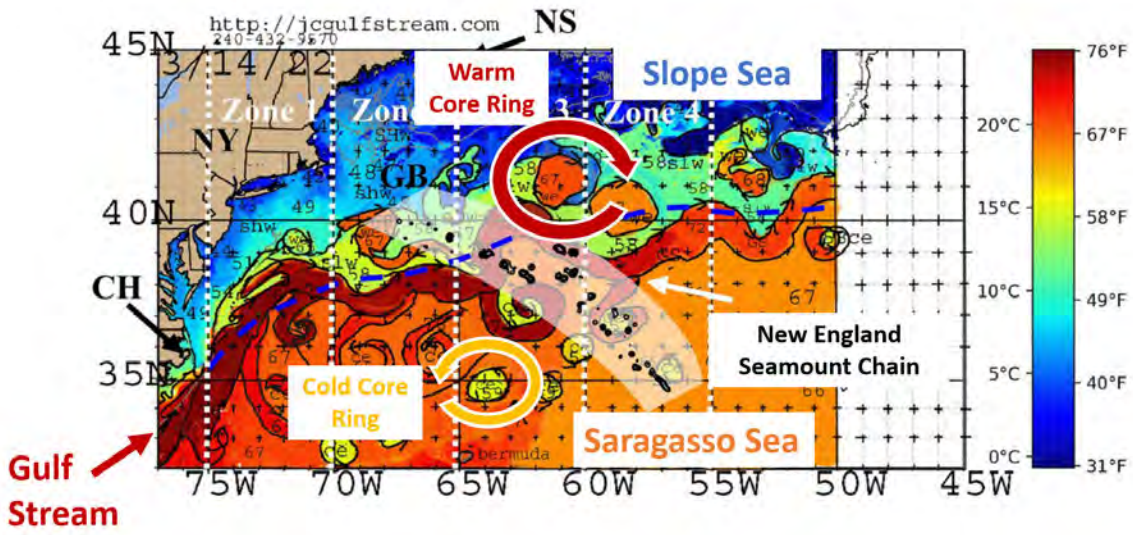

Figure 1: SST plot of the Northeast US continental shelf replicated from Silver et al. 2022 [14], labelling the key topographic and eddying features of the Gulf Stream.

while vortex rings formed east of the seamount chain contain Saragasso Sea Water. This implies that there are different ring formation mechanisms either side of the seamount chain, each of which result in different water mass compositions in the WCRs.

The two mechanisms by which WCRs can form are pinch-offs and aneurysms (Figure 2). In pinch-offs, the Gulf Stream meanders in the North-South direction, and these large meanders can break away from the Gulf Stream, pinching off a core of Saragasso Sea water in the process. In aneurysms, the Gulf Stream itself expands on its northern flank, breaking off into an anti-cyclonic eddy containing primarily Gulf Stream water. It is likely that vortex rings formed west of the seamount chain are formed through aneurysms, while those formed east of the seamount chain are formed through pinch-offs, matching the observations by Silver et al. [14].

Previous research has been conducted on pinch-off formation using contour dynamics [11, 12, 9, 4]. Under the contour dynamical framework, a jet is split into bands of constant PV. The dynamics of a jet is therefore modelled by the dynamics of fronts between layers of constant PV, where the jump in PV at the interfaces is determined by the jet velocity profile. Flierl (1999) [4] in particular use this framework to understand jet instabilities, showing that meanders grow initially through baroclinic instability, but final pinch-offs are dominated by barotropic instability. However, there has not been any research conducted on the formation of aneurysms. This project has therefore aimed to use the contour dynamical framework to understand how aneurysms can be formed in the Gulf Stream, and supplemented this with the use of a pseudospectral QGPV model and SST-Surface QGPV model to verify our hypotheses.

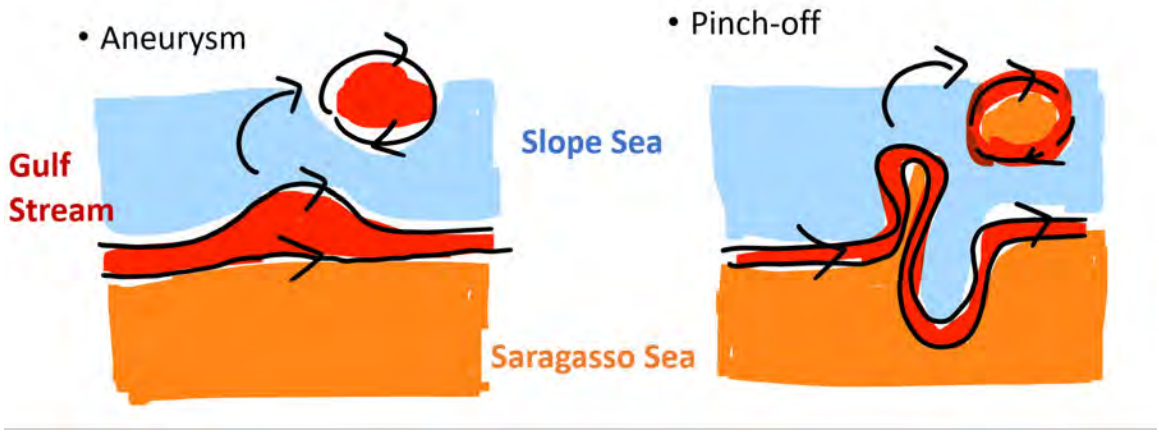

Figure 2: Schematic showing the different formation mechanisms of Warm Core Rings (WCRs) in the Gulf Stream. (Left) WCRs form through Aneurysms as the Gulf Stream bulges out on the northern boundary, detaching to form an WCR consisting of only Gulf Stream water. (Right) WCRs form through pinch-offs when the Gulf Stream meanders in the meridional direction, bringing Saragasso Sea water northwards. When the meander breaks off into a WCR, Saragasso Sea water is also incorporated into the ring, resulting in WCRS with both Gulf Stream water and Sargasso Sea water.

2 Theory and Methods

We primarily use the contour dynamical framework and linear stability theory. First, we construct candidate jet profiles in the contour dynamical framework and predict which produce WCRs through aneurysms. Using the predictions of linear stability theory, we run a full pseudospectral QGPV model to verify if the jets predicted to produce WCRs through aneurysms do so in reality. Section 2 will, therefore, first outline the contour dynamical framework used in this study and its associated assumptions (Section 2.1). We then outline the layered QGPV model (Section 2.2), linear stability theory developed and the eigenvalue problem that allows us to obtain the most unstable mode of the jet system and predict if eddies can be formed through aneurysms (Section 2.3). We finally describe the SST Eady-like model used to produce WCRs through aneurysms in Section 2.5.

2.1 Contour dynamical model of the Gulf Stream

In contour dynamical models of jets, the jet is split into bands of constant potential vorticity (PV) with fronts where discrete jumps in PV occur. Here, we have assumed an f-plane, two-layer system with a flat bottom. In previous work by Flierl [4], a two-layer system with a single PV front in each layer was used, allowing for a symmetric jet profile that exponentially decayed away from the jet core. Pinch-offs formed on both sides of the jet. As aneurysms are only formed on the northern side of the Gulf Stream, we hypothesize that

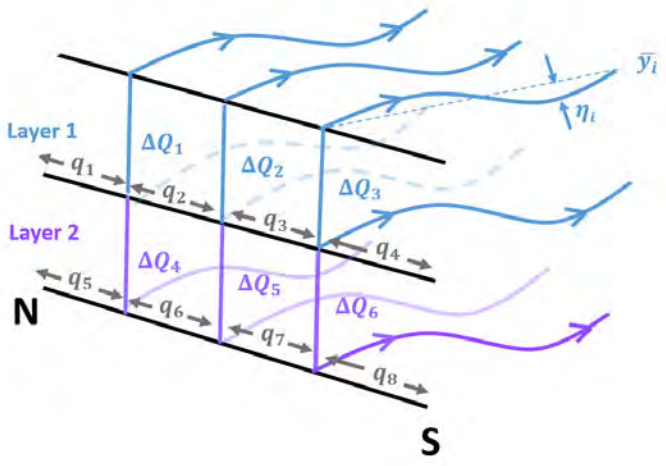

Figure 3: Schematic showing the contour dynamical model of the Gulf Stream. The jet is split into bands of constant PV q_j, with jumps in PV at interface j of ΔQ_j. η_j is the lateral displacement of the PV interface about the mean location $\bar{y}_i$. A two-layered QGPV model is used, with three fronts in each layer to allow for an asymmetry to be imposed on the jet profile.

in linear stability theory, a jet that is asymmetric allows for eddies to form preferentially on one side of the jet, as opposed to an equal probability in either side in the symmetric case. We therefore opted to add two extra fronts in each layer, and the difference in the spacing of the fronts allows the symmetry of the jet to be modified. We make the key assumption that a modelled jet with a northern interface that is displaced more than the southern interface will result in WCR formation through aneurysms, while a set up with equally unstable interfaces results in pinch-offs. We generate candidate jet profiles that may produce WCRs through aneurysms, informed by a parameter sweep, and test the stability of each interface using linear stability theory outlined in Section 2.3. This contour dynamical model set up is pictured in Figure 3, with three PV fronts in each fluid layer and discrete jumps in PV at each interface, marked by ΔQ_i, separating regions of constant PV. Under linearised QGPV, we set up the contour dynamical model by prescribed PV jumps at each interface using candidate jet profiles.

2.2 Two-layered quasi-geostrophic model

We first use the quasi-gesotrophic model as a starting point, using a two-layer system that defines PV q_i in layer i as:

$$q_1 = \nabla^2\psi_1 + F_1(\psi_2 - \psi_1) \tag{1a}$$

$$q_2 = \nabla^2\psi_2 + F_2(\psi_1 - \psi_2) \tag{1b}$$

where $F_1 = f^2/(g'H_1)$ and $F_2 = f^2/(g'H_2) = H_1/H_2F_1 = \delta F_1$ with $g' = g\Delta\rho/\rho_0$ as the reduced gravity of the system, H_1, H_2 as the thicknesses of the upper and lower density layer, respectively, and $f = 10^{-4}s^{-1}$ as the Coriolis parameter.

$F_{1,2}$ can also be defined as $F_1 = \frac{\gamma^2}{1+\delta}$, and $F_2 = \frac{\delta\gamma^2}{1+\delta}$, where δ is the ratio between upper and lower layer thicknesses, and $\gamma^2 = F_1 + F_2 = 1/R_d^2$, and the Rossby deformation radius is $R_d = 40$km. In our model, we set $\delta = 0.2$, obtained from profiles of stratification in the Gulf Stream using methods in work by Flierl (1978) [3].

2.3 Linear stability theory

Under the framework of contour dynamics, we obtain an eigenvalue problem of phase speed c with eigenfunction η, where η is the displacement of the PV contours, and c is the phase speed of the displacement. We initially express everything in terms of a continuous field of PV, and discretise them into the contour dynamical framework at the end.

Starting with the linearised QGPV equations.

$$\frac{\partial q'}{\partial t} + U\frac{\partial q'}{\partial x} + Q_y\frac{\partial \psi}{\partial x} = 0, \tag{2}$$

and substituting $q' \sim -\eta Q_y$ results in a kinematic condition that the displacement of the PV contour, η, is a material line.

$$\frac{\partial \eta}{\partial t} + U\frac{\partial \eta}{\partial x} = \frac{\partial \psi}{\partial x}. \tag{3}$$

The PV equation is then inverted to get an expression for ψ since $L\psi = q'$ as defined in (1); since L is a linear operator,

$$\psi = \int -G(x, y, z|x', y', z')\eta(x', y', z')Q_y(x', y', z')dx'dy'dz', \tag{4}$$

where the z's represent which layer the particular interface occupies and $G(y, z|y', z')$ is derived from the definition of the two-layer QGPV system (1) (See Appendix for derivation). Having linearised, we integrate in x, considering the perturbations in wavenumber k, $\eta \sim e^{ik(x-ct)}$. The stability equation becomes

$$U(y, z)\eta(y, z) + \int G^k(y, z|y', z')\eta(y', z')Q_y(y', z')dy'dz' = c\eta(y, z). \tag{5}$$

Now, we represent the basic state PV as piecewise constant bands, so that Q_y is a set of delta functions

$$Q_y(y, z_i) = \Delta(y_i, z_i)\delta(y - y_i) \tag{6}$$

with Δ being the jump in PV in layer z_i at the mean position y_i of the contour. There-

fore, the stability equation can be expressed in matrix form:

$$M_{ij}\eta_j = c\eta_i \tag{7}$$

$$\text{where } M_{ij} = U(y_i, z_i)\delta_{ij} + G(y_i, z_i|y_j, z_j)\Delta(y_i, z_i)\delta(y - y_i). \tag{8}$$

The procedure for obtaining an expression for $G(y_i, z_i|y_j, z_j)$ is outlined in the appendix. Hence, the kinematic equation for η can be reduced to an eigenvalue problem of phase speed c, with eigenfunctions η_j.

2.4 Pseudospectral QGPV model

The fully non-linear pseudospectral model solves the two-layer QGPV equations as they evolve in time, given an initial velocity field. The velocity field input is motivated by the linear stability analysis, and candidate unstable zonal jets are interpolated to a velocity field to be used to initialize the model, with a peak velocity of 75km/day or 86cm/s. The pseudospectral model is run at 128 $\times$ 128 grid cell resolution in a doubly periodic domain of dimensions 1000km $\times$ 1000km. A small initial perturbation in the PV field is added in the top layer to induce an instability. A Gaussian bump perturbing the PV field was used, but testing variations of this perturbation was outside the scope of this study.

2.5 Surface QGPV SST model

The SST model used surface quasi-geostrophy, where only the temperature evolution on rigid boundary surfaces are modelled. This is an Eady-like model, where we have a region of constant PV and stratification in between two rigid boundary surfaces, similar to the setup used by Tulloch and Smith (2009) [16, 17]. In the boundary surfaces, potential temperature θ is related to the streamfunction ψ by $\partial_z\psi|_{z=0,-H} = \theta|_{z=0,-H}$. The governing equations are:

$$\frac{\partial\theta}{\partial t} + \overline{U}\frac{\partial\theta}{\partial x} + \overline{\Theta}_y\frac{\partial\psi}{\partial x} + J(\psi, \theta) = 0 \text{ for } z = 0, -H \tag{9a}$$

$$\nabla^2\psi + \frac{\partial^2\psi}{\partial z^2} = q, \tag{9b}$$

where we have set $q = 0$ in the domain, with boundary conditions of:

$$\frac{\partial\psi}{\partial z} = \theta_1 \text{ at z = 0} \tag{10a}$$

$$\frac{\partial\psi}{\partial z} = \theta_2 \text{ at z = -H} \tag{10b}$$

These equations are solved in the same pseudospectral methods as in the layered QGPV model. An initial streamfunction field is prescribed to represent an SST gradient, and the surface θ fields are allowed to evolve from this initial condition.

3 Results

3.1 Asymmetry in northern jet flank/formation of cyclonic WCR

We initially hypothesize that adding an asymmetry to the northern flank of the jet would allow for a northern PV interface to be displaced the most in the most unstable mode. Here we have increased the steepness of the northern jet flank by a factor of a as seen in Figure 4. We run the linear stability analysis for a range of w and a values, find the most unstable mode, and calculate the contribution of the northern interface to the amplitude of the eigenfunctions. A summary of these results are shown in Figure 5, where we see that in the symmetric jet, the northern (red line) and southern (blue line) interfaces are displaced by the same amount, while in the asymmetric jet, the northern interface is displaced by a factor of 8 more than the southern interface. This provides some support that adding an asymmetry to a jet can form WCRs through aneurysms, as the northern interface is displaced the most in the most unstable mode of the asymmetric jet.

However, when verifying whether aneurysms are formed in the asymmetric jet, the non-linear psuedospectral model showed cyclonic eddies forming on the northern side instead. Anticyclonic eddies were also formed on the southern side; this is not representative of the Gulf Stream, where anticyclonic eddies are formed on the north, see Figure 6 (a). We found a possible cause to this problem in the PV profiles of the GS in Figure 6 (b); the eddies seen in the simulation were travelling from a local region of high PV to a region of low PV, the downgradient transport of the fluid parcels caused them to be cyclonic to conserve PV. Therefore, we attempted to adjust the PV profile to ensure that eddies formed were anticyclonic, i.e., travelled from regions of low PV to high PV.

3.2 Positive PV jump in northern jet flank/formation of eddies through pinch-offs

Based on results in section 3.1, we wanted to add a positive jump in PV on the northern flank to ensure that anticyclonic eddies are formed, i.e., eddies are travelling up a PV gradient. We do so by adding a positive PV jump in the jet profile on the northern side, instead of pinning the velocity profile to zero, as shown in Figure 4. As $\Delta Q = \frac{\partial^2 U}{\partial y^2}$, by steepening the jet profile at the location of the northern PV interface, we can impose a positive PV jump at the interface, possibly allowing for anticyclonic eddies to form through aneurysms. We again sweep the parameter space for values of w, a and U_{offset}, finding the jet profiles that result in a northern interface with the largest displacement under linear stability theory and anticyclonic eddies forming by having a positive PV jump on the northern interface. As some of these profiles have secondary jets on the northern flank, these have been omitted from our study as they are not representative of the Gulf Stream. These candidate jet profiles are then run in the pseudospectral layered QGPV model.

Snapshots from an example simulation are shown in Figure 8 (a). Anticyclonic eddies are indeed formed, but they are taking up water from the southern side of the jet, in other

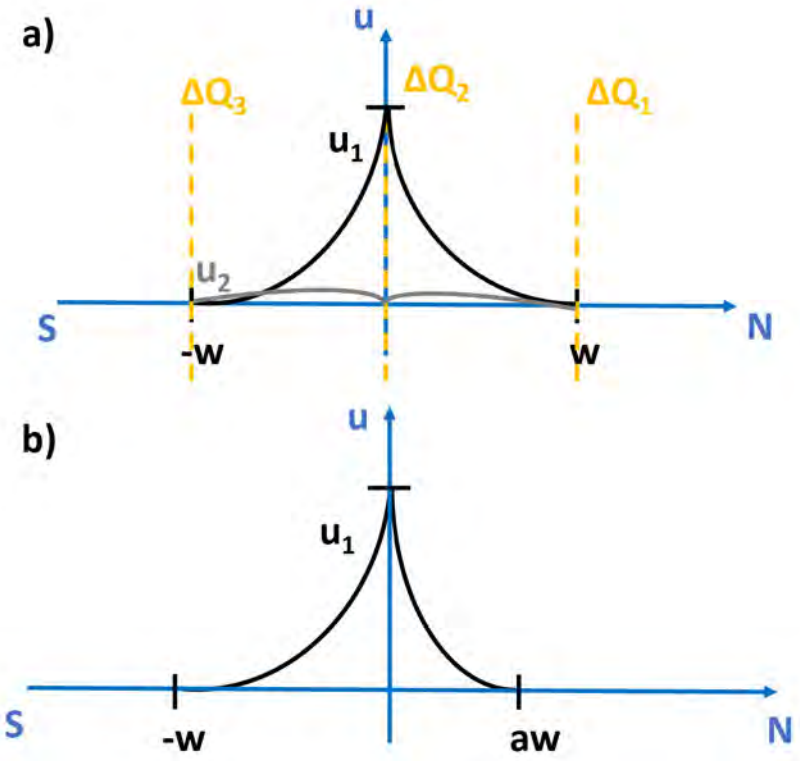

Figure 4: Schematic showing upper layer jet profile in the (a) symmetrical and (b) asymmetrical case. The yellow dotted lines represent the locations of the PV interfaces, where the jumps in PV are calculated. The symmetrical case also shows the lower layer jet profile, where the jumps in PV, and therefore velocities, are pinned to zero at the locations of the PV interfaces.

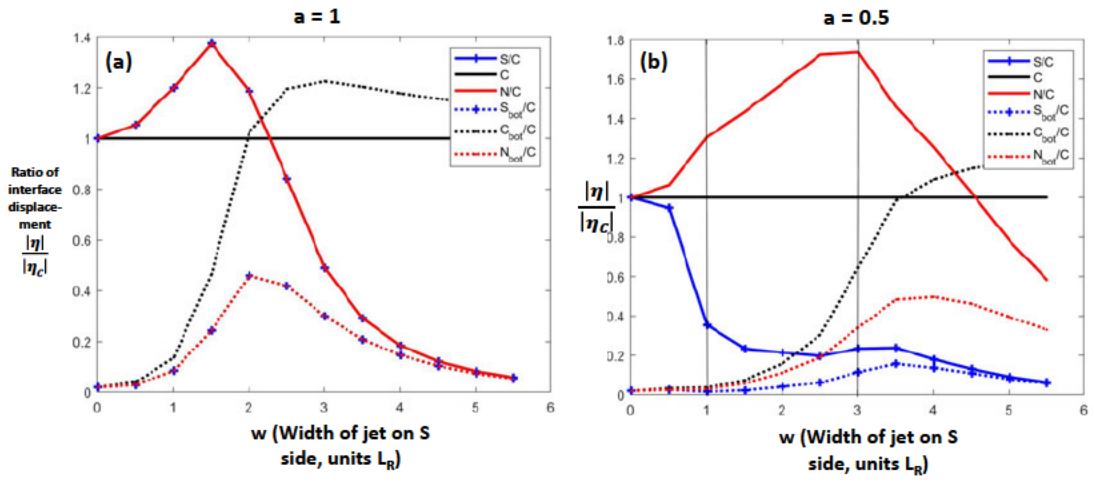

Figure 5: PV interface displacement relative to centre-top interface in the most unstable mode as width of jet w is varied in contour dynamical model of Gulf Stream for (a) symmetrical jet $a = 1$ and (b) asymmetrical jet with $a = 0.5$. The solid lines represent the displacement of upper layer interfaces, and dotted lines that of the lower layer, with the northern (red), southern (blue) and centre (black) interfaces relative displacement colored separately. In the symmetric jet, the blue and red lines overlap exactly, hence the northern and southern interfaces are displaced with the exact same magnitude. For the asymmetric jet, the northern interface is displaced more than the southern interface.

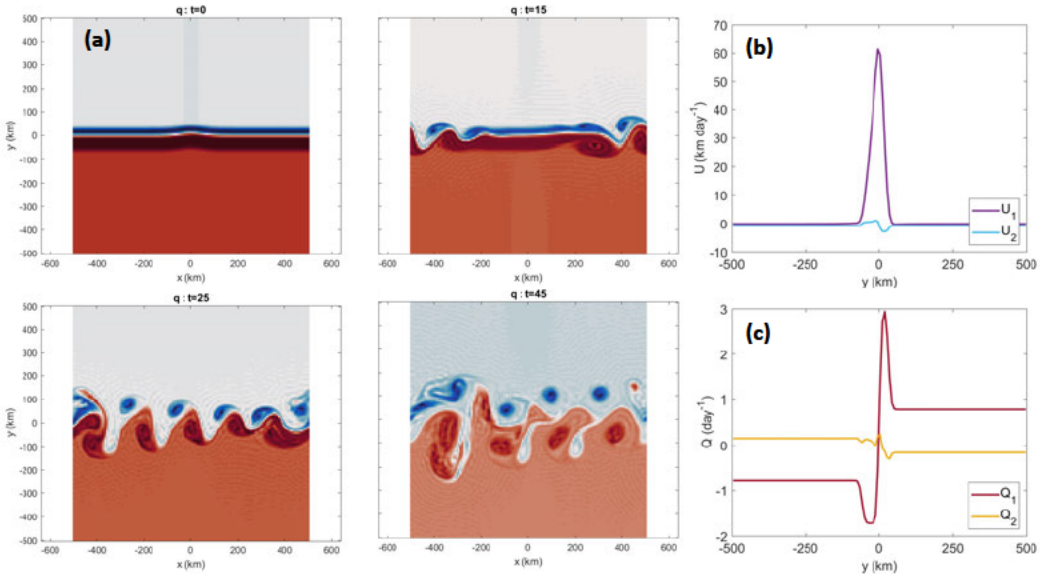

Figure 6: (a) Cyclonic snapshots showing the evolution of pinch-offs in an asymmetrical jet with a positive PV jump in the northern flank, with paramters $w = 1.5, a = 0.5$. The blue represents the high PV regions of the Slope Sea (north side of the Gulf Stream), and the red represents the low PV regions (south of the Gulf Stream.) (b) Initial zonal velocity profiles for upper (purple) and lower (cyan) layer. (c) Initial PV profiles for upper (red) and lower (yellow) layers.

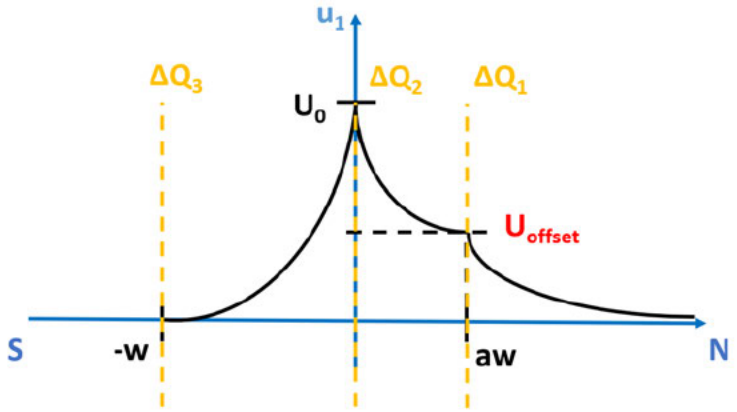

Figure 7: Schematic showing assymetrical jet profile.

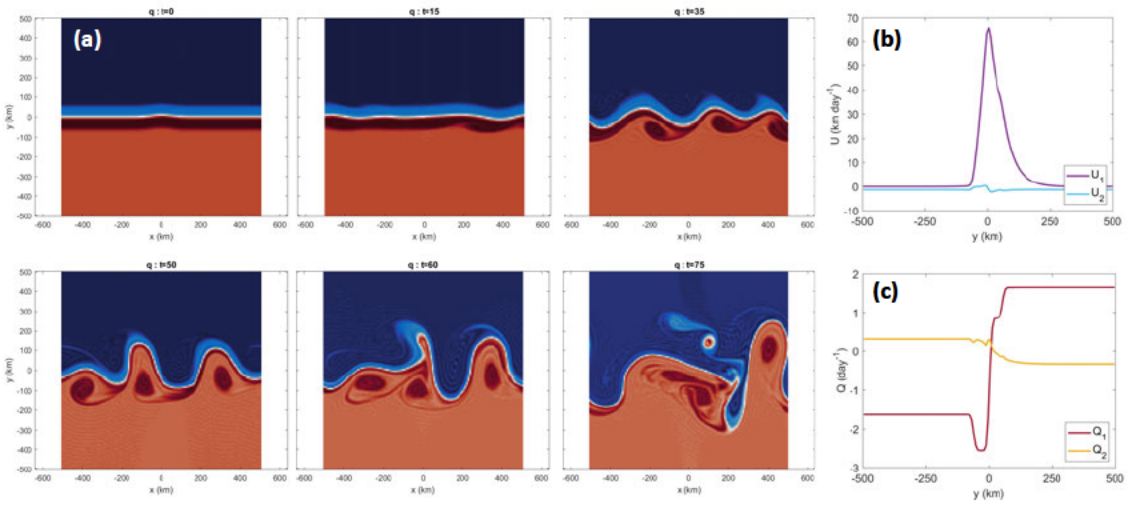

Figure 8: a) Velocity profiles input to the pseudospectral QGPV model: an asymmetrical jet with a positive PV jump on the northern side, interpolated from contour dynamical model of jet with parameters $w = 1.5, a = 0.9$ and $\mathrm{U}_{offset} = 0.5$. b) Initial PV in each layer. c) Snapshots showing the evolution of pinch-offs in an asymmetrical jet with a positive PV jump. The blue represents the high PV regions of the Slope Sea (north side of the Gulf Stream), and the red represents the low PV regions (south of the Gulf Stream.) By $t = 75$, fluid south of the jet has travelled with the meander north and broke off from the center of the jet.

words, eddies are formed through pinch-offs rather than aneursyms. In investigating the cause of this discrepancy between our prediction and the numerical experiments, we find that the PV in the upper layer (see Figure 8 (c)) has a large drop at the southern flank of the jet, there the southern PV interface is located. Hence, anticyclonic eddies are formed as fluid is moved from the low PV region south of the jet to the high PV region north of the jet. Through this pinch-off like mechanism in the Gulf Stream, the water mass of resulting WCRs would contain Saragasso Sea water as well. Therefore, we proposed that removing this dip in PV would allow for anticyclonic WCRs to form from the northern boundary, as tested in the following section 3.3.

3.3 Two positive PV jumps in jet/formation of filaments

We constructed a zonal jet profile incorporating all the previous conditions: asymmetry on the northern flank of the jet, a positive PV jump on the northern side to ensure an anticyclonic eddy formed, and a positive PV jump on the southern side to ensure no eddies are formed through pinch-offs. The generic structure of such a jet is shown in Figure 9. We explored the parameter space of possible jet structures, using the four parameters w, a, U_{offset} and U'_{offset} to find jet profiles that satisfy all conditions. We ran an experiment predicted to form eddies through aneurysms, with two positive PV jumps on either flank of

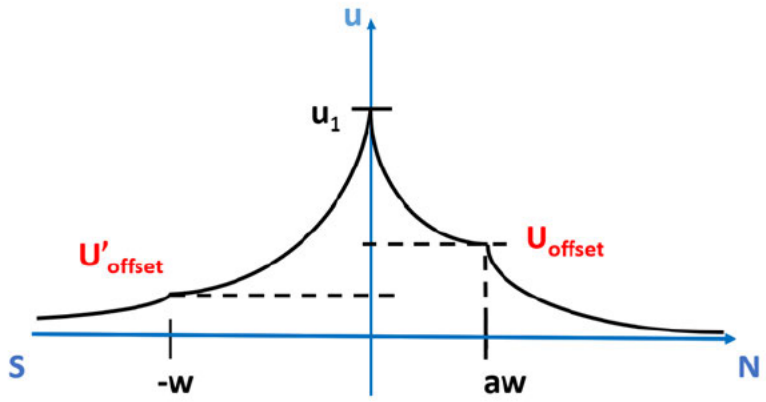

Figure 9: Schematic showing assymetrical jet profile of upper layer with two positive PV jumps to prevent pinch-offs from occurring.

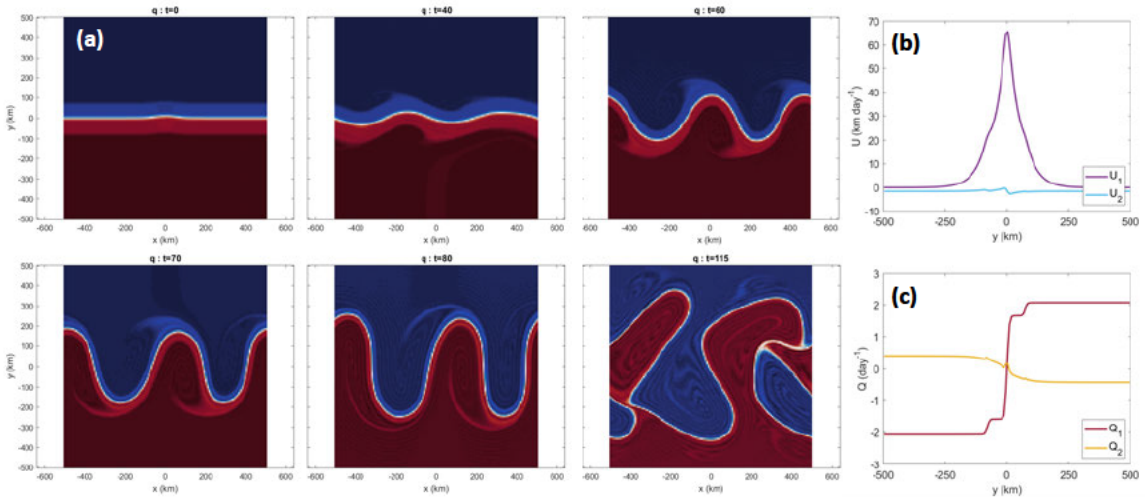

Figure 10: Same as Figure 8 but for the jet with two positive PV jumps, input jet profile was interpolated from contour dynamical model of jet with parameters $w = 2, a = 0.9, \mathrm{U}_{offset} = 0.3$ and $\mathrm{U}'_{offset} = 0.3$.

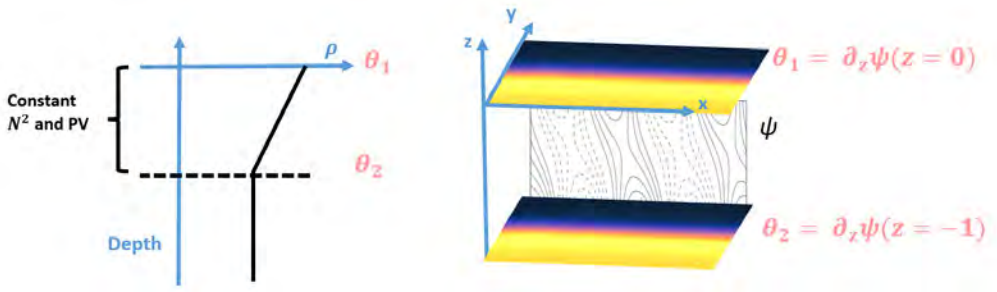

Figure 11: Schematic illustrating the SST-Surface QGPV model. There is constant stratification and PV throughout the depth of the domain, with potential temperature θ defined on the boundary surfaces where it can be advected. A streamfunction throughout the domain is prescribed using boundary conditions imposed by SST gradients, and the system is allowed to evolve over time.

the jet. The snapshots from this experiment are shown in Figure 10. The experiment does not show eddies forming, instead filaments are formed as the Gulf Stream bulges out at the peak of each meander. Eddies do not detach, instead shearing out into filaments before the double-periodic boundary conditions take over and cause the system to blow up. Here we therefore reach the limitations of this experimental setup—there is too much shear in the jet surroundings and eddies are unable to develop independent of the recirculating meander. This could be addressed by modifying the experimental set up to have a set inflow into the channel, but technical difficulties have prevented that work from being completed.

These filaments resemble the shingles/streamers present in the Gulf Stream, where they have been observed on the northern side of the Gulf Stream, with effects on fisheries in the continental shelf region (Silver et al., personal communication). Work by Stern (1985) [15] was able to generate shingles in an equivalent barotropic model[1], under sufficiently large amplitude disturbances and in the presence of large cyclonic shear in the cold water engulfed by the Gulf Stream. As an accidental extension to the previous work, we have found that the necessary but insufficient conditions required for the aneurysms to form appear to also facilitate anticyclonic filament formation in a layered QGPV model.

3.4 SST-Surface QGPV model/formation of WCRs through aneurysms

Given the limitations of the linearised QGPV model, we tried the SST-Eady-like model outlined in Section 2.5 to model the Gulf Stream. We imposed an initial streamfunction with a gradient representative of the meridional SST gradient in the Gulf Stream, with highest temperatures in the centre, warmer in the south, and colder in the north, shown in Figure 12 (c). Running the pseudospectral SST-Surface QGPV model of the Gulf Stream, we see from snapshots in Figure 12 (a) that warm water from the center of the jet, the

[1]Equivalent Barotropic Model: a two-layer model where the jet is confined to the top fluid layer with a motionless lower layer

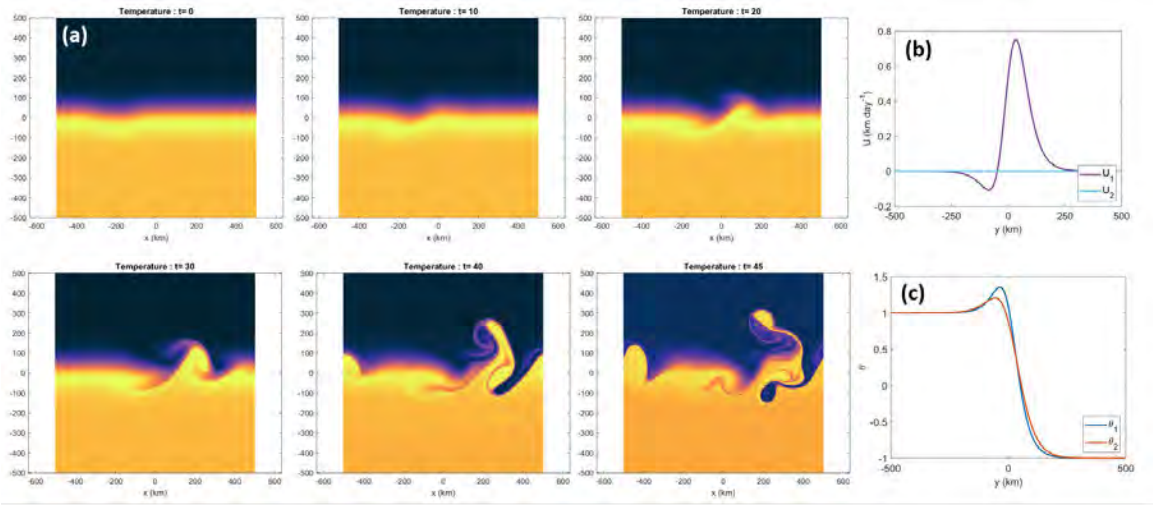

Figure 12: (a) Snapshots of the SST-Surface QGPV model of the Gulf Stream forming eddies through aneurysms: temperature is represented by the warm colors, where the warmest water in the centre of the GS break off and travel north in an anticyclonic WCR. (b) Initial zonal jet velocity profiles in the top (purple) and bottom (cyan) boundary surfaces. (c) Initial zonally averaged θ profiles in the top (blue) and bottom (orange) boundary surfaces.

region of the highest temperature, immediately breaks off northward in an anticyclonic vortex. WCRs are therefore almost immediately formed through aneurysms when an SST gradient is imposed on the boundary surfaces (see Figure 12 (c)).

To verify that the representation of SST is key to the generation of WCRs through aneurysms, we use the initial jet velocity profile from the SST-Surface QGPV (Figure 12 (b)) model as the initial condition of the layered QGPV model. The profile was generated using 2 PV fronts in the top layer, the minimum number required to create the profile with the counterflow seen in the SST-Surface QGPV experiments. The results are shown in Figure 13. WCRs are, however, formed through pinch-offs in this experiment, indicating that the representation of SST could be necessary in aneurysms. Similar to other preliminary experiments, the counterflow in the jet of Figure 13 (b) does not seem to induce the aneurysm formation mechanism as it does not result in a continuously increasing PV profile meridionally, as in Figure 13 (c).

We also note that the formation of eddies through aneurysms is also possible even when the temperature of the GS is lower than that of the Saragasso sea, indicating that only a large SST gradient is important in the formation of aneurysms. This may also imply that the eddy formation through aneurysms is independent of the seasonality of the Gulf Stream; the Gulf Stream SST varies seasonally with a fall maximum in SST [7], but aneurysms formations in our experiments do not appear to be affected by a lower SST in the warm core.

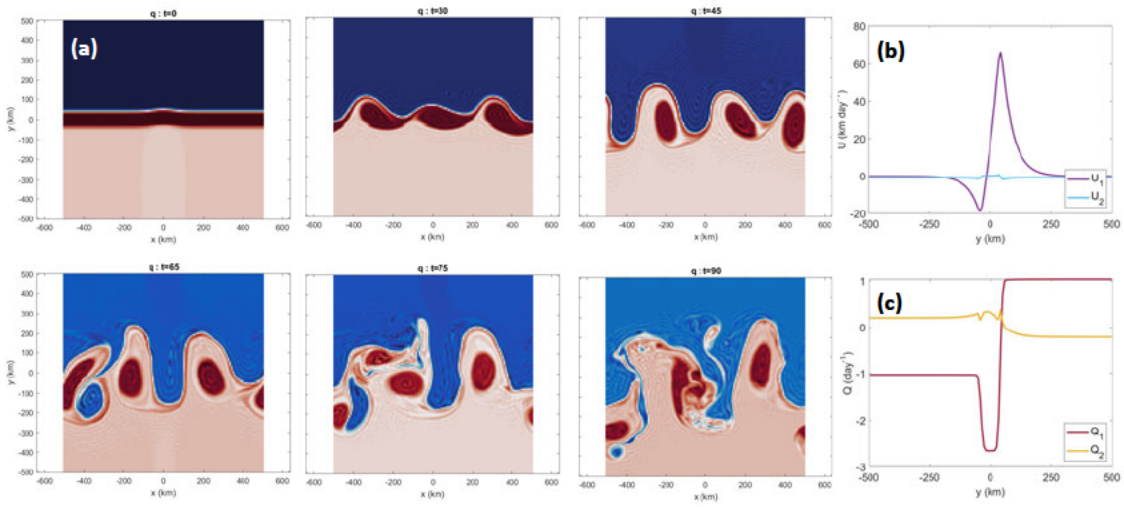

Figure 13: (a) Snapshots of the layered QGPV model of the Gulf Stream using the initial jet profile of the SST-Surface QGPV model. (b) Initial zonal jet velocity profiles in the upper (purple) and lower (cyan) layer, similar to Figure 12. (c) PV in upper (red) and lower (yellow) layer. In this case, pinch-offs are formed as there is a large dip in PV in the upper layer, similar to Figure 8.

4 Conclusion and Discussion

We found that a layered QGPV framework gives us insights into the necessary but insufficient conditions for WCRs to form through aneurysms. Such conditions include: 1) an asymmetrical jet to induce eddy formation on the northern side of the Gulf Stream, 2) a positive jump in PV on the northern flank to allow for anticyclonic WCRs to form, and 3) a positive jump on the southern flank to ensure pinch-offs do not form. Filaments are able to form in this framework, but there seems to be too much shear in the system for WCRs to form. However, the SST-Surface QGPV model allows for WCRs to form through aneurysms in the top surface layer. We found that the SST gradient is necessary in inducing aneurysms, as applying the same jet profile to the original pseudospectral QGPV model did not result in WCR formation through aneurysms.

Limitations of this study include the use of Green's functions as the basis of constructing the jet profiles. In the Gulf Stream, jet profiles are concave and not convex, such as in Figure 4 (a) and (b) in the work by Dong et al. (2019) and others [2, 1, 6]. Generating such a jet profile is not possible in the contour dynamical framework with only three PV fronts due to the exponential nature of the Green's functions, requiring many more PV fronts to be included. Additionally, the pseudospectral layered QGPV model is doubly periodic, which can allow for the instabilities to interact as the current recirculates. Using a larger domain with a constant jet inflow might address this issue, but the implementation of this setup remains a challenge.

An extension of this project would be to combine the SST-Surface QGPV model and the layered QGPV model, such that filaments, as well as WCRs, formed through aneurysms and pinch-offs can all be represented. Modelling this numerically using similar pseudospectral methods is a work in progress. Further work using linear stability theory to understand the phasing of each PV interface displacement might also inform possible mechanisms of WCR formation.

Although the initial attempt to generate WCRs through aneurysms in layered QGPV was unsuccessful, we have found the possibility of generating filaments/shingles in layered QGPV. The SST-Surface QGPV model, however, appears to facilitate the formation of WCRs through aneurysms. Therefore, the development of an idealised Gulf Stream model, which can encompass all these mechanisms of northward warm water transport, remains within reach.

5 Acknowledgements

I would like to acknowledge, and extend a huge thank you to my advisors on this summer project: Ted Johnson and Phil Morrison for your guidance and advice from near and afar, and Glenn Flierl for your immense patience in steering this project. Thank you to Pascale Garaud and Tiffany Shaw for directing this wonderful program, Heather Knutson and Geoff Vallis for the insightful lectures, and to the faculty and visitors for an enriching summer. A final thank you to the GFD fellows, I could not have done this without you all and it has been a joy and a privilege to meet every one of you. I feel so lucky to have had such a wonderful summer together!

References

[1] M. Andres, *On the recent destabilization of the Gulf Stream path downstream of Cape Hatteras*, Geophysical Research Letters, 43 (2016), pp. 9836–9842.

[2] S. Dong, M. O. Baringer, and G. J. Goni, *Slow Down of the Gulf Stream during 1993–2016*, Scientific Reports, 9 (2019).

[3] G. R. Flierl, *Models of vertical structure and the calibration of two-layer models*, Dynamics of Atmospheres and Oceans, 2 (1978), pp. 341–381.

[4] G. R. Flierl, *Thin jet and contour dynamics models of Gulf Stream meandering*, Dynamics of Atmospheres and Oceans, 29 (1999), pp. 189–215.

[5] A. Gangopadhyay, G. Gawarkiewicz, E. N. S. Silva, M. Monim, and J. Clark, *An Observed Regime Shift in the Formation of Warm Core Rings from the Gulf Stream*, Scientific Reports, 9 (2019).

[6] A. Gangopadhyay, A. R. Robinson, and H. G. Arango, *Circulation and Dynamics of the Western North Atlantic. Part I: Multiscale Feature Models*, Journal of Atmospheric and Oceanic Technology, 14 (1997), pp. 1314–1332.

[7] K. A. Kelly, S. Singh, and R. X. Huang, *Seasonal Variations of Sea Surface Height in the Gulf Stream Region**, Journal of Physical Oceanography, 29 (1999), pp. 313–327.

[8] J. M. Klymak, R. K. Shearman, J. Gula, C. M. Lee, E. A. D'Asaro, L. N. Thomas, R. R. Harcourt, A. Y. Shcherbina, M. A. Sundermeyer, J. Molemaker, and J. C. McWilliams, *Submesoscale streamers exchange water on the north wall of the Gulf Stream*, Geophysical Research Letters, 43 (2016), pp. 1226–1233.

[9] S. P. Meacham, *Meander Evolution on Piecewise-Uniform, Quasi-geostrophic Jets*, Journal of Physical Oceanography, 21 (1991), pp. 1139–1170.

[10] L. J. Pietrafesa, *Survey of a Gulf Stream frontal filament*, Geophysical Research Letters, 10 (1983), pp. 203–206.

[11] L. J. Pratt, *Meandering and Eddy Detachment According to a Simple (Looking) Path Equation*, Journal of Physical Oceanography, (1988).

[12] Pratt L J and Stern M, *Dynamics of Potential Vorticity Fronts and Eddy Detachment*, Journal of Physical Oceanography, (1986).

[13] S. L. Salois, K. J. Hyde, A. Silver, B. A. Lowman, A. Gangopadhyay, G. Gawarkiewicz, A. J. Mercer, J. P. Manderson, S. K. Gaichas, D. J. Hocking, B. Galuardi, A. W. Jones, J. Kaelin, G. DiDomenico, K. Almeida, B. Bright, and M. Lapp, *Shelf break exchange processes influence the availability of the northern shortfin squid, Illex illecebrosus, in the Northwest Atlantic*, Fisheries Oceanography, 32 (2023), pp. 461–478.

[14] A. Silver, A. Gangopadhyay, G. Gawarkiewicz, M. Andres, G. Flierl, and J. Clark, *Spatial Variability of Movement, Structure, and Formation of Warm Core Rings in the Northwest Atlantic Slope Sea*, Journal of Geophysical Research: Oceans, 127 (2022).

[15] M. E. Stern, *Lateral Wave Breaking and "Shingle" Formation in Large-Scale Shear Flow*, Journal of Physical Oceanography, 15 (1985), pp. 1274–1283.

[16] R. Tulloch and K. S. Smith, *A note on the numerical representation of surface dynamics in quasigeostrophic turbulence: Application to the nonlinear eady model*, Journal of the Atmospheric Sciences, 66 (2009), pp. 1063–1068.

[17] ——, *Quasigeostrophic turbulence with explicit surface dynamics: Application to the atmospheric energy spectrum*, Journal of the Atmospheric Sciences, 66 (2009), pp. 450–467.

A Evaluating the Green's functions for the two layered QGPV model

In the appendix we detail the steps taken to evaluate the Green's function matrix, using a two layered, two PV front system as an example. A significant portion of this section is from Flierl, Meacham and Paldor, *Instabilities and waves on thin jets: Linear Theory*, in prep.

A.1 Step 1: Find the QGPV equations that describe the system

For linearised two-layer QGPV:

$$q_1 = \nabla^2\psi_1 + F_1(\psi_2 - \psi_1) \tag{11}$$

$$q_2 = \nabla^2\psi_2 + F_2(\psi_1 - \psi_2) \tag{12}$$

$F_1 = f^2/(g'H_1)$ and $F_2 = f^2/(g'H_2) = H_1/H_2F_1 = \delta F_1$, with $\gamma = 1/R_d$.

$F_{1,2}$ can also be expressed as $F_1 = \frac{\gamma^2}{1+\delta}$, and $F_2 = \frac{\delta\gamma^2}{1+\delta}$. Expressed in terms of linear operators $L\psi = \mathbf{q}$, with $\psi = G\mathbf{q}$. When solving for a wave perturbation in ψ, we can write the QGPV equations as

$$(\partial_y^2 - k^2 + L_z)\begin{pmatrix}\psi_1\\ \psi_2\end{pmatrix} = \begin{pmatrix}q_1\\ q_2\end{pmatrix} \tag{13}$$

The matrix defining L_z is therefore

$$L_z = \begin{pmatrix}-F_1 & F_1\\ F_2 & -F_2\end{pmatrix} \tag{14}$$

from the QGPV equations.

A.2 Step 2: Find the vertical eigenmodes of Green's function

From the continuous form of the linear stability problem (2.3),

$$U(y,z)\eta(y,z) + \int G^k(y,z|y',z')\eta(y',z')Q_y(y',z')dy'dz' = c\eta(y,z), \tag{15}$$

where $G^k(y,z|y',z')$ are Green's function for disturbances of wavenumber k, $\eta \sim e^{ik(x-ct)}$.

$$G^k(y,z|y',z') = \int dx' G(x,y,z|x',y',z')exp[ik(x'-x)] \tag{16}$$

Going back to the PV equations expressed in terms of linear operators (1), for perturbations of $\eta \sim e^{-ik(x-ct)}$ in wavenumber k the Green's function should follow:

$$(\partial_y^2 - k^2 + L_z)G^k(y,z|y_i,z_i) = \delta(y-y_i)\delta(z-z_i). \tag{17}$$

The notation now follows the location y, z in the domain and location y_i, z_i of the PV interface i. Focusing on the vertical modes in the two layered problem, we can take the difference between the two PV equations to get the definition of $\psi_{BC} = \psi_1 - \psi_2$ and $\psi_{BT} = \delta\psi_1 + \psi_2$, where

$$\nabla^2\psi_{BC} - (F_1 + F_2)\psi_{BC} = \nabla^2\psi_{BC} - \gamma^2\psi_{BC} = 0 \tag{18a}$$

$$\nabla^2\psi_{BT} = 0 \tag{18b}$$

Therefore, the vertical baroclinic and barotropic eigenmodes have to satisfy $L_z G_z = -\gamma^2 G_z$, where $\gamma^2 = F_1 + F_2 = 1/R_d^2$. This shows that the eigenvalue problem $L_z F_m(z) = \lambda F_m(z)$ of the two layered problem results in eigenvalues of $\lambda = 0, -\gamma^2$, with vertical eigenvectors of $v_1 = (1, 1)$ and $v_2 = (1, -\delta)$, where m is the index for the eigenmodes. We also chose to non-dimensionalise the horizontal and vertical length scales so that the first non-zero eigenvalue is 1. It also follows that $L_z = Z\Omega Z^{-1}$, where Z is the matrix of eigenvectors and Ω is a diagonal matrix with eigenvalues. The Green's function can therefore be decomposed into vertical and horizontal eigenmodes of G_m^k and $F_m(z)$, where

$$G^k(y, z|y', z') = F_m(z) \times G_m^k(y, y') \times F_m(z') \tag{19}$$

with the orthogonality condition of

$$\frac{1}{H}\int dz F_i(z)F_j(z) = \delta_{ij} \tag{20}$$

A.3 Step 3 : Find Green's functions for horizontal modes

From this point onwards, we will use an example with two fronts, one in each layer, to illustrate the procedure used to find the Green's functions. The Green's function should follow:

$$(\partial_y^2 - k^2 + L_z)F_m(z) \times G_m^k(y, y_i) \times F_m(z_i) = \delta(y - y_i)\delta(z - z_i) \tag{21}$$

, where y_i, z_i is the coordinates of the i-th PV interface in the contour dynamical problem.

We go back to this equation, multiplying by $F_m(z)$ and averaging to get for each wavenumber k (not summed)

$$(\partial_y^2 - k^2 + L_z)G_m^k(y, y_i) = \delta(y - y_i) \tag{22}$$

The solution to $G_m^k(y, y_i)$ is

$$G_m^k(y, y_i) = \frac{1}{2\sqrt{k^2 + \gamma^2}} \exp(-\sqrt{k^2 + \gamma^2}|y - y_i|), \tag{23}$$

with the special case of the barotropic, zero wavenumber mode being

$$G_0^0(y, y_i) = \frac{1}{2}|y - y_i|. \tag{24}$$

These form each matrix element of (2.3).

As an example for the two layer system, having already found the vertical modes of the Green's functions, the easiest way to find the Green's functions in the horizontal modes is to look at the Green's function matrix of horizontal modes G^k for a two layer system:

$$G^k = \begin{pmatrix} G_{11} & G_{12} \\ G_{21} & G_{22} \end{pmatrix}, \tag{25a}$$

$$\text{from } L\,G^k = \begin{pmatrix} \delta(y - y_i) & 0 \\ 0 & \delta(y - y_i) \end{pmatrix} \tag{25b}$$

at the $G_{BC} = G_{11} - G_{21}$ and $G_{BT} = \delta G_{11} + G_{21}$ for the upper layer solution. We first focus only an upper layer anomaly in PV of $\Delta_1 \delta(y)\exp(ikx)$, with Green's functions of G_{11} and G_{21}. Physically, G_{11} represents the impact on q in layer 1 on ψ in layer 1 , with G_{21} representing the impact of q in layer 2 on ψ in layer 1. The upper layer problem for (25b) can therefore be written as:

$$\nabla^2 G_{11} - F_1(G_{11} - G_{21}) = \delta(y - y_i) \tag{26}$$

$$\nabla^2 G_{21} - F_2(G_{21} - G_{11}) = 0 \tag{27}$$

There is no source term of PV on the RHS of the equation for G_{21}, as the lower layer does not exchange PV with the upper (analogous to multiplying by $F_m(z)$ in the continuous framework). We then sum and solve to get G_{bt}.

$$\nabla^2 \underbrace{(\delta G_{11} + G_{21})}_{G_{BT}} = \delta\,\delta(y - y_i) \tag{28}$$

$$(\frac{\partial^2}{\partial y^2} - k^2) G_{BT} = \delta\,\delta(y - y_i) \tag{29}$$

$$\rightarrow G_{BT} = \frac{\delta}{2k} e^{(-k|y - y_i|)} \tag{30}$$

For the baroclinic mode $G_{BC} = G_{11} - G_{21}$

$$\nabla^2 G_{BC} - \gamma^2 G_{BC} = \delta(y - y_i) \tag{31}$$

$$(\frac{\partial^2}{\partial y^2} - k^2 - \gamma^2) G_{BC} = \delta(y - y_i) \tag{32}$$

$$\rightarrow G_{BC} = \frac{1}{2\sqrt{k^2+\gamma^2}} e^{(-\sqrt{k^2+\gamma^2}|y-y_i|)} \tag{33}$$

Therefore, the matrix elements G_{11} and G_{21} are:

$$G_{11} = (G_{BC} + G_{BT})\frac{1}{1+\delta} \tag{34a}$$

$$= (\frac{1}{2\sqrt{k^2+\gamma^2}} e^{(-\sqrt{k^2+\gamma^2}|y-y_i|)} + \frac{\delta}{2k} e^{(-k|y-y_i|)})\frac{1}{1+\delta} \tag{34b}$$

$$G_{21} = (G_{BT} - \delta G_{BC})\frac{1}{1+\delta} \tag{34c}$$

$$= (\frac{\delta}{2k} e^{(-k|y-y_i|)} - \frac{\delta}{2\sqrt{k^2+\gamma^2}} e^{(-\sqrt{k^2+\gamma^2}|y-y_i|)})\frac{1}{1+\delta} \tag{34d}$$

Similar methods for a lower layer anomaly of $\Delta_2\delta(y)\exp(ikx)$ allow us to find the Green's functions of G_{21} and $G22$:

$$G_{22} = (\frac{\delta}{2\sqrt{k^2+\gamma^2}} e^{(-\sqrt{k^2+\gamma^2}|y-y_i|)} + \frac{1}{2k} e^{(-k|y-y_i|)})\frac{1}{1+\delta} \tag{35a}$$

$$G_{12} = (\frac{1}{2k} e^{(-k|y-y_i|)} - \frac{1}{2\sqrt{k^2+\gamma^2}} e^{(-\sqrt{k^2+\gamma^2}|y-y_i|)})\frac{1}{1+\delta} \tag{35b}$$

Having computed the matrix elements of the Green's function matrix, we then find the matrix for PV gradient Δ, using Green's function G and basic flow U, and inverting the matrix.

$$U = G_y^0 \mathbf{\Delta} \tag{36}$$

We cannot just directly compute Δ by integrating the chosen velocity profile because of the jumps in potential vorticity.

We are then able to solve the eigenvalue problem in (2.3) to obtain the eigenvalues and get the most unstable growth rate c

$$M_{ij}\eta_j = c\eta_i \tag{37}$$

With the most unstable growth rate, we find its corresponding eigenvector/eigenmode η_i. We then take the amplitude of the eigenmode and look at their relative amplitude of contributions from different layers as outlined in the main text.

Jets on Giant Planets - A Tale of Two Forcings

Yaoxuan Zeng

December 18, 2023

1 Introduction

Giant planets are planets with thick atmosphere primarily made of hydrogen and helium. There are four giant planets in the solar system: two warmer gas giants, Jupiter and Saturn, and two colder ice giants, Uranus and Neptune. Jupiter and Saturn are generally considered to have three layers: a dense core with heavy elements at the center, a metallic hydrogen envelope as the middle layer, and a molecular hydrogen envelope as the outer layer (e.g. [20, 46, 39, 40]). More recent interior models of Jupiter that fit the data from Juno mission suggest Jupiter has a more dilute core – instead of a central core with pure heavy elements, it extends to a larger fraction of the planet and mixes with lighter elements ([3, 57], Fig. 1). Interior structure for Neptune and Uranus are less constrained due to the lack of observational data. Existing interior models universally suggest that the outer envelope of the two ice giants is highly enriched with heavy elements, and the concentration of the heavy elements increases towards the center [25, 38, 37, 42, 24].

Strong winds are observed in the outer envelope of the planets, but the deep interior are quiescent due to Ohmic dissipation (e.g., [35, 13, 52]). The cloud-level atmospheric circulations on the four giant planets are dominated by zonal jets. While there are almost a dozen alternating jets on Jupiter and Saturn, including a central prograde jet at the equator, Uranus and Neptune possess only three jets with the equatorial jet moving in the retrograde direction (e.g. [33, 16, 44, 15, 54, 45]) (Fig. 2). The mechanism behind the distinct jet structures observed on the two gas giants (Jupiter and Saturn) and the two ice giants (Uranus and Neptune) remains inconclusive.

One possible explanation has to do with the two different ways to sustain these zonal jets, one being the convection powered by the internal heating (e.g., [5, 6, 8, 9, 22, 21, 1, 29, 27, 51, 18, 17]) and the other being the baroclinic instability induced by the latitudinal variations of solar radiation (e.g., [58, 7, 49, 48, 32]). Using a thin-shell general circulation model, [47, 36] show that, when the solar forcing dominates, retrograde equatorial jet tends to form as baroclinic eddies pump momentum poleward, and when the parameterized convection dominates, prograde equatorial jet forms instead due to the equatorward momentum convergence by equatorial waves. However, although on Jupiter and Saturn the ratio between internal and solar energy input is much larger than that on Uranus, it is smaller than the ratio on Neptune, which does not seem to be consistent with prograde jet forming on Jupiter and Saturn and retrograde jet forming on Uranus and Neptune (Table 1). Also, with pure solar forcing, equatorial prograde jet is found to be able to form if water

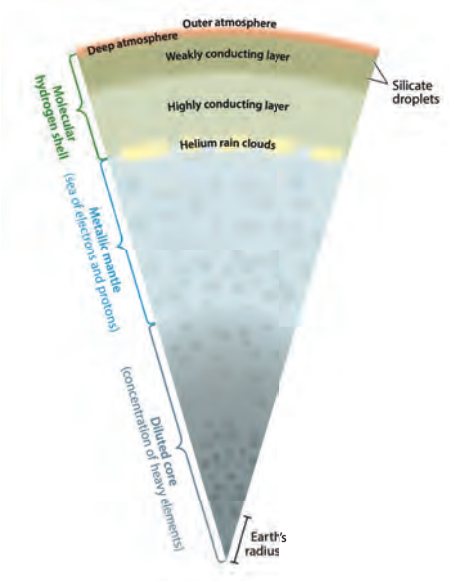

Figure 1: Our present view of Jupiter's internal structure, in the light of the Juno mission. Note the existence of no sharp boundary, but rather a continuous evolution of the material properties and composition along the radial direction. The grey circles in the mantle and core evidence that heavy elements are non-uniformly mixed with helium and hydrogen in these regions. Figure extracted from Fig. 4 in [55].

vapor condensation or large-scale energy dissipation by radiative relaxation is taken into account [48, 32], further complicating the situation. Another way to explain this phenomena is through deep-sphere convection with internal heating only, where the jets form via the momentum transport by the Reynolds stress. Studies have shown that under this scenario, jet can be in either direction depending on the Rayleigh number and Ekman number (e.g., [1, 2]). Challenges are there to couple the thin-shell dynamics and deep-sphere convection together to consider the combined effects of solar and internal heating [28].

Planet	Radius (10^7 m)	Mass (10^{26} kg)	Gravity (m s^{-2})	Rotation period (h)	Internal energy Q_b (W m^{-2})	Solar energy Q_s (W m^{-2})	Ratio Q_b/Q_s
Jupiter	7.13	19.0	22.9	9.84	5.44 ± 0.43	8.14 ± 0.40	0.668
Saturn	6.01	5.68	9.50	10.6	2.01 ± 0.14	2.59 ± 0.12	0.775
Uranus	2.55	0.868	8.69	17.9	0.042 ± 0.047	0.650 ± 0.046	0.065
Neptune	2.48	1.02	11.0	19.2	0.433 ± 0.046	0.268 ± 0.025	1.618

Table 1: Planetary parameters of the giant planets in the solar system. Data are taken from Table 2 & 3 in [43]. The internal energy and the solar energy are taken from [41].

How deep the cloud-level jet can penetrate into the interior is another interesting problem. The jet penetration depth on the giant planets can be determined through the gravity measurement or the Ohmic dissipation constraint. In a fast-rotating system, thermal-wind

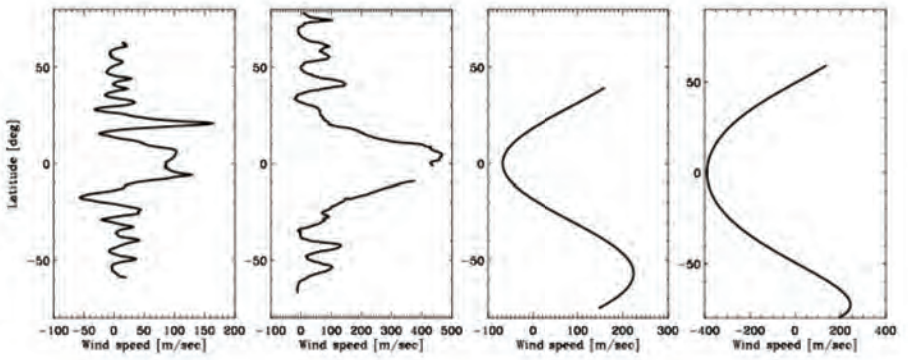

Figure 2: Prograde zonal wind at the cloud level in Jupiter, Saturn, Uranus, and Neptune (from left to right). Figure extracted from Fig. 6 in [50].

balance requires the vertical shear flow to be in balance with the meridional density gradient, which in turn leaves a signature on the gravitational field. Gravity measurement constrained the jet depth on Jupiter and Saturn to be ∼3000 km and ∼9000 km, respectively [31, 14]. Gravity measurement for Uranus and Neptune are much less abundant, leading to an estimate of the jet depth to be no more than about 1000 km for both planets [30]. On the other hand, from the energetic point of view, the Ohmic dissipation should not surpass the net luminosity of the planet, which gives an energy constraint or an entropy constraint (e.g., [34, 52]). For Jupiter and Saturn, the Ohmic dissipation constraint gives the same estimation as the gravitational measurements [35]. For Uranus and Neptune, due to lack of constraint on the electrical conductivity profile on these two ice giants, the es-timation of the penetration depth can vary from ∼2000 km to ∼5000 km for Uranus and from ∼1000 km to ∼4000 km for Neptune [34, 52].

Here, we use a two-layer Boussinesq Quasi-Geostrophic (QG) model to investigate the direction of equatorial jet forced jointly by both solar forcing and convection, and how it is affected by the penetration depth of the jets. Solar forcing is represented by tilting the interface separating the two layers, and convection is represented by stochastic forcing in the lower layer. While being highly idealized, this process-based model allows us to separate key physical processes and the effects of convective forcing and solar forcing much more easily, and additionally, it allows us to get closer to the dynamical regime of giant planets, which is usually hard to achieve in 3D simulations. Section 2 derives the two-layer Boussinesq QG model. Section 3 shows theoretical analysis of the jet formation, jet direction, and jet energy in different scenarios. Section 4 shows numerical simulation results and compares them with the theories. Section 5 provides discussion and concluding remarks.

2 Two-Layer Model for the Atmosphere on Giant Planets

Here, we follow [59] to derive the governing equations of the two-layer QG model under Boussinesq approximation.

2.1 Atmosphere as a two-layer system

We take the atmosphere on giant planets as a two-layer system. The two layers correspond to two forcings on the giant planets: at the very surface, there is a "weather layer" where there is stable stratification set by the solar radiation. Below that, interior heating results in convection that dominates the atmosphere layer, making this "convective layer" unstratified.

We use two coordinate systems in the derivation. The first one is the spherical coordinate $(\boldsymbol{\theta},\ \boldsymbol{\phi},\ \boldsymbol{r})$, where $\boldsymbol{\theta}$ is longitude, $\boldsymbol{\phi}$ is latitude, and $\boldsymbol{r}$ is radius. The second one is a local Cartesian coordinate $(\boldsymbol{x},\ \boldsymbol{y},\ \boldsymbol{z})$, where $\boldsymbol{x}$ is the local azimuthal direction, $\boldsymbol{y}$ is the direction pointing towards the rotational axis, and $\boldsymbol{z}$ is the direction of the planetary rotation. Note that locally $\boldsymbol{\theta}$ and $\boldsymbol{x}$ are the same direction. We take subscript 1 as the upper "weather layer" and 2 as the lower "convective layer", and quantities without prime for the rotational direction and quantities with prime for the radial direction (Fig. 3).

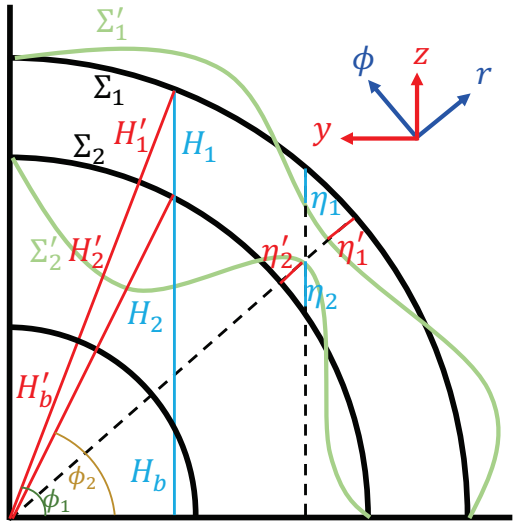

Figure 3: Schematics of the coordinate systems and notations. Σ_1 and Σ_2 are the reference surface of the upper and lower layer, respectively; Σ_1' and Σ_2' are the perturbed surface of the upper and lower layer, respectively. The reference height is $H_1' + H_2' + H_b'$ in the radial direction and $H_1 + H_2 + H_b$ in the direction parallel to rotation for the surface of the upper layer Σ_1, is $H_2' + H_b'$ in the radial direction and $H_2 + H_b$ in the direction parallel to rotation for the interface between two layers Σ_2, and is H_b' in the radial direction and H_b in the direction parallel to rotation for the bottom of the lower layer, respectively. The distance between Σ_1' and Σ_1 is η_1' in the radial direction and η_1 in the direction parallel to rotation. The distance between Σ_2' and Σ_2 is η_2' in the radial direction and η_2 in the direction parallel to rotation.

2.2 QG vorticity equation

We begin with the momentum equation for Boussinesq fluid:

$$\frac{D\boldsymbol{v}}{Dt} + 2\Omega\boldsymbol{z} \times \boldsymbol{v} = -\nabla\Phi + b\boldsymbol{r} + \boldsymbol{F}, \tag{1}$$

where $\boldsymbol{v}$ is the 3-D velocity, Ω is the planetary rotation rate, $\Phi = \delta p/\rho_0$ where δp is the pressure anomaly and ρ_0 is a reference density, $b = -g\delta\rho/\rho_0$ is the buoyancy where g is the gravitational acceleration and $\delta\rho$ is the density anomaly, and $\boldsymbol{F}$ includes all forcing and dissipation terms. Taking the curl of Eq. 1, we have

$$\frac{D\boldsymbol{\omega}}{Dt} = (2\Omega\boldsymbol{z} + \boldsymbol{\omega}) \cdot \nabla\boldsymbol{v} + \nabla \times (b\boldsymbol{r}) + \nabla \times \boldsymbol{F}, \tag{2}$$

where $\boldsymbol{\omega} = \nabla \times \boldsymbol{v}$ is vorticity. By taking z component of the vorticity ($\zeta = \boldsymbol{z} \cdot \boldsymbol{\omega}$) in Eq. 2, we have

$$\frac{D\zeta}{Dt} = (2\Omega + \zeta)\frac{\partial w}{\partial z} + \boldsymbol{\omega_h} \cdot \nabla w + \nabla b \cdot (\boldsymbol{r} \times \boldsymbol{z}) + F, \tag{3}$$

where $\boldsymbol{\omega_h}$ is the horizontal component of the vorticity. The Rossby number of the atmospheric motion on giant planets is much smaller than unity, so that we can make the Quasi-Geostrophic (QG) assumption [56]. In the QG assumption, we assume that the relative vorticity is much smaller than the planetary vorticity ($|\boldsymbol{\omega}| \ll 2\Omega$), and the geostrophic component of the velocity is much larger than the ageostrophic component of the velocity. We hence neglect the ageostrophic component of the velocity in the equation except in the stretching term, $\partial w/\partial z$, and neglect the horizontal component of the vorticity. The geostrophic velocity $\boldsymbol{u_g} = u_g\boldsymbol{x} + v_g\boldsymbol{y}$ is divergent-free, so that we can use a streamfunction Ψ to characterize the flow, where $v_g = \partial\Psi/\partial x$ and $u_g = -\partial\Psi/\partial y$. Eq. 3 then becomes

$$\frac{D\nabla^2\Psi}{Dt} = \frac{\partial\nabla^2\Psi}{\partial t} + J(\Psi, \nabla^2\Psi) = 2\Omega\frac{\partial w}{\partial z} + \nabla b \cdot (\boldsymbol{r} \times \boldsymbol{z}) + F, \tag{4}$$

where $J(\Psi, \nabla^2\Psi) = \partial\Psi/\partial x\ \partial\nabla^2\Psi/\partial y - \partial\Psi/\partial y\ \partial\nabla^2\Psi/\partial x$ is the advection term.

The atmospheric dynamics on giant planets are quite uniform along the axis of rotation in the convective layer with strong rotation. We further reduce the equation into a 2-dimensional system by taking the vertical average of the equation:

$$\frac{D\nabla^2\bar{\Psi}}{Dt} = \frac{2\Omega}{H}(w_t - w_b) + \nabla\bar{b} \cdot (\boldsymbol{r} \times \boldsymbol{z}) + \bar{F}, \tag{5}$$

where $H = \int_{z_b}^{z_t} dz$ is the depth of the layer along the axis of rotation, and overbar indicates averages along z ($\bar{A} = \int_{z_b}^{z_t} A dz / \int_{z_b}^{z_t} dz$). The subscript t indicates the top of the layer and b indicates the bottom of the layer. For simplicity, we will drop the overbar and all quantities will be averages in z.

2.3 Coupling of two layers

The two layers are coupled by the interface displacement. Upward shift of the interface would compress the upper layer and stretch the lower layer and vice versa. The compression and stretching of each layer would alter the relative vorticity as requested by the potential vorticity conservation (note that buoyancy terms drop out as buoyancy anomalies are represented by the interface displacement in the two-layer model):

$$\frac{D\nabla^2\Psi_1}{Dt} = \frac{2\Omega}{H_1}(w_{1t} - w_{1b}) + F_1, \tag{6}$$

$$\frac{D\nabla^2\Psi_2}{Dt} = \frac{2\Omega}{H_2}(w_{2t} - w_{2b}) + F_2. \tag{7}$$

At the boundaries, we have

$$w_{1t} = \frac{D}{Dt}(\eta_1 + H_1 + H_2 + H_b), \tag{8}$$

$$w_{1b} = w_{2t} = \frac{D}{Dt}(\eta_2 + H_2 + H_b), \tag{9}$$

$$w_{2b} = \frac{D}{Dt}H_b. \tag{10}$$

We hence have

$$\frac{D\nabla^2\Psi_1}{Dt} = \frac{2\Omega}{H_1}\frac{D}{Dt}(\eta_1 + H_1 - \eta_2) + F_1, \tag{11}$$

$$\frac{D\nabla^2\Psi_2}{Dt} = \frac{2\Omega}{H_2}\frac{D}{Dt}(\eta_2 + H_2) + F_2. \tag{12}$$

The geostrophic balance allows us to connect the velocity field to the interface perturbation. The geostrophic balance gives

$$\Psi_{1,2} = \frac{p_{1,2}}{2\Omega\rho_{1,2}}, \tag{13}$$

where p is the pressure and ρ is the density. Note that the pressure gradient is determined by the surface perturbation in the two-layer model, and we therefore have

$$p_1 = \rho_1 g\left[(\eta_1 + H_1 + H_2 + H_b)\sin\phi_1 - \int v_1\cos\phi_1 dt\right], \tag{14}$$

$$p_2 = p_1 + (\rho_2 - \rho_1)g\left[(\eta_2 + H_2 + H_b)\sin\phi_2 - \int v_2\cos\phi_2 dt\right], \tag{15}$$

where ϕ_1 and ϕ_2 are the latitudes, and v_1 and v_2 are the meridional velocities at the surface of the upper layer (layer 1, Σ_1) and the lower layer (layer 2, Σ_2), respectively. The last term accounts for the contribution from the radial projection of the interface perturbation in the y direction. Combining Eq. 13-15, we have

$$\frac{D}{Dt}(\eta_1 + H_1 - \eta_2) = \frac{D}{Dt}\left[\frac{2\Omega}{g\sin\phi_1}\Psi_1 - \frac{2\Omega}{g'\sin\phi_2}\left(\Psi_2 - \frac{\rho_1}{\rho_2}\Psi_1\right)\right] + v_1\cot\phi_1 - v_2\cot\phi_2, \tag{16}$$

$$\frac{D}{Dt}(\eta_2 + H_2) = \frac{D}{Dt}\left[\frac{2\Omega}{g'\sin\phi_2}\left(\Psi_2 - \frac{\rho_1}{\rho_2}\Psi_1\right)\right] - \frac{DH_b}{Dt} + v_2\cot\phi_2, \tag{17}$$

where $g' = g(\rho_2 - \rho_1)/\rho_2$ is the reduced gravity. We further assume that $\rho_2 \approx \rho_1$ and $g' \ll g$. Note that H_1, H_2, and H_b are just functions of y, and the shell geometry gives that $\cot\phi_1 = \partial(H_1 + H_2 + H_b)/\partial y$ and $\cot\phi_2 = \partial(H_2 + H_b)/\partial y$. Since v_1 and v_2 are the velocities at the same boundary as ϕ_1 and ϕ_2, we have $v_1 \cot\phi_1 = D(H_1 + H_2 + H_b)/Dt$ and $v_2 \cot\phi_2 = D(H_2 + H_b)/Dt$. The equation becomes

$$\frac{D\nabla^2\Psi_1}{Dt} + \beta_1\frac{\partial\Psi_1}{\partial x} = -\frac{4\Omega^2}{g'H_1}\frac{D}{Dt}\left(\frac{\Psi_2 - \Psi_1}{\sin\phi_2}\right) + F_1, \tag{18}$$

$$\frac{D\nabla^2\Psi_2}{Dt} + \beta_2\frac{\partial\Psi_2}{\partial x} = \frac{4\Omega^2}{g'H_2}\frac{D}{Dt}\left(\frac{\Psi_2 - \Psi_1}{\sin\phi_2}\right) + F_2, \tag{19}$$

where

$$\beta_{1,2} = -\frac{2\Omega}{H_{1,2}}\frac{dH_{1,2}}{dy} \tag{20}$$

is the topographic β. The topographic β is negative outside the tangent cylinder and positive inside the tangent cylinder, where the tangent cylinder is a cylinder that is parallel to the rotational axis and tangent to the bottom of the layer (Fig. 4). We write the model equation at the interface between the two layers so that ϕ_2 is the local latitude, and we will drop the subscript 2 in the rest of the manuscript for simplicity.

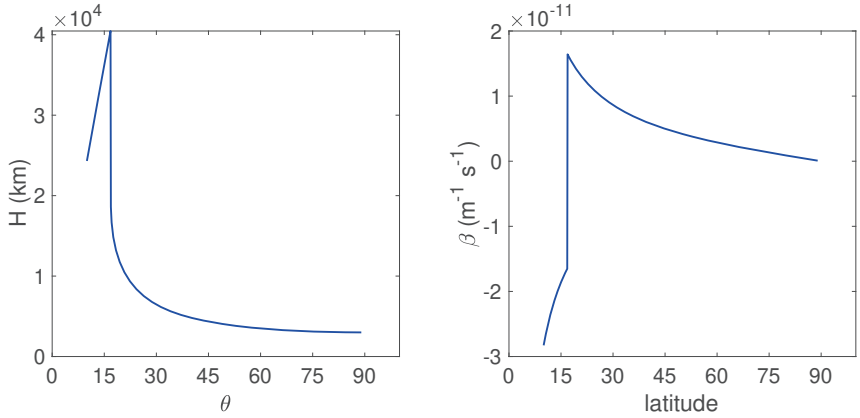

Figure 4: The layer thickness (left) and the topographic β (right) as a function of latitude, using Jupiter's parameter: planetary radius $a = 70000$ km, radial layer depth $d = 3000$ km, and rotation rate $\Omega = 1.7453 \times 10^{-4}$ s^{-1}. Note that β should reach infinity at the tangent cylinder and an approximate solution is shown here.

2.4 Convective forcing

The convective forcing (only applied to the lower layer) is represented by a stochastic forcing following [10, 11, 12, 53]:

$$F_{conv} = \sqrt{\frac{2\epsilon_c k_f^2}{\delta t}}\Sigma_n \frac{e^{-\frac{(k_n - k_f)^2}{2\delta k^2}} e^{i\boldsymbol{k_n}\cdot\boldsymbol{r} + \phi_n}}{C}, \tag{21}$$

where ϵ_c is the bottom energy injection rate per unit mass, k_f is the forcing wave number, $k_n = (k_x^2 + k_y^2)^{1/2}$ is the total wave number, δt is the time step, δk is the forcing wave number bandwidth, ϕ_n is a random phase which is updated after each time step, and C is a normalization factor to make the amplitude of the summation to unity. In our model k_f is chosen as $k_f = 2\pi/(4dL)$ where dL is the resolution (grid scale) of our model so that the scale of the stochastic forcing is small enough to allow for inverse cascade and is large enough to avoid being dissipated by the small-scale hyper-viscosity.

2.5 Solar forcing

The latitudinal variation of the solar heating modifies the meridional temperature gradient and provides potential energy. Since the tilting of the interface represents the meridional temperature gradient in a two-layer model, we apply solar forcing by adding an additional vertical velocity w_s through the interface. When interface is shifted upward, temperature goes down as the lower level cold fluid occupies a larger portion:

$$T' = -\Delta T_z \frac{\eta_2'}{H_1'}. \tag{22}$$

The interface perturbation can be expressed by the streamfunction via the geostrophic balance:

$$\eta_2' = \frac{2\Omega}{g'}(\Psi_2 - \Psi_1), \tag{23}$$

where the reduced gravity can be related to the temperature contrast between the two layers:

$$g' = \alpha_T g \Delta T_z, \tag{24}$$

where α_T is the thermal expansivity. The upper layer heat budget gives

$$\frac{S_0}{\pi}\cos\phi = c_p \rho w_s \Delta T_z + \sigma T^4 \approx c_p \rho w_s \Delta T_z + \sigma T_0^4 + 4\sigma T_0^3 T', \tag{25}$$

where S_0 is the solar constant, c_p is the heat capacity, σ is the Stefan-Boltzmann constant, and T_0 is the radiative equilibrium temperature such that $S_0 = 4\sigma T_0^4$. By solving w_s from Equations 22-25, the solar forcing can therefore be represented by

$$w_s = \frac{2\Omega}{g'}\frac{\Psi_2 - \Psi_1 + \Psi_s}{\tau_{rad}}, \tag{26}$$

where Ψ_s represents the streamfunction corresponding to radiative equilibrium state, and τ_{rad} represents the radiative time scale, following

$$\Psi_s = \frac{\alpha_T g H_1' T_0}{2\Omega}\left(\frac{\cos\phi}{\pi} - \frac{1}{4}\right),\ \tau_{rad} = \frac{c_p \rho H_1'}{4\sigma T_0^3}. \tag{27}$$

This solar-forcing induced vertical pumping w_s would change the vorticity of the two layers through $F_{s1} = -2\Omega w_s/H_1$, $F_{s2} = 2\Omega w_s/H_2$. Including both the convective forcing and the solar forcing to the model equations, we have

$$\frac{D\nabla^2\Psi_1}{Dt} + \frac{4\Omega^2}{g'H_1}\frac{D}{Dt}\left(\frac{\Psi_2-\Psi_1}{\sin\phi_2}\right) + \beta_1\frac{\partial\Psi_1}{\partial x} = -\frac{4\Omega^2}{g'H_1}\frac{\Psi_2-\Psi_1+\Psi_s}{\tau_{rad}} + D_1, \tag{28}$$

$$\frac{D\nabla^2\Psi_2}{Dt} - \frac{4\Omega^2}{g'H_2}\frac{D}{Dt}\left(\frac{\Psi_2-\Psi_1}{\sin\phi_2}\right) + \beta_2\frac{\partial\Psi_2}{\partial x} = \frac{4\Omega^2}{g'H_2}\frac{\Psi_2-\Psi_1+\Psi_s}{\tau_{rad}} + F_{conv} + D_2, \tag{29}$$

where D_1 and D_2 are dissipation terms.

To better illustrate the effect of the solar forcing, we introduce "perturbed" stream functions from the reference stream function Ψ_s, which represents the thermal wind shear in the two layers. We set the background thermal wind velocity in the two layers (U_{1s} and U_{2s}) such that the net zonal momentum is zero ($H_1'U_{1s} + H_2'U_{2s} = 0$). Therefore, we define the perturbed stream functions as $\Psi_1^* = \Psi_1 - (1-\gamma)\Psi_s$ and $\Psi_2^* = \Psi_2 + \gamma\Psi_s$, where $\gamma = H_1'/(H_1' + H_2')$ is the ratio of the upper layer depth to the total depth (in the radial direction). Note that Ψ_s is only a function of y, and that the thermal wind shear

$$U_s = -\frac{\partial\Psi_s}{\partial y} = \frac{\alpha_T g H_1' T_0}{2\pi\Omega(H_2' + H_b')} \tag{30}$$

is a constant. By substituting Ψ_1 and Ψ_2 by Ψ_1^* and Ψ_2^*, we have

$$\begin{aligned}&\left[\frac{D^*}{Dt} + (1-\gamma)U_s\frac{\partial}{\partial x}\right]\nabla^2\Psi_1^* + \frac{4\Omega^2}{g'H_1}\left(\frac{D^*}{Dt} + (1-\gamma)U_s\frac{\partial}{\partial x}\right)\left(\frac{\Psi_2^*-\Psi_1^*}{\sin\phi}\right)\\ &+ (\beta_1+\beta_{1s})\frac{\partial\Psi_1^*}{\partial x} = -\frac{4\Omega^2}{g'H_1}\frac{\Psi_2^*-\Psi_1^*}{\tau_{rad}} + D_1,\end{aligned} \tag{31}$$

$$\begin{aligned}&\left[\frac{D^*}{Dt} - \gamma U_s\frac{\partial}{\partial x}\right]\nabla^2\Psi_2^* - \frac{4\Omega^2}{g'H_2}\left(\frac{D^*}{Dt} - \gamma U_s\frac{\partial}{\partial x}\right)\left(\frac{\Psi_2^*-\Psi_1^*}{\sin\phi}\right)\\ &+ (\beta_2+\beta_{2s})\frac{\partial\Psi_2^*}{\partial x} = F_{conv} + \frac{4\Omega^2}{g'H_2}\frac{\Psi_2^*-\Psi_1^*}{\tau_{rad}} + D_2,\end{aligned} \tag{32}$$

where

$$\beta_{1,2s} = \pm\frac{4\Omega^2}{g'H_{1,2}}\frac{\partial}{\partial y}\frac{\Psi_s}{\sin\phi} = \pm\frac{4\Omega^2 U_s}{g'H_{1,2}\sin^3\phi}\left(1 - \frac{\pi\cos\phi}{4}\right) \tag{33}$$

are the β effect induced by the interface tilt by the solar forcing. Therefore, the solar forcing has three effects: a thermal wind shear U_s which sets the background velocity field, an effective β_s which modulates the planetary vorticity gradient, and a radiative damping term which restores the interface tilt to that induced by differential solar heating (Eq. 31 & 32). We will drop the stars hereafter for simplicity.

2.6 Dissipation

We apply both small-scale hyper-viscosity and large-scale linear damping to our models. In the 2-D system, the energy cascades to large scale and is damped by large-scale dissipation. We set the large-scale dissipation as a linear damping to zero with a time scale of τ_m in our model, representing the effect of Ohmic dissipation at the bottom and the effect of Ekman

layer at the boundary [19]. To ensure numerical stability, we also apply a hyper-viscosity ν_h to dissipate grid-scale noises. By taking all the forcing and dissipation terms into account, the equations are

$$\begin{aligned}&\left[\frac{D}{Dt}+(1-\gamma)U_s\frac{\partial}{\partial x}\right]\nabla^2\Psi_1+\frac{4\Omega^2}{g'H_1}\left(\frac{D}{Dt}+(1-\gamma)U_s\frac{\partial}{\partial x}\right)\left(\frac{\Psi_2-\Psi_1}{\sin\phi}\right)\\&+(\beta_1+\beta_{1s})\frac{\partial\Psi_1}{\partial x}=-\frac{4\Omega^2}{g'H_1}\frac{\Psi_2-\Psi_1}{\tau_{rad}}-\nu_{h1}\nabla^6\Psi_1-\frac{\nabla^2\Psi_1}{\tau_{m1}},\end{aligned}\tag{34}$$

$$\begin{aligned}&\left[\frac{D}{Dt}-\gamma U_s\frac{\partial}{\partial x}\right]\nabla^2\Psi_2-\frac{4\Omega^2}{g'H_2}\left(\frac{D}{Dt}-\gamma U_s\frac{\partial}{\partial x}\right)\left(\frac{\Psi_2-\Psi_1}{\sin\phi}\right)\\&+(\beta_2+\beta_{2s})\frac{\partial\Psi_2}{\partial x}=F_{conv}+\frac{4\Omega^2}{g'H_2}\frac{\Psi_2-\Psi_1}{\tau_{rad}}-\nu_{h2}\nabla^6\Psi_2-\frac{\nabla^2\Psi_2}{\tau_{m2}}.\end{aligned}\tag{35}$$

2.7 Non-dimensionalize the equation

We non-dimensionalize the equations using radius at the layer interface $H_2'+H_b'$ as the length scale and the reverse of the Coriolis parameter $(2\Omega)^{-1}$ as the time scale. As a result, we have the non-dimensional variables

$$\begin{aligned}&\tilde{t}=2\Omega t,\quad(\tilde{x},\tilde{y})=\frac{(x,y)}{H_2'+H_b'},\quad\tilde{U}_s=\frac{U_s}{2\Omega(H_2'+H_b')}=\frac{\alpha_T g H_1' T_0}{4\pi\Omega^2(H_2'+H_b')^2},\\&\tilde{\Psi}=\frac{\Psi}{2\Omega(H_2'+H_b')^2},\quad\tilde{\beta}=\beta\frac{H_2'+H_b'}{2\Omega},\quad\tilde{\epsilon}_c=\frac{\epsilon_c}{8\Omega^3(H_2'+H_b')^2},\\&\tilde{\tau}_{rad}=2\Omega\tau_{rad}=\frac{\Omega c_p\rho H_1'}{2\sigma T_0^3},\quad\tilde{\nu}_h=\frac{\nu_h}{2\Omega(H_2'+H_b')^4},\quad\tilde{\tau}_m=2\Omega\tau_m.\end{aligned}\tag{36}$$

The non-dimensionalized equation becomes

$$\begin{aligned}&\left[\frac{\tilde{D}}{D\tilde{t}}+(1-\gamma)\tilde{U}_s\frac{\partial}{\partial\tilde{x}}\right]\tilde{\nabla}^2\tilde{\Psi}_1+\frac{Fr}{\gamma}\left(\frac{\tilde{D}}{D\tilde{t}}+(1-\gamma)\tilde{U}_s\frac{\partial}{\partial\tilde{x}}\right)\left(\frac{\tilde{\Psi}_2-\tilde{\Psi}_1}{\sin\phi}\right)\\&+\left[B_1(\phi)+\frac{Fr}{\gamma}\tilde{U}_sB_s(\phi)\right]\frac{\partial\tilde{\Psi}_1}{\partial\tilde{x}}=-\frac{Fr}{\gamma}\frac{\tilde{\Psi}_2-\tilde{\Psi}_1}{\tilde{\tau}_{rad}}-\tilde{\nu}_{h1}\tilde{\nabla}^6\tilde{\Psi}_1-\frac{\tilde{\nabla}^2\tilde{\Psi}_1}{\tilde{\tau}_{m1}},\end{aligned}\tag{37}$$

$$\begin{aligned}&\left[\frac{\tilde{D}}{D\tilde{t}}-\gamma\tilde{U}_s\frac{\partial}{\partial\tilde{x}}\right]\tilde{\nabla}^2\tilde{\Psi}_2-\frac{Fr}{1-\gamma}\left[\frac{\tilde{D}}{D\tilde{t}}-\gamma\tilde{U}_s\frac{\partial}{\partial\tilde{x}}\right]\left(\frac{\tilde{\Psi}_2-\tilde{\Psi}_1}{\sin\phi}\right)\\&+\left[B_2(\phi)-\frac{Fr}{1-\gamma}\tilde{U}_sB_s(\phi)\right]\frac{\partial\tilde{\Psi}_2}{\partial\tilde{x}}=\tilde{F}_{conv}-\frac{Fr}{1-\gamma}\frac{\tilde{\Psi}_2-\tilde{\Psi}_1}{\tilde{\tau}_{rad}}-\tilde{\nu}_{h2}\tilde{\nabla}^6\tilde{\Psi}_2-\frac{\tilde{\nabla}^2\tilde{\Psi}_2}{\tilde{\tau}_{m2}},\end{aligned}\tag{38}$$

where

$$B_1(\phi)=B(\phi)=\frac{\cos\phi}{\sin^2\phi},\ B_2=\begin{cases}-B(\phi) & \text{if } |\phi|<|\phi_c|\\ B(\phi) & \text{if } |\phi|>|\phi_c|\end{cases},\ B_s=\frac{1}{\sin^3\phi}\left(1-\frac{\pi\cos\phi}{4}\right)\tag{39}$$

are β profiles as a function of latitude where $\phi_c = \arccos\left(H_b'/(H_b' + H_2')\right)$ is the latitude of the tangent cylinder in the lower layer, and

$$Fr = \frac{4\Omega^2(H_2' + H_b')^2}{g'(H_1' + H_2')} \tag{40}$$

is the Froude number which describes the stratification. Note that the solar-induced effective β is not an independent parameter ($\tilde{\beta}_s \propto Fr\tilde{U}_s$). In the rest of the manuscript, we will use the non-dimensional equations and variables, and drop the tilde for simplicity.

3 Theories of Jet Formation

In this section, we will discuss the factors that determine the jet direction and jet energy.

3.1 Convective forcing

3.1.1 Jet formation

With convective forcing, the jet formation process is associated with the inverse cascade of the energy. In a 2-D system, small-scale turbulence will cascade inversely towards large scale. In the inverse cascade process, the β effect brings in anisotrophy. When the β effect becomes important at the β scale ($k_\beta \sim \epsilon^{-1/5}\beta^{3/5}$ where ϵ is the energy cascade rate), the energy cascades to zonal kinetic energy, forming zonal jets (Fig. 5). Eventually, large-scale dissipation dissipates the energy and the cascades terminates at the frictional Rhines scale ($k_{Rh} \sim \epsilon^{-1/4}\beta^{1/2}\tau^{m1/4}$).

3.1.2 Jet direction

Convective forcing will result in strong mixing in the lower layer, so that the potential vorticity (PV) q, as a conserved quantity, tends to be well mixed. The zonal-mean PV can be written as

$$\bar{q} = \bar{\zeta} + \int \beta dy = -\frac{\partial \bar{u}}{\partial y} + \int \beta dy. \tag{41}$$

Consider a meridional range where the PV is well mixed ($\bar{q}(y) = q_0$), and take $\langle\beta\rangle$ as the average β in the range we consider, we can solve for the zonal-mean zonal velocity profile:

$$\bar{u} = \frac{1}{2}\langle\beta\rangle y^2 - q_0 y + C_u, \tag{42}$$

where C_u is an integral constant to conserve momentum. If we take $q_0 = C_u = 0$, we come up with a scaling of the velocity after the PV mixing process as $\bar{u}^2 \sim \langle\beta\rangle^2 L_y^4$. This energy cannot exceed the initial kinetic energy in the area, so that we have $u_i^2 \sim \langle\beta\rangle^2 L_y^4$ where u_i^2 is the averaged initial kinetic energy. The length scale that PV can be mixed is hence

$$L_y \sim \sqrt{\frac{|u_i|}{\langle\beta\rangle}}. \tag{43}$$

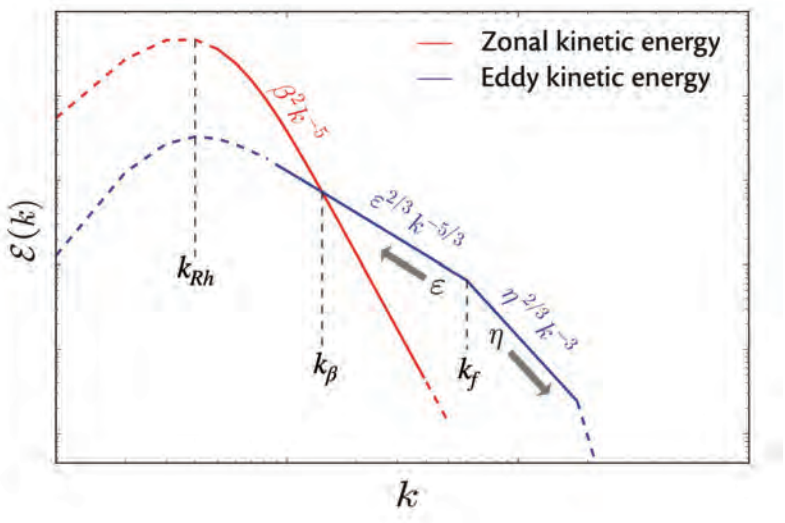

Figure 5: Sketch of the energy spectrum for the inverse cascade of 2-D turbulence on a β-plane. For forced turbulence at the forcing scale k_f, its enstrophy $Z = \zeta^2/2$ will cascade to small scale at a rate of η and its energy $E = |\boldsymbol{u}|^2/2$ will inversely cascade to large scale at a rate of ϵ, where $\eta = k_f^2 \epsilon$. When the inverse cascade hits the β scale k_β, the energy will cascade to zonal kinetic energy. When the cascade hits the frictional Rhines scale k_{Rh}, the energy will be dissipated and the inverse cascade ends. This figure is taken from Fig. 12.5 in [56] with some modification.

If L_y is smaller than the domain size, PV can only be mixed regionally and form staircases, combined with prograde and retrograde jets [56]. Let's consider the PV mixing region at the equator. If we assume symmetry across the equator, $\partial \bar{u}/\partial y = 0$, so that $q_0 = 0$. By further assuming that the mean momentum is zero (which determines the constant C_u), there will be super-rotation ($\bar{u} > 0$ at the equator) if $\langle \beta \rangle < 0$ and sub-rotating ($\bar{u} < 0$ at the equator) if $\langle \beta \rangle > 0$.

If the atmosphere is deep on giant planets, the region outside the tangent cylinder where $\beta < 0$ is large, so that the averaged $\langle \beta \rangle$ is more likely negative and there would more likely be prograde jets at the equator. On the other hand, if the atmosphere is shallow on giant planets, the region outside the tangent cylinder where $\beta < 0$ is small, so that the averaged $\langle \beta \rangle$ is more likely positive and there would more likely be retrograde jets at the equator. Note that in this case, "deep" and "shallow" is compared with the length scale where PV is mixed near the equator.

3.1.3 Jet energy

In a 2-D system, the energy inversely cascades to large scale, so that the energy dissipation is mainly at large scale. If we assume that the large scale dissipation to be linear damping with a momentum damping time scale τ_m, the energy dissipation rate would be

$$\epsilon_{diss} = -\left\langle \boldsymbol{u} \cdot \frac{\boldsymbol{u}}{\tau_m} \right\rangle = -\frac{\langle \boldsymbol{u}^2 \rangle}{\tau_m}, \tag{44}$$

where $\langle\rangle$ denotes domain average. In an equilibrium state, the convective energy injection rate ϵ_c is balanced by the energy dissipation rate ϵ_{diss}, so that

$$\langle \boldsymbol{u}^2 \rangle = \epsilon_c \tau_m. \tag{45}$$

Here $\langle \boldsymbol{u}^2 \rangle$ is the total kinetic energy, and the jet energy (i.e., zonal-mean zonal kinetic energy $\langle \bar{\boldsymbol{u}}^2 \rangle$) is only part of it. The ratio of the jet energy to the total energy can be estimated based on the energy spectrum (Fig. 5). The energy spectrum is

$$E(k) = \begin{cases} K k_\beta^{10/3} \epsilon^{2/3} k^{-5}, & \text{if } k_{Rh} < k < k_\beta, \\ K \epsilon^{2/3} k^{-5/3}, & \text{if } k_\beta < k < k_f, \\ K k_f^{4/3} \epsilon^{2/3} k^{-3}, & \text{if } k_f < k < k_\nu, \end{cases} \tag{46}$$

where K is a constant determined by the total energy and k_ν is the scale where small-scale viscous dissipation dominates. The energy begins to cascade to jet energy at the β scale k_β and ends at the frictional Rhines scale k_{Rh}, so that the jet energy can be estimated by integrating the spectrum from k_{Rh} to k_β. Similarly, the eddy energy can be estimated by integrating the spectrum from k_β to k_ν. The ratio of the jet energy to the total energy is hence

$$\begin{aligned} \frac{E_{jet}}{E_{total}} &= \frac{\int_{k_{Rh}}^{k_\beta} K k_\beta^{10/3} \epsilon^{2/3} k^{-5} dk}{\int_{k_{Rh}}^{k_\beta} K k_\beta^{10/3} \epsilon^{2/3} k^{-5} dk + \int_{k_\beta}^{k_f} K \epsilon^{2/3} k^{-5/3} dk + \int_{k_f}^{k_\nu} K k_f^{4/3} \epsilon^{2/3} k^{-3} dk} \\ &= \frac{k_\beta^{10/3}(k_{Rh}^{-4} - k_\beta^{-4})}{k_\beta^{10/3}(k_{Rh}^{-4} - k_\beta^{-4}) + 6(k_\beta^{-2/3} - k_f^{-2/3}) + 2k_f^{4/3}(k_f^{-2} - k_\nu^{-2})}, \end{aligned} \tag{47}$$

and the jet energy can be estimated given the convective energy injection rate:

$$\langle \bar{\boldsymbol{u}}^2 \rangle = \epsilon_c \tau_m \frac{E_{jet}}{E_{total}}. \tag{48}$$

Besides the quantitative characterization of the ratio E_{jet}/E_{total}, we can have some more intuitive qualitative conclusions. The jet energy is the integral of the energy spectrum from k_{Rh} to k_β, which indicates if other parameters remain unchanged but there is a more clear separation between the frictional Rhines scale and the β scale, we would expect a larger ratio E_{jet}/E_{total}. Therefore, we can consider the ratio k_β/k_{Rh} to qualitatively characterize the ratio E_{jet}/E_{total}. Note that $k_\beta/k_{Rh} \sim \epsilon^{1/20} \beta^{1/10} \tau_m^{1/4}$, we hence have the qualitative conclusion that with a higher energy injection rate, higher β value (i.e. higher rotation rate or smaller planetary radius), or weaker large-scale damping (i.e. larger momentum damping time scale τ_m), there will be more energy stored in the jet energy instead of the eddy energy, and the jet will be more smooth.

3.2 Solar forcing

3.2.1 Jet formation

In Earth's atmosphere, differential solar forcing in latitudes creates the environment for baroclinic instability to develop at mid-latitude, and the resultant eddy momentum flux forms a strong prograde jet there. Similar mechanisms may play a role with solar forcing acting on the atmosphere of giant planets. The differential solar forcing will create meridional temperature gradient and develop potential energy. The meridional temperature gradient potentially makes the system unstable to baroclinic instability, converting potential energy to kinetic energy, triggering eddies and Rossby waves. As Rossby wave propagates and dissipates, the associated eddy momentum flux results in prograde and retrograde jets.

3.2.2 Jet direction

In the solar forcing scenario, jets form due to the momentum convergence and divergence by Rossby waves triggered by baroclinic instability. We calculate the most unstable modes and the associated momentum flux in the shallow and deep scenario (Fig. 6). In the shallow scenario, the most unstable mode locates at the highest latitudes. The eddies tilt northeast-southwest in the northern hemisphere (southeast-northwest in the southern hemisphere), resulting in a poleward momentum flux, converging prograde momentum from low latitudes to high latitudes. We therefore expect a retrograde jet at the equator and a prograde jet at the pole to form. In the deep scenario, instability happens near the critical latitude.

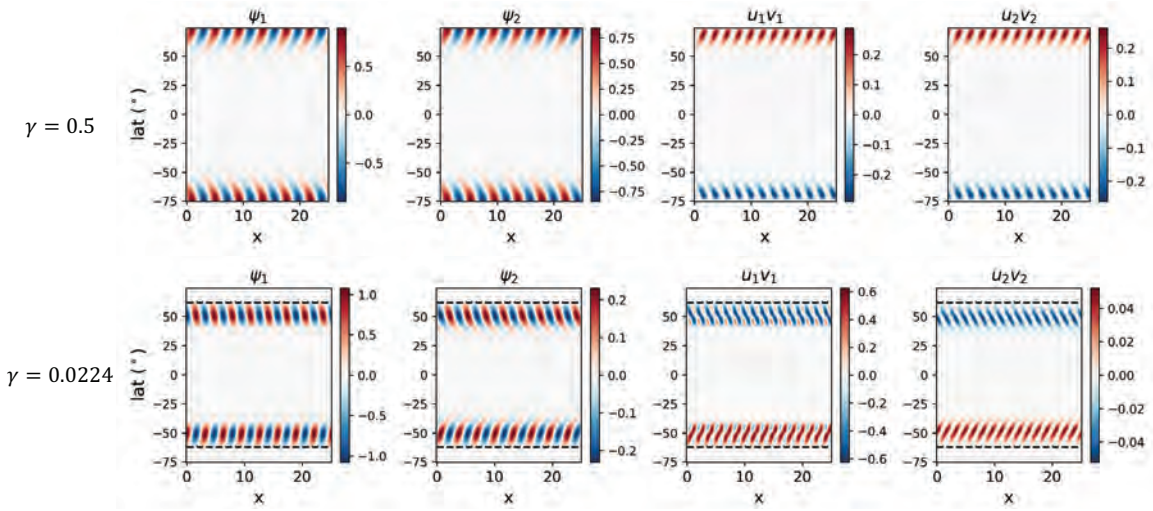

Figure 6: The most unstable mode and the associated momentum flux in the shallow lower layer scenario (upper row, with the same parameter as the simulation Ss_1) and the deep lower layer scenario (lower row, with the same parameter as the simulation Ds_1). The first and second columns show the perturbed stream function of two layers (Ψ_1 and Ψ_2) in the most unstable mode, respectively. The third and fourth columns show the associated momentum flux in two layers (u_1v_1 and u_2v_2), respectively.

The tilting direction of the eddies and hence the momentum flux is opposite to that in the shallow scenario, converging momentum from high latitudes to low latitudes, and we expect a prograde jet at the equator and a retrograde jet at the pole to form.

The momentum flux in the most unstable modes can be understood by the momentum transport associated with the propagation of Rossby waves. Assuming the eddy velocities to be geostrophic, we can define a stream function Ψ to describe the flow such that $u = -\partial\Psi/\partial y$ and $v = \partial\Psi/\partial x$. Taking $\Psi = \Psi_0 e^{i(kx+ly)}$, we have the momentum flux

$$uv^* = -\Psi_0^2 kl \propto -kl, \tag{49}$$

where v^* is the complex conjugate of v. The meridional group velocity of the Rossby wave is

$$c_{gy} = \frac{2\beta kl}{(k^2+l^2)^2}, \tag{50}$$

so that $uv^* \propto -c_{gy}/\beta$. At the wave source region, the energy has to propagate outwards so that the group velocity is divergent. Therefore, there is momentum convergence and prograde jet at the wave source region if $\beta > 0$ (which is the case for Earth) and momentum divergence and retrograde jet at the wave source region if $\beta < 0$. The opposite is true where the Rossby wave dissipates.

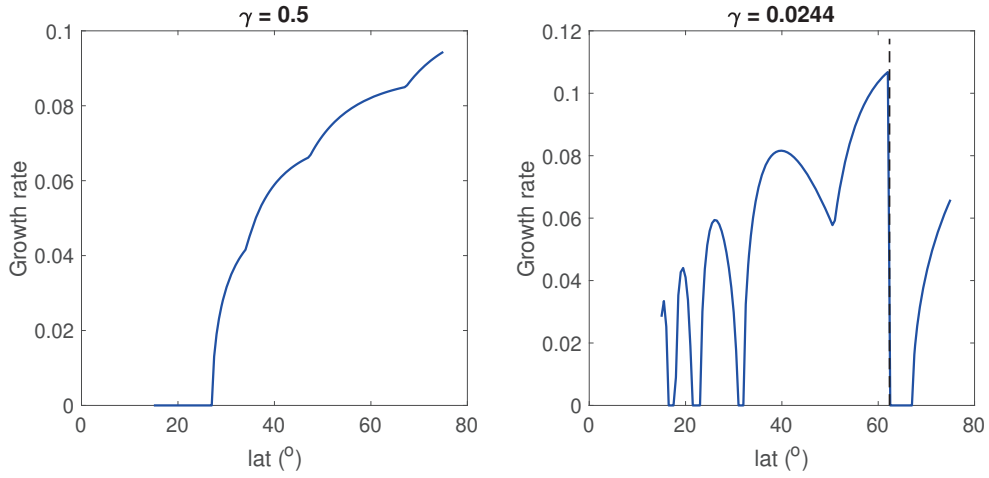

Figure 7: Growth rate of baroclinic instability in the shallow lower layer scenario (left panel, with the same parameter as the simulation Ss_1) and the deep lower layer scenario (right panel, with the same parameter as the simulation Ds_1) using the dispersion relationship derived in [28]. The black dashed line in the right panel shows the critical latitude ϕ_c (ϕ_c in the $\gamma = 0.5$ case is much smaller than 15°).

The remaining problem is hence where the wave source is, i.e. where instability would happen and what the sign of the local β is. In a two-layer system, the necessary condition for baroclinic instability is the upper layer β_{1t} and the lower layer β_{2t} take different signs, where β_t is the sum of the topographic β and the effective β_s induced by the interface tilt due to solar radiation. We calculate the instability growth rate using the dispersion

relationship derived in [28] (Fig. 7). The dispersion relationship in [28] uses a constant β for the entire domain, so we use the β value at each latitude to calculate the local growth rate.

In the shallow scenario, at low latitudes the topographic β_2 is positive, so that there is no instability. As latitude gets higher, the effective β_s begins to reverse the sign of the lower layer β_2 and instability happens. For barotropic Rossby waves, since the topographic β is positive in this case, there will be momentum convergence towards the wave source region, and prograde jets at high-latitudes are expected. The growth rate increases with latitude, indicating the instability is most likely to occur near the pole. Since there is no wave source near the equator, there is likely retrograde jet at the equator, i.e. sub-rotation in the shallow scenario.

In the deep scenario, at low latitudes the topographic β_2 is negative, so instability can occur anywhere outside the lower layer tangent cylinder. Inside the tangent cylinder (at higher latitudes), instability can only happen if the effective β_s can reverse the sign of the topographic β_2, similar to the shallow scenario. Growth rate increases with latitude as topography β_2 weakens. Given the parameters chosen here, the growth rate reaches its maximum near the tangent cylinder. Group velocity of the Rossby wave should always point away from the wave source. This requests an equatorward momentum flux on the poleward side of the wave source, opposite to the group velocity, due to the positive topographic β there. The equatorward side is more complicated because $\beta_1 > 0$ and $\beta_2 < 0$. Since the lower layer depth is much deeper than the upper layer, the barotropic β generally follows the lower layer (negative β), so the momentum flux should also be equatorward, which is in line with the group velocity. Taking both sides into account, we expect a momentum convergence towards low latitude to form prograde jet at the equator. Note that in Fig. 6, the momentum flux poleward of the critical latitude is close to zero, possibly because the topographic β abruptly changes sign at the critical latitude.

3.2.3 Jet energy

The jet speed is controlled by the energy injection rate, which can be estimated by writing down the energy equation of the two-layer system. For simplicity, we neglect the $\sin\phi$ factor and all dissipation terms (including the radiative damping terms):

$$\left[\frac{D}{Dt} + (1-\gamma)U_s\frac{\partial}{\partial x}\right]\left[\nabla^2\Psi_1 + \frac{Fr}{\gamma}(\Psi_2 - \Psi_1)\right] + \left[B_1(\phi) + \frac{Fr}{\gamma}U_sB_s(\phi)\right]\frac{\partial\Psi_1}{\partial x} = 0, \quad (51)$$

$$\left[\frac{D}{Dt} - \gamma U_s\frac{\partial}{\partial x}\right]\left[\nabla^2\Psi_1 - \frac{Fr}{1-\gamma}(\Psi_2 - \Psi_1)\right] + \left[B_2(\phi) - \frac{Fr}{1-\gamma}U_sB_s(\phi)\right]\frac{\partial\Psi_2}{\partial x} = 0. \quad (52)$$

By (51)$\times\gamma\Psi_1$+(52)$\times(1-\gamma)\Psi_2$ and take the global average (symbol $\langle\rangle$), with no-flux or periodic boundary conditions, we have

$$\frac{\partial}{\partial t}\left\langle\gamma\frac{|\nabla\Psi_1|^2}{2} + (1-\gamma)\frac{|\nabla\Psi_2|^2}{2} + Fr\frac{(\Psi_2-\Psi_1)^2}{2}\right\rangle = \gamma(1-\gamma)U_s\langle v_2q_2 - v_1q_1\rangle, \quad (53)$$

where $v_{1,2} = \partial\Psi_{1,2}/\partial x$ is the meridional eddy velocity, $q_1 = \nabla^2\Psi_1 + Fr(\Psi_2 - \Psi_1)/\gamma$ and $q_2 = \nabla^2\Psi_2 - Fr(\Psi_2 - \Psi_1)/(1-\gamma)$ are the eddy PV in two layers, respectively. Note that $\gamma|\nabla\Psi_1|^2/2 + (1-\gamma)|\nabla\Psi_2|^2/2$ is the depth-weighted kinetic energy and $Fr(\Psi_2 - \Psi_1)^2/2$ is the potential energy, Eq. 53 is the equation that describes the energy injection rate by solar forcing ϵ_s. On the right-hand-side, we assume that the eddy PV flux scales as some eddy diffusivity (D_e) multiplied by the background potential vorticity (Q) gradient, $\langle vq\rangle \sim -D_e\langle\partial Q/\partial y\rangle$, we have

$$\epsilon_s \sim \gamma(1-\gamma)U_s D_e \left\langle \frac{\partial Q_1}{\partial y} - \frac{\partial Q_2}{\partial y} \right\rangle \sim \gamma(1-\gamma)U_s D_e \left[B_1(\phi_0) - B_2(\phi_0) + \frac{FrU_s B_s(\phi_0)}{\gamma(1-\gamma)} \right], \tag{54}$$

where we assume that the energy injection happens at latitude ϕ_0 where instability happens. To determine the eddy diffusivity D_e in the above equation, we need an estimate of characteristic length scale and velocity of eddies. Following [23, 26], the length scale scales with the Rhine scale k_{Rh}^{-1}, and the characteristic velocity should be jointly determined by the inverse cascade rate ϵ_s and k_{Rh}, so D_e can be written as

$$D_e = k_{De}\epsilon_s^{1/3} k_{Rh}^{-4/3}, \tag{55}$$

where k_{De} is a pre-factor that needs to be determined from observation or numerical experiments. Substituting D_e into Eq. 54, we can write down the scaling for the energy injection rate by solar radiation

$$\epsilon_s \sim \frac{k_{De}^3 U_s^3 \tau_m}{B(\phi_0)^2}[2\gamma(1-\gamma)B(\phi_0)\chi(\phi_c - \phi_0) + FrU_s B_s(\phi_0)]^3, \tag{56}$$

where $\chi(x)$ is the Heaviside step function such that $\chi(x) = 0$ if $x < 0$ and $\chi(x) = 1$ if $x \geq 0$, and ϕ_c is the critical latitude where the tangent cylinder of the lower layer intersects the interface between the two layers.

4 Numerical Simulations

4.1 Simulation set up

There are 7 independent non-dimensional parameters that control the equations: the layer depth ratio γ, the thermal wind U_s, the Froude number Fr, the bottom energy injection rate ϵ_c, the radiative time scale τ_{rad}, the linear momentum damping time scale τ_m, and the hyper-viscosity ν_h. In our study, we focus on how the convective and solar forcing control the dynamics of the atmosphere, and how the dynamics vary in a deep versus a shallow system. Therefore, we choose 3 parameters: γ that characterizes deep versus shallow system, U_s that characterizes the strength of solar forcing, and ϵ_c that characterizes the strength of convective forcing as control parameters in our work and fix all other parameters.

Since the upper weather layer of the giant planets is expected to be relatively shallow while the lower convective layer depth may vary from planets to planets, we fix the upper layer depth H_1' and modify the lower layer depth H_2'. The ratio of the top layer thickness to the total thickness is measured by $\gamma = H_1'/(H_1' + H_2')$. Consistently, for the Froude number,

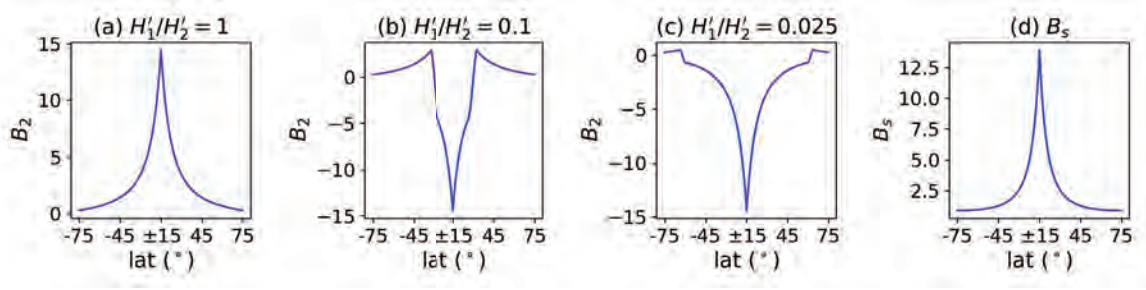

Figure 8: The β profiles in different simulations. (a)-(c): $B_2(\phi)$ in simulations with $\gamma = 0.5$, 0.0909, and 0.0244, respectively. (d): $B_s(\phi)$ in all simulations. Note that the lowest latitude is 15° so that ±15° are the same grid points.

we fix the upper layer $Fr_1 = Fr/\gamma$ instead of fixing Fr. Consequently, when the lower layer depth increases, γ decreases, the critical latitude ϕ_c increases, and the region outside the tangent cylinder expands. The momentum damping time scale τ_m is set to be the same in both layers. The hyper-viscosity in the lower layer ν_{h2} is set based on the energy injection rate ϵ and the grid scale dL so that it can damp grid-scale noises but have as little effect on the stochastic forcing as possible. In the upper layer, there is no small-scale stochastic forcing, and we increase the hyper-viscosity to ensure numerical stability. The model parameters are shown in Table 2 and Table 3.

The topographic β reaches infinity at the equator so that we cannot extend our domain all the way to the equator in the numerical simulations, and we hence set the latitudinal range to be 15 to 75 degrees. We refer to the $H_1'/H_2' = 1$ case as the shallow system because $B_2(\phi) > 0$ everywhere in the domain, and refer to the $H_1'/H_2' = 0.1$ case and the $H_1'/H_2' = 0.025$ case as the deep system because $B_2(\phi) < 0$ at low latitudes (Fig. 8). We apply a local Cartesian coordinate (Fig. 3) and double-periodic boundary conditions. The domain size is 2π in the zonal and 8π in the meridional direction with 64 zonal grids and 256 meridional grids in the simulations with only convective forcing to better resolve the energy spectrum, and is 8π with 128 grids in both zonal and meridional direction in the simulations with only solar forcing and in the coupled simulations to resolve zonal eddies. We then solve the model equations using Dedalus [4].

Upper layer Froude number Fr/γ	Radiative time scale τ_{rad}	Momentum damping time scale τ_m	Lower layer hyper-viscosity ν_{h2}	Upper layer hyper-viscosity ν_{h1}
20	10^4	200	$\epsilon^{1/3} dL^{10/3}/100$	$10\nu_{h2}(\gamma+1)/\gamma$

Table 2: Fixed non-dimensional parameters in the simulations.

Simulation name	Layer depth ratio γ	Convective energy injection rate ϵ_c	Thermal wind shear U_s	Solar forcing strength $\epsilon_{s,est}$
Sc_1	0.5	0.5	0	0
Sc_2	0.5	0.05	0	0
Sc_3	0.5	0.005	0	0
Mc_1	0.0909	0.5	0	0
Mc_2	0.0909	0.05	0	0
Mc_3	0.0909	0.005	0	0
Dc_1	0.0244	0.5	0	0
Dc_2	0.0244	0.05	0	0
Dc_3	0.0244	0.005	0	0
Ss_1	0.5	0	0.22	0.88
Ss_2	0.5	0	0.21	0.67
Ss_3	0.5	0	0.20	0.50
Ss_4	0.5	0	0.18	0.26
Ss_5	0.5	0	0.15	0.089
Ds_1	0.0244	0	0.98	0.80
Ds_2	0.0244	0	0.94	0.62
Ds_3	0.0244	0	0.89	0.45
Ds_4	0.0244	0	0.81	0.26
Ds_5	0.0244	0	0.66	0.075
Sc_1s_1	0.5	0.05	0.22	0.88
Sc_1s_2	0.5	0.05	0.15	0.089
Sc_2s_1	0.5	0.005	0.22	0.88
Sc_2s_2	0.5	0.005	0.15	0.089
Dc_1s_1	0.0244	0.05	0.98	0.80
Dc_1s_2	0.0244	0.05	0.66	0.075
Dc_2s_1	0.0244	0.005	0.98	0.80
Dc_2s_2	0.0244	0.005	0.66	0.075

Table 3: Non-dimensional parameters in the simulations. The upper box shows simulations with only convective forcing, the middle box shows simulations with only solar forcing, and the bottom box shows simulations with both convective and solar forcing. In the simulation name, S indicates Shallow lower layer, i.e. large depth ratio ($\gamma = 0.5$) with $\beta_2 > 0$ everywhere, representing the shallow system; M and D indicate Medium and Deep lower layer, i.e. medium ($\gamma = 0.0909$) and small ($\gamma = 0.0244$) depth ratio with $\beta_2 < 0$ at low latitudes, respectively, representing the deep system. The subscript of c indicates different convective forcing strength and the subscript of s indicates different solar forcing strength. We estimate the solar forcing strength by $\epsilon_{s,est} = k_{De}^3 \tau_m (Fr U_s^2 B_s(\phi_0))^3 / B(\phi_0)^2$, where $k_{De} = 0.073$ and $B(\phi_0) = B_s(\phi_0) = 1$.

4.2 Convective forcing

In the simulations with only convective forcing, the flow fields are mostly barotropic (i.e. the velocities are the same in the upper and lower layer). There is PV mixing phenomenon

in the simulations. For example, in the equilibrium state of the simulation Dc_1, there are prograde and retrograde jets (Fig. 9a), which results in relative vorticity $-\partial\bar{u}/\partial y$ (the blue line in Fig. 9b). The meridional gradient of the relative vorticity compensates for the meridional gradient of the planetary vorticity β, forming PV staircases, which is most significant near the equator (Fig. 9b). In some other simulations, although the meridional gradient of the relative vorticity and the planetary vorticity do not perfectly cancel each other, there are always compensations to some extent.

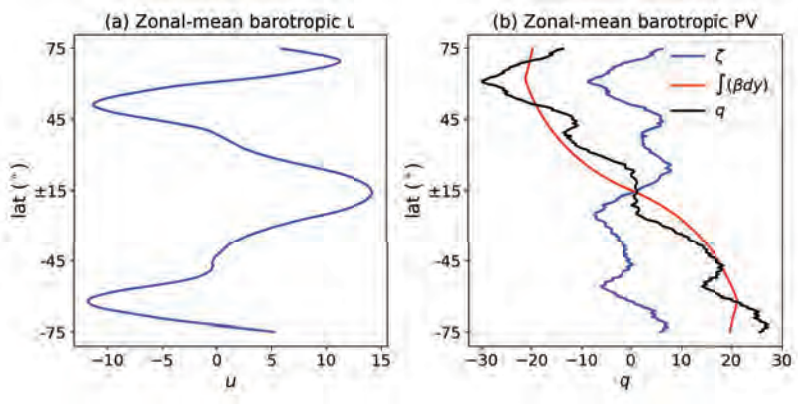

Figure 9: Zonal-mean barotropic zonal velocity $\bar{u}$ (a) and zonal-mean barotropic potential vorticity $\bar{q}$ (b) in the equilibrium state of the simulation Dc_1. In (b), the blue line shows the relative vorticity $-\partial\bar{u}/\partial y$, the red line shows the planetary vorticity $\int(\beta dy)$, and the black line shows the total potential vorticity $\bar{q}$.

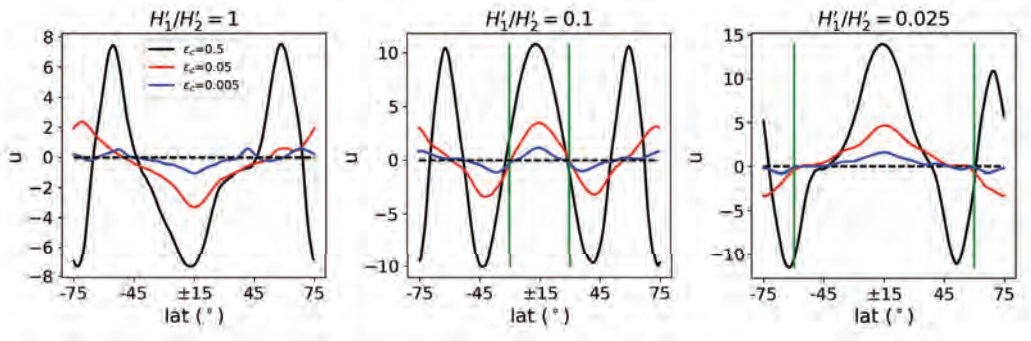

Figure 10: Zonal-mean barotropic zonal velocity u in the equilibrium states of simulations with $\gamma = 0.5$ (left panel), 0.0909 (middle panel), and 0.0244 (right panel), respectively. The vertical green lines indicate the critical latitude ϕ_c. The black lines show simulations with strongest convective forcing ($\epsilon_c = 0.5$), the red lines show simulations with medium convective forcing ($\epsilon_c = 0.05$), and the blue lines show simulations with weakest convective forcing ($\epsilon_c = 0.005$).

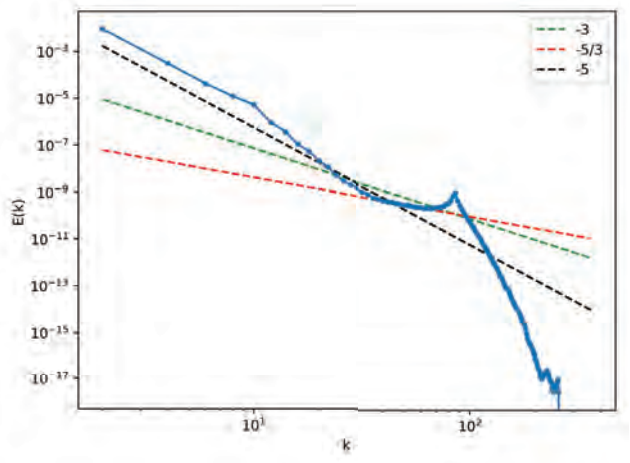

Figure 11: Energy spectrum in a high-resolution (512×2048) one-layer (the lower convective layer) simulation with only convective forcing. The dashed lines indicate slopes of -3 (green), $-5/3$ (red), and -5 (black), respectively. There is a transition from slope -5 to $-5/3$ at k_β, but below the forcing scale k_β, the spectrum drops with a slope much steeper than -3. In the low resolution simulations, k_β is closer to the domain scale so the scale separation is less clear than in this figure.

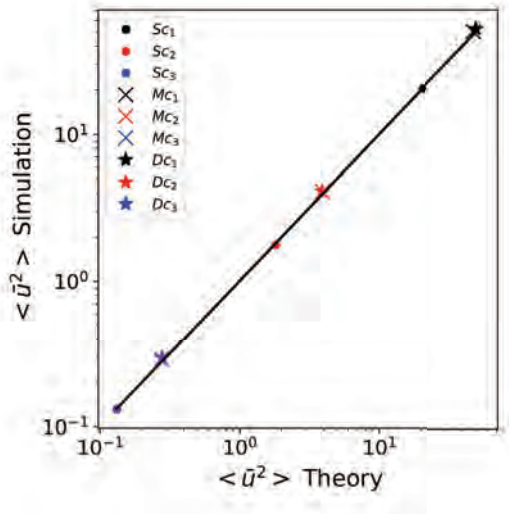

Figure 12: Jet energy in the simulations with only convective forcing compared with Eq. 48. The vertical axis shows the simulation results and the horizontal axis shows the theoretical value predicted by Eq. 48. The black line is the one-to-one line. The dots indicate simulations with $\gamma = 0.5$, the crosses indicate simulations with $\gamma = 0.0909$, and the stars indicate simulations with $\gamma = 0.0244$. Black shows simulations with strongest convective forcing ($\epsilon_c = 0.5$), red shows simulations with medium convective forcing ($\epsilon_c = 0.05$), and blue shows simulations with weakest convective forcing ($\epsilon_c = 0.005$).

In the equilibrium state, prograde equatorial jet develops in the deep scenario, due to the negative B_2 in low-latitudes, and retrograde equatorial jet develops in the shallow scenario, due to the positive B_2 there (Fig. 10). Combined with the PV mixing phenomenon in the simulations, our simulation results confirm our hypothesis that the jet direction at the equator is determined by the PV mixing process and the sign of β near the equator, and there will be super-rotation in the deep system and sub-rotation in the shallow system. The momentum transport may be relevant to the jet structure, so the results may be sensitive to the initial condition. We therefore carry out two sensitivity tests: we take the equilibrium state of the simulations Sc_2 (in which there is sub-rotation) and Dc_2 (in which there is super-rotation) as initial conditions, and use the sub-rotation state as the initial condition for the simulation with parameters same as Dc_2 and use the super-rotation state as the initial condition for the simulation with parameters same as Sc_2. As a result, in the equilibrium state there is still super-rotation in the deep system Dc_2 and sub-rotation in the shallow system Sc_2 (not shown here), which suggests the results presented here are not sensitive to the initial condition.

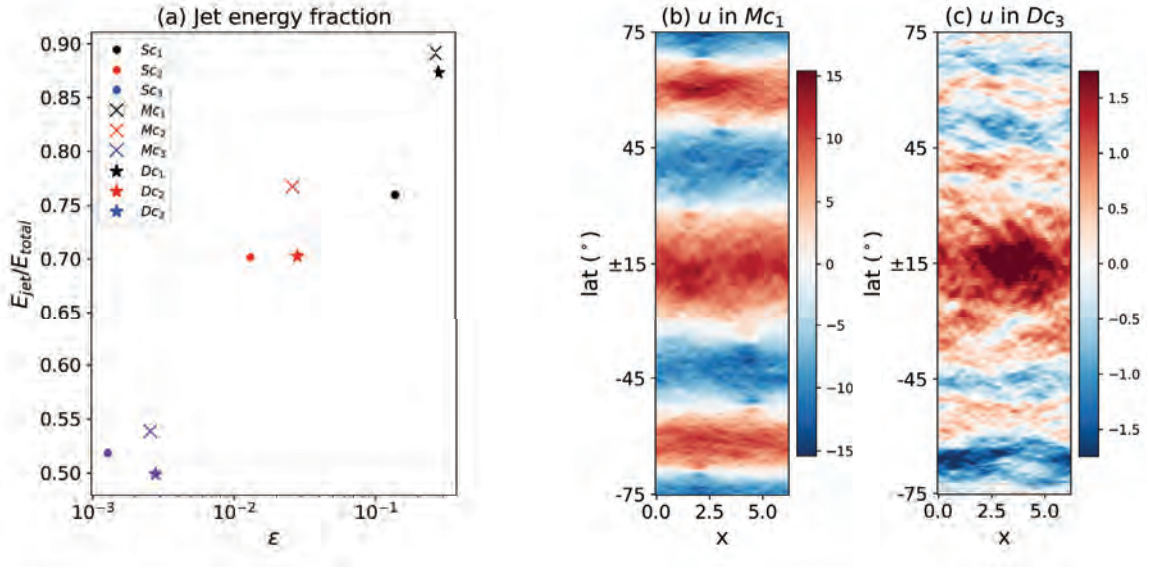

Figure 13: Qualitative comparison of E_{jet}/E_{total} with the energy injection rate. (a) shows the ratio E_{jet}/E_{total} as a function of the energy injection rate ϵ (including the correction of the hyper-viscosity dissipation). (b) and (c) show snapshots of the zonal velocity u in simulation Mc_1 (with the highest E_{jet}/E_{total} ratio) and in simulation Dc_3 (with the lowest E_{jet}/E_{total} ratio), respectively. In (a), the dots indicate simulations with $\gamma = 0.5$, the crosses indicate simulations with $\gamma = 0.0909$, and the stars indicate simulations with $\gamma = 0.0244$. Black shows simulations with strongest convective forcing ($\epsilon_c = 0.5$), red shows simulations with medium convective forcing ($\epsilon_c = 0.05$), and blue shows simulations with weakest convective forcing ($\epsilon_c = 0.005$).

We further examine the jet energy scaling. In our simulations, there are 256 grid points in the meridional direction, but the resolution is still not high enough to precisely resolve the energy spectrum (Fig. 11). Therefore, it is difficult to quantitatively verify the scaling

of jet energy to the total energy with Eq. (47). We therefore diagnostically calculate the ratio E_{jet}/E_{total} using the model output. Note that a non-negligible amount of the energy input by convective forcing is dissipated by small-scale hyper-viscosity, also due to the low resolution, and we take this part of dissipation out so that the real energy input rate in the plot is smaller than prescribed in Table 3. We then compare the zonal jet energy in the simulations with the value predicted in Eq. 48, and we find a almost perfect match (Fig. 12).

Although the quantitative comparison is not applicable with our simulations, we can qualitatively examine the relationship between the jet energy ratio E_{jet}/E_{total} and the energy injection rate. We find that with a higher energy injection rate, which indicates a larger ratio k_β/k_{Rh}, there is more energy stored in jets and the jets are more smooth (Fig. 13), consistent with the theory.

4.3 Solar forcing

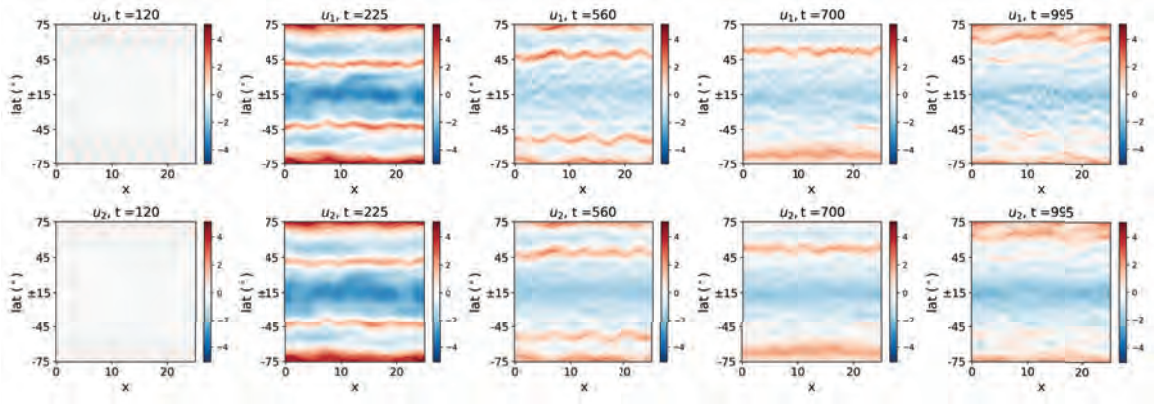

Figure 14: Snapshots of the zonal velocity at different simulation time in the simulation Ss_2.

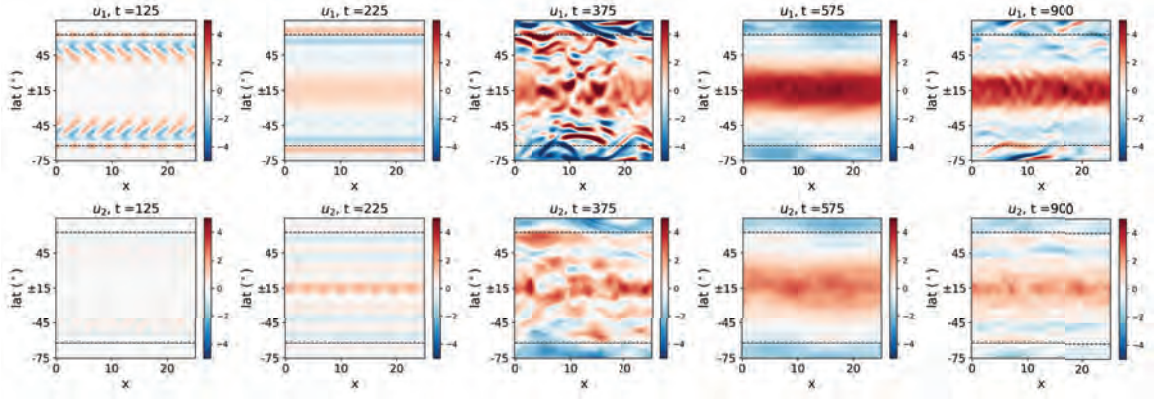

Figure 15: Snapshots of the zonal velocity at different simulation time in the simulation Ds_2. The black dashed lines indicate the critical latitude ϕ_c.

In the simulations with only solar forcing, the zonal velocities in two layers are not barotropic, and the initial jet formation is associated with baroclinic instability (e.g., the left panels in Fig. 14 & 15). As non-linear effects kick in, in the simulation Ss_2, the jet speed weakens with time and multiple prograde jets merge into one wider jet near the pole (Fig. 14). In the simulation Ds_2, the initial jet speed strengthens and some secondary instability occurs (Fig. 15). These phenomena are likely because once the jet forms, the latitude where Rossby wave breaks and hence the momentum flux also changes, which indicates the jet and the momentum flux will co-evolve with each other.

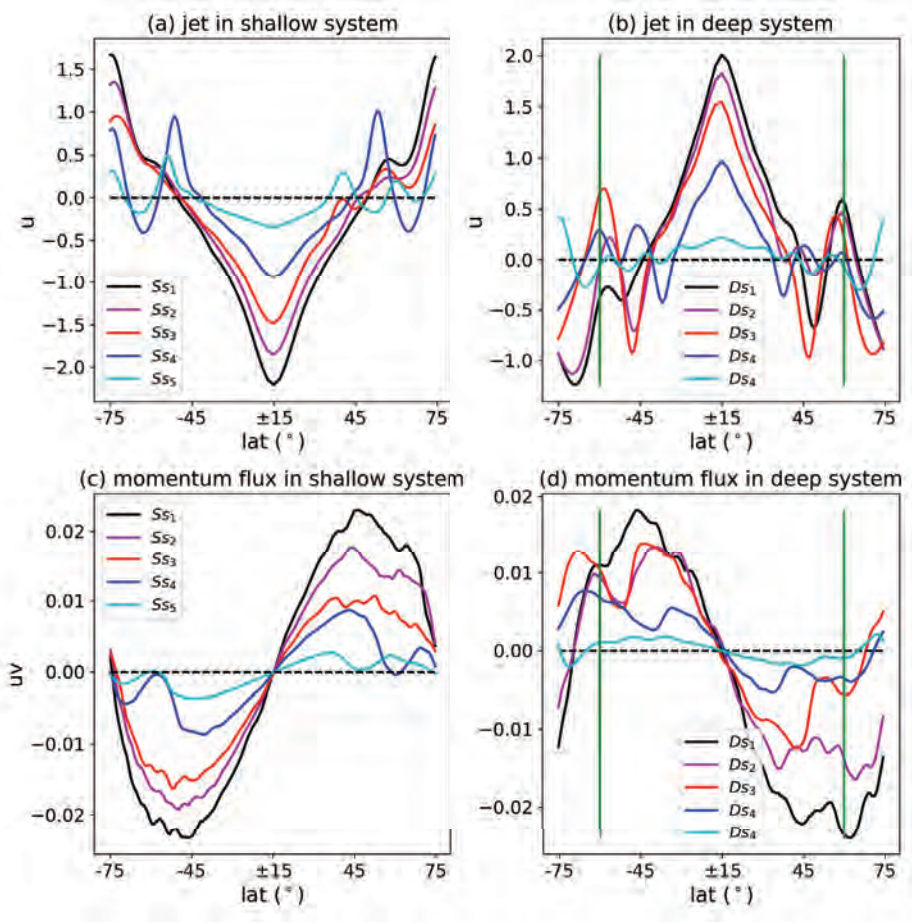

Figure 16: Zonal-mean barotropic zonal velocity (a & b) and momentum flux (c & d) in simulations with only solar forcing. Black, magenta, red, blue and cyan show simulations with strongest solar forcing to the weakest solar forcing. In (b) & (d), the green lines indicate the critical latitude ϕ_c.

Despite the non-linear dynamics discussed above, the jet direction near the equator is consistent with what is expected from the linear analysis: there is super-rotation in the deep system and sub-rotation in the shallow system (Fig. 16a & b). The momentum flux is also consistent with the linear analysis, which is poleward in the shallow system and generally equatorward in the deep system (Fig. 16c & d). The detailed jet structure varies among

simulations, though, because the jet structure and the eddy momentum flux co-evolve with time.

We further examine the scaling for the energy injection rate by solar forcing (Eq. 56). In an equilibrium state, the energy injection rate should be equal to the energy dissipation rate, so we use the energy dissipation rate to estimate the energy injection rate in the simulations. The instability happens near the pole in the shallow system and near the tangent cylinder in the deep system, where $B \sim O(1)$, so we choose $B(\phi_0) = B_s(\phi_0) = 1$ in the theoretical scaling. As a result, we find that if we choose the pre-factor $k_{De} = 0.073$, the simulation results matches well with the theoretical analysis (Fig. 17). Note that here the scaling with Eq. 56 applies only to the total energy. If we want to get the scaling for the jet energy, we need to know the ratio of E_{jet}/E_{total}, which is left for future study.

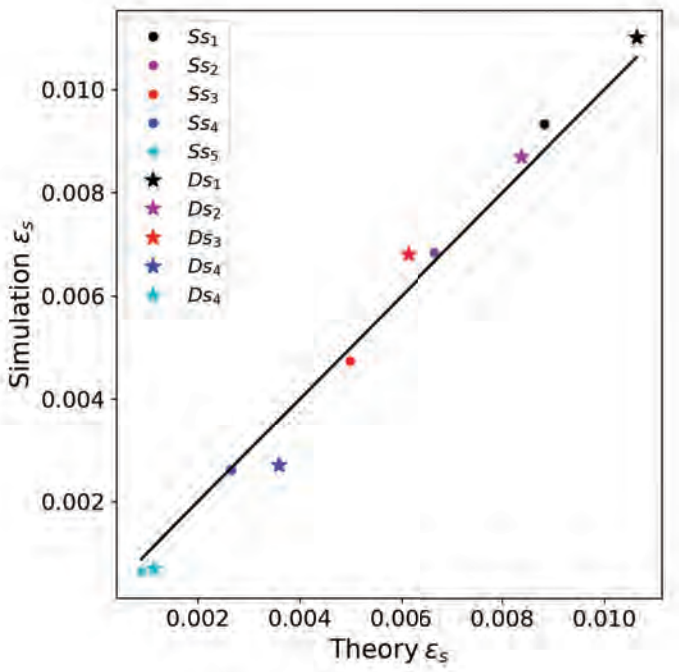

Figure 17: Solar forcing energy injection rate in the simulations with only solar forcing compared with Eq. 56. The vertical axis shows the simulation results and the horizontal axis shows the theoretical value predicted by Eq. 56. The black line is the one-to-one line. The dots indicate simulations with $\gamma = 0.5$, and the stars indicate simulations with $\gamma = 0.0244$. Black, magenta, red, blue and cyan show simulations with strongest solar forcing to the weakest solar forcing.

4.4 Coupled convective and solar forcing

We carried out simulations with both convective and solar forcing (Table 3). In these simulations, there is super-rotation in the deep system and sub-rotation in the shallow system (Fig. 18). Qualitatively, the jet velocity increases with increasing convective forcing

(compare red and blue lines) and with increasing solar forcing (compare solid and dashed lines). The quantitative scaling of the energy is left for future studies.

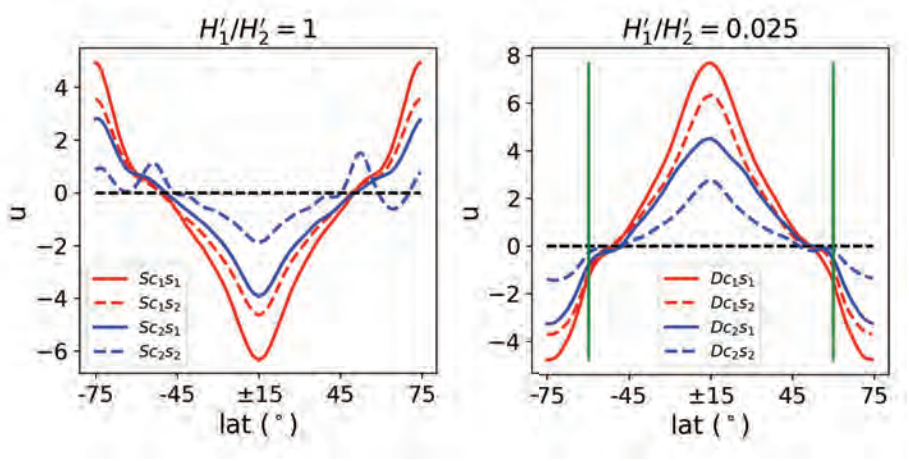

Figure 18: Zonal-mean barotropic zonal velocity in simulations with both convective forcing and solar forcing. Red lines show simulations with stronger convective forcing and blue lines show simulations with weaker convective forcing. Solid lines show simulations with stronger solar forcing and dashed lines show simulations with weaker solar forcing. The green lines indicate the critical latitude ϕ_c.

5 Discussion and Conclusion

Using a two-layer Boussinesq Quasi-Geostrophic model, we systematically investigated what controls the direction and strength of the equatorial jet on giant planets. We find that, no matter the jets are powered by the solar forcing or by convection, prograde jet tends to form in a deep system, and retrograde jet tends to form in a shallow system. When convective forcing dominates, PV mixing flattens out the PV gradient at the low-latitudes, resulting in prograde (retrograde) equatorial jet in a deep (shallow) system because the topographic β is negative (positive) there. When solar forcing dominates, deep system has baroclinic instability peaks around the tangent cylinder, exciting Rossby waves that converge prograde momentum equatorward. For a shallow system, baroclinic instability is most pronounced over the poles, resulting in a poleward momentum transport hence retrograde jet at the equator.

With convective forcing, we find that a stronger energy injection rate leads to concentration of energy in jets relative to eddies, making jets smoother. With solar forcing, we find a scaling of the energy injection rate given the stratification and the thermal wind shear caused by differential solar radiation (Eq. 56). The jet energy to total energy ratio and the detailed momentum flux pattern in the solar forcing scenario, and the quantitative energy injection rate in the coupled convective and solar forcing scenario, are left for future studies.

Our results connect the direction of the equatorial jet with the penetration depth of the

jet on giant planets. We expect the jet on the two gas giants, Jupiter and Saturn, to be relatively deep since they are in super-rotation state. Observations indicate that the jet can penetrate to about 3000 km in Jupiter and about 9000 km in Saturn, comparable to the horizontal scale of the observed jets (about 4000 km in Jupiter and about 10000 km in Saturn), which is consistent with our prediction that super-rotation tends to form in a deep system. Uranus and Neptune are in sub-rotation state, but observations are limited for these ice giants and it is unclear how deep the jets are. The horizontal extend of the equatorial jet is about 2400 km on Uranus and about 9000 km on Neptune. If our results are applicable, we expect the jets to be damped at a much shallower depth compared with the horizontal scale of motion on Uranus and Neptune. Therefore, for Neptune we would expect the conductivity of the outer gas envelope to be high and the jet penetration depth to be near the lower limit (about 1000 km). For Uranus, the estimated penetration depth is comparable to the horizontal scale of motion, suggesting that either the jet is much shallower than current estimation, or some other factors that are not considered in our work (e.g., the high obliquity of Uranus, which suggests a different s olar r adiation d istribution) may play a role in the jet formation.

Acknowledgements

I sincerely thank my advisors Wanying Kang, Glenn Flierl, and Geoff Vallis for their guidance, without which it would have been impossible to finish this project. I also thank Keaton Burns and Daniel Lecoanet for their help in building up the numerical simulations using Dedalus. I would also thank Tiffany Shaw and Pascale Garaud for organizing the GFD summer pro-gram, and my fellow fellows for their companionship during the great summer.

References

[1] J. Aurnou, M. Heimpel, and J. Wicht, *The effects of vigorous mixing in a convective model of zonal flow on the ice giants*, Icarus, 190 (2007), pp. 110–126.

[2] S. Bire, W. Kang, A. Ramadhan, J.-M. Campin, and J. Marshall, *Exploring ocean circulation on icy moons heated from below*, Journal of Geophysical Research: Planets, 127 (2022), p. e2021JE007025.

[3] S. J. Bolton, A. Adriani, V. Adumitroaie, M. Allison, J. Anderson, S. Atreya, J. Bloxham, S. Brown, J. Connerney, E. DeJong, et al., *Jupiter's interior and deep atmosphere: The initial pole-to-pole passes with the juno spacecraft*, Science, 356 (2017), pp. 821–825.

[4] K. J. Burns, G. M. Vasil, J. S. Oishi, D. Lecoanet, and B. P. Brown, *Dedalus: A flexible framework for numerical simulations with spectral methods*, Physical Review Research, 2 (2020), p. 023068.

[5] F. H. Busse, *Thermal instabilities in rapidly rotating systems*, Journal of Fluid Mechanics, 44 (1970), pp. 441–460.

[6] ——, *A simple model of convection in the jovian atmosphere*, Icarus, 29 (1976), pp. 255–260.

[7] J. Y. Cho and L. M. Polvani, *The morphogenesis of bands and zonal winds in the atmospheres on the giant outer planets*, Science, 273 (1996), pp. 335–337.

[8] U. R. Christensen, *Zonal flow driven by deep convection in the major planets*, Geophysical research letters, 28 (2001), pp. 2553–2556.

[9] ——, *Zonal flow driven by strongly supercritical convection in rotating spherical shells*, Journal of Fluid Mechanics, 470 (2002), pp. 115–133.

[10] B. F. Farrell and P. J. Ioannou, *Structure and spacing of jets in barotropic turbulence*, Journal of the Atmospheric Sciences, 64 (2007), pp. 3652–3665.

[11] ——, *Formation of jets by baroclinic turbulence*, Journal of the Atmospheric Sciences, 65 (2008), pp. 3353–3375.

[12] ——, *A stochastic structural stability theory model of the drift wave–zonal flow system*, Physics of Plasmas, 16 (2009).

[13] M. French, A. Becker, W. Lorenzen, N. Nettelmann, M. Bethkenhagen, J. Wicht, and R. Redmer, *Ab initio simulations for material properties along the jupiter adiabat*, The Astrophysical Journal Supplement Series, 202 (2012), p. 5.

[14] E. Galanti, Y. Kaspi, Y. Miguel, T. Guillot, D. Durante, P. Racioppa, and L. Iess, *Saturn's deep atmospheric flows revealed by the cassini grand finale gravity measurements*, Geophysical Research Letters, 46 (2019), pp. 616–624.

[15] E. García-Melendo, S. Pérez-Hoyos, A. Sánchez-Lavega, and R. Hueso, *Saturn's zonal wind profile in 2004–2009 from cassini iss images and its long-term variability*, Icarus, 215 (2011), pp. 62–74.

[16] E. Garcia-Melendo and A. Sánchez-Lavega, *A study of the stability of jovian zonal winds from hst images: 1995–2000*, Icarus, 152 (2001), pp. 316–330.

[17] T. Gastine, M. Heimpel, and J. Wicht, *Zonal flow scaling in rapidly-rotating compressible convection*, Physics of the Earth and Planetary Interiors, 232 (2014), pp. 36–50.

[18] T. Gastine, J. Wicht, and J. Aurnou, *Zonal flow regimes in rotating anelastic spherical shells: An application to giant planets*, Icarus, 225 (2013), pp. 156–172.

[19] N. Gillet and C. Jones, *The quasi-geostrophic model for rapidly rotating spherical convection outside the tangent cylinder*, Journal of Fluid Mechanics, 554 (2006), pp. 343–369.

[20] T. Guillot, *A comparison of the interiors of jupiter and saturn*, Planetary and Space Science, 47 (1999), pp. 1183–1200.

[21] M. Heimpel and J. Aurnou, *Turbulent convection in rapidly rotating spherical shells: A model for equatorial and high latitude jets on jupiter and saturn*, Icarus, 187 (2007), pp. 540–557.

[22] M. Heimpel, J. Aurnou, and J. Wicht, *Simulation of equatorial and high-latitude jets on jupiter in a deep convection model*, Nature, 438 (2005), pp. 193–196.

[23] I. M. Held and V. D. Larichev, *A scaling theory for horizontally homogeneous, baroclinically unstable flow on a beta plane*, Journal of Atmospheric Sciences, 53 (1996), pp. 946–952.

[24] R. Helled, J. D. Anderson, M. Podolak, and G. Schubert, *Interior models of uranus and neptune*, The Astrophysical Journal, 726 (2010), p. 15.

[25] R. Helled and T. Guillot, *Internal structure of giant and icy planets: Importance of heavy elements and mixing*, Handbook of exoplanets, (2018), p. 51.

[26] M. F. Jansen, A. J. Adcroft, R. Hallberg, and I. M. Held, *Parameterization of eddy fluxes based on a mesoscale energy budget*, Ocean Modelling, 92 (2015), pp. 28–41.

[27] C. A. Jones and K. M. Kuzanyan, *Compressible convection in the deep atmospheres of giant planets*, Icarus, 204 (2009), pp. 227–238.

[28] Y. Kaspi, *Turbulent convection in an anelastic rotating sphere: A model for the circulation on the giant planets*, Massachusetts Institute of Technology, 2008.

[29] Y. Kaspi, G. R. Flierl, and A. P. Showman, *The deep wind structure of the giant planets: Results from an anelastic general circulation model*, Icarus, 202 (2009), pp. 525–542.

[30] Y. Kaspi, A. P. Showman, W. B. Hubbard, O. Aharonson, and R. Helled, *Atmospheric confinement of jet streams on uranus and neptune*, Nature, 497 (2013), pp. 344–347.

[31] Y. e. Kaspi, E. Galanti, W. B. Hubbard, D. Stevenson, S. Bolton, L. Iess, T. Guillot, J. Bloxham, J. Connerney, H. Cao, et al., *Jupiter's atmospheric jet streams extend thousands of kilometres deep*, Nature, 555 (2018), pp. 223–226.

[32] Y. Lian and A. P. Showman, *Generation of equatorial jets by large-scale latent heating on the giant planets*, Icarus, 207 (2010), pp. 373–393.

[33] S. S. Limaye, *Jupiter: New estimates of the mean zonal flow at the cloud level*, Icarus, 65 (1986), pp. 335–352.

[34] J. Liu, *Interaction of magnetic field and flow in the outer shells of giant planets*, California Institute of Technology, 2006.

[35] J. Liu, P. M. Goldreich, and D. J. Stevenson, *Constraints on deep-seated zonal winds inside jupiter and saturn*, icarus, 196 (2008), pp. 653–664.

[36] J. Liu and T. Schneider, *Mechanisms of jet formation on the giant planets*, Journal of the Atmospheric Sciences, 67 (2010), pp. 3652–3672.

[37] M. S. Marley, P. Gómez, and M. Podolak, *Monte carlo interior models for uranus and neptune*, Journal of Geophysical Research: Planets, 100 (1995), pp. 23349–23353.

[38] N. Nettelmann, R. Helled, J. Fortney, and R. Redmer, *New indication for a dichotomy in the interior structure of uranus and neptune from the application of modified shape and rotation data*, Planetary and Space Science, 77 (2013), pp. 143–151.

[39] N. Nettelmann, B. Holst, A. Kietzmann, M. French, R. Redmer, and D. Blaschke, *Ab initio equation of state data for hydrogen, helium, and water and the internal structure of jupiter*, The Astrophysical Journal, 683 (2008), p. 1217.

[40] N. Nettelmann, R. Püstow, and R. Redmer, *Saturn layered structure and homogeneous evolution models with different eoss*, Icarus, 225 (2013), pp. 548–557.

[41] J. Pearl and B. Conrath, *The albedo, effective temperature, and energy balance of neptune, as determined from voyager data*, Journal of Geophysical Research: Space Physics, 96 (1991), pp. 18921–18930.

[42] M. Podolak, J. Podolak, and M. Marley, *Further investigations of random models of uranus and neptune*, Planetary and Space Science, 48 (2000), pp. 143–151.

[43] A. Sánchez-Lavega and M. Heimpel, *Atmospheric dynamics of giants and icy planets*, Handbook of exoplanets, (2018), p. 51.

[44] A. Sanchez-Lavega, J. F. Rojas, and P. V. Sada, *Saturn's zonal winds at cloud level*, Icarus, 147 (2000), pp. 405–420.

[45] A. Sánchez-Lavega, L. Sromovsky, A. Showman, A. Del Genio, R. Young, R. Hueso, et al., *Zonal jets in gas giants*, Zonal jets, (2019), pp. 9–45.

[46] D. Saumon and T. Guillot, *Shock compression of deuterium and the interiors of jupiter and saturn*, The Astrophysical Journal, 609 (2004), p. 1170.

[47] T. Schneider and J. Liu, *Formation of jets and equatorial superrotation on jupiter*, Journal of the Atmospheric Sciences, 66 (2009), pp. 579–601.

[48] R. Scott and L. M. Polvani, *Equatorial superrotation in shallow atmospheres*, Geophysical Research Letters, 35 (2008).

[49] A. P. Showman, *Numerical simulations of forced shallow-water turbulence: Effects of moist convection on the large-scale circulation of jupiter and saturn*, Journal of the Atmospheric Sciences, 64 (2007), pp. 3132–3157.

[50] A. P. Showman, J. Y. Cho, and K. Menou, *Atmospheric circulation of exoplanets*, Exoplanets, 526 (2010), pp. 471–516.

[51] K. Soderlund, M. Heimpel, E. King, and J. Aurnou, *Turbulent models of ice giant internal dynamics: Dynamos, heat transfer, and zonal flows*, Icarus, 224 (2013), pp. 97–113.

[52] D. Soyuer, F. Soubiran, and R. Helled, *Constraining the depth of the winds on uranus and neptune via ohmic dissipation*, Monthly Notices of the Royal Astronomical Society, 498 (2020), pp. 621–638.

[53] K. Srinivasan and W. Young, *Zonostrophic instability*, Journal of the atmospheric sciences, 69 (2012), pp. 1633–1656.

[54] L. Sromovsky, I. de Pater, P. Fry, H. Hammel, and P. Marcus, *High s/n keck and gemini ao imaging of uranus during 2012–2014: new cloud patterns, increasing activity, and improved wind measurements*, Icarus, 258 (2015), pp. 192–223.

[55] D. J. Stevenson, *Jupiter's interior as revealed by juno*, Annual Review of Earth and Planetary Sciences, 48 (2020), pp. 465–489.

[56] G. K. Vallis, *Atmospheric and oceanic fluid dynamics*, Cambridge University Press, 2017.

[57] S. M. Wahl, W. B. Hubbard, B. Militzer, T. Guillot, Y. Miguel, N. Movshovitz, Y. Kaspi, R. Helled, D. Reese, E. Galanti, et al., *Comparing jupiter interior structure models to juno gravity measurements and the role of a dilute core*, Geophysical Research Letters, 44 (2017), pp. 4649–4659.

[58] G. P. Williams, *Planetary circulations: 1. barotropic representation of jovian and terrestrial turbulence*, Journal of Atmospheric Sciences, 35 (1978), pp. 1399–1426.

[59] J.-I. Yano and G. R. Flierl, *Jupiter's great red spot: compactness condition and stability*, Annales Geophysicae, 12 (1994), pp. 1–18.

Into the Mix:
How Biological Dynamics Affect Turbulent Transport

Deborah Rhee (née Cotton)

December 5, 2023

1 Introduction

In this report we aim to further the understanding of how the mean flux of biological tracers is linked to the mean tracer concentration in turbulent conditions.

Biological tracers are organisms passively transported in the ocean by turbulent flows. Examples of biological tracers are phytoplankton, zooplankton, mycoplankton and bacterioplankton.

The concentration and flux of biological tracers in the ocean has significant local and global effects. Locally the concentration of biological tracers exerts a strong control on the taxonomic composition and ecological structure of the marine biosphere through their effects on the spatial distributions of nutrients, fixed carbon, and dissolved oxygen [4]. They are also important for mediating the transfer of fixed carbon from the marine photic zone to deeper waters and the seafloor [4]. Globally biological tracers play a significant role in the carbon cycle. It is estimated that carbon fixation by marine phytoplankton accounts for about half the Earth's primary production [3]. The magnitude and nature of the carbon exported to the deep ocean depends on relative abundance and size of phytoplankton [1].

It is thus important to model the local concentration and flux of biological tracers. However, due to the multi-scale nature of turbulent flows, it is infeasible to fully simulate the dispersion of these tracers. Instead, a statistical method is often employed to calculate quantities such as mean tracer fluxes and mean tracer concentrations. To model tracer fluxes, Earth system models require closure relations for the transport of non-local processes [5]. In a similar way to modelling heat flux, one possible closure relation would relate the mean flux of biological tracers to the mean gradient of the tracer concentration. The multi-scale nature of turbulent flows suggests this flux relation may be better modelled using non-local operators. Here, we examine mean tracer flux-gradient relations that result from combining the velocities generated by the stochastic Ornstein-Uhlenbeck process with biological growth processes. Although the Ornstein-Uhlenbeck process does not mirror a real ocean time-dependent velocity field, the conclusions made here about mean tracer flux-gradient

relations can be used to inform parameterisions of biological tracers.

In summary, the aim of this report is to find some non-linear functional relationship between the mean tracer concentration, $\nabla\theta$, and the mean tracer flux, $\langle u\theta\rangle$. In other words we are trying to find some 'effective diffusivity' which relates tracer flux to tracer concentration,

$$\langle u\theta\rangle = \int dx' \mathcal{K}_{eff}(x,\theta,\nabla\theta,x',\theta',\nabla\theta')\nabla\theta'. \tag{1}$$

We can then go through a hierarchy of models to try and find an appropriate representation of $\mathcal{K}$.

In §2 we discuss our method of modelling the stochastic velocity field and our chosen model for biological growth and decay. We then non-dimensionalise this equation. In §3 we discuss some initial results used to inform the rest of the work and demonstrate the competing effects of the two processes. We give our first estimate of $\mathcal{K}_{eff}$ in §4 where we assume that fluctuations in the tracer are negligible and that the tracer flux is directly proportional to the gradient of the tracer concentration. Having shown the failure of this approach we try using asymptotic expansions to get our flux-concentration relationship in §5. We then move on to trying finite-state averaging in §6.

2 Modelling Tracer Transport

We begin by discussing a general model for biological tracers. We model the evolution of the tracer concentration, θ using an advection-diffusion equation coupled with a basic biological model for tracer growth and decay, $B(\theta)$,

$$\frac{\partial\theta}{\partial t} + \frac{\partial(u\theta)}{\partial x} - \kappa\frac{\partial^2\theta}{\partial x^2} = B(\theta), \tag{2}$$

where $u = u(t)$ is a stochastic velocity field and κ is the molecular diffusivity. We assume that the velocity field is incompressible, $\nabla\cdot u = 0$.

2.1 Ornstein-Uhlenbeck process

The stochastic velocity field is modelled using the Ornstein-Uhlenbeck process,

$$du(t) = -ru(t)dt + \sqrt{2K}dW(t). \tag{3}$$

We are interested in the statistical properties of this process; these are calculated by taking an ensemble average, $\langle\rangle$. The first property of the Ornstein-Uhlenbeck processes is $\langle dW(t)\rangle = 0$. Ensemble averaging (3) gives

$$\langle du\rangle = -r\langle u\rangle dt, \tag{4}$$

$$\langle u\rangle = u_0 e^{-rt}. \tag{5}$$

Thus, r can be understood to correspond to the relaxation time of the velocity field and we see that over time $\langle u \rangle \to 0$. We can also take the ensemble average of the covariance of (3),

$$\langle u(t)u(t+\delta)\rangle = \langle u(t)(u(t) - ru(t)\delta + \sqrt{2K}dW)\rangle, \tag{6}$$

$$= \langle u^2(t)\rangle(1 - r\delta), \tag{7}$$

Solving (7) we obtain $\langle u(t)u(t+\delta)\rangle \sim \langle u^2\rangle e^{-r\delta}$, so the covariance decays over timescale $\sim 1/r$. Finally, we can work out the variance of $\langle u \rangle$,

$$\langle u^2(t+dt)\rangle = \langle (u(t) - ru(t)dt + \sqrt{2K}dW)(u(t) - ru(t)dt + \sqrt{2K}dW)\rangle, \tag{8}$$

$$= \langle u^2(t)\rangle(1 - rdt)^2 + 2K\langle dW(t)dW(t)\rangle. \tag{9}$$

Knowing, $\langle dW(t)dW(t)\rangle = dt$ and assuming at equilibrium $\langle u^2(t+dt)\rangle \to \langle u^2(t)\rangle$,

$$\langle u^2(t)\rangle = \frac{K}{r}\left(\frac{1}{1 - \frac{rdt}{2K}}\right). \tag{10}$$

Taking $dt \to 0$,

$$\langle u^2(t)\rangle = \frac{K}{r}. \tag{11}$$

We see that K is a measure of the variance of the velocity field. Intuitively we can understand the variance to increase with K/r as the random processes become more dominant.

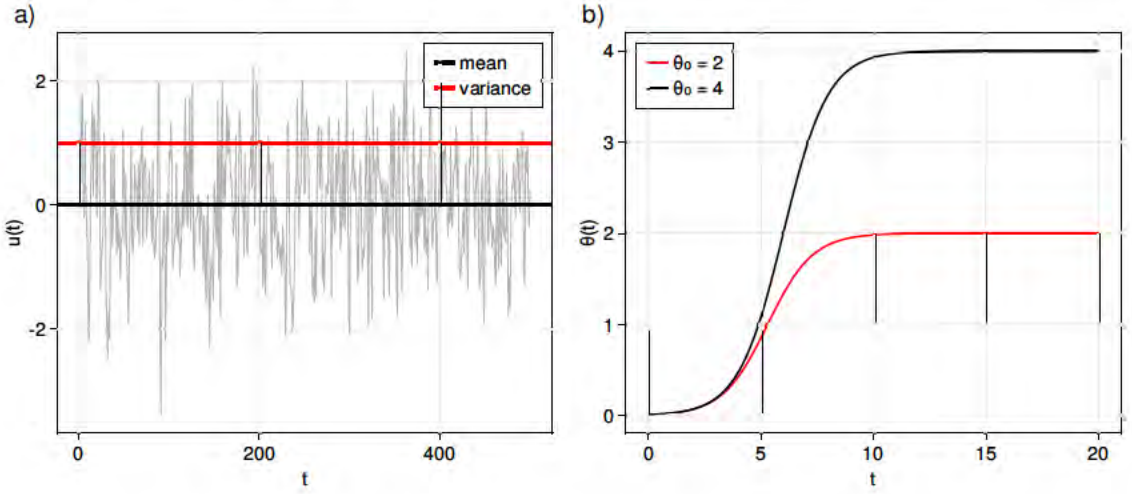

Figure 1: Stochastic velocity field and equation for biological tracer growth and decay used to model the changing tracer concentration. a) Ornstein-Uhlenbeck process for $r = K = 1$, b) Logistic equation for tracer growth and decay, $d\theta/dt = \lambda\theta\,(1 - \theta/\theta_0)$, $\lambda = 1$.

2.2 Tracer growth and decay

We use a model based off Verhulst (1838) [2],

$$B(\theta) = \lambda\theta\left(1 - \frac{\theta}{\theta_{max}}\right). \tag{12}$$

The model suggests that at low tracer concentrations, when there is little competition for resources the tracer concentration grows exponentially from its initial value θ_0, $\theta \sim \theta_0 e^{\lambda t}$. As the concentration of tracer increases and there is more competition for a finite number of resources, the tracer growth rate decreases until the tracer concentration reaches its maximum value, θ_{max}. We introduce some spatial dependence to $\theta_{max} = C(1 + \Delta\cos(kx))$ and define θ_{max} as the local carrying capacity of our system.

2.3 Non-dimensionalising

We now have our full set of equations to model the change in concentration of biological tracers,

$$\frac{\partial\theta}{\partial t} + \frac{\partial(u\theta)}{\partial x} - \kappa\frac{\partial^2\theta}{\partial x^2} = \lambda\theta\left(1 - \frac{\theta}{C(1+\Delta\cos(kx))}\right), \tag{13}$$

$$du(t) = -ru(t)dt + \sqrt{2K}dW(t). \tag{14}$$

We can write everything in terms of dimensionless variables,

$$\hat{\theta} = \frac{\theta}{C}, \qquad \hat{u} = \frac{u}{\sqrt{\langle u^2\rangle}} = u\sqrt{\frac{r}{K}}, \qquad \hat{t} = rt. \tag{15}$$

We obtain,

$$Cr\frac{\partial\hat{\theta}}{\partial\hat{t}} + \sqrt{\langle u^2\rangle}C\frac{\partial(\hat{u}\hat{\theta})}{\partial x} - C\kappa\frac{\partial^2\hat{\theta}}{\partial x^2} = \lambda C\hat{\theta}\left(1 - \frac{C\hat{\theta}}{C(1+\Delta\cos(kx))}\right), \tag{16}$$

$$\sqrt{\langle u^2\rangle}d\hat{u} = -\sqrt{\langle u^2\rangle}\hat{u}d\hat{t} + \sqrt{2r\langle u^2\rangle}\eta(\hat{t})\sqrt{\frac{d\hat{t}}{r}}, \tag{17}$$

where $\eta(t)$ corresponds to Gaussian noise. We can simplify these to,

$$\frac{\partial\hat{\theta}}{\partial\hat{t}} + \frac{\sqrt{\langle u^2\rangle}}{r}\frac{\partial(\hat{u}\hat{\theta})}{\partial x} - \frac{\kappa}{r}\frac{\partial^2\hat{\theta}}{\partial x^2} = \frac{\lambda}{r}\hat{\theta}\left(1 - \frac{\hat{\theta}}{(1+\Delta\cos(kx))}\right), \tag{18}$$

$$d\hat{u} = -\hat{u}d\hat{t} + \sqrt{2}dW(\hat{t}). \tag{19}$$

Removing the $\hat{}$s and letting $U = \sqrt{\langle u^2\rangle}k/r$, $\mathcal{K} = \kappa k^2/r$ and $\Lambda = \lambda/r$, we obtain the final dimensionless equation discussed in the rest of this report,

$$\frac{\partial\theta}{\partial t} + U\frac{\partial(u\theta)}{\partial x} - \mathcal{K}\frac{\partial^2\theta}{\partial x^2} = \Lambda\theta\left(1 - \frac{\theta}{(1+\Delta\cos x)}\right). \tag{20}$$

2.4 Testing parameters and solving the equations

For the cases discussed below we fix $U = 1$ and, as we expect molecular diffusivity not to play a significant role, $\mathcal{K} = 10^{-3}$.

We vary the relative timescale over which the biological processes act, Λ, $0.01 \leq \Lambda \leq 100$ and the strength of the spacial variance of the carrying capacity, Δ, $0.1 \leq \Delta \leq 0.9$.

To find the mean tracer concentration and tracer flux we take an ensemble average. This means that we solve (20) with N different initial choices of $u(t=0)$. We let our choices of $u(t=0)$ to be normally distributed with variance 1 and mean 0. In the limit of averaging a single member over a large time period once the system has evolved for long enough to reach the statistically steady state, taking the ensemble average should be the same as taking a time average. Figure 2 demonstrates the ensemble averaging procedure for $\Lambda = 0.1, 1, 10$. We can split θ and u into a fluctuating component, θ', u' and an ensemble averaged component $\langle\theta\rangle$, $\langle u\rangle$. We denote the ensemble averaged concentration by $\overline{\theta}$ and note that $\langle u\rangle = 0$. By definition, the fluctuating components will have ensemble average 0. Subbing in $\theta = \overline{\theta} + \theta'$, $u = u'$ to (20) and taking the ensemble average we obtain an equation for the mean tracer flux and the mean tracer concentration,

$$\frac{\partial\langle\theta\rangle}{\partial t} + U\frac{\partial\langle u\theta\rangle}{\partial x} - \mathcal{K}\frac{\partial^2\langle\theta\rangle}{\partial x^2} = \Lambda\left\langle\theta\left(1 - \frac{\theta}{1+\Delta\cos x}\right)\right\rangle, \tag{21}$$

$$\frac{\partial\overline{\theta}}{\partial t} + U\frac{\partial\langle u\theta'\rangle}{\partial x} - \mathcal{K}\frac{\partial^2\overline{\theta}}{\partial x^2} = \Lambda\overline{\theta}\left[1 - \frac{1}{1+\Delta\cos x}\left(\overline{\theta} + \frac{\langle\theta'^2\rangle}{\overline{\theta}}\right)\right], \tag{22}$$

where $\langle\rangle$ denotes the ensemble average.

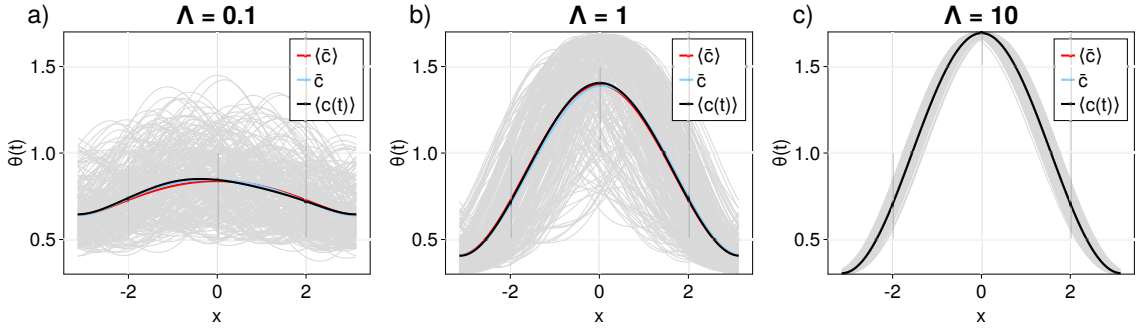

Figure 2: Demonstration of ensemble averaging for the case of $\Delta = 0.7, U = 1$. The grey lines show the tracer concentration at $t = 1000$ for 250 ensemble members. The black line gives the ensemble average at $t = 1000$, the blue line shows the time-averaged (averaged from $t = 100 - 2000$) tracer concentration for a single ensemble member, the red lines shows the time and ensemble averaged tracer concentration. a) $\Lambda = 0.1$, b) $\Lambda = 1.0$, c) $\Lambda = 10.0$.

3 Initial Results

Figure 2 gives some qualitative suggestions about the influence of the stochastic mixing on the tracer growth and decay. In the case where the timescale for the biological growth processes is much shorter than the timescale over which the stochastic mixing occurs ($\Lambda \gg U$), the peak tracer concentration is much higher. The fluctuations are also much smaller. An

explanation for this is given in §5.1. As Λ decreases, the size of the fluctuations seems to increase and the peak tracer concentration decreases. We can understand this by the fact that the velocity field works to smooth out the mean tracer concentration by causing random fluctuations in the tracer field which will have time mean 0. The biological processes cannot act fast enough to damp out these fluctuations.

Figure 3 demonstrates the competing effects of the two processes more quantitatively. In *a*) we see that as the timescale over which the biological processes act decreases ($\Lambda \gg U$), the tracer concentration has much more spatial variance and closely matches $c_0 = 1 + \Delta \cos x$, whilst when turbulence acts on faster timescales ($\Lambda \ll 1$), the tracer concentration has very little spatial variation and a much smaller magnitude. *d*) shows that the spatially averaged tracer concentration has some dependence on the size of the spatial forcing Δ for small values of Λ. In *b*) and *d*) we note that the relative magnitude of the fluctuations is largest around $\Lambda \sim 0.5$ (vertical lines). Finally *c*) shows that the tracer flux is also largest around $\Lambda = 1$. We can understand this by the fact that to have a large flux, we need some spatial dependence to our tracer concentration (requires large Λ) but we also need our velocity to not be too small (requires large U). *f*) verifies that the spatial average of the tracer flux is indeed 0 as we would expect by symmetry (minor fluctuations result from not averaging for long enough).

4 Testing $\langle u\theta' \rangle \propto -\nabla\overline{\theta}$

As a first attempt to relate the gradient of the mean tracer concentration, we assume that the magnitude of the tracer fluctuations $\langle \theta'^2 \rangle$ is negligible and that the tracer flux is proportional to the gradient of the mean tracer concentration multiplied by the variance of the velocity, $\langle u\theta' \rangle \approx -\langle u^2 \rangle \nabla\overline{\theta}$. From (19) $\langle u^2 \rangle = 1$, so (22) becomes,

$$\frac{\partial \overline{\theta}}{\partial t} - (U + \mathcal{K}) \frac{\partial^2 \overline{\theta}}{\partial x^2} = \Lambda \overline{\theta} \left(1 - \frac{\overline{\theta}}{1 + \Delta \cos x} \right). \tag{23}$$

We can then test how well this approximation works for various choices of Λ and Δ. From Figure 3 we choose to do our tests at $\Lambda = 0.01, 0.1, 0.5, 1.0, 10.0, 100.0$ where $\Lambda = 0.5$ is chosen to be close to the peak location where fluctuations become significant. From Figure 4, we see that for large Λ, the ensemble averaged mean tracer concentration (solid lines) is matched fairly well with the approximation (dashed lines). For $\Lambda \lesssim 1$, the approximation becomes much worse. The success of the approximation for large Λ, may be down to the fact that at these values of Λ, u has very little effect on the mean tracer concentration so the parameterisation of $\partial \langle uc \rangle / \partial x$ doesn't really matter for calculating the mean tracer concentration. However, whatever choice we make for Λ, our approximation does a very bad job of reproducing the desired flux-gradient relationship, as shown in the lower panels.

We can however make some further conclusions about the flux-gradient relationship. At large Λ, the relationship is close to bijective and from the plots for $\Lambda = 10$ and 100 in Figure 4, the flux-gradient relationship seems to have some dependence on Λ. As Λ decreases, the relationship becomes surjective and potentially non-local.

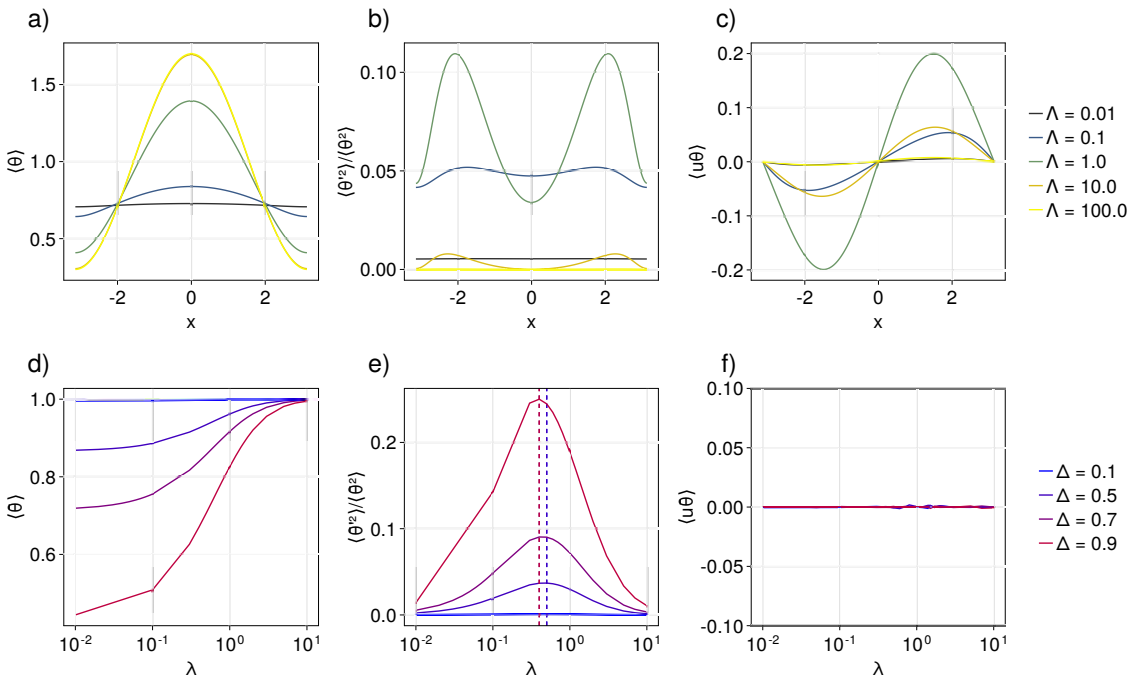

Figure 3: Analysis of the effect changing the timescale over which the biological processes act has on the tracers. a), b) and c) give the spatially dependent time and ensemble mean in the case of $\Delta = 0.7$, $U = 1$ of the, a) tracer concentration, b) magnitude of the fluctuations squared compared to the square of the tracer concentration and c) tracer flux. d), e) and f) give the spatially, time and ensemble mean in the case where $U = 1$ of the, d) tracer concentration, e) magnitude of the fluctuations squared compared to the square of the tracer concentration with the value of Λ at the maximum marked with the dotted lines and f) spatially averaged tracer flux.

5 Asymptotic Expansions

A slightly less naive assumption to work out how the gradient of the mean tracer concentration relates to the tracer flux would be take limits of (20) in the case when $\Lambda \gg U$ and $\Lambda \ll U$. We first consider the limit where $\Lambda \gg U$.

5.1 $\Lambda \gg U$

Physically, $\Lambda \gg U$ means that the biological processes act on much faster timescales than the turbulent processes. As $\Lambda \gg U$, we let $\theta = \theta_0 + U\theta_1 + ...$ Letting $c_0(x) = 1 + \Delta \cos x$, we expand out (20) to increasing order of U. Our zeroth order equation in the statistically steady state gives,

$$0 = \Lambda\theta_0 \left(1 - \frac{\theta_0}{c_0(x)}\right) \Rightarrow \theta_0 = c_0(x) = 1 + \Delta \cos x. \tag{24}$$

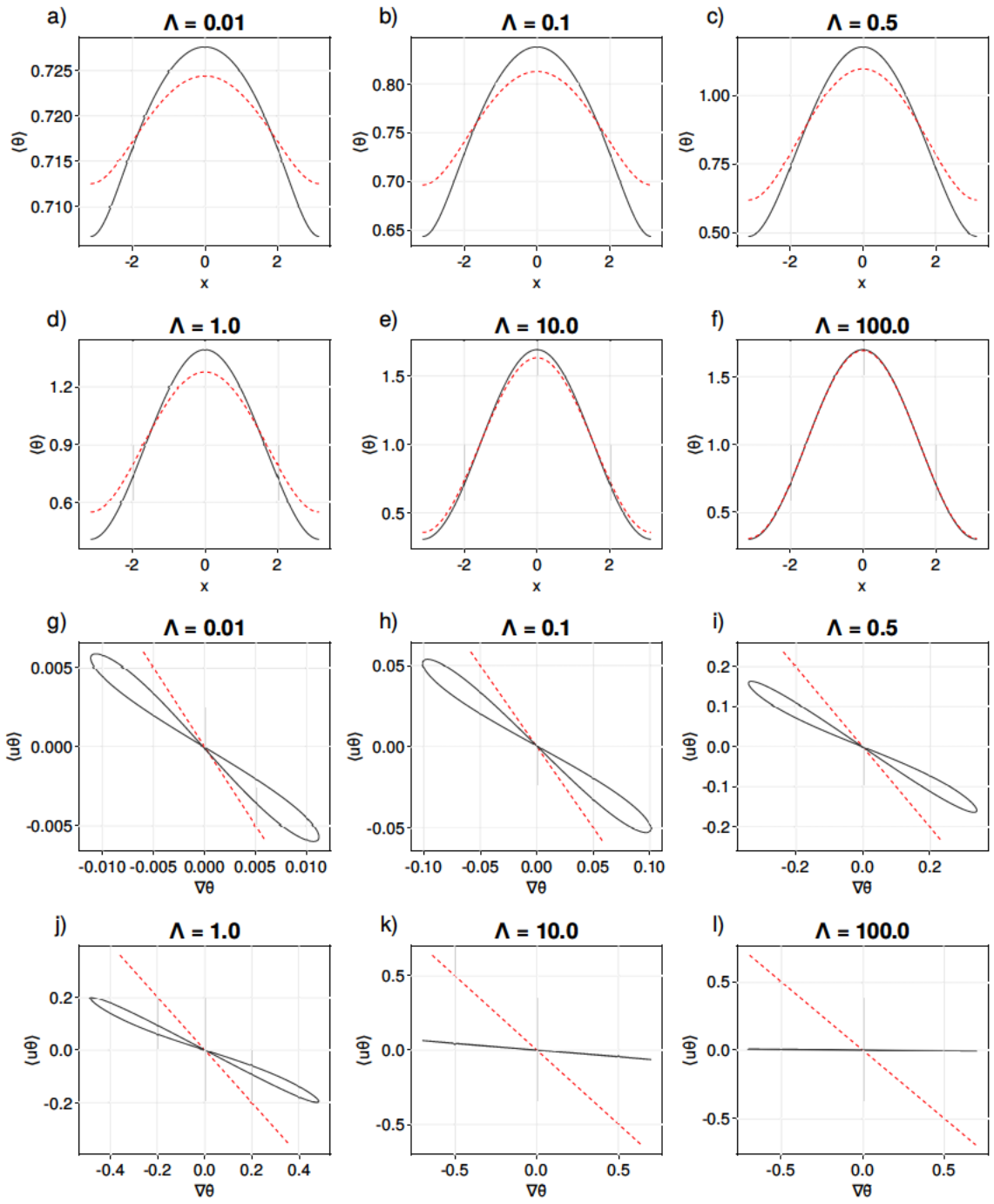

Figure 4: Testing the assumption (red dashed lines), $\langle u\theta' \rangle = -\nabla\overline{\theta}$ that tracer fluctuations can be neglected with the ensemble average (solid lines). $a) - f)$ mean tracer concentration, $g) - l)$ flux-gradient relationship. Here, $\Delta = 0.7, U = 1.0$.

Subbing in θ_0 our $\mathcal{O}(U^1)$ equation is,

$$\frac{\partial \theta_1}{\partial t} = -\Lambda\theta_1 - u(t)\frac{\partial c_0(x)}{\partial x}, \tag{25}$$

which we can solve to give,

$$\theta_1(x,t) = -e^{-\Lambda t}\frac{\partial c_0(x)}{\partial x}\int_{-\infty}^{t} e^{\Lambda t'}u(t')dt', \tag{26}$$

$$u(t)\theta_1(x,t) = -e^{-\Lambda t}\frac{\partial c_0(x)}{\partial x}\int_{-\infty}^{t} e^{\Lambda t'}u(t')u(t)dt'. \tag{27}$$

We ensemble average to obtain,

$$\langle u\theta_1\rangle = -\frac{\partial c_0(x)}{\partial x}\int_{-\infty}^{t} e^{\Lambda(t'-t)}\langle u(t')u(t)\rangle dt' \tag{28}$$

$$= -\frac{\partial c_0(x)}{\partial x}\langle u^2\rangle\int_{-\infty}^{t} e^{\Lambda(t'-t)}e^{t'-t}dt', \tag{29}$$

$$= -\frac{1}{1+\Lambda}\frac{\partial c_0(x)}{\partial x}, \tag{30}$$

where we have used $\langle u^2\rangle = 1$.

We can also obtain an equation for θ_1^2,

$$\frac{\partial \theta_1^2}{\partial t} = -\Lambda\theta_1^2 - \theta_1 u(t)\frac{\partial c_0(x)}{\partial x}. \tag{31}$$

Again ensemble averaging,

$$\frac{\partial\langle\theta_1^2\rangle}{\partial t} = -\Lambda\langle\theta_1^2\rangle - \langle\theta_1 u(t)\rangle\frac{\partial c_0(x)}{\partial x}. \tag{32}$$

In the statistically steady state,

$$\langle\theta_1^2\rangle = \frac{U^2\Delta^2\sin^2 x}{\Lambda(1+\Lambda)}. \tag{33}$$

In summary we now have expressions for $\overline{\theta}$, $\langle u\theta'\rangle$ and $\langle\theta'^2\rangle$ in the limit where $\Lambda \gg U$. Significantly we also have a way of relating the tracer flux to the gradient of the tracer concentration,

$$\overline{\theta} = 1 + \Delta\cos x, \tag{34}$$

$$\langle u\theta'\rangle = -\frac{1}{1+\Lambda}\Delta\sin x, \tag{35}$$

$$\langle\theta'^2\rangle = \frac{U^2\Delta^2\sin^2 x}{\Lambda(1+\Lambda)}, \tag{36}$$

$$U\langle u\theta'\rangle = -\frac{U}{1+\Lambda}\nabla\overline{\theta}. \tag{37}$$

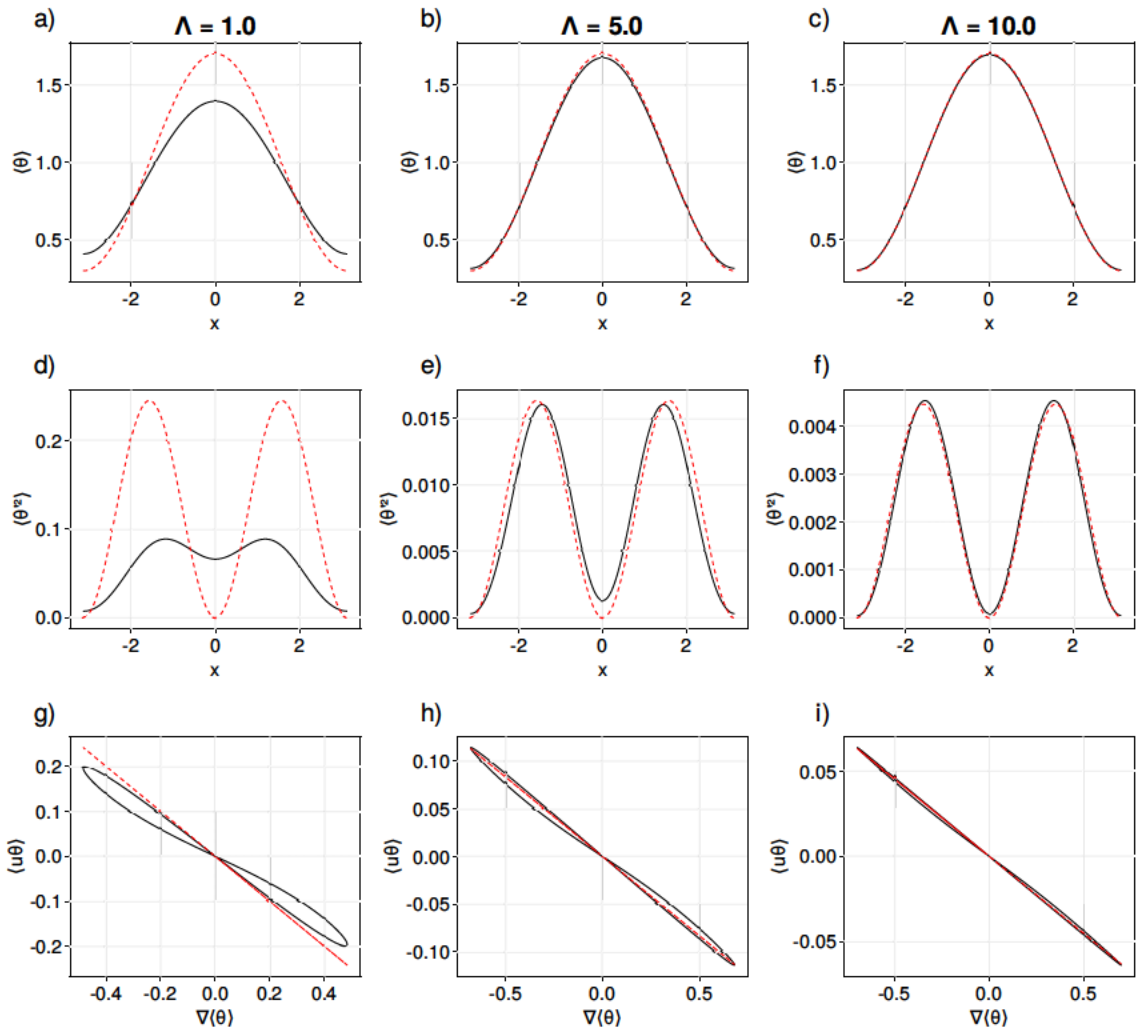

Figure 5: Comparison for the ensemble-averaged (solid lines) and estimated relationships in the limit of $\Lambda \gg U$ (red dashed lines) for, a), b), c), the mean concentration, (34), d), e), f) the tracer fluctuations (36), g), h), i) the flux-gradient relationship (37). Here, $\Delta = 0.7, U = 1.0$.

Figure 5 compares the ensemble-averaged results with the approximations for the tracer mean, fluctuations and flux-gradient relationship. The figure shows overall good spatial agreement in all cases for $\Lambda = 10$, with the prediction of the tracer mean still being good for $\Lambda = 5.0$. For $\Lambda = 1.0$, the spatial agreement in all three aspects is poor.

Figure 6 shows that for $\Lambda \gtrsim 3$, the root-mean-square percentage error (RMSPE) between the prediction and the result indicates that they agree to within 50%, but the prediction significantly worsens for small Λ.

The relative insignificance of the fluctations and the fact that our flux-gradient rela-

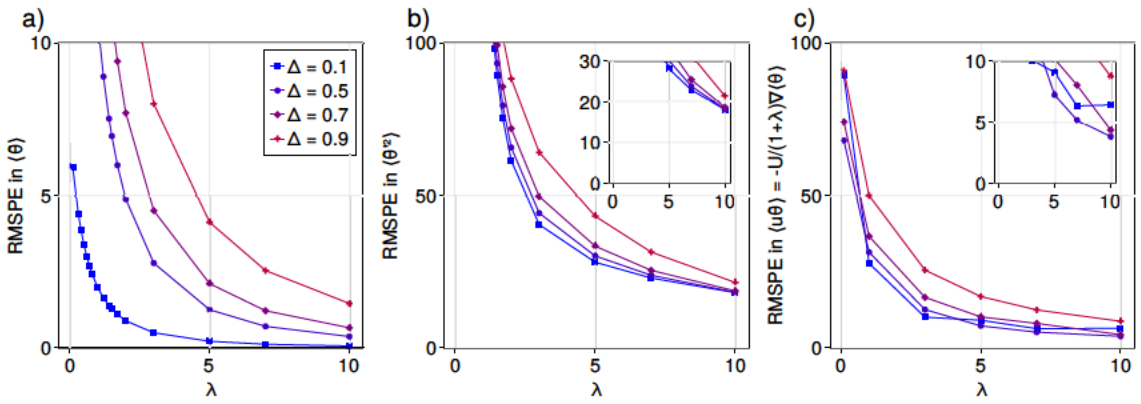

Figure 6: Root-mean-square-percentage-error of the a) ensemble mean and large Λ estimate, (34), b) ensemble mean tracer fluctuations and large Λ estimate, (36), c) ensemble flux-gradient relationship , with the large Λ estimate, (37), for, $\Delta = 0.1, 0.5, 0.7, 0.9, U = 1.0$. The text legend follows for b) and c).

tionship is bijective can be understood by the fact that, when the biological processes act on much shorter timescales, any effects of the turbulent velocity field bringing the tracer concentration away from the carrying capacity are quickly reversed by the speed at which the biological processes act. This means that the fluctuations are small and the flux is dominated by the biological processes which are local.

5.2 $\Lambda \ll U$

We can try the same method in the limit where the turbulent processes act on much faster timescales than the biological processes. In this case we let $\theta = \theta_0 + \Lambda\theta_1 + ...$

To $\mathcal{O}(\Lambda^0)$,

$$\frac{\partial \theta_0}{\partial t} + Uu\frac{\partial \theta_0}{\partial x} = 0. \tag{38}$$

In the steady state $\partial\theta_0/\partial t = 0 \Rightarrow \theta_0 = const.$

To $\mathcal{O}(\Lambda^1)$,

$$\frac{\partial \theta_1}{\partial t} + U\frac{\partial (u\theta_1)}{\partial x} = \theta_0\left(1 - \frac{\theta_0}{1 + \Delta\cos x}\right). \tag{39}$$

Working in the steady state and taking the spatial average,

$$\frac{1}{2\pi}[Uu\theta_1(x)]_{-\pi}^{\pi} = \frac{1}{2\pi}\int_{-\pi}^{\pi}\theta_0\left(1 - \frac{\theta_0}{1 + \Delta\cos x}\right)dx, \tag{40}$$

$$\theta_0 = (1 - \Delta^2)^{1/2}, \tag{41}$$

where we have used the fact that the flux is periodic. We wish to get an expression for the gradient of the tracer concentration and the tracer flux. We can obtain an expression for

the tracer flux by integrating (39) in the steady state. However, to get an expression for the mean tracer concentration gradient, we must solve (39). One way to solve this is using ensemble averaging, a method which is detailed in the next section.

6 Finite-state Averaging

6.1 Description of the method

What is given in this section is only a summary of how finite-state averaging works, for a fuller explanation see [5].

We start off by considering our stochastic velocity field. We can write a Fokker-Plank equation to describe the time evolution of the probability density function (PDF), $\varrho(u,t)$ of the velocity field. $\varrho(u,t)$ gives the probability of the velocity having a value u at time t. For the Ornstein-Uhlenbeck process,

$$\partial_t \varrho(u,t) = \partial_u[u\varrho(u,t) + \partial_u \varrho(u,t)]. \tag{42}$$

Likewise for our tracer concentrations, there will be a joint PDF $\rho(u,\theta(x,t),t)$ giving the probability that at a certain value of x and t, the tracer will have concentration, $\theta(x,t)$ and will be advected with velocity $u(t)$. We have two coupled equations, (19) and (20), which describe the evolution of the tracer concentration. Writing $\partial_t\theta(x,t) = g(u,\theta(x,t))$, the joint PDF for the tracer concentration is given by,

$$\partial_t \rho(u,\theta(x,t),t) = \partial_u[u\rho(u,\theta(x,t),t) + \partial_u \rho(u,\theta(x,t),t)] - \partial_\theta \left[g(u,\theta(x,t))\rho(u,\theta(x,t),t)\right]. \tag{43}$$

We now discretise our velocity field into m different states, $u_1, u_2, ..., u_m$, with $m+1$ different bounding velocities $b_1, b_2, ..., b_{m+1}$, such that,

$$u_1 = b_1 < u \leq b_2, \tag{44}$$
$$u_2 = b_2 < u \leq b_3, \tag{45}$$
$$\vdots \tag{46}$$
$$u_m = b_m < u \leq b_{m+1}. \tag{47}$$

We denote the probability that the velocity field is in state m by $\mathcal{P}_m$,

$$\mathcal{P}_m(t) = \int_{b_m}^{b_{m+1}} \varrho(u,t)du. \tag{48}$$

We now want to use (43), to obtain an equation for the evolution of the joint scaled PDF of $\rho(u,\, \theta(x,\, t),\, t)$, under the constraint that we are only considering ensemble members currently being advected by velocities in the range satisfied by state m. Thus, we are calculating,

$$\int_{b_m}^{b_{m+1}} \partial_t \rho(u,\theta(x,t),t)du = \int_{b_m}^{b_{m+1}} \partial_u \left[u\rho(u,\theta(x,t),t) + \partial_u \rho(u,\theta(x,t),t)\right] du - \int_{b_m}^{b_{m+1}} \partial_\theta \left[g(u,\theta(x,t))\rho(u,\theta(x,t),t)\right] du. \tag{49}$$

Assuming,

$$\int_{b_m}^{b_{m+1}} \partial_\theta \left[g(u, \theta(x,t)) \rho(u, \theta(x,t), t) \right] du \approx \partial_\theta \left[g(u_m, \theta(x,t)) \int_{b_m}^{b_{m+1}} \rho(u, \theta(x,t), t) du \right], \quad (50)$$

and denoting, $\rho_m(\theta(x,t),t) = \int_{b_m}^{b_{m+1}} \rho(u, \theta(x,t), t) du$, we obtain an equation for the evolution of our state constrained scaled PDF,

$$\partial_t \rho_m(\theta(x,t),t) = \partial_u [u \rho_m(\theta(x,t),t) + \partial_u \rho_m(\theta(x,t),t)] - \partial_\theta \left[g(u_m, \theta(x,t)) \rho_m(\theta(x,t),t) \right]. \quad (51)$$

The ∂_u terms describe the process of our system transitioning from one velocity state to another. The $g(u_m, \theta)\partial_\theta \rho_m$ terms account for the effects of advection, diffusion and biological processes on the tracer concentration. Applying a finite volume discretisation to (42) (see [5] for details), we use a matrix to represent the ∂_u terms,

$$\partial_t \mathcal{P}_m = \sum_n Q_{mn} \mathcal{P}_n. \quad (52)$$

For the Ornstein-Uhlenbeck process discretised over $N+1$ states (i.e., for the two-state system $N = 1$), and with the indices in the matrix $(m, n) = 0, 1, ...N$,

$$Q_{mn} = \frac{1}{2}[-N\delta_{nm} + n\delta_{(m+1)n} + (N-n)\delta_{(m-1)n}], \quad (53)$$

$$Q = \frac{1}{2} \begin{pmatrix} -N & 1 & & & & & \\ N & -N & 2 & & & & \\ & N-1 & -N & 3 & & & \\ & & \ddots & \ddots & \ddots & & \\ & & & 3 & -N & (N-1) & \\ & & & & 2 & -N & N \\ & & & & & 1 & -N \end{pmatrix}. \quad (54)$$

Generally, the eigenvalues of this matrix are given by $[0, -1, -2, -3, ..., -(N-1), -N]$ with the left eigenvector associated with eigenvalue 0 given by $(1, 1, ..., 1)$. The steady-state probability distribution is given by the binomial,

$$\mathcal{P}_n = 2^{-N} \binom{N}{n}. \quad (55)$$

Thus, we have a new series of equations to describe the evolution of the $N-1$ state constrained scaled[1] PDF $\rho_m(\theta(x,t),t)$ of $\theta(x,t)$ given that the ensemble members are currently being advected by velocities $b_m < u \leq b_{m+1}$,

$$\partial_t \rho_m = -g(u_m, \theta)\partial_\theta \rho_m + \sum_n Q_{mn} \rho_n, \quad (56)$$

$$\partial_t \theta = g(u, \theta), \quad (57)$$

$$Q_{mn} = \frac{1}{2}[-N\delta_{nm} + n\delta_{(m+1)n} + (N-n)\delta_{(m-1)n}]. \quad (58)$$

[1]Our PDF is scaled because $\int \rho_m(\theta, t) d\theta = \mathcal{P}_m \neq 1$.

Integrating (56) with respect to θ will give the probability $\mathcal{P}_m(t)$, that ensemble members are currently being advected by velocities $b_m < u \leq b_{m+1}$,

$$\mathcal{P}_m(t) = \int d\theta \rho_m(\theta, t). \tag{59}$$

We can also obtain the probability weighted conditional mean, Θ_m which is the mean value of θ given that the ensemble member is currently being advected by velocities $b_m < v \leq b_{m+1}$. In other words Θ_m is the probability weighted conditional mean of $\theta = \theta_m$,

$$\Theta_m(t) = \int d\theta \, \theta \rho_m(\theta, t). \tag{60}$$

The conditional mean $\langle \theta_m \rangle$ of all members being advected with velocities $b_m < u \leq b_{m+1}$ is given by,

$$\langle \theta_m \rangle = \frac{1}{\mathcal{P}_m} \int d\theta \, \theta \rho_m = \frac{\Theta_m}{\mathcal{P}_m}. \tag{61}$$

Thus, $\sum_m \mathcal{P}_m = 1$ and in the limit where $N \to \infty$, $\langle \theta \rangle = \sum_m \Theta_m$, $\langle u\theta \rangle = \sum_m u_m \Theta_m$, where $u_m = \int_{b_m}^{b_{m+1}} u\varrho(u)du$. Therefore, if we can solve (60), we can obtain an expression for our mean tracer concentration and mean tracer flux. For the Ornstein-Uhlenbeck process discretised over $N-1$ states, $u_m = 2/\sqrt{N}(m - N/2)$[5]. Figure 7 demonstrates how finite-state averaging works for the two-state system.

As a general example we consider the case when $g(\theta) = a(x) + b(x)\theta + c(x)\theta^n$, where $n \neq 0, 1$. Integrating by parts,

$$\partial_t \Theta_m(x,t) = \mathcal{P}_m a(x) + b(x)\Theta_m(x,t) + \int \rho_m(\theta) b(x) \theta(x,t)^n d\theta + \sum_n Q_{mn}\Theta_n. \tag{62}$$

Thus, we see that as long as $g(\theta)$ contains only terms $\mathcal{O}(\theta^1)$ and $\mathcal{O}(\theta^0)$ conditional averaging will work well as a method to obtain $\langle u \rangle$ and $\langle u\theta \rangle$.

6.2 Applying the finite-state averaging to the case where $\Lambda \ll U$

In the case where $\Lambda \ll U$, using (39),

$$g(u,\theta) = -U\frac{\partial(u\theta)}{\partial x} + \mathcal{K}\frac{\partial^2 \theta}{\partial x^2} + \theta_0 \left(1 - \frac{\theta_0}{1 + \Delta \cos x}\right). \tag{63}$$

Using (62) and denoting $s(x) = \theta_0(1 - \theta_0(1 + \Delta \cos x)^{-1})$ we obtain an expression for our conditional means,

$$\frac{\partial \Theta_m(x,t)}{\partial t} = \mathcal{P}_m s(x) - U\frac{\partial(u_m \Theta_m)}{\partial x} + \mathcal{K}\frac{\partial^2 \Theta_m}{\partial x^2} + \sum_n Q_{mn}\Theta_n. \tag{64}$$

In this case as $\theta = \theta_0 + \Lambda\theta_1$ and (64) solves for θ_1, $\langle u\theta \rangle = \Lambda \sum_m u_m \Theta_m$ and $\langle \theta \rangle = \sqrt{1 - \Delta^2} + \Lambda \sum_m \Theta_m$. Figure 8 tests the approximation for 2, 3, 10 and 20 states. For $\Lambda \lesssim 0.1$, the flux-gradient relationship is matched very well as the number of states increases,

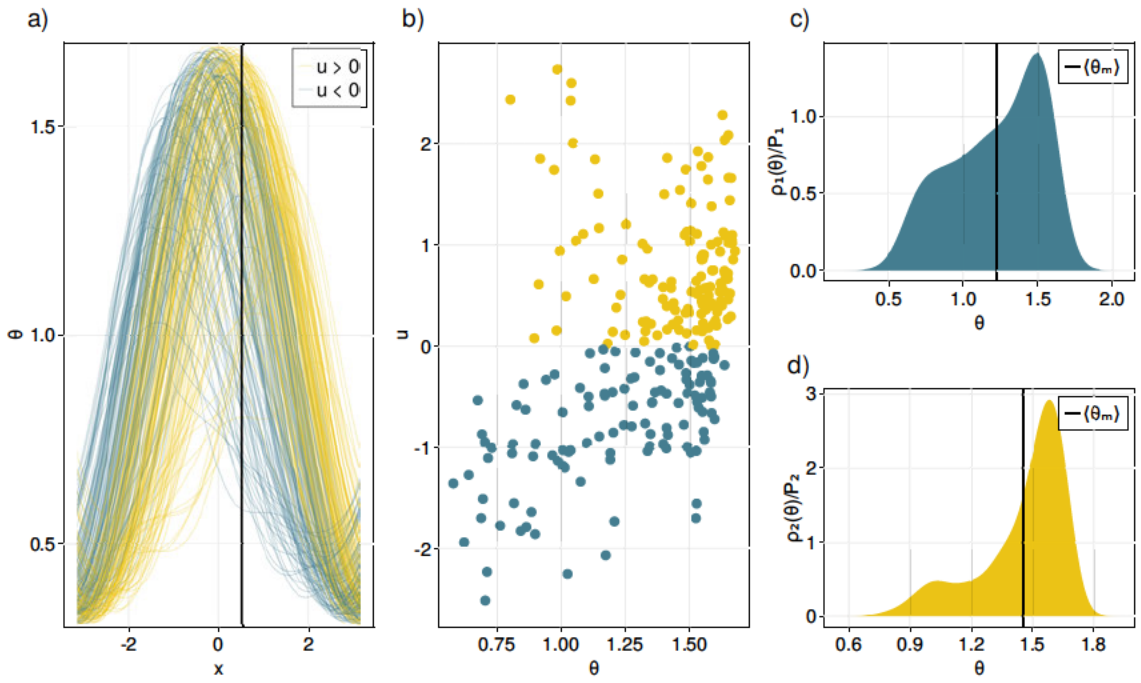

Figure 7: Demonstration of conditional averaging for the two-state system. a) At each instant in time each tracer is being advected with a certain velocity u (yellow and blue lines). We can split our tracers into those with positive velocities (blue lines) and those with negative velocities (yellow lines). At a certain distance, (black line in a) corresponding to $x = 0.53$) we can plot b) the concentration of each tracer and corresponding velocity at each time interval. This can be used to construct the joint PDF $\rho(u, \theta)$. Instead we construct separate PDFs for the concentration in each range of u, i.e., we construct PDFs for the blue c) and yellow d) markers separately. The conditional mean is given by (61) and marked by the straight black lines. If, instead, we wanted to calculate the probability weighted conditional average, Θ_1, Θ_2 we would scale the PDF in c) and d), where instead of $\int \rho d\theta = 1$, $\int \rho d\theta = \mathcal{P}_m$. Here, $t = 1000$, $N = 250$, $\Lambda = U = 1.0$. The same method can be generalised for multiple states.

with the two state approximation consistently not performing well. The approximation consistently overestimates the tracer mean. As Λ increases, the small Λ approximation works less well, as is to be expected.

For the M state system we have M equations and M unknowns, so theoretically we could get an analytical expression for any number of states. However, in order to obtain results which are easier to interpret we choose to solve (64) for the 3-state system, $u_1 = -\sqrt{2}, u_2 = 0, u_3 = \sqrt{2}$.

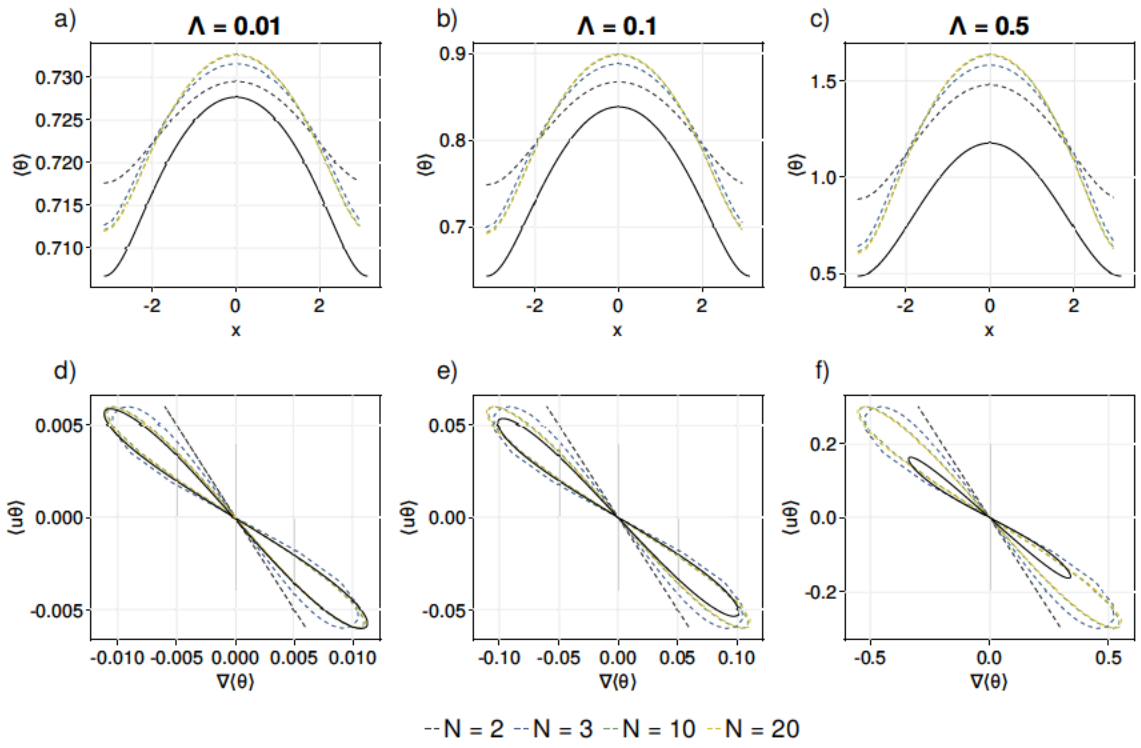

Figure 8: Comparison for the finite-state averaged (black lines) and estimated relationships (dashed coloured lines) for the mean concentration $a) - c)$ and for the flux-gradient relationship $d) - f)$ calculated using (84). Here, $\Delta = 0.7, U = 1.0$.

In matrix form, where $\mathbf{\Theta} = (\Theta_1, \Theta_2, \Theta_3)$,

$$\partial_t \mathbf{\Theta} = \underbrace{\begin{pmatrix} 1/4 \\ 1/2 \\ 1/4 \end{pmatrix}}_{\tilde{S}} s(x) + U \underbrace{\begin{pmatrix} \sqrt{2} & & \\ & 0 & \\ & & -\sqrt{2} \end{pmatrix}}_{\tilde{U}} \partial_x \mathbf{\Theta} + \mathcal{K}\mathbb{I}\partial_{xx}\mathbf{\Theta} + Q\mathbf{\Theta}. \tag{65}$$

We diagonalise $Q = Z^{-1}\Lambda Z$ using the basis transformation $\mathbf{\Theta} = Z\mathbf{f}$ where,

$$Z = 1/4 \begin{pmatrix} 1 & 2 & 1 \\ 2 & 0 & -2 \\ 1 & -2 & 1 \end{pmatrix}. \tag{66}$$

We obtain,

$$\partial_t Z^{-1} Z\mathbf{f} = Z^{-1}\tilde{S}s(x) + UZ^{-1}\tilde{U}Z\partial_x \mathbf{f} + Z^{-1}\mathbb{I}Z\partial_{xx}\mathbf{f} + Z^{-1}QZ\mathbf{f}. \tag{67}$$

Subbing in Z,

$$\partial_t \mathbf{f} = \begin{pmatrix} 1 \\ 0 \\ 0 \end{pmatrix} s(x) + U \begin{pmatrix} 0 & \sqrt{2} & 0 \\ \sqrt{2}/2 & 0 & \sqrt{2}/2 \\ 0 & \sqrt{2} & 0 \end{pmatrix} \partial_x \mathbf{f} + \mathbb{I}\partial_{xx}\mathbf{f} + \begin{pmatrix} 0 & & \\ & -1 & \\ & & -2 \end{pmatrix} \mathbf{f}. \tag{68}$$

Finally we note $f_1 = \Theta_1 + \Theta_2 + \Theta_3 = (\langle\theta\rangle - \theta_0)/\Lambda$ and $f_2 = \Theta_1 - \Theta_3 = -\langle u\theta\rangle/(\sqrt{2}\Lambda)$. In the steady state and neglecting the terms corresponding to diffusion, we obtain,

$$\sqrt{2}U\partial_x f_2 = -s(x), \tag{69}$$

$$U\sqrt{2}\partial_x(f_1 + f_3) = 2f_2, \tag{70}$$

$$\sqrt{2}U\partial_x f_2 = 2f_3. \tag{71}$$

Eliminating f_3 we get an equation for f_1,

$$\frac{\partial f_1}{\partial x} = -\frac{1}{U^2}\int s(x)dx + \frac{1}{2}\frac{\partial s}{\partial x}. \tag{72}$$

Subbing in $s(x)$ and $\nabla\langle\theta\rangle = \Lambda f_1$,

$$\nabla\langle\theta\rangle = -\frac{2\Lambda\theta_0}{U^2}\left[x - 2\arctan\left(\frac{\theta_0}{1+\Delta}\tan\left(\frac{x}{2}\right)\right)\right] + \frac{\Lambda\Delta\theta_0^2}{2}\frac{\sin x}{(1+\Delta\cos x)^2} \tag{73}$$

Rearranging, (69), we also obtain an expression for $\langle u\theta\rangle$, which is the same equation we would have obtained from integrating (39),

$$U\langle u\theta\rangle = 2\Lambda\theta_0\left[x - 2\arctan\left(\frac{\theta_0}{1+\Delta}\tan\left(\frac{x}{2}\right)\right)\right]. \tag{74}$$

Thus, we now have a flux-gradient relation,

$$U\langle u\theta\rangle = -U^2\nabla\langle\theta\rangle + \frac{U^2\Lambda\Delta\theta_0^2}{2}\frac{\sin x}{(1+\Delta\cos x)^2}. \tag{75}$$

We note that ,

$$U\frac{\partial}{\partial x}\left(\frac{\partial\langle u\theta_1\rangle}{\partial x}\right) = \theta_0\frac{\partial}{\partial x}\left(1 - \frac{\theta_0}{1+\Delta\cos x}\right) = \frac{\Delta\theta_0^2\sin\theta}{(1+\Delta\cos x)^2}. \tag{76}$$

Thus,

$$U\langle u\theta\rangle = U^2\left[-\nabla\langle\theta\rangle + \frac{U}{2}\frac{\partial^2}{\partial x^2}\langle u\theta\rangle\right]. \tag{77}$$

We can test the success of this flux-gradient relation by using it to calculate our expected fluxes when we substitute in the ensemble-averaged mean into the right-hand side of (75). Figure 9 tests how well the conditionally averaging method reproduces the ensemble averaged mean (a) and flux-gradient relationship (b). We see that for $\Lambda \lesssim 0.1$, (75) estimates the correct flux-gradient relationship to within $\sim 50\%$ and the ensemble mean to within$\sim 10\%$.

6.3 Finite-state averaging for the general case

We can try and apply the whole procedure for the general case. Our expression for $g(u,\theta)$ is given by,

$$g(u,\theta) = -U\frac{\partial(u\theta)}{\partial x} + \mathcal{K}\frac{\partial^2\theta}{\partial x^2} + \theta\left(1 - \frac{\theta}{1+\Delta\cos x}\right). \tag{78}$$

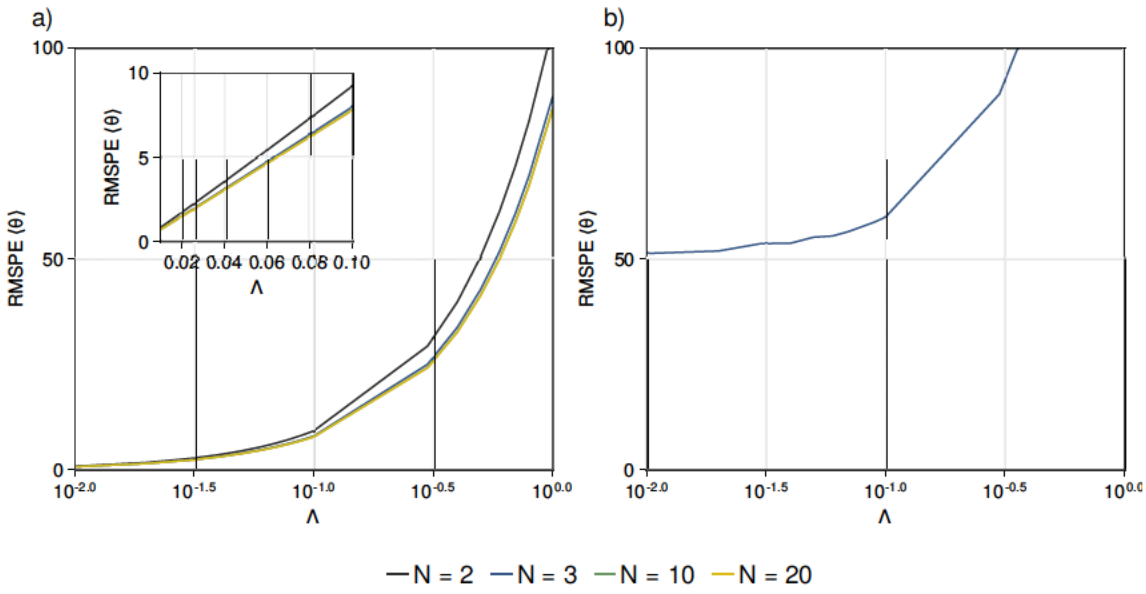

Figure 9: RMSPE for the a) ensemble-averaged mean compared to the estimated mean for 2, 3, 10 and 20 states used in the conditionally averaging method in the small Λ limit, (64). b) the ensemble-averaged flux-gradient compared to the estimated flux-gradient relation for the 3 state system (75). Here, $\Delta = 0.7, U = 1.0$.

Again, using (62) we obtain an expression for our conditional means,

$$\partial_t \Theta_m = -Uu\partial_x \Theta_m + \mathcal{K}\partial_{xx}\Theta_m + \Lambda\Theta_m - \frac{\Lambda}{1+\Delta\cos x}\int \theta^2 \rho_m d\theta + \sum_n Q_{mn}\Theta_n. \tag{79}$$

Here lies the problem, (79) contains an integral with no obvious physical interpretation. In order to progress further, we must approximate this integral.

6.3.1 First approximation, neglect the conditional expectation perturbations

First we note that,

$$\int \theta^2 \rho_m d\theta = \int d\theta \rho_m \left[\left(\theta - \frac{\Theta_m}{\mathcal{P}_m} \right)^2 + \frac{2\theta\Theta_m}{\mathcal{P}_m} - \frac{\Theta_m^2}{\mathcal{P}_m^2} \right]. \tag{80}$$

Using (59) and (60) this simplifies to,

$$\int \theta^2 \rho_m d\theta = \int d\theta \rho_m \left[\left(\theta - \frac{\Theta_m}{\mathcal{P}_m} \right)^2 + \frac{\Theta_m^2}{\mathcal{P}_m} \right], \tag{81}$$

$$= \int d\theta \rho_m \left[(\theta - \langle \theta_m \rangle)^2 + \frac{\Theta_m^2}{\mathcal{P}_m} \right]. \tag{82}$$

If we neglect the conditional expectation perturbations (i.e. we assume that the probability density function is sharply peaked),

$$\int \theta^2 \rho_m d\theta \approx \int \frac{\Theta_m^2}{\mathcal{P}_m}. \tag{83}$$

Thus, we have an approximate conditionally averaged expression for the change in ensemble-averaged tracer concentration,

$$\partial_t \Theta_m = -Uu\partial_x \Theta_m + \mathcal{K}\partial_{xx}\Theta_m + \Lambda\Theta_m - \Lambda\Theta_m - \frac{\Lambda}{1+\Delta\cos x}\frac{\Theta_m^2}{\mathcal{P}_m} + \sum_n Q_{mn}\Theta_n \tag{84}$$

Figure 10 shows the approximation for the $2, 3, 10$ and 20 state system. We note that the method does a very good job for matching the gradient-flux relation when the number of states is large. However, it is less successful at reproducing the correct mean tracer concentration and seems to over-predict the concentration in all cases apart for the two state system.

6.3.2 Second approximation, using the equation for $\langle 1/\theta \rangle$

Using a change of variables, $\phi = \theta^{-1}$, (20) becomes,

$$\partial_t \phi = -Uu\partial_x \phi + \mathcal{K}\left[\partial_{xx}\phi - \frac{2}{\phi}(\partial_x \phi)^2\right] - \Lambda\phi + \frac{\Lambda}{1+\Delta\cos x}. \tag{85}$$

When $\mathcal{K}$ is negligible, this equation becomes linear so we have no problems applying a conditional average to this equation.

Assuming $\theta' \ll \overline{\theta}$, we note that,

$$\left\langle \frac{1}{\theta} \right\rangle = \left\langle \frac{1}{\overline{\theta}+\theta'} \right\rangle, \tag{86}$$

$$= \frac{1}{\overline{\theta}}\left\langle 1 - \frac{\theta'}{\overline{\theta}} + \left(\frac{\theta'}{\overline{\theta}}\right)^2 + \ldots \right\rangle, \tag{87}$$

$$\approx \frac{1}{\overline{\theta}^3}\left\langle \overline{\theta}^2 + \theta'^2 \right\rangle, \tag{88}$$

$$\approx \frac{1}{\overline{\theta}^3}\langle \theta^2 \rangle. \tag{89}$$

Considering our conditional means $\langle \theta_m \rangle$, and assuming that $\theta_m' \ll \overline{\theta_m}$, where $\overline{\theta_m} = \langle \theta_m \rangle$ and θ_m' corresponds to the concentration fluctuations, considering only tracers being advected by velocities $b_m < v \leq b_{m+1}$, we argue,

$$\left\langle \frac{1}{\theta_m} \right\rangle \approx \frac{1}{\langle \theta_m \rangle^3}\langle \theta_m^2 \rangle. \tag{90}$$

Thus, denoting $\Phi_m/\mathcal{P}_m = \phi_m = \langle 1/\theta_m \rangle$ we obtain a second approximation for modeling our θ^2 term,

$$\int \theta^2 \rho_m d\theta = \mathcal{P}_m \langle \theta_m^2 \rangle, \tag{91}$$

$$\approx \mathcal{P}_m \left\langle \frac{1}{\theta_m} \right\rangle \langle \theta_m \rangle^3, \tag{92}$$

$$\approx \mathcal{P}_m \frac{\Phi_m}{\mathcal{P}_m} \frac{\Theta_m^3}{\mathcal{P}_m^3}, \tag{93}$$

$$\approx \frac{\Phi_m \Theta_m}{\mathcal{P}_m^2} \frac{\Theta_m^2}{\mathcal{P}_m}. \tag{94}$$

Thus, we have a new equation for our conditional averages,

$$\partial_t \Theta_m = -Uu\partial_x \Theta_m + \mathcal{K}\partial_{xx}\Theta_m + \Lambda\Theta_m - \frac{\Lambda \mathcal{P}_m}{1+\Delta\cos x}\left(\frac{\Theta_m^2}{\mathcal{P}_m^2}\frac{\Phi_m\Theta_m}{\mathcal{P}_m^2}\right) + \sum_n Q_{mn}\Theta_n. \tag{95}$$

To solve this equation, we also need to have an expression for Φ_m which we obtain from neglecting $\mathcal{K}$ in (85) and using (62),

$$\partial_t \Phi_m = -Uu\partial_x \Phi_m - \Lambda\Phi_m + \frac{\mathcal{P}_m \Lambda}{1+\Delta\cos x} + \sum_n Q_{mn}\Phi_n. \tag{96}$$

We note that the equation for the conditionally averaged inverse means, Φ_m does not depend on the conditional means, Θ_m. Thus, (96) can be solved first and the solution put into (95).

Figure 11 demonstrates the success of this approximation. We see that as the number of states increase, the conditionally estimated mean maps very closely onto the true ensemble mean. The flux-gradient relationships also do a very good job of mirroring the ensemble -averaged flux-gradient relationships.

We can compare the two methods (84) and (95) in Figure 12. We see that the method using $\langle 1/\theta \rangle$ to correct for the fluctuations reduces the RMSPE to be $< 0.5\%$ in the case when $N = 20$. The RMSPE is still relatively small $\sim 5\%$ for the method which avoids using the inverse.

6.4 Analytical flux-gradient relationships

Having demonstrated the success of the finite-state averaging method in reproducing the desired tracer flux-gradient relationship. We now examine the finite-state averaged equations to see if we can make any analytical headway. We note that, theoretically, you could solve for $\langle u\theta \rangle = \int dx' \mathcal{K}_{eff}(x,t,\bar{\theta},x',t')\nabla\theta$ for any number of states, however, this becomes increasingly challenging and it is harder to make useful interpretations of the result. For the analysis we again let $c_0 = 1 + \Delta\cos x$.

6.4.1 Two-state system

We begin by considering the two state system for (84). In this case $\langle\theta\rangle = \Theta_1 + \Theta_2$ and $\langle u\theta\rangle = -\Theta_1 + \Theta_2$. Our two-equations are,

$$\partial_t\Theta_1 \approx +U\partial_x\Theta_1 + \mathcal{K}\partial_{xx}\Theta_1 + \Lambda\Theta_1 - \Lambda\frac{(\Theta_1)^2}{\mathcal{P}_1 c_0} - \frac{\Theta_1}{2} + \frac{\Theta_2}{2}, \tag{97}$$

$$\partial_t\Theta_1 \approx -U\partial_x\Theta_2 + \mathcal{K}\partial_{xx}\Theta_2 + \Lambda\Theta_2 - \Lambda\frac{(\Theta_2)^2}{\mathcal{P}_2 c_0} - \frac{\Theta_2}{2} + \frac{\Theta_1}{2}, \tag{98}$$

$$\tag{99}$$

where here we have used $u_0 = -1$, $u_1 = +1$. In the steady state $\mathcal{P}_0 = \mathcal{P}_1 = 0.5$. We can solve to find the operator $\mathcal{K}_{eff}(\langle\theta\rangle)$,

$$\mathcal{K}_{eff}(\langle\theta\rangle) = -U\left[-\mathcal{K}\partial_{xx} - \Lambda + 1 + \frac{2\Lambda}{c_0}\langle\theta\rangle\right]^{-1}. \tag{100}$$

K_{eff} is now non-linear as it depends on $\langle\theta\rangle$. We note that when $\Lambda \gg U$ and $\langle\theta\rangle \sim c_0$, $\mathcal{K}_{eff} \approx -U/(1+\Lambda)$, in agreement with (37).

Figure 13 shows the RMSPE when (100) is used to estimate the flux-gradient relationship, given the gradient of the tracer concentration taken from the finite-state averaging process. We see that the model correctly predicts the flux-gradient r elationship t o within an order of magnitude.

6.4.2 Three-state system

Now considering the three state system for (84)

$$\partial_t\mathcal{P}_1 = -\mathcal{P}_1 + \frac{\mathcal{P}_2}{2}, \tag{101}$$

$$\partial_t\mathcal{P}_2 = -\mathcal{P}_2 + \mathcal{P}_1 + \mathcal{P}_3, \tag{102}$$

$$\partial_t\mathcal{P}_3 = -\mathcal{P}_3 + \frac{\mathcal{P}_2}{2}, \tag{103}$$

$$\partial_t\Theta_1 \approx +U\sqrt{2}\partial_x\Theta_1 + \mathcal{K}\partial_{xx}\Theta_1 + (\Lambda-1)\Theta_1 - \Lambda\frac{(\Theta_1)^2}{\mathcal{P}_1 c_0} + \frac{\Theta_2}{2}, \tag{104}$$

$$\partial_t\Theta_2 \approx +0U\partial_x\Theta_2 + \mathcal{K}\partial_{xx}\Theta_2 + (\Lambda-1)\Theta_2 - \Lambda\frac{(\Theta_2)^2}{\mathcal{P}_2 c_0} + \frac{\Theta_1}{2} + \frac{\Theta_3}{2}, \tag{105}$$

$$\partial_t\Theta_3 \approx -U\sqrt{2}\partial_x\Theta_3 + \mathcal{K}\partial_{xx}\Theta_3 + (\Lambda-1)\Theta_3 - \Lambda\frac{(\Theta_3)^2}{\mathcal{P}_2 c_0} + \frac{\Theta_2}{2}, \tag{106}$$

where here we have used $u_1 = -\sqrt{2}$, $u_2 = 0$, $u_3 = +\sqrt{2}$. In the steady state $\mathcal{P}_1 = \mathcal{P}_3 = 0.25$, $\mathcal{P}_2 = 0.5$.

We apply the same approach as used in §6.2. We write our set of equations in matrix form,

$$\partial_t \boldsymbol{\Theta} = U \begin{pmatrix} \sqrt{2} & & \\ & 0 & \\ & & -\sqrt{2} \end{pmatrix} \partial_x \boldsymbol{\Theta} + \lambda \mathbb{I} \boldsymbol{\Theta} - \frac{\lambda}{c_0} \begin{pmatrix} 4 & & \\ & 2 & \\ & & 4 \end{pmatrix} \begin{pmatrix} \Theta_1^2 \\ \Theta_2^2 \\ \Theta_3^2 \end{pmatrix} + Q\boldsymbol{\Theta}, \tag{107}$$

and diagonalise, $Q = Z^{-1}\Lambda Z$, $\boldsymbol{\Theta} = Z\mathbf{f}$.

$$\partial_t \mathbf{f} = U \begin{pmatrix} 0 & \sqrt{2} & 0 \\ \sqrt{2}/2 & 0 & \sqrt{2}/2 \\ 0 & \sqrt{2} & 0 \end{pmatrix} \partial_x \mathbf{f} + \lambda \mathbb{I} \mathbf{f} - \frac{\lambda}{c_0} \begin{pmatrix} 2 & 1 & 2 \\ 2 & 0 & -2 \\ 2 & -1 & 2 \end{pmatrix} \begin{pmatrix} \Theta_1^2 \\ \Theta_2^2 \\ \Theta_3^2 \end{pmatrix} + \begin{pmatrix} 0 & & \\ & -1 & \\ & & -2 \end{pmatrix} \mathbf{f}. \tag{108}$$

We note that $f_1 = \langle\theta\rangle$, $f_2 = -\langle u\theta\rangle/\sqrt{2}$. Thus, we wish to express $\partial_x f_1$ in terms of f_2. The maths for this is quite complicated but we eventually find,

$$L^{-1} = \left[\Lambda\left(1 - \frac{2\langle\theta\rangle}{c_0}\right) - 2 + \mathcal{K}\partial_x^2\right]^{-1}, \tag{109}$$

$$\underbrace{\left(\Lambda\left(1 - 2\frac{\langle\theta\rangle}{c_0}\right) - 1 + \mathcal{K}\partial_x^2 - U^2\partial_x L^{-1}\partial_x\right)\frac{\langle u\theta\rangle}{\sqrt{2}}}_{L_2[\langle u\theta\rangle]}$$
$$\underbrace{- \left(\frac{U}{\sqrt{2}}\frac{\partial}{\partial x} + \frac{\sqrt{2}\Lambda}{c_0}\langle u\theta\rangle\right) L^{-1}\left[\frac{\Lambda}{c_0}\langle u\theta\rangle^2\right]}_{\mathcal{N}_2[\langle u\theta\rangle]} = \frac{\sqrt{2}}{2}U\frac{\partial}{\partial x}\langle\theta\rangle, \tag{110}$$

where the flux-gradient relationship has been split into a linear and non-linear term. It is hard to make any general conclusions about this equation but we can take the limit of $\Lambda \gg U$ and $\Lambda \ll U$. We can write this equation as,

$$L_2[\langle u\theta\rangle] + \mathcal{N}_2[\langle u\theta\rangle] = U\frac{\sqrt{2}}{2}\partial_x\langle\theta\rangle. \tag{111}$$

In the limit $\Lambda \gg U$, we expect $\langle u\theta\rangle \sim 1/\Lambda$. Therefore, we note that the the second term is of $\mathcal{O}(1/\Lambda^2)$ whilst the first term is $\mathcal{O}(1/\Lambda)$ and the multiplier for L^{-1} in L_2 is $\mathcal{O}(U^2)$ both these terms can be neglected and we obtain the same result for $\mathcal{K}_{eff}$ as in the two-state case.

In the opposite case, $\Lambda \ll U$ we neglect the terms $\mathcal{O}(\Lambda)$,

$$\left(-1 + \mathcal{K}\partial_x^2 - U^2\partial_x[-2 + \mathcal{K}\partial_x^2]^{-1}\partial_x\right)\langle u\theta\rangle = U\partial_x\langle\theta\rangle \tag{112}$$

In the limit $\mathcal{K} \to 0$, we obtain our flux-gradient relationship in the small Λ limit, (77). Thus, we can conclude that as Λ decreases, the flux-gradient relationship starts to become non-local.

Noting that the non-linear term doesn't matter in both limits, the three state system can be written in a simplified form which catches K_{eff} in both limits,

$$\left(\Lambda\left(1 - 2\frac{\langle\theta\rangle}{c_0}\right) - 1 + \mathcal{K}\partial_x^2 - U^2\partial_x[-2 + \mathcal{K}\partial_x^2]^{-1}\partial_x\right)\langle u\theta\rangle = U\partial_x\langle\theta\rangle. \tag{113}$$

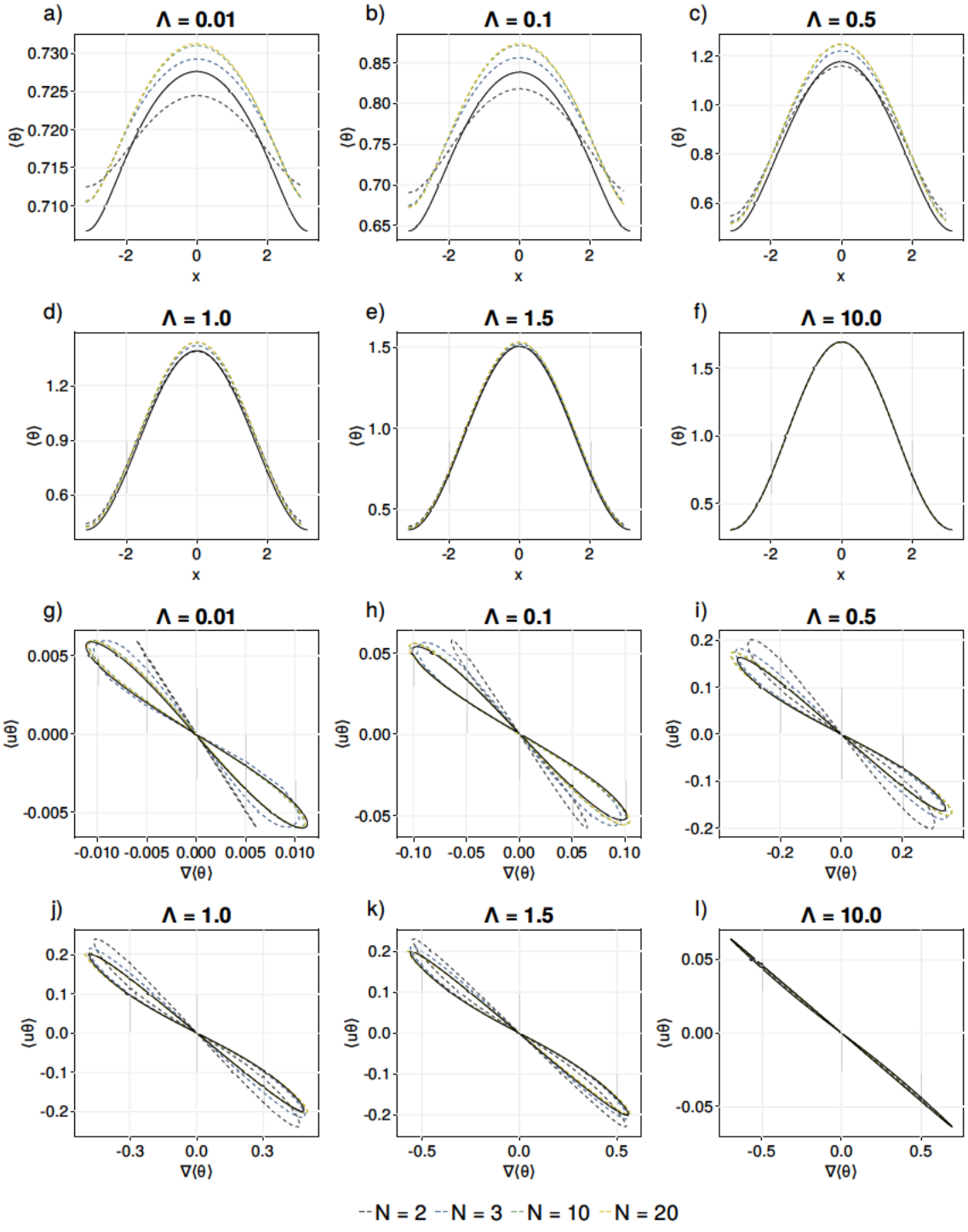

Figure 10: Comparison for the ensemble averaged (black lines) and estimated relationships (dashed coloured lines) for the mean concentration $a) - f)$ and for the flux-gradient relationship $g) - l)$ calculated using (84). Here, $\Delta = 0.7, U = 1.0$.

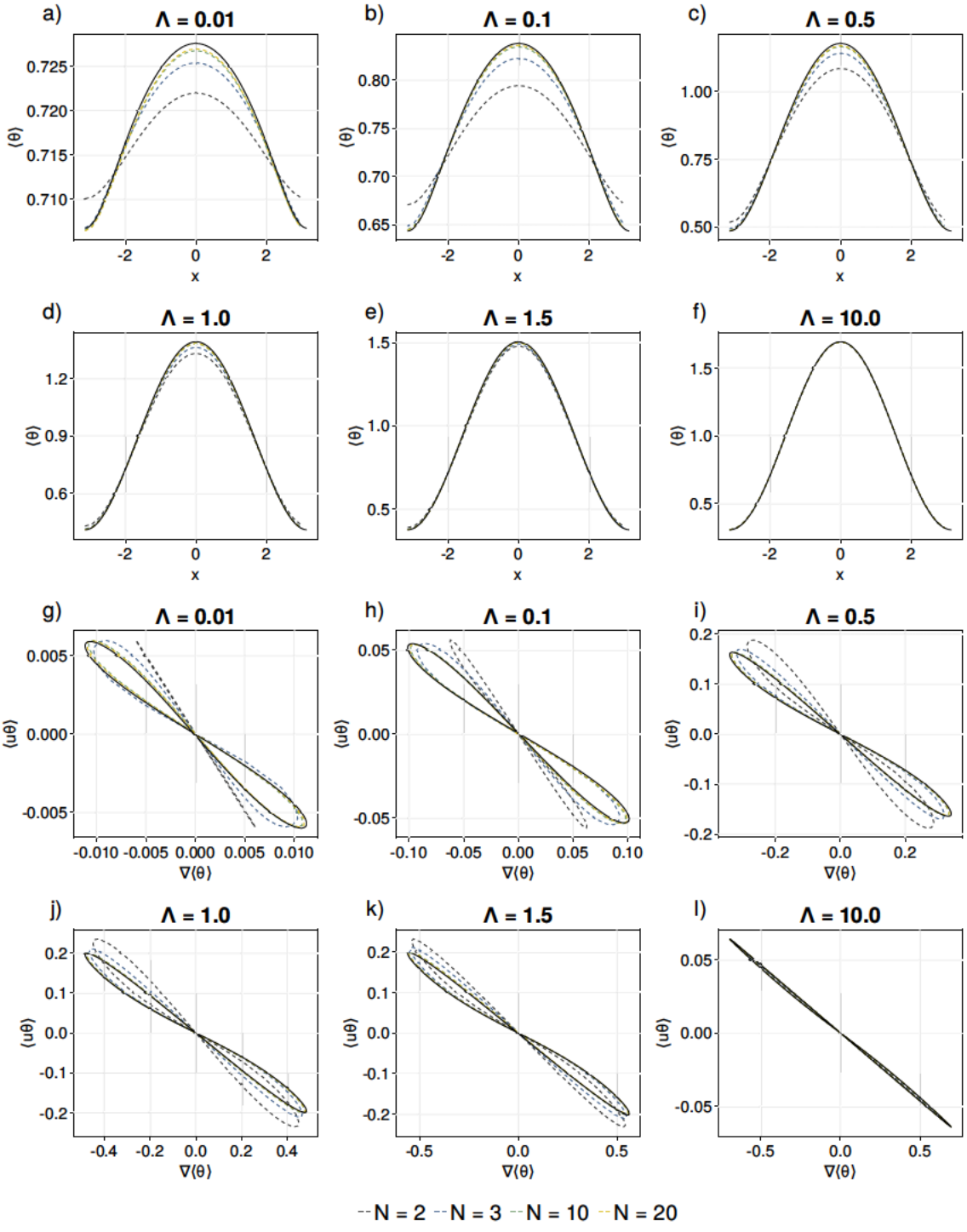

Figure 11: Comparison for the ensemble-averaged (black lines) and estimated relationships (dashed coloured lines) for the mean concentration $a) - f)$ and for the flux-gradient relationship $g) - l)$ calculated using (95). Here, $\Delta = 0.7, U = 1.0$.

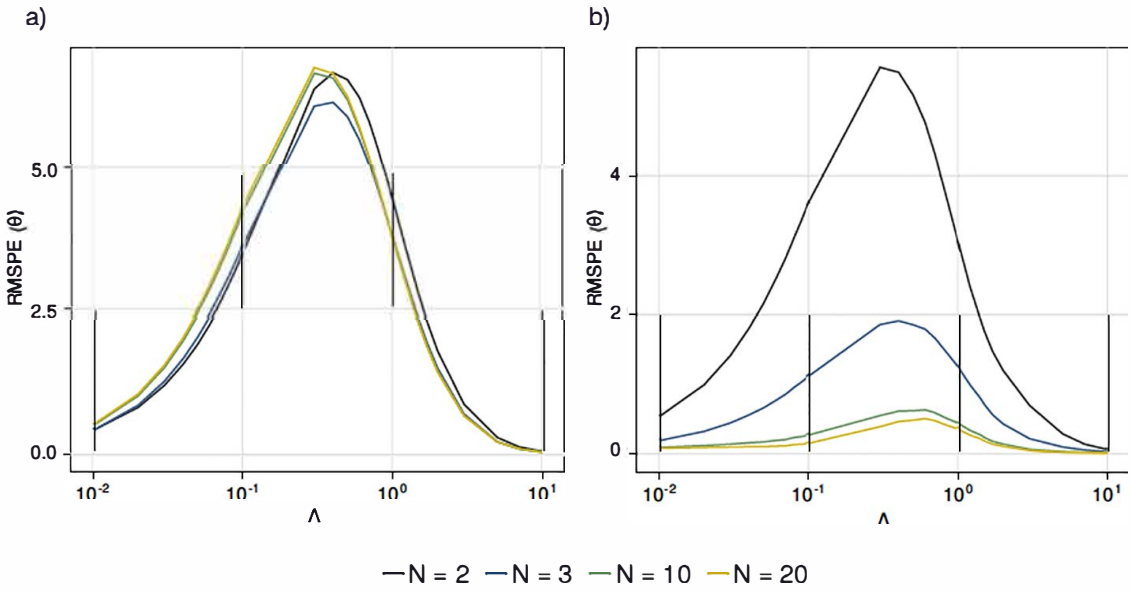

Figure 12: Root-mean-square-percentage-error for the estimated means using *a*) (84) and *b*) (95). N corresponds to the number of different velocities allowed in the ensemble-averaged system. Here, $\Delta = 0.7, U = 1.0$.

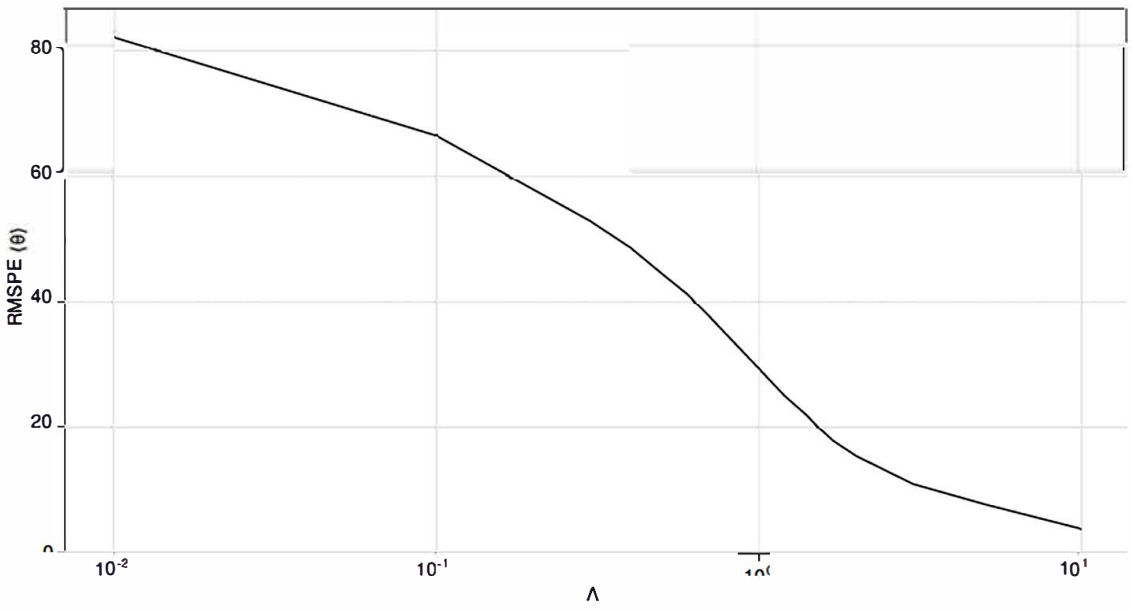

Figure 13: RMSPE for two-state approximation for the flux-gradient relationship, (100). Here, $\Delta = 0.7, U = 1.0$.

6.5 Two-state system (corrected)

Making analytical headway with the second approximation for the finite-state average is more challenging due to the Θ^3 terms in (95). As such the analytical solutions are not discussed in this report and left for later work.

7 Conclusion

This report focuses on furthering our understanding about how the flux of biological tracers is related to the tracer concentration. The tracers are advected by a turbulent velocity field and grow and decay under a logistic model of tracer growth. We model the turbulent velocity field using the Ornstein-Uhlenbeck process. We have demonstrated that using these methods to model the tracers results in a non-trivial relationship between the flux of biological tracers and the gradient of the mean tracer concentration. In particular, that the tracer flux cannot be assumed to be proportional to the variance of the stochastic velocity field multiplied by the gradient mean tracer concentration.

We show that, in the limit where biological processes act on much faster timescales than the turbulence, the mean tracer flux is proportional to the gradient of the tracer mean, $\langle U\theta\rangle = -U/(1+\Lambda)\nabla\bar{\theta}$. However, in the limit where the biological processes act on similar or slower timescales to the turbulence, asymptotic expansions can no longer be easily employed as a method to obtain tracer flux-gradient relationships and instead we demonstrate the power of finite-state averaging.

We first consider the case where turbulence acts on much faster timescales than the biological processes. In this case we demonstrate that when the velocity field is discretised into a large number of states, finite-state averaging works well to capture the flux-gradient relationship but overestimates the tracer mean. We have analytically solved for the flux-tracer relationship in the case when the velocity field is discretised into three states and obtain a non-local tracer flux-gradient relationship, $\langle U\theta\rangle = U^2(-\nabla\bar{\theta} + \nabla^2\langle U\theta\rangle)$.

For intermediate relative timescales, we examine two different finite-state averaging methods. In the first case we assume that the probability density functions for the velocity discretised tracer concentration are sharply peaked, in the second case we relate the tracer fluctuations to the inverse of the tracer concentration. Both methods do a very successful job of capturing the tracer flux-gradient relationship as well as the tracer means (the second method obtains the means correct to within $\sim 0.5\%$ and the first to within $\sim 5\%$). The second method is more challenging to obtain analytical tracer flux-gradient relationships which are easy to interpret, but from the first method we can obtain relationships for both the two state and three state system. Applying the relationship obtained using the three state system in the limit where biological processes act on much slower timescales than turbulence leads to a non-local gradient flux relationship. In the limit where biological processes act on much faster timescales than turbulence the mean concentration enters the equation for the effective diffusivity so $\mathcal{K}_{eff}$ becomes non-linear. In both these cases we recover the equations obtained by asymptotic expansions in the fast/slow timescale limits.

Combining the fast/slow limit relationships gives an overall flux gradient relationship (113) that agrees within an order of magnitude to that obtained by averaging the full stochastic model.

8 Acknowledgements

My first thanks goes to the 9 other fellows who made WHOI GFD 2023 such a fun and enriching experience, especially to my roommate Ellie for some amazing cooking and lots of great conversations. Secondly, I'm incredibly grateful for the work that Tiffany and Pascale put into organising the programme. Thirdly, to Geoff and Heather for their engaging lectures. Fourthly, to the rest of the staff for making me feel very welcome and especially Claudia and Karl for lending me their bikes. Finally, I would like to thank my supervisors Andre and Glenn (and Alexis who joined for a few of our meetings) for their patience and guidance as I tried to learn how to use Julia and attempted to understand how stochastic processes work. They have both taught me valuable lessons and skills that I will use for the rest of my PhD and into the future.

References

[1] E. Acevedo-Trejos, G. Brandt, J. Bruggeman, and A. Merico, *Mechanisms shaping size structure and functional diversity of phytoplankton communities in the ocean*, Scientific Reports, 5 (2015), p. 8918.

[2] B. Delmas, *Pierre-françois verhulst et la loi logistique de la population*, Mathématiques et sciences humaines, (2004).

[3] S. Irion, U. Christaki, H. Berthelot, S. L'Helguen, and L. Jardillier, *Small phytoplankton contribute greatly to co2-fixation after the diatom bloom in the southern ocean*, The ISME Journal, 15 (2021), pp. 2509–2522.

[4] K. M. Meyer, A. Ridgwell, and J. L. Payne, *The influence of the biological pump on ocean chemistry: implications for long-term trends in marine redox chemistry, the global carbon cycle, and marine animal ecosystems*, Geobiology, 14 (2016), pp. 207–219.

[5] A. N. Souza, T. Lutz, and G. R. Flierl, *Statistical non-locality of dynamically coherent structures*, Journal of Fluid Mechanics, 966 (2023), p. A44.